JAERI-M
90-051

EFFECTS OF HIGH TEMPERATURE ECC INJECTION ON SMALL AND LARGE BREAK BWR LOCA SIMULATION TESTS IN ROSA-III PROGRAM (RUNS 940 AND 941)

March 1990

Mitsuhiro SUZUKI, Hideo NAKAMURA, Hiroshige KUMAMARU
Yoshinari ANODA, Taisuke YONOMOTO, Hideo MURATA
and Kanji TASAKA

日 本 原 子 力 研 究 所
Japan Atomic Energy Research Institute

編集兼発行　日本原子力研究所
印　　刷　ニッセイエブロ株式会社

Effects of High Temperature ECC Injection on Small and Large Break BWR LOCA Simulation Tests in ROSA-III Program (RUNs 940 and 941)

Mitsuhiro SUZUKI, Hideo NAKAMURA, Hiroshige KUMAMARU
Yoshinari ANODA, Taisuke YONOMOTO, Hideo MURATA
and Kanji TASAKA

Department of Reactor Safety Research
Tokai Research Establishment
Japan Atomic Energy Research Institute
Tokai-mura, Naka-gun, Ibaraki-ken

(Received February 13, 1990)

The ROSA-III program, of which principal results are summarized in a report of JAERI 1307, conducted small and large-break loss-of-coolant experiments (RUNs 940 and 941) with high water temperature of the emergency core cooling system (ECCS) as one of the parametric study with respect to the ECCS effect on core cooling.

This report presents all the experiment results of these two tests and describes additional finding with respect to the hot ECC effects on core cooling phenomena. By comparing these two tests (water temperature of 393 K) with the standard ECC tests of RUNs 922 and 926 (water temperature of 313 K), it was found that the ECC subcooling variation had a small influence on the core cooling phenomena in 5% small break tests but had larger influence on them in 200% break tests. The ECC subcooling effects described in the previous report are reviewed and the temperature distribution in the pressure vessel is investigated for these four tests.

Keywords: ROSA-III, BWR, LOCA, ECCS, Simulation Test, Experiment Data, ECC Subcooling, Core Cooling, Small Break, Large Break

ROSA－Ⅲで実施されたBWRの大小破断LOCA模擬実験における高温ECC注入の影響（RUN　940，941）

日本原子力研究所東海研究所原子炉安全工学部
鈴木　光弘・中村　秀夫・熊丸　博滋・安濃田良成
与能本泰介・村田　秀男・田坂　完二

（1990年2月13日受理）

ROSA－Ⅲ計画では，炉心冷却に及ぼす非常用炉心冷却系（ECCS）の効果を調べるパラメーター実験の1種として，高温ECC水を準備したBWRの大・小破断LOCA模擬実験（RUNs 940，941）を実施した（ROSA－Ⅲ計画の主要な成果はJAERI 1307レポートに記されている）。

本報はこれら2実験の全実験結果を示すとともに，炉心冷却に及ぼす高温ECC注入の影響に関する上記レポート以外の指摘事項についても示す。これら2実験（ECC水温393K）と対応する2標準実験，RUNs 922，926（ECC水温313K）とを比較することにより次のことを明らかにした。5％小破断実験では炉心冷却に及ぼすECC水サブクール度の影響は小さいが，200％破断実験では大きな影響がみられた。ECC水サブクール度についての既報の結論を再評価し，圧力容器内の温度分布について詳細な検討を行った。

東海研究所：〒319－11　茨城県那珂郡東海村白方字白根2－4

Contents

目　　次

ABBREVIATIONS

ADS	Automatic Depressurization System
AT	Air Tank
AV	Air Actuation Valve
(2)B	(2) inches pipe of Schedule 80
BN	Boron Nitride
BWR	Boiling Water Reactor
CA	Chromel-Alumel
CCFL	Counter Current Flow Limiting
CHV	Check Valve
CP	Conductivity Prove
CV	Control Valve
CWT	Cooling Water Tank
D	Differential Pressure
d	Diameter
DF	Density of Fluid
DL(+100)	Elevation (+100 mm) from the bottom of PV
ECCS	Emergency Core Cooling System
ESF	Engineered Safety Features
EX	Heat Exchanger
F	Flow Rate
Fig.	Figure
FS	Full Scale
FW	Feedwater
FWLF	Feedwater Line Flashing
FWP	Feedwater Pump
FWT	Feedwater Tank
HPCS	High Pressure Core Spray
HPCSP	High Pressure Core Spray Pump
HPCST	High Pressure Core Spary Tank

HPWP	High Pressure Water Pump
ID	Inner diameter
INC 600	Inconel 600
JP	Jet Pump
K	Kelvin
kg	Kilogram
kPa	Kilopascal
kW	Kilowatt
L	Liter
LB	Liquid Level in Channel Box
LBWR	Large Boiling Water Reactor
LL	Liquid Level
LOCA	Loss-of-Coolant Accident
LOCE	Loss-of-Coolant Experiment
LP	Lower Plenum
LPCI	Low Pressure Coolant Injection
LPCIP	Low Pressure Coolant Injection Pump
LPCIT	Low Pressure Coolant Injection Tank
LPCS	Low Pressure Core Spray
LPCSP	Low Pressure Core Spary Pump
LPCST	Low Pressure Core Spary Tank
LPF	Lower Plenum Flashing
LTP	Lower Tie Plate
M	Momentum Flux
m	Meter
mm	Milimeter
MLHR	Maximum Linear Heat Rate
MPa	Megapascal
MRP	Main Recirculation Pump
MSIV	Main Steam Isolation Valve
MSL	Main Steam Line

MW	Megawatt
N	Rotation Speed
OR	Orifice
P	Pressure
	Power
PCT	Peak Cladding Temperature
PV	Pressure Vessel
PWT	Pure Water Tank
QOBV	Quick Opening Blowdown Valve
QSV	Quick Shut-off Valve
RCN	Rapid Condencer
ROSA	Rig of Safety Assessment
rpm	Revolution per Minute
S	Signal
s	Second
Sch	Schedule
SUS	Stainless Steel
T	Temperature
T/C	Thermocouple
TC	Temperature of Fluid
TF	Temperature of Fuel
TS	Temperature of Structure Material
UTP	Upper Tie Plate
V	Valve
VF	Void Fraction
W	Watt
WL	Water Level
WSP	Water Supply Pump

List of Tables for RUNs 940 and 941

List of Figures for RUNs 940 and 941

1. Introduction

The Rig-of-Safety Assessment (ROSA)-III program(1)(2) was initiated in 1976 to study the thermal-hydraulic behavior of a boiling water reactor (BWR)(3) during a postulated loss-of-coolant accident (LOCA) with the emergency core cooling system (ECCS) actuation, and to provide the data base to evaluate the predictability of computer codes developed for reactor safety analysis. To meet these objectives, various kinds of LOCA tests have been performed with test parameters of (1) break area, (2) break location, (3) break configuration, (4) core heat generation rate, (5) failure mode of ECCSs including the automatic depressurization system (ADS), (6) different initial fluid conditions and (7) different ECC temperatures. Also the tests were conducted for transients and natural circulation. Most of these test results have been studied and published.(4)-(57)

This report presents the experimental results of small and large break LOCA tests, RUNs 940 and 941, with an objective to clarify the effects of the parameter (7) of ECC temperature on core cooling phenomena. These two tests were conducted with assumptions of hot ECC temperature (393 K) and failure on the high pressure core spray (HPCS). The break location was at the recirculation pump suction line in one of the two recirculation loops and their break areas were 5 and 200% of the 1/424 scaled BWR recirculation line pipe flow area. These two tests are compared with the standard LOCA tests of RUNs 922 and 926 (ECC temperature of 313 K) to study the effects of ECC temperature. The effects of hot ECC injection on LOCA phenomena described in the previous study(57) are reviewed and temperature distribution in the pressure vessel is precisely studied for these four tests in this report.

The characteristic features of RUNs 940 and 941 are briefly described in Chapters 4 and 5. The effects of hot ECC is shown in Chapter 6. All of the measurements and calculated data of these two tests are listed in Appendix I. Most of the experimental results and data processing methods are shown in Appendix II. Distributions of the maximum heater rod surface temperature at each thermocouple in RUNs 940 and 941 are shown in Appendix III.

2. ROSA-III Test Facility

The ROSA-III test facility with an electrically heated core is a 1/424 volumetrically-scaled BWR system and is designed to study the thermal-hydraulic responses of the primary system the core during the postulated LOCA. Details of the test facility can be refered to the reference (2).

The test facility consists of four subsystems of (a) pressure vessel (PV), (b) steam line and the feedwater line, (c) recirculation loops and (d) ECCS. Figures 2.1, 2.2 and 2.3 illustrate configuration of the test facility, PV internals and the piping schematics, respectively. Table 2.1 compares the major dimensions of the ROSA-III test facility to the corresponding dimensions of the reference BWR (3800 MWt). The ROSA-III PV includes various components simulating the internal structures of the BWR vessel as shown in Fig.2.4. The interior of the vessel is divided into the core, core bypass, lower plenum, upper plenum, downcomer annulus, steam separator, steam dome and the steam dryer simulator.

The core consists of four simulated fuel assemblies of half length and a control rod simulator. Each fuel assembly contains 62 heater rods (Fig. 2.5) and 2 water rods spaced in a 8 x 8 square array and it is supported by spacers and upper and lower tie plates. The heater rod is heated electrically with chopped cosine power distribution along the effective heated length is 1880 mm (Fig.2.6). Two kinds of power systems are supplied to the core . The high power supply system with maximum power of 1.26 MWt was used for the fuel assembly "A" with a radial peaking factor of 1.4 and the average power supply system with the maximum power of 3.15 MWt was used for other three bundles "B", "C" and "D" with radial peaking factor of 1.0. The heater rods in each assembly are divided into three groups with respect to the local heat generation rates as shown in Fig.2.7. The local peaking factor of the heater rods in each bundle are 1.1, 1.0 and 0.875. The total electric power is controlled along the predetermined power curve (see Fig.3.1) and is limitted as 4.24 MW by limitation of the power supply system. The orifice plate with 44 mm I.D. in one assembly is inserted at each core inlet to control the core inlet flow.

The steam line is connected to the steam dome of the pressure vessel. A control valve (CV-130) is installed in the steam line to control the steam dome pressure in the steady state before the initiation of the tests, and in the transient state to simulate both the pressure control system

(PCS) and the safety/relief valve (SRV) operation. The main steam isolation valve (MSIV) is simulated by quickly closing the CV-130 valve. The steam line has a branch of the automatic depressurization system (ADS), of which flow area is simulated by the orifice of OR-4. The operation of valves in the steam line is described in Chapter 3. The feedwater is supplied from the feedwater tank (FWT) through the feedwater line (Fig.2.8) and feedwater sparger (Fig.2.9).

Figure 2.10 shows the recirculation lines consisted of two loops. Each line has a recirculation pump and two jet pumps. The jet pumps are installed outside the pressure vessel to simulate their relative volume and relative height to the core in addition to simulate their performances. Two break simulators and a quick shut-off valve (QSV) are installed in one of these loops to simulate the various break conditions. Each break simulator consists of nozzle or orifice to determine the break size and a quick opening blowdown valve (QOBV) to initiate the test. The break mode (double-ended or split), the break size and the break location can be changed as test parameters. The diameter of the largest nozzle and orifice is 26.2 mm for 100% break area in one break unit. Several flow nozzles and orifices of different size are prepared to vary the break size.

The ROSA-III test facility is furnished with all kinds of the ECCS's available in the BWR system, i.e., the high pressure core spray (HPCS), the low pressure core spray (LPCS), the low pressure coolant injection (LPCI), and the ADS. The HPCS and the LPCS spray the cooling water in the upper plenum. The LPCI injects the cooling water into the core bypass. Each ECCS except for the ADS consists of a pump, a tank, piping, and a control system.

The water level in the upper downcomer was measured by a differential pressure transducer and used for actuations of MSIV and ECCS's. The LPCS and LPCI in the BWR/6 system are simulated by the low low downcomer level signal (L1) accompanied with the pressure of 2.16 MPa and 1.57 MPa, respectively. The standard ADS and the MSIV were actuated as follows. The low downcomer level (L2) for the MSIV closure is 4.76 m above PV bottom.

LPCS Actuation = (L1 + 40 s) + (P less than 2.16 MPa)
LPCI Actuation = (L1 + 40 s) + (P less than 1.57 MPa)
ADS Actuation = L1 + 120 s
MSIV Closure = L2 + 3 s

3. Instrumentation

The instrumentation of the ROSA-III is designed to obtain thermal-hydraulic data during the simulated BWR LOCA. The data obtained from the experiments will contribute to assess the analytical computer codes for LOCA analyses and to investigate the transient fluid and fuel responses during the simulated LOCA. Table 3.1 summarizes instrumentation list for the No.4 simulated fuel assembly used in the present tests. The measurement list including the core instrumentation and calculated data list are shown in Appendix II (Table A.1 through A.3). Instrumentation locations are shown in Fig.3.1 through Fig.3.6. Typical measured parameters in the ROSA-III are pressure, differential pressure, flow rate, electric power, pump speed, fluid and metal temperatures, collapsed liquid level, two-phase mixture level, fluid density and trip signals.

Pressure and differential pressure transducers are two-wire, direct-current type which convert diaphragm displacement to electric capacitance. The pressure lead pipes are either the standard single, cylindrical pipes used in conjunction with condensate pots, or dual concentric cylinders capable of the circulation of cooling water to prevent flashing of the fluid.

The flow rate is measured by four types of instrumentations, i.e., turbine flow meter, orifice type flow meter, Venturi type flow meter and momentum flux measurement equipment depending on the fluid conditions and measuring locations. The turbine flow meter is used for subcooled water flow such as ECCS injection flow and feedwater flow. The orifice type flow meter is used for both flows i.e, one is steam line flow including ADS flow and another one is jet pump discharge flow in the broken loop. The Venturi flow meters are used for recirculation flows in both loops and jet pump discharge flow in the intact loop. The momentum flux measurement using drag-disk is used for the break flow (see Appendix II).

The temperatures of the fluid, structural material and heater rod cladding are measured with chromel-alumel thermocouples (CA T/C) of 1.6 or 1.0 mmφ. The thermocouples for heater rod cladding temperatures are imbedded at the surface of the cladding as shown in Fig.2.5. There are seven (maximum) thermocouples for one heater rod along the axial direction.

Liquid levels are measured by either differential pressure transducers, described above or needle type electrical conductivity probes (CP) developed in the ROSA-III program. The probes are distributed along the vessel height to detect existence of the water or vapor at different levels.

The electric power supplied to the simulated fuel rods is controlled to follow the predetermined power curve with function of time and measured by a fast response electric power meter.

Pump speed is measured by a pulse generator integral of the pump. Trip signals such as selected valve positions and pump coastdown initiation are detected in order to record the exact actuation times of trip signals.

Fluid density in the pipe is measured by means of gamma densitometers. Preliminary studies indicate that two-beam and three-beam densitometers should be used to determine the flow regime. Figures 3.7 and 3.8 show the beam directions of the three-beam and two-beam gamma densitometers. The gamma-ray source is ^{137}Cs and the detector is a water cooled NaI(Tl) scintillation counter.

Momentum flux is measured by a drag disk as shown in Fig.3.9. The combination of signals from a drag disk and a gamma densitometer is used to determine the two-phase flow rate as shown in Fig.3.10.

The data acquisition system (DATAC 2000B, Iwasaki Tsushinki Co.) scans all of signals with the frequency up to 30 Hz. The data recorded on magnetic tape are processed into 1000 points for data plotting by the FACOM M780 system computer at JAERI by off-line control. After evaluation, for example by comparing the initial and final pressure values with standard values, the data is reprocessed using the correct conversion factors as determined from the consistency examination.

More detailed information on the data processing procedure are shown in Appendix II and are available in reference (55).

4. Test Conditions and Procedure

The test conditions of RUNs 940 and 941 are the same except for the break areas as shown in Table 4.1. The valve characteristics and control sequences for the steam line valves are shown in Tables 4.2 and 4.3, respectively.

4.1 5% Break Test with Hot ECC Injection (RUN 940)

The break orifice of 5.9 mm I.D. was used at the break unit B for RUN 940. The measured initial test conditions were; steam dome pressure of 7.36 MPa, total core power of 3.97 MW, core inlet mass flow of 16.5 kg/s, core inlet subcooling of 10.2 K, main steam flow of 2.04 kg/s, feedwater flow of 2.04 kg/s, and corrected PV water level of 5.11 m. The initial average fluid quality in the upper plenum was estimated as 12.5%. The initial core power corresponds to 44% of the 1/424 scaled BWR/6 rated power. The initial core flow was lowered to establish the similar enthalpy distribution across the core as in the BWR rated condition.

RUN 940 was performed by the following procedures (refer Table 5.1). Break was initiated by quickly opening the QOBV in the break unit B. At the same time, the power supply to both recirculation pumps was terminated and the pump speed coasted down rapidly. After the break, the steady state core power was maintained for 9.0 seconds and then decreased along the power curve shown in Fig.4.1, which simulated the heat transfer rate to coolant during a hypothetical BWR/LOCA.(56) The steam flow to heat up the feedwater from the third steam line was manually stopped immerdiately after the break by closing the valves CV-1 and CV-2. The pressure control valve (CV-130) in the same line was fully opened immediately after the break to simulate the 1/424 scaled steam flow by using the orifice (OR-3). The feedwater supply was terminated during 2 and 4 s after the break.

The MSIV was tripped to close at 23 s after the break by L2 trip level with time delay of 4 s. ADS was actuated at 162 s after the break by L1 level trip with a time delay of 123 s. The LPCS was actuated at 330 s after the break (at 2.2 MPa of the system pressure) and LPCI was actuated at 443 s after the break (at 1.7 MPa of the system pressure).

4. Test Conditions and Procedure

The test conditions of RUNs 940 and 941 are the same except for the break areas as shown in Table 4.1. The valve characteristics and control sequences for the steam line valves are shown in Tables 4.2 and 4.3, respectively.

4.1 5% Break Test with Hot ECC Injection (RUN 940)

The break orifice of 5.9 mm I.D. was used at the break unit B for RUN 940. The measured initial test conditions were; steam dome pressure of 7.36 MPa, total core power of 3.97 MW, core inlet mass flow of 16.5 kg/s, core inlet subcooling of 10.2 K, main steam flow of 2.04 kg/s, feedwater flow of 2.04 kg/s, and corrected PV water level of 5.11 m. The initial average fluid quality in the upper plenum was estimated as 12.5%. The initial core power corresponds to 44% of the 1/424 scaled BWR/6 rated power. The initial core flow was lowered to establish the similar enthalpy distribution across the core as in the BWR rated condition.

RUN 940 was performed by the following procedures (refer Table 5.1). Break was initiated by quickly opening the QOBV in the break unit B. At the same time, the power supply to both recirculation pumps was terminated and the pump speed coasted down rapidly. After the break, the steady state core power was maintained for 9.0 seconds and then decreased along the power curve shown in Fig.4.1, which simulated the heat transfer rate to coolant during a hypothetical BWR/LOCA.(56) The steam flow to heat up the feedwater from the third steam line was manually stopped immerdiately after the break by closing the valves CV-1 and CV-2. The pressure control valve (CV-130) in the same line was fully opened immediately after the break to simulate the 1/424 scaled steam flow by using the orifice (OR-3). The feedwater supply was terminated during 2 and 4 s after the break.

The MSIV was tripped to close at 23 s after the break by L2 trip level with time delay of 4 s. ADS was actuated at 162 s after the break by L1 level trip with a time delay of 123 s. The LPCS was actuated at 330 s after the break (at 2.2 MPa of the system pressure) and LPCI was actuated at 443 s after the break (at 1.7 MPa of the system pressure).

The test was performed on September 11, 1981. The experiment data acquisition system started 120 s prior to the break initiation and terminated after completion of core reflooding (at 933 s after the break). Most of the instruments functioned successfully.

4.2 200% Break LOCA Test with Hot ECC Injection (RUN 941)

The break nozzles (Fig.4.2) of 26.2 mm I.D. were used at the break units of A and B. The measured initial test conditions were almost the same as in RUN 940, i.e., the steam dome pressure of 7.35 MPa, total core power of 3.96 MW, core inlet mass flow of 16.5 kg/s, core inlet subcooling of 10.2 K, main steam flow of 2.02 kg/s, feedwater flow of 2.04 kg/s, and corrected PV water level of 5.11 m. The initial average fluid quality in the upper plenum was estimated as 12.5% and the initial enthalpy distribution in the system in RUN 941 was the same as in RUN 940.

RUN 941 was performed as follows (ref. Table 5.2). The break was initiated by quickly opening two QOBVs in the break units A and B. At the same time, the quick shut valve (QSV) between the two break units was quickly closed and the recirculation pumps began to coast down was quickly closed and the recirculation pumps began to coast down rapidly. The same core power curve (Fig.4.1) was used. The steam line valves, CV-1 and CV-2 were closed quickly after the break. The MSIV was tripped at 5.4 s after the break. The LPCS was actuated at 70 s after break (at 2.3 MPa of the system pressure) and the LPCI was actuated at 95 s after the break (at 1.7 MPa of the system pressure).

The test was performed on July 8, 1981. The experimental data acquisition system was started 111 s prior to the break initiation and continued up to 854 s after the break. Most of the instrumentation functioned successfully.

5. Test Results of RUNs 940 and 941

5.1 Test Results of RUN 940

Characteristic phenomena of the 5% recirculation pump suction line break test (RUN 940) are described in this section with respect to (1) the pressure responses and related major events, (2) fluid the flow rates and densities, (3) the water levels and mass inventory in PV, and (4) the heater rod (simulated fuel rod) temperature responses related to the core mixture level. Typical experiment data of RUN 940 are shown in Figs.5.1 through 5.20 and a chronology of major events and test procedures are shown in Table 5.1 (Most of the experiment data of RUN 940 are presented in Appendix II).

(1) Pressure Responses and Major Events

Shown in Fig.5.1 is the steam dome pressure responses which is representative of all the primary system in RUN 940. Timings of the following events are also shown in the figure, i.e., closure of the main steam isolation valve (MSIV, 23 s), actuation of the automatic depressurization system (ADS, 162 s), and actuations of the LPCS (330 s) and LPCI (443 s). The core dryout occurred twice in the test period of RUN 940, i.e., a temporary dryout at the top of core between 137 s and 166 s (4 s after the ADS actuation) and an overall dryout due to level decrease between 213 s and 474 s (31 s after the LPCI actuation). The core dryout and quench phenomena are described later in detail.

The system pressure responses are related to these major events as shown below. The break was initiated by quickly opening the break valve (QOBV) in the break unit B at time zero and the primary fluid flowed into the break area from the two paths, i.e., one is from the downcomer through the main recirculation pump (MRP) suction line, and another one is from the lower plenum through the jet pumps and MRP discharge line. In spite of this water discharge through the break area and an additional increas of the steam discharge through the main steam line (MSL), the system pressure was kept at 7.3 MPa due to the continuing heat generation in the core until 9 s after the break. The system pressure began to decrease at this time due to the core power decay (see Fig. 5.2).

At the same time of break initiation, the two MRPs began to coast down resultig in the rapid core flow decrease (see next section). The feedwater supply was stopped between 1.7 and 3.1 s after the break.

The system pressure decreased to 6.7 MPa at 21 s after the break and was kept to the level by the pressure control system (PCS) for a short time. The MSIV closure, which was tripped by the L2 level signal with a time delay of 4 s, caused the rapid pressure increase until the relief valve (RV) began to operate at the system pressure of 8.18 MPa. Thereafter, the system pressure was maintained higher then 8 MPa until the ADS actuation. During this high-pressure period, the RV operation was terminated (at 126 s) according to the lowered steam generation in the core and thereafter, the system pressure began to decrease gradually (by L1 level signal with a time delay of 123 s).

The ADS opening at 162 s after the break caused rapid depressurization as shown in Fig. 5.1. Two-phase flow began to discharge through the break area immediately after the ADS actuation. As the ADS orifice (15.5 mm I.D.) flow area was 6.9 times of the break area, the steam flow rate through the ADS (see Fig. 5.4) had controlling effect on the depressurization rate after the ADS opening. The lower plenum flashing (LPF) began to initiate between 170 and 180 after the break and thereafter lowered the depressurization rate. The LPCS and LPCI were tripped to actuate by the L1 level signal with a time delay of 40 s and actuated at their designed pressures of 2.3 and 1.7 MPa, respectively. Their actuation timings were 168 s and 281 s after the ADS actuation timing, respectively.

(2) Fluid Flows and Fluid Densities

Shown in Figs. 5.3 and 5.4 are the total break flow rate and steam discharge flow rate, respectively. The break flow was almost constant for the initial 162 s and abruptly decreased after ADS actuation. The nagative break flow rate after the ADS actuation is incorrect and this reason may be ascribable to an error of the rapidly changed momentum flux data after flashing initiation in the break flow (see upstream-side fluid density in Fig. 5.11). The steam flow was slightly increased immediately after the break due to fully opened pressure control valve (CV-130) and decreased after the MSIV closure operation. A small steam flow was discharged during the RV opeation period (from 69 to 126 s). The ADS steam flow is shown after 162 s.

The injected flow rates for the feedwater and ECCSs are shown in Figs. 5.5 and 5.6, respectively. Although the feedwater flow was completely stopped at 3.1 s after the break, some amount of two-phase fluid flowed into the downcomer after initiation of the feedwater flashing (see some spikes between 357 and 454 s). The initial feedwater temperature was 489 K. The injection flows of the LPCS and LPCI systems (Fig. 5.6) were measured by the turbine flow meters. The LPCI flow rate was approximately 3 times of the LPCS flow rate. The total ECC flow rate is also shown in Fig. 5.6.

The core inlet flow rates are shown in Figs. 5.7 and 5.8. These mass flow data are valuable for a single-phase water flow condition (before the LPF initiation at 170 s and after the LPCI actuation at 443 s). The total core inlet flow rate rapidly decreased after the MRP coastdown initiation. As the forced circulation flow almost stopped within 10 s after the break, the positive flow after this shows a natural circulation flow through the core. The core inlet flow became almost zero for the RV operation period (from 69 to 126 s). After the LPCS initiation, a large coherent flow oscillation was observed among the four bundles and guide tube region. Similar flow oscillation was observed after the LPCS actuation. The net core inlet flow rate bacame negative after the LPCS actu- ation. It is shown that the channel A inlet flow rate was slightly higher than the others for all the test period and especially higher after the LPCI actuation.

Shown in Figs. 5.9 through 5.11 are fluid densities at the JP1, 2 outlet region, MRP side of the break and PV side of the break. These fluid densities showed almost constant before the ADS opening corresponding to each water condition. The break flow shown in Fig. 5.3 is mainly controlled by the PV-side discharge flow with the density shown in Fig. 5.11. The PV-side discharge flow became almost steam flow after the ADS actuation (the downcomer water level already reached the recirculation line nozzle elevation at 155 s after the break). The significant density recovery was observed after the LPF initiation. On the other hand, the JP1, 2 outlet fluid density showed that significant water mass remained in the jetpumps even after the LPF initiation. The break density increase was observed at 417 s (87 s after the LPCS actuation) at the PV side of the break.

(3) Water Level and Mass Inventory in PV

Collapsed water level was measured in the upper and lower downcomer regions as shown in Fig. 5.12. The upper downcomer level (between 3.9 and 6.0 m above the PV bottom) became zero at 46 s after the break and at the same time, the lower downcomer level (between 0.94 and 3.9m) began to decrease. The L2 level (4.76 m above PV bottom) tripped at 19 s and the L1 level (4.25 m above PV bottom) tripped at 39 s after the break. The lower downcomer level decreased below the jet pump suction line (2.8 m above PV bottom) at 114 s after the break and thereafter it decreased faster than the previouse time period. The downcomer mass recovery is shown at 444 s after the break.

Shown in Fig. 5.13 are the differential pressures (DPs) between the lower plenum and upper plenum (0.1 and 4.25m, PD21), and between the upper plenum and steam dome (4.25 and 6.04 m, PD22), respectively. A sum of these two DPs is equivallent to a collapsed level inside the core-shroud (see LM728 in Fig. 5.14). From these DP responses, it is shown that the mixture level inside the core shroud became lower than 4.25 m at 68 s after the break. It is also shown from the heater rod temperature resposes that the core top part (Pos. 1, 3.42 m abve PV bottom) became uncovered at 137 s. Thus, the mixture level passed through the upper plenum during 68 and 137 s. As the collapsed water level inside core-shroud (LM 728) was 3.28 m at 137 s after the break, it is shown that the mixuture level was close to the collapsed level inside the core-shroud before the ADS actuation timing.

A large upward steam (or high quality two-phase) flow passed through the steam separator toward the MSL after the ADS actuation and increased the PD22 value. As the fluid mass decreased. PD 21 and PD 22 became lower. The downcomer collapsed level (LM 727 in Fig. 5.14) is a sum of LM 68 and LM 69 shown in Fig. 5.12. These are used for estimation of the mass inventory in the downcomer and inside the core-shroud shown in Fig. 5.15.

Mass inventory in the downcomer region is correct in the blowdown phase, whereas that inside the core-shroud is incorrect through the test period because of void distributions through and above the core. However, these data can be used for rough estimation of the PV mass inventory. The PV mass inventory was approximately 300 kg at the temporary core dryout initiation time of 137 s (at the constant system pressure of 8 MPa) and was approximately 44% of the total initial mass inventory of 678 kg (ref. 1 excluding the feedwater line volume). In the depressurization process after the ADS actuation, the core top part showed the second dryout (213 s) at the PV mass inventory of approximately 230 kg (34% of the total initial mass inventory). And the PV mass inventory at the final core quench (474 s) was approximately 250 kg (37% of the total initial mass inventory). It is shown that both of the overall core dryout initiation and quench completion were observed at a mass inventory ratio (compared to the initial total mass) between 30 and 40% in the depressurization process after the ADS actuation, and that there may be no core dryout in a case of larger mass inventory ratio than 40%.

(4) Heater Rod Temperature Responses and Core Mixture Level

Shown in Fig. 5.16 through 5.18 are the surface temperatures of heater rods, A11, A22 and C22. A11 rod is a high power rod (local peaking factor of 1.1) and A22 rod is an average power rod (local peaking factor of 1.0). Both of these are in the high power bundle A (radial peaking factor of 1.4). C22 rod has local and radial peaking factors of 1.0 and 1.0, respectively. Shown in Fig. 5.19 are the water rod surface temperatures of A45 rod. Shown in Fig. 5.20 are the liquid level (mixture level) data measured by the conduction probes at seven elevations corresonding to the surface temperature measurements for A11, A22, C22 and A45 rods.

It is shown from these figures that (1) the dryout and quench timings of the heater rods for both temporary and overall core dryout periods are closely related to the mixture level trajectories given by the conduction probe data, (2) the LPCS water contributed to partial cooling of heater rods, especially in the upper core region, (3) the middle and lower core regions were quenched later than the upper core region, and (4) all the heater rods were quenched within 31 s after the LPCI actuation. The peak cladding temperature (PCT) was observed as 842 K at 415 s (85 s after the LPCS actuation) at A71 rod position 4 (the highest power region, see Table 5.2).

5.2 Test Results of RUN 941

Characteristic phenomena of the 200% recirculation pump suction line break test (RUN 941) are similarly described in this section as of RUN 940 in the previous section. Typical eperiment data of RUN 941 are shown in Figs. 5.21 thrugh 5.40 and a chronology of major events and test procedures is shown in Table 5.3 (Most of the experiment data of RUN 941 are presented in Appendix II).

(1) Pressure Responses and Major Events

Shown in Fig. 5.21 is the steam dome pressure, which is representative of all the system except for the broken recirculation loop in RUN 941. Timings of major events such as the MSIV closure (5.4 s), recirculation-pump suction line uncovery (RLU, 13.5 s), lower plenum flashing (LPF, 17 s), feedwater line flashing (68 s), LPCS actuation (70 s), LPCI actuation (95 s) and ADS opening (131 s), are shown in Fig. 5.21. Time periods for the temporary core dryout (from 3.2 to 30 s) and the overall core dryout (from 35 to 179 s) are also shown in Fig. 5.21.

The system pressure responses are related to these major events as shown below. The break was initiated by quickly opening two break valves (QOBVs) at time zero and quickly closing the quick shut valve (QSV) located between the two break units. Thereafter, the primary fluid flowed out through the two break areas (26.2 mm I.D. for one break). The MRP side discharge flow was limitted by the critical flow choking at the narrow flow area of the jet pump drive nozzles, of which total area was 21 % of the 100 % break area. As the PV side discharge flow was limitted at the 100 % break area, the effective choking flow area( ) for this 200 % guilltone break LOCA was reduced to 121 %. The broken loop pressure was, therefore, slightly lower in the PV side break flow path and significantly lower in another break flow passed through the jet pump drive nozzles.

After break initiation, the steam dome (system) pressure began to decrease until initiation of the MSIV closure, which changed the pressure to increase. The system pressure began to rapidly decrease after the recirculation line uncovery (RLU) at 13.5 s. After the LPF initiation at 17 s, the depressurization rate temporary decreased.

At the same time of break initiation, the two MRPs began to coastdown resulting in the rapid core flow decrease. The feedwater supply was stopped similarly as in RUN 940. The core power was controlled as shown in Fig. 5.22.

The system depressurization was temporarily stopped at 68 s due to initiation of feedwater line flashing (at the system pressure of 2.15 MPa) and the LPCS actuation was slightly delayed from this. The small amount of remained feedwater (30 kg) had a little affect on the depressurization rate at the significantly-degraded mass inventory condition for the primary system. (At 68 s, there was no water mass in the downcomer and almost all the core was uncovered. The roughly estimated mass inside core-shroud (ref. Fig. 5.35) was approximately 100 kg at this time and the estimated mass of LM 728 in the figure was significantly over estimated during the time period before the feedwater flashing initiation).

The system pressure decreased slightly after the LPCI actuation due to condensation in the core bypass region. After a while, the system pressure was kept almost constant under the continuing core power supply and mass recovery in PV.

(2) Fluid Flows and Fluid Densities

Shown in Figs. 5.23 and 5.24 are the total break flow rate and steam discharge flow rate, respectively. The total break flow rate was mainly controlled at the PV side discharge flow rate, which showed rapid decrease after the RLU (see fluid density of DE 704 in Fig. 5.31). The MSL steam flow was stopped by the MSIV closure until the ADS actuation at 131 s. As the ADS flow area was 29 % of the total effective choking flow area in RUN 941 and the system pressure already decreased to lower value (0.9 MPa) at 131 s, the ADS effect was very small on the pressure responses.

The injected flow rates for the feedwater and ECCSs are shown in Figs. 5.25 and 5.26, respectively. The violent flashing in the feedwater line was shown at 68 s in Fig. 5.25. However, the mass flow rate after the flashing is not correct because the flow rate was measured by a turbine flow meter for a single-phase water flow. The LPCS and LPCI injection flows were measured also by turbine flow meters. A total ECC injection flow rate is also shown in Fig. 5.26.

The core inlet flow rates are shown in Figs. 5.27 and 5.28. These data are valuable for the water flow condition before the LPF initiation and can be used for qualitative or relative fluid behaviors for two-phase flows after the LPF initiation. After the MRP coast down at time zero, the total core flow rate (Fig. 5.28) rapidly decreased and became almost zero after the MSIV closure. After the LPF initiation, a large upward flow was induced at the core inlets. Each channel inlet flow after 30 s (after the LPF effect being moderated) was, however, was very different as shown in Fig. 5.27, i.e., the highest core flow in channe A, a slightly lower core flow in channel C, nearly zero flow in channel D and a downward flow in channel B. This indicate different flow patterns among the four parallel channels under the condition of lower total core inlet flow rate. During this time period, the overall core dryout was initiated in each heater rod bundle.

The feedwater flashing, which caused steam-generation in the upper downcomer, contributed to suppress steam generation in the lower plenum region and consequently caused the CCFL break at all the channel inlets). This mass discharge from the core into the lower plenum resulted in additional dryout initiation at the lower core region. After a short time from the LPCS actuation at 70 s, upward core inlet flow was induced in all the channels. After the LPCI actuation at 95 s, contrary flow directions wre observed between the high-power channel A and other three channels as shown in Fig. 5.27. The total core inlet flow direction was downward after the LPCI actuation (Fig. 5.28).

Shown in Figs. 5.29, 5.30 and 5.31 are the fluid density data measured at the intact loop jet pump outlet, upstream of the MRP side break, and upsteam of the PV side break, respectively. It is shown in Fig. 5.29 that there was a significant fluid mass remaining in the intact loop jet pump outlet for all the test period. On the other hand, there was little water mass in the broken loop after the steam discharge at RLU initiation (see Figs. 5.30 and 5.31). The MRP side discharge flow was almost steam flow, whereas the PV side discharge flow showed density increase at 50 s after the LPCI actuation.

(3) Water Level and Mass Inventory in PV

Collapsed water level was measured in upper and lower downcomer as shown in Fig. 5.32. In the first 8 s after the break, the upper downcomer level became zero and the L2 and L1 trip signals were sent at 3.0 and 7.7 s, respectively. The lower downcomer level reached the recirculation line nozzle elevetion (0.94 m above the PV bottom) at 13.5 s after the break. Due to large downcomer flow toward the break units, these collapsed water levels include some frictional pressure loss and therefore shifted slightly from the correct level data (if there were no frictional pressure loss, the level changes should be consistent at the boundary of upper and lower downcomer level measurements as shown in the 5 % break test of RUN 940). The downcomer water mass was almost zero even 100 s after the LPCI actuation. Mass recovery in the lower downcomer was observed at 200 s after the break.

Differential pressures between the lower plenum and upper plenum (PD 21), and between the upper plenum and steam dome (PD 22) are shown in Fig. 5.33. A sum of these two differential pressures is consistent to the collapsed level the inside core-shroud (LM 728) in Fig. 5.34. The collapsed level in the downcomer (LM 727) is reduced from the water levels (LM 68 and LM 69) shown in Fig. 5.32. Thus, LM 727 also include frictional pressure loss effect. The pressure loss through the core region is found in the collapsed water level of LM 728. Namely, the collapsed level inside core shroud abruptly increased by 085 m after the LPF initiation (17 s) and abruptly decreased by 0.75 m after the feedwater flashing initiation (68 s) despite of small mass change during a short time. Therefore, the actual collapsed level inside core shroud may be lower than the LM 728 data by 0.7 - 0.9 m.

Shown in Fig. 5.35 are the estimated mass inventories in the downcomer and core-shroud regions. The mass inside the core-shroud (EV 730) is over-estimated during a time period between 17 and 68 s due to a reason shown above. Actual mass inside core shroud can be roughly corrected as a broken line in Fig. 5.35.

It can be shown that the mass inventory inside core shroud was approximately 190 kg at the timing of overall core dryout initiation (35 s) and it corresponded to approximately 28 % of the total initial mass inventory for the primary system. This mass inventory ratio is slightly lower than that in the 5 % break LOCA test of RUN 940 (approimately 34 %). And the mass inventory inside core shroud in RUN 941 was approximately 300 kg (44 % of the initial value) at the time of final core quench at 179 s. This mass inventory ratio at the final core quench in RUN 941 was slightly higher than in RUN 940 (37 % of the initial value). Thus, the differences between the mass inventories of two tests are within 10 % of the total initial mass inventory for initiation or completion of the overall core dryout.

(4) Heater Rod Temperature Responses and Core Mixture Level

Shown in Figs. 5.36, 5.37 and 5.38 are the surface temperatures of heater rods of A11, A22 and C22, respectively. Shown in Fig. 5.39 are the surface temperatures of the water rod A45. Shown in Fig. 5.40 are the liquid level (mixture level) data measured by the conduction probes at the same elevations as the heater rod surface temperatures shown above.

It is shown from these figures that (1) the dryout and quench timings of heater rods are closely related to the mixture level trajectory, (2) temporary core dryout was observed soon after the core flow coast down in the upper core region (positions 1 through 3) and completely diminished by swelled mixture level in the core at 13 s after the LPF initiation, (3) the whole core was uncovered just after the feedwater flashing initiation (during 35 s from the core top dryout initiation), (4) the core quench was partially conducted in the upper core by the LPCS injection and completely conducted by the LPCI injection (within 84 s from the LPCI injection time). The peak cladding temperature (PCT) was observed as 790 K at 116 s (21 s after the LPCI actuation) at A71 rod position 4 (the highest power region) as shown in Table 5.4.

6. Effects of Hot ECC Injection on LOCA Phenomena

Effects of hot ECC water injection on both small and large break LOCA phenomena were previously studied in the report(57) and are reviewed at first in this chapter. The experiment results of hot ECC tests of RUNs 940 and 941 are compared with those of the standard (cold ECC) tests of RUNs 922 and 926, in which RUN 922 is a 5% small break test and RUN 926 is a 200% break test. The test conditions of these four tests are the same except for the ECC water temperatures and break areas as shown in Tables 4.1 and 6.1. Secondly, subcooling temperature distribution in the pressure vessel are studied for these four tests in Section 6.2.

6.1 Review of Previous Study on Hot ECC Injection Tests

In the previous report, the hot ECC injection effects were studied especially on the condensation-depressurization phenomena and on the core cooling capability of the ECCSs deriving the following conclusions.

(A) The ECC temperature had no direct influence on the core cooling, since ECC became nearly saturated before reaching the core, because of vapor condensation on, and stored heat release to ECC. However, the ECC temperature affected indirectly the ECCS core cooling performance by changing the vessel pressure responses.

(B) A high ECC temperature resulted in delayed core level recovery in the upper core region, because it caused a slower depressurization, and thus resulted in smaller ECC flow rate, delayed LPCI initiation and earlier CCFL break down at the core inlet.

(C) The PCT occurred at the core mid-plane where the timing of rod surface quenching was essentially unaffected by the ECC temperature. The measured peak cladding temperature was not affected by the ECC temperature for both large and small break experiments.

Reviewing the conclusions (A) and (B), some different results are obtained with respect to the ECC subcooling effects on the pressure responses, core cooling behaviors and ECC injection flow rates as shown below.

(1) Effect of ECC Subcooling on Pressure Responses

Effect of high temperature ECC injection on the system pressure responses was observed approximately 60 s after the LPCS actuation in the 5% break tests (see Fig.6.1) and approximately 20 s after the LPCI actuation in the 200% break tests (see Fig.6.2), respectively. As these pressure deviations did not change the actuation timing of each effective ECCS (the LPCS for the 5% break tests, and three LPCIs for the 200% break tests under the assumption of HPCS single-failure) in these tests, there were very small influences on the peak cladding temperature (PCT) and its timing (see Table 6.2) by changing the ECC temperature as shown previously.

However, two different results from the previous conclusions can be derived for the 200% break LOCA tests. One is a difference of core cooling process, which was observed in the upper core region after initiation of the LPCS injection between the two tests of RUN 941 and 926. This difference was observed not only in the later reflooding phase (after their system pressures largely deviated) but also in the earlier refill/reflood phase (before their system pressures largely deviated) due to the different condensation effect on the CCFL break at the upper tie plate (UTP) between them. Thus, the ECC subcooling directly affected the core cooling behaviors in the 200 % break tests (see next section).

The second is the estimation of large stored-heat release on the ECC heat-up, which was pointed out as one of the reasons of "no direct influence of the ECC water subcooling on core cooling", in the previous study. Shown in Fig.6.3 is the previous result on depressurization rate components after LPCS actuation for 200% break tests. The calculated stored-heat release rates for two large-break tests (Fig.6.4) were 3 to 5 times as large as the total core power even in a test period between the LPCS and LPCI actuation timings. These stored-heat release rates are significantly larger than the actual value. In the ROSA-III facility, there are three kinds of metal heat sources, i.e., thick PV wall, thin internal structures and heater rods including the heater leading parts. The mixture level transients in the core, downcomer and lower plenum in RUN 926 are shown in Figs.6.5 and 6.6 and can be compared with those of RUN 941 in Figs.B.156 and B.157 in Appendix.II. The amount of metal fluid contact area for each metal component is directly related to the mixture levels shown in these figures.

It should be noted that the ECC mainly contacted thin structual materials, such as the core-shroud (4 or 6 mm t; thickness), channel boxes (3 mm t), stand pipe and steam separator (6 and 3 mm t). A possible stored-heat released from these thin materials, which form boundaries of upper plenum, core bypass and steam separator, is roughly estimated from their heat capacity between the LPCS and LPCI actuation timings by assuming the surface temperatures as the saturated temperature, as,

$$Q = \rho C \Sigma V_i \times \Delta T$$
$$= 5.4 \times 10^3 \quad (\mathrm{kJ}),$$

where ρC is the material specific heat per unit volume (4.2×10^3 kJ/m^{3}K for the stainless steel at 473 K), V_i is each metal volume (m^3, see Table 6.3), and ΔT is saturated temperature change (K), respectively. For the time period between the LPCS and LPCI actuation timings (25 s), ΔT is 15 K. Thus, an averaged heat release rate from these thin materials is obtained as,

$$dQ/dt = 0.216 \quad \mathrm{MW}.$$

On the other hand, the stored-heat release from the thick PV wall was analytically estimated(58) by the RELAP5 code for the main steam line (MSL) break test (RUN 952), which showed the similar pressure response as that of RUN 926. The PV wall heat release in this analysis increased as the system pressure decreased and became equal to the core heat release rate of 0.6 MW at 75 s after the break (at the system pressure of approximately 2 MPa). The PV wall heat release in RUN 926 is much smaller than this value (except for the feedwater flashing effect shown later) because the downcomer water level already decreased to bottom, whereas the PV wall was covered by swelled mixture level in RUN 952.

The stored-heat release rate from the core during a period before the LPCI actuation was not large because most of the heater rods were uncovered in the middle height core region with higher heat generation rate.

It is evident that the wall heat release from the PV wall, thin materials and heater rods was significantly small at the timing of LPCS actuation because these metals were uncovered by mixture levels at this timing except for the feedwater flashing effect shown later. By accounting these facts, it can be concluded that the wall heat release rates in the previous report were over-estimated.

In the previous study, the wall heat release term $(dP/dt)_{wall}$ was obtained as a residual of the actual depressurization rate of dP/dt and other three terms of $(dP/dt)_{core}$, $(dP/dt)_{ECCS}$ and $(dP/dt)_{break}$. Therefore, the term of $(dP/dt)_{wall}$ in the previous study includes not only the wall heat effect but also the effects of feedwater flashing and other factor which produces discrepancy between the previous calculation and the actual system conditions.

There are two possible reasons for this large stored-heat effect as shown below. One is a feedwater flashing effect on the system pressure responses, which was not accounted both in the 100% MSL break analysis and the previous study. The feedwater flashing, which was initiated 2 s prior to the LPCS actuation in the 200% break test, largely changed the depressurization rate as shown in Section 5.2 because it added steam not only by the evaporation of the feedwater but also by receiving stored heat energy from the uncovered hot PV wall. However, both of the mass increase and the steam generation due to the feedwater flashing were not separately accounted in the depressurization analysis. Thus, the feedwater flashing should be correctly accounted for this analysis.

The second reason on the large stored-heat effect is an over-estimation of average enthalpy in the previous study due to the assumption of saturated fluid condition. In fact, large subcooling temperatures were observed in the core bypass region after the LPCI actuation in RUNs 941 and 926 as shown in Figs.6.7 and 6.8, respectively (see Section 6.2). When the saturated fluid condition is assumed for the subcooling fluid, the average fluid enthalpy should be calculated higher than the actual value in the condition of the same mass inventories and the same pressure responses between the two cases. Thus, the higher average enthalpy resulted in an increase of the residual component of $(dP/dt)_{wall}$ in the previous study.

Concludingly, the stored-heat release to the injected ECC water is not so prominent as the previous conclusion. The feedwater flashing effect should be correctly accounted in the depressurization analysis. And the discrepancy from the assumed saturated condition should be corrected for the analysis.

(2) Different Core Cooling Behaviors Affected by ECC Subcooling

As shown previously, it was concluded that there was no direct influence of ECC subcooling on the core cooling phenomena in both small and large-break LOCA tests except for an indirect influence after initiation of the pressure response deviation between the two tests with different ECC subcoolings. This is correct for the 5% break tests (RUNs 940 and 922). Moreover, a perfect repeatability was confirmed not only on the dryout and quench timings of the heater rods, but also on most of the heater rod surface temperatures during a time period between the timings of LPCS and LPCI actuations for these tests. However, obviously different core cooling behaviors were observed between the two 200% break tests (RUNs 941 and 926) even in a time period of the same pressure responses between them.

The heater rod surface temperatures of A22, B22, C22 and D22 rods in RUN 941 are compared with those in RUN 926 as shown in Figs.6.9 through 6.12. The following can be derived through these comparisons.

(a) In a time period prior to the LPCI actuation (between 70 and 95 s in RUN 941, and between 71 and 96 s in RUN 926), the hot ECC injection resulted in improved core cooling in the upper half core region of three channels (D, C and A) and slightly deteriorated cooling in the channel B comparing with those in the cold ECC test. This may be ascribable to a result of different CCFL break at the upper tie plate (UTP) caused by the hot ECC. These heater rod temperature behaviors indicate larger amount of ECC flowed into the core in the hot ECC test than in the cold ECC test.

(b) The CCFL break at the UTP was also influenced by the feedwater flashing initiated 2 s prior to the LPCS actuation. This effect to increase the ECC downflow due to decreasing the upward core flow is common for the two tests of cold and hot ECC injection.

(c) In a time period after the LPCI actuation, improved core cooling was observed in all the channel D and both upper and lower regions of the channel A (the middle core region was remained unimporoved) in the hot ECC test. As the PCT was observed at the middle core region (position 4) of channel A in both tests, there was no important difference between their PCTs. On the other hand, the core cooling in channel C was partly improved and partly deteriorated by the hot ECC injection and almost deteriorated in channel B in RUN 941 (heater rods in channel B in RUN 926 were cooled best among the four channels). Thus, the hot LPCI injection resulted in core cooling improvement in channels A and D, in which the heater rods were not well cooled in RUN 926, and core cooling deterioration in channels B and C, in which the heater rods were cooled well relatively in RUN 926.

(d) Consequently, larger difference of the heater rod temperature responses observed among the four channels in RUN 926 was changed into a smaller difference among them (i.e., moderated or averaged responses) by the hot ECC injection in the 200% break test.

Shown in Figs.6.13 and 6.14 are the liquid level signals measured at the inner surface of channel boxes A and C in RUN 926 (ref. Figs.6.5 and 6.6). These liquid signals are similar between the two channels in RUN 926. However, the heatewr rod temperatures in these channels were not similar as shown above due to the different heat generation rates between them. By comparing these data with those in RUN 941 (Figs.6.15 and 6.16), the following are derived. Namely, slightly much signals of liquid were observed at the upper core region of channel A in RUN 941, whereas much less liquid signals were observed at the upper core region of channel C in RUN 941 comparing with those in RUN 926. These are consistent to the improved core cooling at the upper region of channel A and the deteriorated cooling at the upper region of channel C in RUN 941. And these liquid level signals in two test indicate different fluid distribution in the channel boxes due to the difference of ECC subcoolings between them.

(3) ECC Injection Flow Rate and Mass Inventory in Two 200% Break Tests

Shown in Figs.6.17 and 6.18 are the total ECC injection (volumetric) flow rates of 5 and 200% break tests, respectively. By assuming average system pressures during the core reflooding phase as 2 MPa for the 5% break tests and 1 MPa for the 200% break tests, the ECC density for each test is obtained as,

ρ = 943.8 kg/m^3 for RUN 940,
ρ = 993.1 kg/m^3 for RUN 922,
ρ = 943.2 kg/m^3 for RUN 941,
ρ = 992.7 kg/m^3 for RUN 926.

Shown in Figs.6.19 and 6.20 are the injected ECC mass for 5 and 200% break tests, respectively. It is clear from these figures that the injected ECC mass was slightly smaller in the cold ECC tests than in the hot ECC tests despite of the lower system pressures in the formers. The reason of smaller ECC mass flow rate in the cold ECC test may be ascribable to the ECCS pumps performances, i.e., the larger water density and larger viscosity of the cold water resulted in smaller pumping mass flow rate under the same pump powers comparing with the hot ECC injection. Thus, the previous conclusion of "smaller ECC injection flow rate caused by the slower depressurization in the hot ECC test" is not correct in these tests. On the contrary, the hot ECC water resulted in slightly larger injection flow rate than the cold ECC.

Shown in Fig.6.21 are the collapsed water levels in the downcomer and inside the core-shroud in RUN 926 (ref. Fig.5.34 for RUN 941). It is shown that the collapsed water level inside the core-shroud in RUN 941 was slightly lower than in RUN 926 in the reflooding phase (especially from 120 s after the break). The estimated mass inventories in the downcomer and inside the core-shroud in RUN 941 (Fig.5.35) are also slightly smaller than those in RUN 926 shown in Fig.6.22. This is a result of more larger discharging mass flow in RUN 941 than in RUN 926 despite of the condition of slightly larger ECC injection mass flow in RUN 941 than in RUN 926. The larger discharging mass flow rate is caused by the higher system pressure in RUN 941 than RUN 926 (see Fig.6.2). Therefore, it is shown that the relatively improved core cooling was accomplished in RUN 941 rather than in RUN 926 under the condition of slightly smaller mass inventory for the former.

6.2 Temperature Distribution in PV

Subcooling temperature distribution in PV after the LPCS actuation is experimentally studied for the four tests (RUNs 940, 922, 941 and 926) in this section. The cold ECC (313 K) had a subcooling of 176 K at the LPCS actuation pressure of 2.16 MPa and a subcooling of 161 K at the LPCI actuation pressure of 1.57 MPa, respectively. On the other hand, the hot ECC (393 K) had a subcooling of 96 K at the LPCS actuation and had a subcooling of 81 K at the LPCI actuation, respectively. Non-homogeneous temperature conditions in PV and measured maximum subcooling are shown below.

(1) Temperature Distribution in 5% Small Break Tests

After description of experiment results of RUNs 940 and 922, summary of findings is described.

Shown in Figs.6.23 and 6.24 are the fluid temperatures along two ECC discharging paths in RUN 940, i.e., one is from the upper plenum to the downcomer and another one is from the upper plenum and core bypass to jet pumps (JPs) through the lower plenum. It is found that the temperatures in the lower downcomer (TE 142), lower plenum inlet from the JPs (TE 138), and broken loop JP outlet (TE 149) were nearly equal to a saturated temperature for all test period. On the other hand, super-heat temperatures were found in the top of upper plenum (TE 139) and steam dome (TE 140) even after the LPCI actuation at 443 s after the break. Slight subcoolings (18 K in maximum) were found in the lower plenum (in the heater rod lead bundles; TE 545, 549, 550) after the completion of final core quench at 474 s after the break.

Shown in Figs.6.25 and 6.26 are the outer surface temperatures measured at the channel boxes A and C in RUN 940, respectively. These surface temperatures showed super-heat corresponding to the core heat-up shown in Section 5.1 and became saturated value after the LPCS actuation. Large subcooling were shown in these figures after the LPCI actuation. The measured lowest temperature (the largest subcooling) was close to the ECC at the top of channel box C and the highest temperature was detected at the lowest region of channel boxes A and C. It is shown that the subcooling was slightly larger on the channel box C than on the channel box A. At the final core quench time, the largest subcooling was 71 K and the smallest one was 6 K in RUN 940.

Shown in Figs.6.27 and 6.28 are fluid temperatures at the top surface of the upper tie plate (UTP) in channels A and C, respectively. Reason of larger super heat in channel A before the LPCS actuation and smaller subcooling after the LPCI actuation can be ascribable to larger upward flow in the high-power bundle A comparing with those in the average-power bundle C. The subcooling was detected in these region after completion of the final core quench.

Shown in Figs.6.29 and 6.30 are the temperature distribution on both inner and outer surfaces at the channel boxes A and C, respectively. The higher temperatures on the outer surface were observed than on the inner surface before the LPCS actuation because of different water distribution in each channel. Namely, the outer surface temperatures were measured at the middle of channel box wall width, whereas the inner surface temperatures were measured at the corner for both channels A and C. These results indicate that there was relatively larger water mass in the channel box corner than on the flat channel box wall before the LPCS actuation. After actuation of LPCI, larger subcooling was observed on the outer surface than on the inner surface.

Shown in Figs.6.31 through 6.38 are the similar temperature responses of RUN 922 as in RUN 940.

The saturated temperature in RUN 922 was found at the lower downcomer (TE 142 in Fig.6.31) and broken loop JP outlet (TE 149 in Fig.6.32). The super-heat temperature was found for all test period at the top of steam dome (TE 140) and for 400 s at the top of upper plenum (TE 139). These are similar to the results of RUN 940. However, larger subcooling was observed at the upper plenum top in the last 150 s of test in RUN 922. Slight subcoolings were observed in the upper downcomer (TE 141) and lower plenum (TE 138, 545, 549 550). These results are different from those in RUN 940.

Shown in Figs.6.33 and 6.34 are the outer surface temperatures measured at the channel boxes A and C in RUN 922, respectively. The super-heat temperatures before the LPCS actuation and the subcooling after the LPCI actuation are similar in both tests of RUNs 922 and 940. However, the subcooling detection at the outer surfaces was slightly earlier and the subcooling was larger in RUN 922 than in RUN 940. The largest and the smallest subcoolings at the final core quench time were the same in both tests. Thereafter the subcooling in RUN 922 became larger time to time than in RUN 940.

Shown in Figs.6.35 and 6.36 are fluid temperatures at the top surface of the upper tie plate (UTP) in channels A and C, respectively. Similar rends for the super-heat temperatures before the LPCS actuation and the subcooling after the LPCI actuation were found in RUN 922 as in RUN 940. The subcoolings in RUN 922 were, however, obviously large in RUN 922 due to the cold ECC temperature than in RUN 940.

Shown in Figs.6.37 and 6.38 are the temperature distribution on both inner and outer surfaces at the channel boxes A and C. Similar trends are found for these temperatures as those in RUN 940 except for the larger subcooling in RUN 922.

Following conclusions can be derived through these data comparisons between the two 5% break tests.

(a) Fluid and metal temperatures in PV were quite similar during a time period before the completion of final core quench in these two tests. Therefore, the ECC subcooling effect on these temperature responses was very small during the core reflooding phase of this 5% small break test.

(b) The evident subcooling was detected in the core bypass region and on the UTP in both tests. The subcooling and super-heat temperature distributions in PV are shown in Figs.6.39 and 6.40 for RUN 940 and RUN 922, respectively. The lower downcomer andJP outlet region were kept in a saturated condition and the steam dome top was kept in a super-heated condition for all test period in both tests. Thus, there are larger temperature disribution on the PV wall and PV internals after the core quench time than those in the earlier time period.

(c) The lowest surface temperature at the top of the channel box C was close to the ECC tempertature in the hot ECC test and it was kept almost constant (the subcooling was larger than 60 K) after 470 s. On the other hand, the largest subcooling in the cold ECC test was more than 90 K after 480 s. The cold ECC was significantly heated up before it reached top of the channel box.

(2) Temperature Distribution in 200% Break Tests

After description of experiment results of RUNs 941 and 926, summary of findings is described.

Shown in Figs.6.41 and 6.42 are the fluid temperatures along two ECC discharging paths in RUN 941. It is found that the lower downcomer temperature (TE 142) was kept saturated for all test period except for a short time between 105 and 125 s. The temperatures at the lower plenum (TE 138) and broken loop JP outlet (TE 149) were the same as this. Large super-heat temperatures were found in the steam dome (TE 140) for most of test period, and partly in the upper plenum top (TE 139) and upper downcomer (TE 141). Slight subcoolings were observed in the lower plenum (TE 545, 549, 550) after the completion of final core quench at 179 s after the break.

Shown in Figs.6.43 and 6.44 are the outer surface temperatures measured at the channel boxes A and C in RUN 941, respectively. It is found that larger subcooling was observed at the top of channel box C than the channel box A. The largest subcooling measured in the core bypass region during the core reflooding phase of RUN 941 was 43 K at 150 s after the break (the lowest temperature was 7 K higher than the ECC temperature). It is clear that all the core bypass region was kept in a subcooling condition for all test period after the LPCI actuation.

Shown in Figs.6.45 and 6.46 are fluid temperatures at the top surface of the upper tie plate (UTP) in channels A and C, respectively. The fluid temperature was kept in almost saturated condition until 170 s after the break. The measured subcooling above the UTP of channel box C was larger than that of channel A after 170 s.

Shown in Figs.6.47 and 6.48 are the temperature distribution on both inner and outer surfaces at the channel boxes A and C. The inner surface temperatures were higher than the outer surface temperatures at both channels. The temperature differences across the channel box wall was larger in the upper region than in the lower region. The measured maximum temperature difference was approximately 40 K at the top of channel box C.

Shown in Figs.6.49 through 6.56 are the similar temperature responses of RUN 926 as in RUN 941.

The saturated temperature in RUN 926 was found at the lower downcomer

(TE 142 in Fig.6.49) and broken loop JP outlet (TE 149 in Fig.6.50). Observed super-heat temperature in the steam dome (TE 140) was higher than the saturated temperature by 58 K at 250 s in RUN 926. The upper plenum fluid (TE 139) showed saturated temperatures in two times (before 152 s and between 178 and 253 s) and subcooling in the later period. The subcoolings in the lower plenum (TE 545, 549, 550) were observed after the final core quench at 188 s after the break and were larger than those in RUN 941 due to the larger ECC subcooling in the former.

Shown in Figs.6.51 and 6.52 are the outer surface temperatures measured at the channel boxes A and C in RUN 926, respectively. Slightly super-heated temperatures were observed before the LPCS actuation. Large subcoolings were observed after the LPCI actuation at 96 s in both channels. The subcooling was larger on the channel box C than the channel box A as in RUN 941. However, these subcoolings were significantly larger in RUN 926 than in RUN 941. The largest subcooling during the core reflooding phase was found as 100 K at 137 s after the break at the channel box C. The smallest subcooling was similar at the bottom of both channel boxes.

Shown in Figs.6.53 and 6.54 are fluid temperatures at the top surface of the upper tie plate (UTP) in channels A and C, respectively. Super-heat temperatures before the LPCS actuation, which were observed in RUN 941, were not observed in RUN 926. The subcooling was observed at 133 s and it became large after 160 s. The subcoolings were similar at both channels A and C. These subcoolings above the UTPs became larger than those at the bottom of core bypass region after completion of final core quench at 188 s indicating the ECC water flow-down through both core bypass and core top region. At the channel box A, the subcooling above the UTP were rather larger than all of the channel box outer surface temperatures (Fig.6.51) after 210 s.

Shown in Figs.6.55 and 6.56 are the temperature distribution on both inner and outer surfaces of channel box A and C, respectively. Larger temperature difference was observed across the channel box C than across the channel box A. The measured maximum subcooling was 90 K at 137 s after the break. The inner surface temperatures were higher than the outer surface temperatures for most of test period after the LPCI actuation at both channels.

Following conclusions can be derived through these data comparisons between the two 200% break tests.

(a) Fluid temperatures in PV (except for the upper plenum, core bypass and core) were slightly changed by the ECC subcooling variation except for the different saturation temperatures after 120 s in the two 200% break tests.

(b) The metal temperatures of channel box outer surface were significantly changed by the ECC subcooling as shown in Figs.6.57 and 6.58. The largest subcooling of the channel box wall was 43 K in the hot ECC test of RUN 941 during the core reflooding phase, whereas it was 100 K in RUN 926. The smallest subcoolings were slightly changed between the two tests. The largest subcooling was kept almost constant through the test period in each test.

(c) The temperature distribution in PV was contracted in the hot ECC test than in the cold ECC test as shown in Figs.6.57 and 6.58. The super-heat temperature and the core bypass subcooling became small in RUN 941 compared with those in RUN 926. The maximum temperature difference between the steam dome and the core bypass regions in RUN 941 was approximately a half of RUN 926.

By comparing the results of 200% break tests with those of 5% break tests, the following results can be derived.

(d) Similar subcoolings (approximately 100K) were observed at the core bypass region in 5 and 200% break tests with the cold ECC injection despite of the significantly different pressure responses between them. Similar subcoolings were also observed in the lower plenum after the final core quench in these two tests.

(e) For the hot ECC injection tests, on the other hand, larger subcooling was observed at the core bypass and lower plenum regions in 5% break test than those in 200% break test because of the higher system pressure in the former. The lowest surface temperatures of channel box in these two tests were very close to the hot ECC temperature for a time period after the final core quench. These are different from the subcooling conditions in the cold ECC tests.

7. Conclusions

Effects of ECC subcooling on small and large break LOCA phenomena were experimentally studied by comparing the test results of RUNs 940 and 941 with hot ECC (393 K) with those of RUNs 922 and 926 with cold ECC (313 K). From the previous study(57) and present work, following conclusions were derived.

(1) The ECC subcooling variation had a small impact on the peak cladding temperature (PCT) and its timing in both 5 and 200% break tests. However, a larger influence of the ECC subcooling was found on the core cooling behaviors in the four bundles in the 200% break test. The hot ECC injection considerably improved the core cooling and averaged the quite different core cooling patterns among the four bundles, which was observed in the 200% break cold ECC test.

(2) The measured largest subcooling during the core reflooding phase was 71 K in the two 5% break tests, 43 K in 200% break hot ECC test and 100 K in 200% break cold ECC test. The maximum temperature difference between the super-heat temperature in the steam dome top and the lowest temperature, i.e., largest subcooling at the core bypass top was approximately 80 K in the hot ECC tests, whereas it was more than 120 K in the cold ECC tests. Thus, the hot ECC injection reduced the temperature distribution by more than 50% comparing with the cold ECC tests.

(3) The stored-heat release from the metal walls to the ECC water was over-estimated in the previous study. The feedwater flashing, which began prior to the LPCS actuation, significantly affected the system pressure responses in the 200% break tests. The ECC injection flow rates in the hot ECC tests were slightly higher than in the cold ECC tests.

Acknowledgment

The authors are grateful to Mr.H.ASAHI, T.ODAIRA, T.TAKAYASU, Y.KITANO and T.NUMATA of Nuclear Engineering Corporation for their assistance in conducting the experiments, to Mr.K.HIYAMA, E.UMEKI andd T.NAKAJIMA of Information System Laboratory Corporation for preparing the data plots, and to Ms.T.KUROSAWA and M.KIKUCHI of Nihon Computer Bureau for preparing the typings.

References

(1) K.TASAKA, et al., "Study on the Similarity between ROSA-III Experiment and BWR LOCA", JAERI-M 6703 (1976) (in Japanese).

(2) Y.ANODA, et al.,"ROSA-III System Description for Fuel Assembly No. 4", JAERI-M 9363 (1981) (in Japanese).

(3) General Electric Company, "General Electric Standard Safety Analysis Report, BWR/6", DOCKET-STN-50477 (1978).

(4) K.TASAKA, et al.,"ROSA-III Base Test Series for a Large Break Loss of Coolant Accident in a Boiling Water Reactor", Nucl. Technol. 57, 179-191 (1982).

(5) K.SODA, et al.,"Boiling Water Reactor Loss of Coolant Test (Single Failure Test with ROSA-III)", J. Nucl. Sci. Technol. 20, 537-558 (1983).

(6) K.TASAKA, et al.,"Simulation Experiment of Five Percent Small Break LOCA of BWR", J. Nucl. Sci. Technol. 20, 89-104 (1983).

(7) K.TASAKA, et al.,"ROSA-III Double-Ended Break Test Series for a Loss-of-Coolant Accident in a Boiling Water Reactor", Nucl. Technol. 68, 77-93 (1985).

(8) M.SUZUKI, et al.,"Recirculation Pump Discharge Line Break Tests at ROSA-III for a Boiling Water Reactor", Nucl. Technol. 70, 189-203 (1985).

(9) Y.KOIZUMI, et al., "Experiment Analysis of Power Curve Sensitivity Test Series at ROSA-III", Nucl. Eng. and Design 86, 267-287 (1985)

(10) H.KUMAMARU, et al.,"Five Percent Break BWR LOCA/ECC Test at

Acknowledgment

The authors are grateful to Mr.H.ASAHI, T.ODAIRA, T.TAKAYASU, Y.KITANO and T.NUMATA of Nuclear Engineering Corporation for their assistance in conducting the experiments, to Mr.K.HIYAMA, E.UMEKI andd T.NAKAJIMA of Information System Laboratory Corporation for preparing the data plots, and to Ms.T.KUROSAWA and M.KIKUCHI of Nihon Computer Bureau for preparing the typings.

References

(1) K.TASAKA, et al., "Study on the Similarity between ROSA-III Experiment and BWR LOCA", JAERI-M 6703 (1976) (in Japanese).

(2) Y.ANODA, et al.,"ROSA-III System Description for Fuel Assembly No. 4", JAERI-M 9363 (1981) (in Japanese).

(3) General Electric Company, "General Electric Standard Safety Analysis Report, BWR/6", DOCKET-STN-50477 (1978).

(4) K.TASAKA, et al.,"ROSA-III Base Test Series for a Large Break Loss of Coolant Accident in a Boiling Water Reactor", Nucl. Technol. 57, 179-191 (1982).

(5) K.SODA, et al.,"Boiling Water Reactor Loss of Coolant Test (Single Failure Test with ROSA-III)", J. Nucl. Sci. Technol. 20, 537-558 (1983).

(6) K.TASAKA, et al.,"Simulation Experiment of Five Percent Small Break LOCA of BWR", J. Nucl. Sci. Technol. 20, 89-104 (1983).

(7) K.TASAKA, et al.,"ROSA-III Double-Ended Break Test Series for a Loss-of-Coolant Accident in a Boiling Water Reactor", Nucl. Technol. 68, 77-93 (1985).

(8) M.SUZUKI, et al.,"Recirculation Pump Discharge Line Break Tests at ROSA-III for a Boiling Water Reactor", Nucl. Technol. 70, 189-203 (1985).

(9) Y.KOIZUMI, et al., "Experiment Analysis of Power Curve Sensitivity Test Series at ROSA-III", Nucl. Eng. and Design 86, 267-287 (1985)

(10) H.KUMAMARU, et al.,"Five Percent Break BWR LOCA/ECC Test at

ROSA-III without HPCS Actuation---Two Dimensional Core Thermal Hydraulic Phenomena", Nucl. Eng. and Design 86, 219-239 (1985).

(11) K.TASAKA, et al.,"Analysis of ROSA-III Break Area Spectrum Experiments on BWR Loss-of-Coolant Accident", Nucl. Technol. 71, 3, 628-643 (1985).

(12) T.YONOMOTO, et al.,"Investigation of BWR/LOCA at ROSA-III---Effect of Break Configuration on System Transient---", Nucl. Eng. and Design 92, 195-205 (1986).

(13) M.SUZUKI, et al.,"Similarity Study of Large Steam Line Break LOCAs in ROSA-III, FIST and BWR/6", Nucl. Eng. and Design 98,1, 39-56 (1986).

(14) Y.KOIZUMI et al.,"Investigation of Break Location Effects on Thermal-Hydraulics during Intermediate Break Loss-of-Coolant Accident Experiments at ROSA-III", J. Nucl. Sci. Technol., 23 11, 1008-1019 (1986).

(15) H.KUMAMARU et al.,"Investigation of Effect of Pressure Control System on BWR LOCA Phenomena Using ROSA-III Facility", J. Nucl. Sci. Technol., 24 10, 844-858 (1987).

(16) T.YONOMOTO et al.,"Core Heat Transfer Analysis during a BWR LOCA Simulation Experiment at ROSA-III", Nucl. Eng. and Design, 103 2, 239-250 (1987).

(17) Y.KOIZUMI et al.,"BWR Small Break LOCA Counterpart Test at ROSA-III and FIST Test Facilities", Nucl. Eng. and Design, 102, 151-163 (1987).

(18) H.KUMAMARU et al.,"BWR Large Break LOCA/ECC Counterpart Test at ROSA-III and FIST", Nucl. Eng. and Design, 102 2, 223-238 (1987).

(19) Y.KOIZUMI et al.,"Effect of Heat Generation Difference among Fuel Bundles on Core Thermal-Hydraulics during 200% and 5% Loss-of-Coolant Accident Experiments", J. Nucl. Sci. Technol., 24 1, 61-74 (1987).

(20) K.TASAKA et al.,"ROSA-III Experimental Program for BWR LOCA/ECCS Integral Tests", JAERI 1307 (1987).

(21) H.NAKAMURA et al.,"Effectiveness of Automatic Depressurization System on Core Cooling in Small Break Loss-of-Coolant Accident of Boiling Water Reactor", to be published in Nucl. Eng. and Design.

(22) M.SOBAJIMA et al.,"Experiment Test Data of ROSA-III Test RUN 701 (Decay Heat Simulation Test with ECCS Actuation)", JAERI-M 8604 (1979).

(23) Y.ANODA et al.,"Experiment Data of ROSA-III Test RUN 703 (Split

Break Simulation Test with ECCS Actuation)", JAERI-M 8967 (1980).
(24) Y.ANODA et al.,"Experiment Data of ROSA-III Test RUN 704 (Standard Test with ECCS Actuation)", JAERI-M 8968 (1980).
(25) M.OKAZAKI et al.,"Experimet Test Data of ROSA-III Integral Test RUN 705 (Isothermal Blowdown Test without ECCS Actuation)", JAERI-M 8723 (1980).
(26) M.SUZUKI et al.,"Experiment Data of ROSA-III Integral Test, RUN 706", JAERI-M 8737 (1980).
(27) M.OKAZAKI et al.,"Experiment Data of ROSA-III Integral Test RUN 708 (Standard Test without ECCS Actuation)", JAERI-M 8738 (1980).
(28) Y.KOIZUMI et al.,"Experiment Data of ROSA-III Integral Test, RUN 710", JAERI-M 9249 (1981).
(29) Y.ANODA et al.,"Experimet Data of ROSA-III Integral Test RUN912 (5% Split Break Test without HPCS Actuation)", JAERI-M 82-010 (1982).
(30) H.NAKAMURA et al.,"Experiment Data of ROSA-III Integral Test RUN 901 (200% Double-Ended Break with Full ECCS Actuation)", JAERI-M 84-007 (1984).
(31) H.NAKAMURA et al.,"Experiment Data of ROSA-III Integral Test RUN 926 (200% Double-Ended Break with HPCS Failure)", JAERI-M 84-008 (1984).
(32) M.SUZUKI et al.,"Experiment Data of 200% Recirculation Pump Discharge Line Break Integral Test RUN 961 with HPCS Failure at ROSA-III and Comparison with Results of Suction Line Break Tests", JAERI-M 84-045, (1984).
(33) M.SUZUKI, et al.,"Recirculation Pump Suction Line 2.8% Break Integral Test at ROSA-III with HPCS Failure, RUN 984", JAERI-M 84-100, (1984).
(34) M.SUZUKI, et al.,"Recirculation Pump Suction Line 200% Break Integral Test at ROSA-III with Two LPCI Failures, RUN 983", JAERI-M 84-135, (1984).
(35) M.KAWAJI, et al.,"A Main Steam Line Break Experiment at ROSA-III RUN 952 (Standard Run with Full ECCS)", JAERI-M 84-229, (1984).
(36) M.KAWAJI, et al.,"A Main Steam Line Break Experiment at ROSA-III, RUN 953 (100% Break with an HPCS Failure)", JAERI-M 85-029 (1985).
(37) M.SUZUKI, et al.,"BWR Recirculation Loop Discharge Line Break LOCA Tests with Break Areas of 50 and 100% Assuming HPCS Failure at ROSA-III Facility", JAERI-M 85-037, (1985).
(38) T.YONOMOTO, et al.,"ROSA-III 50% Break Integral Test RUN 916 (Break

Area Parameter Test)", JAERI-M 85-109, (1985).

(39) H.NAKAMURA, et al.,"Recirculation Pump Suction Line 5% Split Break Test of ROSA-III (RUNs 922 and 932 with HPCS Failure)", JAERI-M 85-128, (1985).

(40) T.YONOMOTO, et al.,"ROSA-III 50% Break Integral Test RUN 928 (Break Configuration Sensitivity Test)", JAERI-M 85-151 (1985).

(41) K.TASAKA, et al.,"Comparison of ROSA-III and FIST BWR Loss of Coolant Accident Simulation Tests", JAERI-M 85-158 (1985).

(42) M.SUZUKI, et al.,"BWR Main Steam Line Break LOCA Tests RUNs 951, 954 and 956 at ROSA-III (Beak Area Effects with HPCS Failure)", JAERI-M 85-202 (1985).

(43) H.NAKAMURA et al.,"Recirculation Pump Suction Line 1% Split Break LOCA Test of ROSA-III (RUNs 921 and 931 with HPCS Failure)", JAERI-M 85-209 (1986).

(44) M.SUZUKI, et al.,"BWR 200% Recirculation Pump Suction Line Break LOCA Tests, RUNs 942 and 943 at ROSA-III without HPCS (Effects of Initial Fluid Conditions on LOCA)", JAERI-M 86-038 (1986).

(45) M.SUZUKI, et al.,"BWR LOCA Integral Test Simulating a 100% Main Steam Line Break outside Reactor Containment Vessel in ROSA-III Program, RUN 955 (Analogy of Steam and Recirculation Line Small Break LOCAs)", JAERI-M 87-044 (1987).

(46) T.YONOMOTO, et al.,"ROSA-III 100% Break Integral Test RUN 914 (Break (Break Area Parameter Test)), JAERI-M 87-072 (1987).

(47) M.SUZUKI, et al.,"BWR Main Recirculation Line Break LOCA Tests, RUNs 917 and 918 without HPCS at ROSA-III Program (Effects of ADS Delay in Small Break LOCA)", JAERI-M 88-141 (1988).

(48) M.SUZUKI, et al.,"BWR LOCA Simulation Test (RUN 992) in ROSA-III Program for a 10% Main Steam Line Break with ECCS Double Failures", JAERI-M 89-034 (1989).

(49) T.YONOMOTO, et.al.,"Experiment Data of ROSA-III Integral Test RUN 913 (15% Split Break without HPCS Actuation)", JAERI-M 89-125 (1989).

(50) H.NAKAMURA, et.al.,"Loss of Off-Site Power Test of ROSA-III (RUN 971 with HPCS Failure)", JAERI-M 89-130 (1989).

(51) H.NAKAMURA et al.,"Recirculation Pump Suction Line 75 and 25% Split Break LOCA Test of ROSA-III (RUNs 929 and 930 with HPCS Failure)", JAERI-M 89-131 (1989).

(52) M.SUZUKI, et al.,"Heat Loss and Fluid Leakage Tests of the ROSA-III

Facility", JAERI-M 9834 (1981).

(53) M.SUZUKI, et al.,"Characteristics of the ROSA-III Test Facility (Characteristics Test of the Jet Pumps in Normal and Reverse Flow)", JAERI-M 8670, (1980) (in Japanese).

(54) M.SUZUKI, et al.,"Evaluation of a Jet Pump Model for RELAP5 Code", JAERI-M 84-245, (1985) (in Japanese).

(55) M.SOBAJIMA et al.,"Instrumentation and Data Processing Method of the ROSA-III Test", JAERI-M 8499 (1979) (in Japanese).

(56) N.ABE et al.,"Electric Power Tansient Curve for ROSA-III Tests", JAERI-M 8728 (1980).

(57) K.TASAKA, et.al.,"ROSA-III Experimental Program for BWR LOCA/ECCS Integral Simulation Tests", JAERI 1307 (1987).

(58) H.MURATA, et.al.,"An Analysis of 100% Steam Line Break Test in the ROSA-III Program by Using RELAP5/Mod1 Code (Analysis of RUN 952, an HPCS Injection Test)", JAERI-M 83-210 (1983).

Table 2.1 Primary chracteristics of ROSA-III and BWR/6

Items	Unit	BWR*	ROSA-III	BWR / ROSA-III
Number of Recirc. Loops	-	2	2	1
Number of Jet Pumps	-	24	4	6
Number of Separators	-	212	1	212
Number of Fuel Assemblies	-	848	4	212
Active Fuel Length	m	3.76	1.88	2
Total Fluid Volume	m^3	621	1.42	437
Maximum Core Power	MW	3800	< 4.40	> 864
Steam Dome Pressure	MPa	7.23	7.23	1
Total core Flow Rate	kg/s	15400	< 36.4	> 424
Recirc. Flow Rate/Loop	kg/s	2240	< 5.26	> 424
Total Steam Flow Rate	kg/s	2060	< 4.86	> 424
Feedwater Temperature	K	489	489	1

* BWR/6 (251-848)

Table 3.1 ROSA-III instrumentation summary list

ITEM	SENSOR	NUMBER	NOTE
Pressure	Pressure Transducer	20	
Differential Pressure	DP Cell	60	PV and Loop 44 Level Measurement 5 Flow Meter 11
Fluid Temperature	CA Thermocouple	129	Primary Loop 23 DTT 4 Tie Rod 28 Upper Plenum 10 Lower Plenum 10 Tie Plate 40 Bypass 14
Fuel Rod Temperature	CA Thermocouple	213	
Slab Surface Temperature	CA Thermocouple	70	Core Barrel 24 Pressure Vessel 3 Channel Box 35 Shroud Support 8
Slab Inner Temperature	CA Thermocouple	9	JP Diffuser 4 PV Wall 5
Volumetric Flow Rate	Turbine Flow Meter Venturi Flow Meter Orifice Flow Meter	3 4 6	ECCS Loop 3 Primary Loop 10
Mass Flow Rate	Turbine Flow Meter Orifice Flow Meter	4 3	Recirculation Loop 4 Main Steam Line 3
Liquid Level	Conductivity Probe Capacitance Probe	138 2	
Density	Gamma Densitometer	10	2 Beam GD 2 3 Beam GD 2
Momentum Flux	Drag Disk	4	JP Spool Piece 2 Break Spool Piece 4 Break Orifice 1
Signal	ON/OFF Switch	14	
Pump Speed	Revolution Counter	2	
Electric Core Power	VA Meter	2	
TOTAL		693	

Table 4.1 Test conditions of RUNs 940 and 941

Test Parameters	Unit	RUN 940	RUN 941
Break Conditions			
Break Location		MRP Suction	MRP Suction
Break Diameter/Area	mm/%	5.9/5	2x26.2/200
Initial Conditions			
Steam Dome Pressure	MPa	7.36	7.36
Lower Plenum Temperature	K	553.7	553.6
Lower Plenum Subcooling	K	10.2	10.2
Core Inlet Flow Rate	kg/s	16.5	16.5
Total Core Power	MW	3.97	3.96
Max. Linear Heat Rate	kW/m	16.68	16.63
Upper Plenum Quality	%	12.5	12.5
Downcomer Water Level*	m	5.04	5.04
Steam Flow Rate	kg/s	2.04	2.02
Feedwater Flow Rate	kg/s	2.04	2.04
Feedwater Temperature	K	489	489
Transient Conditions			
MRP Trip	s	0.0	0.0
MSIV Closure Trip	s	L2+3	L2+3
ECC Conditions			
HPCS Actuation		Failure	Failure
LPCS Actuation Logic	s	L1+40	L1+40
LPCS Actuation Pressure	MPa	2.16	2.16
LPCI Actuation Logic	s	L1+40	L2+40
LPCI Actuation Pressure	MPa	1.57	1.57
ECC Water Temperature	K	393	393
ADS Actuation Logic	s	L1+120	L1+120
ADS Orifice Diameter	mm	15.5	15.5

L1 Level = 4.25 m, L2 Level = 4.76 m.

* Actual downcomer level is corrected to 5.11 m for both tests.

Table 4.2 Characteristics of steam discharge line valves

Valve	Close to Open	Open to Close
AV165	0.1 s	1.5 s
AV168 (Steady Line)	-	0.1 s
AV169 (ADS)	0.3 s	2.0 s

Table 4.3 Control sequence for steam line valves in RUNs 940 and 941

Valves	Simulation	Before Break	After Break
CV-130	MSIV,PCS	open	Control
AV-168		open	open
AV-165		Close	Close
AV-169	ADS	Close	Open by L1 + 120s
CV-1		Open	Close
CV-2		Open	Close

Table 5.1 Major events and test procedures of RUN 940

Time (s)	Events
- 120	· Initiation of data recording
- 10	· Initiation of data plotting
0	· Initiation of break, MRP trip and closure of valves (CV-1,2)
9	· Core power decay
19	· L2 level trip
21	· Pressure control (P ≧ 6.7 MPa)
23	· MSIV closure
39	· L1 level trip
69	· Relief valve operation (P ≦ 8.13 MPa)
137	· Temporary core dryout
156	· DC level at recirculation line
162	· ADS actuation
170～180	· Lower plenum flashing
213	· Second core dryout initiation
330	· LPCS injection
415	· PCT recorded at A-71 rod Pos. 4 (841.6 K)
443	· LPCI injection
474	· Completion of core quench (A77 rod, position 2)
690	· Completion of data plotting
933	· Completion of data recording

Table 5.2 PCT in RUN 940

```
** Order of PCT  (RUN 940) **

 No. 1      A-71 rod    Pos. 4      PCT =  841.6 (K)      Time =   415.1 (s)
 No. 2      A-57 rod    Pos. 4      PCT =  836.0 (K)      Time =   444.5 (s)
 No. 3      A-31 rod    Pos. 4      PCT =  833.2 (K)      Time =   395.5 (s)
 No. 4      A-11 rod    Pos. 4      PCT =  832.3 (K)      Time =   425.6 (s)
 No. 5      A-17 rod    Pos. 4      PCT =  832.3 (K)      Time =   445.9 (s)
 No. 6      A-68 rod    Pos. 4      PCT =  817.2 (K)      Time =   443.1 (s)
 No. 7      A-28 rod    Pos. 4      PCT =  810.7 (K)      Time =   401.8 (s)
 No. 8      A-51 rod    Pos. 4      PCT =  807.9 (K)      Time =   420.7 (s)
 No. 9      A-84 rod    Pos. 4      PCT =  806.9 (K)      Time =   395.5 (s)
 No.10      A-85 rod    Pos. 4      PCT =  806.9 (K)      Time =   381.5 (s)
```

Table 5.3 Major events and test procedures of RUN 941

Time (s)	Events
- 111.0	· Initiation of data recording
- 10.0	· Initiation of data plotting
0.0	· Initiation of break, MRP trip and closure of valves (CV-1, 2)
1.7	· Feedwater line closure (~3.1 s)
3.0	· L2 level trip
3.2	· First core dryout (~30 s)
5.4	· MSIV closure
7.7	· L1 level trip
13.5	· Recirculation suction line uncovered
17	· Lower plenum flashing
35	· Second core dryout
68	· Feedwater line flashing
70	· LPCS injection
95	· LPCI injection
116	· PCT at A-71 rod, Position 4 (790.0 K)
131	· ADS opening
179	· Completion of core quench (B-22 rod Position 1)
590	· Completion of data plotting
854	· Completion of data recording

Table 5.4 PCT in RUN 941

```
** Order of PCT  (RUN 941) **

 No. 1      A-71 rod    Pos. 4     PCT =  790.0 (K)     Time =  116.4 (s)
 No. 2      A-31 rod    Pos. 4     PCT =  783.5 (K)     Time =  115.8 (s)
 No. 3      A-11 rod    Pos. 4     PCT =  778.3 (K)     Time =  118.2 (s)
 No. 4      B-11 rod    Pos. 3     PCT =  776.9 (K)     Time =  155.4 (s)
 No. 5      A-85 rod    Pos. 3     PCT =  768.5 (K)     Time =  115.8 (s)
 No. 6      A-51 rod    Pos. 4     PCT =  767.5 (K)     Time =  116.4 (s)
 No. 7      A-88 rod    Pos. 3     PCT =  767.5 (K)     Time =  120.0 (s)
 No. 8      A-28 rod    Pos. 4     PCT =  766.6 (K)     Time =  115.2 (s)
 No. 9      A-84 rod    Pos. 4     PCT =  766.6 (K)     Time =  116.4 (s)
 No.10      A-88 rod    Pos. 2     PCT =  766.6 (K)     Time =   19.2 (s)
```

Table 6.1 Test conditions of small and large-break LOCA tests (RUNs 922 and 926) with cold ECC water injection

Test Parameters	Unit	RUN 922	RUN926
Break Conditions			
Break Location		MRP Suction	MRP Suction
Break Diameter/Area	mm/%	5.9 / 5.0	2x26.2 / 200.0
Initial Conditions			
Steam Dome Pressure	MPa	7.35	7.37
Lower Plenum Temperature	K	552.4	553.0
Lower Plenum Subcooling	K	9.8	10.0
Core Inlet Flow Rate	kg/s	16.4	16.3
Total Core Power	MW	3.96	3.97
Max. Linear Heat Rate	kW/m	16.65	16.69
Upper Plenum Quality	%	14.1	13.9
Downcomer Water Level*	m	5.04	5.04
Steam Flow Rate	kg/s	2.06	2.08
Feedwater Flow Rate	kg/s	2.05	2.03
Feedwater Temperature	K	490.0	489.0
Transient Conditions			
MRP Trip	s	0.0	0.0
MSIV Closure Trip	s	L2 + 3	L2 + 3
ECC Conditions			
HPCS Actuation		Failure	Failure
LPCS Actuation Logic	s	L1 + 40	L1 + 40
LPCS Actuation Pressure	MPa	2.27	2.13
LPCI Actuation Logic	s	L1 + 40	L1 + 40
LPCI Actuation Pressure	MPa	1.72	1.45
ECC Water Temperature	K	313	313
ADS Actuation Logic		L1 + 120	L1 + 120
ADS Orifice Diameter	mm	15.5	15.5

L1 Level = 4.25 m, L2 Level = 4.76 m

Actual DC. Level was corrected to 5.11 m in two tests.

Table 6.2 Comparison of major event timings between RUNs 940 and and 922, and between RUNs 941 and 926

Events (Time; s)	5% Break Tests		200% Break Tests	
	RUN 940	RUN 922	RUN 941	RUN 926
Break Initiation	0.0 s	0.0 s	0.0 s	0.0 s
MSIV Closure Completion	25	25	9.0	8.6
ADS Actuation	162	162	131	130*
RLU (Recirculation Line Uncovery)	162	162	13.5*	13.0*
LPF (Lower Plenum Flashing)	170~180*	171	17.0*	17.0*
1st Core Dryout Initiation	137	125	3.2	3.2
2nd Core Dryout Initiation	213	200	35	34
LPCS Actuation	330	330	70	71
LPCI Actuation	443*	426	95	96
PCT Time	415*	431	116	119
Completion of Quench	474	456	179*	188*

PCT (K)	841.6	830.3	790.0	783.5

Table 6.3 Metal volumes of structures surrounding upper plenum steam separator and core bypass in ROSA-III facility

Components	Thickness (m)	Length (m)	Contact Surface(m^2)	Metal Volume (m^3)
Core Shroud (total)			5.4	0.051
· Core Region	6×10^{-3}	2.24	2.8	0.017
· Upper Plenum	4×10^{-3}	0.75	1.2	0.020
· Lower Plenum	6×10^{-3}	1.36	1.4	0.014
Separator (total)			2.1	0.007
· Stand Pipe	6×10^{-3}	1.12	0.6	0.003
· Separator	3×10^{-3}	0.71	1.5	0.004
Channel Boxes	3×10^{-3}	2.38	5.3	0.016
Guide Tube	8×10^{-3}	1.07	1.5	0.012
Total	-	-	14.3	0.086

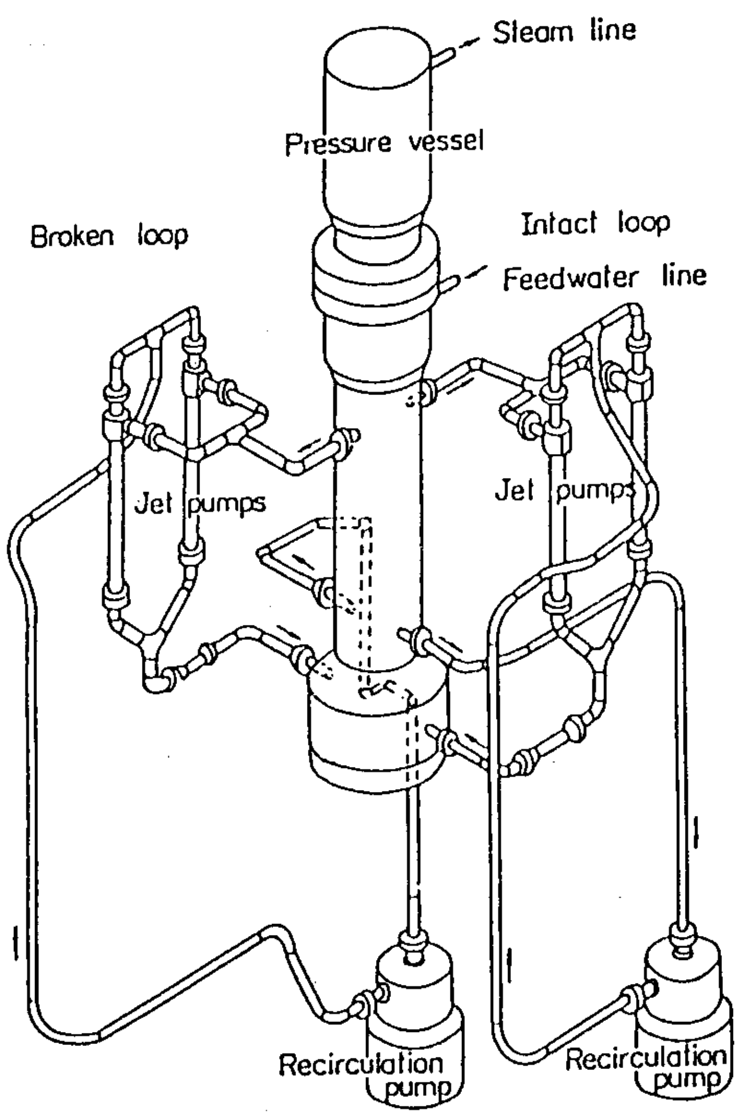

Fig. 2.1 Schematic diagram of ROSA-III test facility

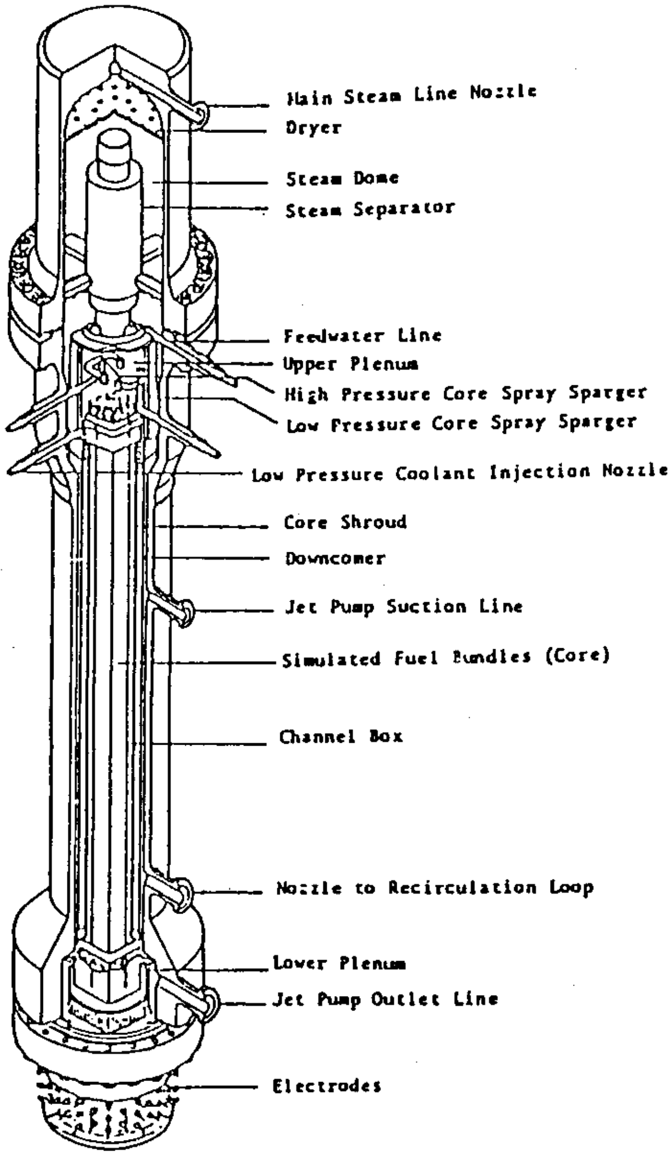

Fig. 2.2 Internal structure of pressure vessel of ROSA-III

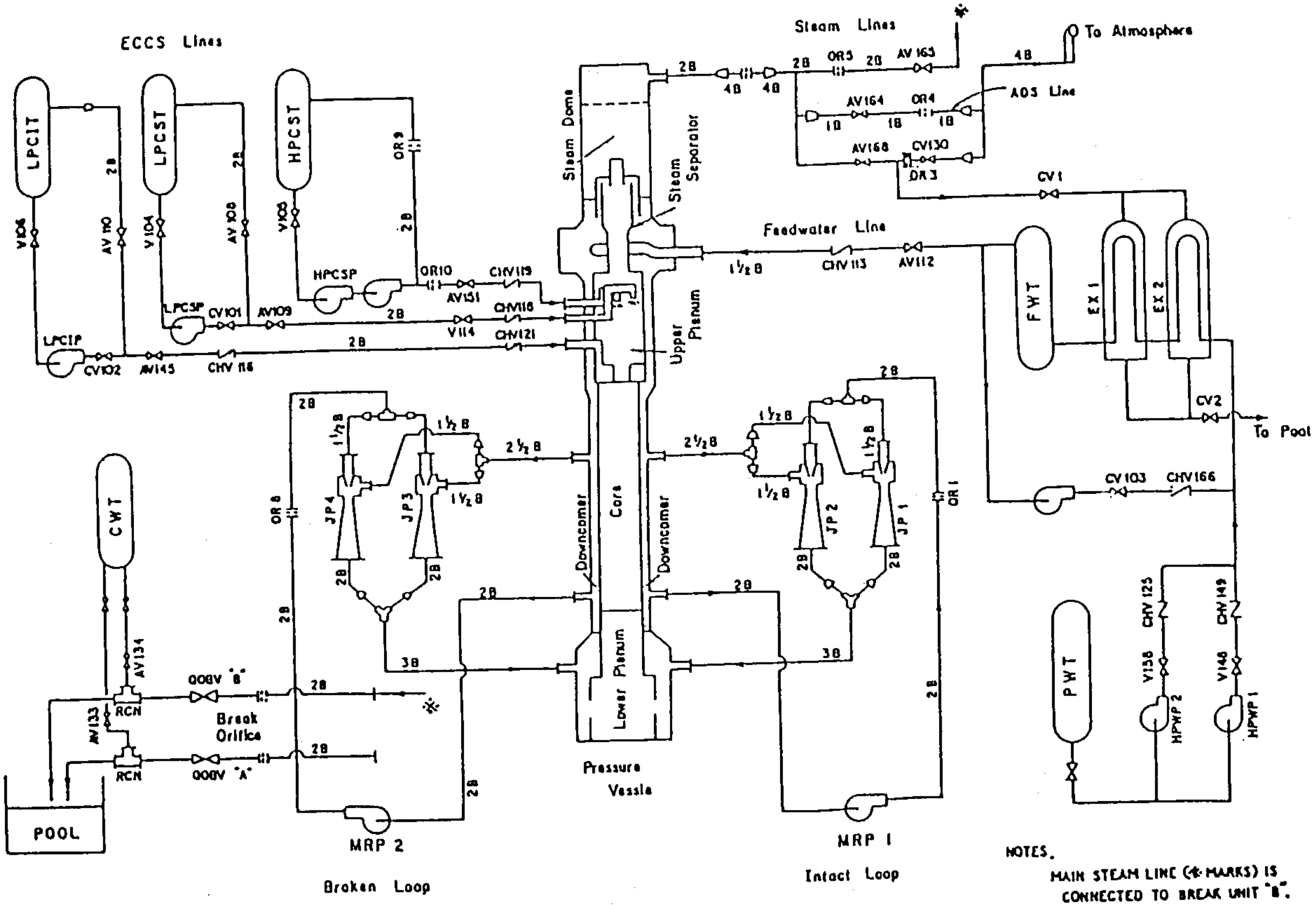

Fig. 2.3 ROSA-III piping schematic

NOTES.
MAIN STEAM LINE (※ MARKS) IS CONNECTED TO BREAK UNIT "B".

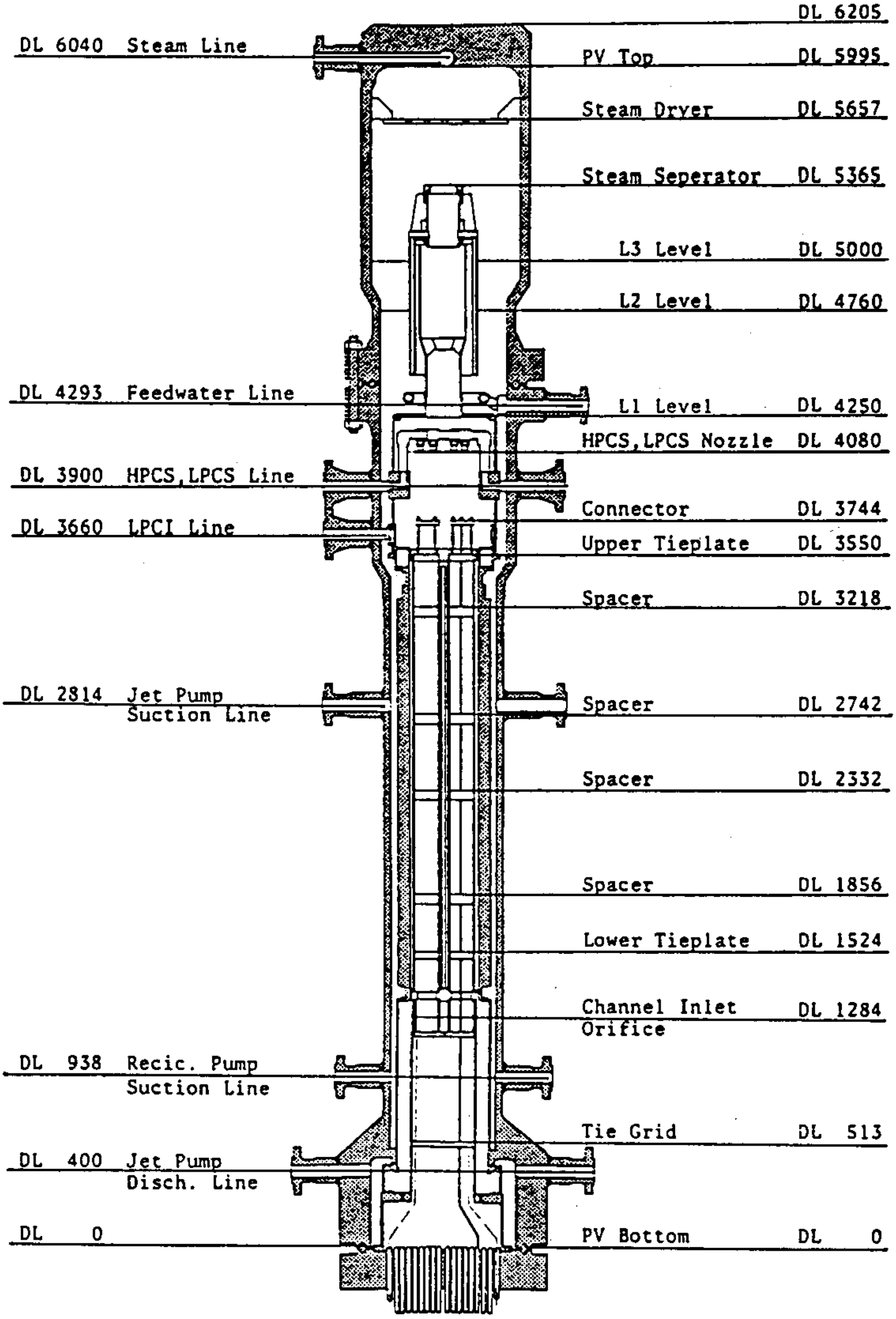

Fig. 2.4 Pressure vessel internals arrangement

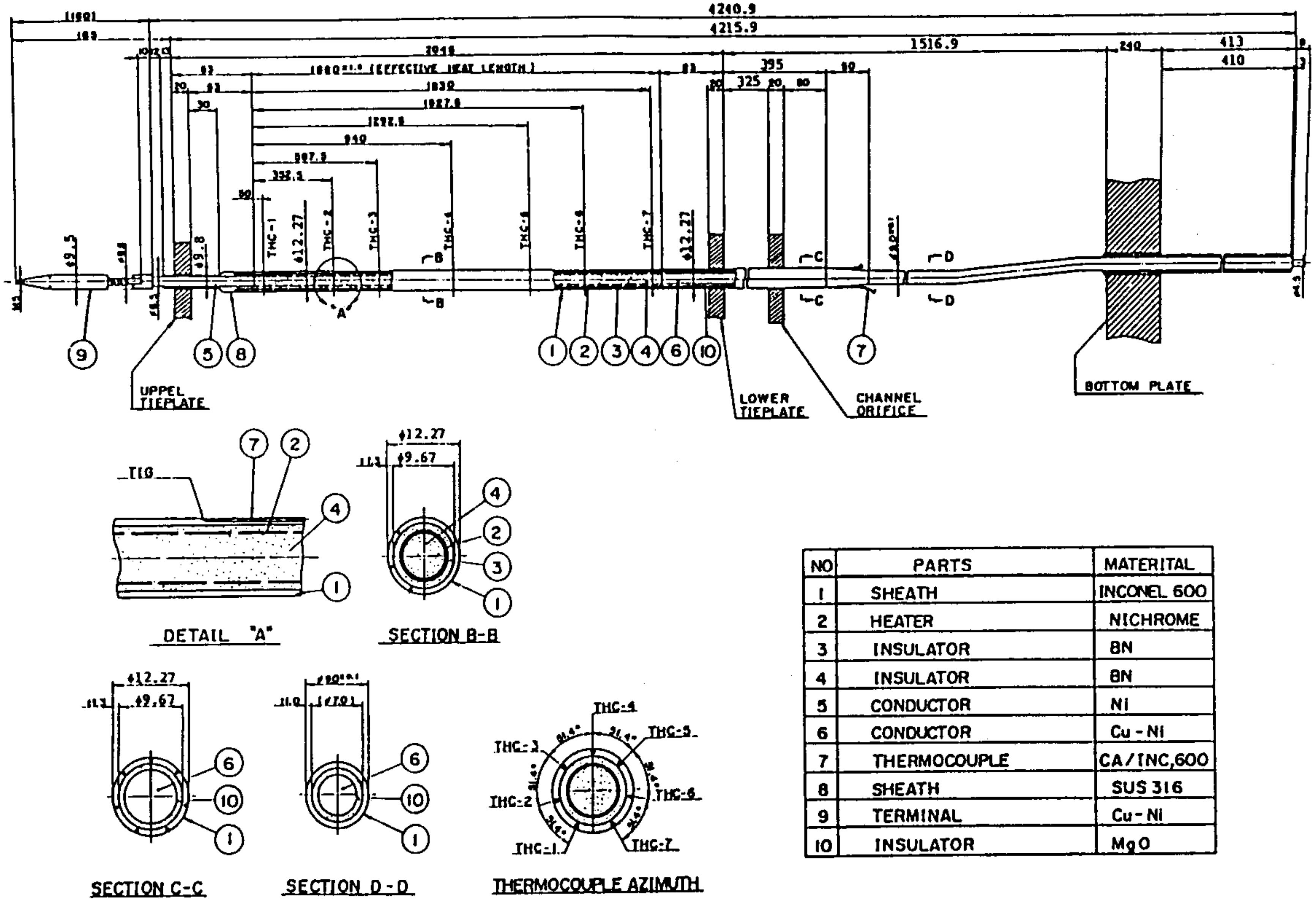

NO	PARTS	MATERITAL
1	SHEATH	INCONEL 600
2	HEATER	NICHROME
3	INSULATOR	BN
4	INSULATOR	BN
5	CONDUCTOR	Ni
6	CONDUCTOR	Cu - Ni
7	THERMOCOUPLE	CA/INC,600
8	SHEATH	SUS 316
9	TERMINAL	Cu - Ni
10	INSULATOR	MgO

Fig. 2.5 Simulated fuel rod of ROSA-III

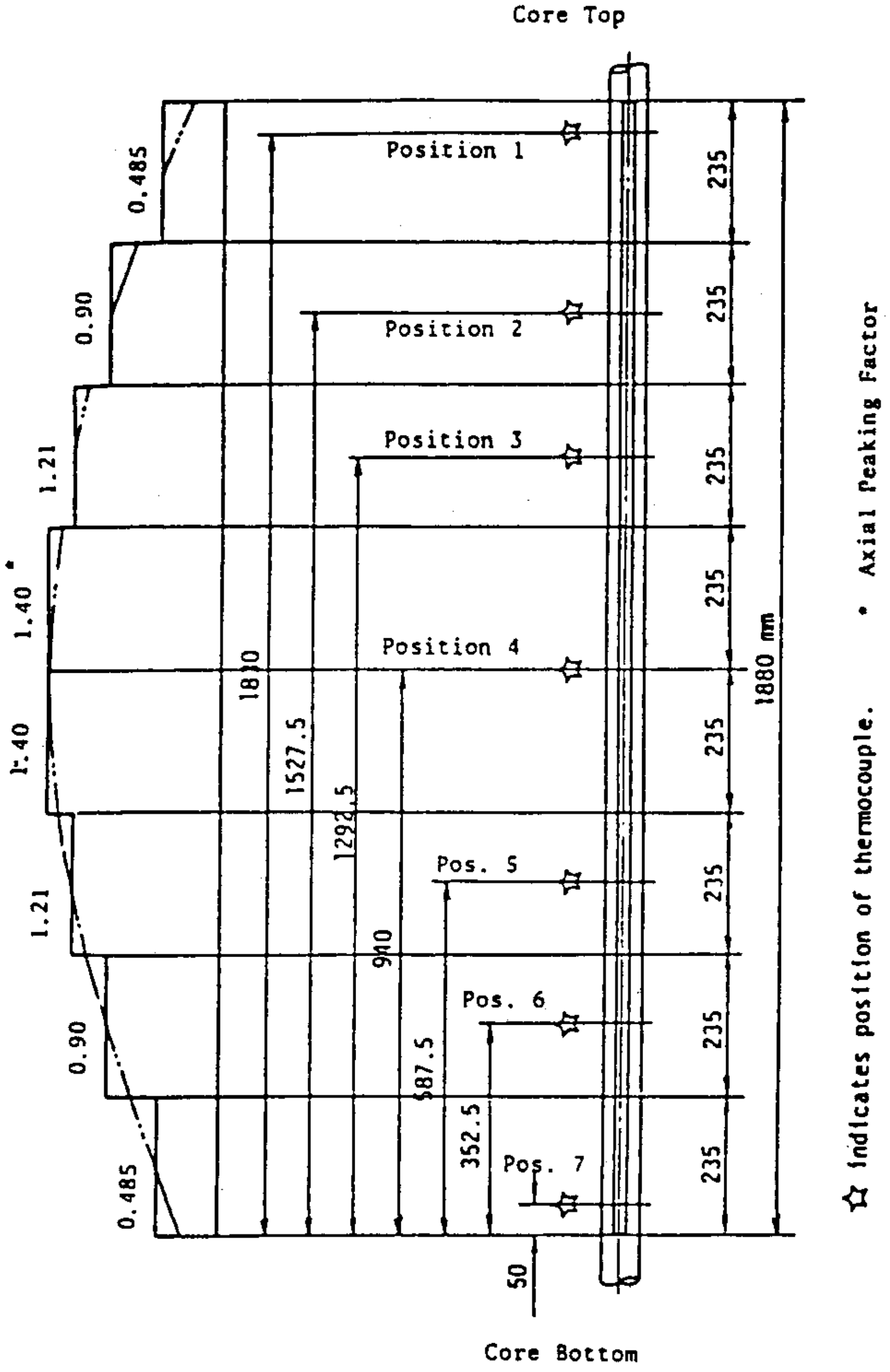

Fig. 2.6 Axial power distribution of heater rod

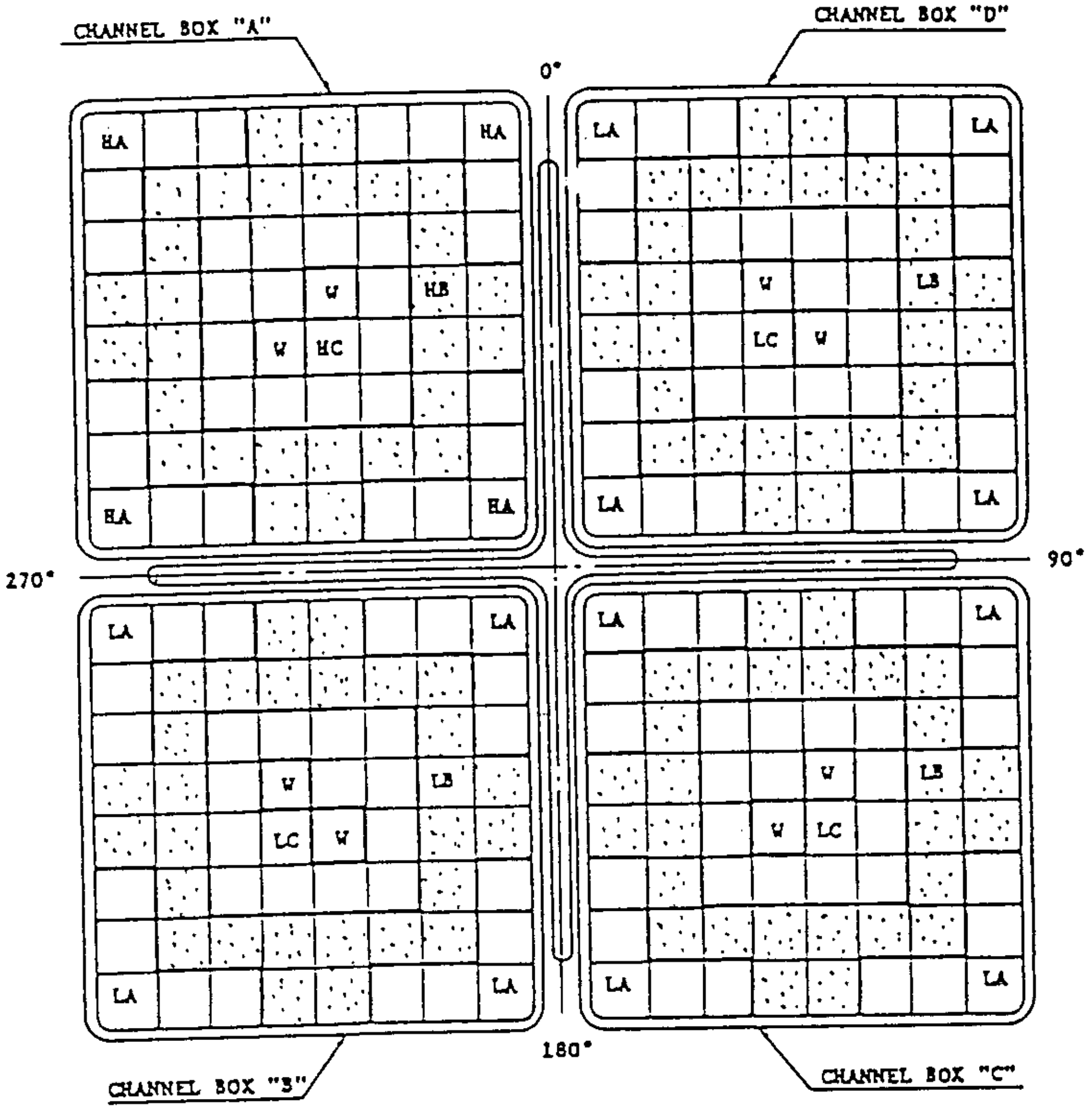

Region	HA	HB	HC	LA	LB	LC	W
Lenear Heat Rate (kW/m)	18.5	16.81	14.41	13.21	12.01	10.29	0.0
Local peaking factor	1.1	1.0	0.875	1.1	1.0	0.875	0.0
No. of Rods	20	28	14	60	84	.42	8

* note : Radial peaking factor is 1.4

Fig. 2.7 Radial power distribution of core

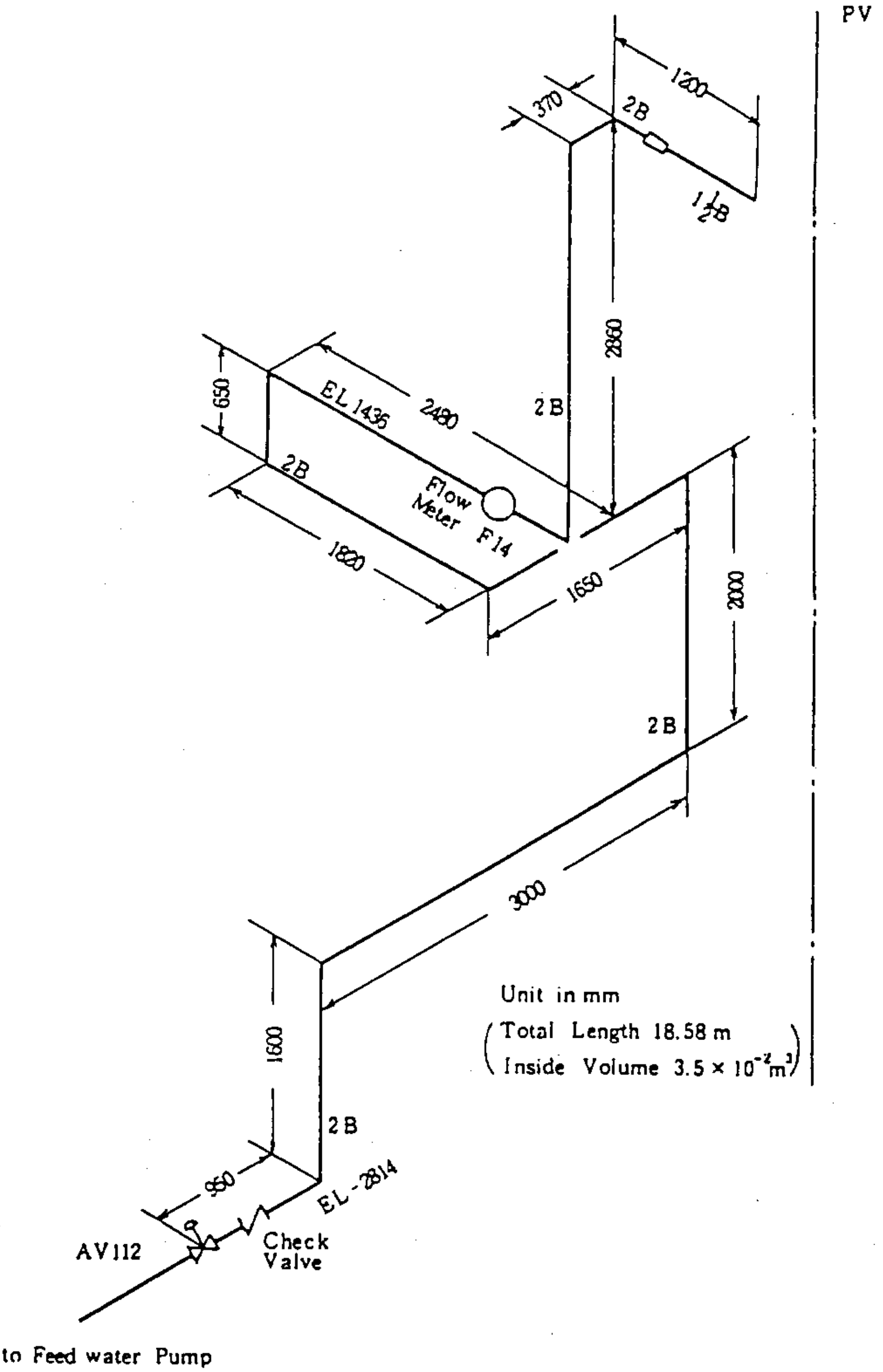

Unit in mm
(Total Length 18.58 m
Inside Volume $3.5 \times 10^{-2} m^3$)

Fig. 2.8 Feedwater line between PV and AV-112

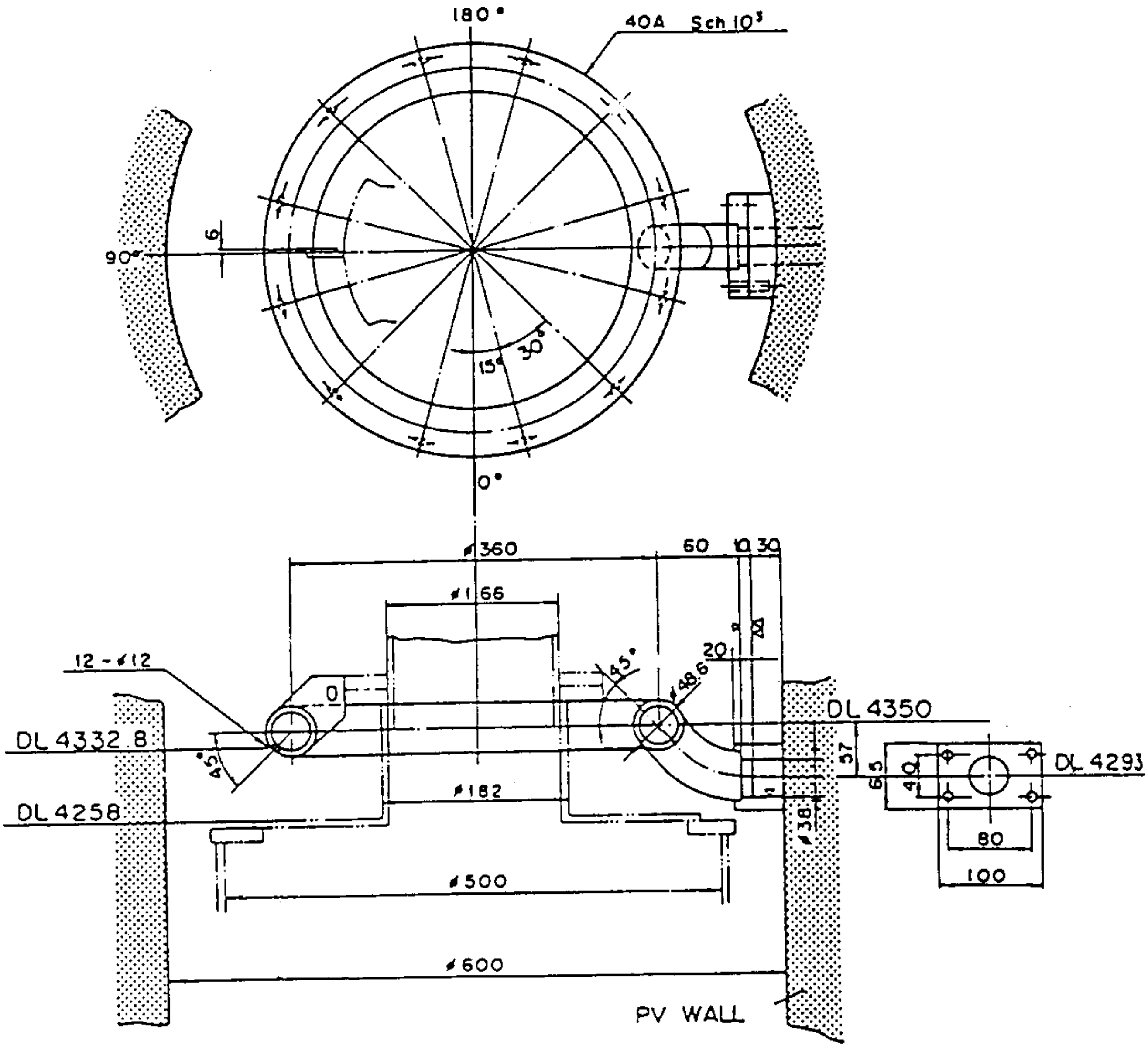

Fig. 2.9 Feedwater sparger configuration

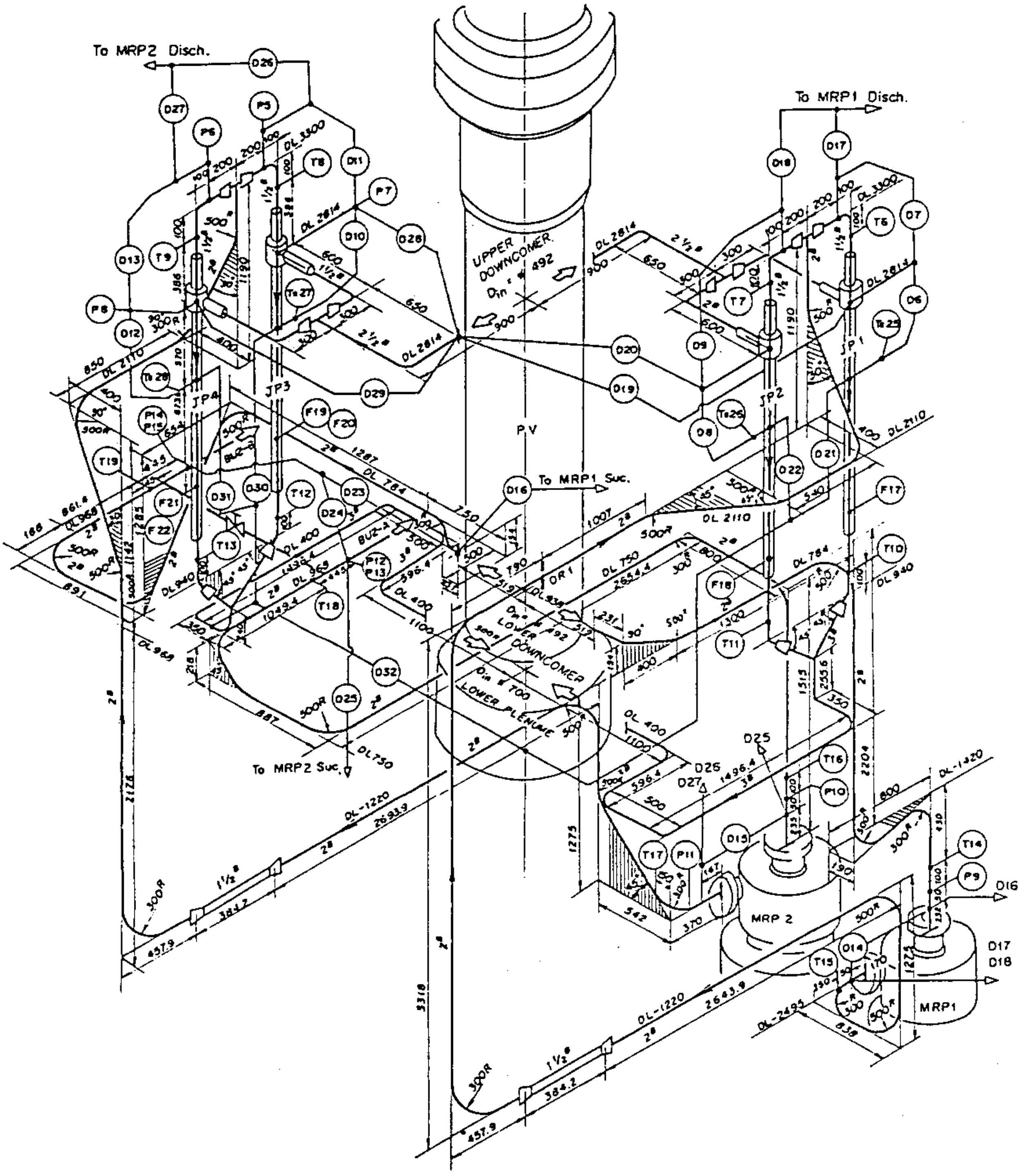

Fig. 2.10 Details of ROSA-III system piping

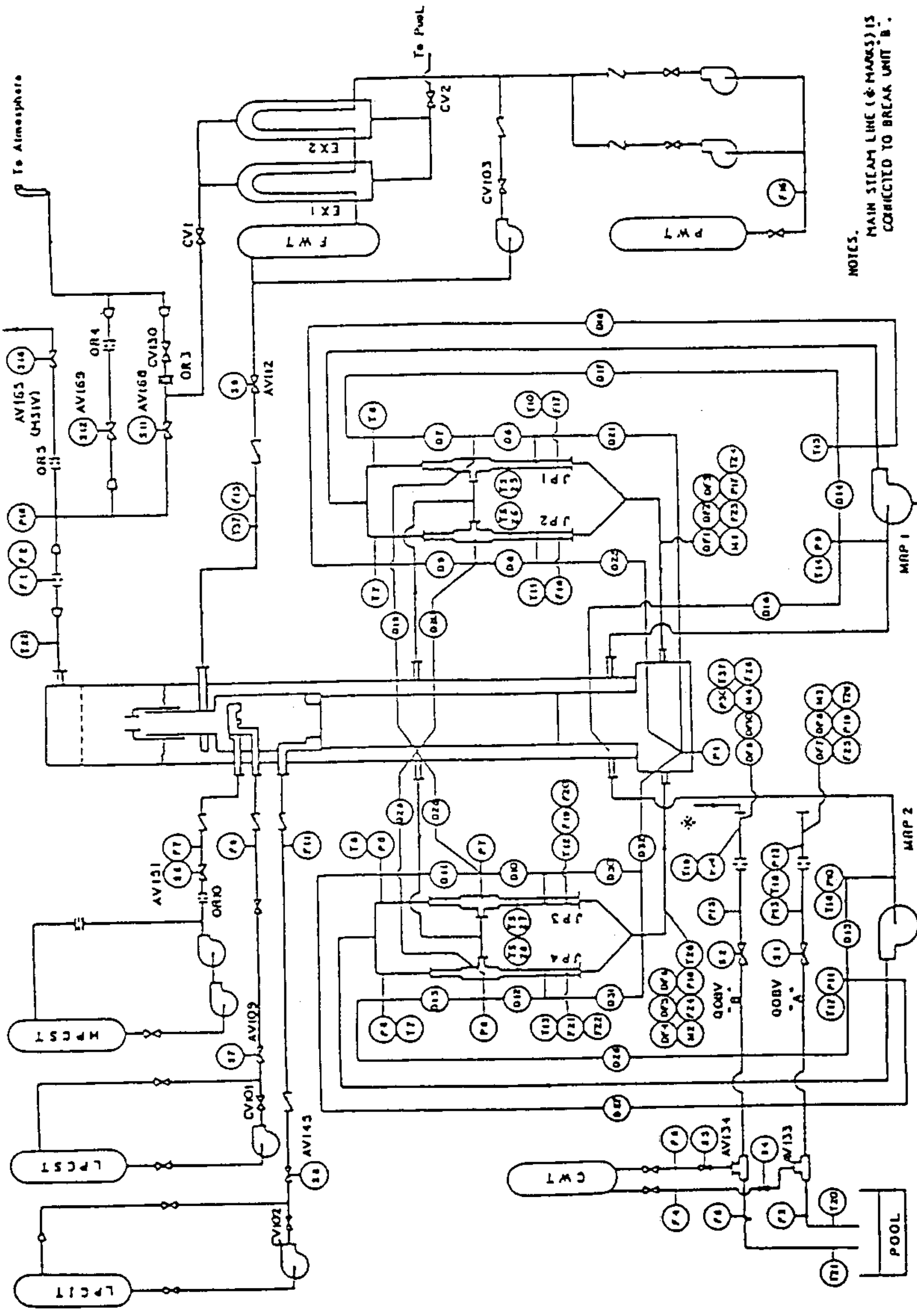

NOTES.
MAIN STEAM LINE (※-MARKS) IS CONNECTED TO BREAK UNIT "B".

Fig. 3.1 Instrumentation location of ROSA-III test facility

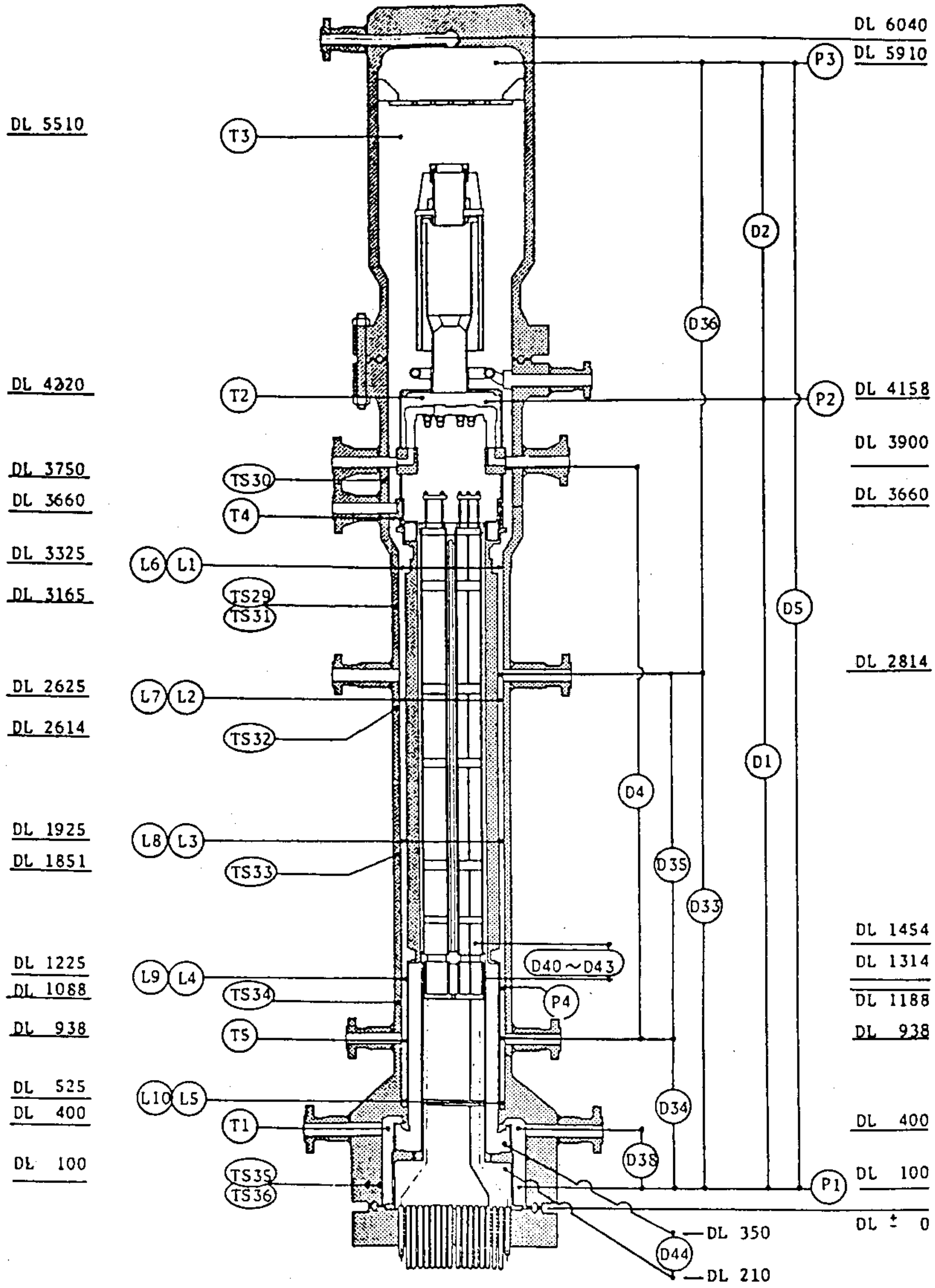

Fig. 3.2 Instrumentation location in pressure vessel

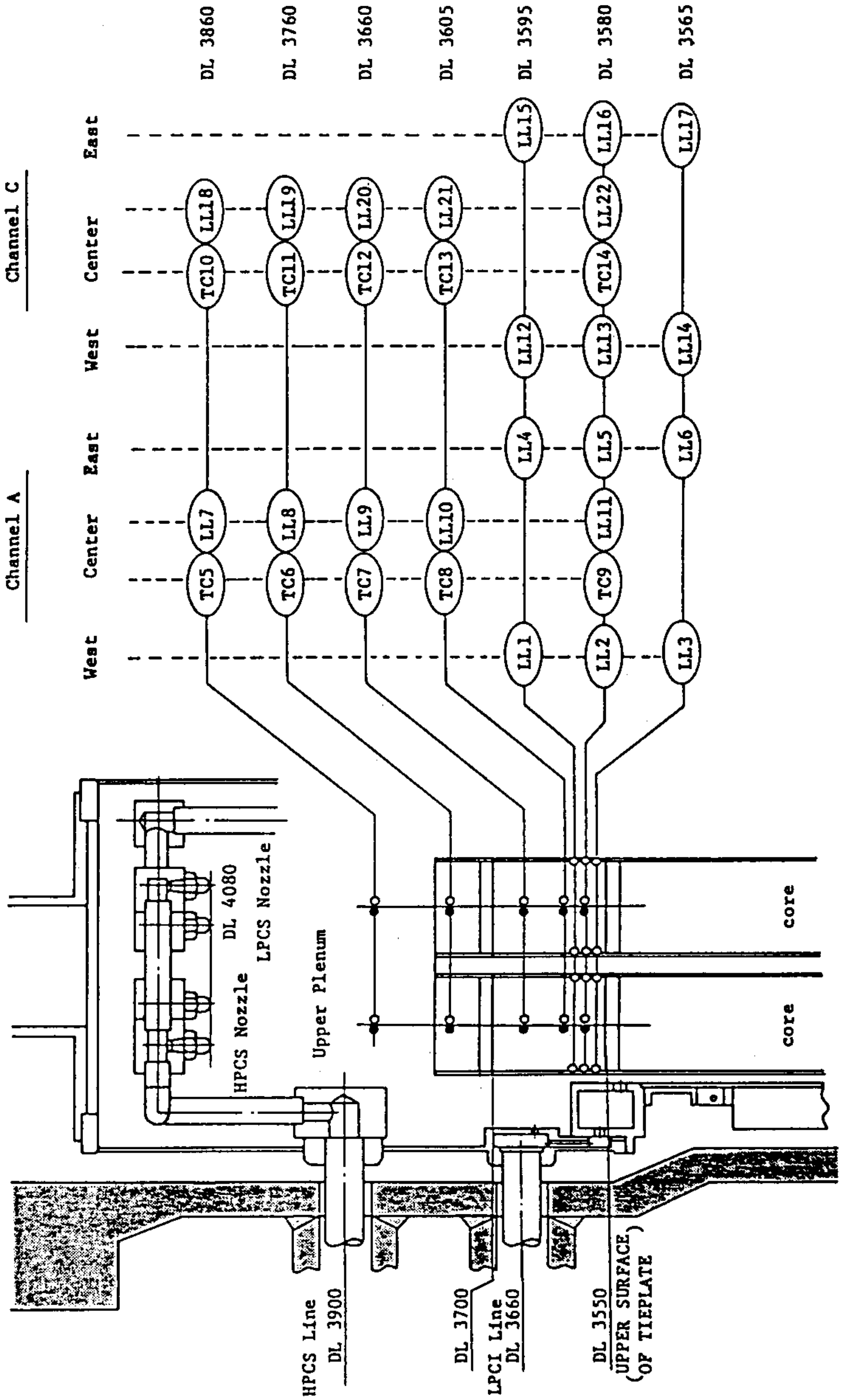

Fig. 3.3 Upper plenum instrumentation

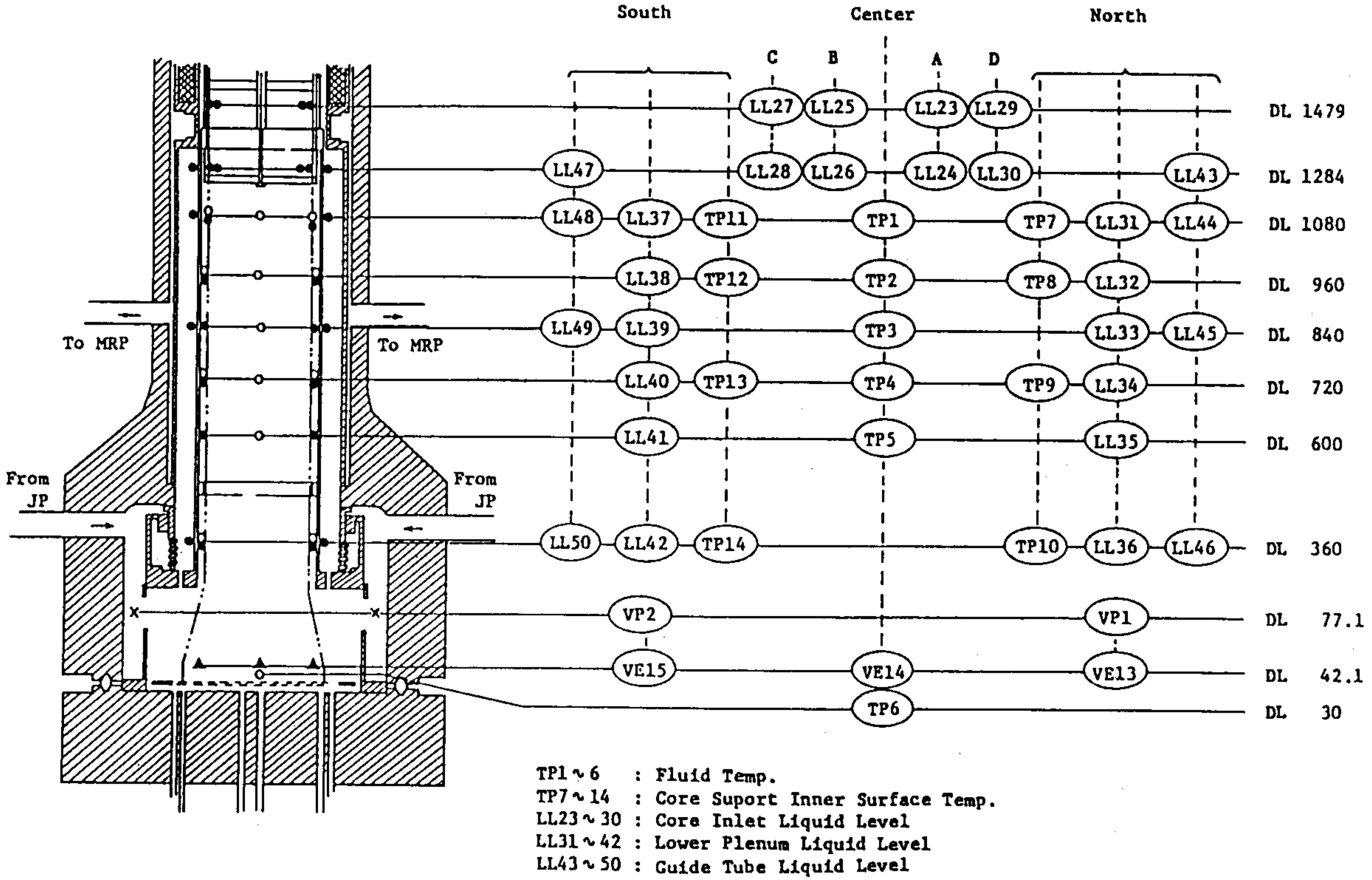

TP1～6 : Fluid Temp.
TP7～14 : Core Suport Inner Surface Temp.
LL23～30 : Core Inlet Liquid Level
LL31～42 : Lower Plenum Liquid Level
LL43～50 : Guide Tube Liquid Level

Fig. 3.4 Lower plenum instrumentation

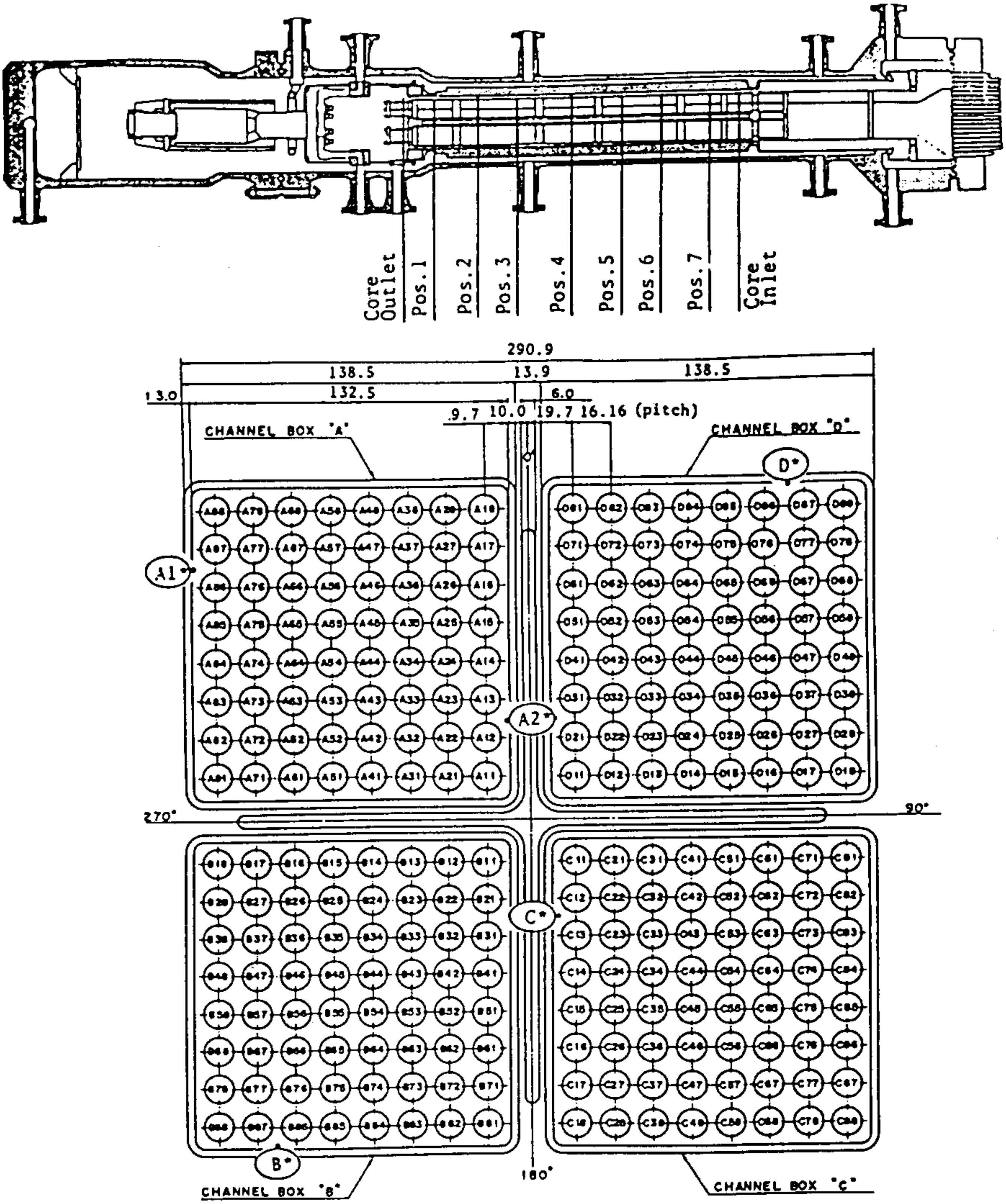

Heater rod O.D. is 12.27mm

A54,B54,C54 and D54 are water rod simulators with void probes, O.D.= 15.01mm

A45,B45,C45 and D45 are water rod simulators with thermocouples, O.D.= 15.01mm

Fig. 3.5 Core instrumentation

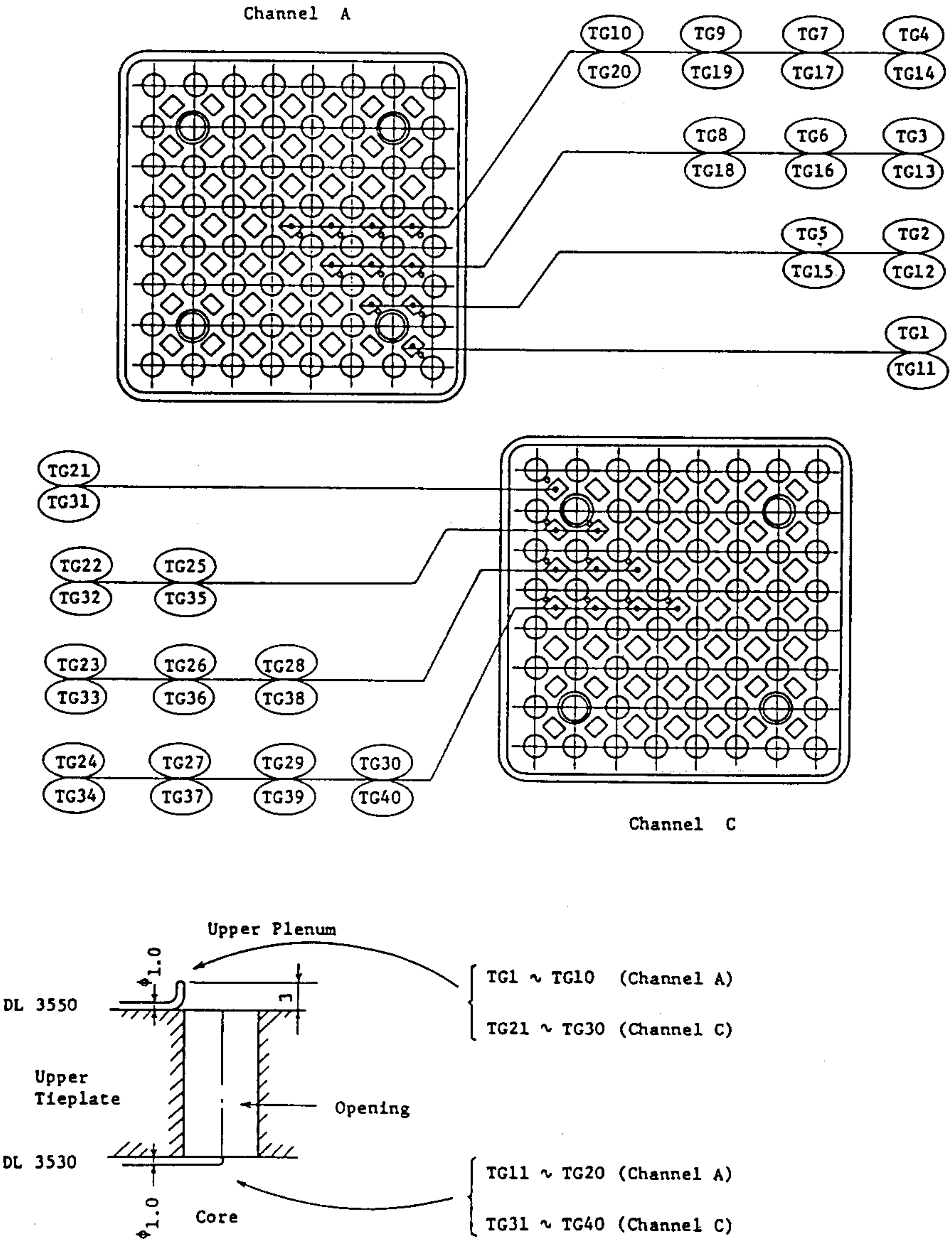

Fig. 3.6 Upper tieplate instrumentations

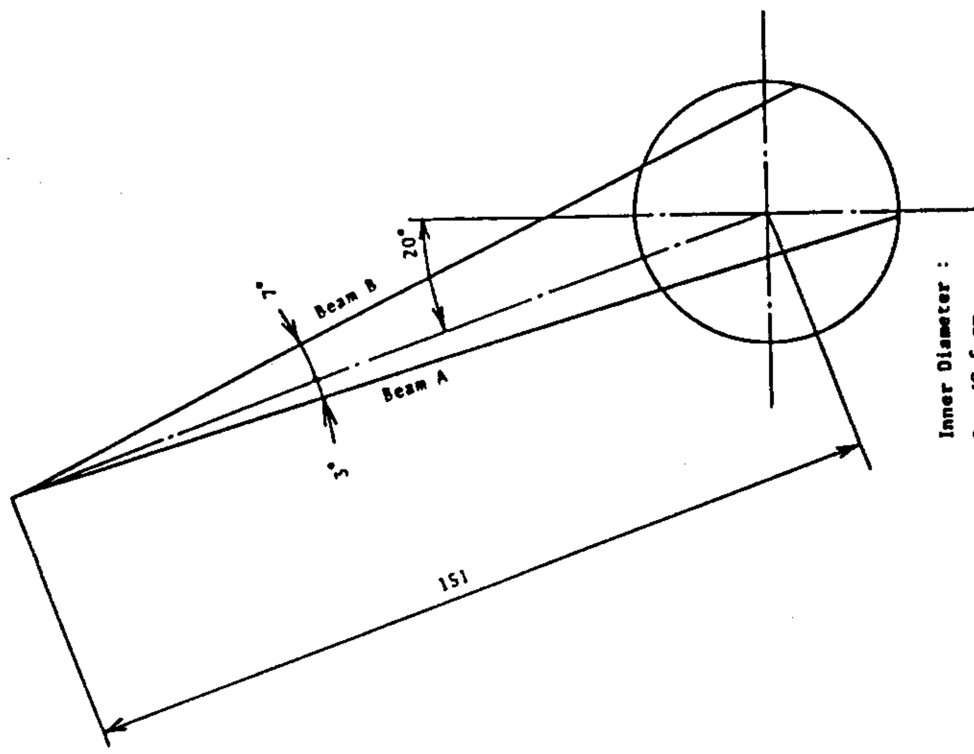

Fig. 3.8 Beam directions of two-beam gamma densitometer

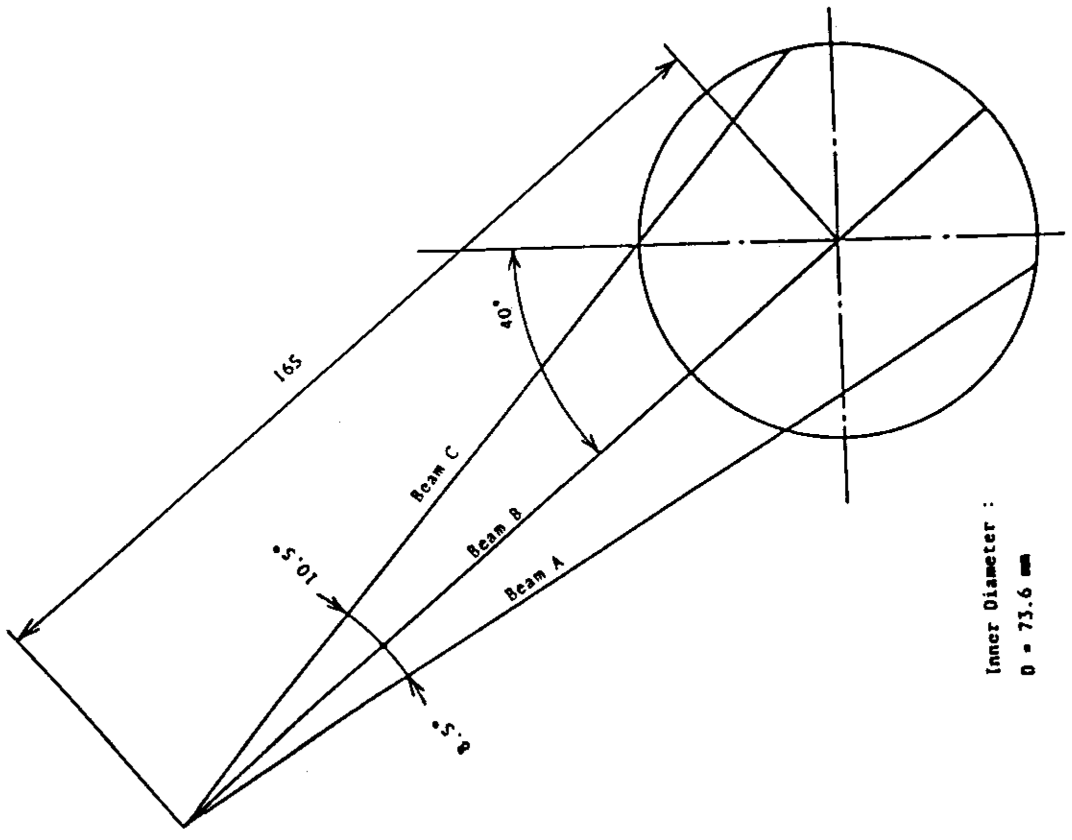

Fig. 3.7 Beam directions of three-beam gamma densitometer

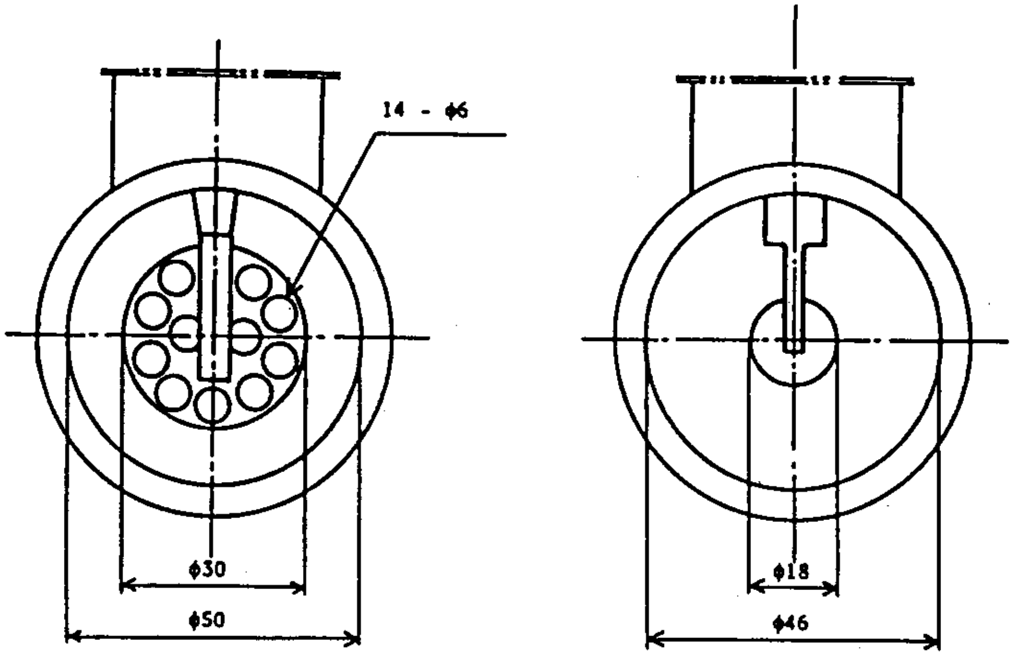

(a) High Range Drag Disc

(b) Low Range Drag Disc

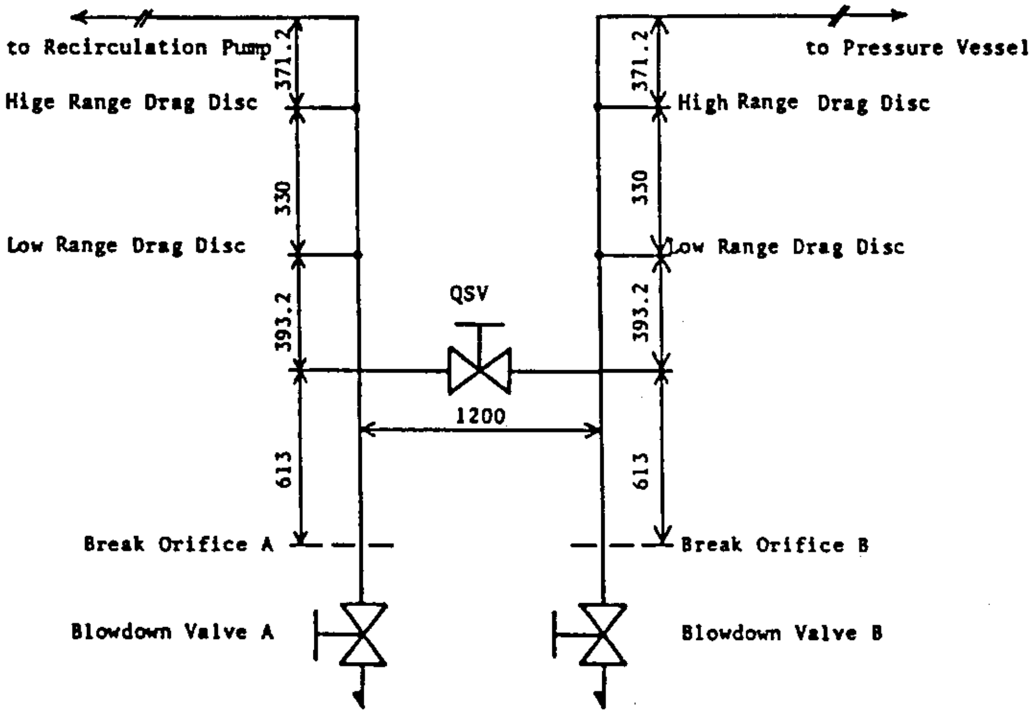

(c) Location of Drag Discs

Fig. 3.9 Arrangement and location of drag disks

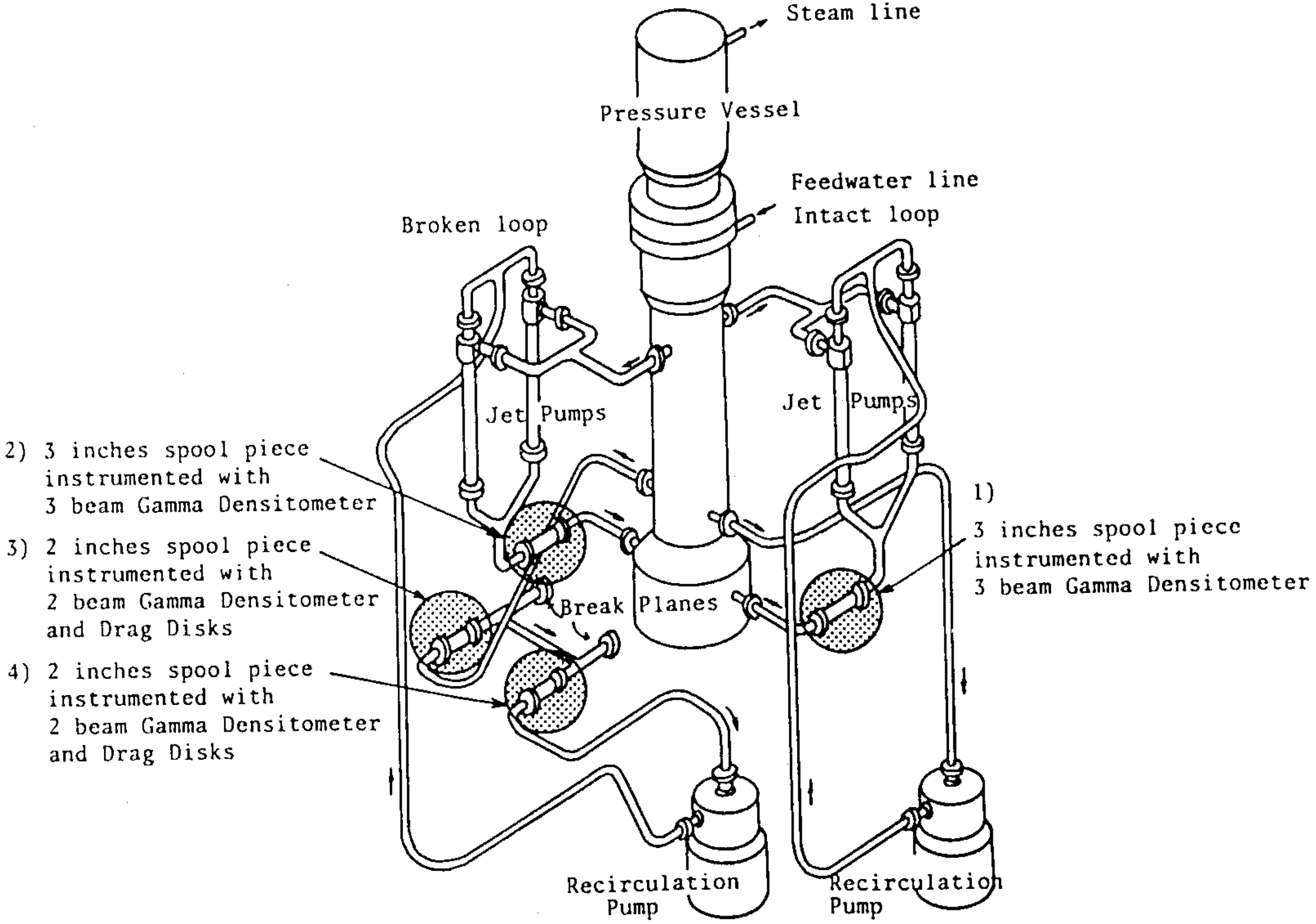

Fig. 3.10 Location of two-phase flow measurement spool pieces

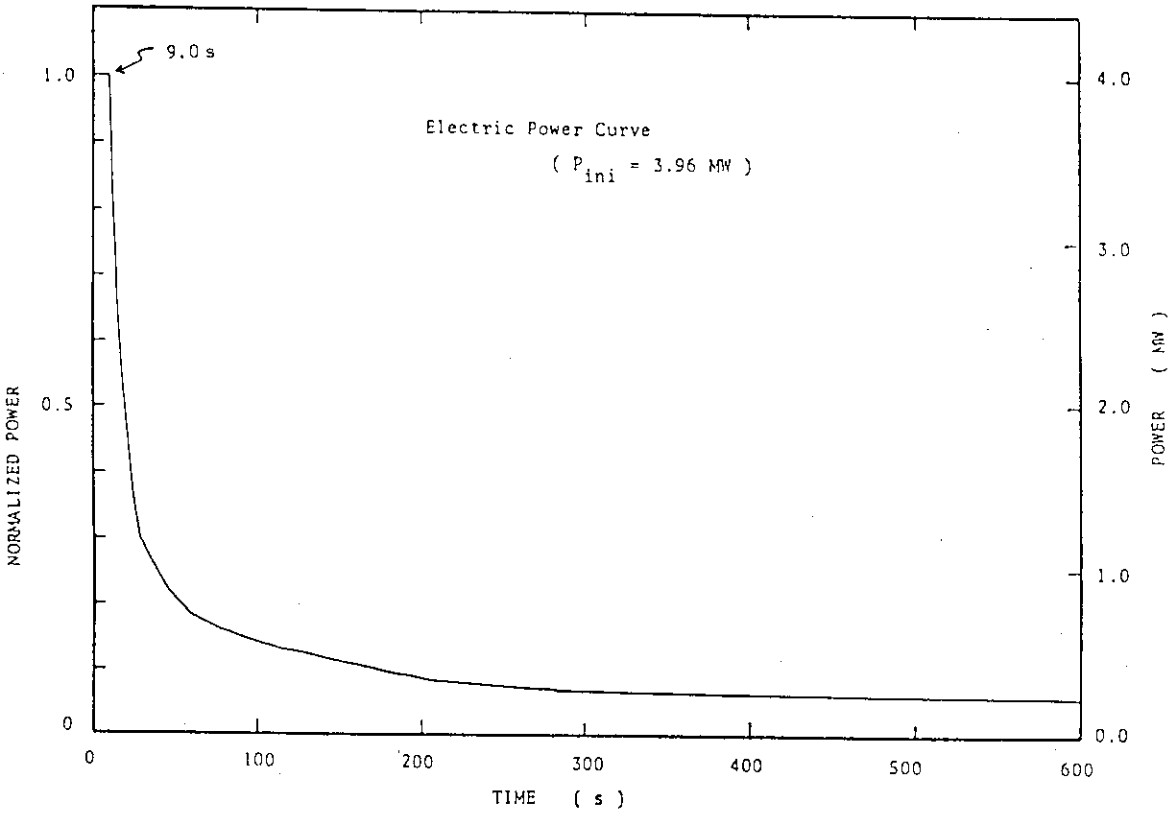

Fig. 4.1 Normalized power transient for ROSA-III

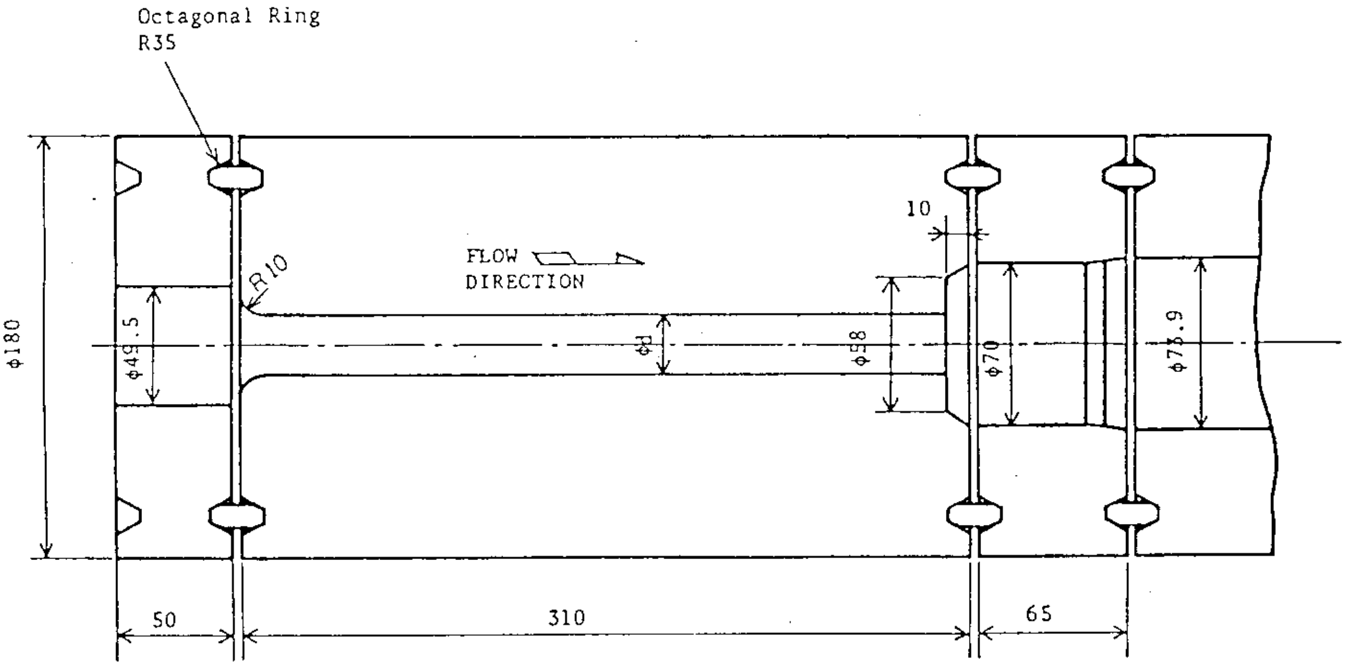

Material SUS304
Dimension in mm

Break area ratio (%)	d (mm)
100	26.2

Fig. 4.2 Break nozzle details

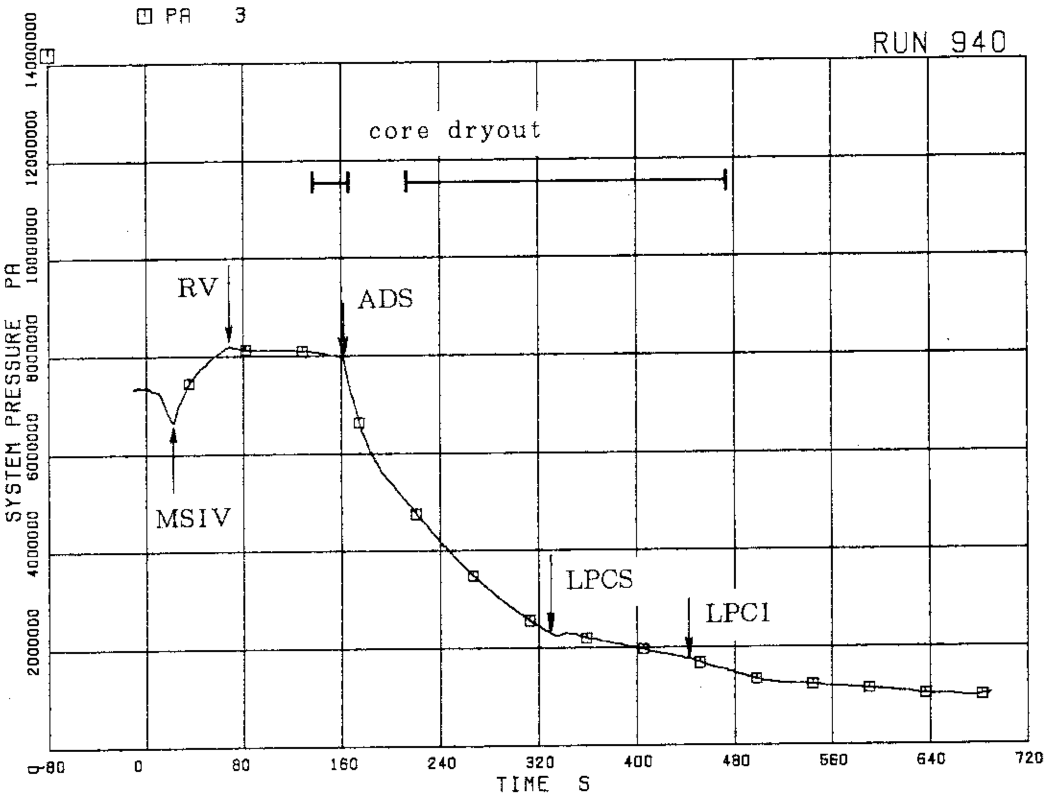

Fig. 5.1 System pressure in steam dome in RUN 940

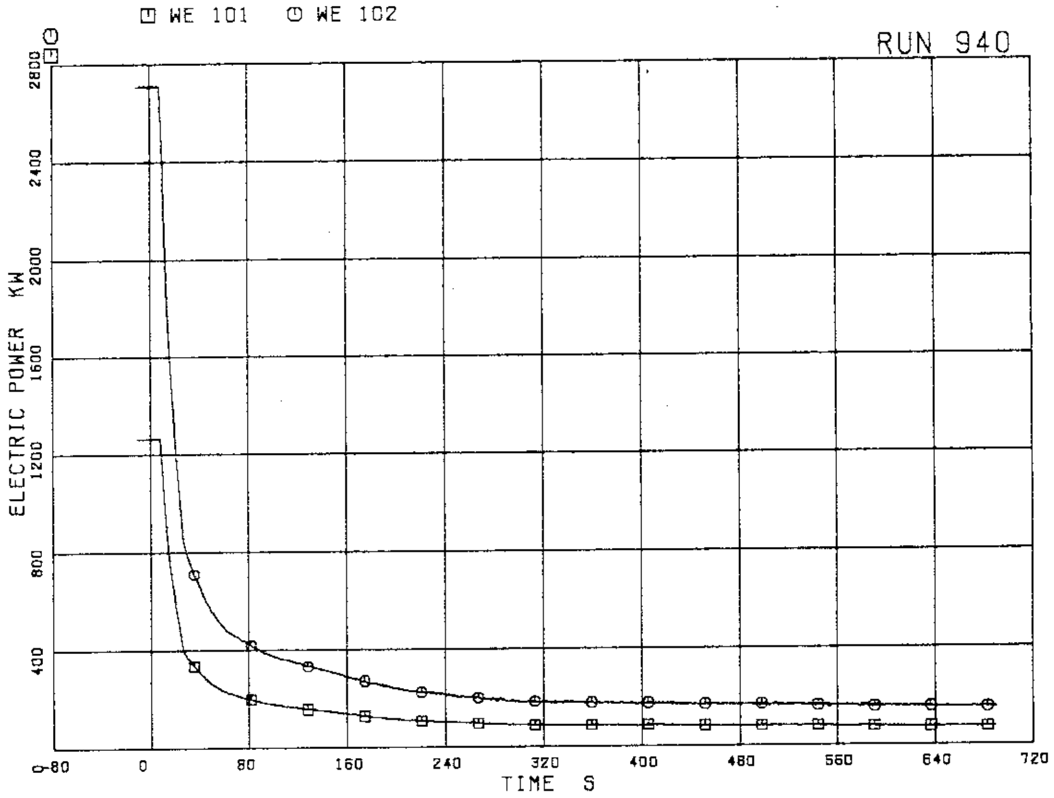

Fig. 5.2 Core power for bundle A (WE 101) and other three bundles (WE 102) in RUN 940

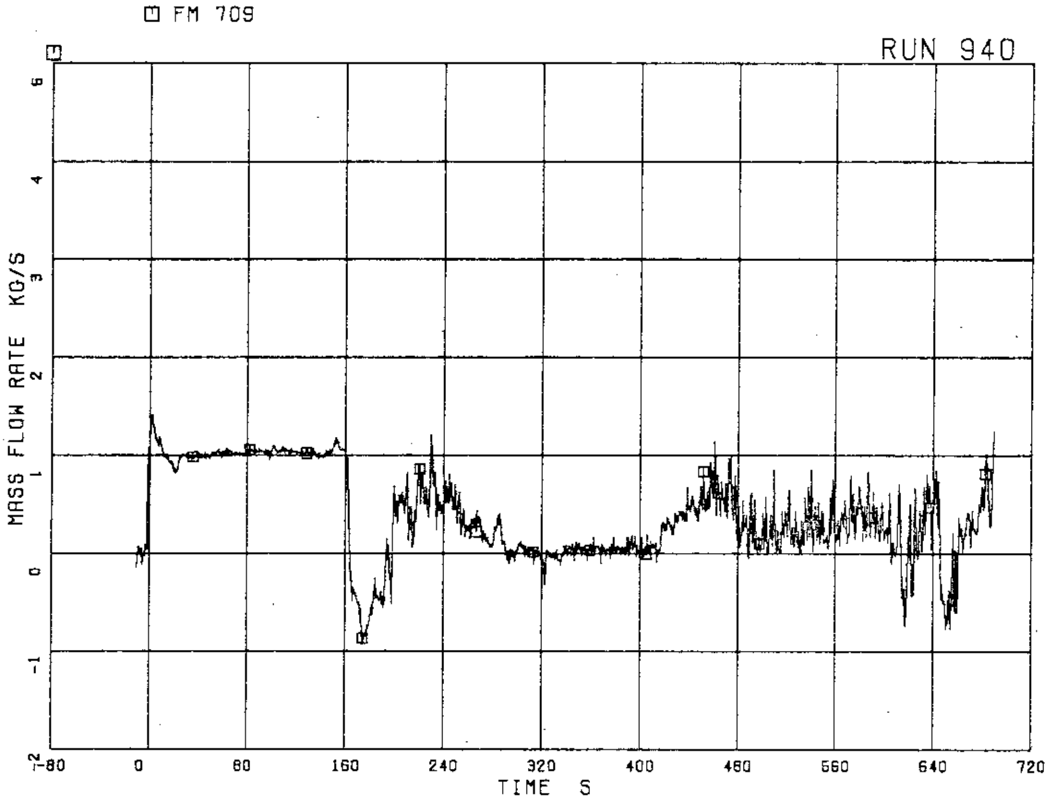

Fig. 5.3 Total discharge flow rate from break in RUN 940 (low range drag disk data)

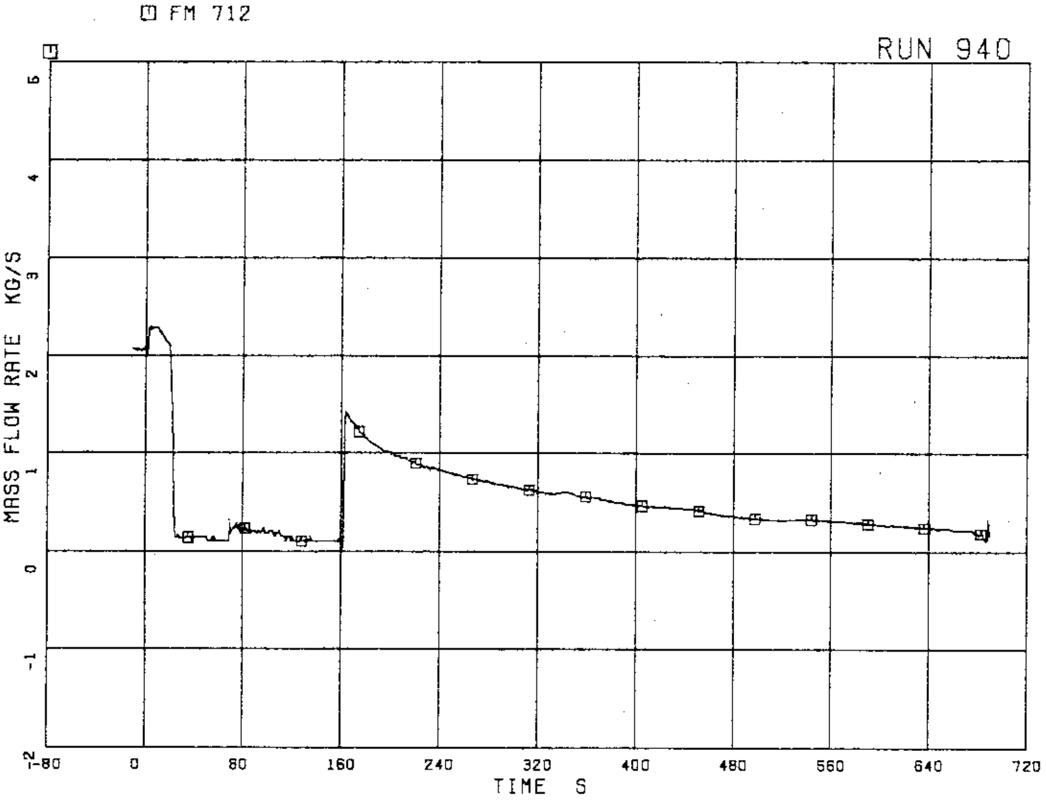

Fig. 5.4 Steam discharge flow rate through MSL in RUN 940

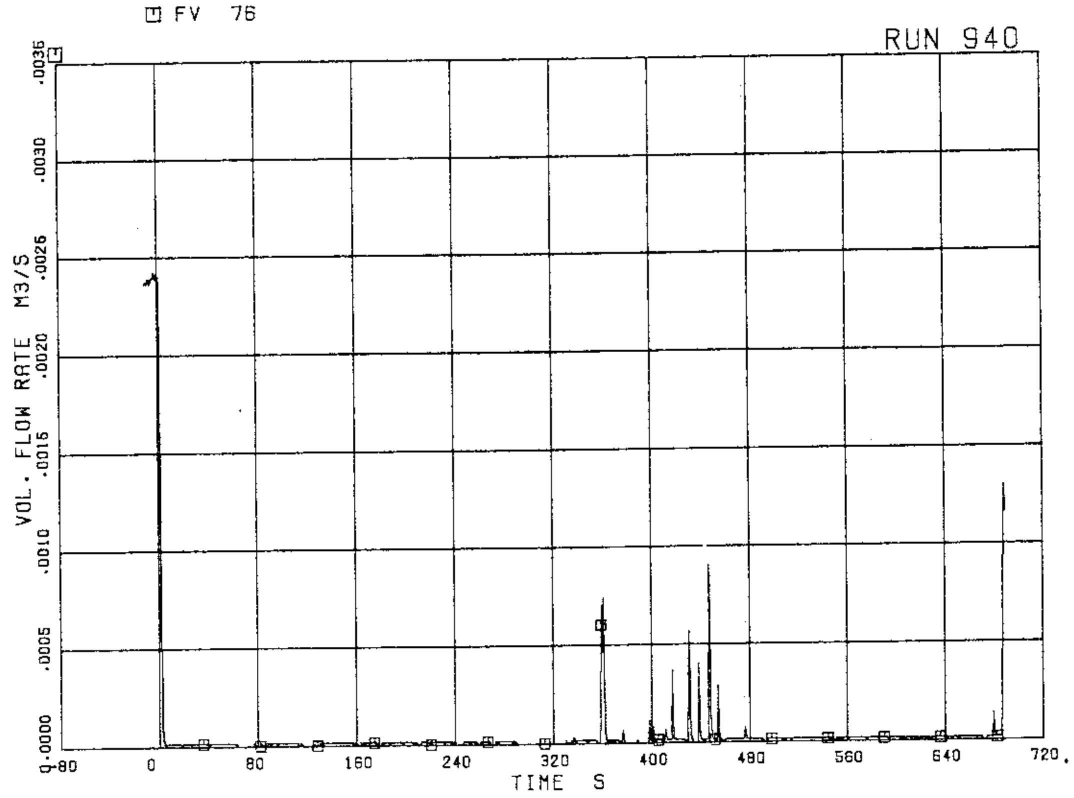

Fig. 5.5 Feedwater flow rate in RUN 940

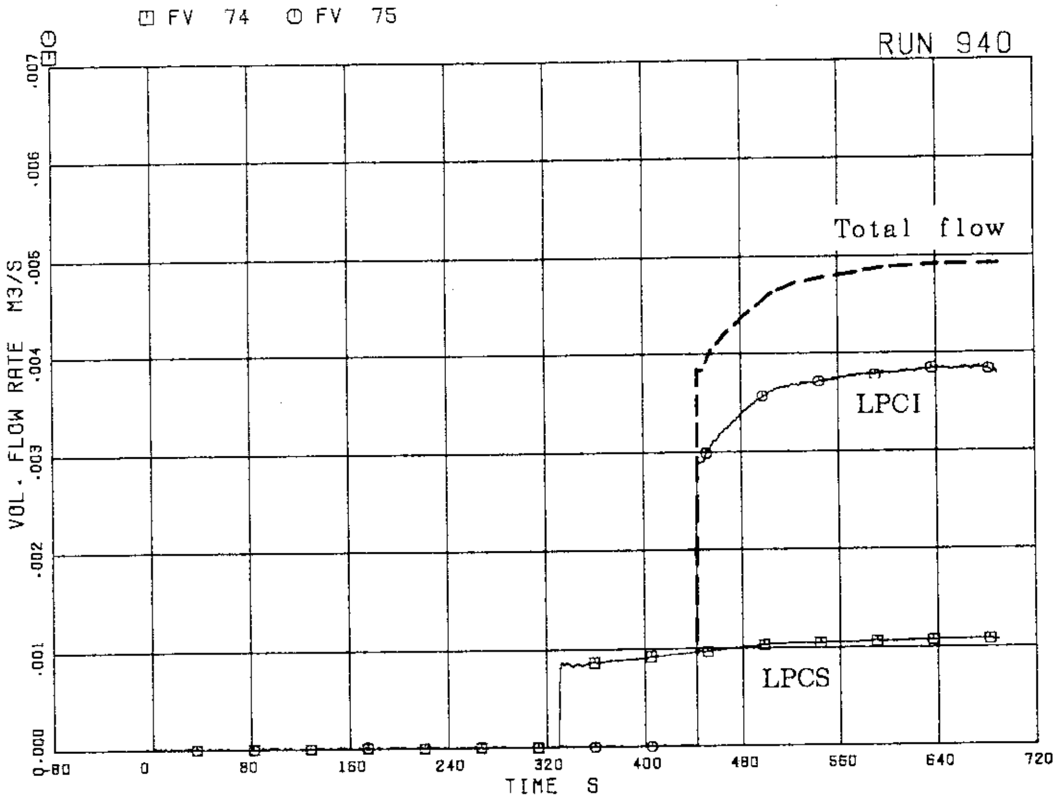

Fig. 5.6 Injection flow rates of LPCS and LPCI in RUN 940

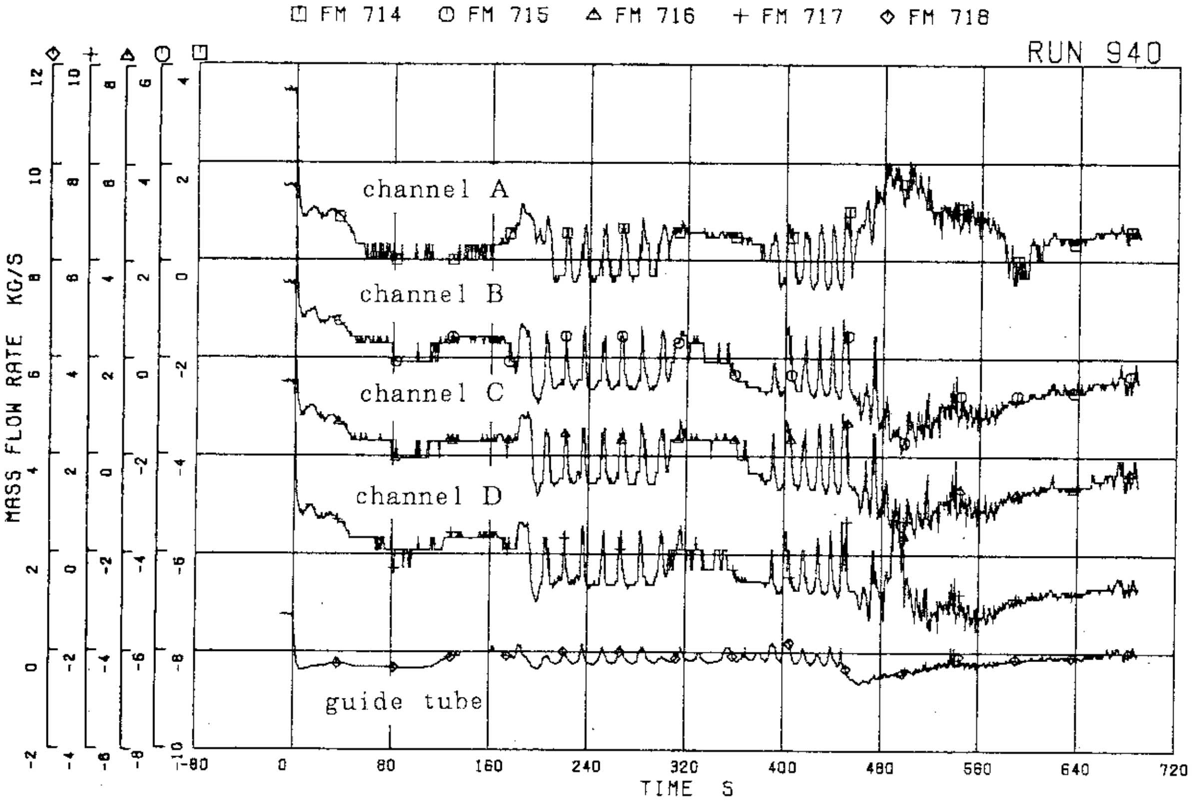

Fig. 5.7 Flow rates at core inlet orifices and bottom of guide tube in RUN 940

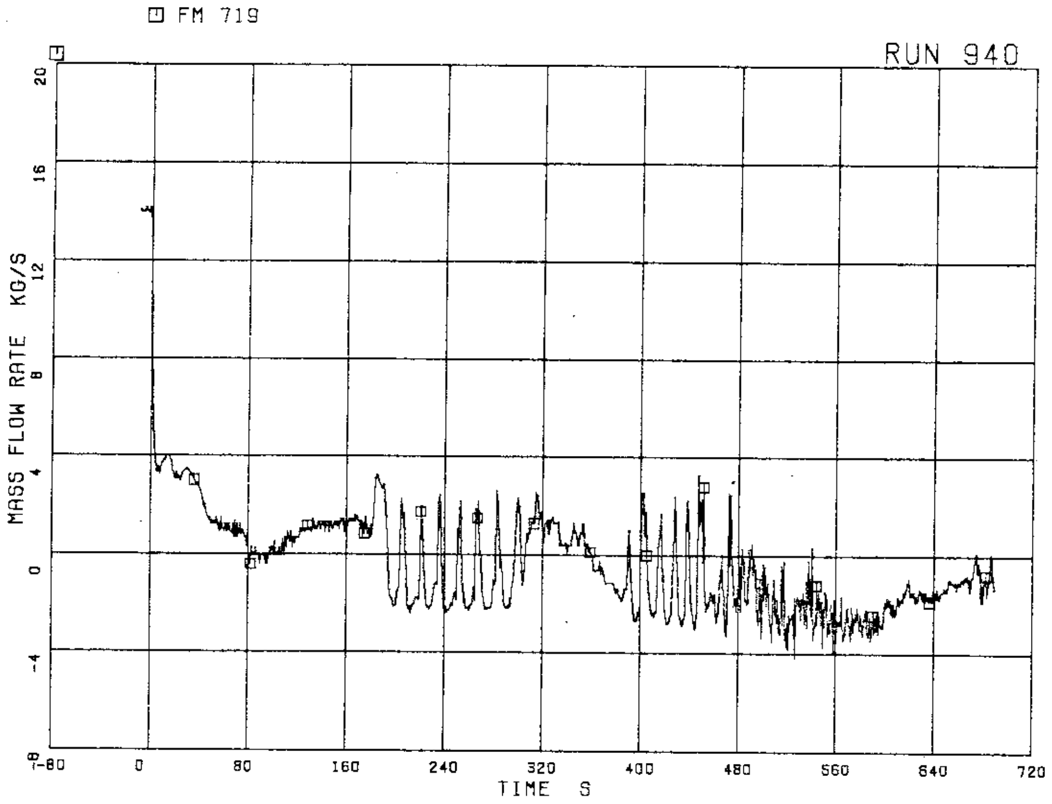

Fig. 5.8 Total channel inlet flow rate in RUN 940

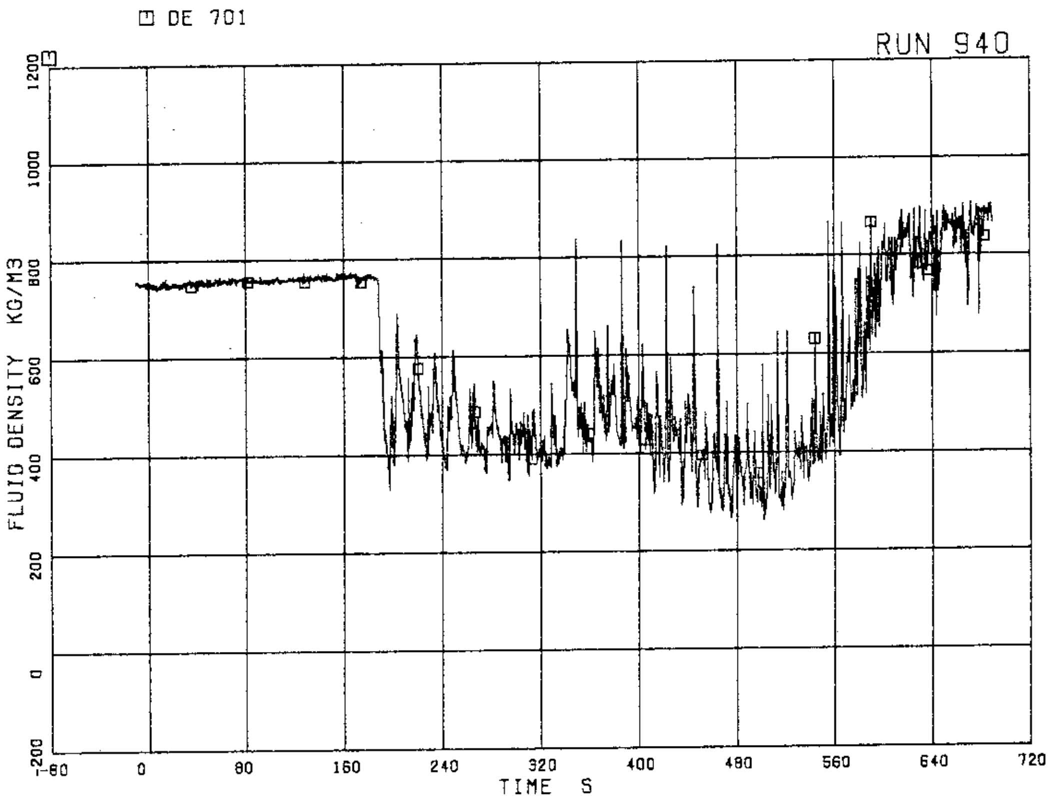

Fig. 5.9 Average density at JP-1,2 outlet in RUN 940

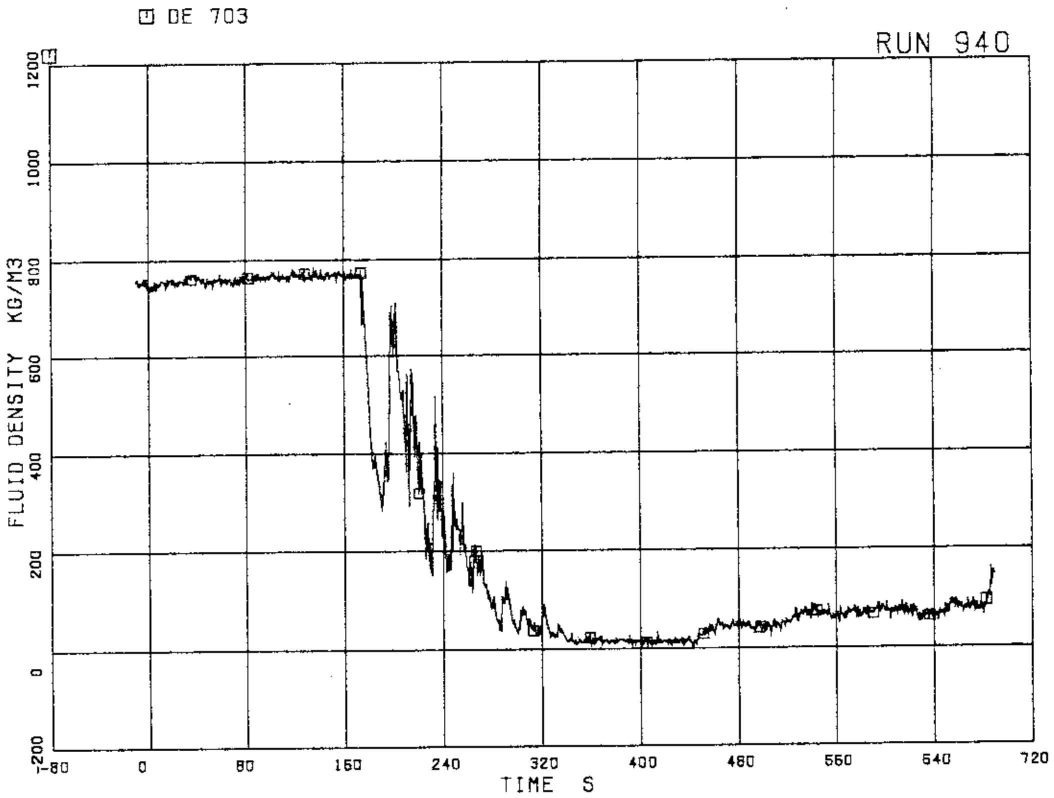

Fig. 5.10 Average density at MRP side of break in RUN 940

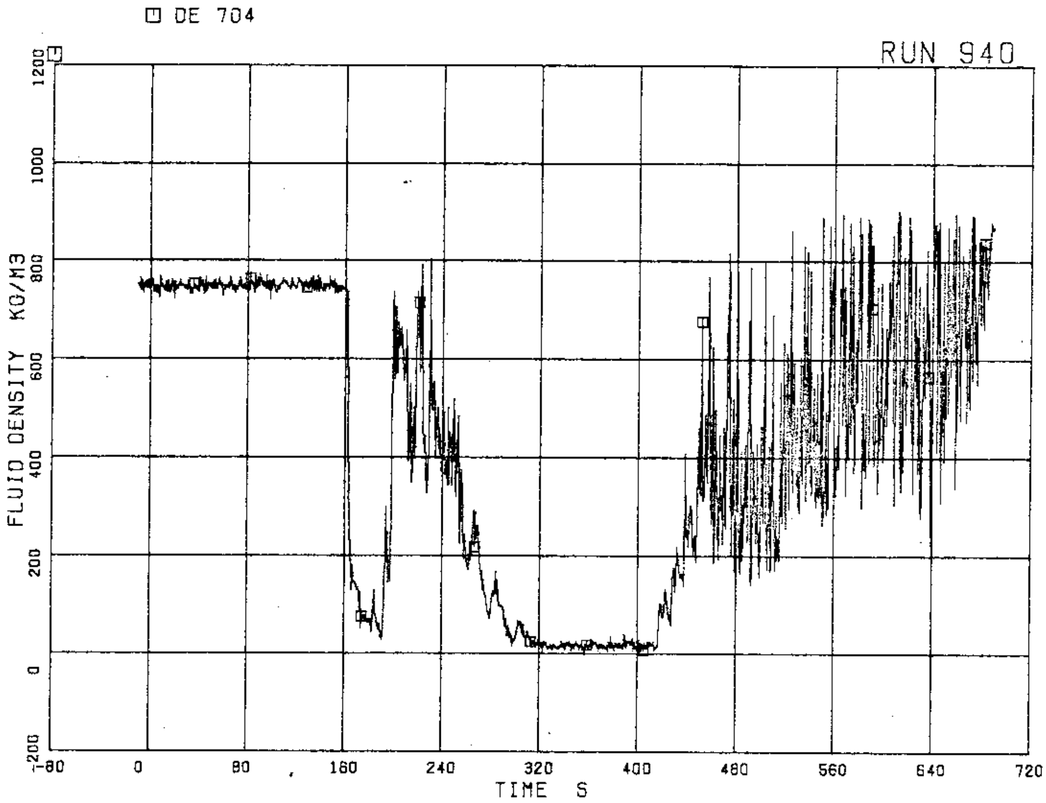

Fig. 5.11 Average density at PV side of break in RUN 940

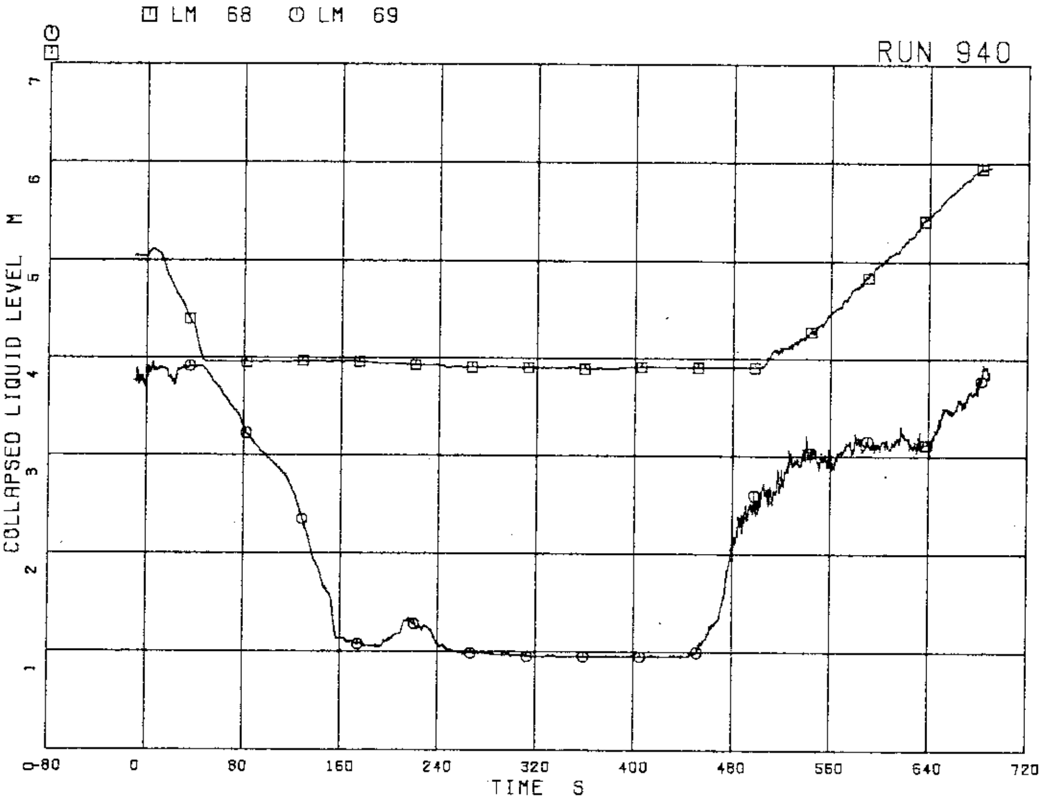

Fig. 5.12 Collapsed liquid level in downcomer in RUN 940

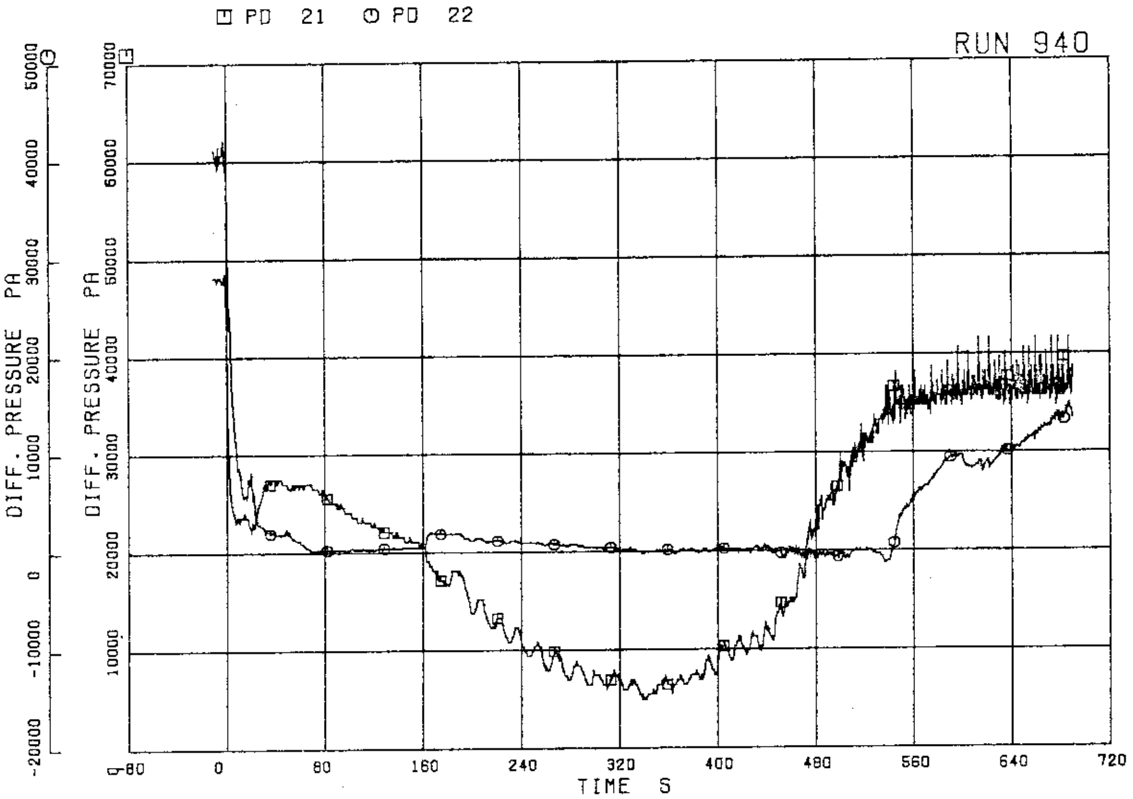

Fig. 5.13 Differential pressure between LP and UP, and between UP and steam dome in RUN 940

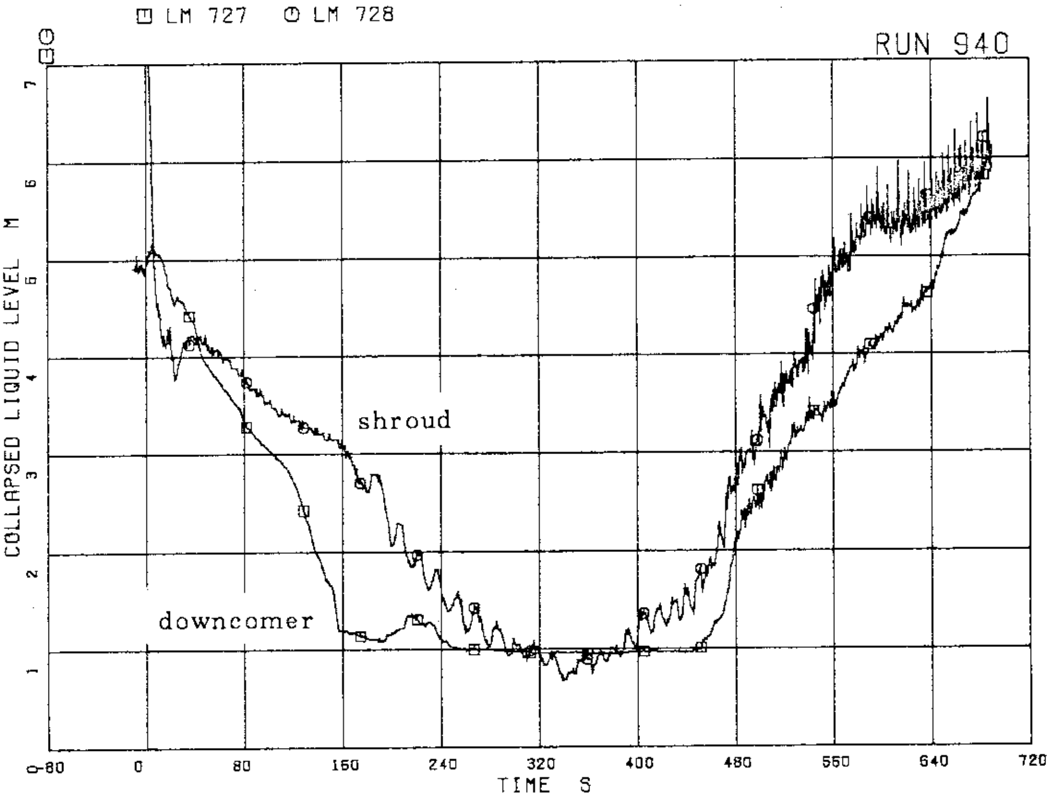

Fig. 5.14 Collapsed levels in downcomer and shroud in RUN 940

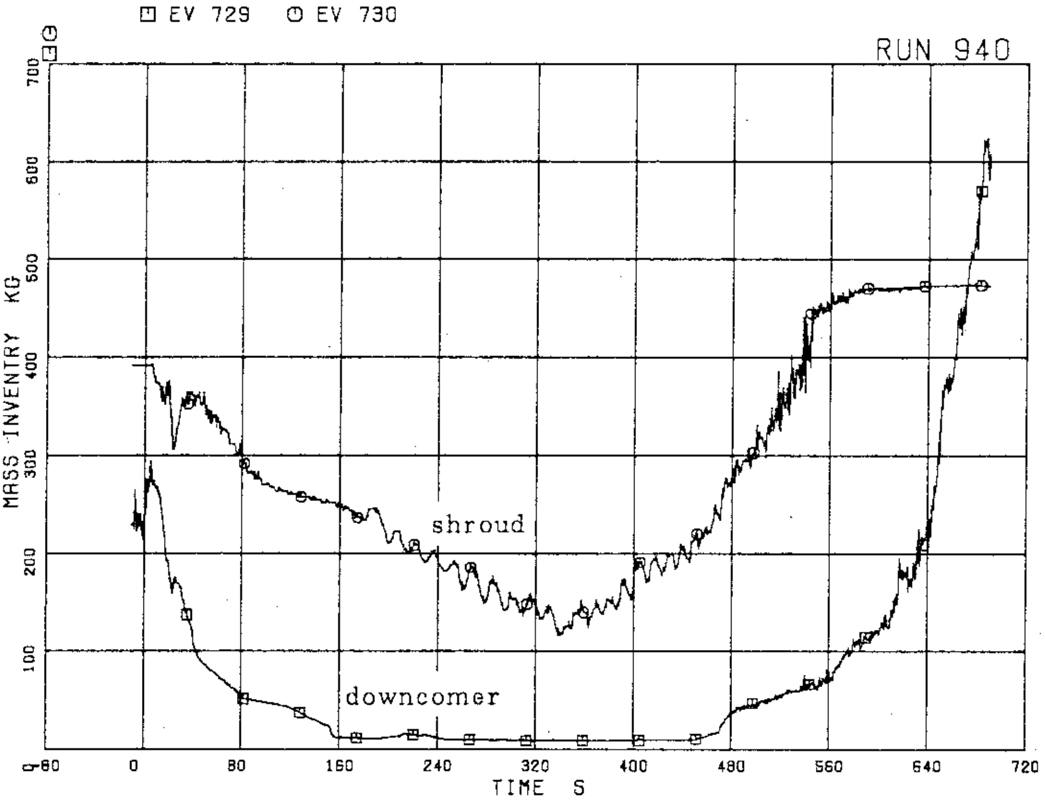

Fig. 5.15 Fluid inventory in downcomer and shroud in RUN 940

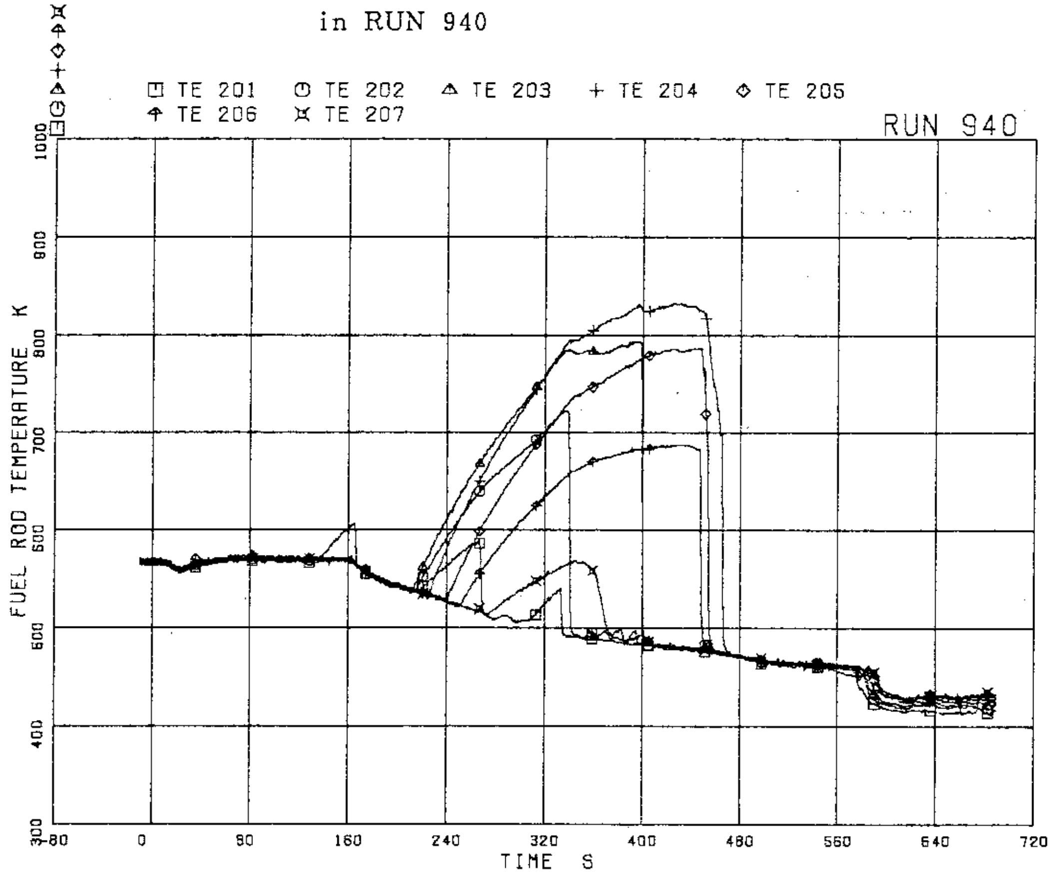

Fig. 5.16 Surface temperatures at A11 rod in RUN 940

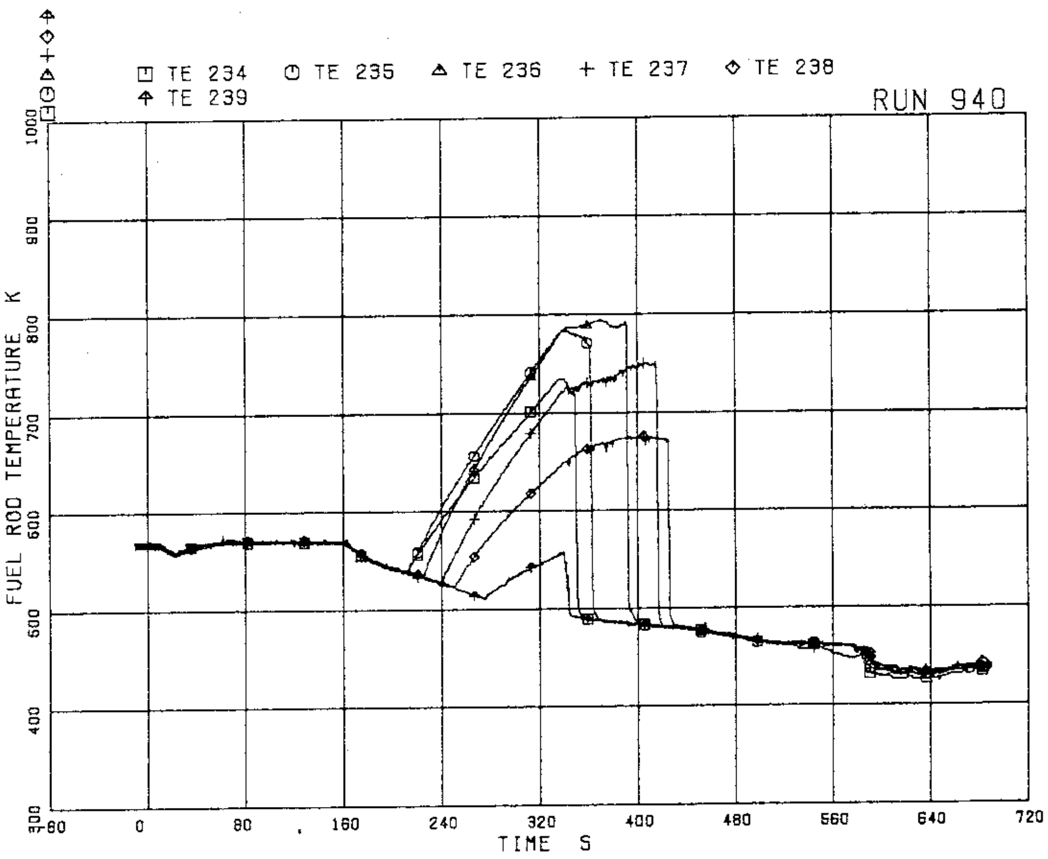

Fig. 5.17 Surface temperatures at A22 rod in RUN 940

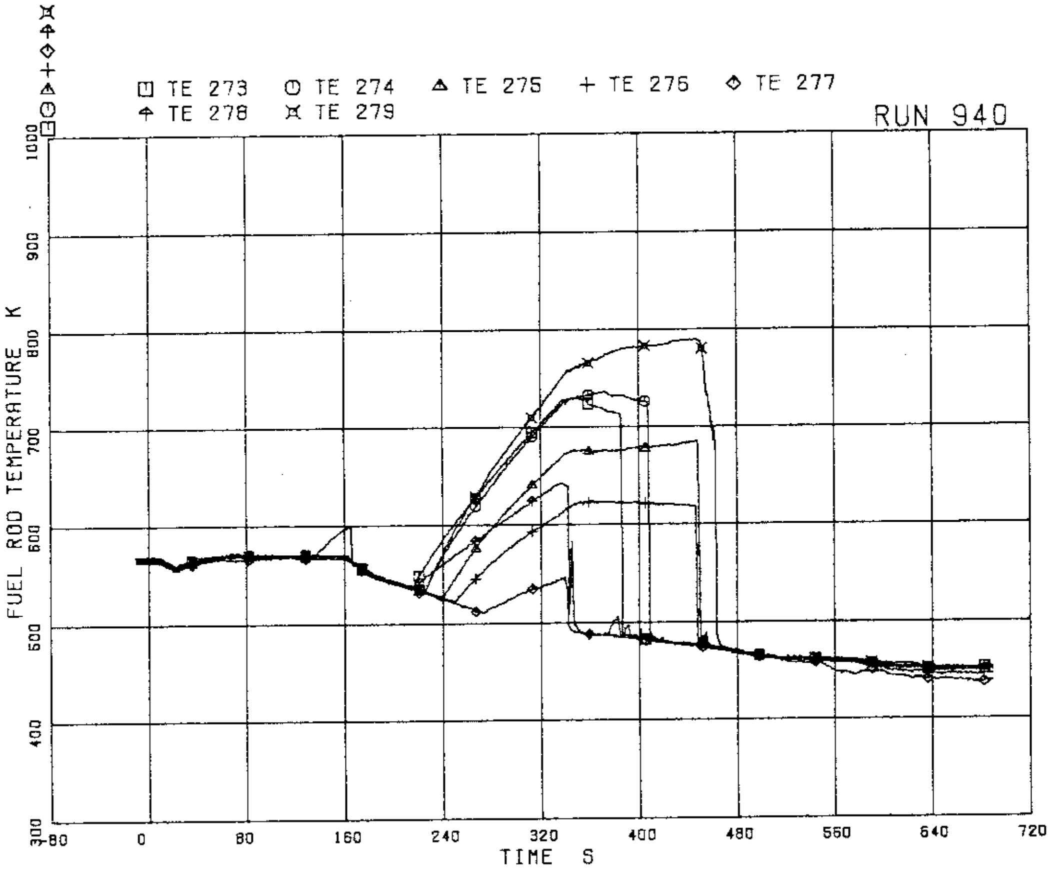

Fig. 5.18 Surface temperatures at C22 rod in RUN 940

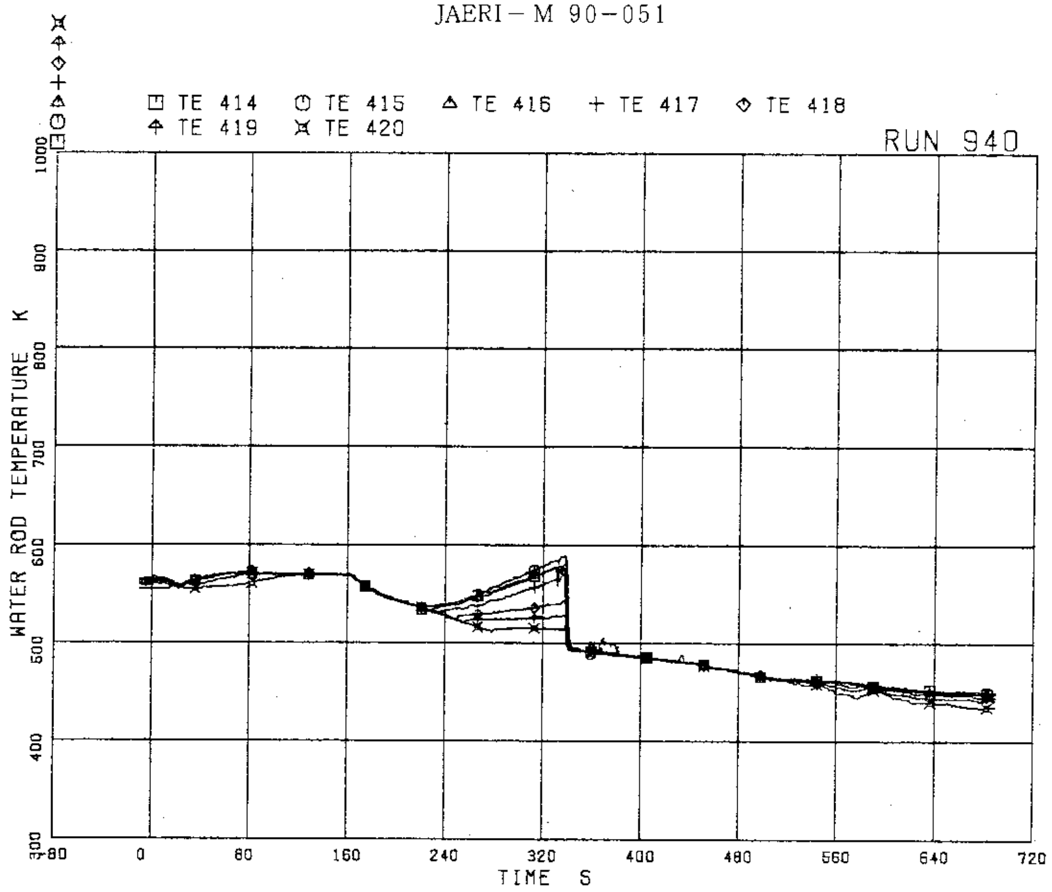

Fig. 5.19 Surface temperatures at A45 rod in RUN 940

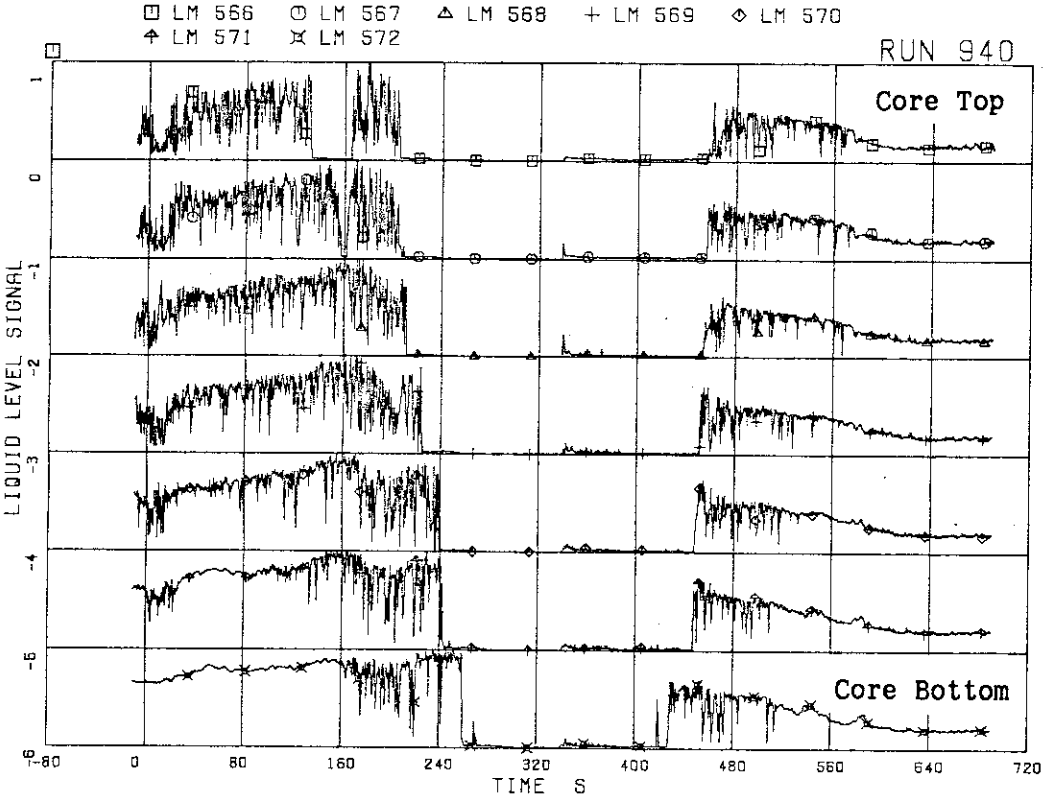

Fig. 5.20 Liquid level signals in channel box A (location A2) in RUN 940

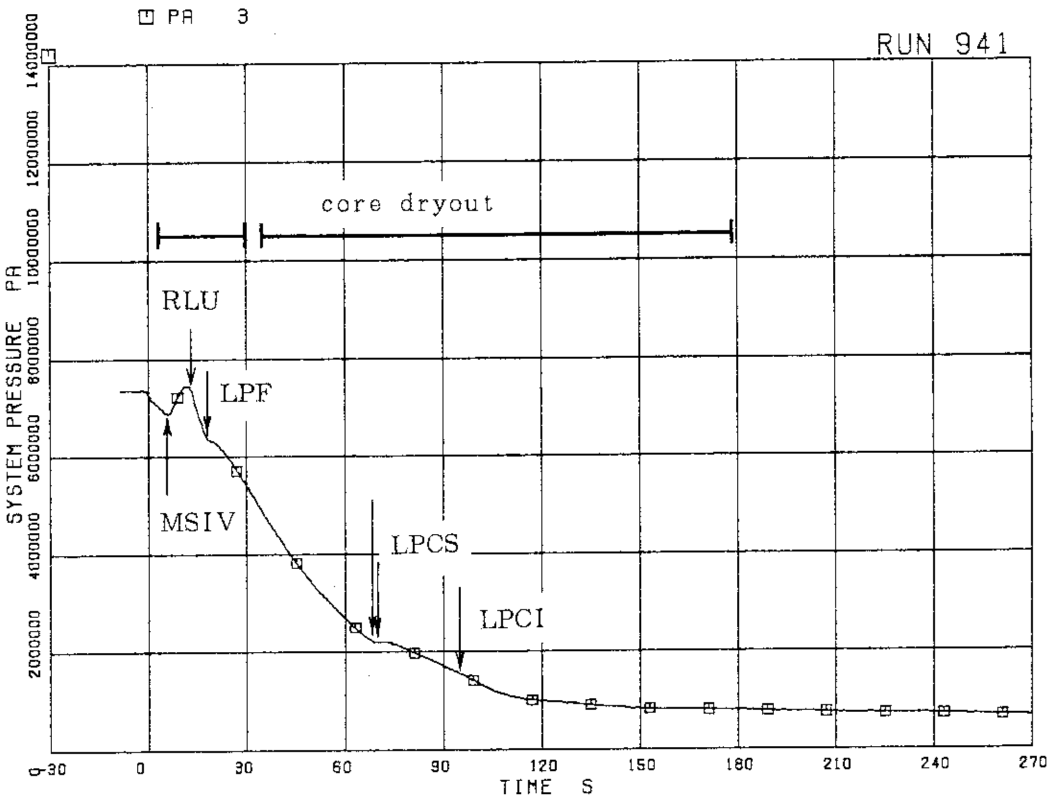

Fig. 5.21 System pressure in steam dome in RUN 941

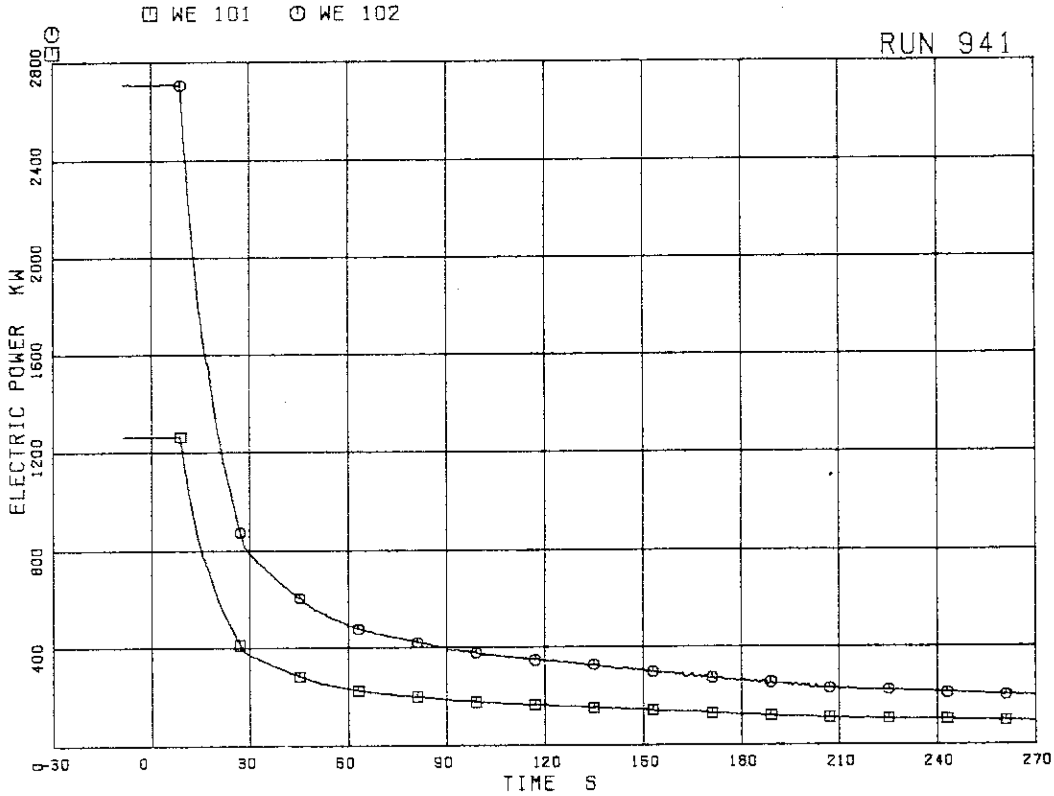

Fig. 5.22 Core power for bundle A (WE 101) and other three bundles (WE 102) in RUN 941

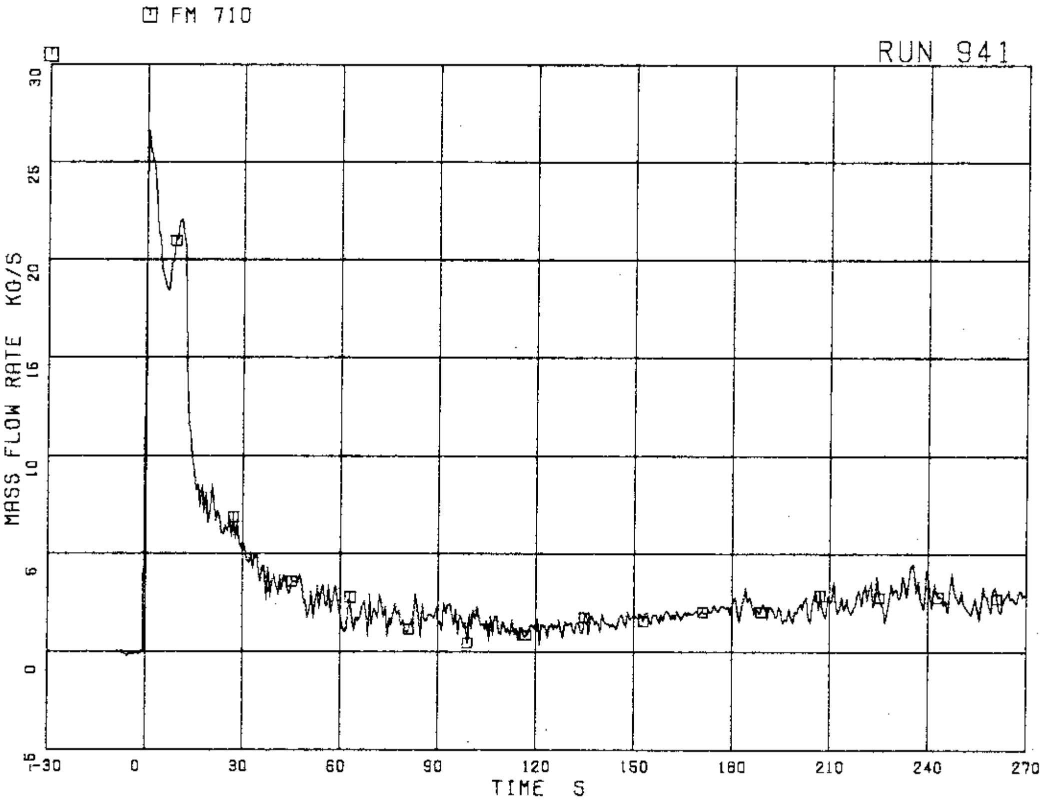

Fig. 5.23 Total discharge flow rate from break in RUN 941 (high range drag disk data)

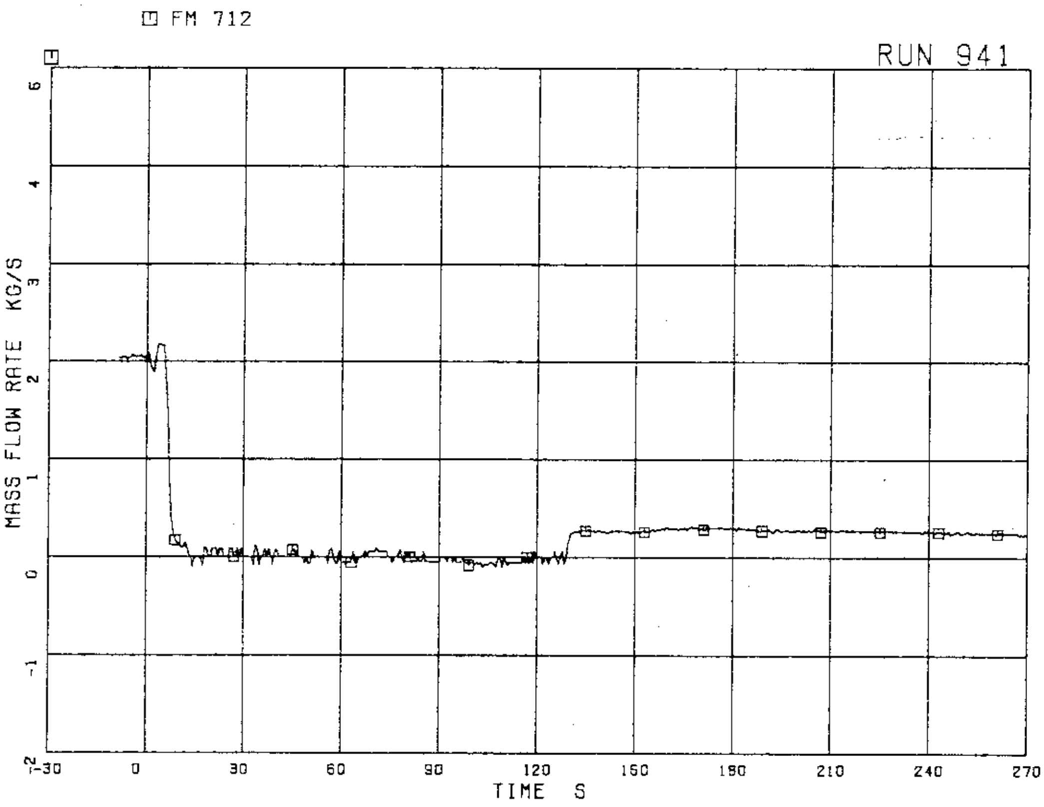

Fig. 5.24 Steam discharge flow rate through MSL in RUN 941

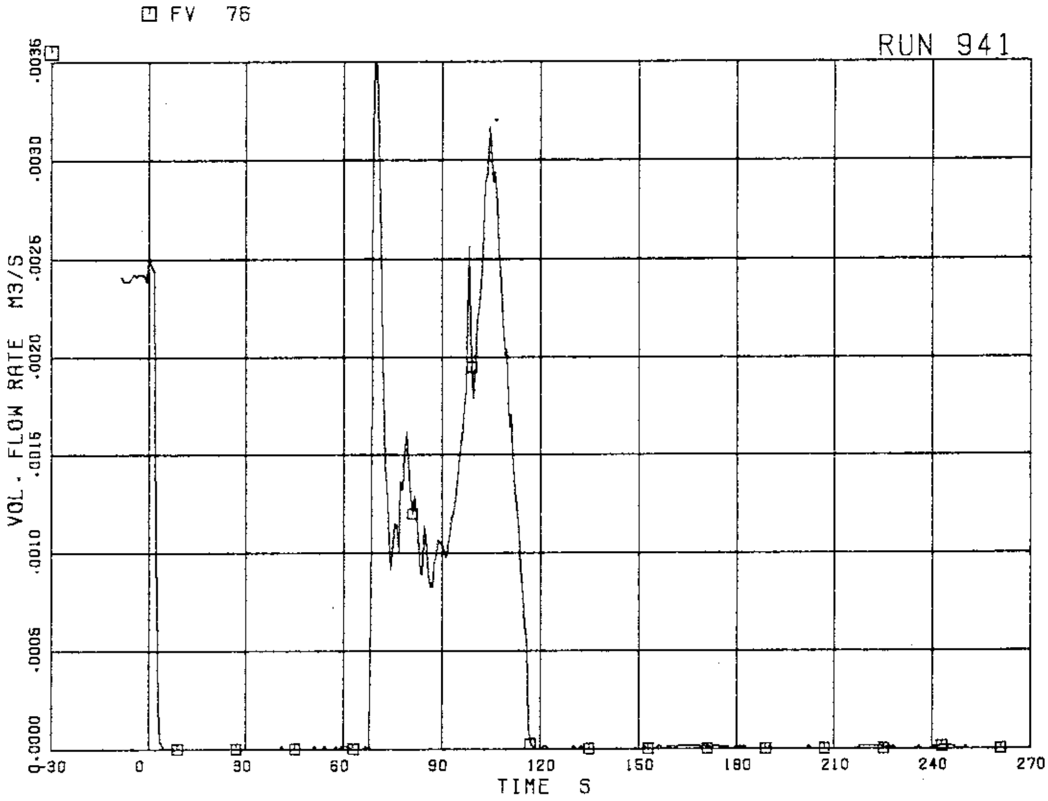

Fig. 5.25 Feedwater flow rate in RUN 941

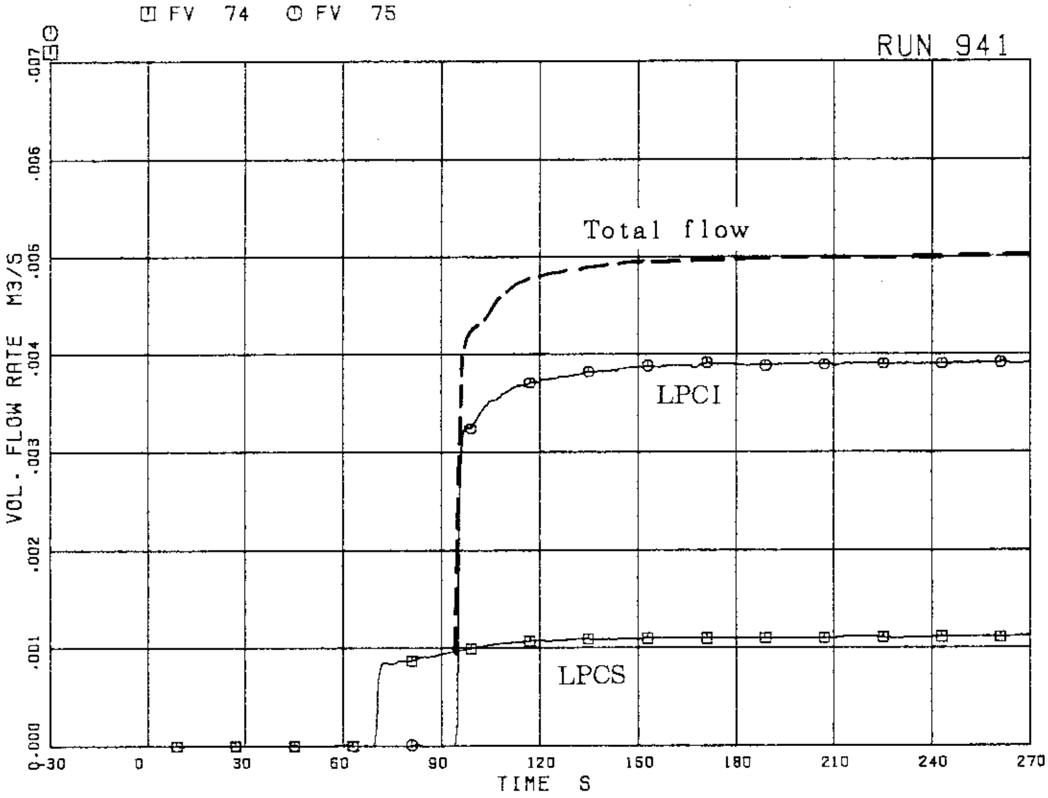

Fig. 5.26 Injection flow rates of LPCS and LPCI in RUN 941

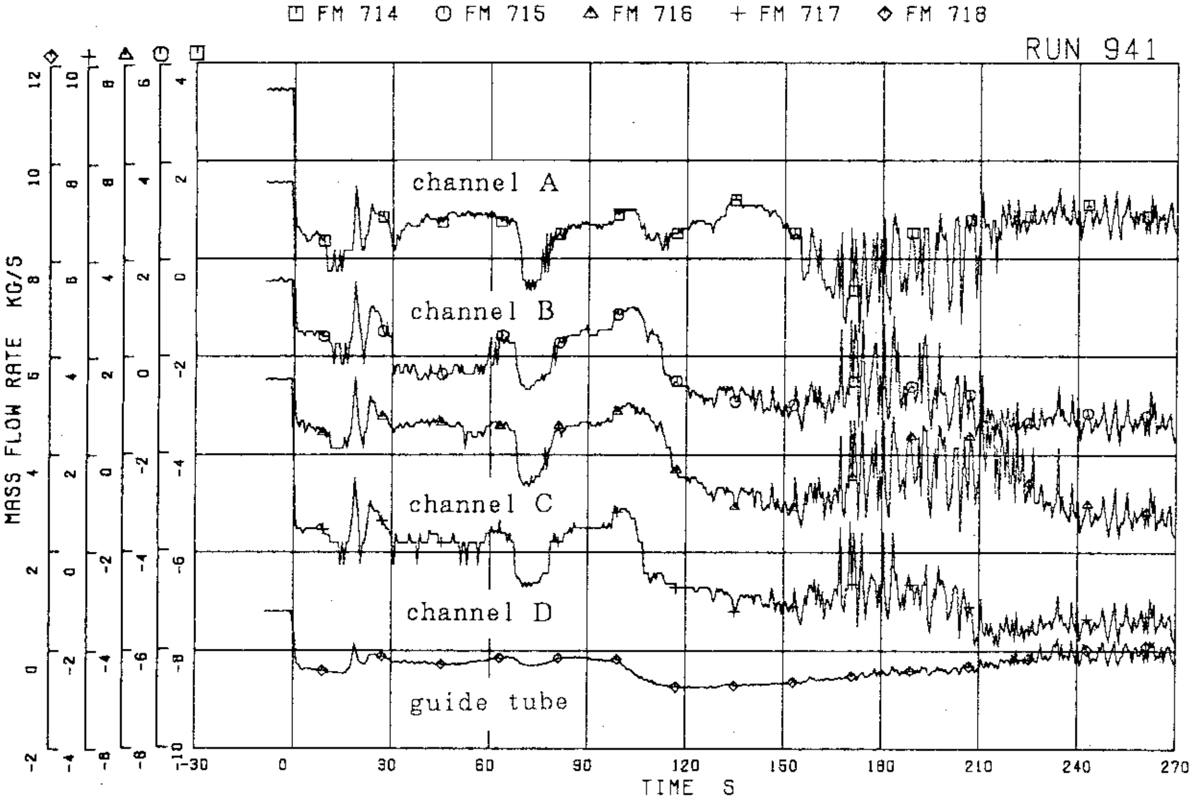

Fig. 5.27 Flow rates at core inlet orifices and bottom of guide tube in RUN 941

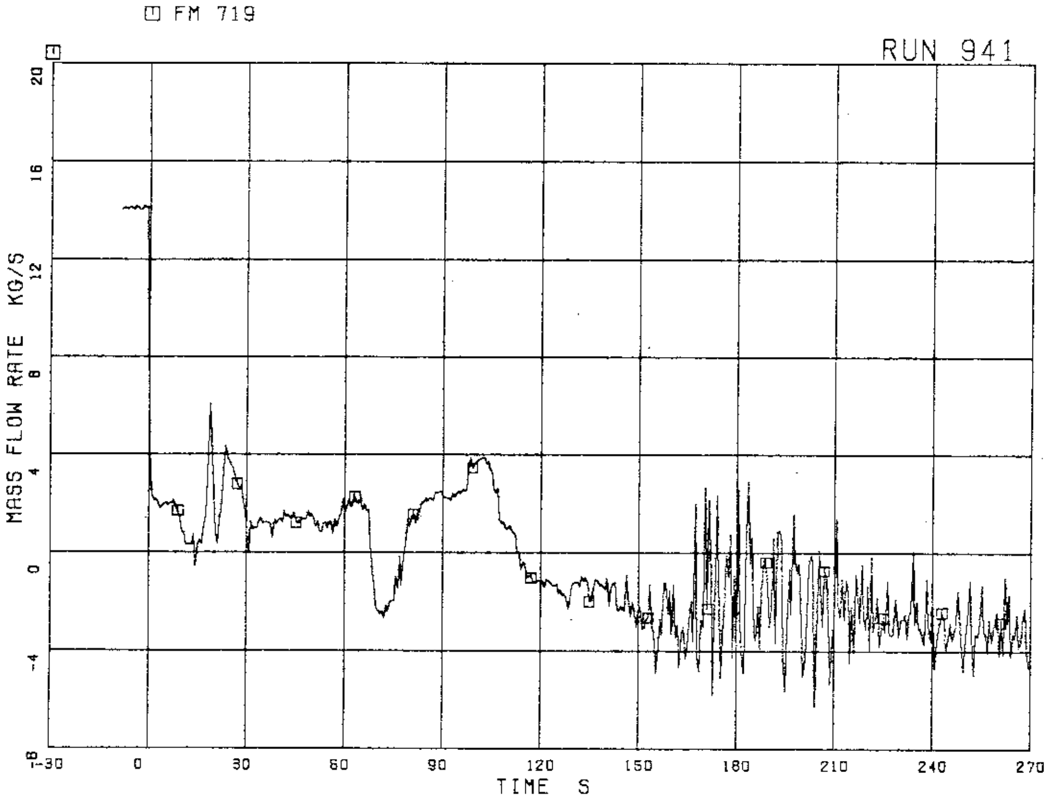

Fig. 5.28 Total channel inlet flow rate in RUN 941

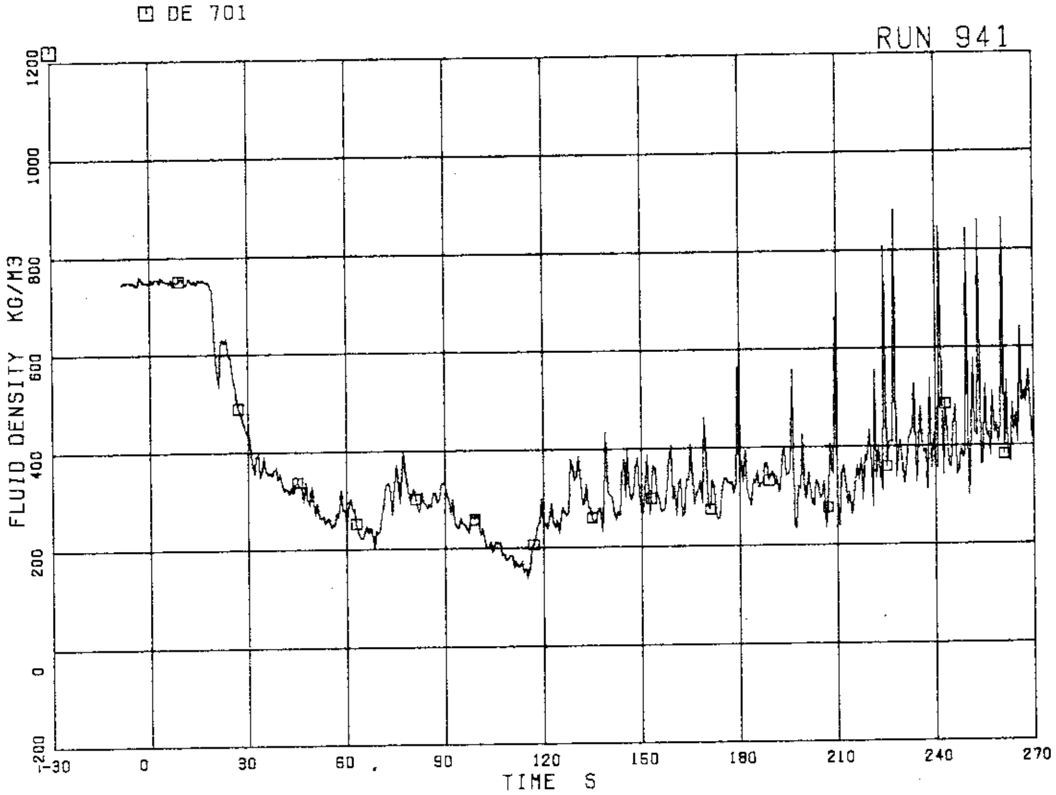

Fig. 5.29 Average density at JP-1,2 outlet in RUN 941

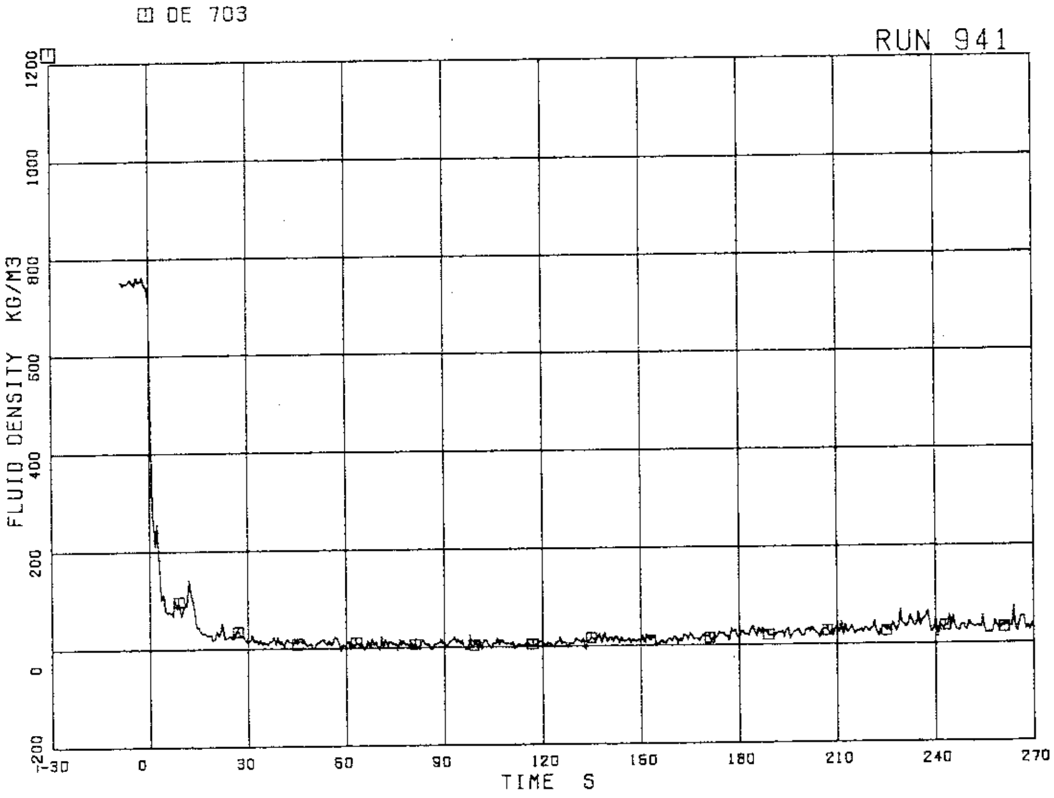

Fig. 5.30 Average density at MRP side of break in RUN 941

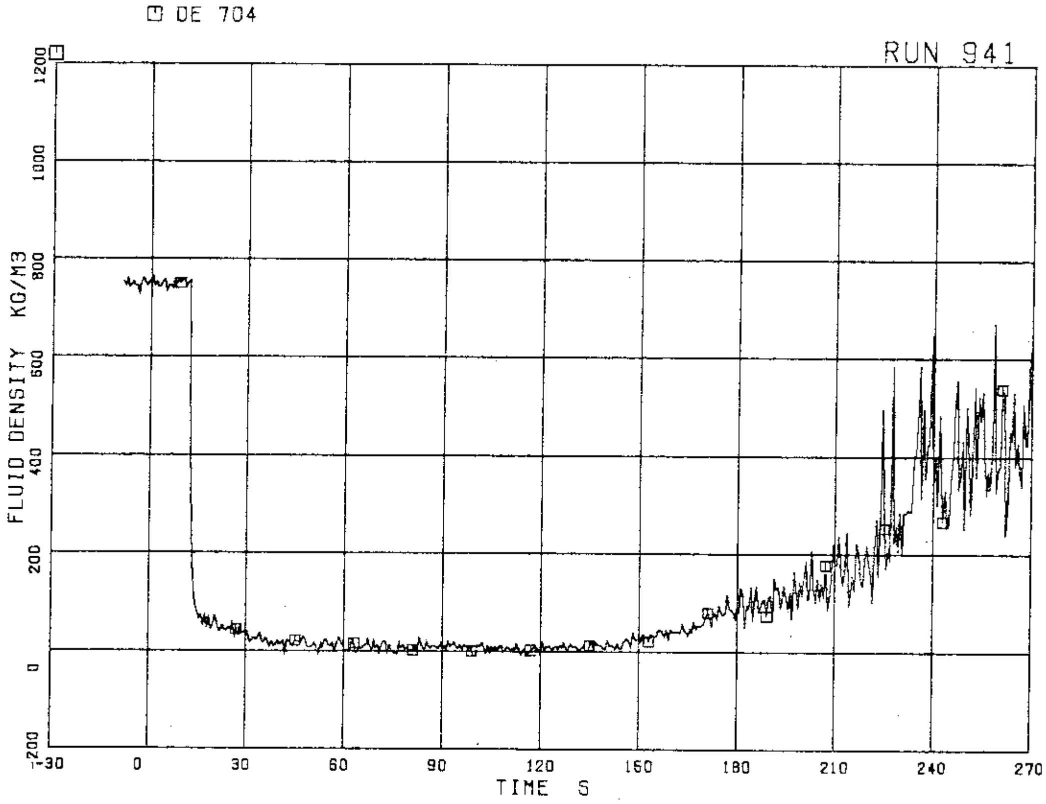

Fig. 5.31 Average density at PV side of break in RUN 941

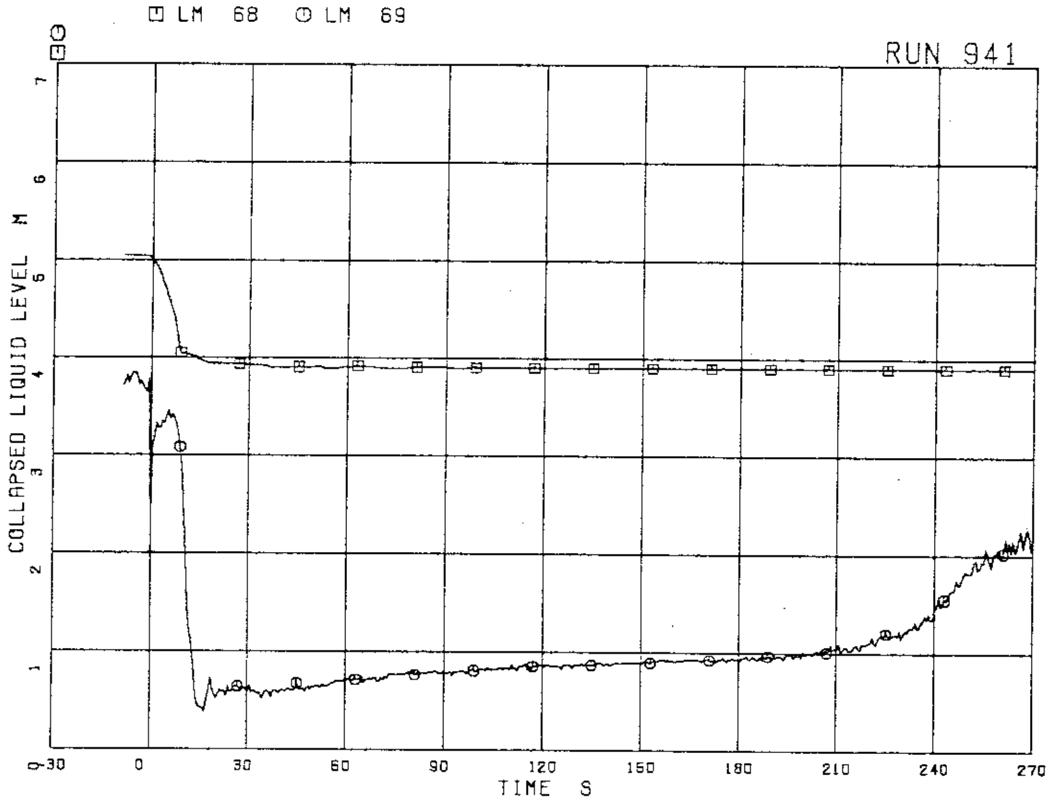

Fig. 5.32 Collapsed liquid level in downcomer in RUN 941

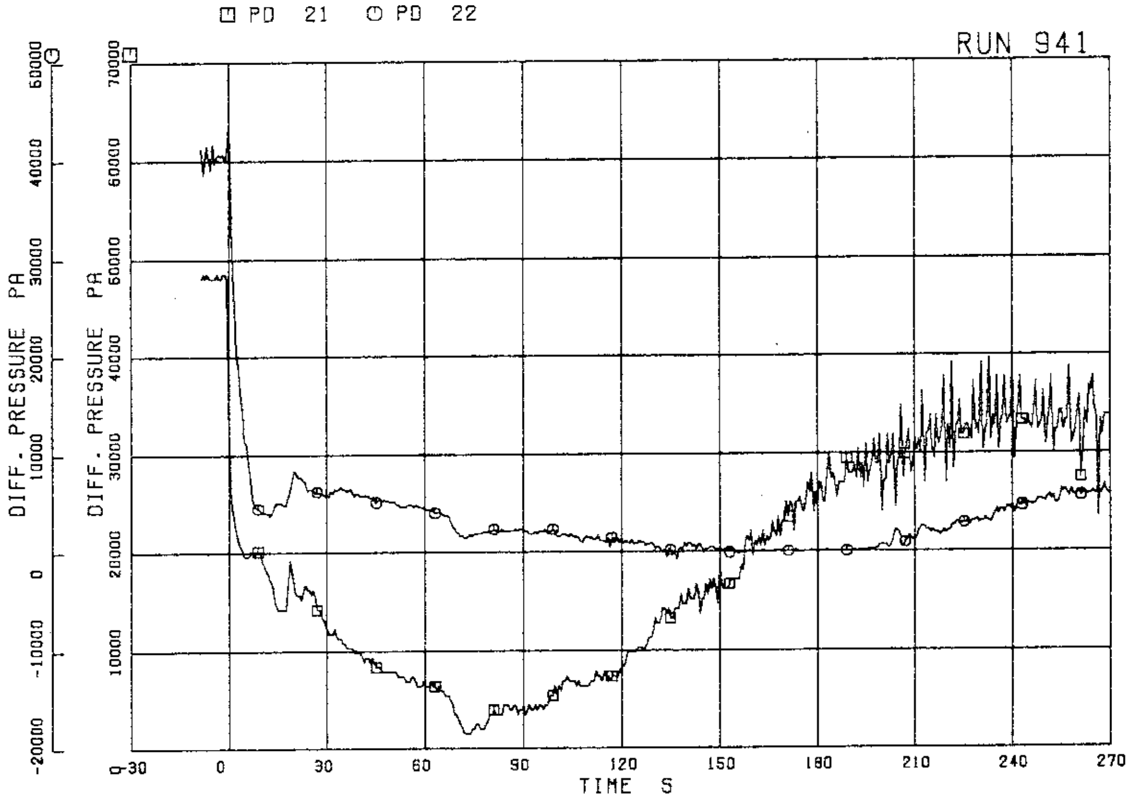

Fig. 5.33 Differential pressure between LP and UP, and between UP and steam dome in RUN 941

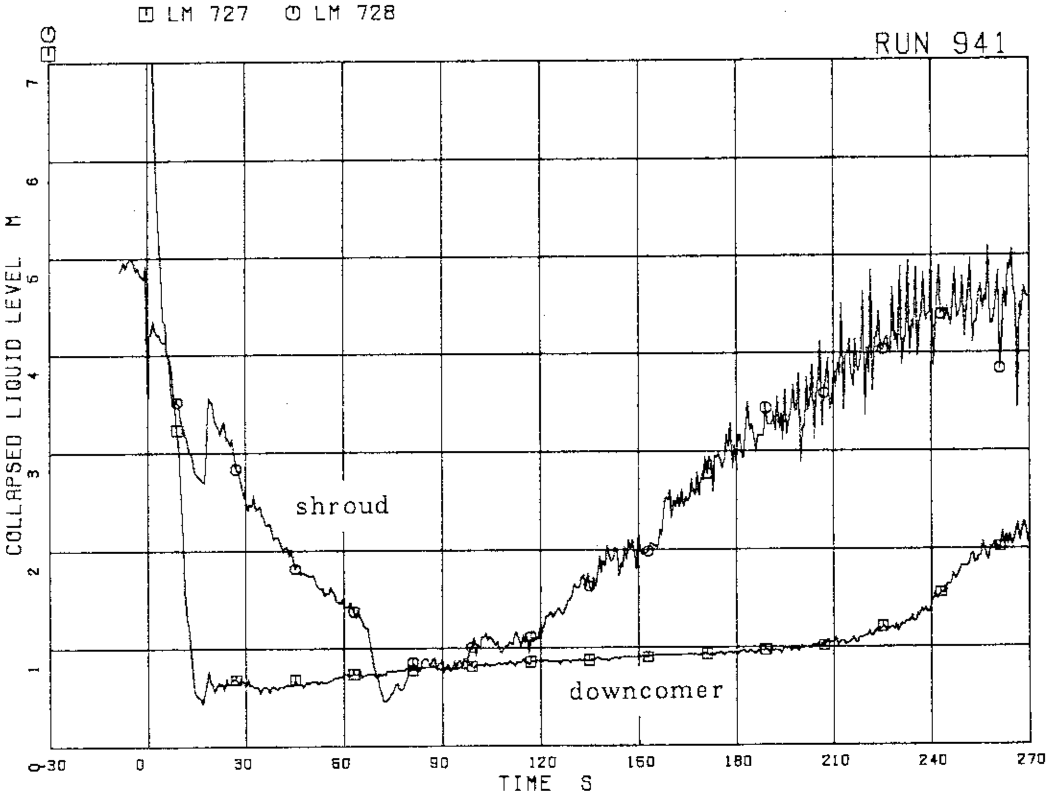

Fig. 5.34 Collapsed levels in downcomer and shroud in RUN 941

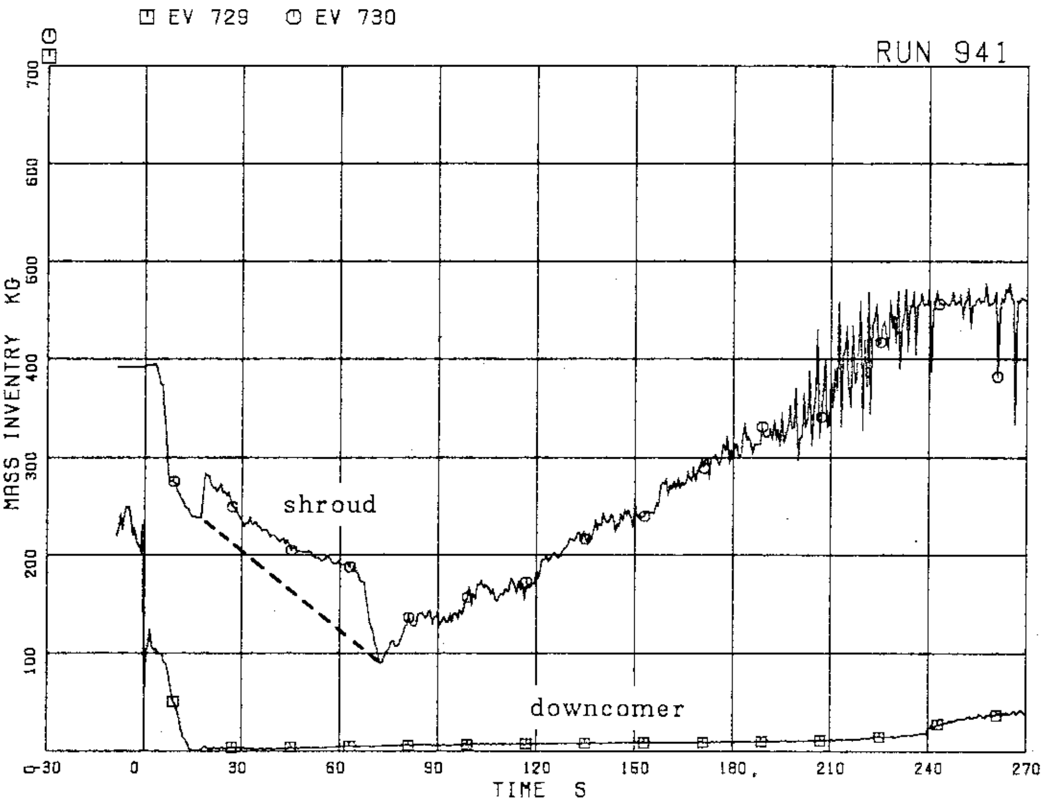

Fig. 5.35 Fluid inventory in downcomer and shroud in RUN 941

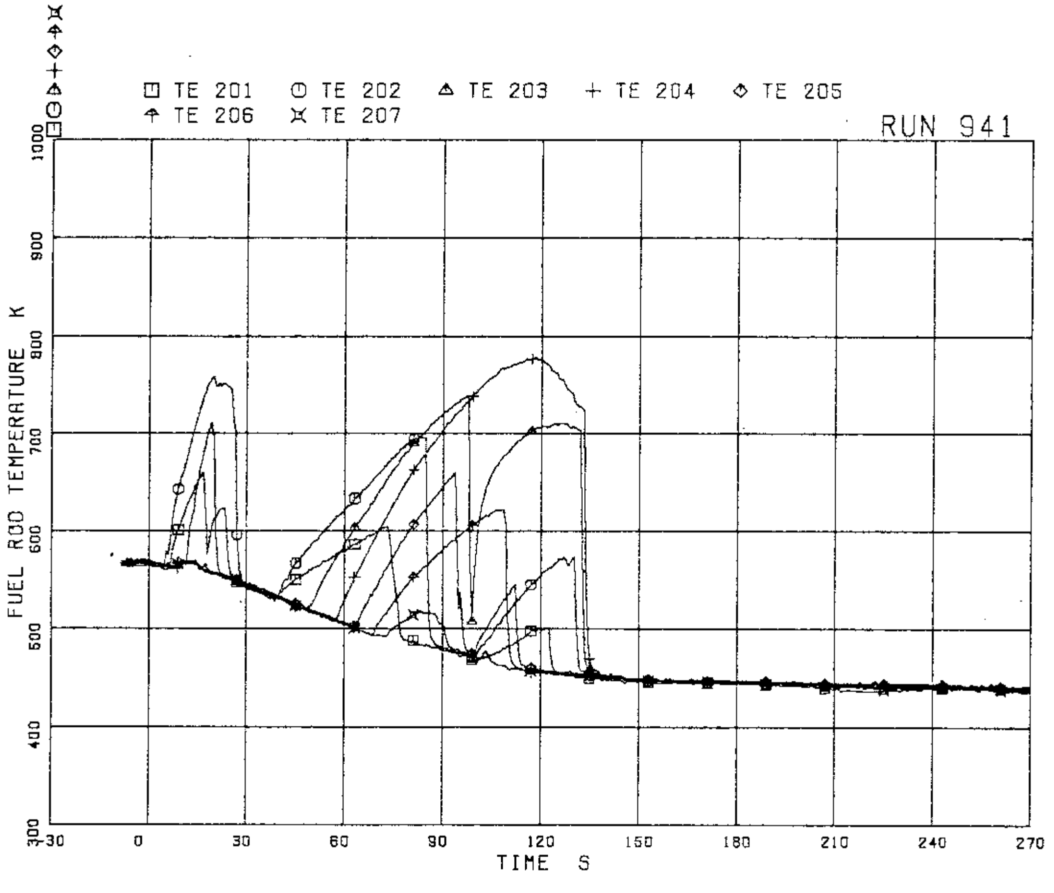

Fig. 5.36 Surface temperatures at A11 rod in RUN 941

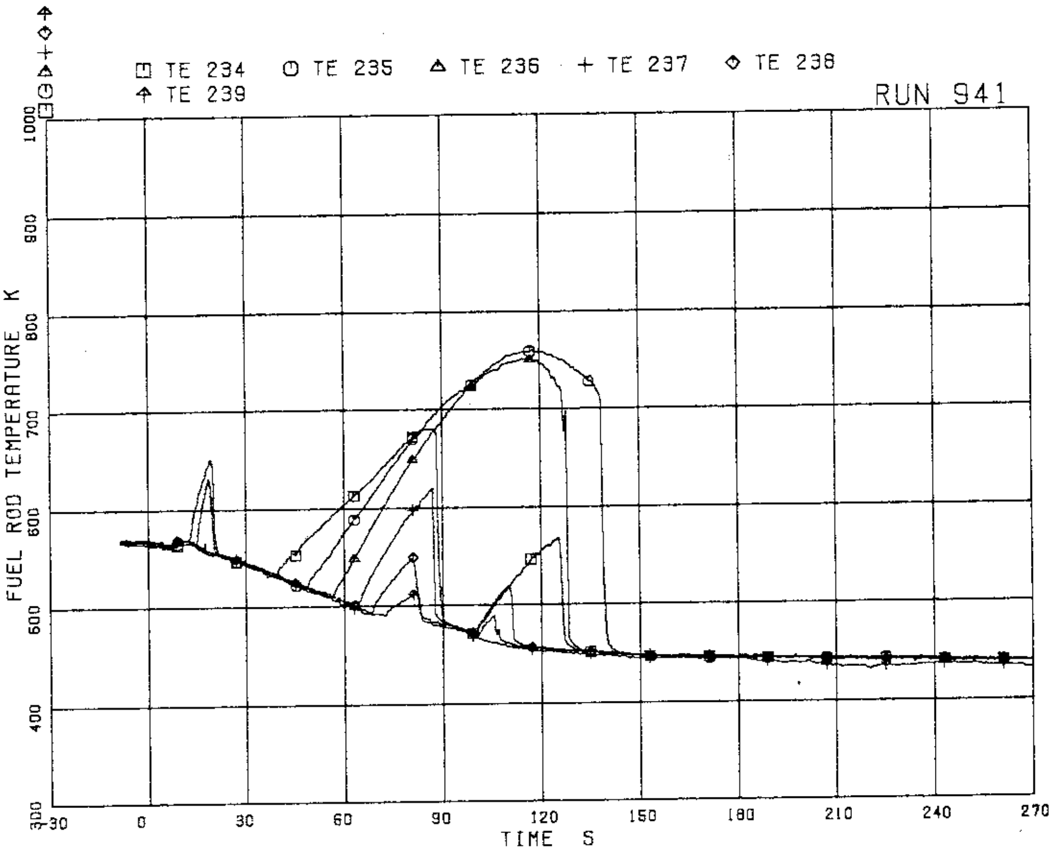

Fig. 5.37 Surface temperatures at A22 rod in RUN 941

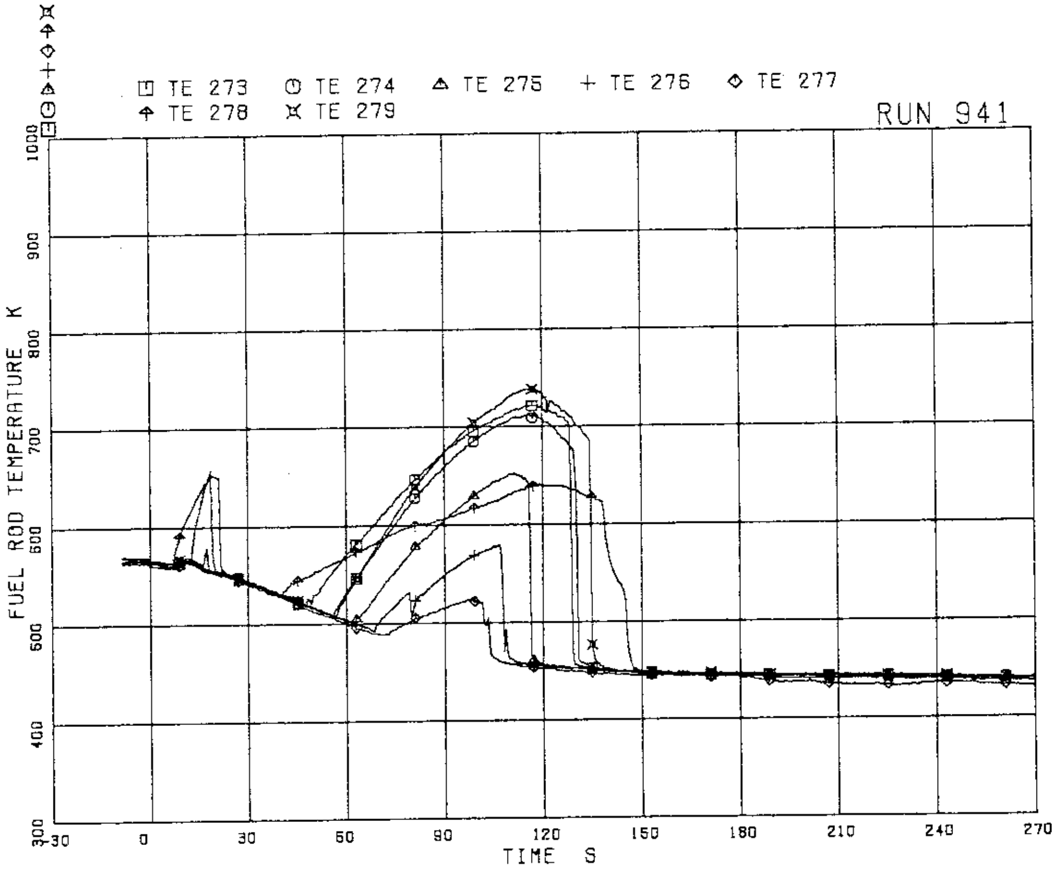

Fig. 5.38 Surface temperatures at C22 rod in RUN 941

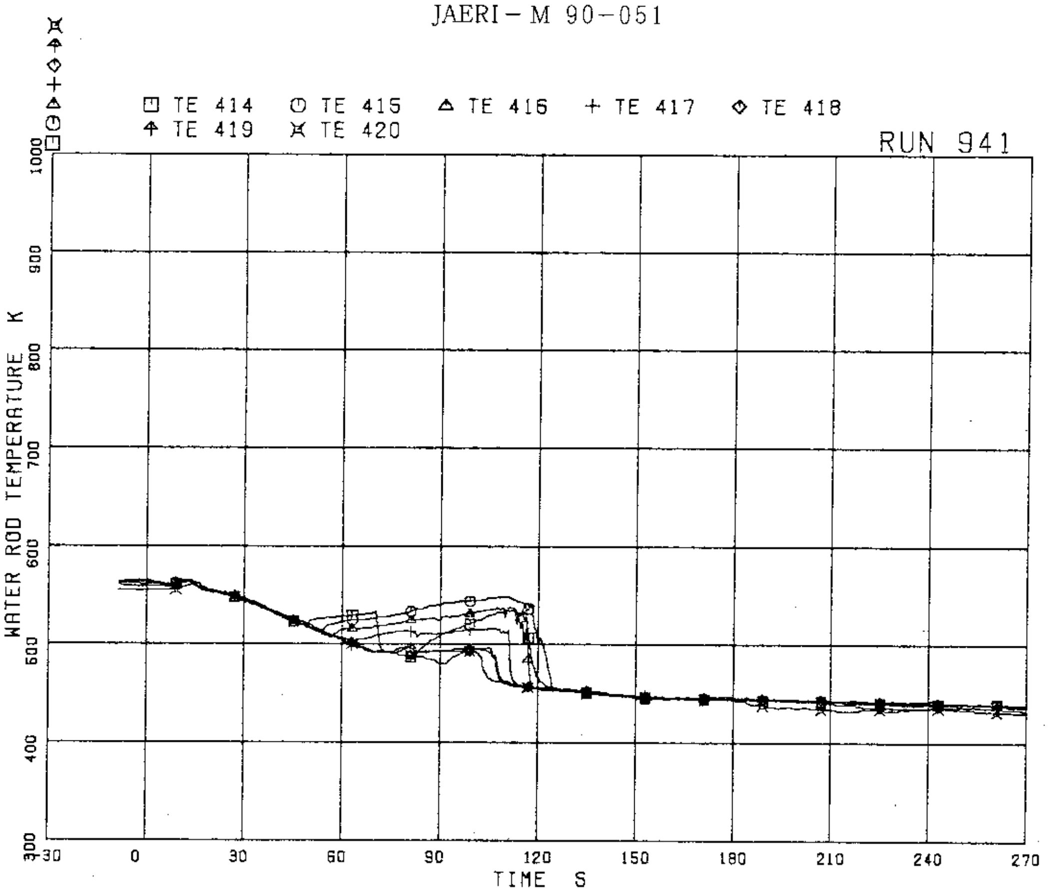

Fig. 5.39 Surface temperatures at A45 rod in RUN 941

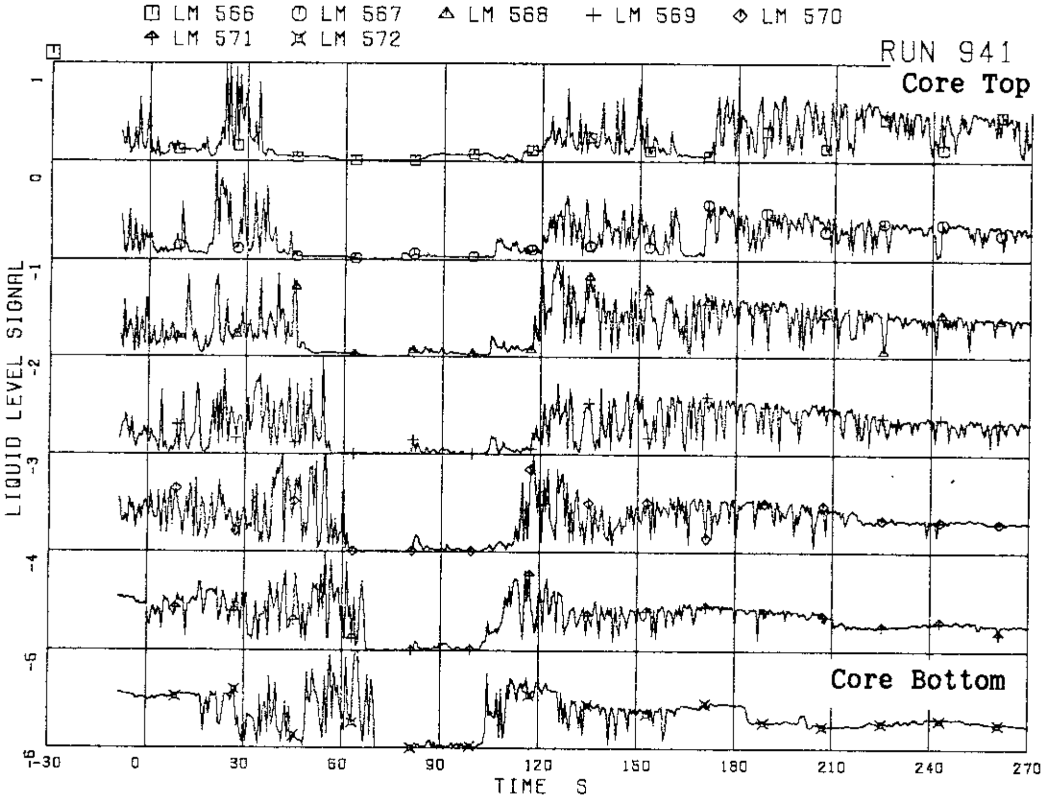

Fig. 5.40 Liquid level signals in channel box A (location A2) in RUN 941

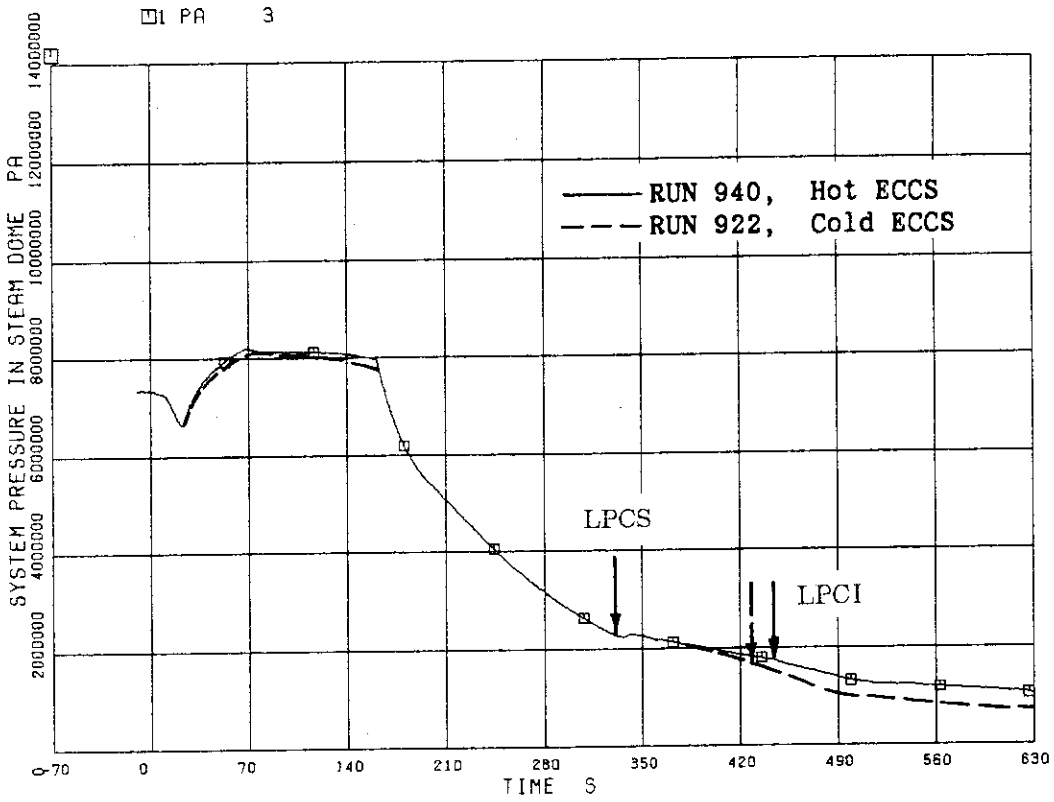

Fig. 6.1 Effect of hot ECC injection on system pressure in 5% small-break tests

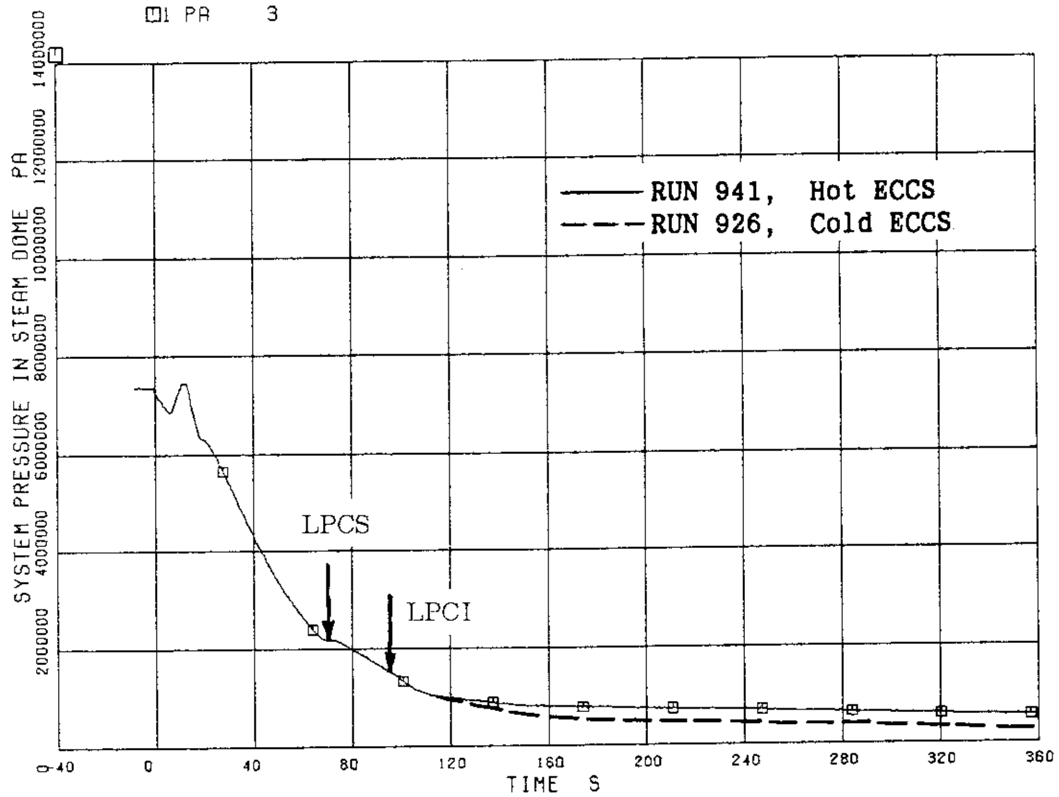

Fig. 6.2 Effect of hot ECC injection on system pressure in 200% break tests

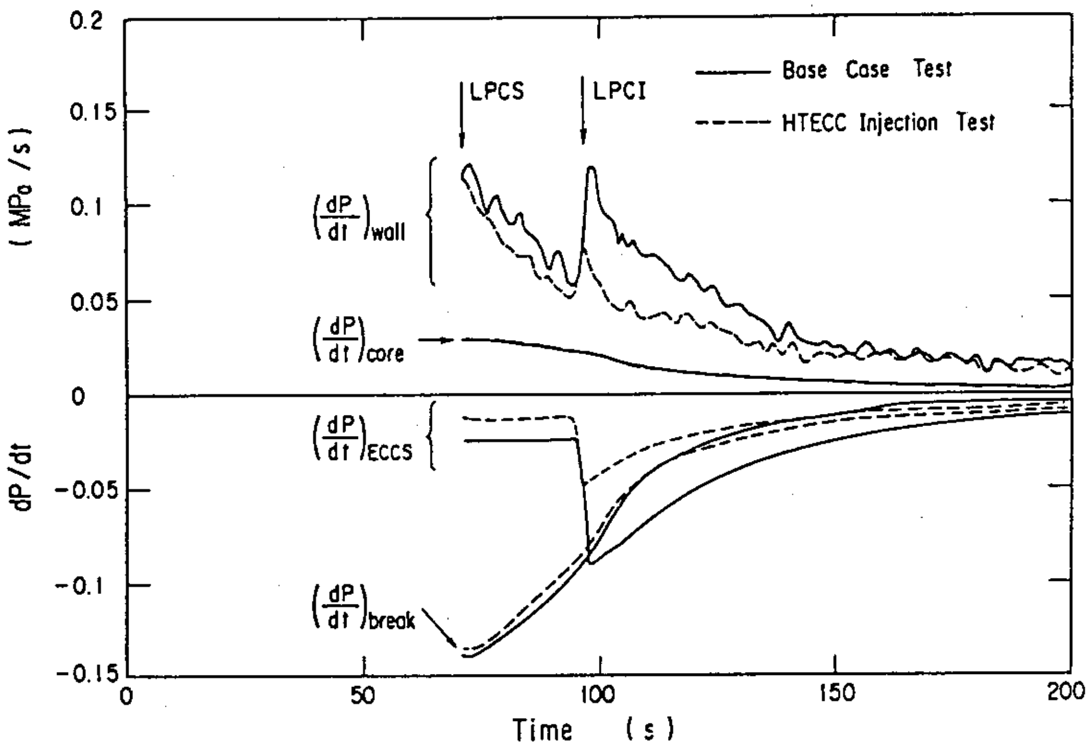

Fig. 6.3 Previous study on depressurization effects in 200% break tests

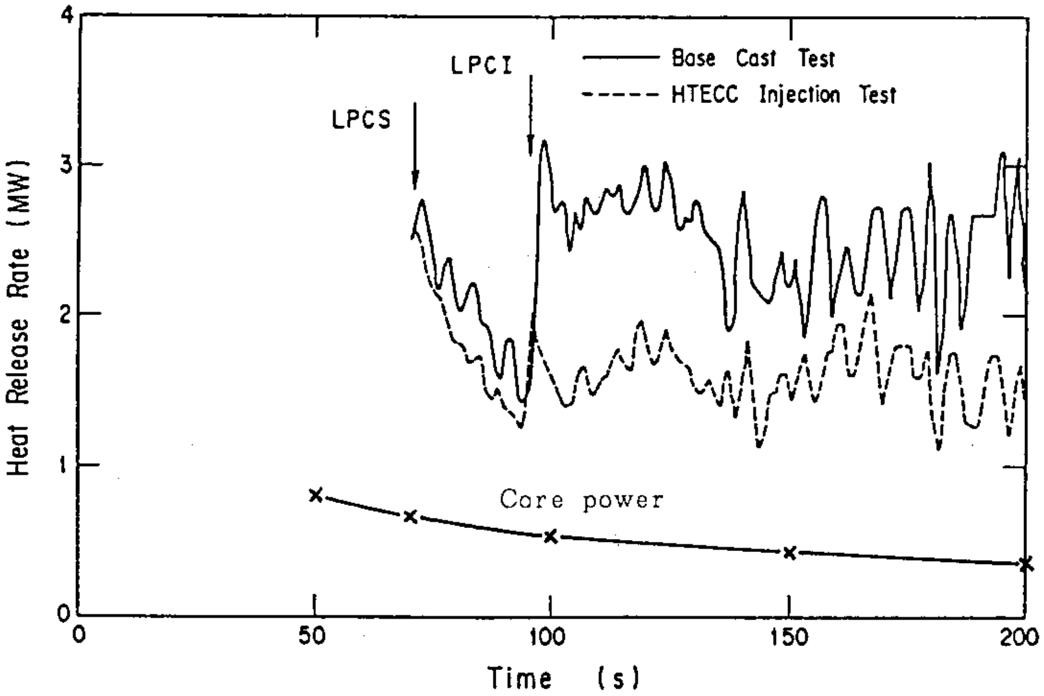

Fig. 6.4 Previous study on stored-heat release in 200% break tests and core power

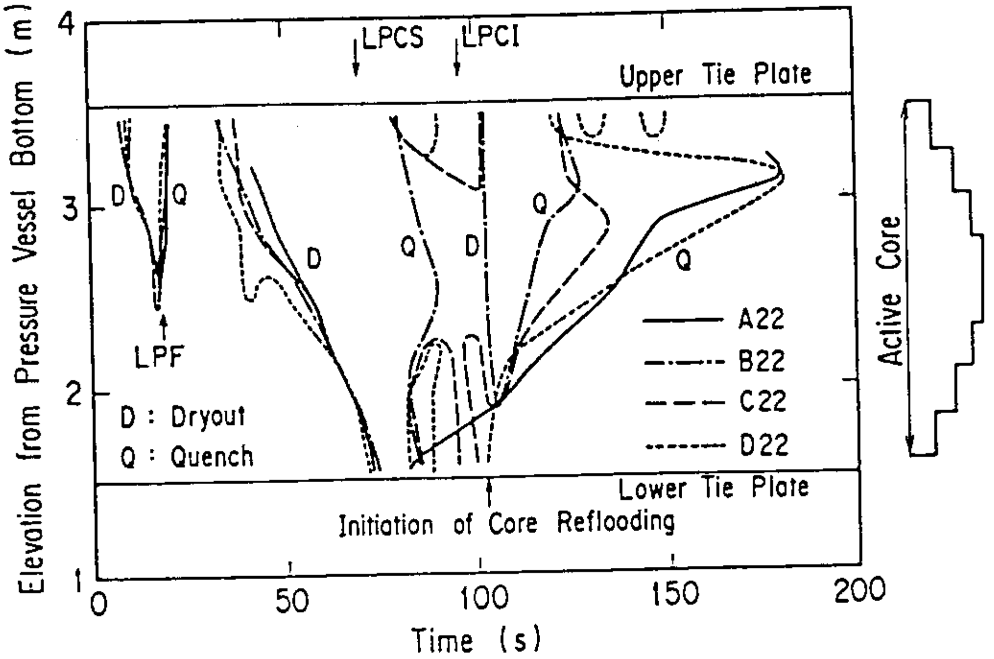

Fig. 6.5 Dryout and quench fronts on A22, B22, C22 and D22 rods in RUN 926

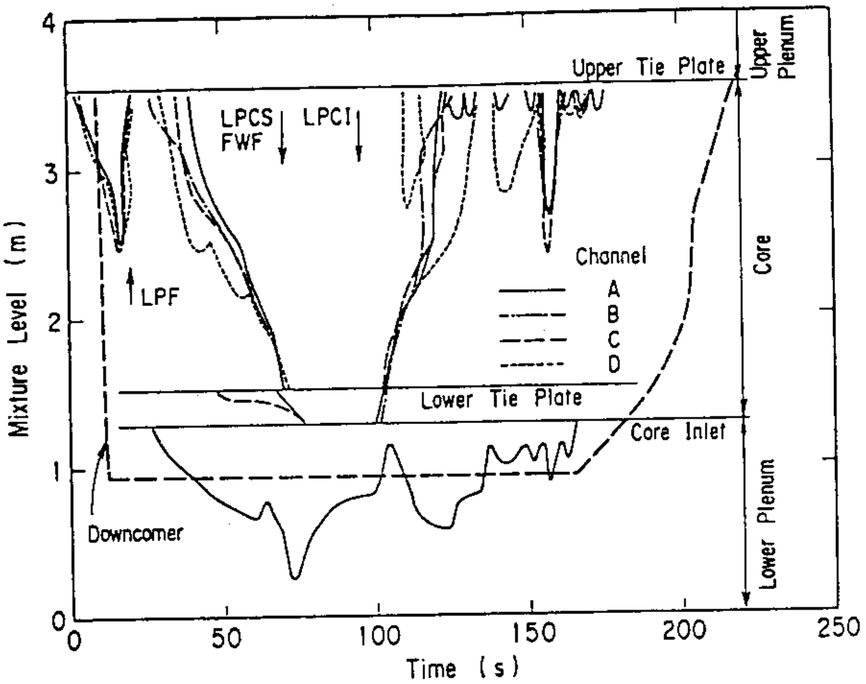

Fig. 6.6 Mixture level transients in PV in RUN 926

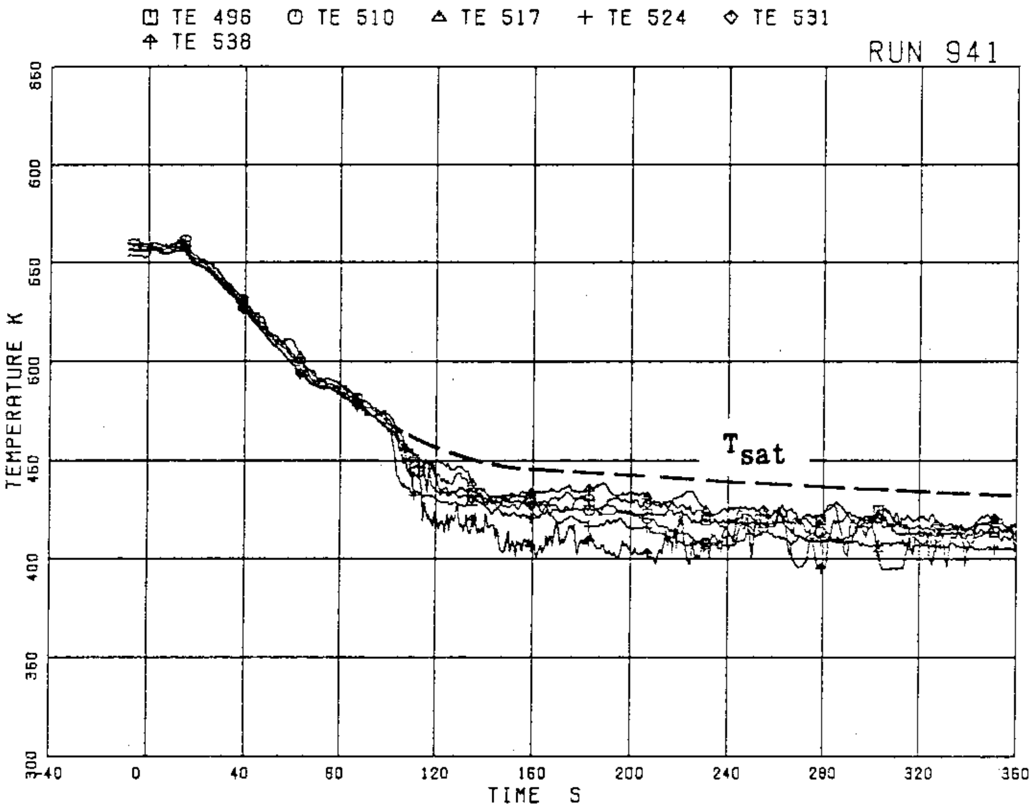

Fig. 6.7 Inner and outer surface temperatures of channel box at pos. 1 in RUN 941

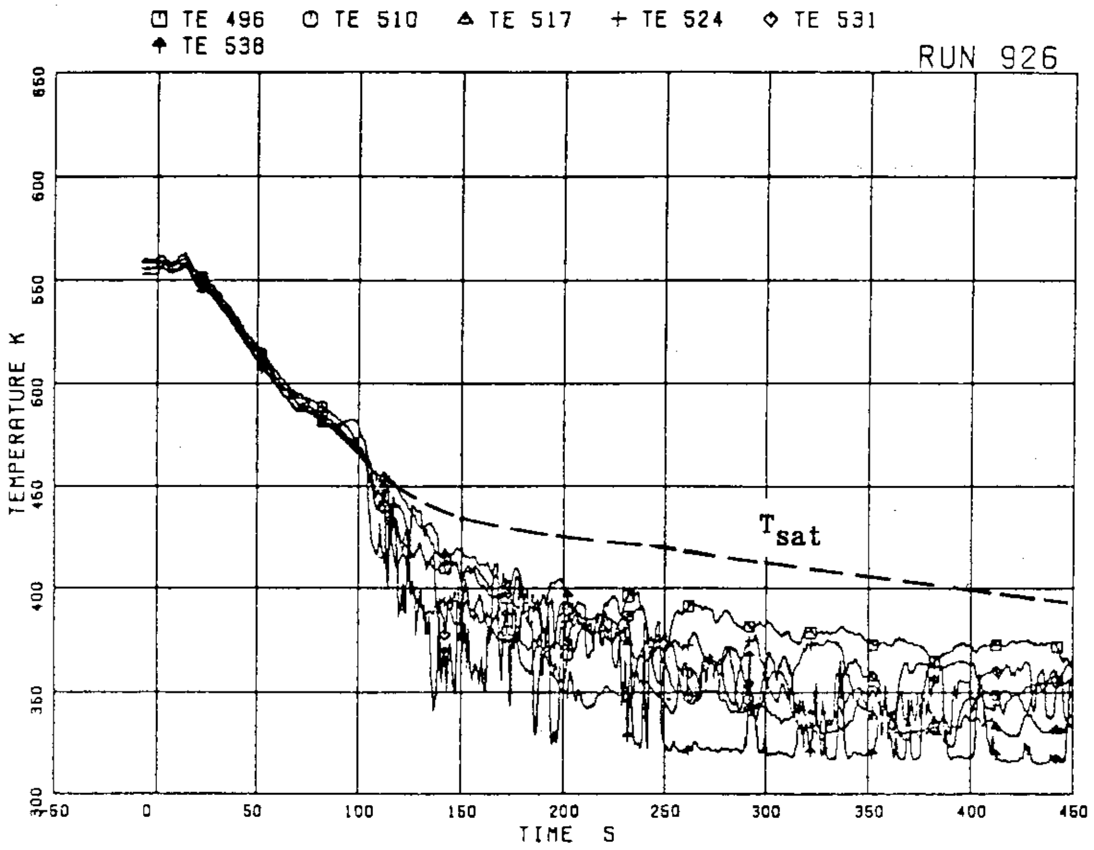

Fig. 6.8 Inner and outer surface temperatures of channel box at pos. 1 in RUN 926

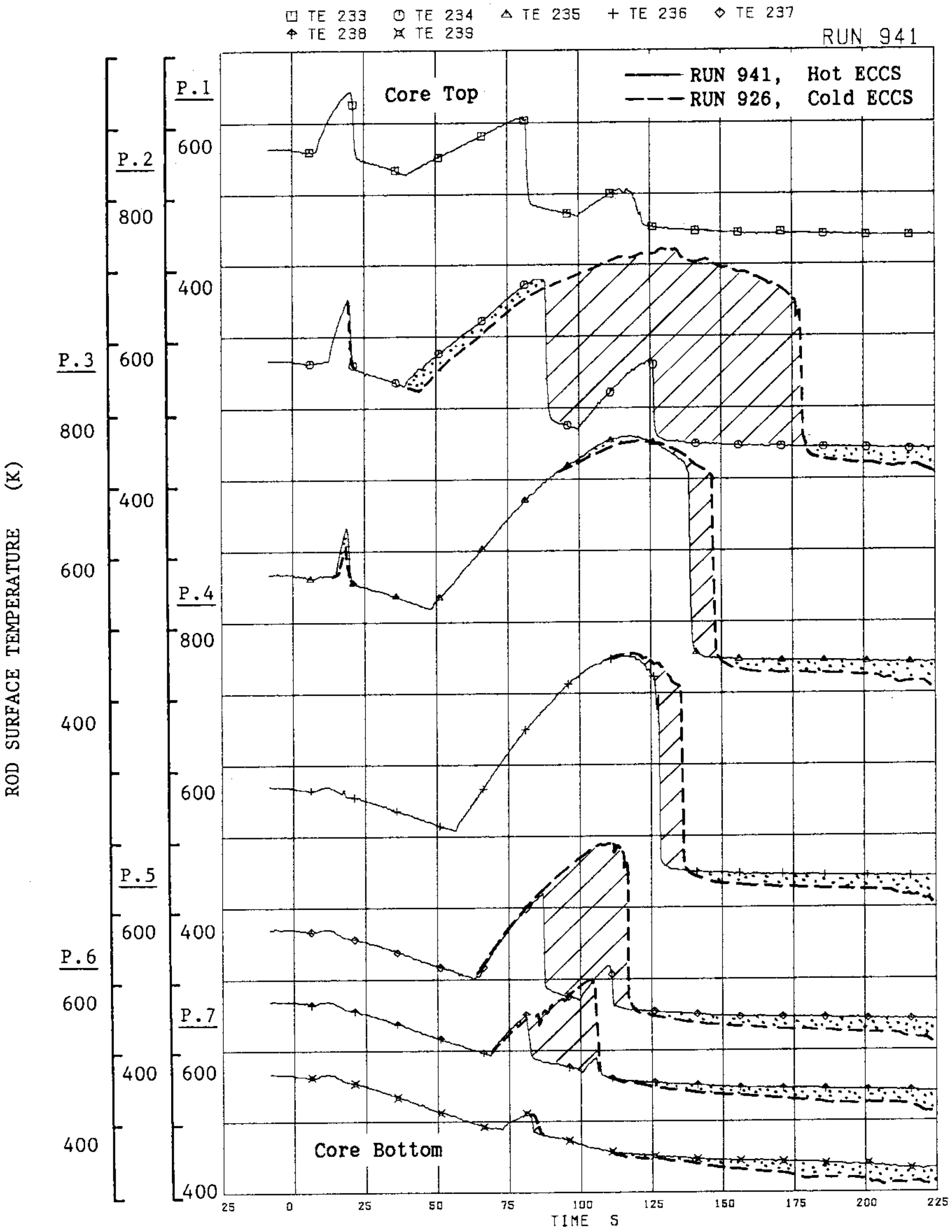

Fig. 6.9 Comparison of A22 rod temperatures between hot and cold ECC tests

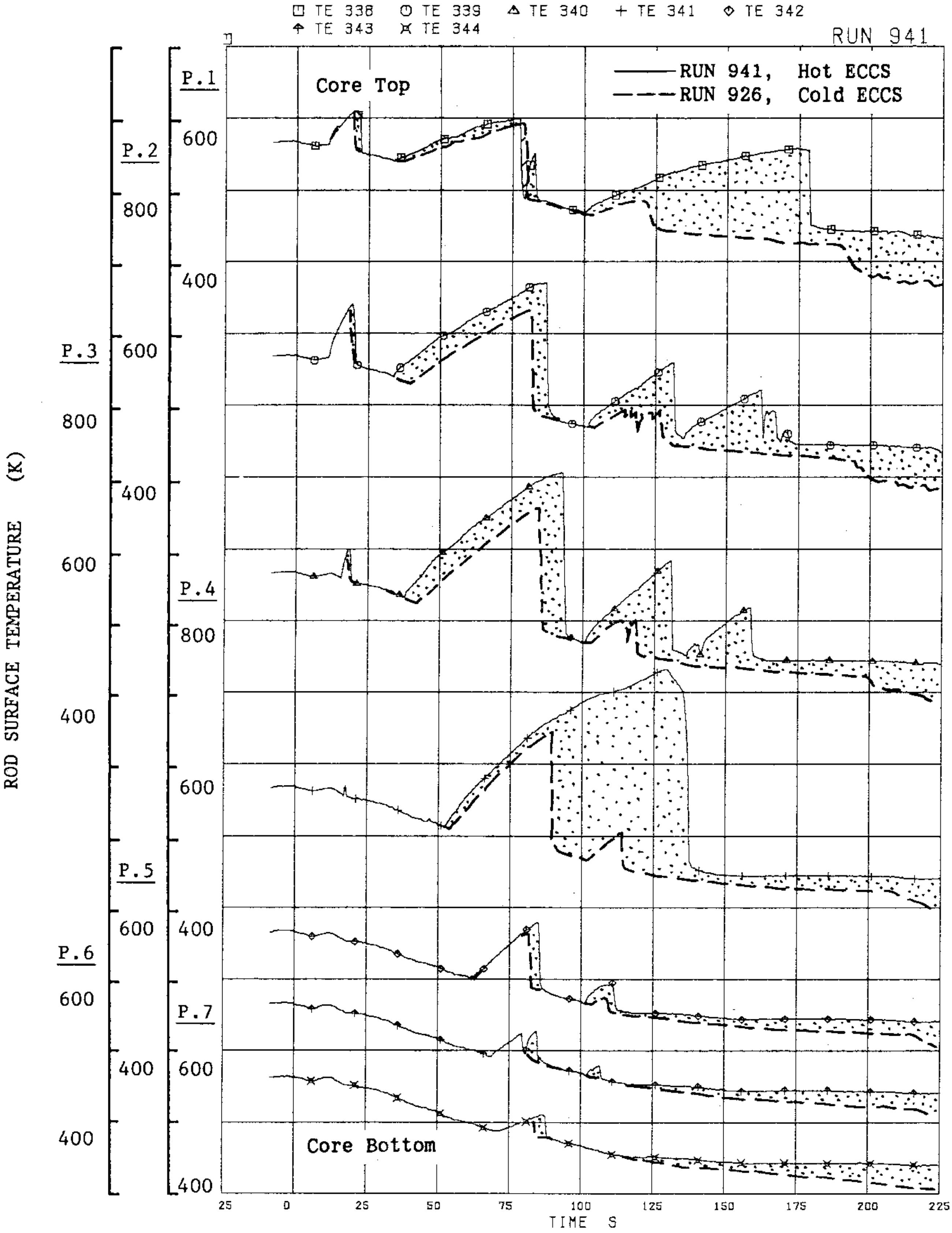

Fig. 6.10 Comparison of B22 rod temperatures between hot and cold ECC tests

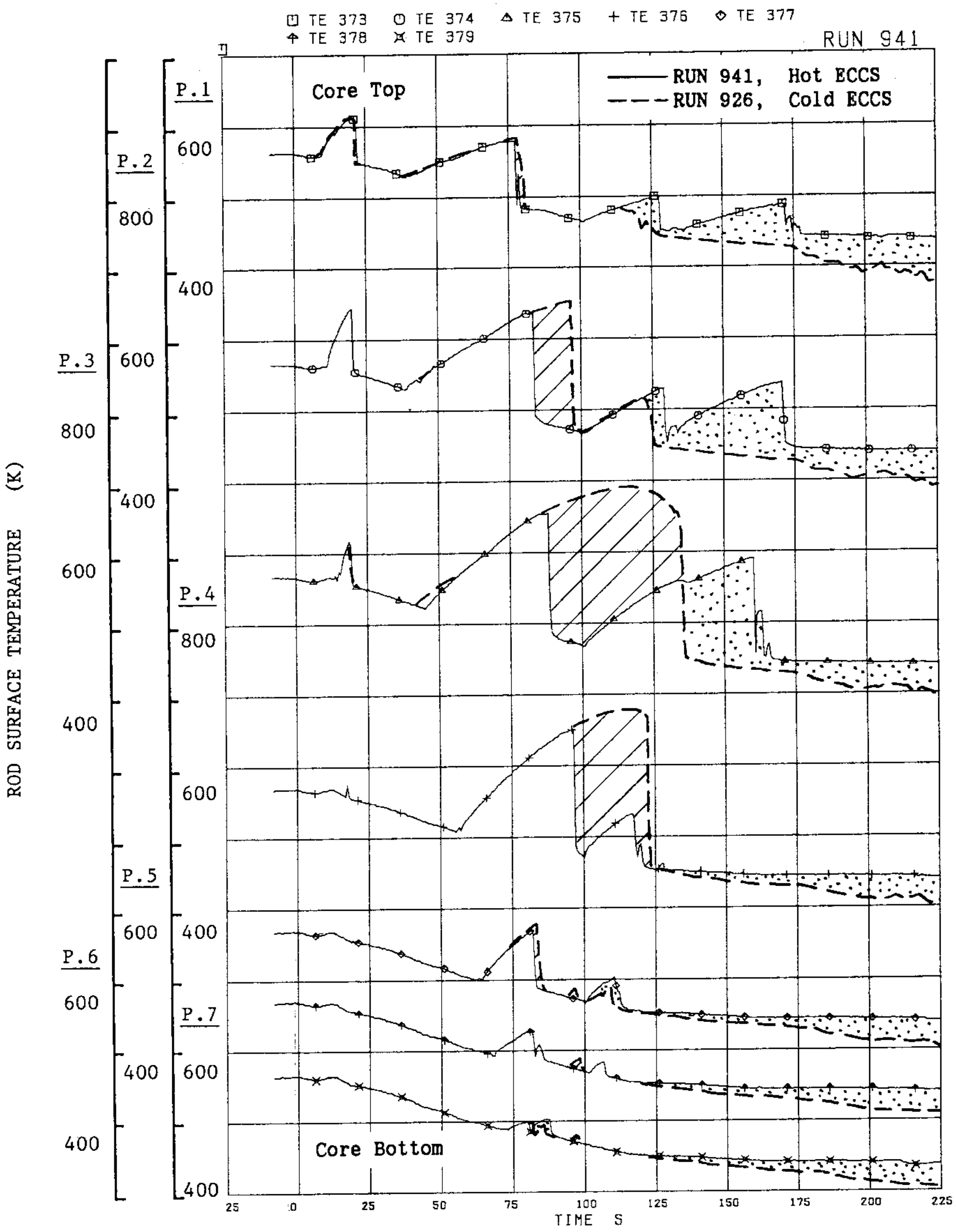

Fig. 6.11 Comparison of C22 rod temperatures between hot and cold ECC tests

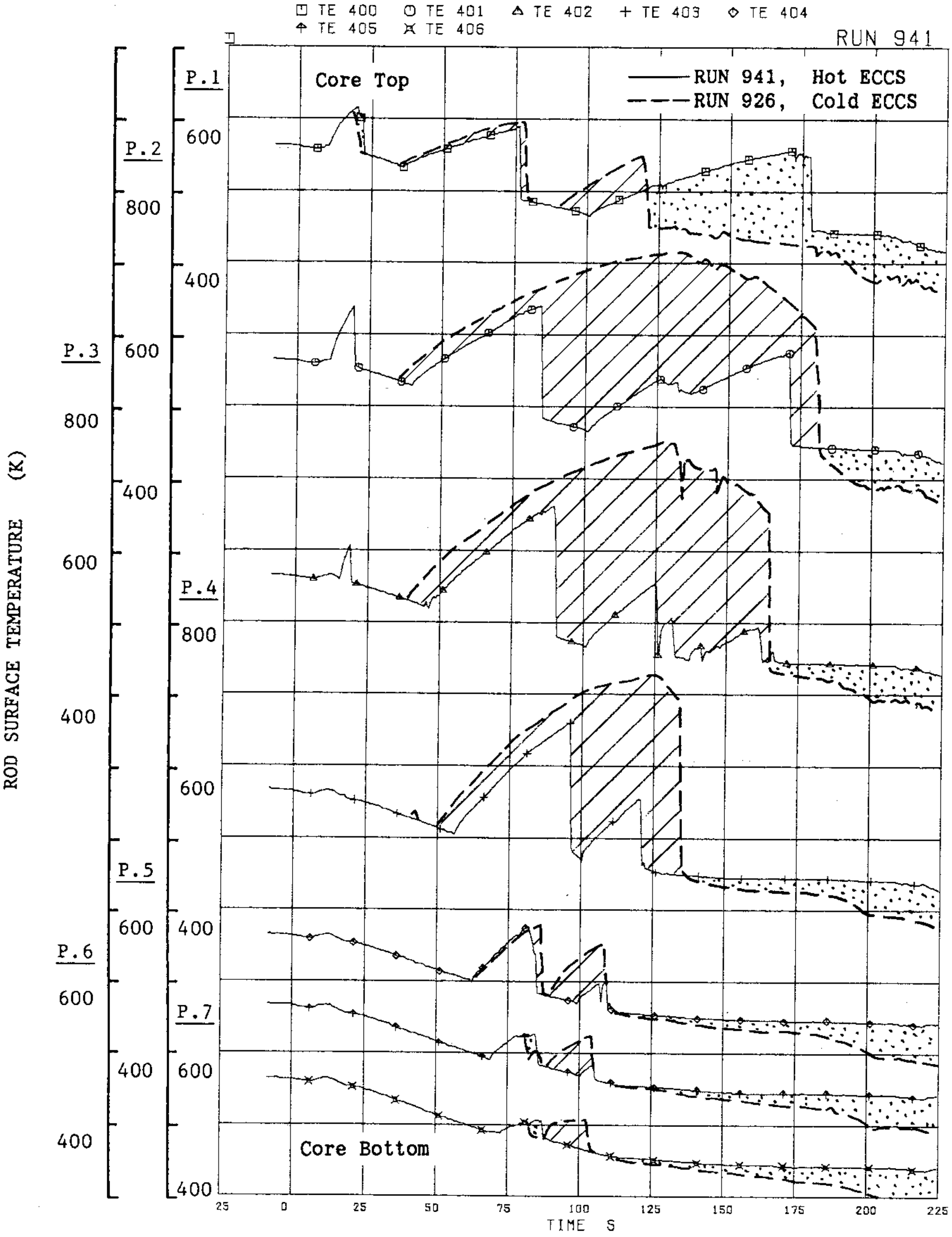

Fig. 6.12 Comparison of D22 rod temperatures between hot and cold ECC tests

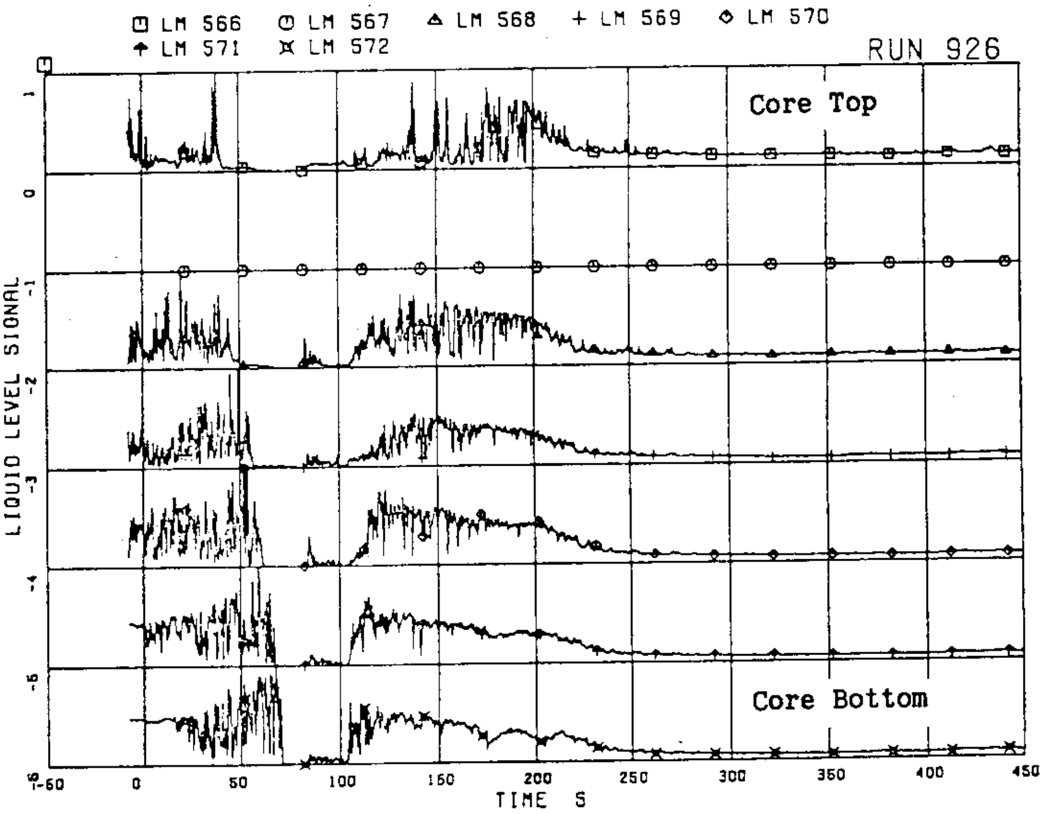

Fig. 6.13 Liquid level signals in channel box A in RUN 926

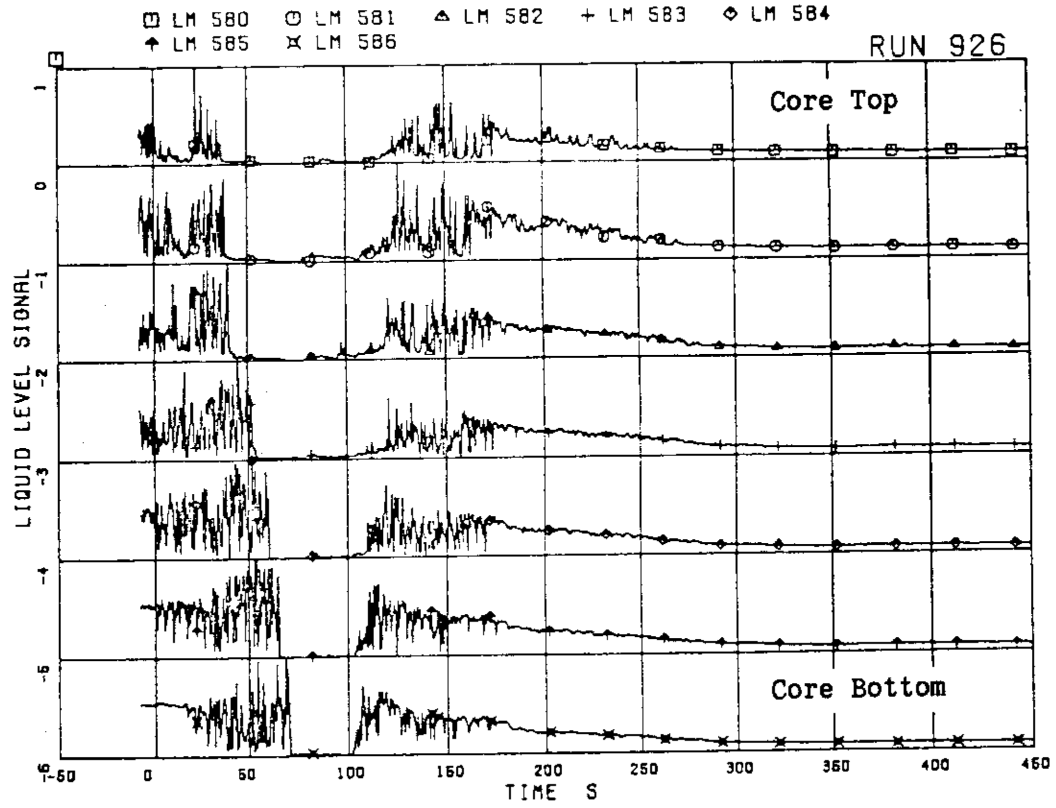

Fig. 6.14 Liquid level signals in channel box C in RUN 926

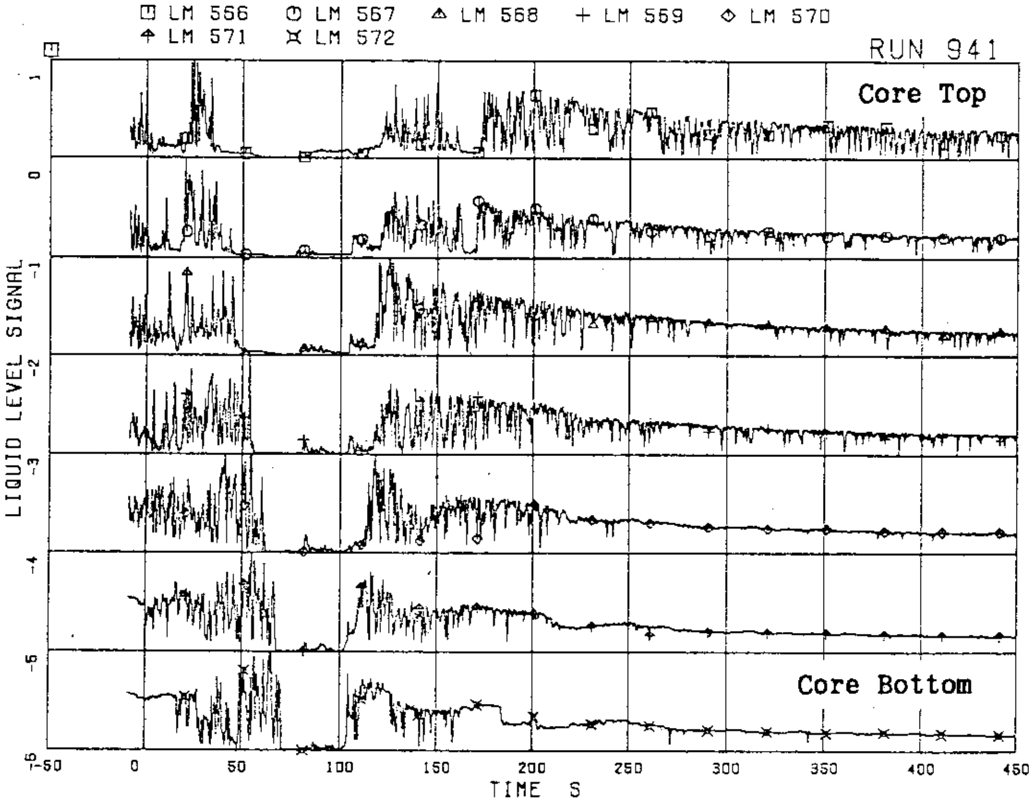

Fig. 6.15 Liquid level signals in channel box A in RUN 941

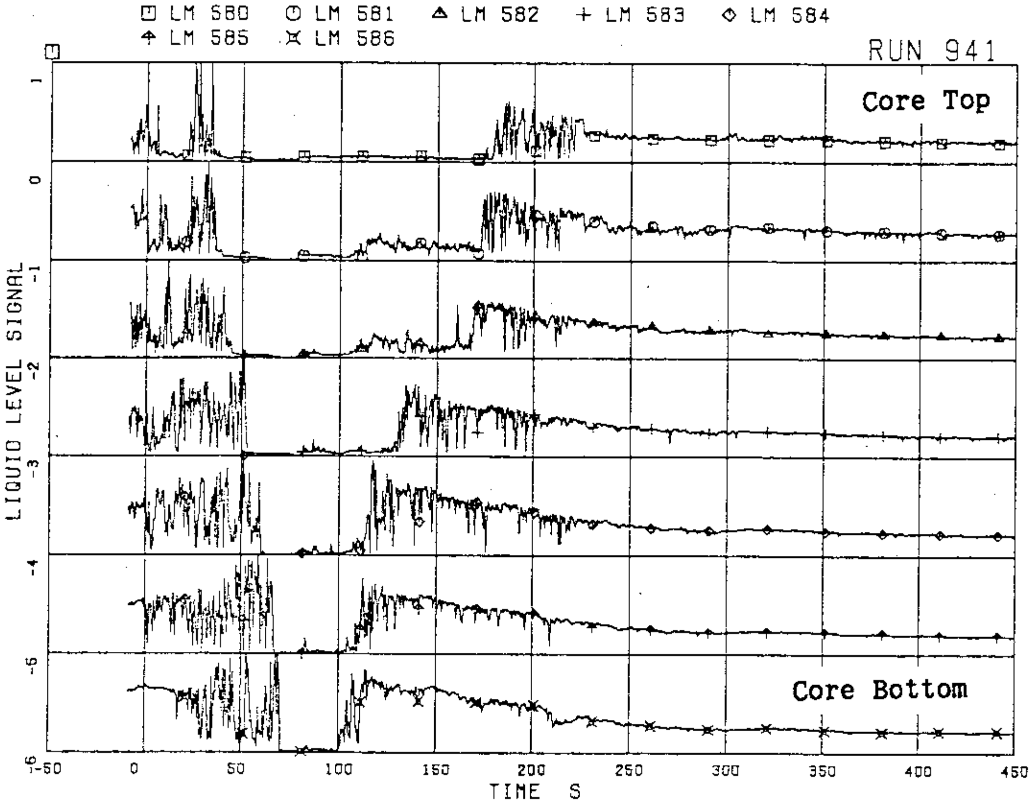

Fig. 6.16 Liquid level signals in channel box C in RUN 941

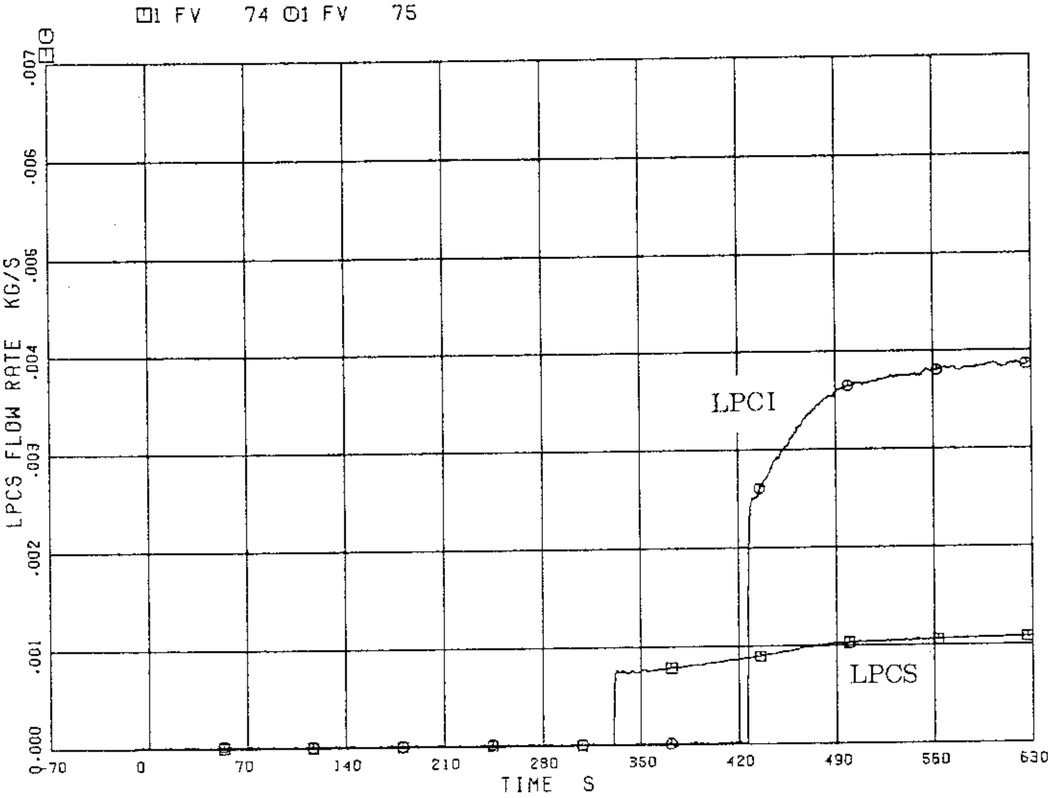

Fig. 6.17 Volumetric flow rates of LPCS and LPCI in RUN 922

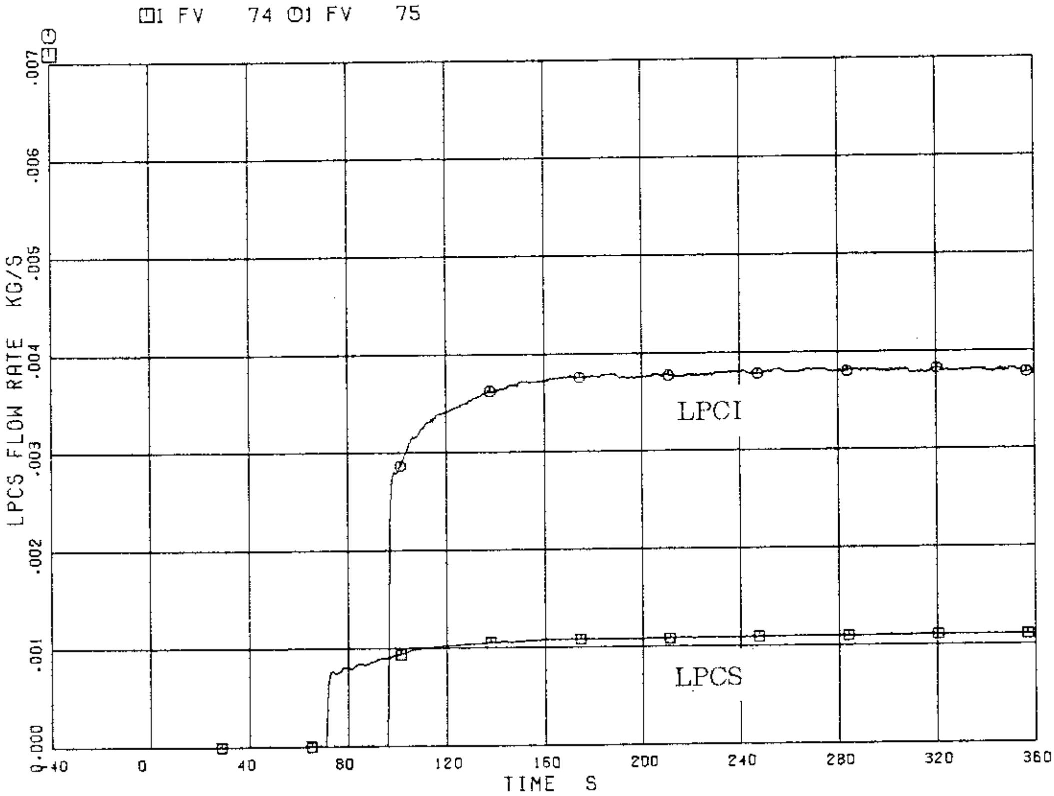

Fig. 6.18 Volumetric flow rates of LPCS and LPCI in RUN 926

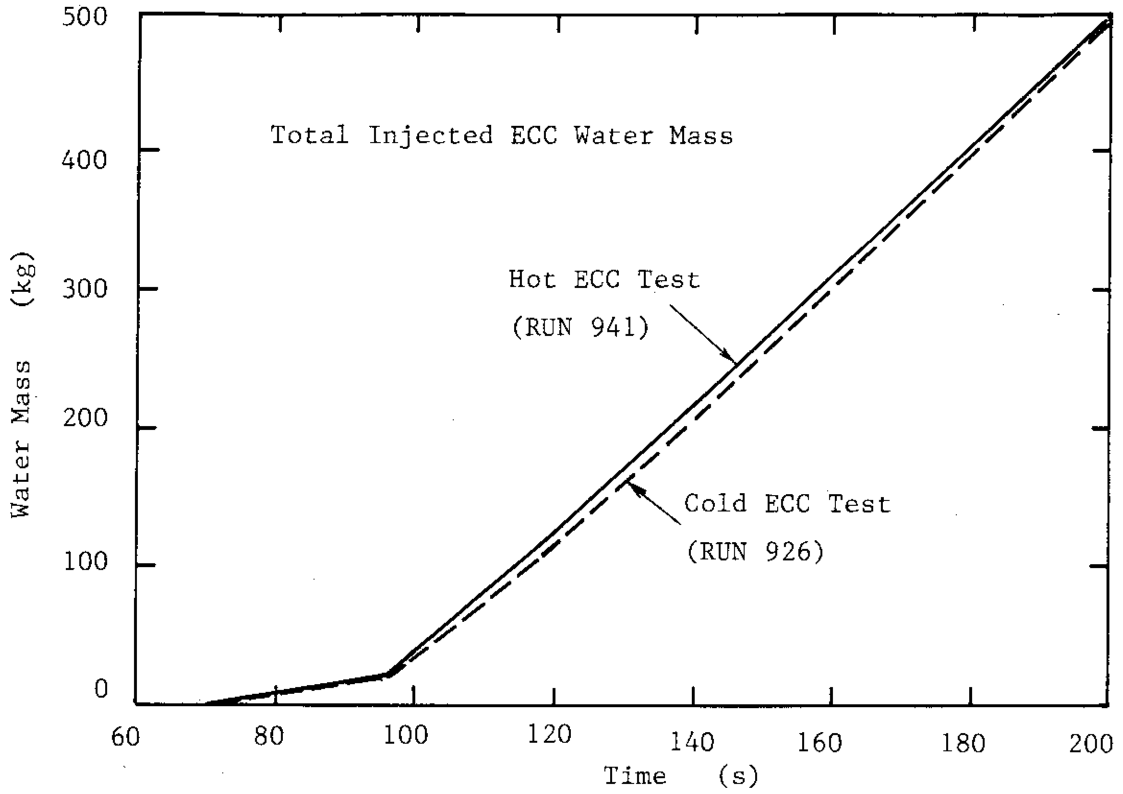

Fig. 6.19 Comparison of injected ECC mass between RUNs 941 and 926

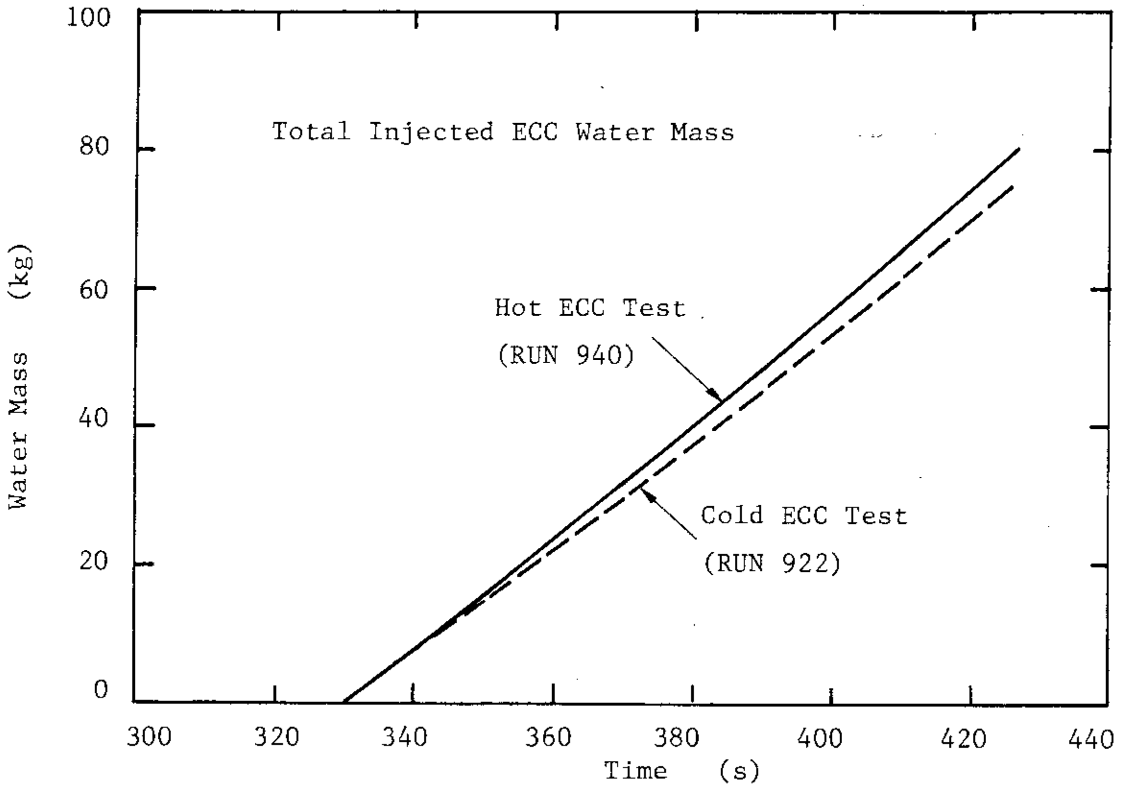

Fig. 6.20 Comparison of injected ECC mass between RUNs 940 and 922

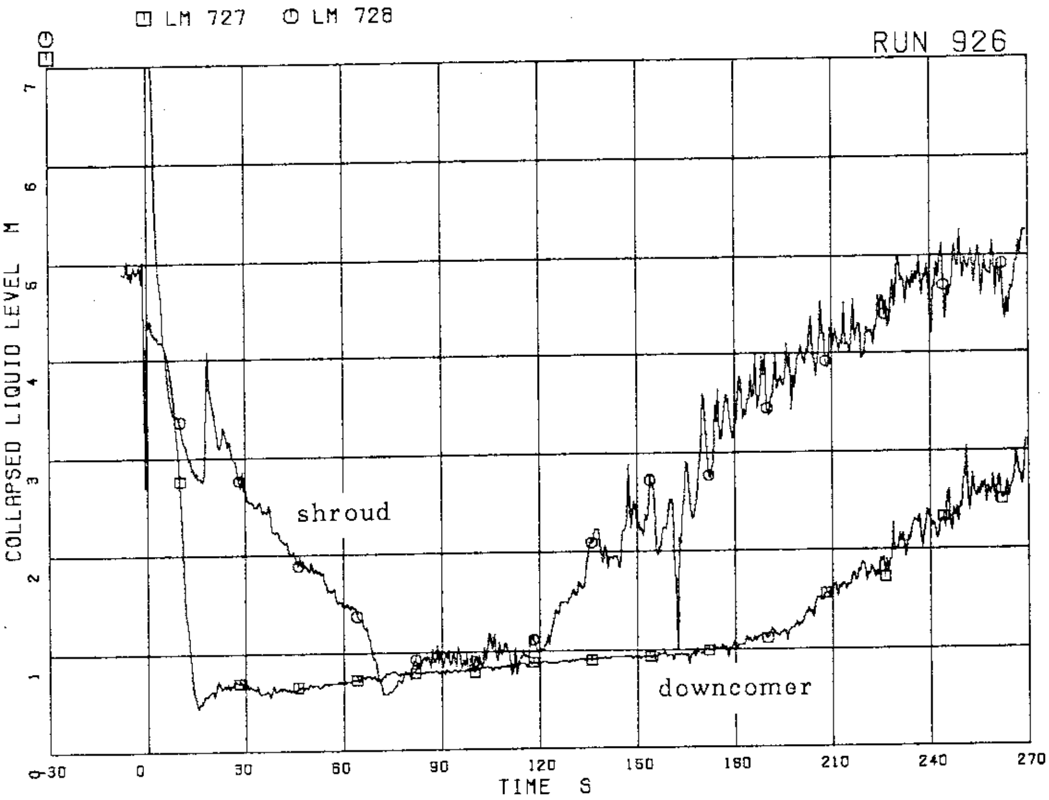

Fig. 6.21 Collapsed levels in downcomer and shroud in RUN 926

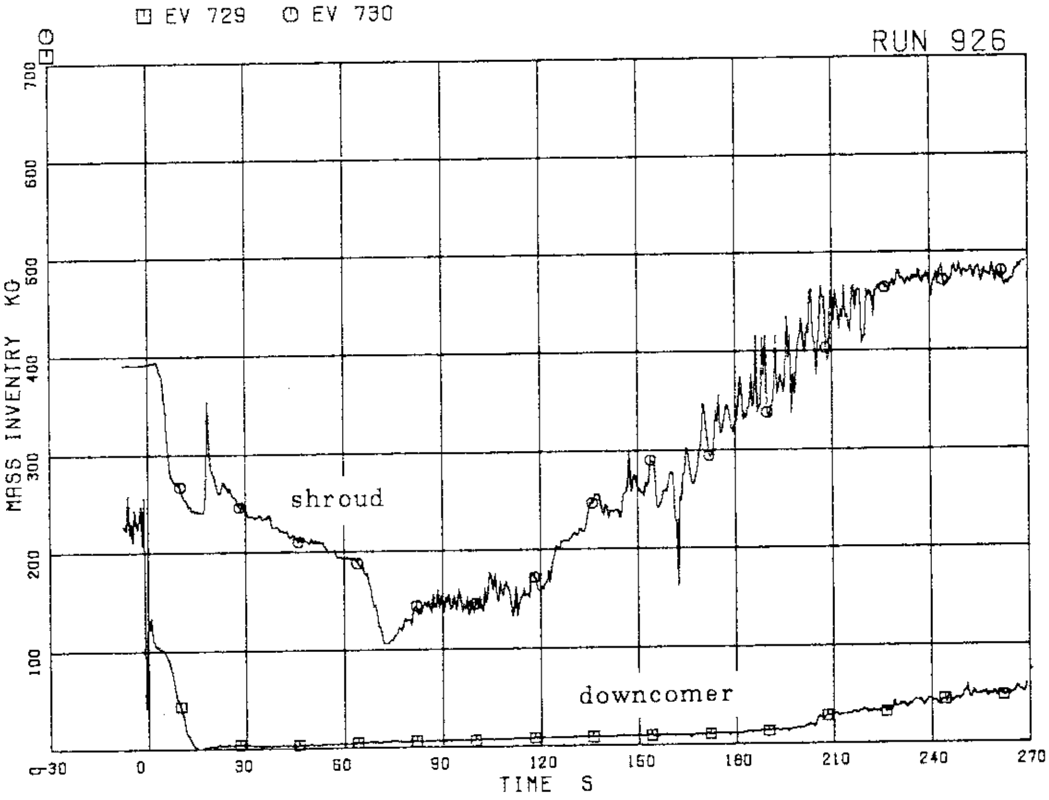

Fig. 6.22 Fluid inventory in downcomer and shroud in RUN 926

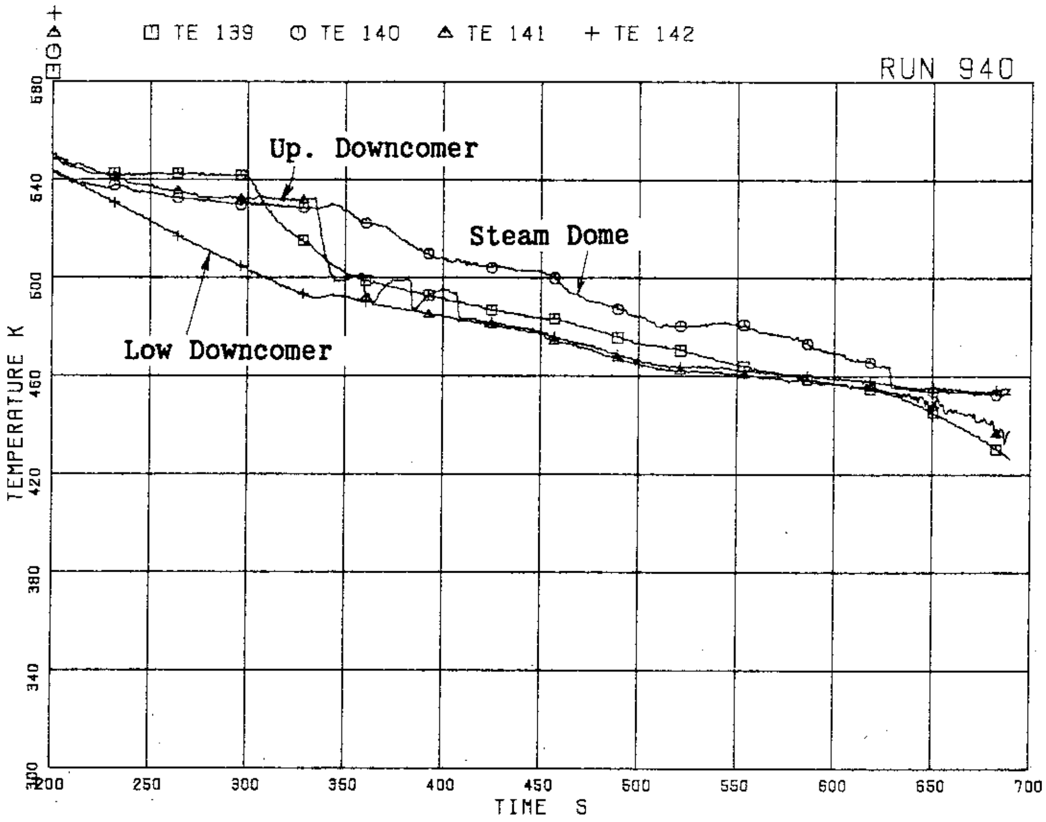

Fig. 6.23 Fluid temperature distribution in u.plenum, steam dome and downcomer in RUN 940

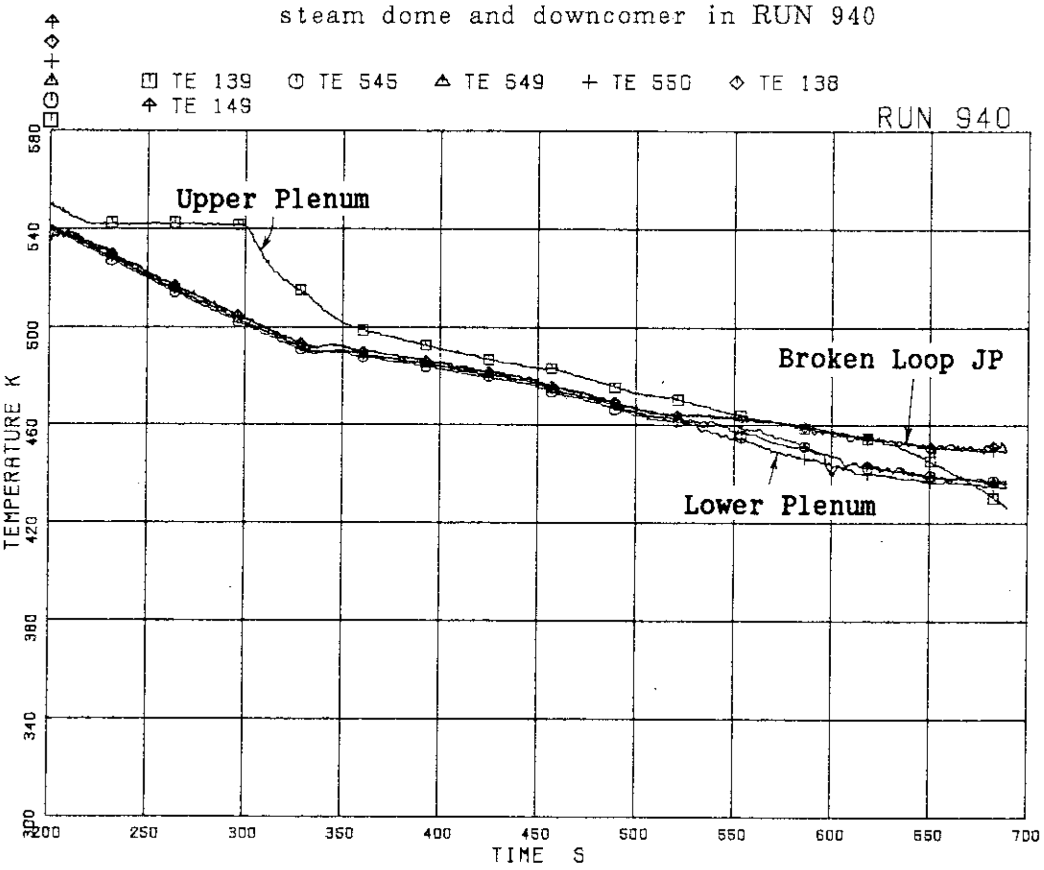

Fig. 6.24 Fluid temperature distribution in upper and lower plenua and broken loop JP in RUN 940

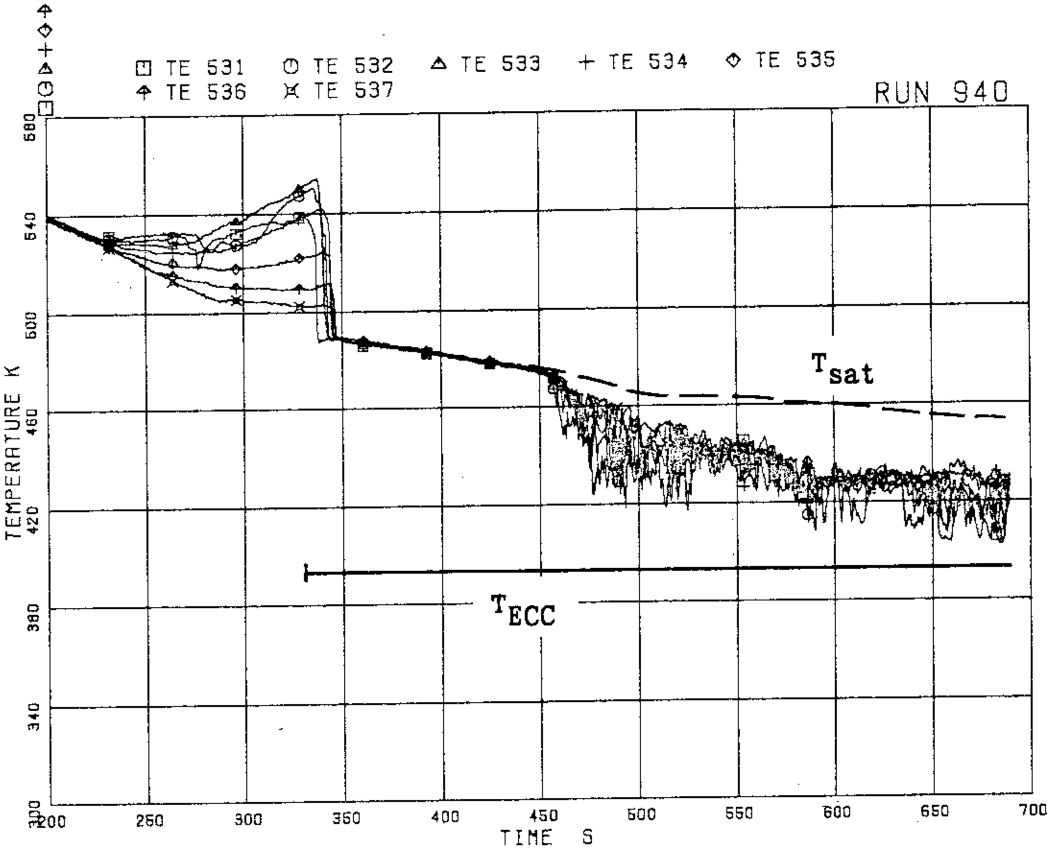

Fig. 6.25 Outer surface temperatures of channel box A (Pos.1 － 7) in RUN 940

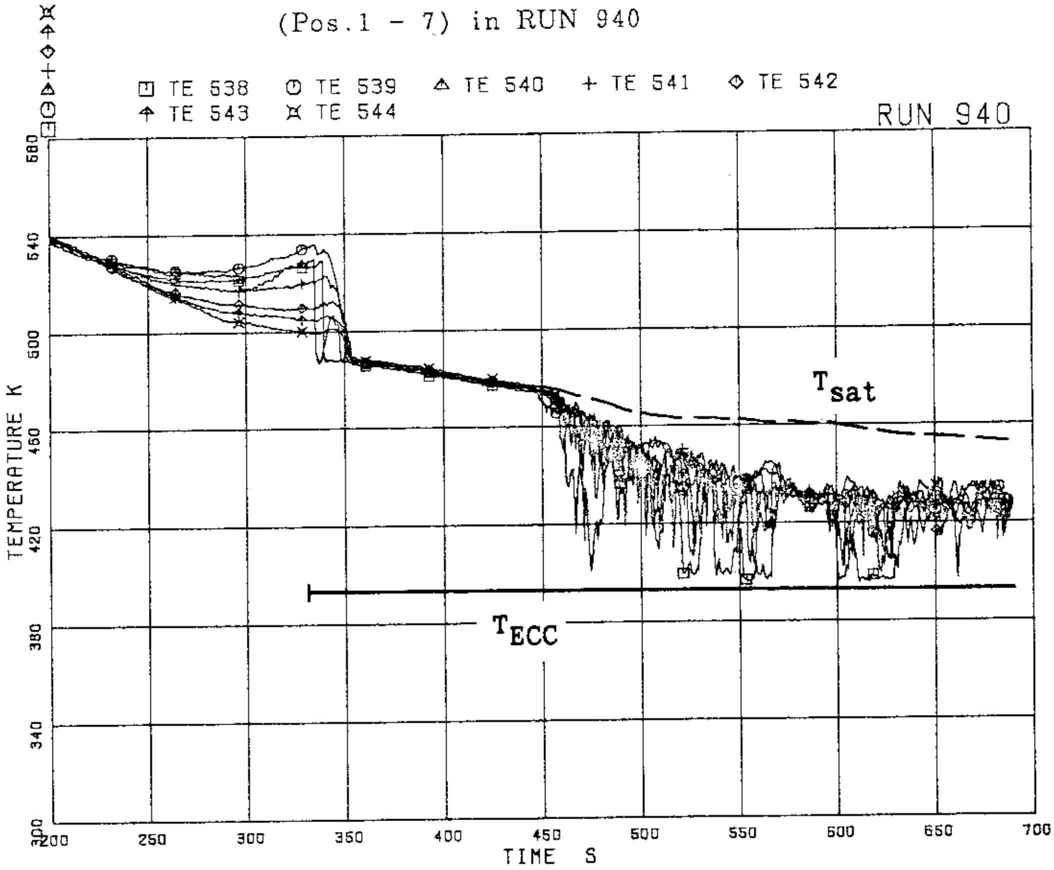

Fig. 6.26 Outer surface temperatures of channel box C (Pos.1 － 7) in RUN 940

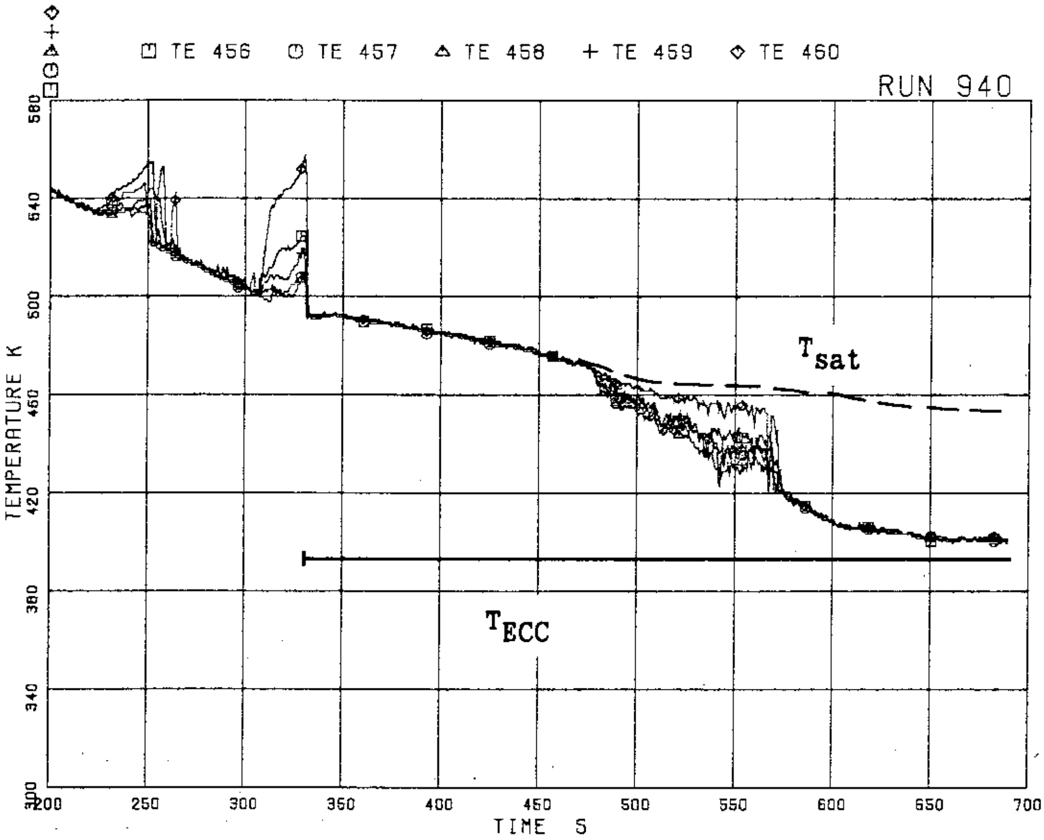

Fig. 6.27 Fluid temperatures above UTP of channel A, openings 1 to 5 in RUN 940

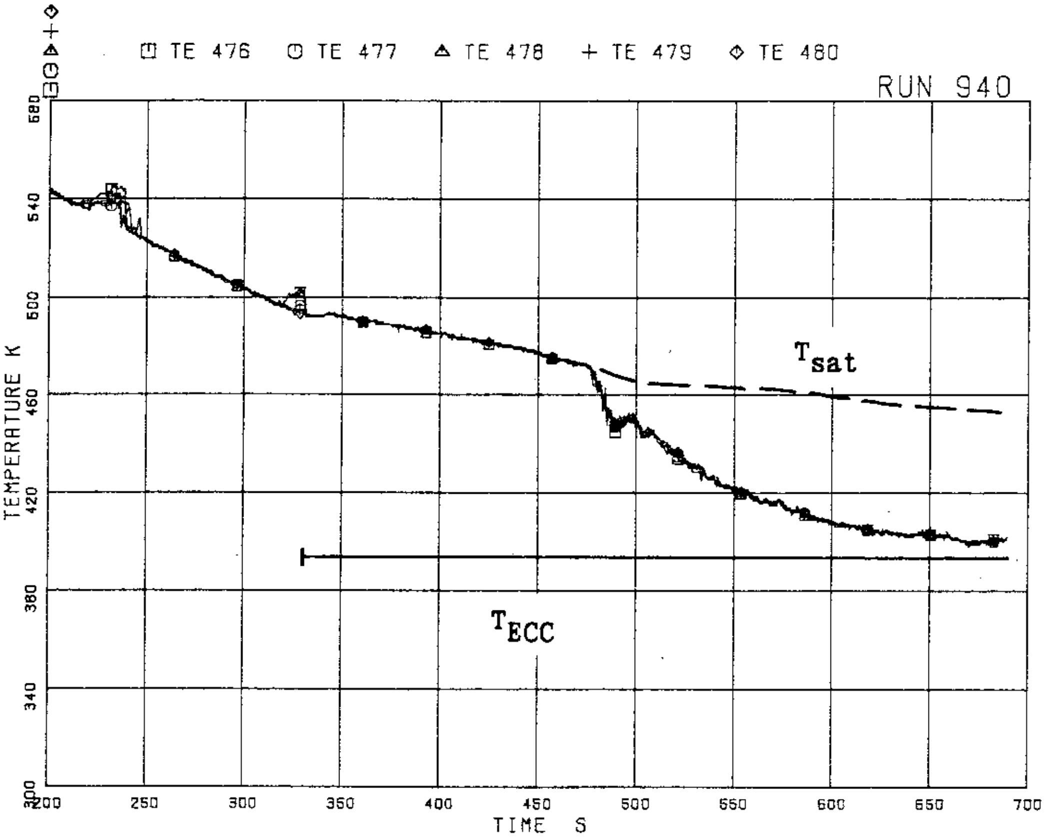

Fig. 6.28 Fluid temperatures above UTP of channel C, openings 1 to 5 in RUN 940

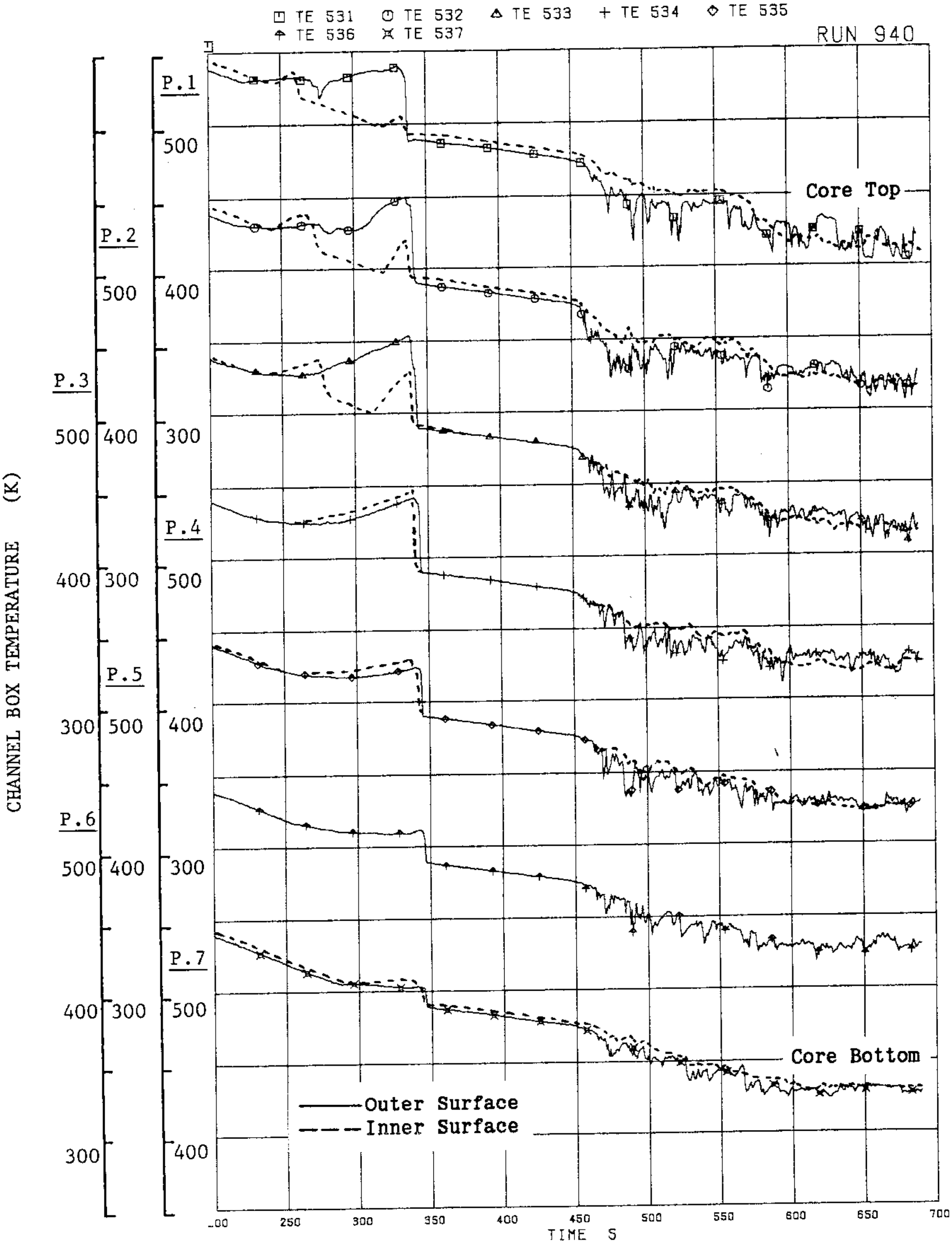

Fig. 6.29 Outer and inner surface temperatures of channel

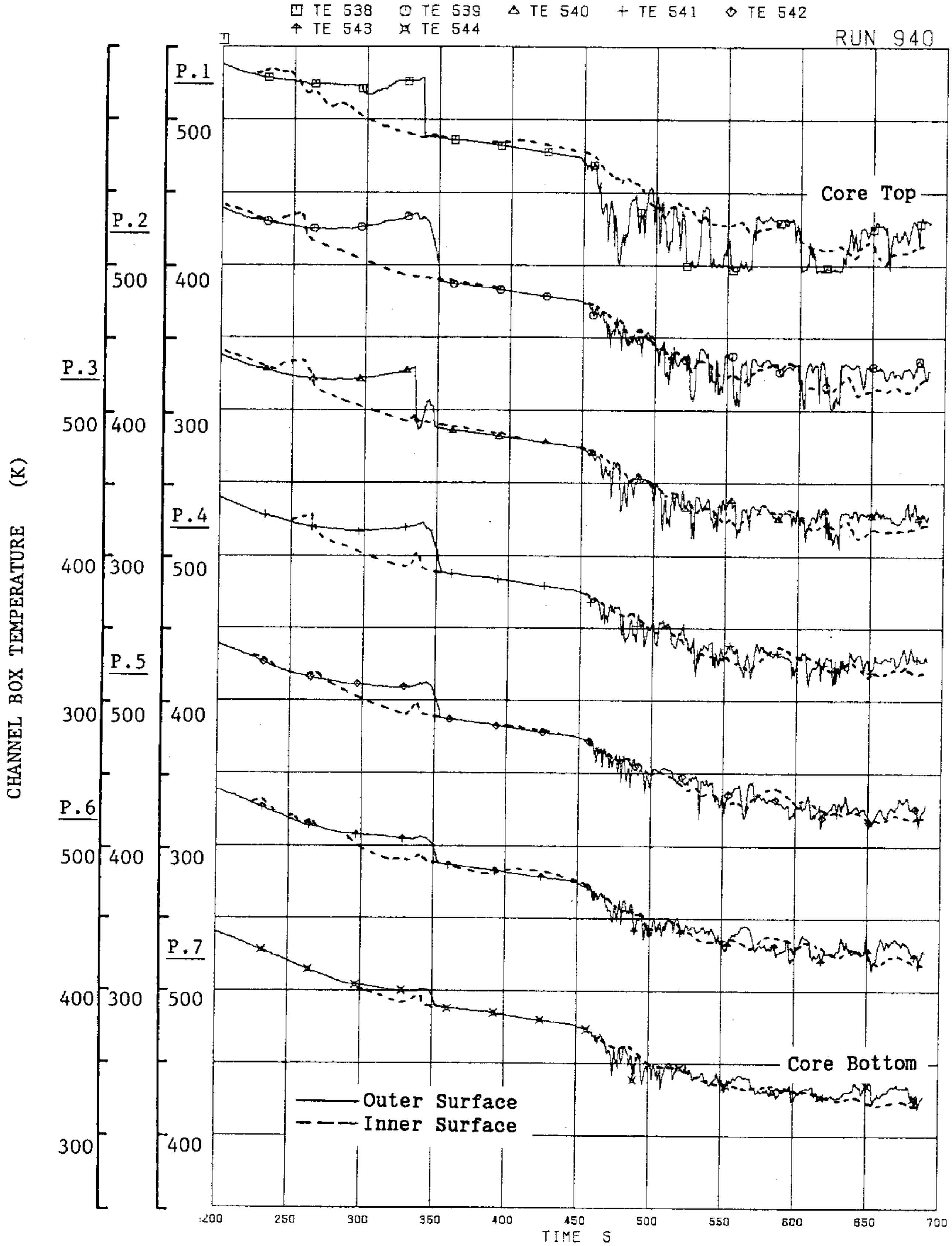

Fig. 6.30 Outer and inner surface temperatures of channel box C in RUN 940

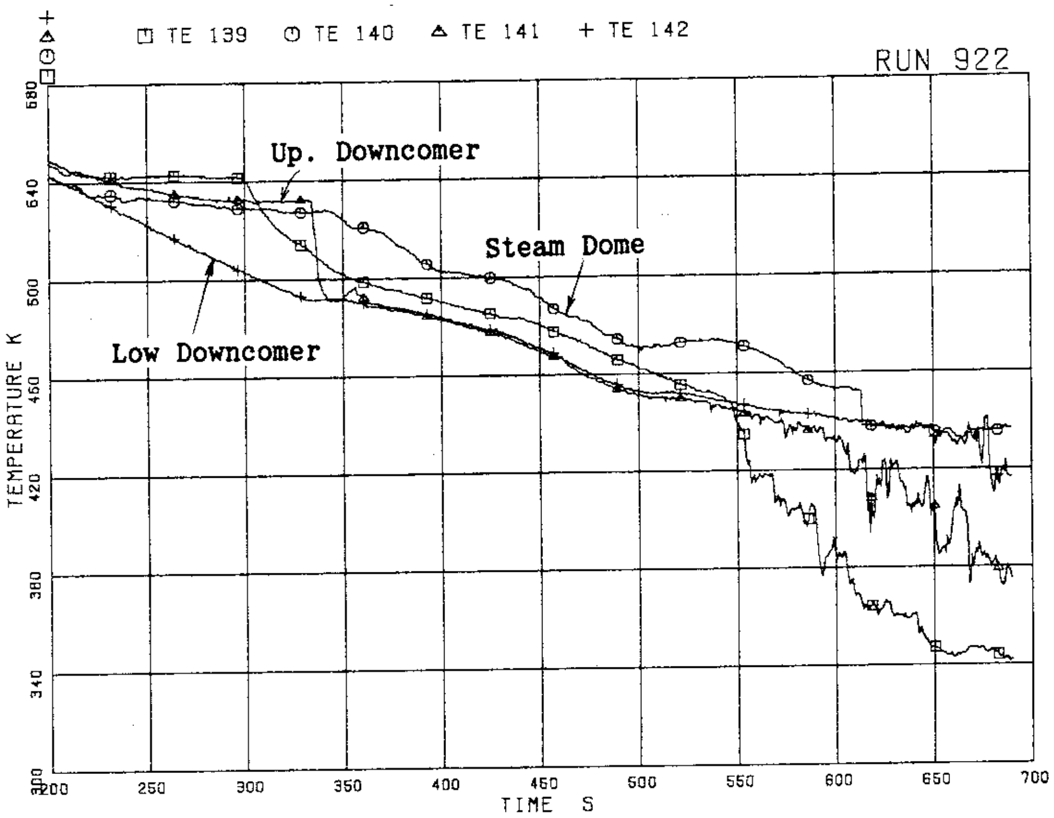

Fig. 6.31 Fluid temperature distribution in u.plenum, steam dome and downcomer in RUN 922

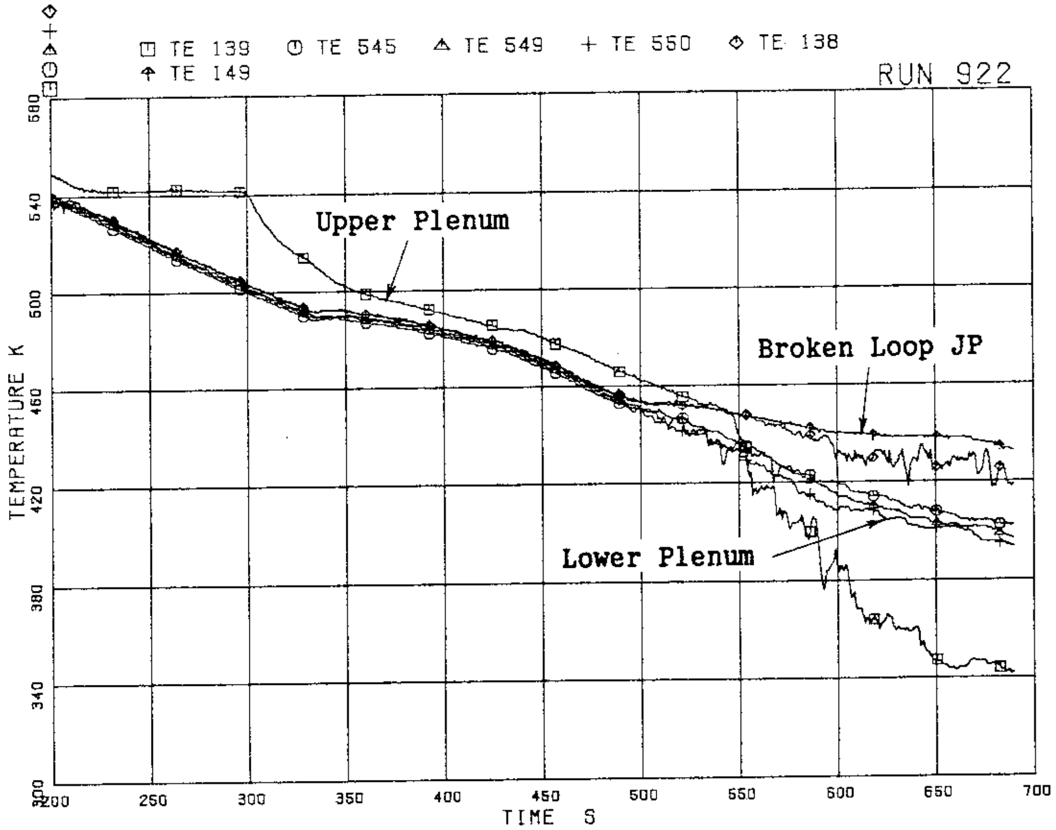

Fig. 6.32 Fluid temperature distribution in upper and lower plenua and broken loop JP in RUN 922

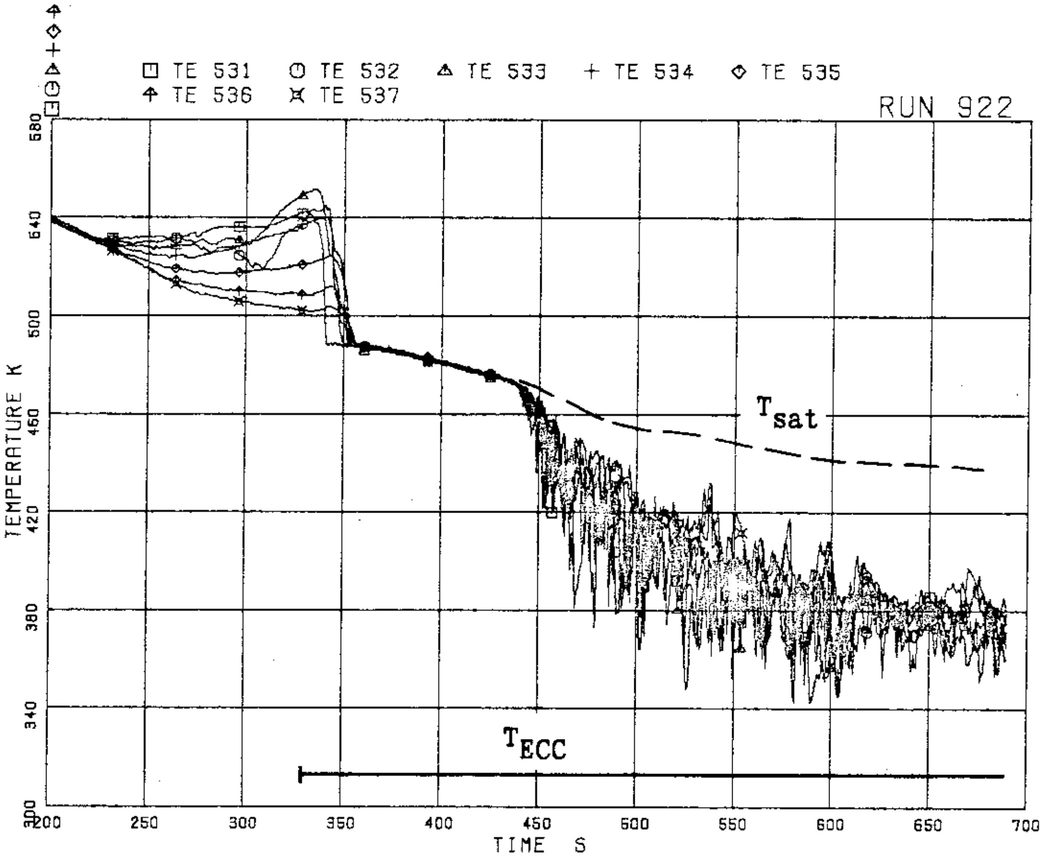

Fig. 6.33 Outer surface temperatures of channel box A (Pos.1 － 7) in RUN 922

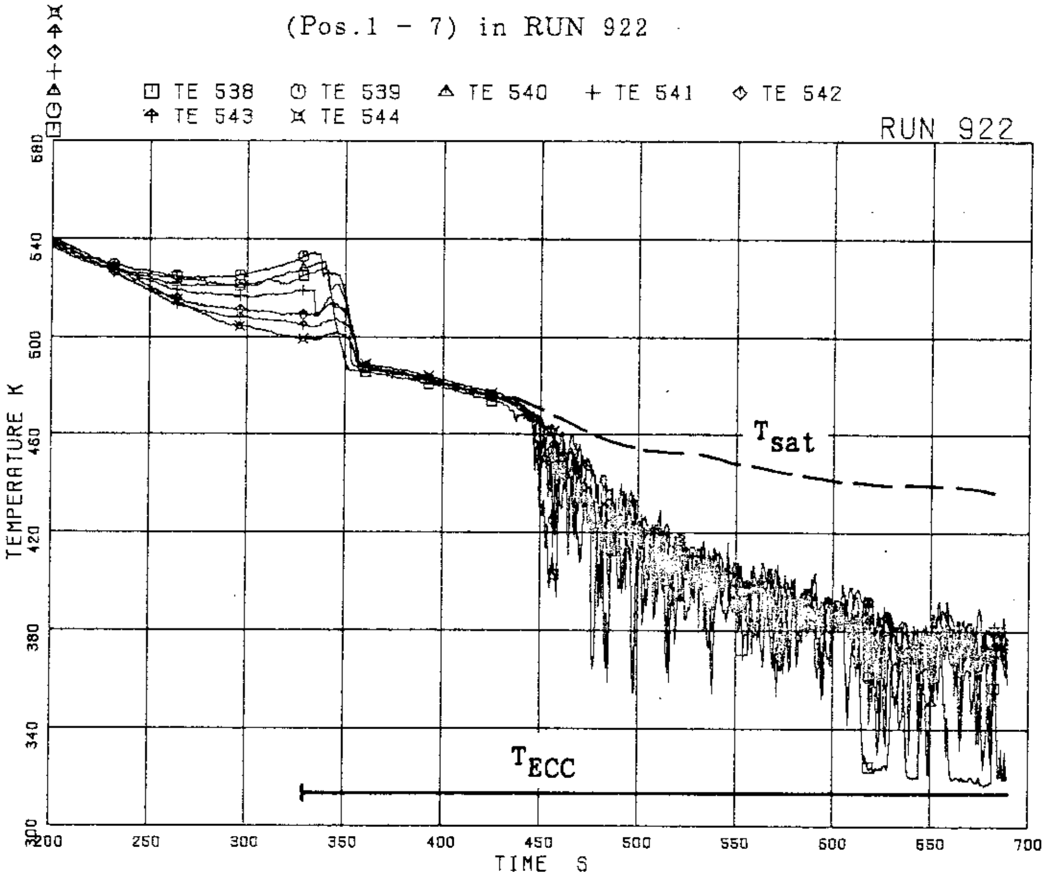

Fig. 6.34 Outer surface temperatures of channel box C (Pos.1 － 7) in RUN 922

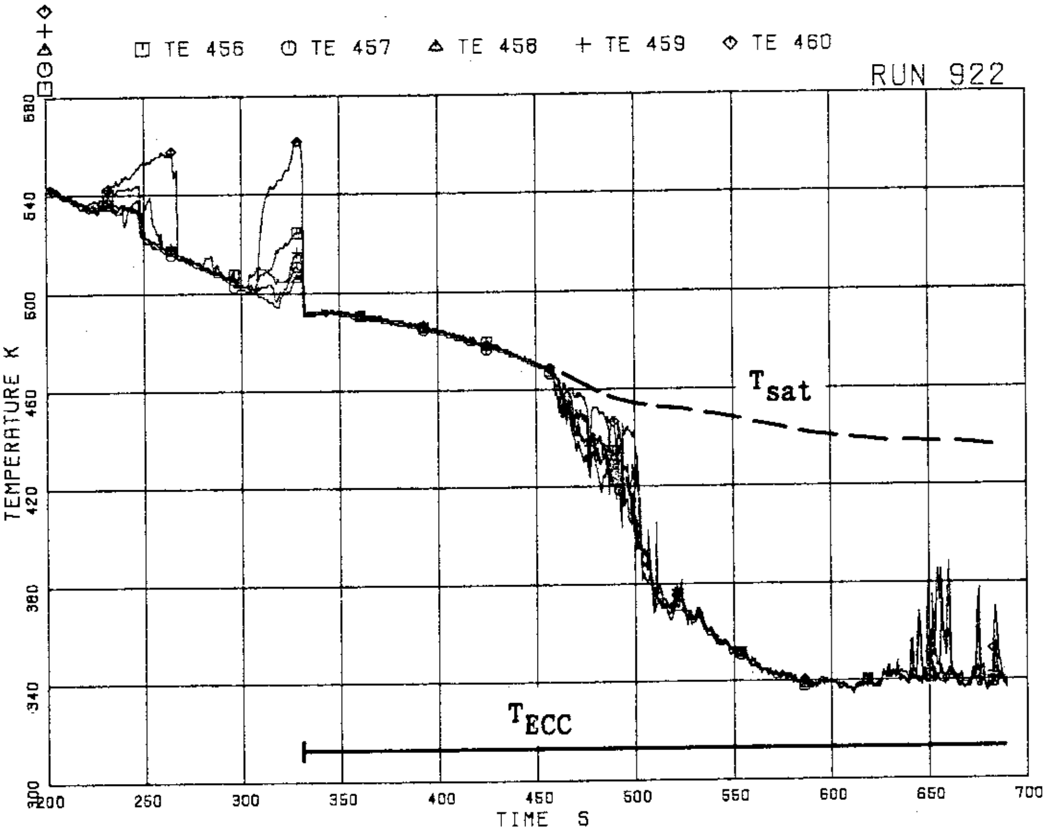

Fig. 6.35 Fluid temperatures above UTP of channel A, openings 1 to 5 in RUN 922

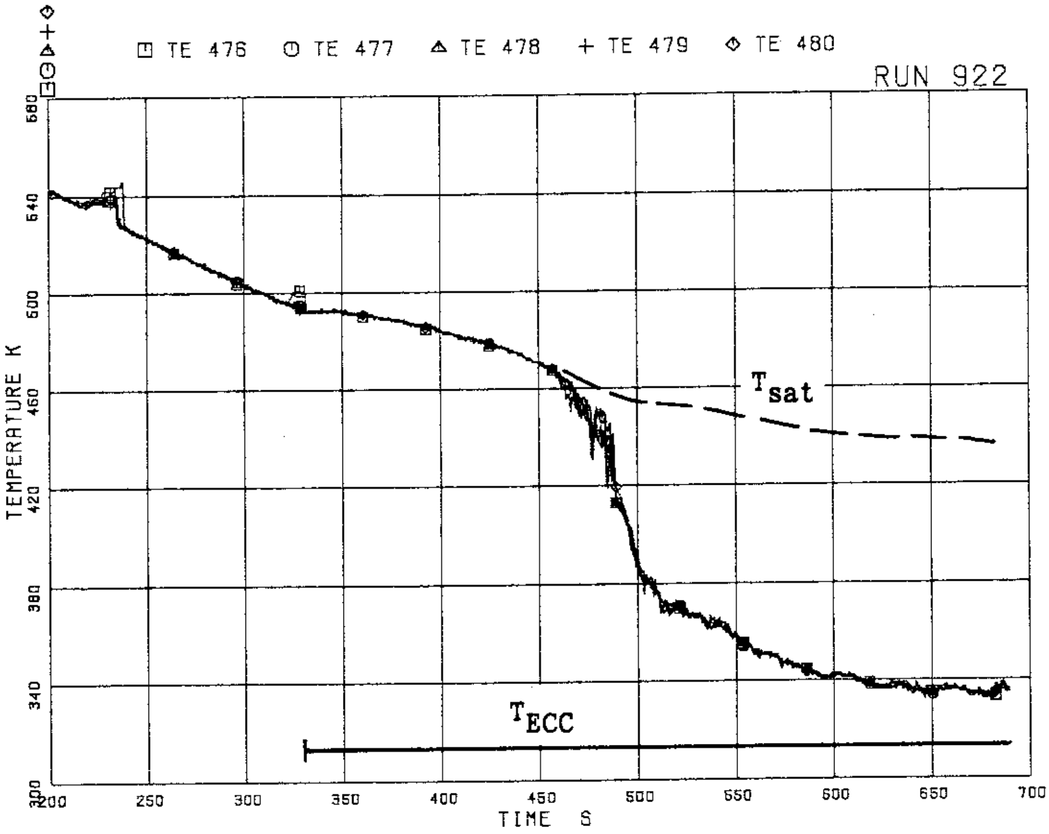

Fig. 6.36 Fluid temperatures above UTP of channel C, openings 1 to 5 in RUN 922

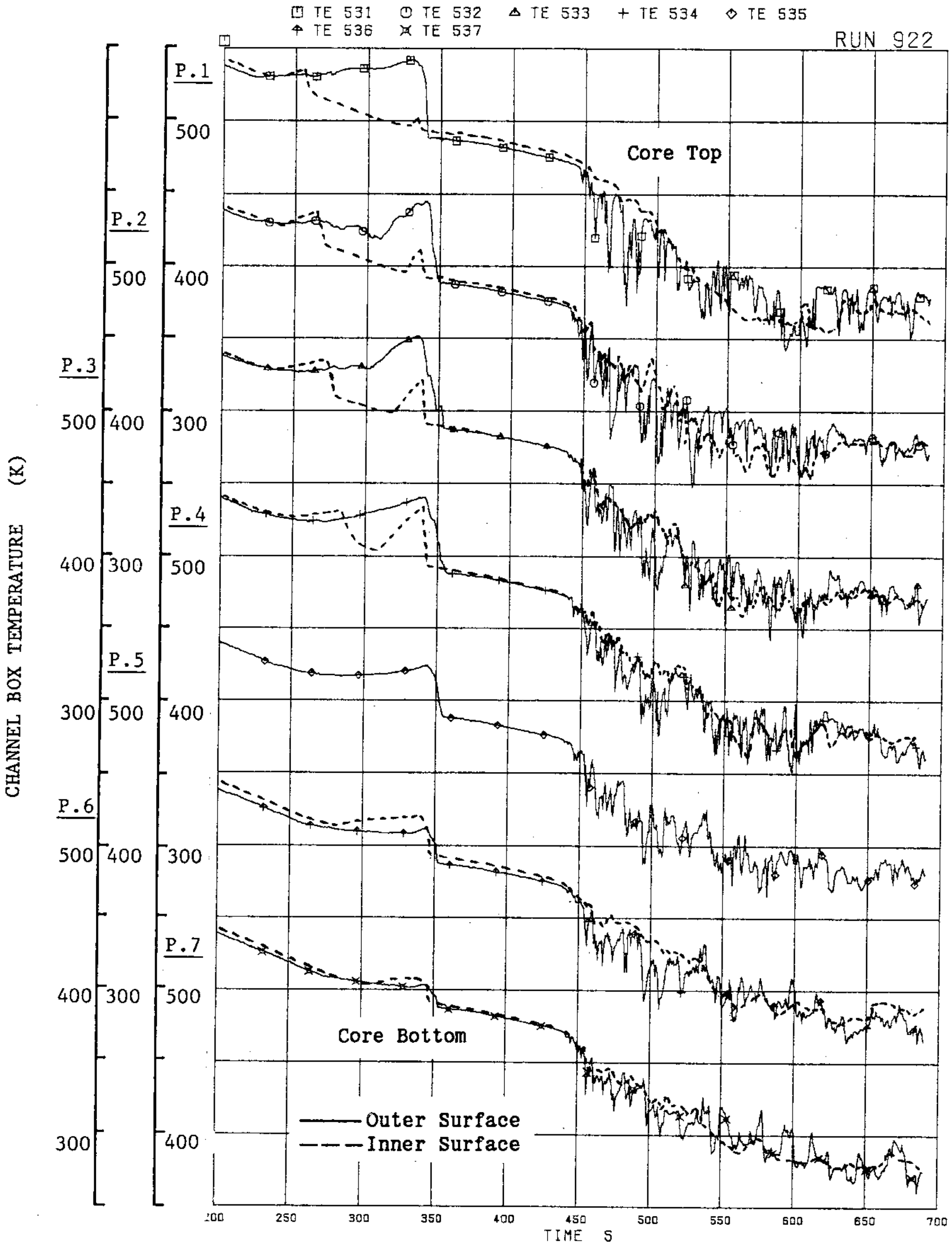

Fig. 6.37 Outer and inner surface temperatures of channel box A in RUN 922

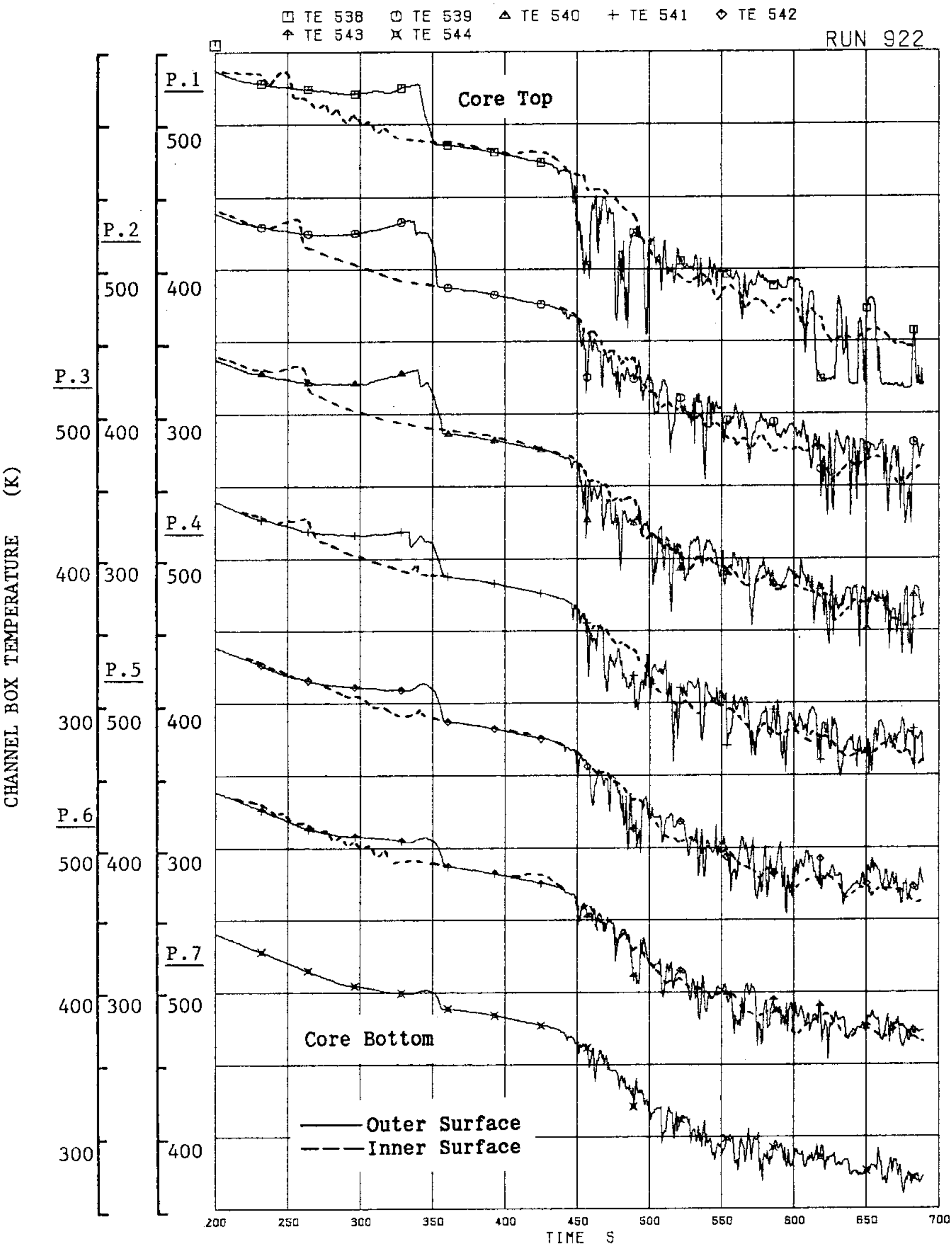

Fig. 6.38 Outer and inner surface temperatures of channel box C in RUN 922

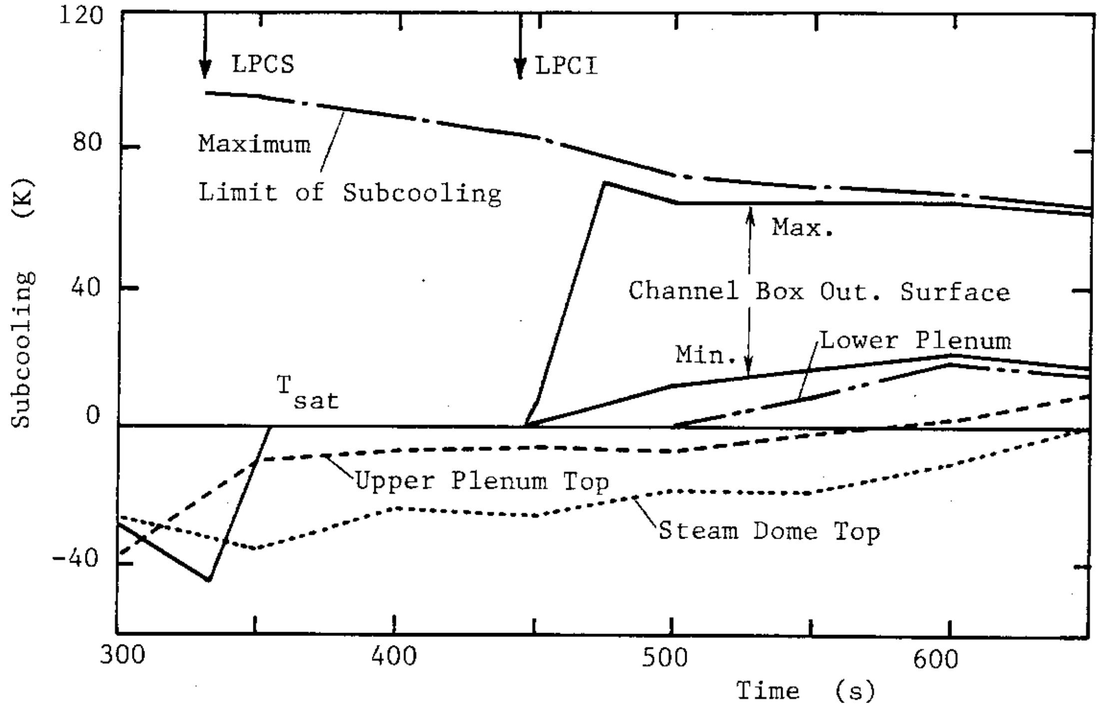

Fig. 6.39 Subcooling Distribution after ECC injection in RUN 940

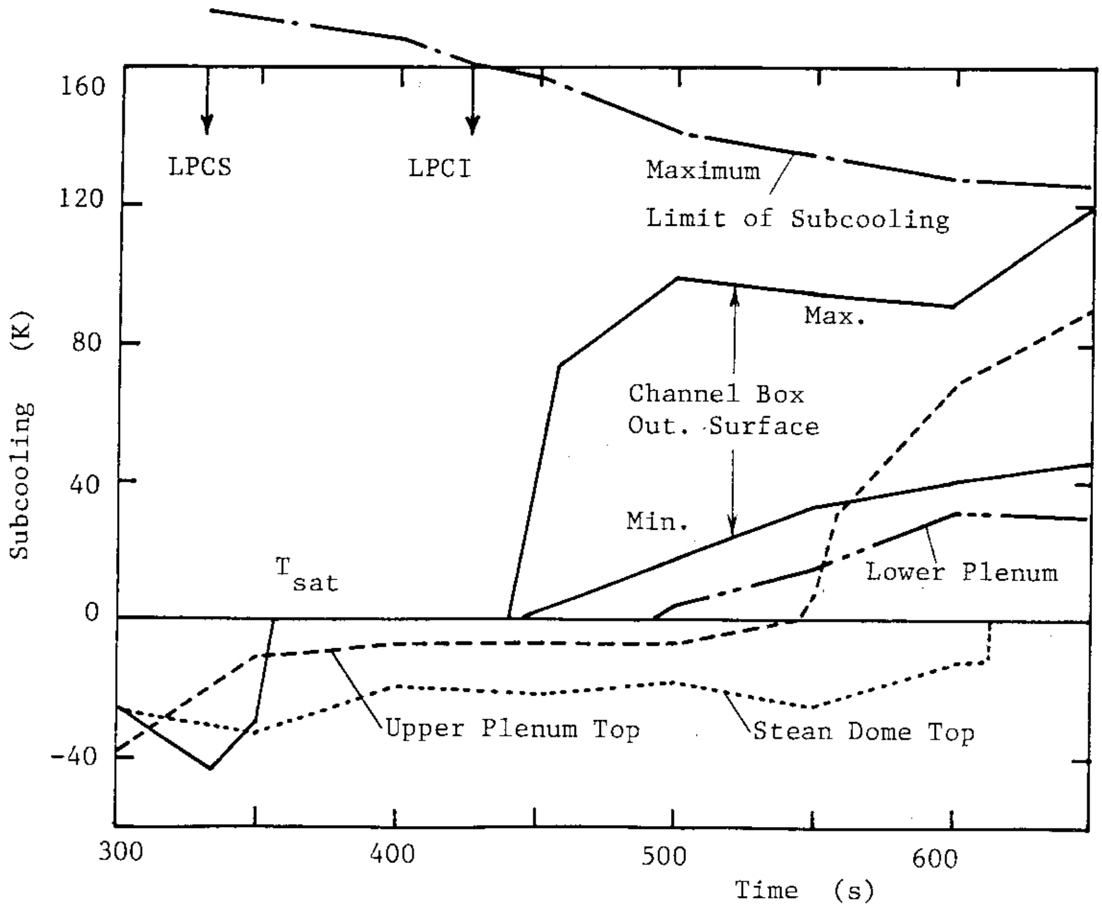

Fig. 6.40 Subcooling Distribution after ECC injection in RUN 922

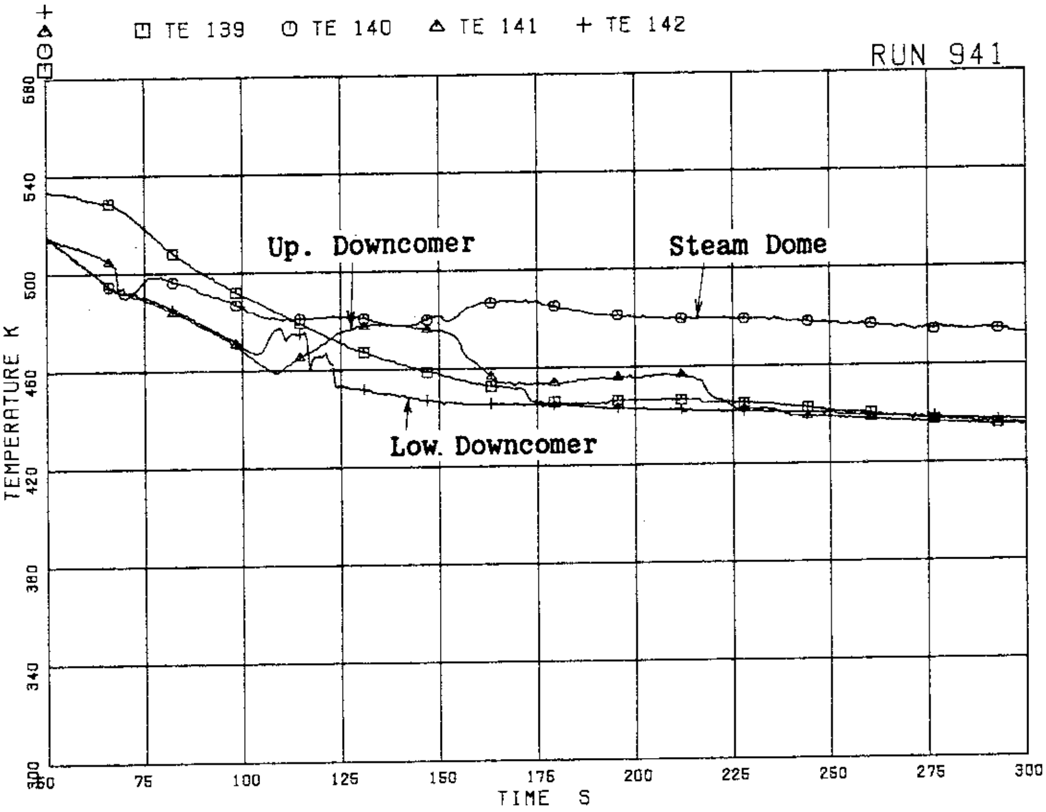

Fig. 6.41 Fluid temperature distribution in u.plenum, steam dome and downcomer in RUN 941

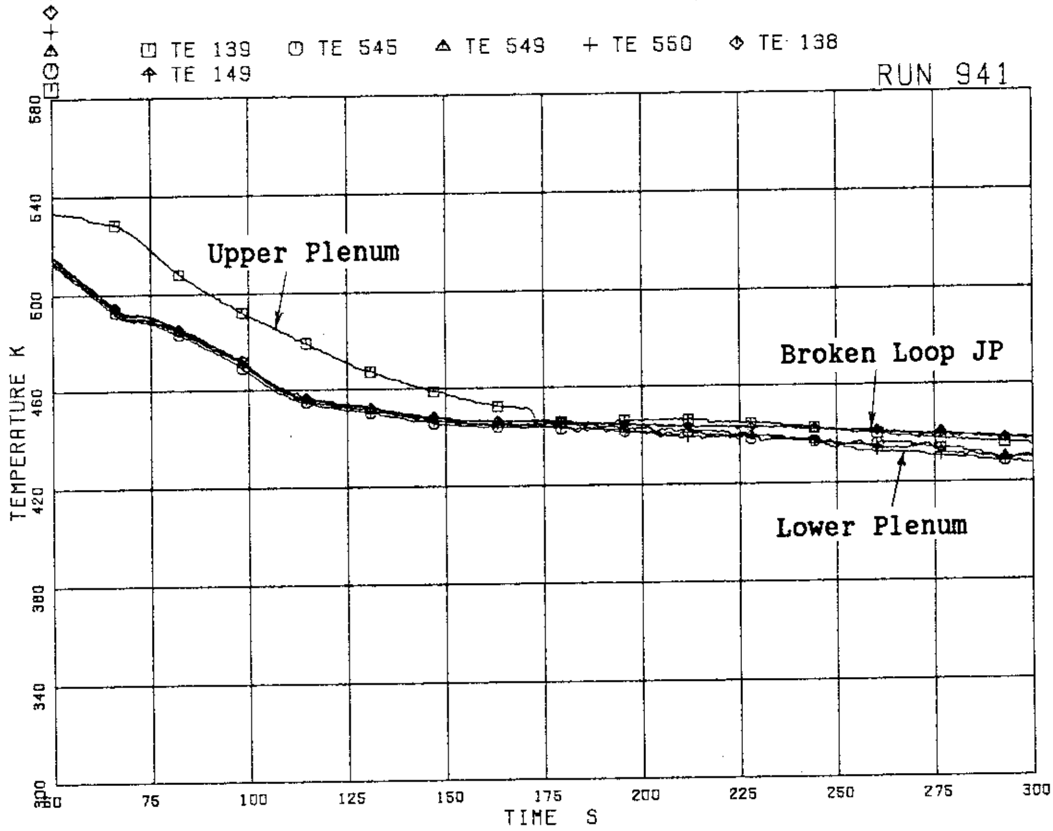

Fig. 6.42 Fluid temperature distribution in upper and lower plenua and broken loop JP in RUN 941

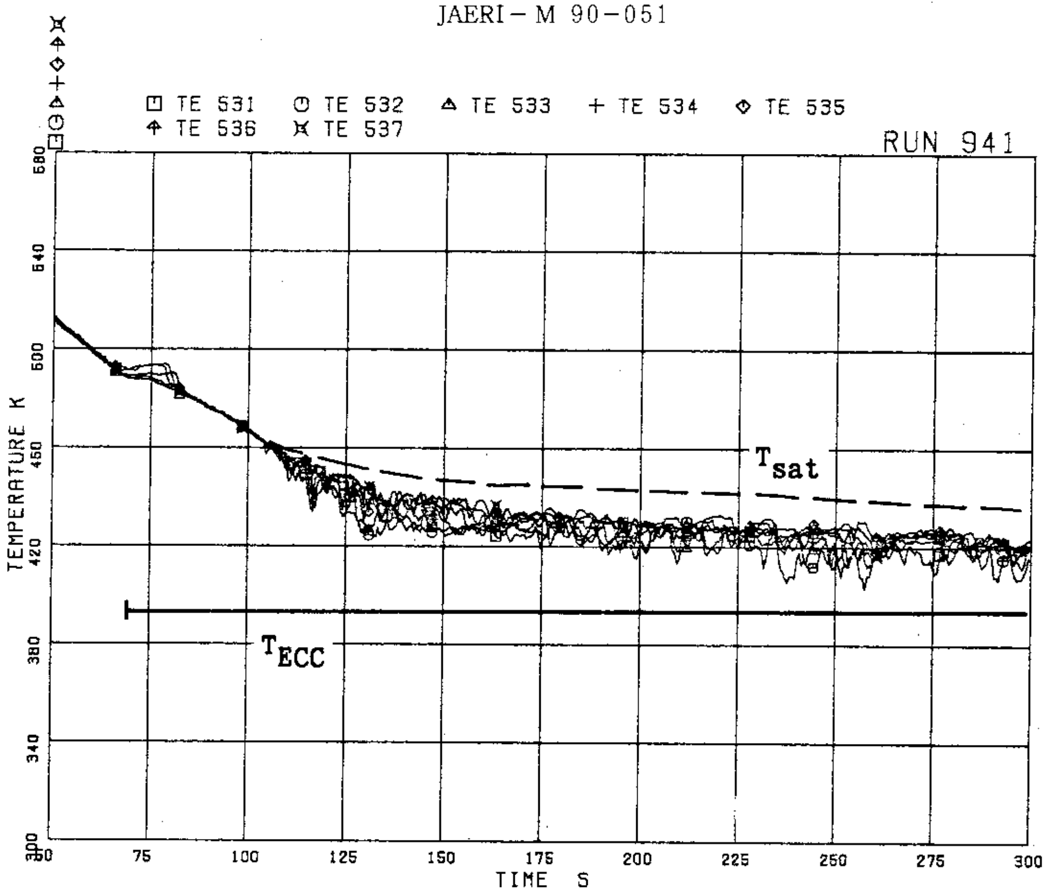

Fig. 6.43 Outer surface temperatures of channel box A (Pos.1 – 7) in RUN 941

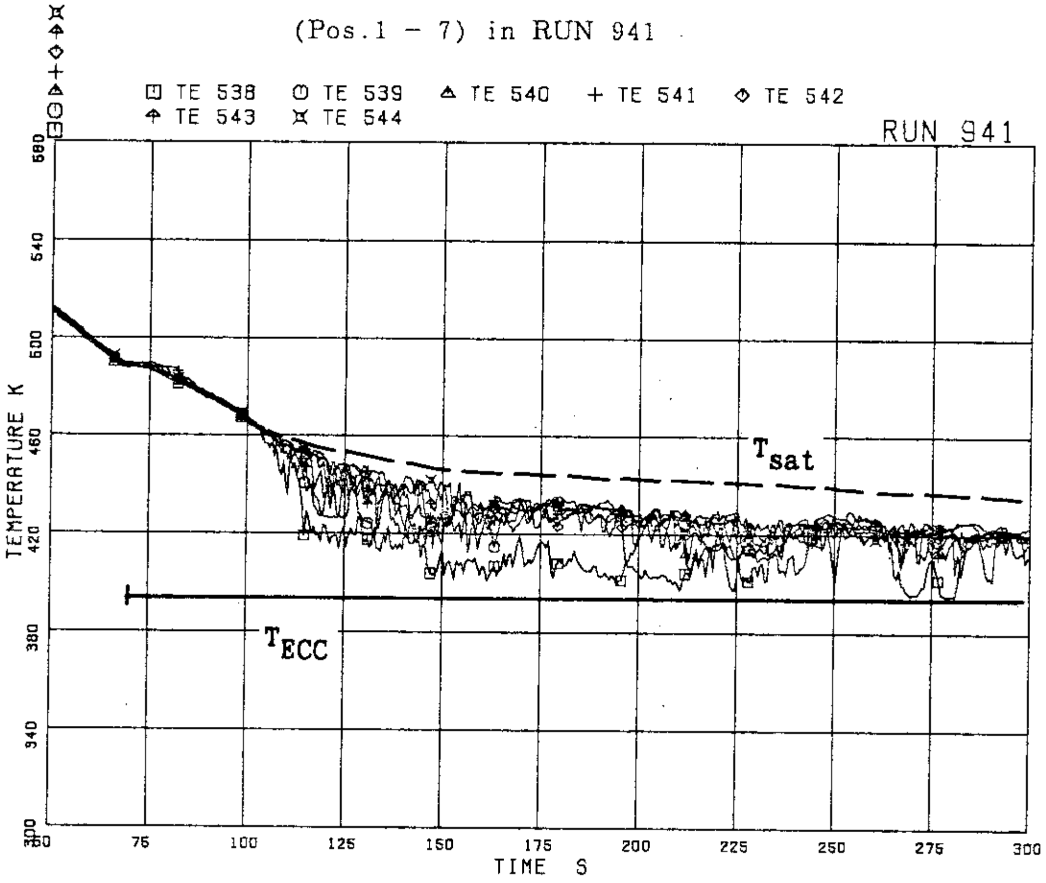

Fig. 6.44 Outer surface temperatures of channel box C (Pos.1 – 7) in RUN 941

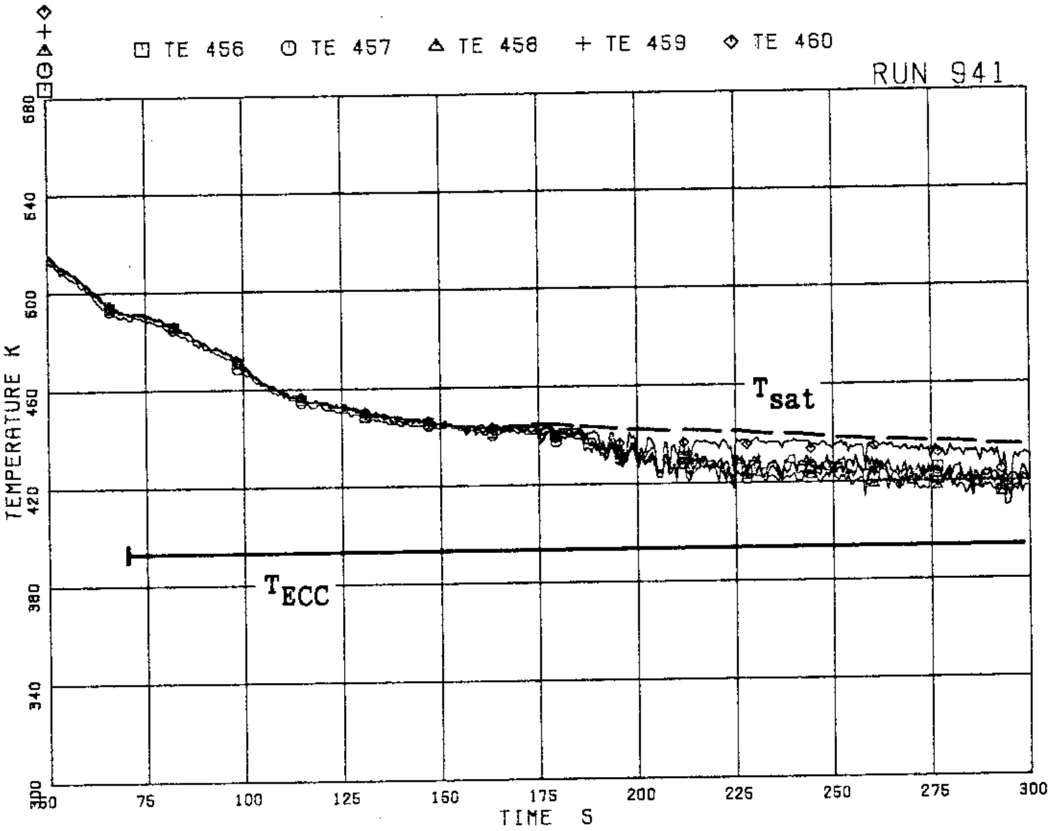

Fig. 6.45 Fluid temperatures above UTP of channel A, openings 1 to 5 in RUN 941

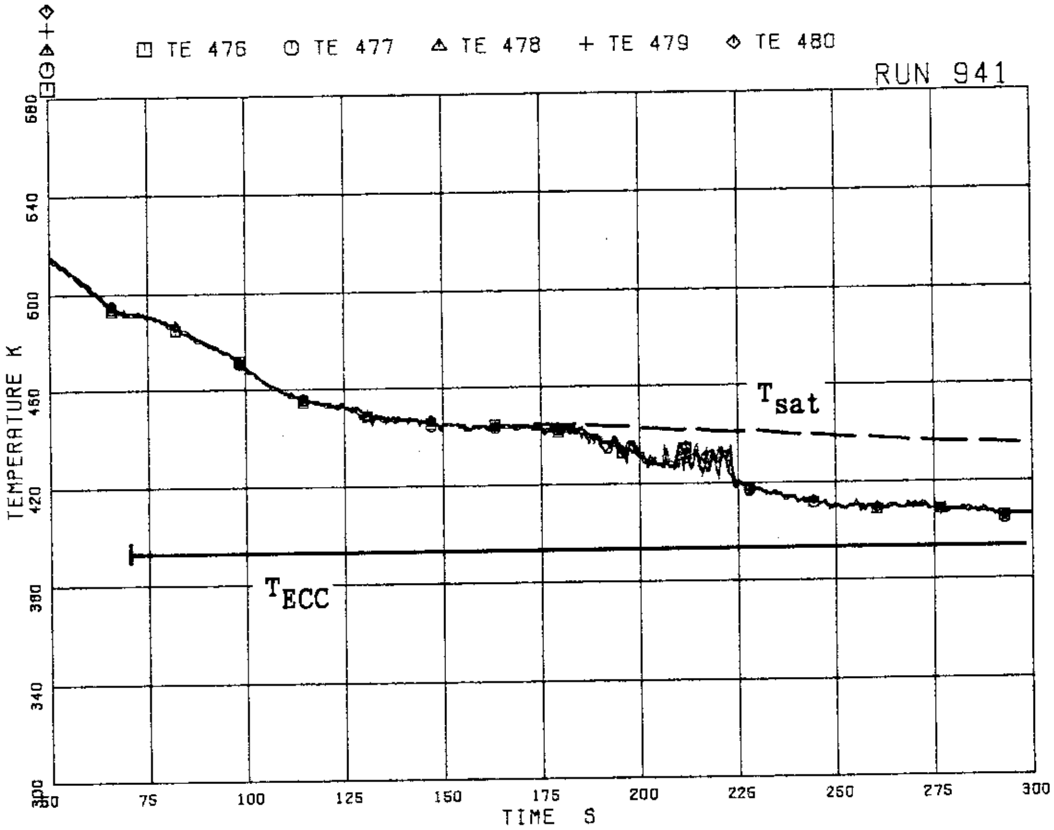

Fig. 6.46 Fluid temperatures above UTP of channel C, openings 1 to 5 in RUN 941

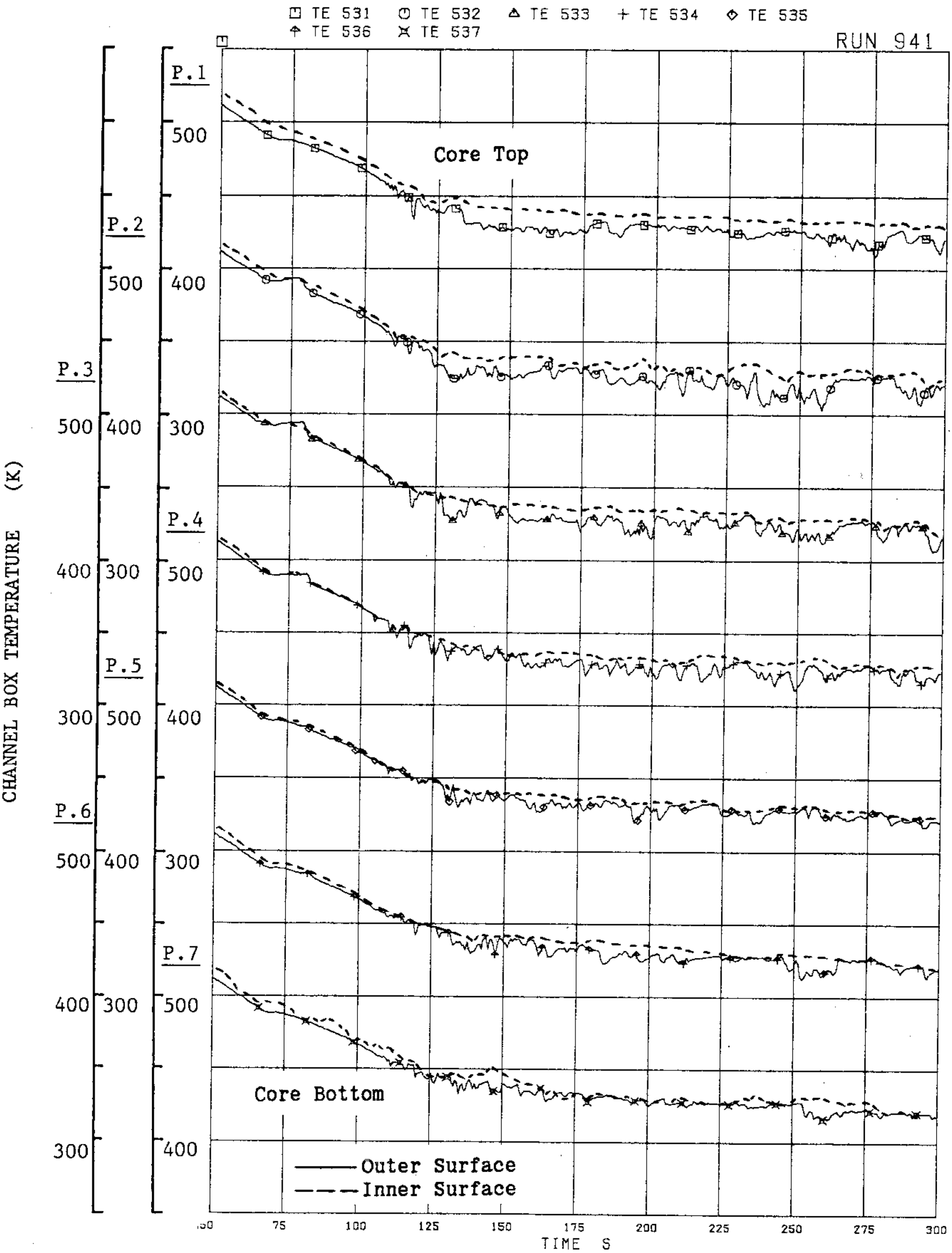

Fig. 6.47 Outer and inner surface temperatures of channel box A in RUN 941

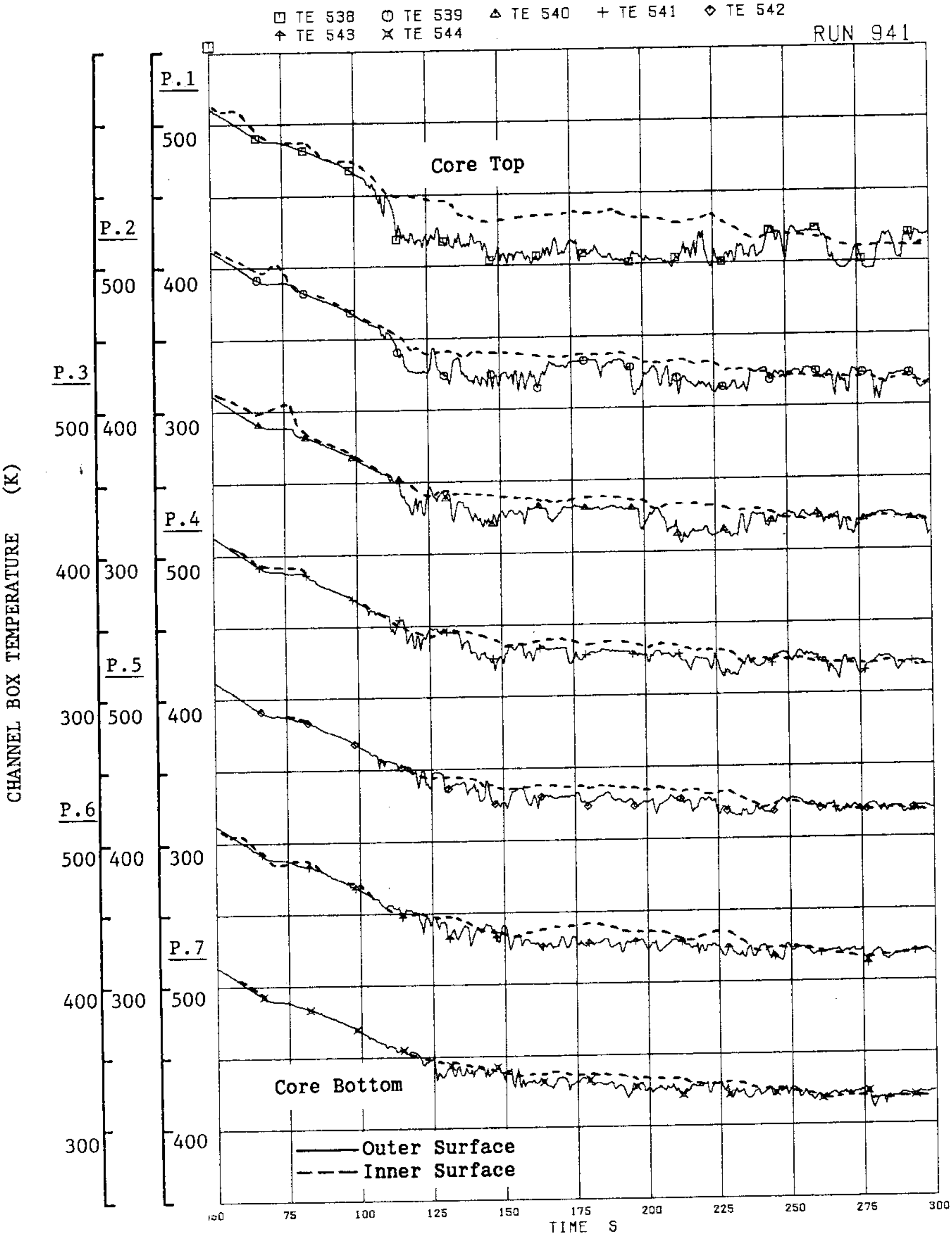

Fig. 6.48 Outer and inner surface temperatures of channel box C in RUN 940

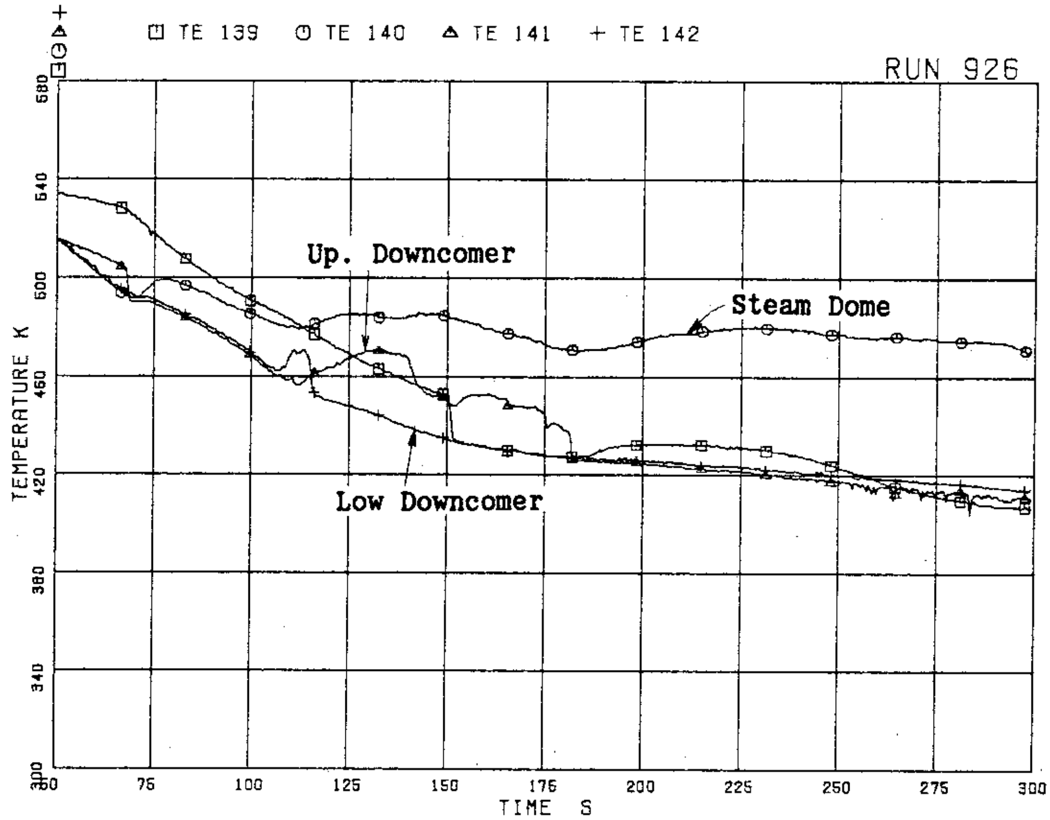

Fig. 6.49 Fluid temperature distribution in u.plenum, steam dome and downcomer in RUN 926

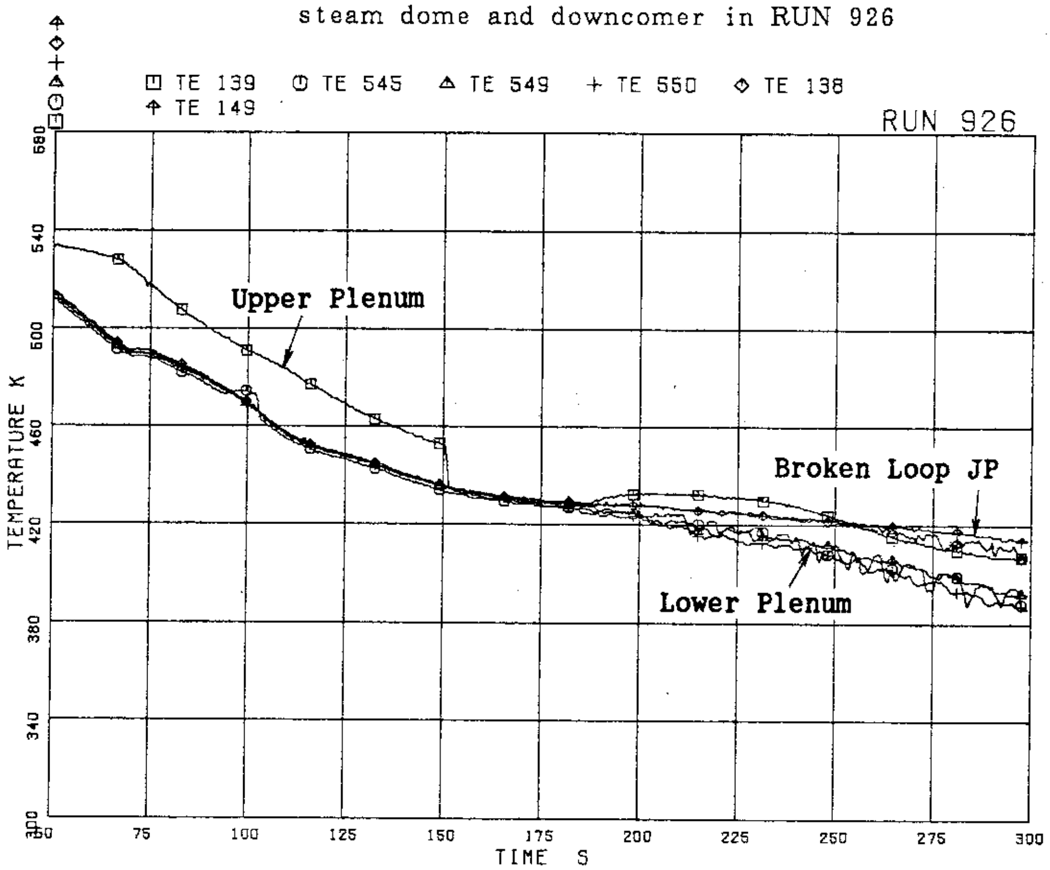

Fig. 6.50 Fluid temperature distribution in upper and lower plenua and broken loop JP in RUN 926

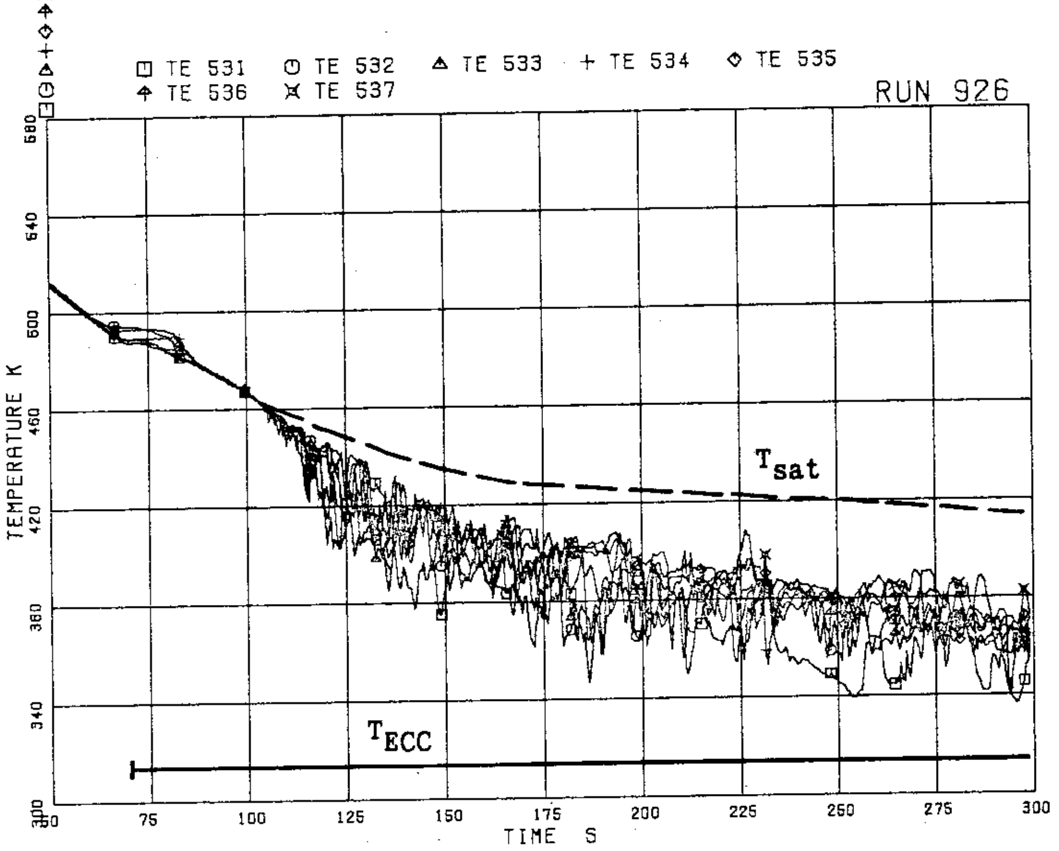

Fig. 6.51 Outer surface temperatures of channel box A (Pos.1 － 7) in RUN 926

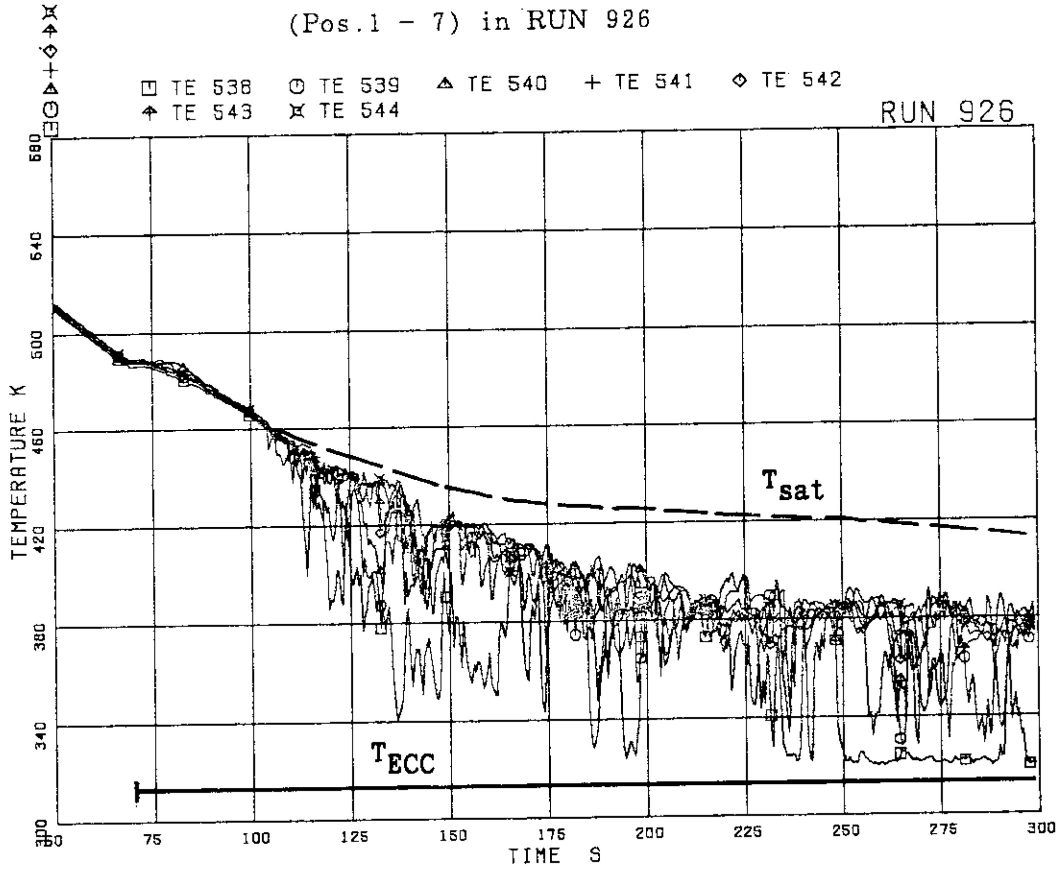

Fig. 6.52 Outer surface temperatures of channel box C (Pos.1 － 7) in RUN 926

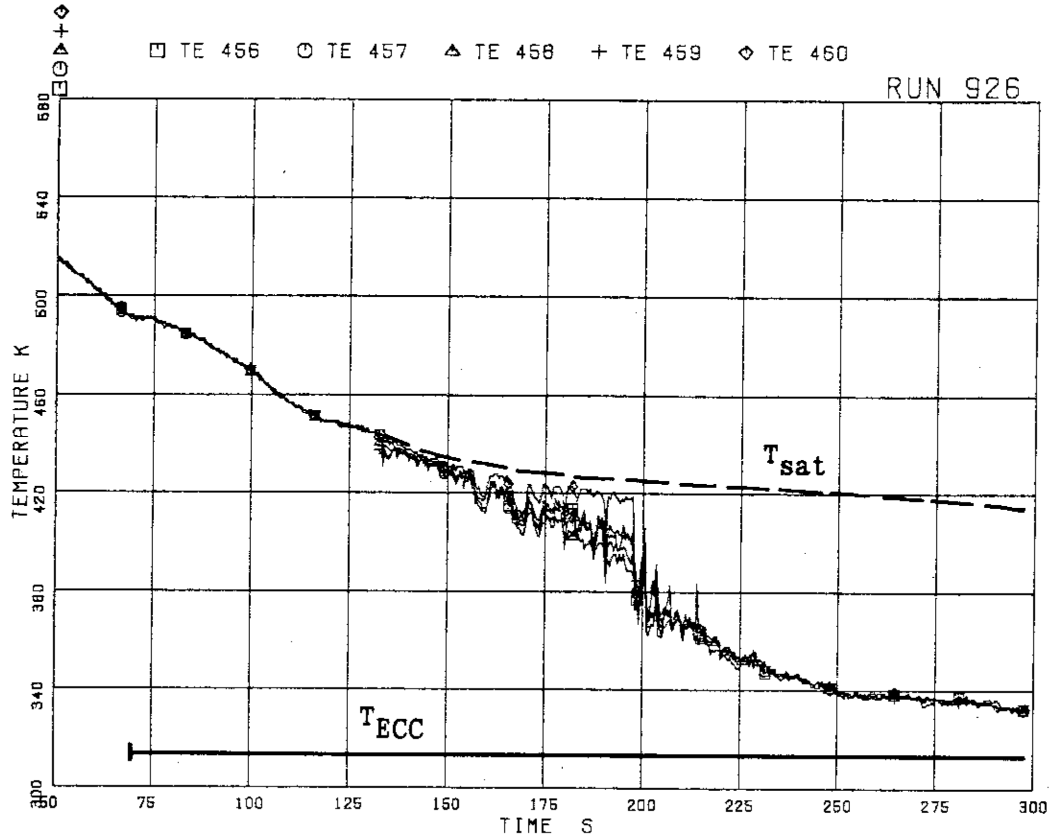

Fig. 6.53 Fluid temperatures above UTP of channel A, openings 1 to 5 in RUN 926

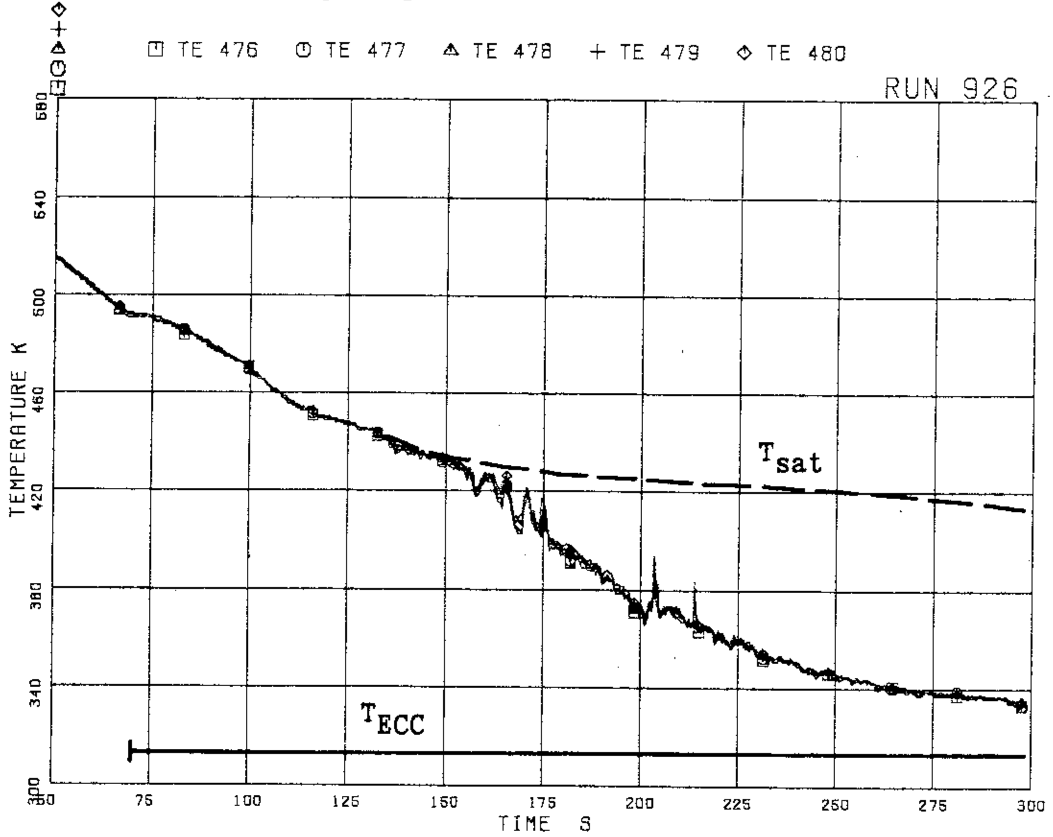

Fig. 6.54 Fluid temperatures above UTP of channel C, openings 1 to 5 in RUN 926

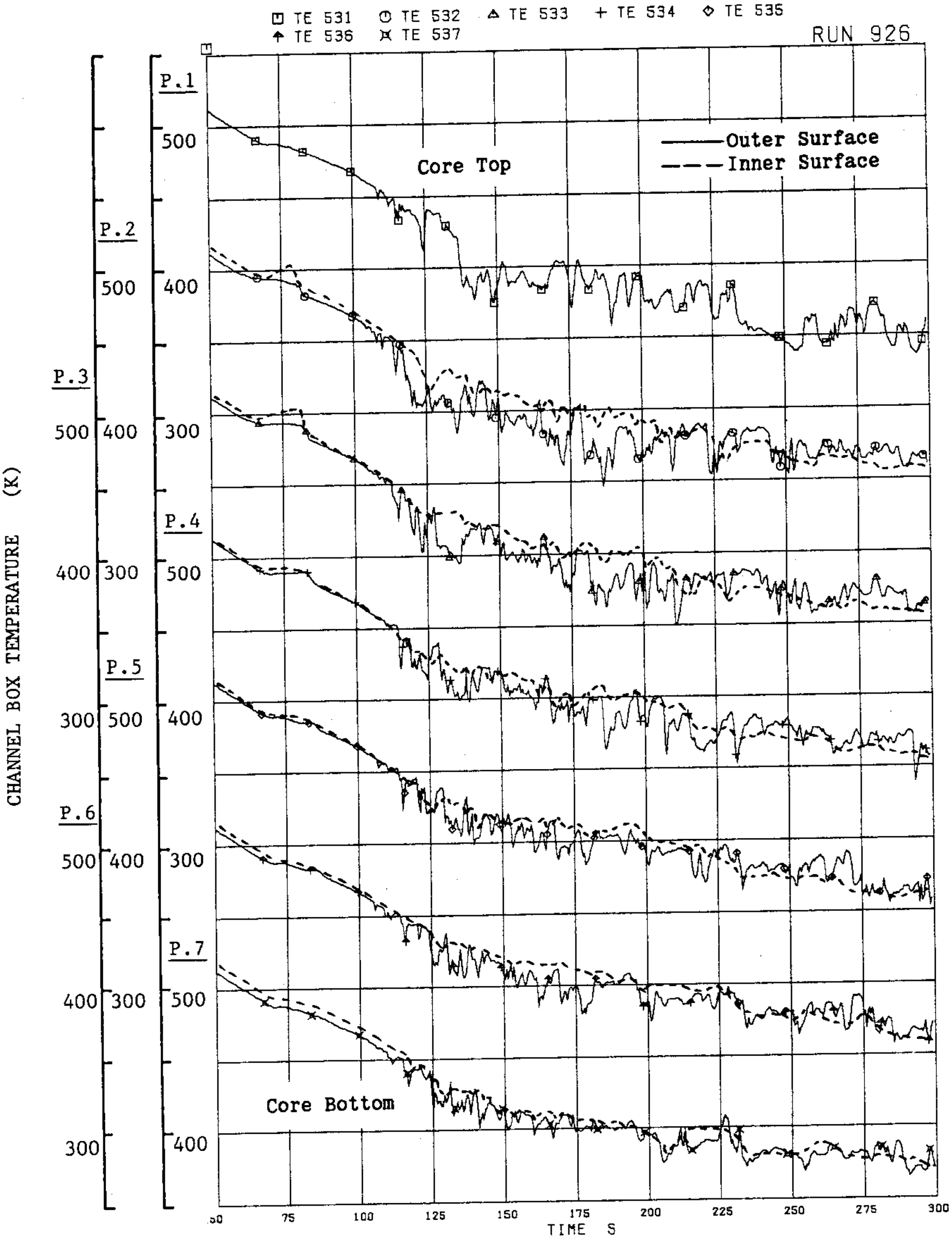

Fig. 6.55 Outer and inner surface temperatures of channel box A in RUN 926

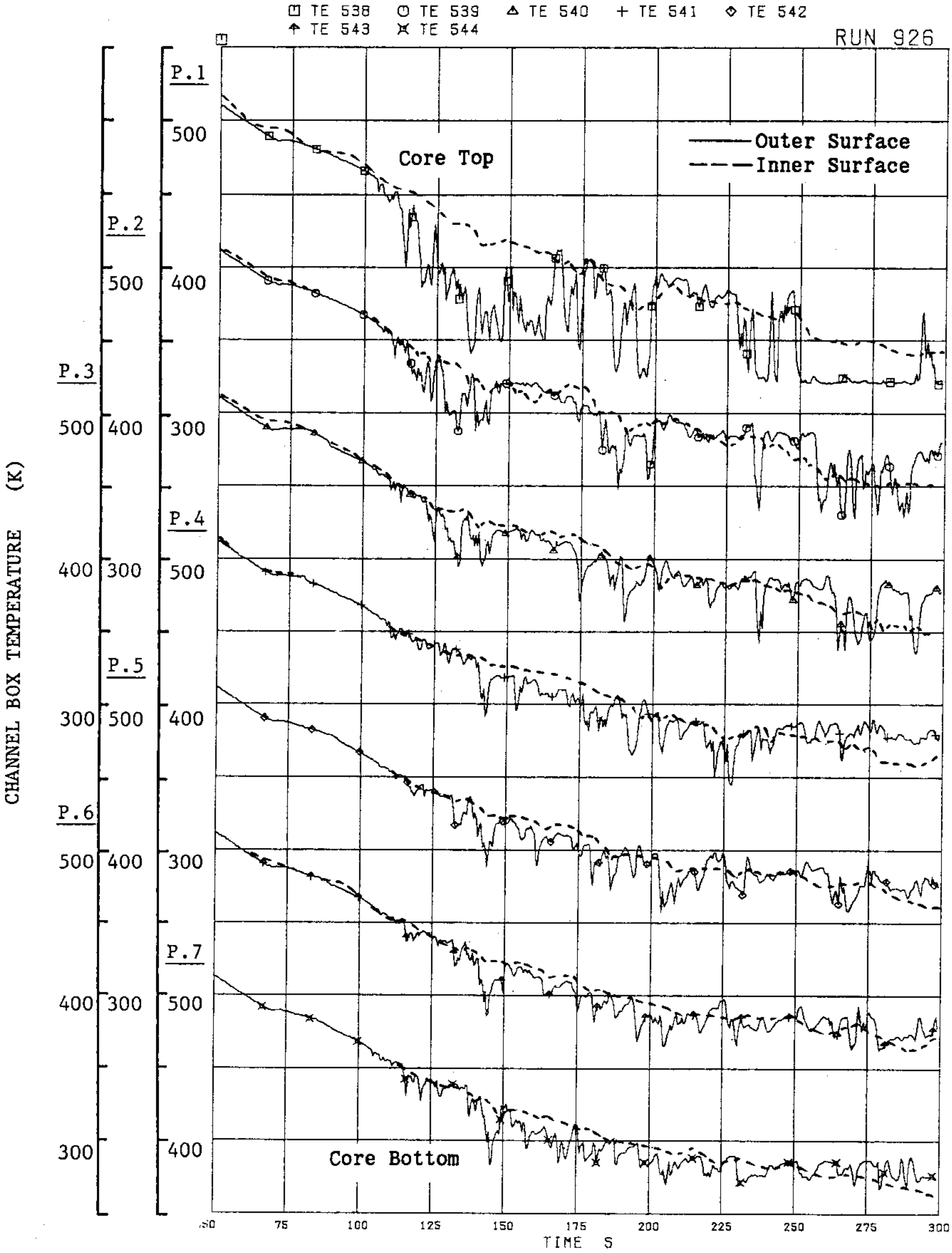

Fig. 6.56 Outer and inner surface temperatures of channel box C in RUN 926

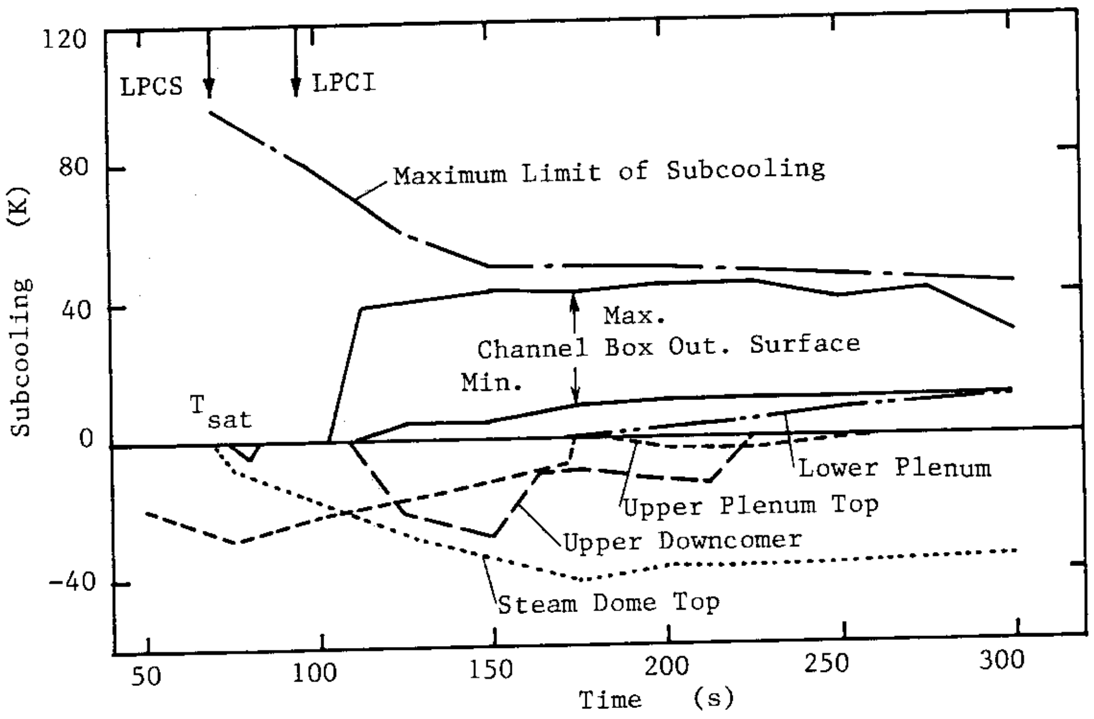

Fig. 6.57 Subcooling Distribution after ECC injection in RUN 941

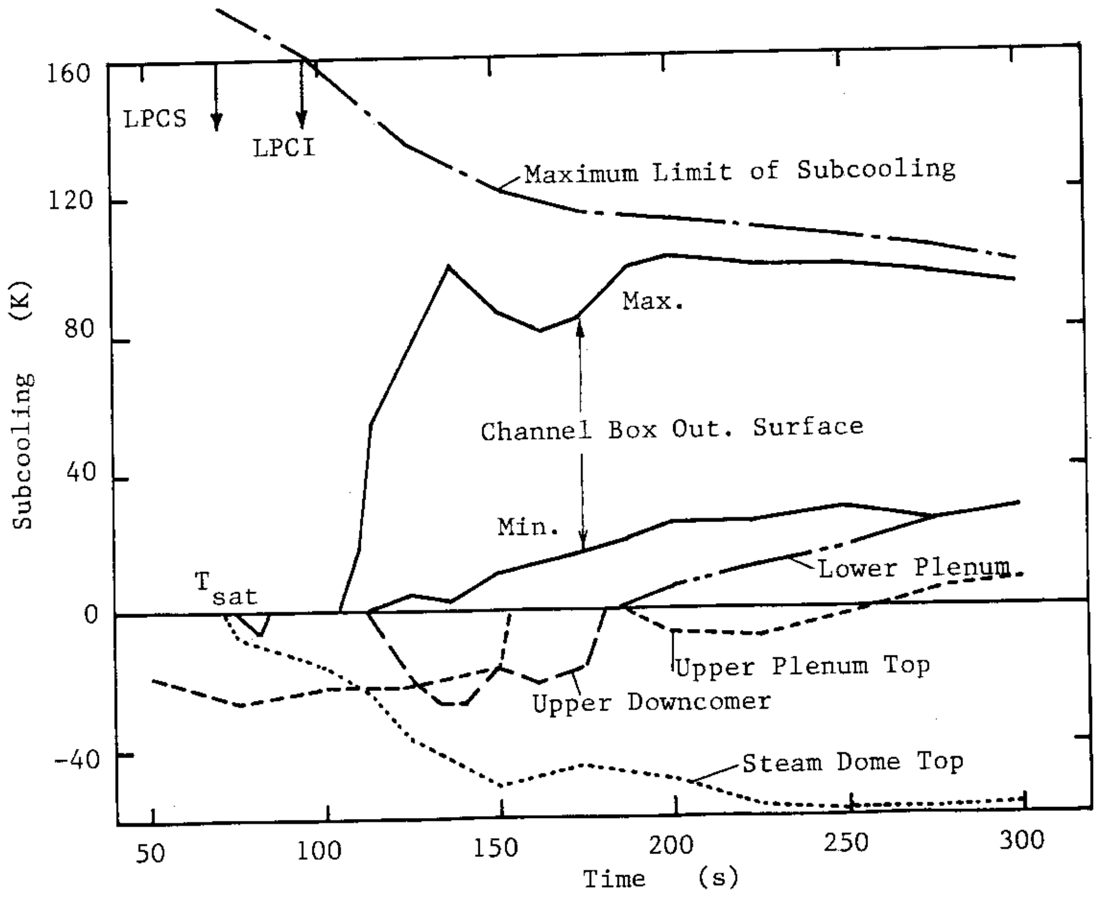

Fig. 6.58 Subcooling Distribution after ECC injection in RUN 926

Appendix I List of Measurements and Calculated Data in RUNs 940 and 941

All of the measurements (Channels 1 through 698) in RUNs 940 and 941 are listed in Table A.1. The figure number of RUN 940 data (see Appendix II; Figs.A.1 through A.157) is shown as A.XXX. As all the experiment data of RUN 941 (see Appendix II; Figs.B.1 through B.157) are shown similarly as those of RUN 940, the figure number of RUN 941 can be read by changing the letter "A" to "B" in Table A.1. The signatures of NM, NU and FL in the figure number column of Table A.1 mean "not measured", "not used" and "failure", respectively. The blank data mean that the recorded data were not shown in this report because those data were similar and could be represented by the other data shown in this report. Shown in Table A.2 is a list of calculated data by using the experimental results shown in Table A.1. The core instrumentations including the heater rod surface temperatures and fluid mixture level are listed in Table A.3.

Table A.1	Measurement List for RUNs 940 and 941
Table A.2	Calculated Data in RUNs 940 and 941
Table A.3	Core Instrumentation List

Table A.1 Measurement list for RUNs 940 and 941

1Ch.- 50Ch.

Ch.	Item	Symbol	ID.		Location	Fig.No.	Range	Unit	Accuracy
1	Press.	P- 1	PA	1	Lower Plenum	A. 1	0.100 - 10.0	MPa	1.08%FS
2	Press.	P- 2	PA	2	Upper Plenum	A. 1	0.100 - 10.0	MPa	1.08%FS
3	Press.	P- 3	PA	3	Steam Dome	A. 1	0.100 - 10.0	MPa	1.08%FS
4	Press.	P- 4	PA	4	Downcomer Bottom	A. 1	0.100 - 10.0	MPa	1.08%FS
5	Press.	P- 5	PA	5	JP-3 Drive	A. 2	0.100 - 10.0	MPa	1.08%FS
6	Press.	P- 6	PA	6	JP-4 Drive	A. 2	0.100 - 10.0	MPa	1.08%FS
7	Press.	P- 7	PA	7	JP-3 Suction	A. 2	0.100 - 10.0	MPa	1.08%FS
8	Press.	P- 8	PA	8	JP-4 Suction	A. 2	0.100 - 10.0	MPa	1.08%FS
9	Press.	P- 9	PA	9	MRP-1 Suction	A. 3	0.100 - 10.0	MPa	1.08%FS
10	Press.	P-10	PA	10	MRP-2 Suction	A. 3	0.100 - 10.0	MPa	1.08%FS
11	Press.	P-11	PA	11	MRP-2 Delivery	A. 3	0.100 - 10.0	MPa	1.08%FS
12	Press.	P-12	PA	12	Break A Upstream	NM	0.100 - 10.0	MPa	1.08%FS
13	Press.	P-13	PA	13	Break A Downstream	A. 4	0.100 - 10.0	MPa	1.08%FS
14	Press.	P-14	PA	14	Break B Upstream	A. 5	0.100 - 10.0	MPa	1.08%FS
15	Press.	P-15	PA	15	Break B Downstream	A. 5	0.100 - 10.0	MPa	1.08%FS
16	Press.	P-16	PA	16	Steam Line		0.100 - 10.0	MPa	1.08%FS
17	Press.	P-17	PA	17	JP-1,2 Outlet Spool		0.100 - 10.0	MPa	1.08%FS
18	Press.	P-18	PA	18	JP-3,4 Outlet Spool		0.100 - 10.0	MPa	1.08%FS
19	Press.	P-19	PA	19	Break A Spool Piece	A. 4	0.100 - 10.0	MPa	1.08%FS
20	Press.	P-30	PA	20	Break B Spool Piece	A. 5	0.100 - 10.0	MPa	1.08%FS
21	Diff.P.	D- 1	PD	21	Lower Pl.-Upper Pl.	5.13,33	-50.0 - 350.	kPa	0.63%FS
22	Diff.P.	D- 2	PD	22	Upper Pl.-Steam Dome	5.13,33	-10.0 - 90.0	kPa	0.63%FS
23	Diff.P.	D- 3	PD	23	Lower Plenum Head	NM			
24	Diff.P.	D- 4	PD	24	Downcomer Head	A. 6	0.0 - 100.	kPa	0.63%FS
25	Diff.P.	D- 5	PD	25	PV Bottom-Top	A. 7	-100. - 900.	kPa	0.63%FS
26	Diff.P.	D- 6	PD	26	JP-1 Disch.-Suction	A. 8	-100. - 300.	kPa	0.63%FS
27	Diff.P.	D- 7	PD	27	JP-1 Drive -Suction	A. 9	0.0 - 2.50	MPa	0.63%FS
28	Diff.P.	D- 8	PD	28	JP-2 Disch.-Suction	A. 8	-100. - 300.	kPa	0.63%FS
29	Diff.P.	D- 9	PD	29	JP-2 Drive -Suction	A. 9	0.0 - 2.50	MPa	0.63%FS
30	Diff.P.	D-10	PD	30	JP-3 Disch.-Suction	A. 10	-100. - 300.	kPa	0.63%FS
31	Diff.P.	D-11	PD	31	JP-3 Drive -Suction	A. 11	-4.00 - 2.00	MPa	0.63%FS
32	Diff.P.	D-12	PD	32	JP-4 Disch.-Suction	A. 10	-100. - 300.	kPa	0.63%FS
33	Diff.P.	D-13	PD	33	JP-4 Drive -Suction	A. 11	-4.00 - 2.00	MPa	0.63%FS
34	Diff.P.	D-14	PD	34	MRP-1 Deliv.-Suction	A. 12	-0.100 - 2.50	MPa	0.63%FS
35	Diff.P.	D-15	PD	35	MRP-2 Deliv.-Suction	A. 12	-0.100 - 2.50	MPa	0.63%FS
36	Diff.P.	D-16	PD	36	DC Bottom- MRP-1 Suc.	A. 13	-50.0 - 50.0	kPa	0.63%FS
37	Diff.P.	D-17	PD	37	MRP1 Deliv.-JP1 Drive	A. 14	0.0 - 250.	kPa	0.63%FS
38	Diff.P.	D-18	PD	38	MRP1 Deliv.-JP2 Drive	A. 14	0.0 - 250.	kPa	0.63%FS
39	Diff.P.	D-19	PD	39	DC Middle-JP1 Suction	A. 15	0.0 - 250.	kPa	0.63%FS
40	Diff.P.	D-20	PD	40	DC Middle-JP2 Suction	A. 15	0.0 - 250.	kPa	0.63%FS
41	Diff.P.	D-21	PD	41	JP1 Disch.-Lower Pl.	A. 16	-100. - 100.	kPa	0.63%FS
42	Diff.P.	D-22	PD	42	JP2 Disch.-Lower Pl.	A. 16	-100. - 100.	kPa	0.63%FS
43	Diff.P.	D-23	PD	43	DC Bottom- Break B	A. 17	-60.0 - 540.	kPa	0.63%FS
44	Diff.P.	D-24	PD	44	Break B- Break A	A. 18	0.0 - 100.	kPa	0.63%FS
45	Diff.P.	D-25	PD	45	Break A- MRP2 Suction	A. 19	-500. - 100.	kPa	0.63%FS
46	Diff.P.	D-26	PD	46	MRP2 Deliv.-JP3 Drive	A. 20	-500. - 500.	kPa	0.63%FS
47	Diff.P.	D-27	PD	47	MRP2 Deliv.-JP4 Drive	A. 20	-500. - 500.	kPa	0.63%FS
48	Diff.P.	D-28	PD	48	DC Middle-JP3 Suction	A. 21	-250. - 250.	kPa	0.63%FS
49	Diff.P.	D-29	PD	49	DC Middle-JP4 Suction	A. 21	-250. - 250.	kPa	0.63%FS
50	Diff.P.	D-30	PD	50	JP3 Disch.-Confluence	A. 22	-100. - 100.	kPa	0.63%FS

Table A.1 Measurement list for RUNs 940 and 941 (Cont'd)

51Ch.- 100Ch.

Ch.	Item	Symbol	ID.		Location	Fig.No.	Range	Unit	Accuracy
51	Diff.P.	D-31	PD	51	JP4 Disch.-Confluence	A. 22	-100. - 100.	kPa	0.63%FS
52	Diff.P.	D-32	PD	52	Confluence -Lower Pl.	A. 23	-50.0 - 50.0	kPa	0.63%FS
53	Diff.P.	D-33	PD	53	Lower Pl.-DC Middle	A. 24	-250. - 250.	kPa	0.63%FS
54	Diff.P.	D-34	PD	54	Lower Pl.-DC Bottom	A. 25	-250. - 250.	kPa	0.63%FS
55	Diff.P.	D-35	PD	55	DC Bottom-DC Middle	A. 26	-50.0 - 50.0	kPa	0.63%FS
56	Diff.P.	D-36	PD	56	DC Middle-Steam Dome	A. 27	-50.0 - 50.0	kPa	0.63%FS
57	Diff.P.	D-37	PD	57	Lower Pl.Mid-Upper PL	NM			
58	Diff.P.	D-38	PD	58	Lower Pl.Bottom-Mid.	A. 28	0.0 - 50.0	kPa	0.63%FS
59	Diff.P.	D-39	PD	59	Upper Pl.-DC High	NM	-20.0 - 100.	kPa	0.63%FS
60	Diff.P.	D-40	PD	60	Channel Orifice A		-50.0 - 50.0	kPa	0.63%FS
61	Diff.P.	D-41	PD	61	Channel Orifice B		-50.0 - 50.0	kPa	0.63%FS
62	Diff.P.	D-42	PD	62	Channel Orifice C		-25.0 - 75.0	kPa	0.63%FS
63	Diff.P.	D-43	PD	63	Channel Orifice D		-50.0 - 50.0	kPa	0.63%FS
64	Diff.P.	D-44	PD	64	Bypass Hole		-100. - 100.	KPA	0.63%FS
65	Level	WL- 1	LM	65	HPCS Tank	NU	0.0 - 2.30	m	1.00%FS
66	Level	WL- 2	LM	66	LPCS Tank	A. 29	0.0 - 2.30	m	1.00%FS
67	Level	WL- 3	LM	67	LPCI Tank	A. 29	0.0 - 4.25	m	1.00%FS
68	Level	WL- 4	LM	68	Upper Downcomer	5.12,32	3.90 - 6.04	m	1.00%FS
69	Level	WL- 5	LM	69	Lower Downcomer	5.12,32	0.938 - 3.90	m	1.00%FS
70	Mass.F.	F- 1	FM	70	Steam Line (Low Range)		0.0 - 1.13	kg/s	0.92%FS
71	Mass.F.	F- 2	FM	71	Steam Line(High Range)		0.0 - 3.00	kg/s	0.92%FS
72	Mass.F.	F- 3	FM	72	Steam Line (Mid Range)		0.0 - 1.94	kg/s	1.40%FS
73	Vol.F.	F- 7	FV	73	HPCS (Upper Plenum)	NU	0.0 - 0.250E-02	m3/s	0.79%FS
74	Vol.F.	F- 9	FV	74	LPCS (Upper Plenum)	5. 6,26	0.0 - 0.250E-02	m3/s	0.79%FS
75	Vol.F.	F-11	FV	75	LPCI (Core Bypass)	5. 6,26	0.0 - 0.830E-02	m3/s	0.79%FS
76	Vol.F.	F-15	FV	76	Feedwater	5. 5,25	0.0 - 0.100E-01	m3/s	0.79%FS
77	Vol.F.	F-16	FV	77	PWT Flow	NU	0.0 - 0.420E-02	m3/s	0.79%FS
78	Vol.F.	F-17	FV	78	JP1 Discharge	A. 30	0.0 - 0.170E-01	m3/s	0.88%FS
79	Vol.F.	F-18	FV	79	JP2 Discharge	A. 30	0.0 - 0.170E-01	m3/s	0.88%FS
80	Vol.F.	F-19	FV	80	JP3 Disch. Positive	A. 31	0.0 - 0.170E-01	m3/s	0.92%FS
81	Vol.F.	F-20	FV	81	JP3 Disch. Negative	A. 32	0.0 - 0.500E-02	m3/s	0.92%FS
82	Vol.F.	F-21	FV	82	JP4 Disch. Positive	A. 31	0.0 - 0.170E-01	m3/s	0.92%FS
83	Vol.F.	F-22	FV	83	JP4 Disch. Negative	A. 32	0.0 - 0.500E-02	m3/s	0.92%FS
84	Mass.F.	F-23	FM	84	JP1,2 Outlet Spool	NM	0.0 - 30.0	kg/s	1.40%FS
85	Mass.F.	F-24	FM	85	JP3,4 Outlet Spool	NM	0.0 - 30.0	kg/s	1.40%FS
86	Mass.F.	F-25	FM	86	Break A Spool Piece	NM	0.0 - 30.0	kg/s	1.40%FS
87	Mass.F.	F-26	FM	87	Break B Spool Piece	NM	0.0 - 30.0	kg/s	1.40%FS
88	Vol.F.	F-27	FV	88	MRP-1	A. 33	0.0 - 0.120E-01	m3/s	0.88%FS
89	Vol.F.	F-28	FV	89	MRP-2	A. 33	0.0 - 0.120E-01	m3/s	0.63%FS
90	Diff.P.	D-F1	PD	90	F1 Orifice		0.0 - 4.90	kPa	0.63%FS
91	Diff.P.	D-F2	PD	91	F2 Orifice		0.0 - 34.9	kPa	0.63%FS
92	Diff.P.	D-F3	PD	92	F3 Orifice		0.0 - 14.6	kPa	0.63%FS
93	Diff.P.	D-F17	PD	93	F17 Venturi		0.0 - 98.1	kPa	0.63%FS
94	Diff.P.	D-F18	PD	94	F18 Venturi		0.0 - 98.1	kPa	0.63%FS
95	Diff.P.	D-F19	PD	95	F19 Orifice		0.0 - 147.	kPa	0.63%FS
96	Diff.P.	D-F20	PD	96	F20 Orifice		0.0 - 13.2	kPa	0.63%FS
97	Diff.P.	D-F21	PD	97	F21 Orifice		0.0 - 147.	kPa	0.63%FS
98	Diff.P.	D-F22	PD	98	F22 Orifice		0.0 - 13.2	kPa	0.63%FS
99	Diff.P.	D-F27	PD	99	F27 Venturi		0.0 - 200.	kPa	0.63%FS
100	Diff.P.	D-F28	PD	100	F28 Venturi		0.0 - 200.	kPa	0.63%FS

Table A.1 Measurement list for RUNs 940 and 941 (Cont'd)

101Ch.- 150Ch.

Ch.	Item	Symbol	ID.	Location	Fig.No.	Range	Unit	Accuracy
101	Power	W- 1	WE 101	2100 kW Power Supplier	5. 2,22	0.0 - 0.210E+04	kW	1.00%FS
102	Power	W- 2	WE 102	3150 kW Power Supplier	5. 2,22	0.0 - 0.315E+04	kW	1.00%FS
103					NU			
104	Rev.	N- 1	SR 104	MRP-1 Revolution	A. 34	0.0 - 0.500E+04	RPM	1.08%FS
105	Rev.	N- 2	SR 105	MRP-2 Revolution	A. 34	0.0 - 0.500E+04	RPM	1.08%FS
106	Signal	S- 1	EV 106	Break Signal A	A. 35			
107	Signal	S- 2	EV 107	Break Signal B	A. 35			
108	Signal	S- 3	EV 108	QSV Signal	A. 35			
109	Signal	S- 6	EV 109	HPCS Valve	NU			
110	Signal	S- 7	EV 110	LPCS Valve	A. 36			
111	Signal	S- 8	EV 111	LPCI Valve	A. 36			
112	Signal	S- 9	EV 112	Feedwater Control	A. 35			
113	Signal	S-10	EV 113	MSIV Signal	A. 35			
114	Signal	S-11	EV 114	Steam Line Valve				
115	Signal	S-12	EV 115	ADS Valve	A. 36			
116	Signal	S-13	EV 116	MRP-1 Power OFF	A. 37			
117	Signal	S-14	EV 117	MRP-2 Power OFF	A. 37			
118	Signal	RD- 1	EV 118	MRP-1 Rev. Direction	NU			
119	Signal	RD- 2	EV 119	MRP-2 Rev. Direction	NU			
120	Density	DF- 1	DE 120	JP1,2 Outlet Beam A	A. 38	0.0 - 0.100E+04	kg/m3	1.00%FS
121	Density	DF- 2	DE 121	JP1,2 Outlet Beam B	A. 39	0.0 - 0.100E+04	kg/m3	1.00%FS
122	Density	DF- 3	DE 122	JP1,2 Outlet Beam C	A. 40	0.0 - 0.100E+04	kg/m3	1.00%FS
123	Density	DF- 4	DE 123	JP3,4 Outlet Beam A	A. 41	0.0 - 0.100E+04	kg/m3	1.00%FS
124	Density	DF- 5	DE 124	JP3,4 Outlet Beam B	A. 42	0.0 - 0.100E+04	kg/m3	1.00%FS
125	Density	DF- 6	DE 125	JP3,4 Outlet Beam C	A. 43	0.0 - 0.100E+04	kg/m3	1.00%FS
126	Density	DF- 7	DE 126	Break A Beam A	A. 44	0.0 - 0.100E+04	kg/m3	1.00%FS
127	Density	DF- 8	DE 127	Break A Beam B	A. 45	0.0 - 0.100E+04	kg/m3	1.00%FS
128	Density	DF- 9	DE 128	Break B Beam A	A. 46	0.0 - 0.100E+04	kg/m3	1.00%FS
129	Density	DF-10	DE 129	Break B Beam B	A. 47	0.0 - 0.100E+04	kg/m3	1.00%FS
130	Mo.Flux	M- 1	MF 130	JP1,2 Outlet Spool	A. 48	0.0 - 0.220E+05	kg/ms2	1.00%FS
131	Mo.Flux	M- 2	MF 131	JP3,4 Outlet Spool	A. 49	0.0 - 0.220E+05	kg/ms2	1.00%FS
132	Mo.Flux	M- 3	MF 132	Break A (Low Range)	A. 50	0.0 - 0.220E+05	kg/ms2	1.00%FS
133	Mo.Flux	M- 4	MF 133	Break B (Low Range)	A. 51	0.0 - 0.220E+05	kg/ms2	1.00%FS
134	Mo.Flux	M- 5	MF 134	Break A (High Range)	A. 52	0.0 - 0.220E+06	kg/ms2	1.00%FS
135	Mo.Flux	M- 6	MF 135	Break B (High Range)	A. 53	0.0 - 0.220E+06	kg/ms2	1.00%FS
136	Mo.Flux	M- 7	MF 136	Break Orifice	NM	0.0 - 0.220E+05	kg/ms2	1.00%FS
137								
138	Fluid T.	T- 1	TE 138	Lower Plenum	A. 54	273. - 673.	K	0.64%FS
139	Fluid T.	T- 2	TE 139	Upper Plenum	A. 54	273. - 673.	K	0.64%FS
140	Fluid T.	T- 3	TE 140	Steam Dome	A. 55	273. - 673.	K	0.64%FS
141	Fluid T.	T- 4	TE 141	Upper Downcomer	A. 56	273. - 673.	K	0.64%FS
142	Fluid T.	T- 5	TE 142	Lower Downcomer	A. 56	273. - 673.	K	0.64%FS
143	Fluid T.	T- 6	TE 143	JP-1 Drive	A. 57	273. - 673.	K	0.64%FS
144	Fluid T.	T- 7	TE 144	JP-2 Drive	A. 57	273. - 673.	K	0.64%FS
145	Fluid T.	T- 8	TE 145	JP-3 Drive	A. 58	273. - 673.	K	0.64%FS
146	Fluid T.	T- 9	TE 146	JP-4 Drive	A. 58	273. - 673.	K	0.64%FS
147	Fluid T.	T-10	TE 147	JP-1 Discharge	A. 59	273. - 673.	K	0.64%FS
148	Fluid T.	T-11	TE 148	JP-2 Discharge	A. 59	273. - 673.	K	0.64%FS
149	Fluid T.	T-12	TE 149	JP-3 Discharge	A. 60	273. - 673.	K	0.64%FS
150	Fluid T.	T-13	TE 150	JP-4 Discharge	A. 60	273. - 673.	K	0.64%FS

Table A.1 Measurement list for RUNs 940 and 941 (Cont'd)

151Ch.- 200Ch.

Ch.	Item	Symbol	ID.	Location	Fig.No.	Range	Unit	Accuracy
151	Fluid T.	T-14	TE 151	MRP-1 Suction	A. 57	273. - 673.	K	0.64%FS
152	Fluid T.	T-15	TE 152	MRP-1 Delivery	A. 57	273. - 673.	K	0.64%FS
153	Fluid T.	T-16	TE 153	MRP-2 Suction	A. 58	273. - 673.	K	0.64%FS
154	Fluid T.	T-17	TE 154	MRP-2 Delivery	A. 58	273. - 673.	K	0.64%FS
155	Fluid T.	T-18	TE 155	Break A Upstream	A. 61	273. - 673.	K	0.64%FS
156	Fluid T.	T-19	TE 156	Break B Upstream	A. 61	273. - 673.	K	0.64%FS
157	Fluid T.	T-20	TE 157	RCN A Condenced Water	NU	273. - 698.	K	0.64%FS
158	Fluid T.	T-21	TE 158	RCN B Condenced Water	NU	273. - 698.	K	0.64%FS
159	Fluid T.	T-22	TE 159	Discharged Steam	A. 55	273. - 673.	K	0.64%FS
160	Fluid T.	T-24	TE 160	JP-1,2 Outlet Spool	A. 59	273. - 763.	K	0.64%FS
161	Fluid T.	T-25	TE 161	JP-3,4 Outlet Spool	A. 60	273. - 763.	K	0.64%FS
162	Fluid T.	T-26	TE 162	Break A Spool Piece	A. 61	273. - 763.	K	0.64%FS
163	Fluid T.	T-27	TE 163	Break B Spool Piece	A. 61	273. - 763.	K	0.64%FS
164	Fluid T.	T-28	TE 164	Feedwater	A. 62	273. - 673.	K	0.64%FS
165	Fluid T.	T-29	TE 165	Break Orifice 1	NM	273. - 673.	K	0.64%FS
166	Fluid T.	T-30	TE 166	Break Orifice 2	NM	273. - 673.	K	0.64%FS
167	Fluid T.	T-31	TE 167	Break A Down DD(Low)	NM	273. - 673.	K	0.64%FS
168	Fluid T.	T-32	TE 168	Break B Down DD(Low)	NM	273. - 673.	K	0.64%FS
169	Fluid T.	T-33	TE 169	Break A Up. DD(High)	NM	273. - 673.	K	0.64%FS
170	Fluid T.	T-34	TE 170	Break B Up. DD(High)	NM	273. - 673.	K	0.64%FS
171	Fluid T.	T-F17	TE 171	JP1 Fluid D. Correc.	NM	273. - 673.	K	0.64%FS
172	Fluid T.	T-F18	TE 172	JP2 Fluid D. Correc.	NM	273. - 673.	K	0.64%FS
173	Fluid T.	T-F19	TE 173	JP3 Fluid D. Correc.	NM	273. - 673.	K	0.64%FS
174	Fluid T.	T-F21	TE 174	JP4 Fluid D. Correc.	NM	273. - 673.	K	0.64%FS
175	Slab T.	TS-11	TE 175	Core Barrel A Pos.5	NM	273. - 673.	K	0.64%FS
176	Slab T.	TS-12	TE 176	Core Barrel A Pos.6	NM	273. - 673.	K	0.64%FS
177	Slab T.	TS-13	TE 177	Filler Block C Pos.1	NM	273. - 673.	K	0.64%FS
178	Slab T.	TS-14	TE 178	Filler Block C Pos.2	NM	273. - 673.	K	0.64%FS
179	Slab T.	TS-15	TE 179	Filler Block C Pos.3	NM	273. - 673.	K	0.64%FS
180	Slab T.	TS-16	TE 180	Filler Block C Pos.4	NM	273. - 673.	K	0.64%FS
181	Slab T.	TS-17	TE 181	Filler Block C Pos.5	NM	273. - 673.	K	0.64%FS
182	Slab T.	TS-18	TE 182	Filler Block C Pos.6	NM	273. - 673.	K	0.64%FS
183	Slab T.	TS-19	TE 183	Filler Block A Pos.1	NM	273. - 673.	K	0.64%FS
184	Slab T.	TS-20	TE 184	Filler Block A Pos.2	NM	273. - 673.	K	0.64%FS
185	Slab T.	TS-21	TE 185	Filler Block A Pos.3	NM	273. - 673.	K	0.64%FS
186	Slab T.	TS-22	TE 186	Filler Block A Pos.4	NM	273. - 673.	K	0.64%FS
187	Slab T.	TS-23	TE 187	Filler Block A Pos.5	NM	273. - 673.	K	0.64%FS
188	Slab T.	TS-24	TE 188	Filler Block A Pos.6	NM	273. - 673.	K	0.64%FS
189	Slab T.	TS-25	TE 189	JP-1 Diffuser Wall	NM	273. - 673.	K	0.64%FS
190	Slab T.	TS-26	TE 190	JP-2 Diffuser Wall	NM	273. - 673.	K	0.64%FS
191	Slab T.	TS-27	TE 191	JP-3 Diffuser Wall	NM	273. - 673.	K	0.64%FS
192	Slab T.	TS-28	TE 192	JP-4 Diffuser Wall	NM	273. - 673.	K	0.64%FS
193	Slab T.	TS-29	TE 193	PV Wall Inside 1-1	NM	273. - 673.	K	0.64%FS
194	Slab T.	TS-30	TE 194	PV Inner Surface 1-2	NM	273. - 673.	K	0.64%FS
195	Slab T.	TS-31	TE 195	PV Inner Surface 1-3	NM	273. - 673.	K	0.64%FS
196	Slab T.	TS-32	TE 196	PV Wall Inside 2	NM	273. - 673.	K	0.64%FS
197	Slab T.	TS-33	TE 197	PV Wall Inside 3	NM	273. - 673.	K	0.64%FS
198	Slab T.	TS-34	TE 198	PV Wall Inside 4	NM	273. - 673.	K	0.64%FS
199	Slab T.	TS-35	TE 199	L.P. Inner Surface	NM	273. - 673.	K	0.64%FS
200	Slab T.	TS-36	TE 200	L.P. Wall Inside	NM	273. - 673.	K	0.64%FS

Table A.1 Measurement list for RUNs 940 and 941 (Cont'd)

201Ch.- 250Ch.

Ch.	Item	Symbol	ID.	Location	Fig.No.	Range	Unit	Accuracy
201	Temp.	TF- 1	TE 201	A11 Fuel Rod Pos.1	A. 63, 83	273. - 0.147E+04	K	0.64%FS
202	Temp.	TF- 2	TE 202	A11 Fuel Rod Pos.2	A. 63, 84	273. - 0.147E+04	K	0.64%FS
203	Temp.	TF- 3	TE 203	A11 Fuel Rod Pos.3	A. 63, 85	273. - 0.147E+04	K	0.64%FS
204	Temp.	TF- 4	TE 204	A11 Fuel Rod Pos.4	A. 63, 86	273. - 0.147E+04	K	0.64%FS
205	Temp.	TF- 5	TE 205	A11 Fuel Rod Pos.5	A. 63, 87	273. - 0.147E+04	K	0.64%FS
206	Temp.	TF- 6	TE 206	A11 Fuel Rod Pos.6	A. 63, 88	273. - 0.147E+04	K	0.64%FS
207	Temp.	TF- 7	TE 207	A11 Fuel Rod Pos.7	A. 63, 89	273. - 0.147E+04	K	0.64%FS
208	Temp.	TF- 8	TE 208	A12 Fuel Rod Pos.1	A. 64, 83	273. - 0.147E+04	K	0.64%FS
209	Temp.	TF- 9	TE 209	A12 Fuel Rod Pos.2	A. 64, 84	273. - 0.147E+04	K	0.64%FS
210	Temp.	TF- 10	TE 210	A12 Fuel Rod Pos.3	A. 64, 85	273. - 0.147E+04	K	0.64%FS
211	Temp.	TF- 11	TE 211	A12 Fuel Rod Pos.4	A. 64, 86	273. - 0.147E+04	K	0.64%FS
212	Temp.	TF- 12	TE 212	A12 Fuel Rod Pos.5	A. 64, 87	273. - 0.147E+04	K	0.64%FS
213	Temp.	TF- 13	TE 213	A12 Fuel Rod Pos.6	A. 64, 88	273. - 0.147E+04	K	0.64%FS
214	Temp.	TF- 14	TE 214	A12 Fuel Rod Pos.7	A. 64, 89	273. - 0.147E+04	K	0.64%FS
215	Temp.	TF- 15	TE 215	A13 Fuel Rod Pos.1	A. 65, 83	273. - 0.147E+04	K	0.64%FS
216	Temp.	TF- 16	TE 216	A13 Fuel Rod Pos.2	A. 65, 84	273. - 0.147E+04	K	0.64%FS
217	Temp.	TF- 17	TE 217	A13 Fuel Rod Pos.3	A. 65, 85	273. - 0.147E+04	K	0.64%FS
218	Temp.	TF- 18	TE 218	A13 Fuel Rod Pos.4	A. 65, 86	273. - 0.147E+04	K	0.64%FS
219	Temp.	TF- 19	TE 219	A13 Fuel Rod Pos.5	A. 65, 87	273. - 0.147E+04	K	0.64%FS
220	Temp.	TF- 20	TE 220	A13 Fuel Rod Pos.6	A. 65, 88	273. - 0.147E+04	K	0.64%FS
221	Temp.	TF- 21	TE 221	A13 Fuel Rod Pos.7	A. 65, 89	273. - 0.147E+04	K	0.64%FS
222	Temp.	TF- 22	TE 222	A14 Fuel Rod Pos.1	A. 66	273. - 0.147E+04	K	0.64%FS
223	Temp.	TF- 23	TE 223	A14 Fuel Rod Pos.2	A. 66	273. - 0.147E+04	K	0.64%FS
224	Temp.	TF- 24	TE 224	A14 Fuel Rod Pos.3	A. 66	273. - 0.147E+04	K	0.64%FS
225	Temp.	TF- 25	TE 225	A14 Fuel Rod Pos.4	A. 66	273. - 0.147E+04	K	0.64%FS
226	Temp.	TF- 26	TE 226	A14 Fuel Rod Pos.5	A. 66	273. - 0.147E+04	K	0.64%FS
227	Temp.	TF- 27	TE 227	A14 Fuel Rod Pos.6	A. 66	273. - 0.147E+04	K	0.64%FS
228	Temp.	TF- 28	TE 228	A14 Fuel Rod Pos.7	NM	273. - 0.147E+04	K	0.64%FS
229	Temp.	TF- 29	TE 229	A15 Fuel Rod Pos.1		273. - 0.147E+04	K	0.64%FS
230	Temp.	TF- 30	TE 230	A15 Fuel Rod Pos.4		273. - 0.147E+04	K	0.64%FS
231	Temp.	TF- 31	TE 231	A17 Fuel Rod Pos.1		273. - 0.147E+04	K	0.64%FS
232	Temp.	TF- 32	TE 232	A17 Fuel Rod Pos.4		273. - 0.147E+04	K	0.64%FS
233	Temp.	TF- 33	TE 233	A22 Fuel Rod Pos.1	A. 67, 90	273. - 0.147E+04	K	0.64%FS
234	Temp.	TF- 34	TE 234	A22 Fuel Rod Pos.2	A. 67, 91	273. - 0.147E+04	K	0.64%FS
235	Temp.	TF- 35	TE 235	A22 Fuel Rod Pos.3	A. 67, 92	273. - 0.147E+04	K	0.64%FS
236	Temp.	TF- 36	TE 236	A22 Fuel Rod Pos.4	A. 67, 93	273. - 0.125E+04	K	0.64%FS
237	Temp.	TF- 37	TE 237	A22 Fuel Rod Pos.5	A. 67, 94	273. - 0.125E+04	K	0.64%FS
238	Temp.	TF- 38	TE 238	A22 Fuel Rod Pos.6	A. 67, 95	273. - 0.125E+04	K	0.64%FS
239	Temp.	TF- 39	TE 239	A22 Fuel Rod Pos.7	A. 67, 96	273. - 0.125E+04	K	0.64%FS
240	Temp.	TF- 40	TE 240	A24 Fuel Rod Pos.1	A. 68	273. - 0.125E+04	K	0.64%FS
241	Temp.	TF- 41	TE 241	A24 Fuel Rod Pos.2	A. 68	273. - 0.125E+04	K	0.64%FS
242	Temp.	TF- 42	TE 242	A24 Fuel Rod Pos.3	A. 68	273. - 0.125E+04	K	0.64%FS
243	Temp.	TF- 43	TE 243	A24 Fuel Rod Pos.4	A. 68	273. - 0.125E+04	K	0.64%FS
244	Temp.	TF- 44	TE 244	A24 Fuel Rod Pos.5	A. 68	273. - 0.125E+04	K	0.64%FS
245	Temp.	TF- 45	TE 245	A24 Fuel Rod Pos.6	A. 68	273. - 0.125E+04	K	0.64%FS
246	Temp.	TF- 46	TE 246	A24 Fuel Rod Pos.7	A. 68	273. - 0.125E+04	K	0.64%FS
247	Temp.	TF- 47	TE 247	A26 Fuel Rod Pos.1		273. - 0.125E+04	K	0.64%FS
248	Temp.	TF- 48	TE 248	A26 Fuel Rod Pos.4		273. - 0.125E+04	K	0.64%FS
249	Temp.	TF- 49	TE 249	A28 Fuel Rod Pos.1		273. - 0.125E+04	K	0.64%FS
250	Temp.	TF- 50	TE 250	A28 Fuel Rod Pos.4		273. - 0.125E+04	K	0.64%FS

Table A.1 Measurement list for RUNs 940 and 941 (Cont'd)

251Ch.- 300Ch.

Ch.	Item	Symbol	ID.	Location	Fig.No.	Range	Unit	Accuracy
251	Temp.	TF- 51	TE 251	A31 Fuel Rod Pos.1		273. - 0.125E+04	K	0.64%FS
252	Temp.	TF- 52	TE 252	A31 Fuel Rod Pos.4		273. - 0.125E+04	K	0.64%FS
253	Temp.	TF- 53	TE 253	A33 Fuel Rod Pos.1	A. 69	273. - 0.125E+04	K	0.64%FS
254	Temp.	TF- 54	TE 254	A33 Fuel Rod Pos.2	A. 69	273. - 0.125E+04	K	0.64%FS
255	Temp.	TF- 55	TE 255	A33 Fuel Rod Pos.3	A. 69	273. - 0.125E+04	K	0.64%FS
256	Temp.	TF- 56	TE 256	A33 Fuel Rod Pos.4	A. 69	273. - 0.125E+04	K	0.64%FS
257	Temp.	TF- 57	TE 257	A33 Fuel Rod Pos.5	A. 69	273. - 0.125E+04	K	0.64%FS
258	Temp.	TF- 58	TE 258	A33 Fuel Rod Pos.6	A. 69	273. - 0.125E+04	K	0.64%FS
259	Temp.	TF- 59	TE 259	A33 Fuel Rod Pos.7	A. 69	273. - 0.125E+04	K	0.64%FS
260	Temp.	TF- 60	TE 260	A34 Fuel Rod Pos.1	A. 70	273. - 0.125E+04	K	0.64%FS
261	Temp.	TF- 61	TE 261	A34 Fuel Rod Pos.2	A. 70	273. - 0.125E+04	K	0.64%FS
262	Temp.	TF- 62	TE 262	A34 Fuel Rod Pos.3	A. 70	273. - 0.125E+04	K	0.64%FS
263	Temp.	TF- 63	TE 263	A34 Fuel Rod Pos.4	A. 70	273. - 0.125E+04	K	0.64%FS
264	Temp.	TF- 64	TE 264	A34 Fuel Rod Pos.5	A. 70	273. - 0.125E+04	K	0.64%FS
265	Temp.	TF- 65	TE 265	A34 Fuel Rod Pos.6	A. 70	273. - 0.125E+04	K	0.64%FS
266	Temp.	TF- 66	TE 266	A34 Fuel Rod Pos.7	A. 70	273. - 0.125E+04	K	0.64%FS
267	Temp.	TF- 67	TE 267	A37 Fuel Rod Pos.1		273. - 0.125E+04	K	0.64%FS
268	Temp.	TF- 68	TE 268	A37 Fuel Rod Pos.4		273. - 0.125E+04	K	0.64%FS
269	Temp.	TF- 69	TE 269	A42 Fuel Rod Pos.1		273. - 0.125E+04	K	0.64%FS
270	Temp.	TF- 70	TE 270	A42 Fuel Rod Pos.4		273. - 0.125E+04	K	0.64%FS
271	Temp.	TF- 71	TE 271	A44 Fuel Rod Pos.1	A. 71	273. - 0.125E+04	K	0.64%FS
272	Temp.	TF- 72	TE 272	A44 Fuel Rod Pos.2	A. 71	273. - 0.125E+04	K	0.64%FS
273	Temp.	TF- 73	TE 273	A44 Fuel Rod Pos.3	A. 71	273. - 0.125E+04	K	0.64%FS
274	Temp.	TF- 74	TE 274	A44 Fuel Rod Pos.4	A. 71	273. - 0.125E+04	K	0.64%FS
275	Temp.	TF- 75	TE 275	A44 Fuel Rod Pos.5	A. 71	273. - 0.125E+04	K	0.64%FS
276	Temp.	TF- 76	TE 276	A44 Fuel Rod Pos.6	A. 71	273. - 0.125E+04	K	0.64%FS
277	Temp.	TF- 77	TE 277	A44 Fuel Rod Pos.7	A. 71	273. - 0.125E+04	K	0.64%FS
278	Temp.	TF- 78	TE 278	A48 Fuel Rod Pos.1		273. - 0.125E+04	K	0.64%FS
279	Temp.	TF- 79	TE 279	A48 Fuel Rod Pos.4		273. - 0.125E+04	K	0.64%FS
280	Temp.	TF- 80	TE 280	A51 Fuel Rod Pos.1		273. - 0.125E+04	K	0.64%FS
281	Temp.	TF- 81	TE 281	A51 Fuel Rod Pos.4		273. - 0.125E+04	K	0.64%FS
282	Temp.	TF- 82	TE 282	A53 Fuel Rod Pos.1		273. - 0.125E+04	K	0.64%FS
283	Temp.	TF- 83	TE 283	A53 Fuel Rod Pos.4		273. - 0.125E+04	K	0.64%FS
284	Temp.	TF- 84	TE 284	A57 Fuel Rod Pos.1		273. - 0.125E+04	K	0.64%FS
285	Temp.	TF- 85	TE 285	A57 Fuel Rod Pos.4		273. - 0.125E+04	K	0.64%FS
286	Temp.	TF- 86	TE 286	A62 Fuel Rod Pos.1		273. - 0.125E+04	K	0.64%FS
287	Temp.	TF- 87	TE 287	A62 Fuel Rod Pos.4		273. - 0.125E+04	K	0.64%FS
288	Temp.	TF- 88	TE 288	A66 Fuel Rod Pos.1		273. - 0.125E+04	K	0.64%FS
289	Temp.	TF- 89	TE 289	A66 Fuel Rod Pos.4		273. - 0.125E+04	K	0.64%FS
290	Temp.	TF- 90	TE 290	A68 Fuel Rod Pos.1		273. - 0.125E+04	K	0.64%FS
291	Temp.	TF- 91	TE 291	A68 Fuel Rod Pos.4		273. - 0.125E+04	K	0.64%FS
292	Temp.	TF- 92	TE 292	A71 Fuel Rod Pos.1		273. - 0.125E+04	K	0.64%FS
293	Temp.	TF- 93	TE 293	A71 Fuel Rod Pos.4		273. - 0.125E+04	K	0.64%FS
294	Temp.	TF- 94	TE 294	A73 Fuel Rod Pos.1		273. - 0.125E+04	K	0.64%FS
295	Temp.	TF- 95	TE 295	A73 Fuel Rod Pos.4		273. - 0.125E+04	K	0.64%FS
296	Temp.	TF- 96	TE 296	A75 Fuel Rod Pos.1		273. - 0.125E+04	K	0.64%FS
297	Temp.	TF- 97	TE 297	A75 Fuel Rod Pos.4		273. - 0.125E+04	K	0.64%FS
298	Temp.	TF- 98	TE 298	A77 Fuel Rod Pos.1	A. 72, 97	273. - 0.125E+04	K	0.64%FS
299	Temp.	TF- 99	TE 299	A77 Fuel Rod Pos.2	A. 72, 98	273. - 0.125E+04	K	0.64%FS
300	Temp.	TF-100	TE 300	A77 Fuel Rod Pos.3	A. 72, 99	273. - 0.125E+04	K	0.64%FS

Table A.1 Measurement list for RUNs 940 and 941 (Cont'd)

301Ch.- 350Ch.

Ch.	Item	Symbol	ID.	Location	Fig.No.	Range	Unit	Accuracy
301	Temp.	TF-101	TE 301	A77 Fuel Rod Pos.4	A. 72,100	273. - 0.125E+04	K	0.64%FS
302	Temp.	TF-102	TE 302	A77 Fuel Rod Pos.5	A. 72,101	273. - 0.125E+04	K	0.64%FS
303	Temp.	TF-103	TE 303	A77 Fuel Rod Pos.6	A. 72,102	273. - 0.125E+04	K	0.64%FS
304	Temp.	TF-104	TE 304	A77 Fuel Rod Pos.7	FL	273. - 0.125E+04	K	0.64%FS
305	Temp.	TF-105	TE 305	A82 Fuel Rod Pos.1		273. - 0.125E+04	K	0.64%FS
306	Temp.	TF-106	TE 306	A82 Fuel Rod Pos.4	FL	273. - 0.125E+04	K	0.64%FS
307	Temp.	TF-107	TE 307	A84 Fuel Rod Pos.1		273. - 0.125E+04	K	0.64%FS
308	Temp.	TF-108	TE 308	A84 Fuel Rod Pos.4		273. - 0.125E+04	K	0.64%FS
309	Temp.	TF-109	TE 309	A85 Fuel Rod Pos.1		273. - 0.125E+04	K	0.64%FS
310	Temp.	TF-110	TE 310	A85 Fuel Rod Pos.2		273. - 0.125E+04	K	0.64%FS
311	Temp.	TF-111	TE 311	A85 Fuel Rod Pos.3		273. - 0.125E+04	K	0.64%FS
312	Temp.	TF-112	TE 312	A85 Fuel Rod Pos.4		273. - 0.125E+04	K	0.64%FS
313	Temp.	TF-113	TE 313	A85 Fuel Rod Pos.5		273. - 0.125E+04	K	0.64%FS
314	Temp.	TF-114	TE 314	A85 Fuel Rod Pos.6		273. - 0.125E+04	K	0.64%FS
315	Temp.	TF-115	TE 315	A85 Fuel Rod Pos.7		273. - 0.125E+04	K	0.64%FS
316	Temp.	TF-116	TE 316	A87 Fuel Rod Pos.1	A. 83	273. - 0.125E+04	K	0.64%FS
317	Temp.	TF-117	TE 317	A87 Fuel Rod Pos.2	A. 84	273. - 0.125E+04	K	0.64%FS
318	Temp.	TF-118	TE 318	A87 Fuel Rod Pos.3	A. 85	273. - 0.125E+04	K	0.64%FS
319	Temp.	TF-119	TE 319	A87 Fuel Rod Pos.4	A. 86	273. - 0.125E+04	K	0.64%FS
320	Temp.	TF-120	TE 320	A87 Fuel Rod Pos.5	A. 87	273. - 0.125E+04	K	0.64%FS
321	Temp.	TF-121	TE 321	A87 Fuel Rod Pos.6	A. 88	273. - 0.125E+04	K	0.64%FS
322	Temp.	TF-122	TE 322	A87 Fuel Rod Pos.7	A. 89	273. - 0.125E+04	K	0.64%FS
323	Temp.	TF-123	TE 323	A88 Fuel Rod Pos.1	A. 73, 83	273. - 0.125E+04	K	0.64%FS
324	Temp.	TF-124	TE 324	A88 Fuel Rod Pos.2	A. 73, 84	273. - 0.125E+04	K	0.64%FS
325	Temp.	TF-125	TE 325	A88 Fuel Rod Pos.3	A. 73, 85	273. - 0.125E+04	K	0.64%FS
326	Temp.	TF-126	TE 326	A88 Fuel Rod Pos.4	A. 73, 86	273. - 0.125E+04	K	0.64%FS
327	Temp.	TF-127	TE 327	A88 Fuel Rod Pos.5	A. 73, 87	273. - 0.125E+04	K	0.64%FS
328	Temp.	TF-128	TE 328	A88 Fuel Rod Pos.6	A. 73, 88	273. - 0.125E+04	K	0.64%FS
329	Temp.	TF-129	TE 329	A88 Fuel Rod Pos.7	A. 73, 89	273. - 0.125E+04	K	0.64%FS
330	Temp.	TF-130	TE 330	B11 Fuel Rod Pos.1		273. - 0.125E+04	K	0.64%FS
331	Temp.	TF-131	TE 331	B11 Fuel Rod Pos.2		273. - 0.125E+04	K	0.64%FS
332	Temp.	TF-132	TE 332	B11 Fuel Rod Pos.3		273. - 0.125E+04	K	0.64%FS
333	Temp.	TF-133	TE 333	B11 Fuel Rod Pos.4		273. - 0.125E+04	K	0.64%FS
334	Temp.	TF-134	TE 334	B11 Fuel Rod Pos.5		273. - 0.125E+04	K	0.64%FS
335	Temp.	TF-135	TE 335	B11 Fuel Rod Pos.6		273. - 0.125E+04	K	0.64%FS
336	Temp.	TF-136	TE 336	B11 Fuel Rod Pos.7		273. - 0.125E+04	K	0.64%FS
337	Temp.	TF-137	TE 337	B13 Fuel Rod Pos.4		273. - 0.125E+04	K	0.64%FS
338	Temp.	TF-138	TE 338	B22 Fuel Rod Pos.1	A. 74, 90	273. - 0.125E+04	K	0.64%FS
339	Temp.	TF-139	TE 339	B22 Fuel Rod Pos.2	A. 74, 91	273. - 0.125E+04	K	0.64%FS
340	Temp.	TF-140	TE 340	B22 Fuel Rod Pos.3	A. 74, 92	273. - 0.125E+04	K	0.64%FS
341	Temp.	TF-141	TE 341	B22 Fuel Rod Pos.4	A. 74, 93	273. - 0.125E+04	K	0.64%FS
342	Temp.	TF-142	TE 342	B22 Fuel Rod Pos.5	A. 74, 94	273. - 0.125E+04	K	0.64%FS
343	Temp.	TF-143	TE 343	B22 Fuel Rod Pos.6	A. 74, 95	273. - 0.125E+04	K	0.64%FS
344	Temp.	TF-144	TE 344	B22 Fuel Rod Pos.7	A. 74, 96	273. - 0.125E+04	K	0.64%FS
345	Temp.	TF-145	TE 345	B31 Fuel Rod Pos.4		273. - 0.125E+04	K	0.64%FS
346	Temp.	TF-146	TE 346	B33 Fuel Rod Pos.4		273. - 0.125E+04	K	0.64%FS
347	Temp.	TF-147	TE 347	B51 Fuel Rod Pos.4		273. - 0.125E+04	K	0.64%FS
348	Temp.	TF-148	TE 348	B53 Fuel Rod Pos.4		273. - 0.125E+04	K	0.64%FS
349	Temp.	TF-149	TE 349	B66 Fuel Rod Pos.4		273. - 0.125E+04	K	0.64%FS
350	Temp.	TF-150	TE 350	B77 Fuel Rod Pos.1	A. 97	273. - 0.125E+04	K	0.64%FS

Table A.1 Measurement list for RUNs 940 and 941 (Cont'd)

351Ch.- 400Ch.

Ch.	Item	Symbol	ID.	Location	Fig.No.	Range	Unit	Accuracy
351	Temp.	TF-151	TE 351	B77 Fuel Rod Pos.2	A. 98	273. - 0.125E+04	K	0.64%FS
352	Temp.	TF-152	TE 352	B77 Fuel Rod Pos.3	A. 99	273. - 0.125E+04	K	0.64%FS
353	Temp.	TF-153	TE 353	B77 Fuel Rod Pos.4	A.100	273. - 0.125E+04	K	0.64%FS
354	Temp.	TF-154	TE 354	B77 Fuel Rod Pos.5	A.101	273. - 0.125E+04	K	0.64%FS
355	Temp.	TF-155	TE 355	B77 Fuel Rod Pos.6	A.102	273. - 0.125E+04	K	0.64%FS
356	Temp.	TF-156	TE 356	B77 Fuel Rod Pos.7	A.103	273. - 0.125E+04	K	0.64%FS
357	Temp.	TF-157	TE 357	B86 Fuel Rod Pos.4		273. - 0.125E+04	K	0.64%FS
358	Temp.	TF-158	TE 358	C11 Fuel Rod Pos.1	A. 75	273. - 0.125E+04	K	0.64%FS
359	Temp.	TF-159	TE 359	C11 Fuel Rod Pos.2	A. 75	273. - 0.125E+04	K	0.64%FS
360	Temp.	TF-160	TE 360	C11 Fuel Rod Pos.3	A. 75	273. - 0.125E+04	K	0.64%FS
361	Temp.	TF-161	TE 361	C11 Fuel Rod Pos.4	A. 75	273. - 0.125E+04	K	0.64%FS
362	Temp.	TF-162	TE 362	C11 Fuel Rod Pos.5	A. 75	273. - 0.125E+04	K	0.64%FS
363	Temp.	TF-163	TE 363	C11 Fuel Rod Pos.6	A. 75	273. - 0.125E+04	K	0.64%FS
364	Temp.	TF-164	TE 364	C11 Fuel Rod Pos.7	A. 75	273. - 0.125E+04	K	0.64%FS
365	Temp.	TF-165	TE 365	C13 Fuel Rod Pos.1	A. 76	273. - 0.125E+04	K	0.64%FS
366	Temp.	TF-166	TE 366	C13 Fuel Rod Pos.2	A. 76	273. - 0.125E+04	K	0.64%FS
367	Temp.	TF-167	TE 367	C13 Fuel Rod Pos.3	A. 76	273. - 0.125E+04	K	0.64%FS
368	Temp.	TF-168	TE 368	C13 Fuel Rod Pos.4	A. 76	273. - 0.125E+04	K	0.64%FS
369	Temp.	TF-169	TE 369	C13 Fuel Rod Pos.5	A. 76	273. - 0.125E+04	K	0.64%FS
370	Temp.	TF-170	TE 370	C13 Fuel Rod Pos.6	A. 76	273. - 0.125E+04	K	0.64%FS
371	Temp.	TF-171	TE 371	C13 Fuel Rod Pos.7	A. 76	273. - 0.125E+04	K	0.64%FS
372	Temp.	TF-172	TE 372	C15 Fuel Rod Pos.4		273. - 0.125E+04	K	0.64%FS
373	Temp.	TF-173	TE 373	C22 Fuel Rod Pos.1	A. 77, 90	273. - 0.125E+04	K	0.64%FS
374	Temp.	TF-174	TE 374	C22 Fuel Rod Pos.2	A. 77, 91	273. - 0.125E+04	K	0.64%FS
375	Temp.	TF-175	TE 375	C22 Fuel Rod Pos.3	A. 77, 92	273. - 0.125E+04	K	0.64%FS
376	Temp.	TF-176	TE 376	C22 Fuel Rod Pos.4	A. 77, 93	273. - 0.125E+04	K	0.64%FS
377	Temp.	TF-177	TE 377	C22 Fuel Rod Pos.5	A. 77, 94	273. - 0.125E+04	K	0.64%FS
378	Temp.	TF-178	TE 378	C22 Fuel Rod Pos.6	A. 77, 95	273. - 0.125E+04	K	0.64%FS
379	Temp.	TF-179	TE 379	C22 Fuel Rod Pos.7	A. 77, 96	273. - 0.125E+04	K	0.64%FS
380	Temp.	TF-180	TE 380	C31 Fuel Rod Pos.4		273. - 0.125E+04	K	0.64%FS
381	Temp.	TF-181	TE 381	C33 Fuel Rod Pos.1	A. 78	273. - 0.125E+04	K	0.64%FS
382	Temp.	TF-182	TE 382	C33 Fuel Rod Pos.2	A. 78	273. - 0.125E+04	K	0.64%FS
383	Temp.	TF-183	TE 383	C33 Fuel Rod Pos.3	A. 78	273. - 0.125E+04	K	0.64%FS
384	Temp.	TF-184	TE 384	C33 Fuel Rod Pos.4	A. 78	273. - 0.125E+04	K	0.64%FS
385	Temp.	TF-185	TE 385	C33 Fuel Rod Pos.5	A. 78	273. - 0.125E+04	K	0.64%FS
386	Temp.	TF-186	TE 386	C33 Fuel Rod Pos.6	A. 78	273. - 0.125E+04	K	0.64%FS
387	Temp.	TF-187	TE 387	C33 Fuel Rod Pos.7	A. 78	273. - 0.125E+04	K	0.64%FS
388	Temp.	TF-188	TE 388	C35 Fuel Rod Pos.4		273. - 0.125E+04	K	0.64%FS
389	Temp.	TF-189	TE 389	C66 Fuel Rod Pos.4		273. - 0.125E+04	K	0.64%FS
390	Temp.	TF-190	TE 390	C68 Fuel Rod Pos.4		273. - 0.125E+04	K	0.64%FS
391	Temp.	TF-191	TE 391	C77 Fuel Rod Pos.1	A. 79, 97	273. - 0.125E+04	K	0.64%FS
392	Temp.	TF-192	TE 392	C77 Fuel Rod Pos.2	A. 79, 98	273. - 0.125E+04	K	0.64%FS
393	Temp.	TF-193	TE 393	C77 Fuel Rod Pos.3	A. 79, 99	273. - 0.125E+04	K	0.64%FS
394	Temp.	TF-194	TE 394	C77 Fuel Rod Pos.4	A. 79,100	273. - 0.125E+04	K	0.64%FS
395	Temp.	TF-195	TE 395	C77 Fuel Rod Pos.5	A. 79,101	273. - 0.125E+04	K	0.64%FS
396	Temp.	TF-196	TE 396	C77 Fuel Rod Pos.6	A. 79,102	273. - 0.125E+04	K	0.64%FS
397	Temp.	TF-197	TE 397	C77 Fuel Rod Pos.7	A. 79,103	273. - 0.125E+04	K	0.64%FS
398	Temp.	TF-198	TE 398	D11 Fuel Rod Pos.4		273. - 0.125E+04	K	0.64%FS
399	Temp.	TF-199	TE 399	D13 Fuel Rod Pos.4		273. - 0.125E+04	K	0.64%FS
400	Temp.	TF-200	TE 400	D22 Fuel Rod Pos.1	A. 80, 90	273. - 0.125E+04	K	0.64%FS

Table A.1 Measurement list for RUNs 940 and 941 (Cont'd)

401Ch.- 450Ch.

Ch.	Item	Symbol	ID.	Location	Fig.No.	Range	Unit	Accuracy
401	Temp.	TF-201	TE 401	D22 Fuel Rod Pos.2	A. 80, 91	273. - 0.125E+04	K	0.64%FS
402	Temp.	TF-202	TE 402	D22 Fuel Rod Pos.3	A. 80, 92	273. - 0.125E+04	K	0.64%FS
403	Temp.	TF-203	TE 403	D22 Fuel Rod Pos.4	A. 80, 93	273. - 0.125E+04	K	0.64%FS
404	Temp.	TF-204	TE 404	D22 Fuel Rod Pos.5	A. 80, 94	273. - 0.125E+04	K	0.64%FS
405	Temp.	TF-205	TE 405	D22 Fuel Rod Pos.6	A. 80, 95	273. - 0.125E+04	K	0.64%FS
406	Temp.	TF-206	TE 406	D22 Fuel Rod Pos.7	A. 80, 96	273. - 0.125E+04	K	0.64%FS
407	Temp.	TF-207	TE 407	D31 Fuel Rod Pos.4		273. - 0.125E+04	K	0.64%FS
408	Temp.	TF-208	TE 408	D33 Fuel Rod Pos.4		273. - 0.125E+04	K	0.64%FS
409	Temp.	TF-209	TE 409	D51 Fuel Rod Pos.4		273. - 0.125E+04	K	0.64%FS
410	Temp.	TF-210	TE 410	D53 Fuel Rod Pos.4		273. - 0.125E+04	K	0.64%FS
411	Temp.	TF-211	TE 411	D66 Fuel Rod Pos.4		273. - 0.125E+04	K	0.64%FS
412	Temp.	TF-212	TE 412	D77 Fuel Rod Pos.4	NM	273. - 0.125E+04	K	0.64%FS
413	Temp.	TF-213	TE 413	D86 Fuel Rod Pos.4		273. - 0.125E+04	K	0.64%FS
414	Fluid T.	TW- 1	TE 414	A45 Tie Rod Pos.1	A. 81	273. - 0.125E+04	K	0.64%FS
415	Fluid T.	TW- 2	TE 415	A45 Tie Rod Pos.2	A. 81	273. - 0.125E+04	K	0.64%FS
416	Fluid T.	TW- 3	TE 416	A45 Tie Rod Pos.3	A. 81	273. - 0.125E+04	K	0.64%FS
417	Fluid T.	TW- 4	TE 417	A45 Tie Rod Pos.4	A. 81	273. - 0.125E+04	K	0.64%FS
418	Fluid T.	TW- 5	TE 418	A45 Tie Rod Pos.5	A. 81	273. - 0.125E+04	K	0.64%FS
419	Fluid T.	TW- 6	TE 419	A45 Tie Rod Pos.6	A. 81	273. - 0.125E+04	K	0.64%FS
420	Fluid T.	TW- 7	TE 420	A45 Tie Rod Pos.7	A. 81	273. - 0.125E+04	K	0.64%FS
421	Fluid T.	TW- 8	TE 421	B45 Tie Rod Pos.1		273. - 0.125E+04	K	0.64%FS
422	Fluid T.	TW- 9	TE 422	B45 Tie Rod Pos.2		273. - 0.125E+04	K	0.64%FS
423	Fluid T.	TW-10	TE 423	B45 Tie Rod Pos.3		273. - 0.125E+04	K	0.64%FS
424	Fluid T.	TW-11	TE 424	B45 Tie Rod Pos.4		273. - 0.125E+04	K	0.64%FS
425	Fluid T.	TW-12	TE 425	B45 Tie Rod Pos.5		273. - 0.125E+04	K	0.64%FS
426	Fluid T.	TW-13	TE 426	B45 Tie Rod Pos.6		273. - 0.125E+04	K	0.64%FS
427	Fluid T.	TW-14	TE 427	B45 Tie Rod Pos.7		273. - 0.125E+04	K	0.64%FS
428	Fluid T.	TW-15	TE 428	C45 Tie Rod Pos.1	A. 82	273. - 0.125E+04	K	0.64%FS
429	Fluid T.	TW-16	TE 429	C45 Tie Rod Pos.2	A. 82	273. - 0.125E+04	K	0.64%FS
430	Fluid T.	TW-17	TE 430	C45 Tie Rod Pos.3	A. 82	273. - 0.125E+04	K	0.64%FS
431	Fluid T.	TW-18	TE 431	C45 Tie Rod Pos.4	A. 82	273. - 0.125E+04	K	0.64%FS
432	Fluid T.	TW-19	TE 432	C45 Tie Rod Pos.5	A. 82	273. - 0.125E+04	K	0.64%FS
433	Fluid T.	TW-20	TE 433	C45 Tie Rod Pos.6	A. 82	273. - 0.125E+04	K	0.64%FS
434	Fluid T.	TW-21	TE 434	C45 Tie Rod Pos.7	A. 82	273. - 0.125E+04	K	0.64%FS
435	Fluid T.	TW-22	TE 435	D45 Tie Rod Pos.1		273. - 0.125E+04	K	0.64%FS
436	Fluid T.	TW-23	TE 436	D45 Tie Rod Pos.2		273. - 0.125E+04	K	0.64%FS
437	Fluid T.	TW-24	TE 437	D45 Tie Rod Pos.3	NM	273. - 0.125E+04	K	0.64%FS
438	Fluid T.	TW-25	TE 438	D45 Tie Rod Pos.4	NM	273. - 0.125E+04	K	0.64%FS
439	Fluid T.	TW-26	TE 439	D45 Tie Rod Pos.5	NM	273. - 0.125E+04	K	0.64%FS
440	Fluid T.	TW-27	TE 440	D45 Tie Rod Pos.6	NM	273. - 0.125E+04	K	0.64%FS
441	Fluid T.	TW-28	TE 441	D45 Tie Rod Pos.7	NM	273. - 0.125E+04	K	0.64%FS
442	Fluid T.	TC- 1	TE 442	Channel Box A Inlet	A.104	273. - 0.125E+04	K	0.64%FS
443	Fluid T.	TC- 2	TE 443	Channel Box B Inlet	A.104	273. - 0.125E+04	K	0.64%FS
444	Fluid T.	TC- 3	TE 444	Channel Box C Inlet	A.104	273. - 0.125E+04	K	0.64%FS
445	Fluid T.	TC- 4	TE 445	Channel Box D Inlet	A.104	273. - 0.125E+04	K	0.64%FS
446	Fluid T.	TC- 5	TE 446	Channel Box Outlet A-1	A.105	273. - 0.125E+04	K	0.64%FS
447	Fluid T.	TC- 6	TE 447	Channel Box Outlet A-2	A.105	273. - 0.125E+04	K	0.64%FS
448	Fluid T.	TC- 7	TE 448	Channel Box Outlet A-3	A.105	273. - 0.125E+04	K	0.64%FS
449	Fluid T.	TC- 8	TE 449	Channel Box Outlet A-4	A.105	273. - 0.125E+04	K	0.64%FS
450	Fluid T.	TC- 9	TE 450	Channel Box Outlet A-6	A.105	273. - 0.125E+04	K	0.64%FS

Table A.1 Measurement list for RUNs 940 and 941 (Cont'd)

451Ch.- 500Ch.

Ch.	Item	Symbol	ID.	Location	Fig.No.	Range	Unit	Accuracy
451	Fluid T.	TC-10	TE 451	Channel Box Outlet C-1	A.106	273. - 0.125E+04	K	0.64%FS
452	Fluid T.	TC-11	TE 452	Channel Box Outlet C-2	A.106	273. - 0.125E+04	K	0.64%FS
453	Fluid T.	TC-12	TE 453	Channel Box Outlet C-3	A.106	273. - 0.125E+04	K	0.64%FS
454	Fluid T.	TC-13	TE 454	Channel Box Outlet C-4	A.106	273. - 0.125E+04	K	0.64%FS
455	Fluid T.	TC-14	TE 455	Channel Box Outlet C-6	A.106	273. - 0.125E+04	K	0.64%FS
456	Fluid T.	TG- 1	TE 456	Upper Tieplate A Up.1	A.107	273. - 0.125E+04	K	0.64%FS
457	Fluid T.	TG- 2	TE 457	Upper Tieplate A Up.2	A.107	273. - 0.125E+04	K	0.64%FS
458	Fluid T.	TG- 3	TE 458	Upper Tieplate A Up.3	A.107	273. - 0.125E+04	K	0.64%FS
459	Fluid T.	TG- 4	TE 459	Upper Tieplate A Up.4	A.107	273. - 0.125E+04	K	0.64%FS
460	Fluid T.	TG- 5	TE 460	Upper Tieplate A Up.5	A.107	273. - 0.125E+04	K	0.64%FS
461	Fluid T.	TG- 6	TE 461	Upper Tieplate A Up.6	A.108	273. - 0.125E+04	K	0.64%FS
462	Fluid T.	TG- 7	TE 462	Upper Tieplate A Up.7	A.108	273. - 0.125E+04	K	0.64%FS
463	Fluid T.	TG- 8	TE 463	Upper Tieplate A Up.8	A.108	273. - 0.125E+04	K	0.64%FS
464	Fluid T.	TG- 9	TE 464	Upper Tieplate A Up.9	A.108	273. - 0.125E+04	K	0.64%FS
465	Fluid T.	TG-10	TE 465	Upper Tieplate A Up.10	A.108	273. - 0.125E+04	K	0.64%FS
466	Fluid T.	TG-11	TE 466	Upper Tieplate A Lo.1	A.109	273. - 0.125E+04	K	0.64%FS
467	Fluid T.	TG-12	TE 467	Upper Tieplate A Lo.2	A.109	273. - 0.125E+04	K	0.64%FS
468	Fluid T.	TG-13	TE 468	Upper Tieplate A Lo.3	A.109	273. - 0.125E+04	K	0.64%FS
469	Fluid T.	TG-14	TE 469	Upper Tieplate A Lo.4	A.109	273. - 0.125E+04	K	0.64%FS
470	Fluid T.	TG-15	TE 470	Upper Tieplate A Lo.5	A.109	273. - 0.125E+04	K	0.64%FS
471	Fluid T.	TG-16	TE 471	Upper Tieplate A Lo.6	A.110	273. - 0.125E+04	K	0.64%FS
472	Fluid T.	TG-17	TE 472	Upper Tieplate A Lo.7	A.110	273. - 0.125E+04	K	0.64%FS
473	Fluid T.	TG-18	TE 473	Upper Tieplate A Lo.8	A.110	273. - 0.125E+04	K	0.64%FS
474	Fluid T.	TG-19	TE 474	Upper Tieplate A Lo.9	A.110	273. - 0.125E+04	K	0.64%FS
475	Fluid T.	TG-20	TE 475	Upper Tieplate A Lo.10	A.110	273. - 0.125E+04	K	0.64%FS
476	Fluid T.	TG-21	TE 476	Upper Tieplate C Up.1	A.111	273. - 0.125E+04	K	0.64%FS
477	Fluid T.	TG-22	TE 477	Upper Tieplate C Up.2	A.111	273. - 0.125E+04	K	0.64%FS
478	Fluid T.	TG-23	TE 478	Upper Tieplate C Up.3	A.111	273. - 0.125E+04	K	0.64%FS
479	Fluid T.	TG-24	TE 479	Upper Tieplate C Up.4	A.111	273. - 0.125E+04	K	0.64%FS
480	Fluid T.	TG-25	TE 480	Upper Tieplate C Up.5	A.111	273. - 0.125E+04	K	0.64%FS
481	Fluid T.	TG-26	TE 481	Upper Tieplate C Up.6	A.112	273. - 0.125E+04	K	0.64%FS
482	Fluid T.	TG-27	TE 482	Upper Tieplate C Up.7	A.112	273. - 0.125E+04	K	0.64%FS
483	Fluid T.	TG-28	TE 483	Upper Tieplate C Up.8	A.112	273. - 0.125E+04	K	0.64%FS
484	Fluid T.	TG-29	TE 484	Upper Tieplate C Up.9	A.112	273. - 0.125E+04	K	0.64%FS
485	Fluid T.	TG-30	TE 485	Upper Tieplate C Up.10	A.112	273. - 0.125E+04	K	0.64%FS
486	Fluid T.	TG-31	TE 486	Upper Tieplate C Lo.1	A.113	273. - 0.125E+04	K	0.64%FS
487	Fluid T.	TG-32	TE 487	Upper Tieplate C Lo.2	A.113	273. - 0.125E+04	K	0.64%FS
488	Fluid T.	TG-33	TE 488	Upper Tieplate C Lo.3	A.113	273. - 0.125E+04	K	0.64%FS
489	Fluid T.	TG-34	TE 489	Upper Tieplate C Lo.4	A.113	273. - 0.125E+04	K	0.64%FS
490	Fluid T.	TG-35	TE 490	Upper Tieplate C Lo.5	A.113	273. - 0.125E+04	K	0.64%FS
491	Fluid T.	TG-36	TE 491	Upper Tieplate C Lo.6	A.114	273. - 0.125E+04	K	0.64%FS
492	Fluid T.	TG-37	TE 492	Upper Tieplate C Lo.7	A.114	273. - 0.125E+04	K	0.64%FS
493	Fluid T.	TG-38	TE 493	Upper Tieplate C Lo.8	A.114	273. - 0.125E+04	K	0.64%FS
494	Fluid T.	TG-39	TE 494	Upper Tieplate C Lo.9	A.114	273. - 0.125E+04	K	0.64%FS
495	Fluid T.	TG-40	TE 495	Upper Tieplate C Lo.10	A.114	273. - 0.125E+04	K	0.64%FS
496	Slab T.	TB- 1	TE 496	C.B. A1 Inner ,Pos.1	A.115	273. - 0.125E+04	K	0.64%FS
497	Slab T.	TB- 2	TE 497	C.B. A1 Inner ,Pos.2	A.116	273. - 0.125E+04	K	0.64%FS
498	Slab T.	TB- 3	TE 498	C.B. A1 Inner ,Pos.3	A.117	273. - 0.125E+04	K	0.64%FS
499	Slab T.	TB- 4	TE 499	C.B. A1 Inner ,Pos.4	A.118	273. - 0.125E+04	K	0.64%FS
500	Slab T.	TB- 5	TE 500	C.B. A1 Inner ,Pos.5	A.119	273. - 0.125E+04	K	0.64%FS

Table A.1 Measurement list for RUNs 940 and 941 (Cont'd)

501Ch.- 550Ch.

Ch.	Item	Symbol	ID.	Location	Fig.No.	Range	Unit	Accuracy
501	Slab T.	TB- 6	TE 501	C.B. A1 Inner ,Pos.6	A.120	273. - 0.125E+04	K	0.64%FS
502	Slab T.	TB- 7	TE 502	C.B. A1 Inner ,Pos.7	A.121	273. - 0.125E+04	K	0.64%FS
503	Slab T.	TB- 8	TE 503	C.B. A2 Inner ,Pos.1	A.115	273. - 0.125E+04	K	0.64%FS
504	Slab T.	TB- 9	TE 504	C.B. A2 Inner ,Pos.2	A.116	273. - 0.125E+04	K	0.64%FS
505	Slab T.	TB-10	TE 505	C.B. A2 Inner ,Pos.3	A.117	273. - 0.125E+04	K	0.64%FS
506	Slab T.	TB-11	TE 506	C.B. A2 Inner ,Pos.4	A.118	273. - 0.125E+04	K	0.64%FS
507	Slab T.	TB-12	TE 507	C.B. A2 Inner ,Pos.5	A.119	273. - 0.125E+04	K	0.64%FS
508	Slab T.	TB-13	TE 508	C.B. A2 Inner ,Pos.6	A.120	273. - 0.125E+04	K	0.64%FS
509	Slab T.	TB-14	TE 509	C.B. A2 Inner ,Pos.7	A.121	273. - 0.125E+04	K	0.64%FS
510	Slab T.	TB-15	TE 510	C.B. B Inner ,Pos.1	A.115	273. - 0.125E+04	K	0.64%FS
511	Slab T.	TB-16	TE 511	C.B. B Inner ,Pos.2	A.116	273. - 0.125E+04	K	0.64%FS
512	Slab T.	TB-17	TE 512	C.B. B Inner ,Pos.3	A.117	273. - 0.125E+04	K	0.64%FS
513	Slab T.	TB-18	TE 513	C.B. B Inner ,Pos.4	A.118	273. - 0.125E+04	K	0.64%FS
514	Slab T.	TB-19	TE 514	C.B. B Inner ,Pos.5	A.119	273. - 0.125E+04	K	0.64%FS
515	Slab T.	TB-20	TE 515	C.B. B Inner ,Pos.6	A.120	273. - 0.125E+04	K	0.64%FS
516	Slab T.	TB-21	TE 516	C.B. B Inner ,Pos.7	A.121	273. - 0.125E+04	K	0.64%FS
517	Slab T.	TB-22	TE 517	C.B. C Inner ,Pos.1	A.115	273. - 0.125E+04	K	0.64%FS
518	Slab T.	TB-23	TE 518	C.B. C Inner ,Pos.2	A.116	273. - 0.125E+04	K	0.64%FS
519	Slab T.	TB-24	TE 519	C.B. C Inner ,Pos.3	A.117	273. - 0.125E+04	K	0.64%FS
520	Slab T.	TB-25	TE 520	C.B. C Inner ,Pos.4	A.118	273. - 0.125E+04	K	0.64%FS
521	Slab T.	TB-26	TE 521	C.B. C Inner ,Pos.5	A.119	273. - 0.125E+04	K	0.64%FS
522	Slab T.	TB-27	TE 522	C.B. C Inner ,Pos.6	A.120	273. - 0.125E+04	K	0.64%FS
523	Slab T.	TB-28	TE 523	C.B. C Inner ,Pos.7	A.121	273. - 0.125E+04	K	0.64%FS
524	Slab T.	TB-29	TE 524	C.B. D Inner ,Pos.1	A.115	273. - 0.125E+04	K	0.64%FS
525	Slab T.	TB-30	TE 525	C.B. D Inner ,Pos.2	A.116	273. - 0.125E+04	K	0.64%FS
526	Slab T.	TB-31	TE 526	C.B. D Inner ,Pos.3	A.117	273. - 0.125E+04	K	0.64%FS
527	Slab T.	TB-32	TE 527	C.B. D Inner ,Pos.4	A.118	273. - 0.125E+04	K	0.64%FS
528	Slab T.	TB-33	TE 528	C.B. D Inner ,Pos.5	A.119	273. - 0.125E+04	K	0.64%FS
529	Slab T.	TB-34	TE 529	C.B. D Inner ,Pos.6	A.120	273. - 0.125E+04	K	0.64%FS
530	Slab T.	TB-35	TE 530	C.B. D Inner ,Pos.7	A.121	273. - 0.125E+04	K	0.64%FS
531	Fluid T.	TB-36	TE 531	C.B. A Outer ,Pos.1	A.115	273. - 0.125E+04	K	0.64%FS
532	Fluid T.	TB-37	TE 532	C.B. A Outer ,Pos.2	A.116	273. - 0.125E+04	K	0.64%FS
533	Fluid T.	TB-38	TE 533	C.B. A Outer ,Pos.3	A.117	273. - 0.125E+04	K	0.64%FS
534	Fluid T.	TB-39	TE 534	C.B. A Outer ,Pos.4	A.118	273. - 0.125E+04	K	0.64%FS
535	Fluid T.	TB-40	TE 535	C.B. A Outer ,Pos.5	A.119	273. - 0.125E+04	K	0.64%FS
536	Fluid T.	TB-41	TE 536	C.B. A Outer ,Pos.6	A.120	273. - 0.125E+04	K	0.64%FS
537	Fluid T.	TB-42	TE 537	C.B. A Outer ,Pos.7	A.121	273. - 0.125E+04	K	0.64%FS
538	Fluid T.	TB-43	TE 538	C.B. C Outer ,Pos.1	A.115	273. - 0.125E+04	K	0.64%FS
539	Fluid T.	TB-44	TE 539	C.B. C Outer ,Pos.2	A.116	273. - 0.125E+04	K	0.64%FS
540	Fluid T.	TB-45	TE 540	C.B. C Outer ,Pos.3	A.117	273. - 0.125E+04	K	0.64%FS
541	Fluid T.	TB-46	TE 541	C.B. C Outer ,Pos.4	A.118	273. - 0.125E+04	K	0.64%FS
542	Fluid T.	TB-47	TE 542	C.B. C Outer ,Pos.5	A.119	273. - 0.125E+04	K	0.64%FS
543	Fluid T.	TB-48	TE 543	C.B. C Outer ,Pos.6	A.120	273. - 0.125E+04	K	0.64%FS
544	Fluid T.	TB-49	TE 544	C.B. C Outer ,Pos.7	A.121	273. - 0.125E+04	K	0.64%FS
545	Fluid T.	TP- 1	TE 545	Lower Pl. Center 1	A.122	273. - 0.125E+04	K	0.64%FS
546	Fluid T.	TP- 2	TE 546	Lower Pl. Center 2	A.122	273. - 0.125E+04	K	0.64%FS
547	Fluid T.	TP- 3	TE 547	Lower Pl. Center 3	A.122	273. - 0.125E+04	K	0.64%FS
548	Fluid T.	TP- 4	TE 548	Lower Pl. Center 4	A.122	273. - 0.125E+04	K	0.64%FS
549	Fluid T.	TP- 5	TE 549	Lower Pl. Center 5	A.122	273. - 0.125E+04	K	0.64%FS
550	Fluid T.	TP- 6	TE 550	Lower Pl. Center 7	A.122	273. - 0.125E+04	K	0.64%FS

Table A.1 Measurement list for RUNs 940 and 941 (Cont'd)

551Ch.- 600Ch.

Ch.	Item	Symbol	ID.	Location	Fig.No.	Range	Unit	Accuracy
551	Slab T.	TP- 7	TE 551	Lower Pl. North 1		273. - 0.125E+04	K	0.64%FS
552	Slab T.	TP- 8	TE 552	Lower Pl. North 2		273. - 673.	K	0.64%FS
553	Slab T.	TP- 9	TE 553	Lower Pl. North 4		273. - 673.	K	0.64%FS
554	Slab T.	TP-10	TE 554	Lower Pl. North 6		273. - 673.	K	0.64%FS
555	Slab T.	TP-11	TE 555	Lower Pl. South 1		273. - 673.	K	0.64%FS
556	Slab T.	TP-12	TE 556	Lower Pl. South 2		273. - 673.	K	0.64%FS
557	Slab T.	TP-13	TE 557	Lower Pl. South 4		273. - 673.	K	0.64%FS
558	Slab T.	TP-14	TE 558	Lower Pl. South 6		273. - 673.	K	0.64%FS
559	Level	LB- 1	LM 559	C.B.Liquid Level A1-1	A.123			
560	Level	LB- 2	LM 560	C.B.Liquid Level A1-2	A.123			
561	Level	LB- 3	LM 561	C.B.Liquid Level A1-3	A.123			
562	Level	LB- 4	LM 562	C.B.Liquid Level A1-4	A.123			
563	Level	LB- 5	LM 563	C.B.Liquid Level A1-5	A.123			
564	Level	LB- 6	LM 564	C.B.Liquid Level A1-6	A.123			
565	Level	LB- 7	LM 565	C.B.Liquid Level A1-7	A.123			
566	Level	LB- 8	LM 566	C.B.Liquid Level A2-1	A.124			
567	Level	LB- 9	LM 567	C.B.Liquid Level A2-2	A.124			
568	Level	LB-10	LM 568	C.B.Liquid Level A2-3	A.124			
569	Level	LB-11	LM 569	C.B.Liquid Level A2-4	A.124			
570	Level	LB-12	LM 570	C.B.Liquid Level A2-5	A.124			
571	Level	LB-13	LM 571	C.B.Liquid Level A2-6	A.124			
572	Level	LB-14	LM 572	C.B.Liquid Level A2-7	A.124			
573	Level	LB-15	LM 573	C.B.Liquid Level B-1	A.125			
574	Level	LB-16	LM 574	C.B.Liquid Level B-2	A.125			
575	Level	LB-17	LM 575	C.B.Liquid Level B-3	A.125			
576	Level	LB-18	LM 576	C.B.Liquid Level B-4	A.125			
577	Level	LB-19	LM 577	C.B.Liquid Level B-5	A.125			
578	Level	LB-20	LM 578	C.B.Liquid Level B-6	A.125			
579	Level	LB-21	LM 579	C.B.Liquid Level B-7	A.125			
580	Level	LB-22	LM 580	C.B.Liquid Level C-1	A.126			
581	Level	LB-23	LM 581	C.B.Liquid Level C-2	A.126			
582	Level	LB-24	LM 582	C.B.Liquid Level C-3	A.126			
583	Level	LB-25	LM 583	C.B.Liquid Level C-4	A.126			
584	Level	LB-26	LM 584	C.B.Liquid Level C-5	A.126			
585	Level	LB-27	LM 585	C.B.Liquid Level C-6	A.126			
586	Level	LB-28	LM 586	C.B.Liquid Level C-7	A.126			
587	Level	LB-29	LM 587	C.B.Liquid Level D-1	A.127			
588	Level	LB-30	LM 588	C.B.Liquid Level D-2	A.127			
589	Level	LB-31	LM 589	C.B.Liquid Level D-3	A.127			
590	Level	LB-32	LM 590	C.B.Liquid Level D-4	A.127			
591	Level	LB-33	LM 591	C.B.Liquid Level D-5	A.127			
592	Level	LB-34	LM 592	C.B.Liquid Level D-6	A.127			
593	Level	LB-35	LM 593	C.B.Liquid Level D-7	A.127			
594	Level	LL- 1	LM 594	Ch.Box Outlet A1-5	A.128			
595	Level	LL- 2	LM 595	Ch.Box Outlet A1-6	A.128			
596	Level	LL- 3	LM 596	Ch.Box Outlet A1-7	FL			
597	Level	LL- 4	LM 597	Ch.Box Outlet A2-5	A.129			
598	Level	LL- 5	LM 598	Ch.Box Outlet A2-6	A.129			
599	Level	LL- 6	LM 599	Ch.Box Outlet A2-7	A.129			
600	Level	LL- 7	LM 600	Ch.Box Outlet A-1	A.130			

Table A.1 Measurement list for RUNs 940 and 941 (Cont'd)

601Ch.- 650Ch.

Ch.	Item	Symbol	ID.	Location	Fig.No.	Range	Unit	Accuracy
601	Level	LL- 8	LM 601	Ch.Box Outlet A-2	NM			
602	Level	LL- 9	LM 602	Ch.Box Outlet A-3	A.130			
603	Level	LL-10	LM 603	Ch.Box Outlet A-4	A.130			
604	Level	LL-11	LM 604	Ch.Box Outlet A-6	A.130			
605	Level	LL-12	LM 605	Ch.Box Outlet C1-5	A.131			
606	Level	LL-13	LM 606	Ch.Box Outlet C1-6	A.131			
607	Level	LL-14	LM 607	Ch.Box Outlet C1-7	A.131			
608	Level	LL-15	LM 608	Ch.Box Outlet C2-5	A.132			
609	Level	LL-16	LM 609	Ch.Box Outlet C2-6	A.132			
610	Level	LL-17	LM 610	Ch.Box Outlet C2-7	A.132			
611	Level	LL-18	LM 611	Ch.Box Outlet C-1	A.133			
612	Level	LL-19	LM 612	Ch.Box Outlet C-2	A.133			
613	Level	LL-20	LM 613	Ch.Box Outlet C-3	A.133			
614	Level	LL-21	LM 614	Ch.Box Outlet C-4	A.133			
615	Level	LL-22	LM 615	Ch.Box Outlet C-6	A.133			
616	Level	LL-23	LM 616	Ch.Box Inlet A-1	A.134			
617	Level	LL-24	LM 617	Ch.Box Inlet A-2	A.134			
618	Level	LL-25	LM 618	Ch.Box Inlet B-1	A.135			
619	Level	LL-26	LM 619	Ch.Box Inlet B-2	A.135			
620	Level	LL-27	LM 620	Ch.Box Inlet C-1	A.136			
621	Level	LL-28	LM 621	Ch.Box Inlet C-2	A.136			
622	Level	LL-29	LM 622	Ch.Box Inlet D-1	A.137			
623	Level	LL-30	LM 623	Ch.Box Inlet D-2	A.137			
624	Level	LL-31	LM 624	Lower Pl. North 1	A.138			
625	Level	LL-32	LM 625	Lower Pl. North 2	A.138			
626	Level	LL-33	LM 626	Lower Pl. North 3	A.138			
627	Level	LL-34	LM 627	Lower Pl. North 4	A.138			
628	Level	LL-35	LM 628	Lower Pl. North 5	A.138			
629	Level	LL-36	LM 629	Lower Pl. North 6	A.138			
630	Level	LL-37	LM 630	Lower Pl. South 1	A.139			
631	Level	LL-38	LM 631	Lower Pl. South 2	A.139			
632	Level	LL-39	LM 632	Lower Pl. South 3	A.139			
633	Level	LL-40	LM 633	Lower Pl. South 4	A.139			
634	Level	LL-41	LM 634	Lower Pl. South 5	A.139			
635	Level	LL-42	LM 635	Lower Pl. South 6	A.139			
636	Level	LL-43	LM 636	Guide Tube North 0	A.140			
637	Level	LL-44	LM 637	Guide Tube North 1	A.140			
638	Level	LL-45	LM 638	Guide Tube North 3	A.140			
639	Level	LL-46	LM 639	Guide Tube North 6	A.140			
640	Level	LL-47	LM 640	Guide Tube South 0	A.141			
641	Level	LL-48	LM 641	Guide Tube South 1	A.141			
642	Level	LL-49	LM 642	Guide Tube South 3	A.141			
643	Level	LL-50	LM 643	Guide Tube South 6	A.141			
644	Level	L- 1	LM 644	Downcomer D-Side 1	A.142			
645	Level	L- 2	LM 645	Downcomer D-Side 2	A.142			
646	Level	L- 3	LM 646	Downcomer D-Side 3	A.142			
647	Level	L- 4	LM 647	Downcomer D-Side 4	A.142			
648	Level	L- 5	LM 648	Downcomer D-Side 5	FL			
649	Level	L- 6	LM 649	Downcomer B-Side 1	A.143			
650	Level	L- 7	LM 650	Downcomer B-Side 2	A.143			

Table A.1 Measurement list for RUNs 940 and 941 (Cont'd)

651Ch.- 700Ch.

Ch.	Item	Symbol	ID.	Location	Fig.No.	Range	Unit	Accuracy
651	Level	L- 8	LM 651	Downcomer B-Side 3	A.143			
652	Level	L- 9	LM 652	Downcomer B-Side 4	A.143			
653	Level	L-10	LM 653	Downcomer B-Side 5	FL			
654	Void	VF- 1	VD 654	A54 Tie Rod Pos.1	NM	0.0 - 1.00		
655	Void	VF- 2	VD 655	A54 Tie Rod Pos.2	NM	0.0 - 1.00		
656	Void	VF- 3	VD 656	A54 Tie Rod Pos.3	NM	0.0 - 1.00		
657	Void	VF- 4	VD 657	A54 Tie Rod Pos.4	NM	0.0 - 1.00		
658	Void	VF- 5	VD 658	A54 Tie Rod Pos.5	NM	0.0 - 1.00		
659	Void	VF- 6	VD 659	A54 Tie Rod Pos.6	NM	0.0 - 1.00		
660	Void	VF- 7	VD 660	A54 Tie Rod Pos.7	NM	0.0 - 1.00		
661	Void	VF- 8	VD 661	B54 Tie Rod Pos.1	NM	0.0 - 1.00		
662	Void	VF- 9	VD 662	B54 Tie Rod Pos.2	NM	0.0 - 1.00		
663	Void	VF-10	VD 663	B54 Tie Rod Pos.3	NM	0.0 - 1.00		
664	Void	VF-11	VD 664	B54 Tie Rod Pos.4	NM	0.0 - 1.00		
665	Void	VF-12	VD 665	B54 Tie Rod Pos.5	NM	0.0 - 1.00		
666	Void	VF-13	VD 666	B54 Tie Rod Pos.6	NM	0.0 - 1.00		
667	Void	VF-14	VD 667	B54 Tie Rod Pos.7	NM	0.0 - 1.00		
668	Void	VF-15	VD 668	C54 Tie Rod Pos.1	NM	0.0 - 1.00		
669	Void	VF-16	VD 669	C54 Tie Rod Pos.2	NM	0.0 - 1.00		
670	Void	VF-17	VD 670	C54 Tie Rod Pos.3	NM	0.0 - 1.00		
671	Void	VF-18	VD 671	C54 Tie Rod Pos.4	NM	0.0 - 1.00		
672	Void	VF-19	VD 672	C54 Tie Rod Pos.5	NM	0.0 - 1.00		
673	Void	VF-20	VD 673	C54 Tie Rod Pos.6	NM	0.0 - 1.00		
674	Void	VF-21	VD 674	C54 Tie Rod Pos.7	NM	0.0 - 1.00		
675	Void	VF-22	VD 675	D54 Tie Rod Pos.7	NM	0.0 - 1.00		
676	Void	VF-23	VD 676	D54 Tie Rod Pos.7	NM	0.0 - 1.00		
677	Void	VF-24	VD 677	D54 Tie Rod Pos.7	NM	0.0 - 1.00		
678	Void	VF-25	VD 678	D54 Tie Rod Pos.7	NM	0.0 - 1.00		
679	Void	VF-26	VD 679	D54 Tie Rod Pos.7	NM	0.0 - 1.00		
680	Void	VF-27	VD 680	D54 Tie Rod Pos.7	NM	0.0 - 1.00		
681	Void	VF-28	VD 681	D54 Tie Rod Pos.7	NM	0.0 - 1.00		
682	Void	VE- 1	VD 682	Channel A Outlet 1	NM	0.0 - 1.00		
683	Void	VE- 2	VD 683	Channel A Outlet 2	NM	0.0 - 1.00		
684	Void	VE- 3	VD 684	Channel A Outlet 3	NM	0.0 - 1.00		
685	Void	VE- 4	VD 685	Channel B Outlet 1	NM	0.0 - 1.00		
686	Void	VE- 5	VD 686	Channel B Outlet 2	NM	0.0 - 1.00		
687	Void	VE- 6	VD 687	Channel B Outlet 3	NM	0.0 - 1.00		
688	Void	VE- 7	VD 688	Channel C Outlet 1	NM	0.0 - 1.00		
689	Void	VE- 8	VD 689	Channel C Outlet 2	NM	0.0 - 1.00		
690	Void	VE- 9	VD 690	Channel C Outlet 3	NM	0.0 - 1.00		
691	Void	VE-10	VD 691	Channel D Outlet 1	NM	0.0 - 1.00		
692	Void	VE-11	VD 692	Channel D Outlet 2	NM	0.0 - 1.00		
693	Void	VE-12	VD 693	Channel D Outlet 3	NM	0.0 - 1.00		
694	Void	VE-13	VD 694	Lower Plenum Bottom 1	NM	0.0 - 1.00		
695	Void	VE-14	VD 695	Lower Plenum Bottom 2	NM	0.0 - 1.00		
696	Void	VE-15	VD 696	Lower Plenum Bottom 3	NM	0.0 - 1.00		
697	Void	VP- 1	VD 697	Lower Plenum Inlet	NM	0.0 - 1.00		
698	Void	VP- 2	VD 698	Lower Plenum Inlet	NM	0.0 - 1.00		

Table A.2 Calculated Data in RUNs 940 and 941

No.	Item	Symbol	Location	Fig. No.	Unit
1	Density	DE 701	JP1,2 Outlet, Average	5.9, 29	kg/m^3
2	Density	DE 702	JP3,4 Outlet, Average		kg/m^3
3	Density	DE 703	MRP-Side Break, Average	5.10, 30	kg/m^3
4	Density	DE 704	PV-Side Break, Average	5.11, 31	kg/m^3
5	Flow Rate	FM 705	MRP-Side Break, (Low)	A/B.144	kg/s
6	Flow Rate	FM 706	PV-Side Break, (Low)	A/B.145	kg/s
7	Flow Rate	FM 707	MRP-Side Break, (High)	A/B.146	kg/s
8	Flow Rate	FM 708	PV-Side Break, (High)	A/B.147	kg/s
9	Flow Rate	FM 709	Total Break Flow (Low)	5.3, 21	kg/s
10	Flow Rate	FM 710	Total Break Flow (High)	A/B.149	kg/s
11	Flow Rate	FM 711	Steam Flow (Low)		kg/s
12	Flow Rate	FM 712	Steam Flow (High)	5.4, 24	kg/s
13	Flow Rate	FM 713	Steam Flow (Middle)		kg/s
14	Flow Rate	FM 714	Channel A Inlet	5.7, 27	kg/s
15	Flow Rate	FM 715	Channel B Inlet	5.7, 27	kg/s
16	Flow Rate	FM 716	Channel C Inlet	5.7, 27	kg/s
17	Flow Rate	FM 717	Channel D Inlet	5.7, 27	kg/s
18	Flow Rate	FM 718	Bypass Hole Flow	5.7, 27	kg/s
19	Flow Rate	FM 719	Total Core Flow	5.8, 28	kg/s
20	Flow Rate	FM 720	JP1 Outlet (Pos. Flow)		kg/s
21	Flow Rate	FM 721	JP2 Outlet (Pos. Flow)		kg/s
22	Flow Rate	FM 722	JP3 Outlet (Pos. Flow)		kg/s
23	Flow Rate	FM 723	JP3 Outlet (Neg. Flow)		kg/s
24	Flow Rate	FM 724	JP4 Outlet (Pos. Flow)		kg/s
25	Flow Rate	FM 725	JP4 Outlet (Neg. FLow)		kg/s
26	Flow Rate	FM 726	Total JP Outlet Flow	A/B.150	kg/s
27	Water Level	LM 727	Collapsed DC Level	5.14, 34	m
28	Water Level	LM 728	Collapsed In-Shroud Level	5.14, 34	m
29	Fluid Mass	EV 729	Downcomer Mass	5.15, 35	kg
30	Fluid Mass	EV 730	In-Shroud Mass	5.15, 35	kg
31	Fluid Mass	EV 731	Total Mass in PV	A/B.155	kg
32	Fluid Mass	EV 732	Mass Balance in PV		kg
33	Fluid Mass	EV 733	Discharged Mass		kg
34	Flow Rate	FM 734	Discharged Flow Rate		kg/s
35	Flow Rate	FM 735	Discharged Flow Rate		kg/s

Table A.3 Core Instrumentation List

Item	Pos. DL Rod NO.	Core Outlet	Pos.1	Pos.2	Pos.3	Pos.4	Pos.5	Pos.6	Pos.7	Core Inlet
		3660	3417	3114.5	2879.5	2527	2174.5	1939.5	1637	1454
Surface Temp.	A11		TF 1	TF 2	TF 3	TF 4	TF 5	TF 6	TF 7	
	A12		TF 8	TF 9	TF 10	TF 11	TF 12	TF 13	TF 14	
	A13		TF 15	TF 16	TF 17	TF 18	TF 19	TF 20	TF 21	
	A14		TF 22	TF 23	TF 24	TF 25	TF 26	TF 27	TF 28	
	A15		TF 29			TF 30				
	A17		TF 31			TF 32				
	A22		TF 33	TF 34	TF 35	TF 36	TF 37	TF 38	TF 39	
	A23		TF 40	TF 41	TF 42	TF 43	TF 44	TF 45	TF 46	
	A24		TF 47	TF 48	TF 49	TF 50	TF.51	TF 52	TF 53	
	A26		TF 54			TF 55				
	A28		TF 56			TF 57				
	A31		TF 58			TF 59				
	A33		TF 60	TF 61	TF 62	TF 63	TF 64	TF 65	TF 66	
	A34		TF 67	TF 68	TF 69	TF 70	TF 71	TF 72	TF 73	
	A35		TF 74			TF 75				
	A37		TF 76			TF 77				
	A42		TF 78			TF 79				
Fluid Temp.	A44	TC 1	TF180	TF181	TF182	TF183	TF184	TF185	TF186	TC 2
Surface Temp.	A45		TF 80			TF 81				
	A46		TF 82			TF 83				
	A48		TF 84			TF 85				
	A51		TF 86			TF 87				
	A53		TF 88			TF 89				
	A54		TF 90							
	A57		TF 91			TF 92				
	A62		TF 93			TF 94				
	A64		TF 95			TF 96				
	A66		TF 97			TF 98				
	A68		TF 99			TF100				
	A71		TF101			TF102				
	A73		TF103			TF104				
	A75		TF105			TF106				
	A77		TF107			TF108				

Table A.3 Core Instrumentation list (Cont'd)

Item	Pos.	Core Outlet	Pos.1	Pos.2	Pos.3	Pos.4	Pos.5	Pos.6	Pos.7	Core Inlet
	Rod NO. \ DL	3660	3417	3114.5	2879.5	2527	2174.5	1939.5	1637	1454
Surface Temp.	A82		TF109			TF110				
	A84		TF111			TF112				
	A86		TF113			TF114				
	A88		TF115			TF116				
	B11					TF117				
	B13					TF118				
	B15		TF119	TF120	TF121	TF122	TF123	TF124	TF125	
	B31					TF126				
	B33					TF127				
	B35					TF128				
Fluid Temp.	B44	TC 3	TF187	TF188	TF189	TF190	TF191	TF192	TF193	TC 4
Surface Temp.	B51					TF129				
	B53					TF130				
	B85		TF131	TF132	TF133	TF134	TF135	TF136	TF137	
	C11					TF138				
	C13					TF139				
	C15					TF140				
	C31					TF141				
	C33		TF142	TF143	TF144	TF145	TF146	TF147	TF148	
	C35					TF149				
Fluid Temp.	C44	TC 5	TF194	TF195	TF196	TF197	TF198	TF199	TF200	TC 6
Surface Temp.	C51					TF150				
	C53					TF151				
	C77		TF152	TF153	TF154	TF155	TF156	TF157	TF158	
	D11					TF159				
	D13					TF160				
	D27		TF161	TF162	TF163	TF164	TF165	TF166	TF167	
	D31					TF168				
	D33					TF169				
	D35					TF170				
Fluid Temp.	D44	TC 7	TF201	TF202	TF203	TF204	TF205	TF206	TF207	TC 8
Surface Temp.	D51					TF171				
	D53					TF172				
	D88		TF173	TF174	TF175	TF176	TF177	TF178	TF179	

Table A.3 Core Instrumentation list (Cont'd)

Item	Pos.	Core Outlet	Pos.1	Pos.2	Pos.3	Pos.4	Pos.5	Pos.6	Pos.7	Core Inlet
	Rod NO. DL	3660	3417	3114.5	2879.5	2527	2174.5	1939.5	1673	1454
Void	A55		VF 1	VF 2	VF 3	VF 4	VF 5	VF 6	VF 7	
	B55		VF 8	VF 9	VF 10	VF 11	VF 12	VF 13	VF 14	
	C55		VF 15	VF 16	VF 17	VF 18	VF 19	VF 20	VF 21	
	D55		VF 22	VF 23	VF 24	VF 25	VF 26	VF 27	VF 28	
Channel Box Surface Temp.	A1*		TB 1	TB 2	TB 3	TB 4	TB 5	TB 6	TB 7	
	A2*		TB 8	TB 9	TB 10	TB 11	TB 12	TB 13	TB 14	
	B*		TB 15	TB 16	TB 17	TB 18	TB 19	TB 20	TB 21	
	C*		TB 22	TB 23	TB 24	TB 25	TB 26	TB 27	TB 28	
	D*		TB 29	TB 30	TB 31	TB 32	TB 33	TB 34	TB 35	
Liquid Level in the Channel Box	A1*		LB 1	LB 2	LB 3	LB 4	LB 5	LB 6	LB 7	
	A2*		LB 8	LB 9	LB 10	LB 11	LB 12	LB 13	LB 14	
	B*		LB 15	LB 16	LB 17	LB 18	LB 19	LB 20	LB 21	
	C*		LB 22	LB 23	LB 24	LB 25	LB 26	LB 27	LB 28	
	D*		LB 29	LB 30	LB 31	LB 32	LB 33	LB 34	LB 35	

Appendix II Data Processing and Experiment Data for RUNs 940 and 941

In Appendix II, most of the experiment data of RUNs 940 and 941 and their data processing methods are shown. Some of the experiment data of these two tests are shown in Chapters 5 and 6. The data acquisition frequency was 10 Hz for both tests. The test data were processed and reduced to 1000 data points in each data channel for computer plotting.

The test data of RUN 940 are shown in Figs. A.1 through A.157. In these figures, the measured quantity is identified by the channel number and the alphabetic characters (ref. Table A.1). The test data of RUN 941 are described after the description of RUN 940 data, in Figs. B.1 through B.157.

(1) Experiment Data of RUN 940, A 5% Break LOCA Test

Figures A.1 through A.5 show the pressure data in the pressure vessel (PV), recirculation loops and main steam line (MSL). Figures A.6 through A.28 show differential pressure data between various positions in the pressure vessel and the recirculation loops. Figure A.29 shows the liquid levels in the ECCS tanks. Figures A.30 through A.33 show the jet pump discharge flows and recirculation line flows. The pump speed of the recirculation pump is shown in Fig.A.34. The trip signals such as the break initiation signal and the valve positioning signals are shown in Figs. A.35 through A.37. Figures A.38 through A.47 show the fluid densities measured by the gamma densitometer at the jet pump outlets and break units. The fluid density data are corrected at two known points, one is the initial condition and another is a steam-phase condition or a water single phase condition. Figures A.48 through A.53 show momentum fluxes measured by drag-disks at the jet pump outlets and break units. The drag-disk data are similarly corrected as the fluid density at two known points, one is the initial condition, in which the volumetric flow rate for the initial water flow is known, and another one is the final test condition, in which the recirculation flow was terminated by closing the QSV after the end of test period. Figures A.54 through A.62 show the fluid temperatures at various positions in the system. The surface temperatures of heater rods and water rods are measured at positions 1 through 7 as given in Figs. A.63 through A.82. Figures A.83 through A.103 show the heater rod temperatures in the same vertical axis. Figures A.104 through A.106 show the fluid temperatures at both outlet and inlet of the channel boxes. The fluid temperatures above and below the upper tieplate (UTP) in both A and C channels are shown in Figs.A.107 through A.114 (thermocouple locations of these are shown in Fig.3.6). The channel box surface temperatures both on inner and outer walls are compared each other at the same elevation in Figs.A.115 through A.121. Fluid temperatures in the lower plenum are compared in Fig.A.122. The liquid level signals in the core, the upper and lower plena, the guide tube and the downcomer are shown in Figs. A.123 through A.143.

Quantities reduced from the test data are shown in Figs. A.144 through A.157. The average densities (see Figs.5.9 through 5.11 in Chapter 5) are calculated as an arithmetic mean of the densities in multi-directions with the weight of each cord length (see Figs.A.38 through A.47).

For the three-beam densitometer at the jet pump outlet spool,

$$\rho_{av} = 0.3221\rho_A + 0.43\rho_B + 0.2479\rho_C \qquad (A.1)$$

where,

ρ_{av}: average density obtained from the three-beam gamma densitometer,
ρ_A : density measured by beam A (bottom),
ρ_B : density measured by beam B (middle).
ρ_C : density measured by beam C (top).

For the two-beam densitometer at the break spool piece,

$$\rho_{av} = 0.5863\rho_A + 0.4137\rho_B \qquad (A.2)$$

where,

ρ_{av}: average density obtained from the two-beam gamma densitometer,
ρ_A : density measured by beam A (bottom),
ρ_B : density measured by beam B (top).

Figures A.144 through A.147 show flow rates measured by the low and high-range drag-disks. The flow rates are computed from the drag-disk data and the gamma densitometer data by using the following equation,

$$G = C_D \cdot A \cdot \sqrt{\rho_{av} \cdot \rho V^2} \tag{A.3}$$

where,

G : mass flow rate,

C_D : drag coefficient (= 1.13),

A : flow area (= 1.923×10^{-3} m^2),

ρ_{av} : average density from gamma densitometer,

ρV^2 : momentum flux from drag disk.

The total break flow rates shown in Figs.A.148 and A.149 are derived from these flow rates as follows,

$$G_B = G_P - G_V \tag{A.4}$$

where,

G_B : break flow,

G_P : flow rate at the pump side of the break,

G_V : flow rate at the vessel side of the break.

The fluid flow rates at the main steam line, channel inlet orifices, bypass hole and jet pump outlets (see Figs.5.4, 5.7, 5.8 and Fig.A.150) are calculated from the test data which are the pressure drop across the orifices or venturi flow meters and the liquid density obtained from the temperature and the pressure condition. The equation used for the calculation is as follows :

$$G = C_D \cdot A \cdot \sqrt{2g \cdot \rho_l \cdot \Delta P} \tag{A.5}$$

where,

G : flow rate,

ΔP : pressure drop across the orifice,

C_D : discharge coefficient,

= 0.6552 (the orifice to measure the steam discharge flow rate)

= 0.4761 (the channel inlet orifice)

= 0.8032 (the bypass hole)

= 0.7383 (the orifice to measure jet pump outlet flow)

= 1.1260 (the venturi to measure jet pump outlet flow)

A : flow area (m^2)

$= 2.875 \times 10^{-3}$ (the orifice to measure the steam discharge flow rate)

$= 1.521 \times 10^{-3}$ (the channel inlet orifice)

$= 1.758 \times 10^{-4}$ (the bypass hole)

$= 1.133 \times 10^{-3}$ (the jet pump outlet orifice)

$= 9.095 \times 10^{-4}$ (the jet pump outlet venturi)

g : gravitational acceleration ($= 9.807\ m/s^2$),
ρ_l : density of the single-phase liquid (kg/m^3).

This calculation method is not applicable for two-phase flow condition after the LPF initiation at the channel inlet orifice and the bypass hole. Those calculated values show only a trend in two-phase flow condition. Total channel inlet flow rate presents the sum of four channel inlet flow rates and a bypass hole flow rate.

Figures A.151 and A.152 show the collapsed water levels in downcomer and inside the core-shroud, respectively. Each level is obtained from the corresponding differential pressure. The differential pressure may include the flow resistance effect, however, the flow resistance becomes negligible after slowdown of the recirculation pump speed and lower plenum flashing.

Figure A.153 shows the fluid mass inventory in downcomer. The fluid mass inventory is determined from the density and configurational data outside the core shroud,

$$M = \rho_l \cdot Q \qquad (A.6)$$

where,
M : fluid inventory,
ρ_l : liquid density estimated from the satulation temperature and/or pressure,
Q : liquid volume calculated from the liquid level.

The volume Q (m^3) inside the shroud is also given as a function of collapsed water level in downcomer (L),

$$Q = 0.0 \qquad (L \leqq 0.494)$$
$$Q = 0.0225L - 0.0111 \qquad (0.494 < L \leqq 1.384)$$

$$
\begin{array}{ll}
Q = 0.0697L - 0.0769 & (\ 1.384 < L \leqq 1.519\ ) \\
Q = 0.0225L - 0.0048 & (\ 1.519 < L \leqq 3.355\ ) \\
Q = 0.0801L - 0.1980 & (\ 3.355 < L \leqq 4.250\ ) \\
Q = 0.2443L - 0.8959 & (\ 4.250 < L \leqq 4.413\ ) \\
Q = 0.2611L - 0.9700 & (\ 4.413 < L \leqq 4.578\ ) \\
Q = 0.2504L - 0.9211 & (\ 4.578 < L \leqq 4.654\ ) \\
Q = 0.2375L - 0.8610 & (\ 4.654 < L \leqq 4.815\ ) \\
Q = 0.2866L - 1.0974 & (\ 4.815 < L \leqq 4.915\ ) \\
Q = 0.3396L - 1.3580 & (\ 4.915 < L \leqq 5.143\ ) \\
Q = 0.3607L - 1.4665 & (\ 5.143 < L \leqq 5.365\ ) \\
Q = 0.3848L - 1.5960 & (\ 5.365 < L \leqq 5.995\ ) \\
Q = 0.7111 & (\ 5.995 < L\ )
\end{array}
\qquad (A.7)
$$

Figure A.154 shows the fluid mass inventory inside core shroud. The fluid mass inventory is determined from the density and configurational data inside the core-shroud,

$$M = \rho_l \cdot Q \qquad (A.8)$$

where,

M : fluid inventory,

ρ_l : liquid density estimated from the saturation temperature and/or pressure,

Q : liquid volume calculated from the liquid level.

The volume Q (m^3) inside the shroud is also given as a function of collapsed water level inside core-shroud (L),

$$
\begin{array}{ll}
Q = 0.0 & (\ L \leqq 0.0\ ) \\
Q = 0.2350L & (\ 0.0 < L \leqq 0.497\ ) \\
Q = 0.1245L + 0.0549 & (\ 0.497 < L \leqq 1.354\ ) \\
Q = 0.0698L + 0.1290 & (\ 1.354 < L \leqq 3.589\ ) \\
Q = 0.1648L - 0.2120 & (\ 3.589 < L \leqq 3.744\ ) \\
Q = 0.1963L - 0.3299 & (\ 3.744 < L \leqq 4.243\ ) \\
Q = 0.0196L + 0.4199 & (\ 4.243 < L \leqq 4.578\ ) \\
Q = 0.0186L + 0.4244 & (\ 4.578 < L \leqq 4.654\ ) \\
Q = 0.0410L + 0.3201 & (\ 4.654 < L \leqq 5.099\ ) \\
Q = 0.0196L + 0.4292 & (\ 5.099 < L \leqq 5.365\ )
\end{array}
\qquad (A.9)
$$

$Q = 0.5344 \qquad (5.365 < L \qquad)$

Figure A.155 shows a total fluid inventory in PV, which is a sum of fluid mass in downcomer (see Fig. A.153) and inside core-shroud (see Fig. A.154).

Figures A.156 and A.157, which are shown in Chapter 13 of the previous report(57), show the dryout and quench fronts on the heater rods of A22, B22, C22 and D22 and mixture level transients in four bundles, respectively.

(2) Experiment Data of RUN 941, A 200% Break LOCA Test

The experiment data and reduced data for RUN 941 are similarly shown in Figs.B.1 through B.157 as for RUN 940 in the previous section. As the data processing methods are common for these two tests, the description of the experiment data for RUN 941 are omitted.

List of Figures of Experiment Data for RUN 940 (Appendix II)

List of Figures of Experiment Data for RUN 941 (Appendix II)

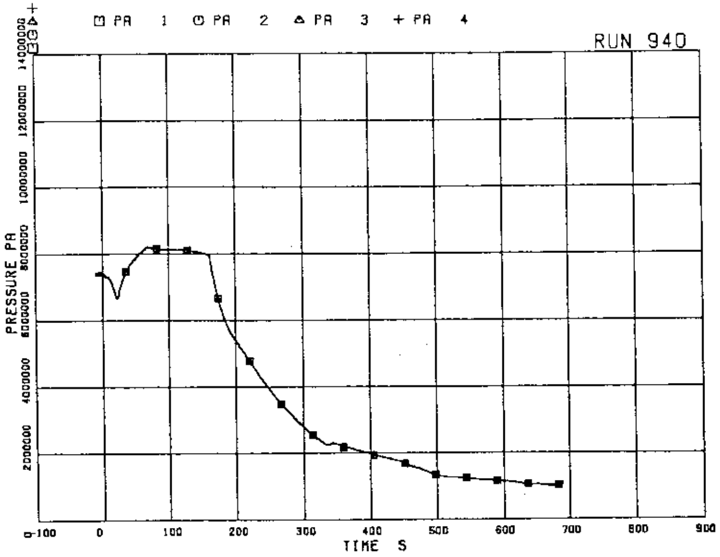

Fig.A.1 Pressure in PV (pressure vessel)

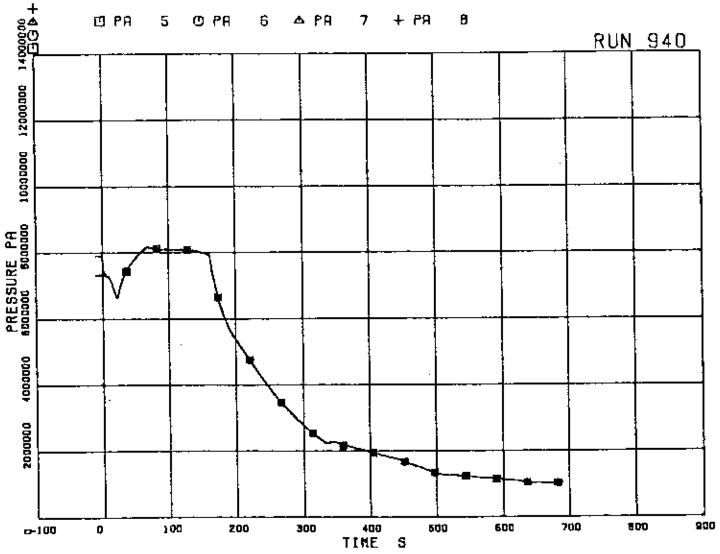

Fig.A.2 Pressure in broken loop JP (Jet Pump)

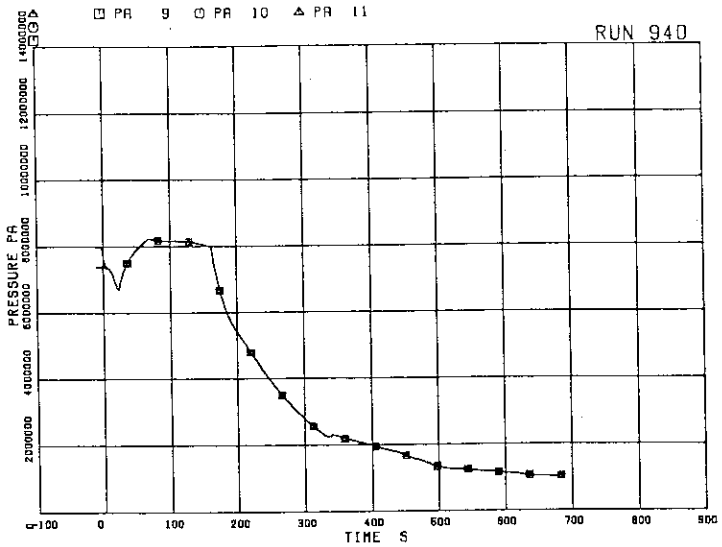

Fig.A.3 Pressure near MRP (Main Recirculation Loop)

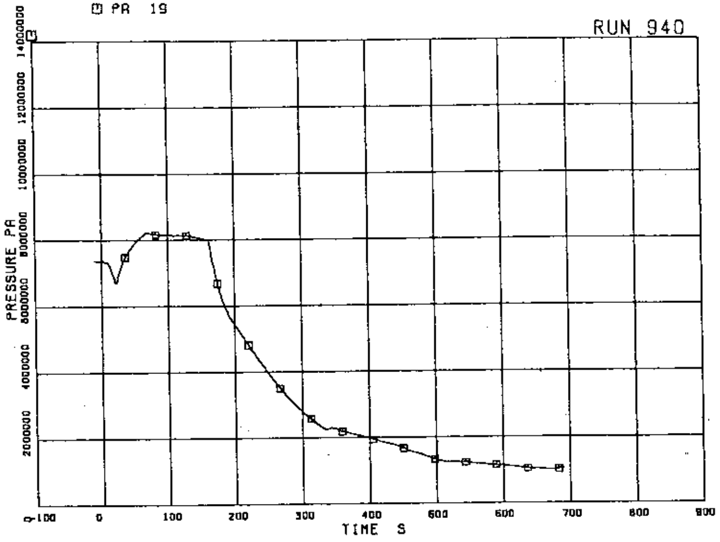

Fig.A.4 Pressure at MRP side of break

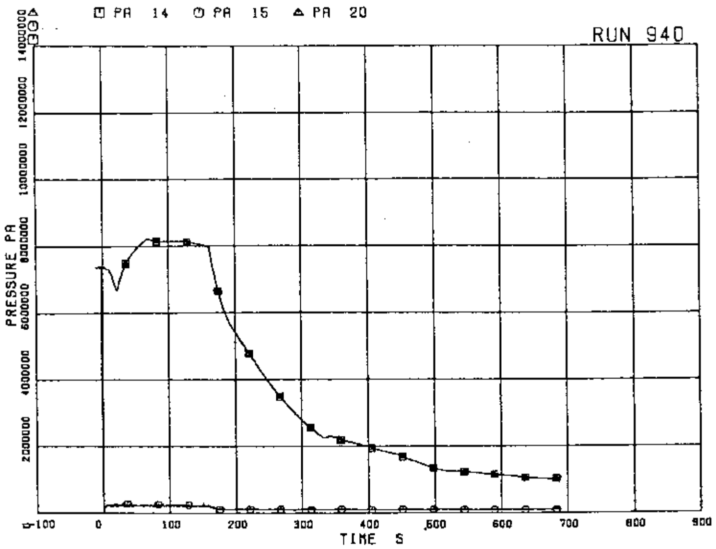

Fig.A.5 Pressure at PV side of break

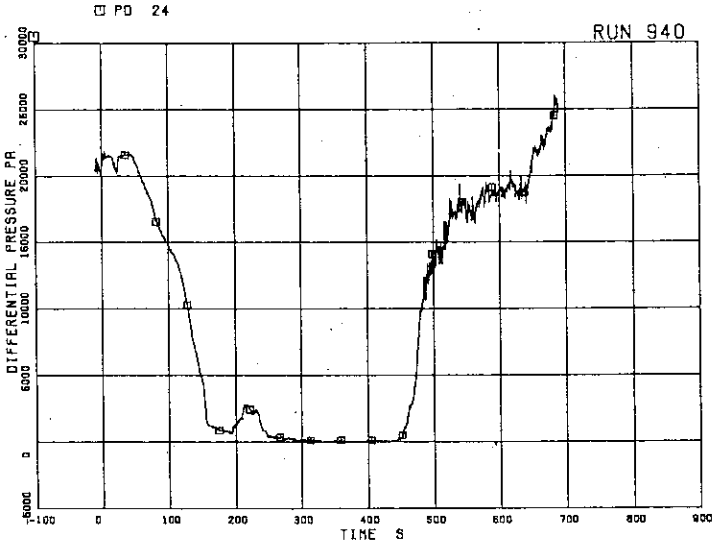

Fig.A.6 (DC) Downcomer Head

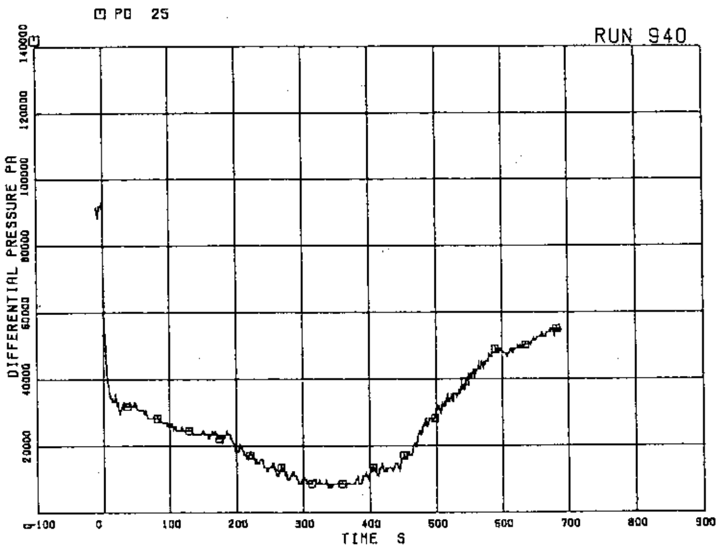

Fig.A.7 Differential pressure between PV bottom and top

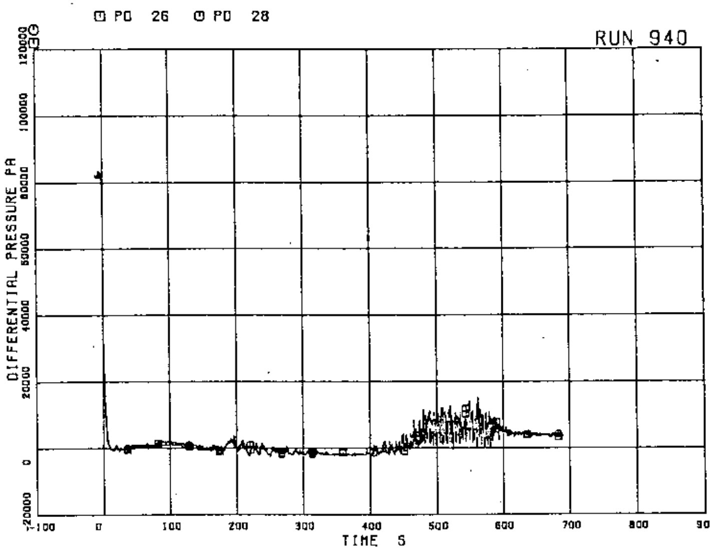

Fig.A.8 Differential pressure between JP-1,2 discharge and suction

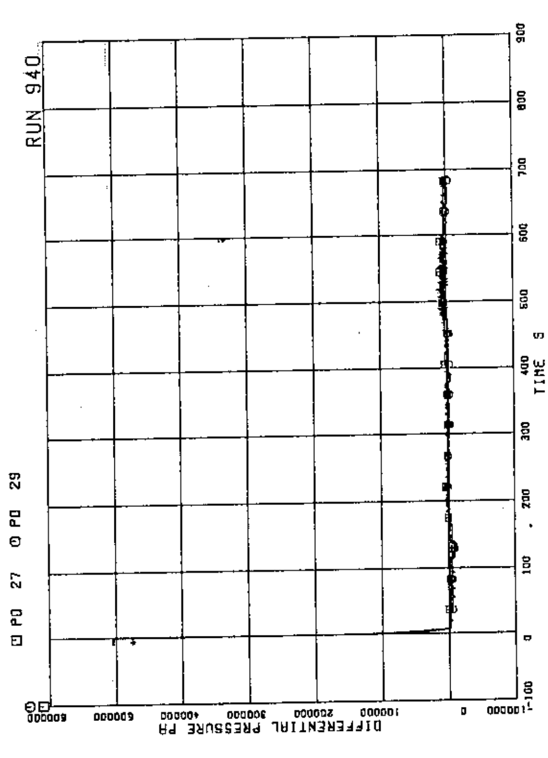

Fig.A.9 Differential pressure between JP-1,2 drive and suction

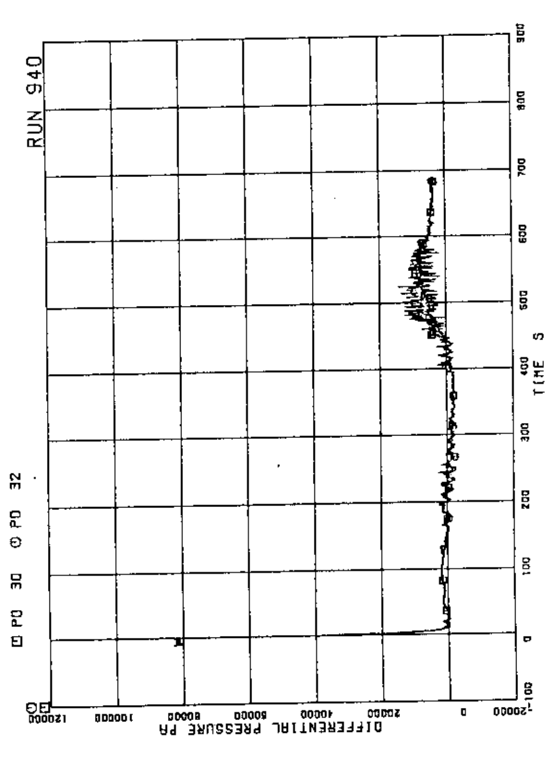

Fig.A.10 Differential pressure between JP-3,4 discharge and suction

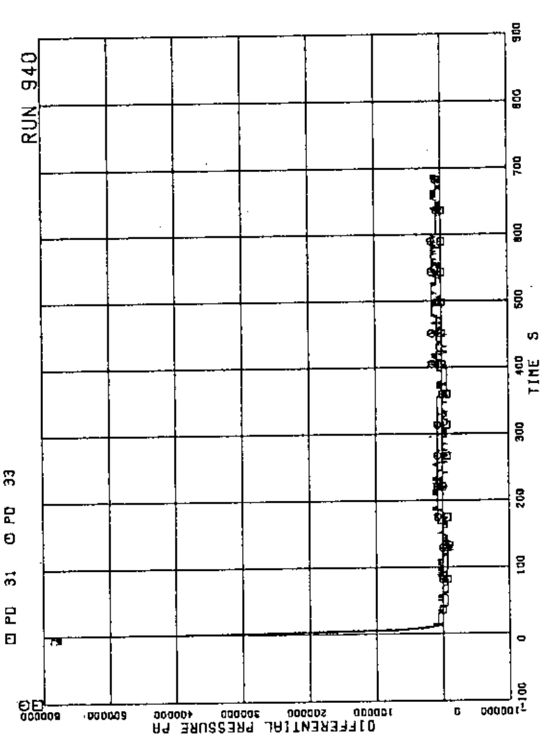

Fig.A.11 Differential pressure between JP-3,4 drive and suction

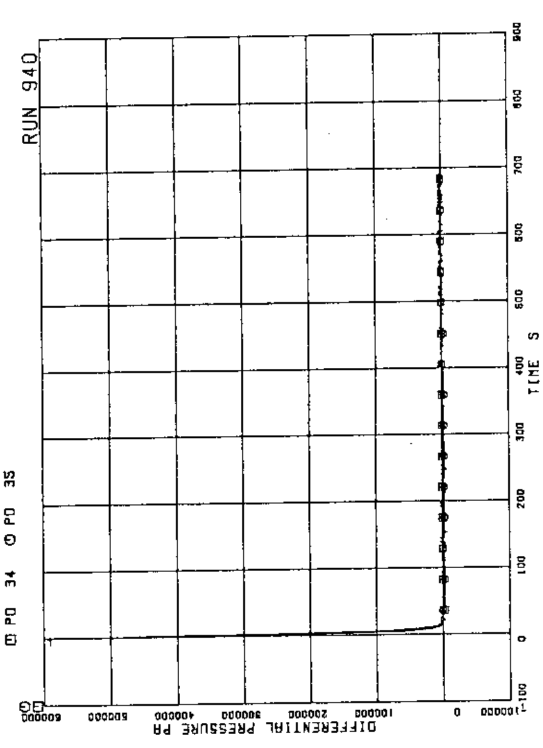

Fig.A.12 Differential pressure beetween MRP delivery and suction

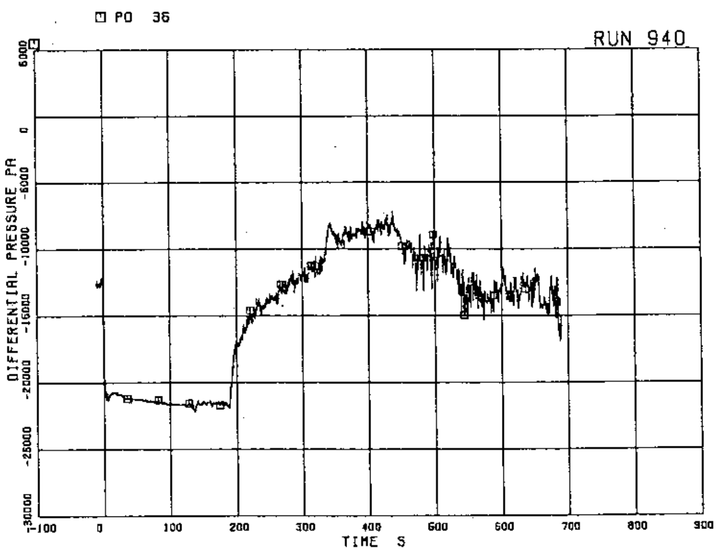

Fig.A.13　Differential pressure between downcomer bottom and MRP1 suction

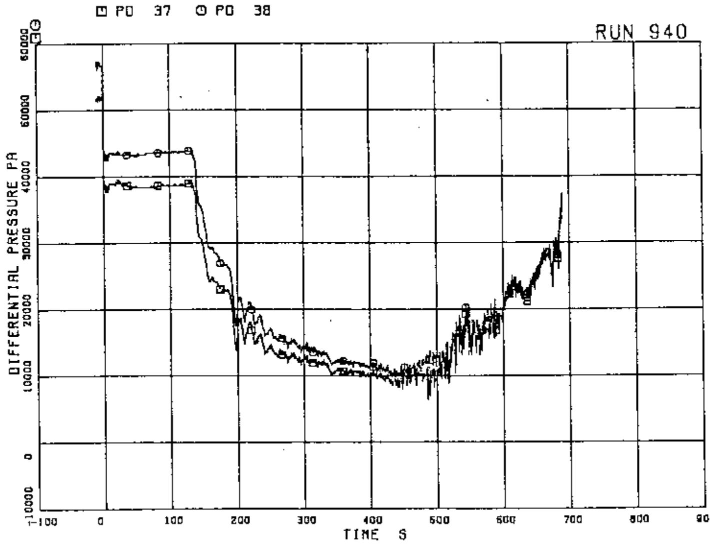

Fig.A.14　Differential pressure between MRP1 delivery and JP-1,2 drive

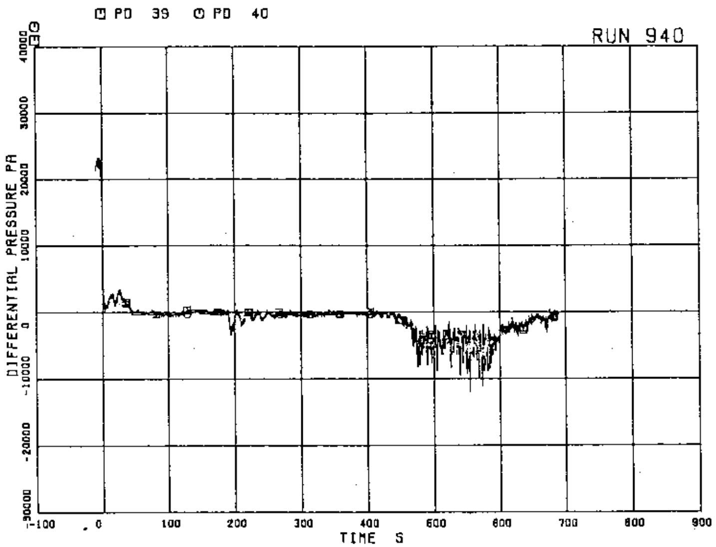

Fig.A.15　Differential pressure between downcomer middle and JP-1,2 suction

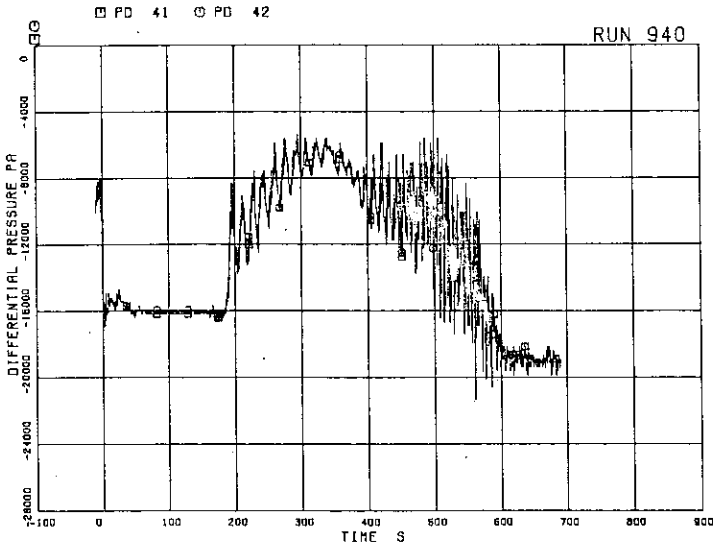

Fig.A.16　Differential pressure between JP-1,2 discharge and LP

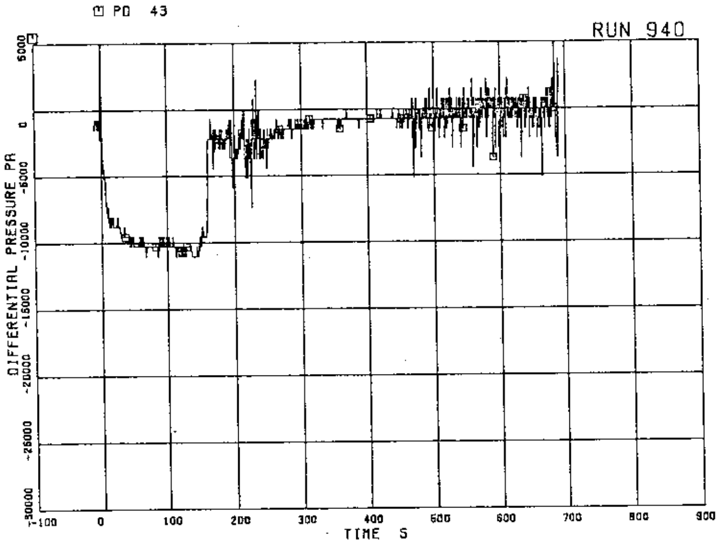

Fig.A.17 Differential pressure between downcomer bottom and break B

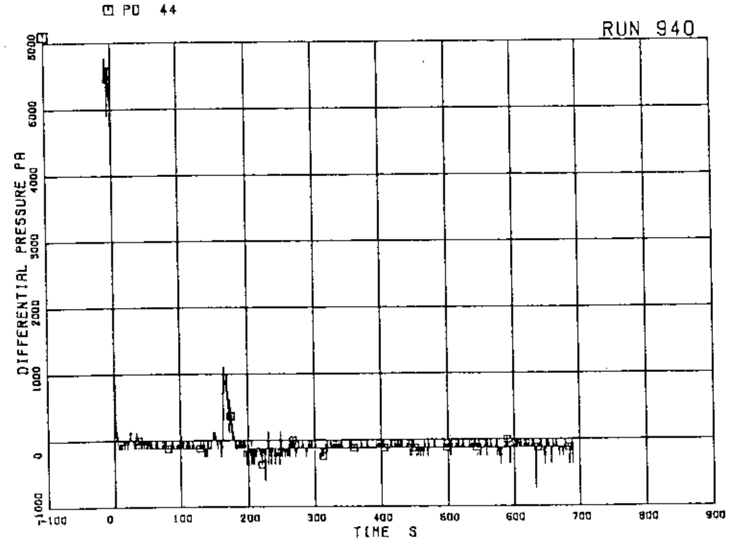

Fig.A.18 Differential pressure between breaks A and B

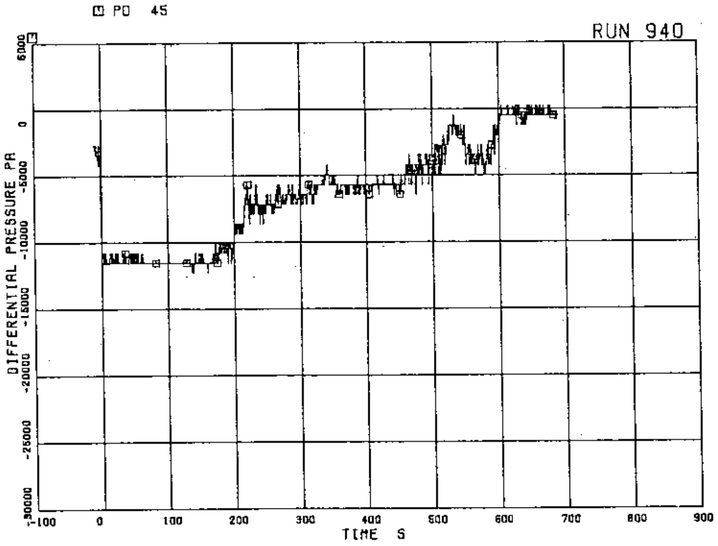

Fig.A.19 Differential pressure between break A and MRP2 suction

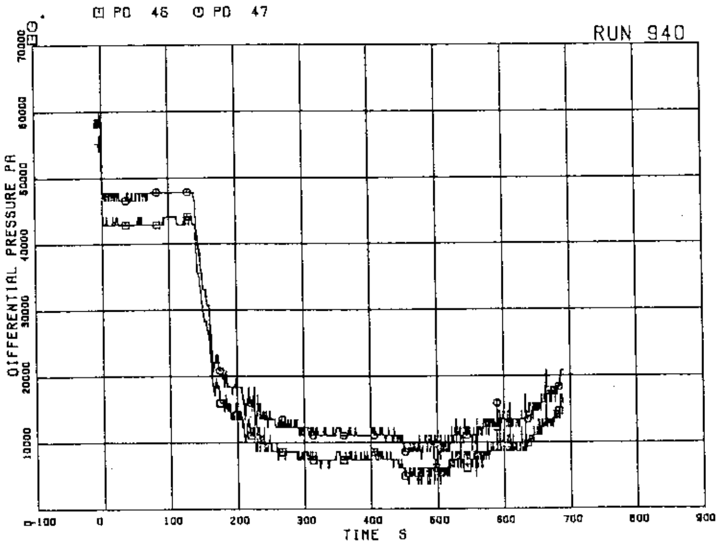

Fig.A.20 Differential pressure between MRP2 dilivery and JP-3,4 drive

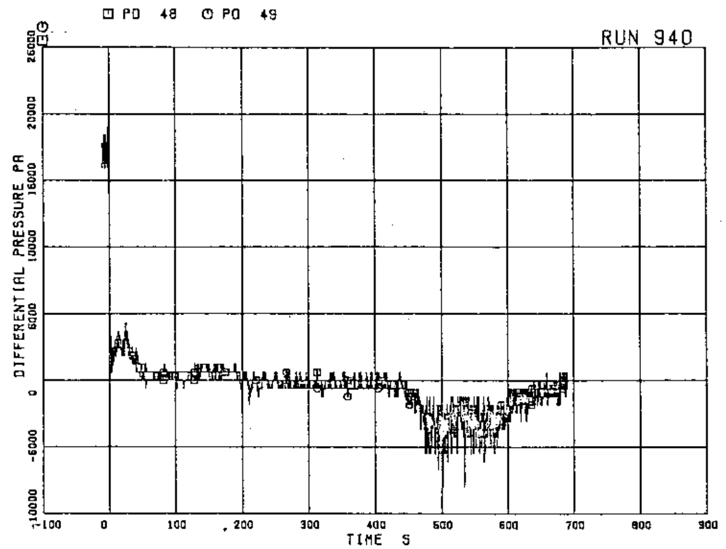

Fig.A.21 Differential pressure between downcomer middle and JP-3,4 suction

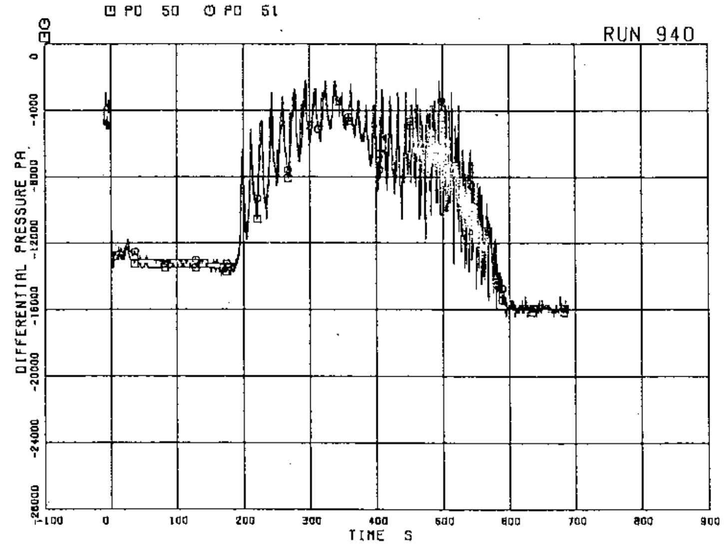

Fig.A.22 Differential pressures between JP-3,4 discharge and confluence

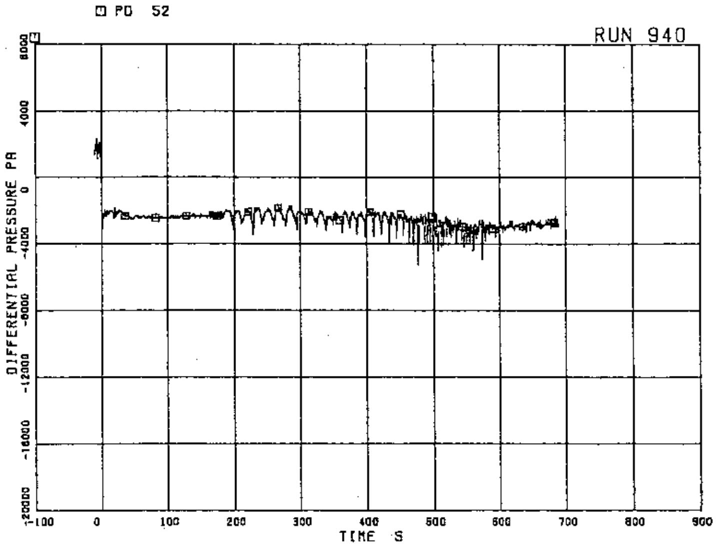

Fig.A.23 Differential pressure between JP-3,4 confluence in broken loop and LP

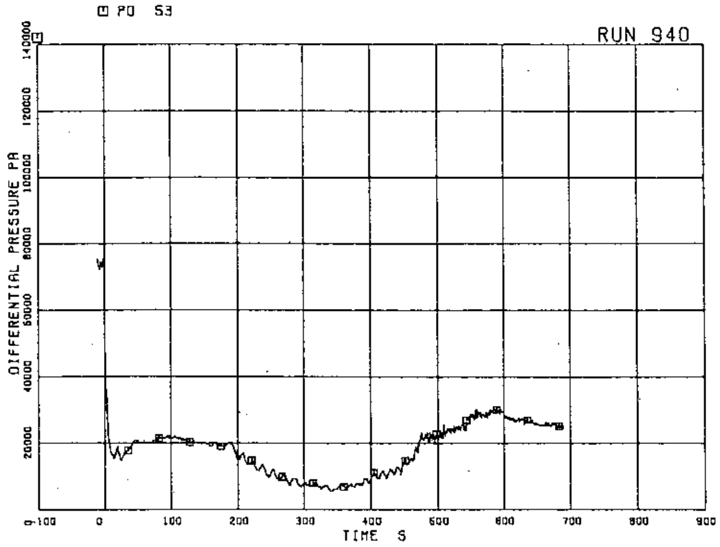

Fig.A.24 Differential pressure between lower plenum and

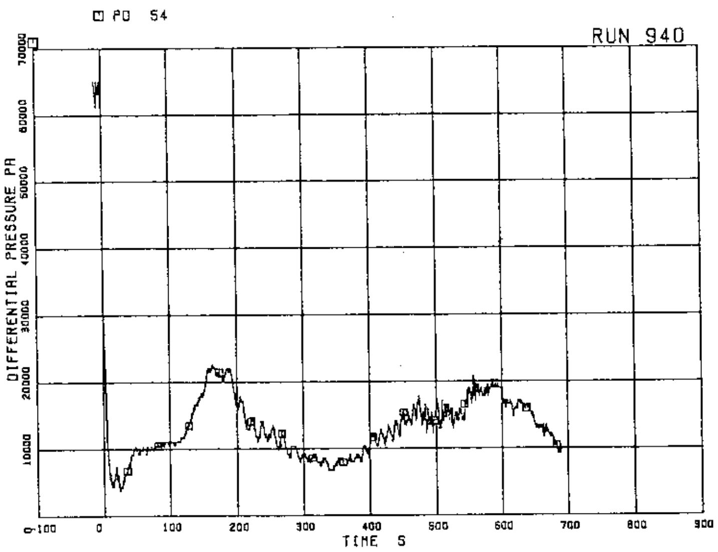

Fig.A.25 Differential pressure between lower plenum and downcomer bottom

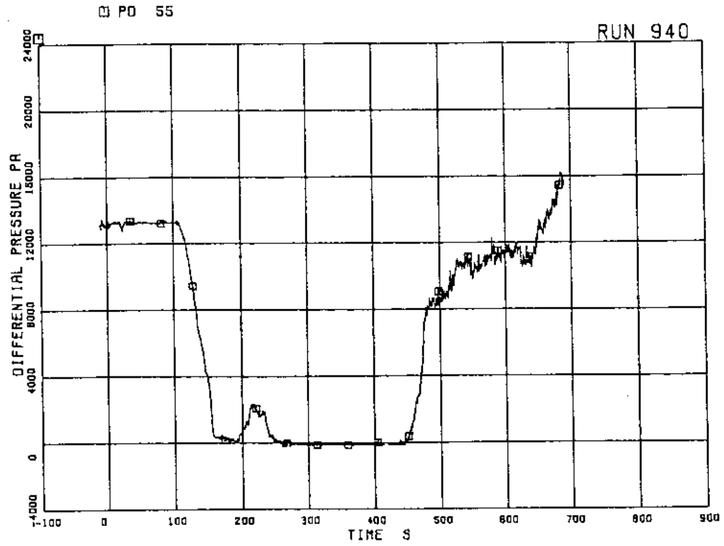

Fig.A.26 Differential pressure between downcomer bottom and downcomer middle

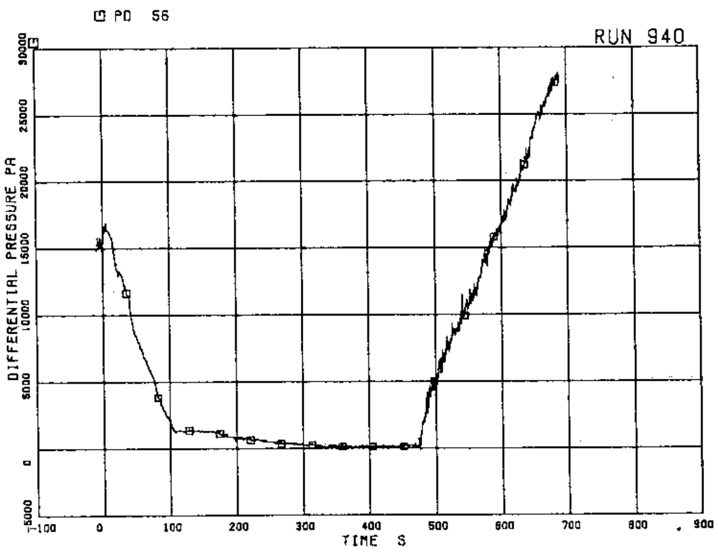

Fig.A.27 Differential pressure between downcomer middle and steam dome

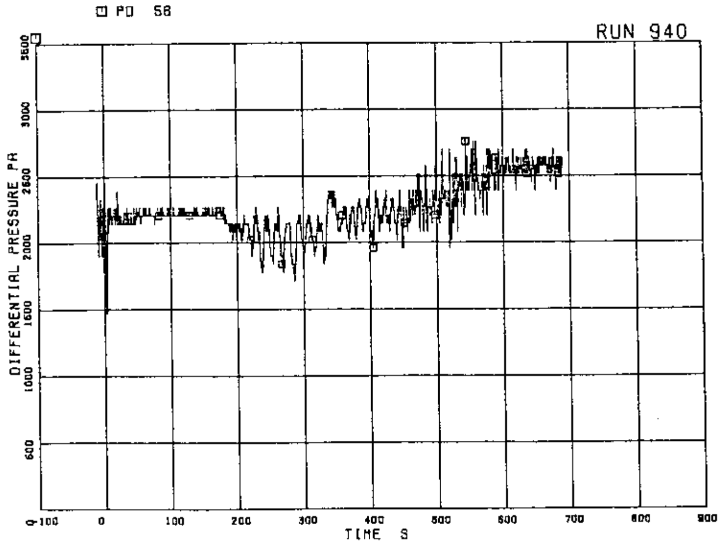

Fig.A.28 Differential pressure between LP bottom and LP middle

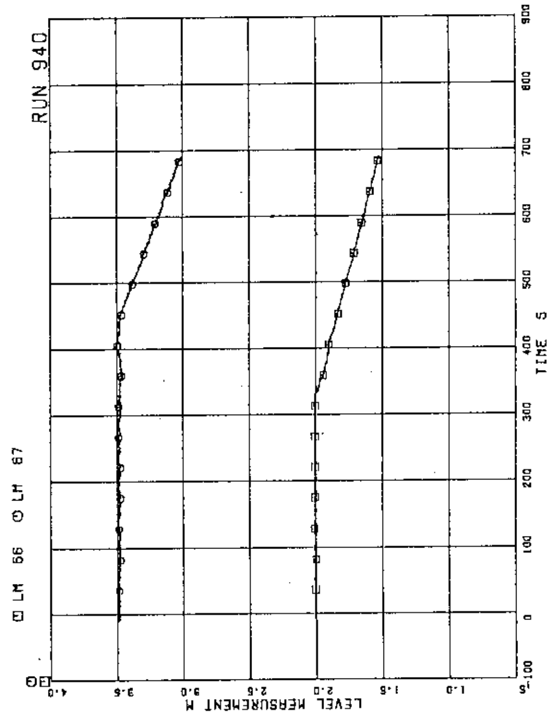

Fig.A.29 Liquid levels in ECCS tanks

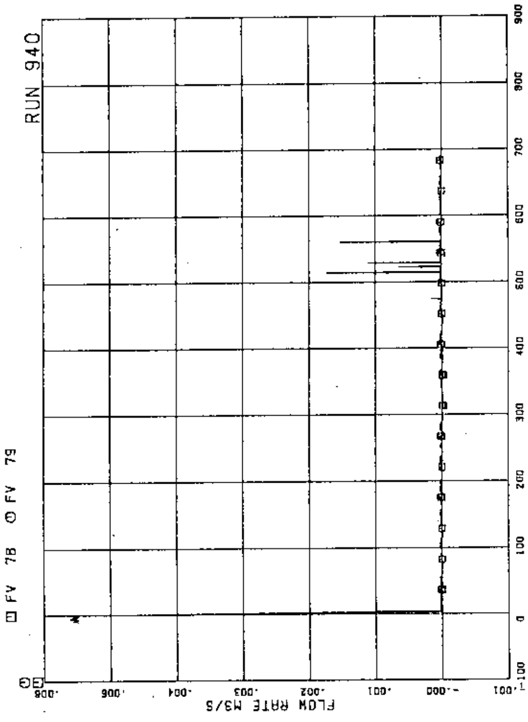

Fig.A.30 JP-1,2 discharge flow rates (pos. flow)

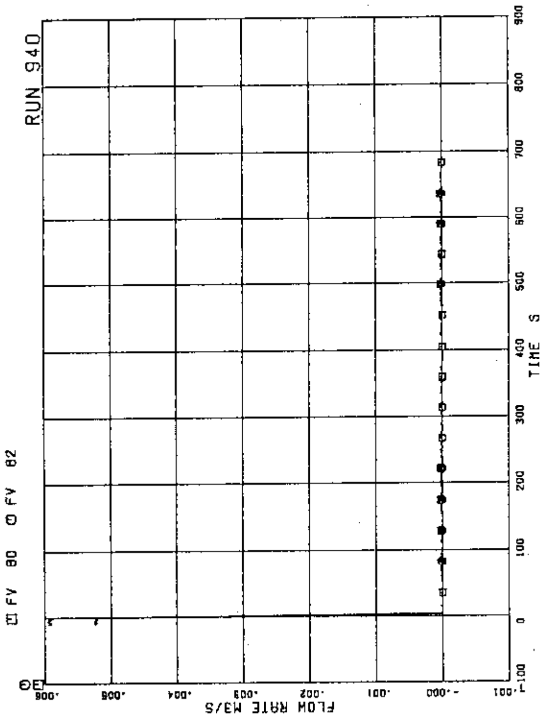

Fig.A.31 JP-3,4 discharge flow rates (pos. flow)

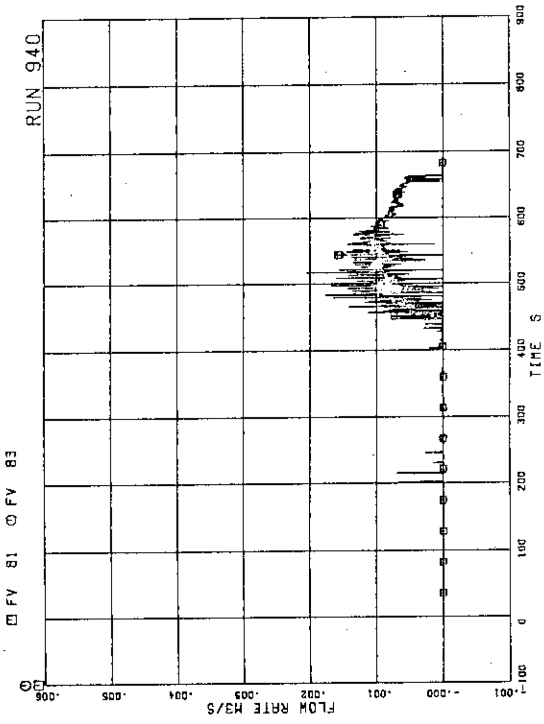

Fig.A.32 JP-3,4 discharge flow rates (neg. flow)

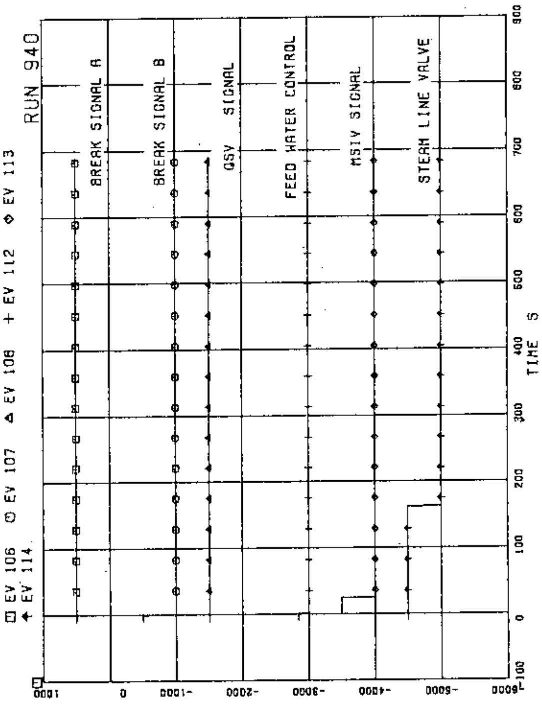

Fig.A.35 Valve operation signals

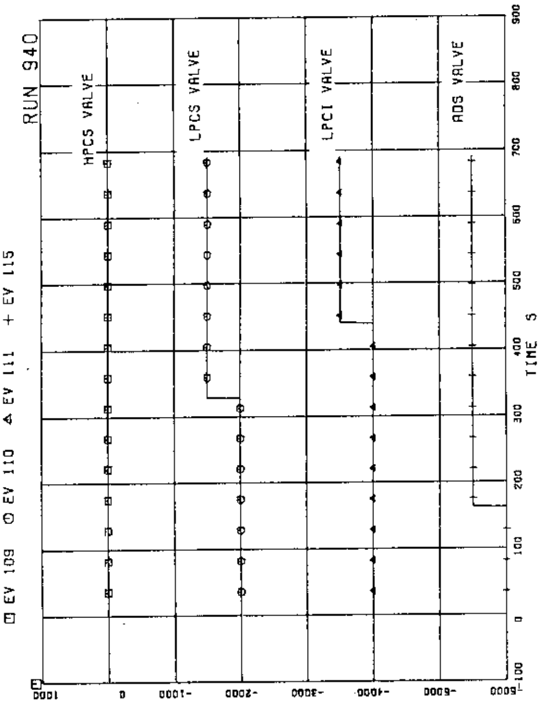

Fig.A.36 ECCS operation signals

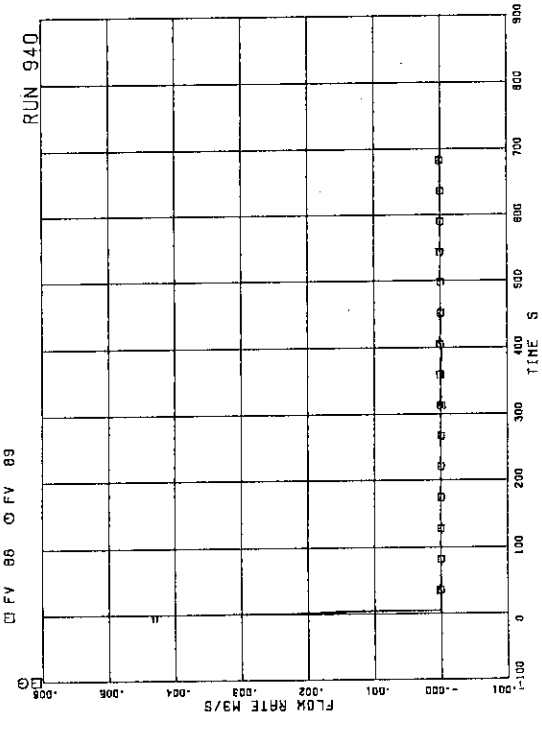

Fig.A.33 MRP discharge flow rate

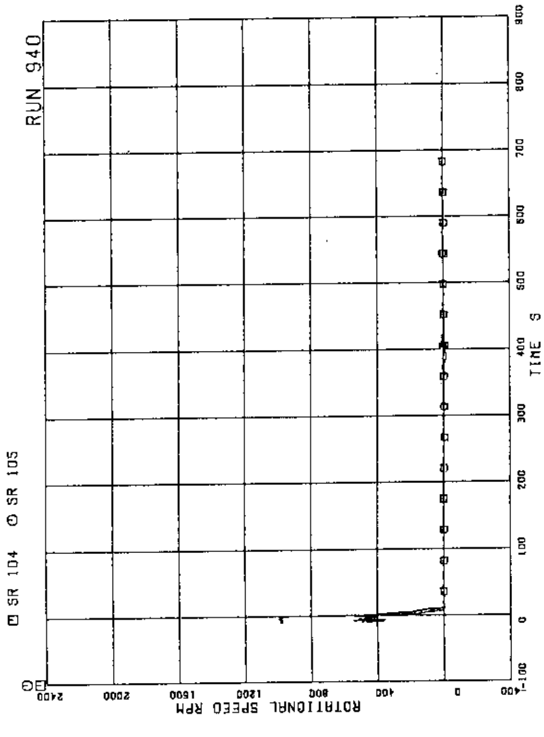

Fig.A.34 MRP pump speeds

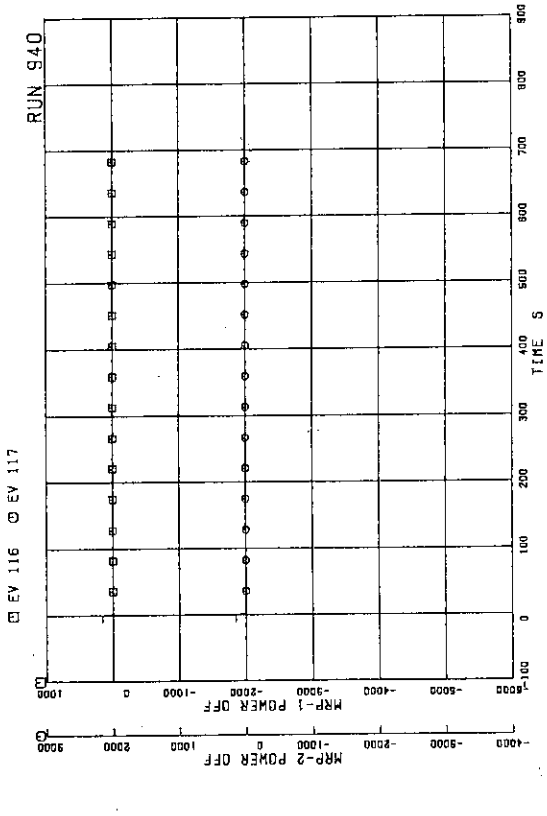

Fig.A.37 MRP operation signals

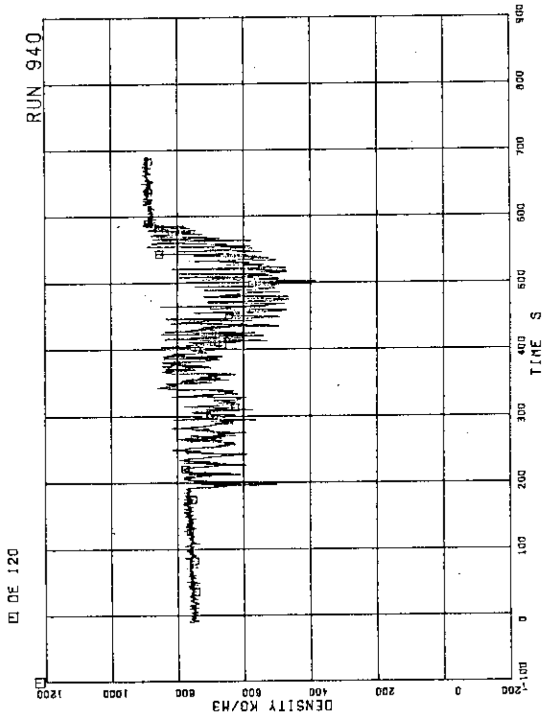

Fig.A.38 Fluid density at JP-1,2 outlet, beam A

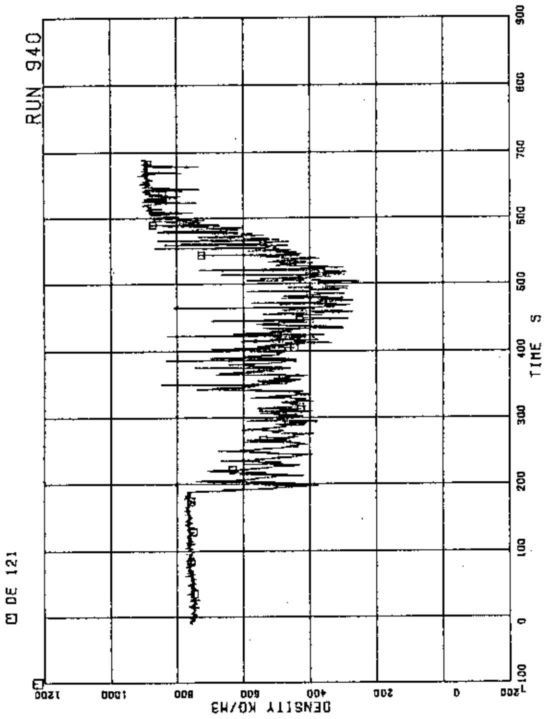

Fig.A.39 Fluid density at JP-1.2 outlet, beam B

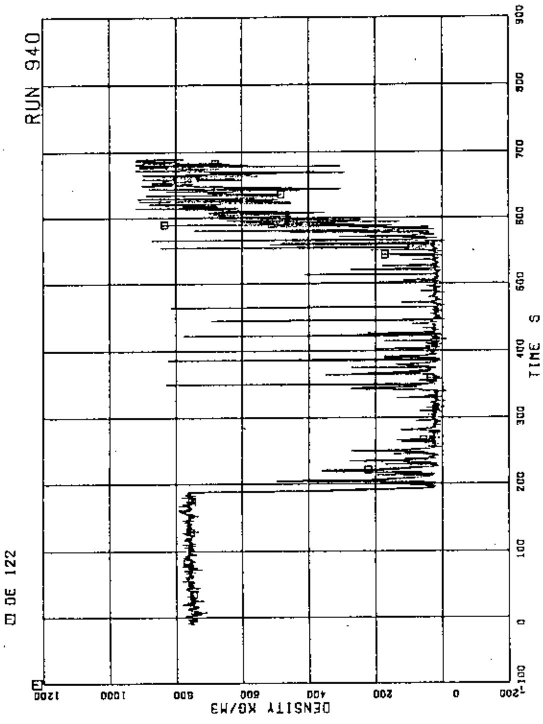

Fig.A.40 Fluid density at JP-1.2 outlet, beam C

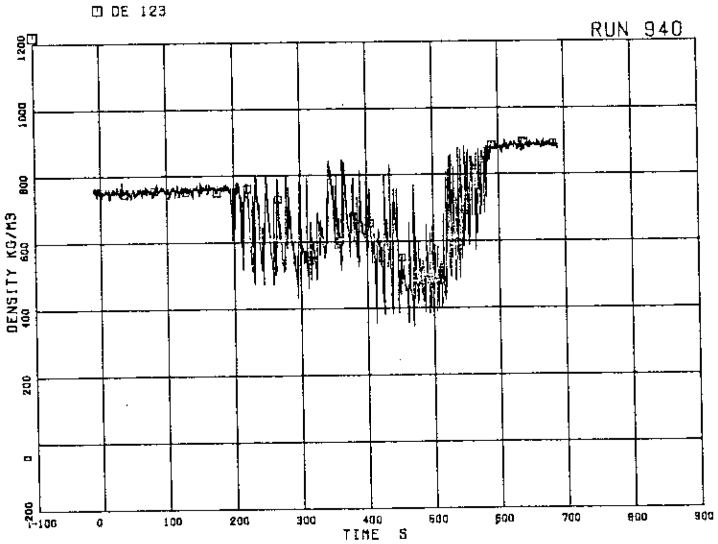

Fig.A.41 Fluid density at JP-3,4 outlet, beam A

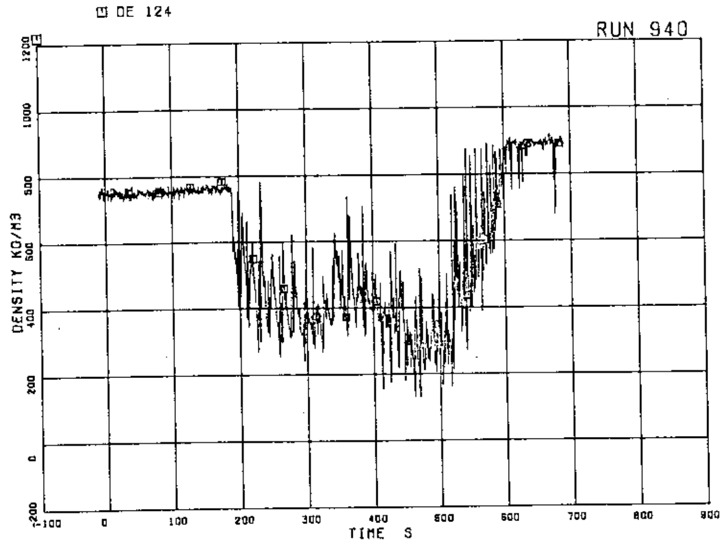

Fig.A.42 Fluid density at JP-3,4 outlet, beam B

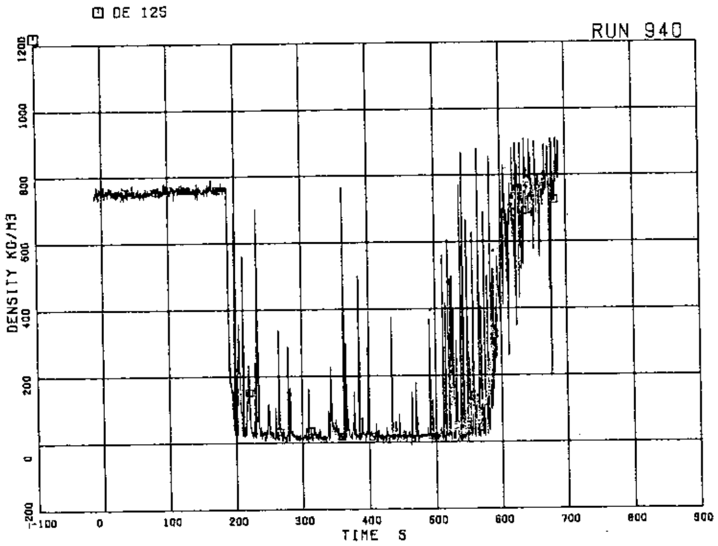

Fig.A.43 Fluid density at JP-3,4 outlet, beam C

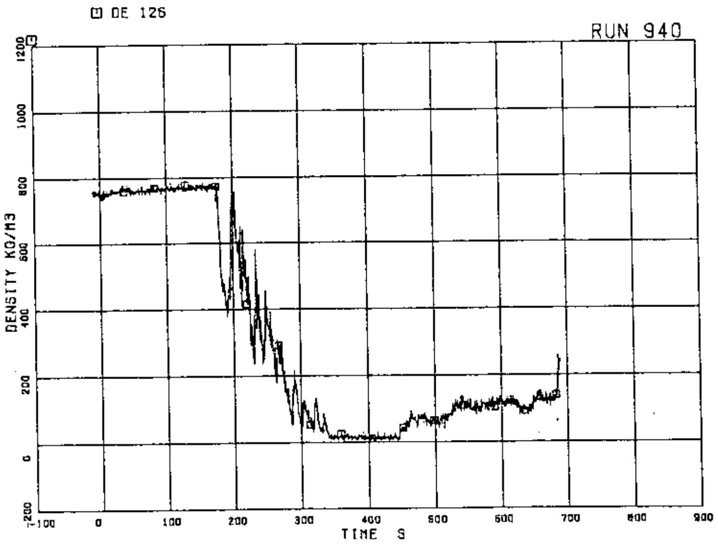

Fig.A.44 Fluid density at MRP-side of break, beam A

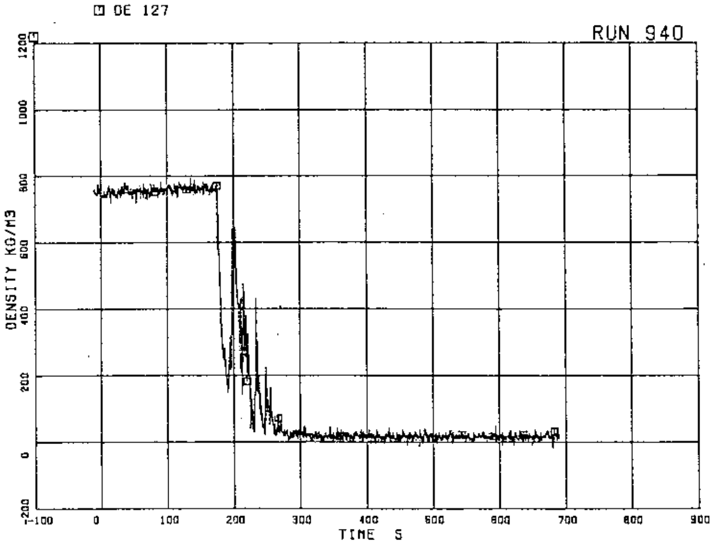

Fig.A.45 Fluid density at MRP-side of break, beam B

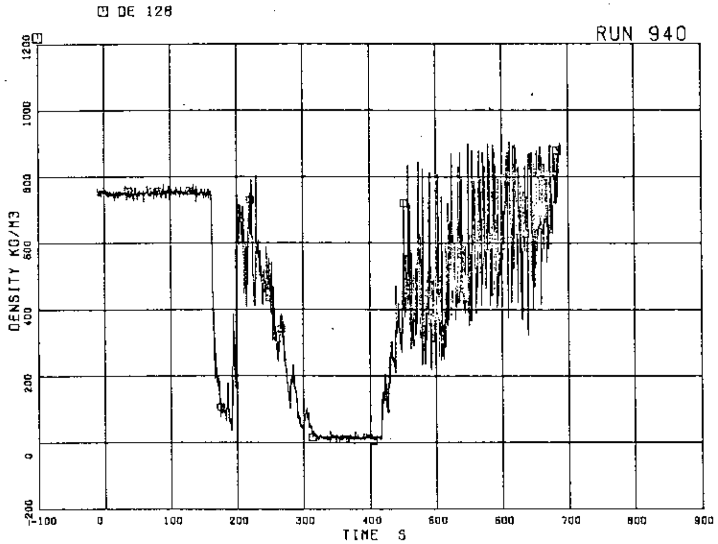

Fig.A.46 Fluid density at PV side of break, beam A

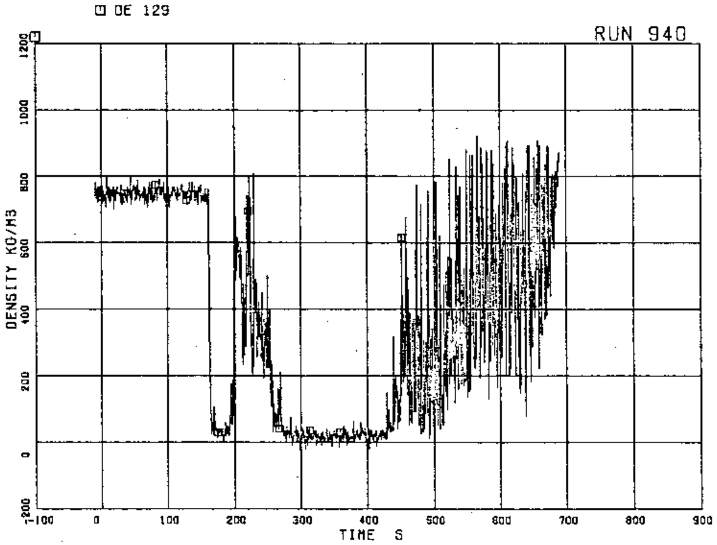

Fig.A.47 Fluid density at PV side of break, beam B

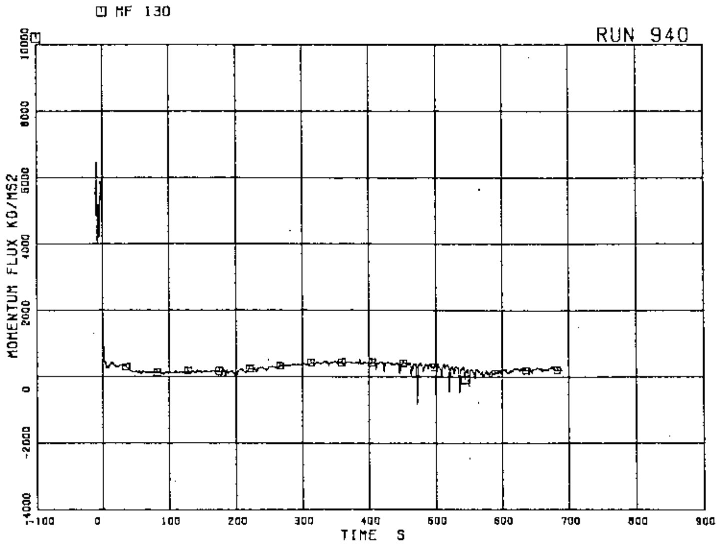

Fig.A.48 Momentum flux at JP 1,2 outlet spool

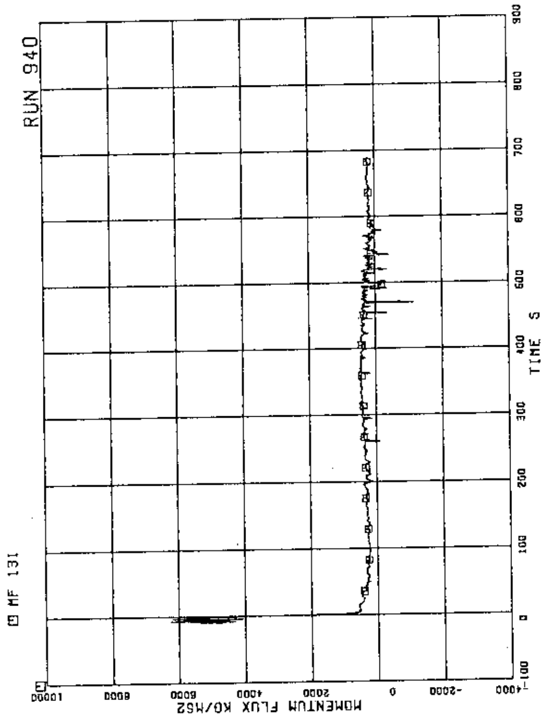

Fig.A.49 Momentum flux at JP 3,4 outlet spool

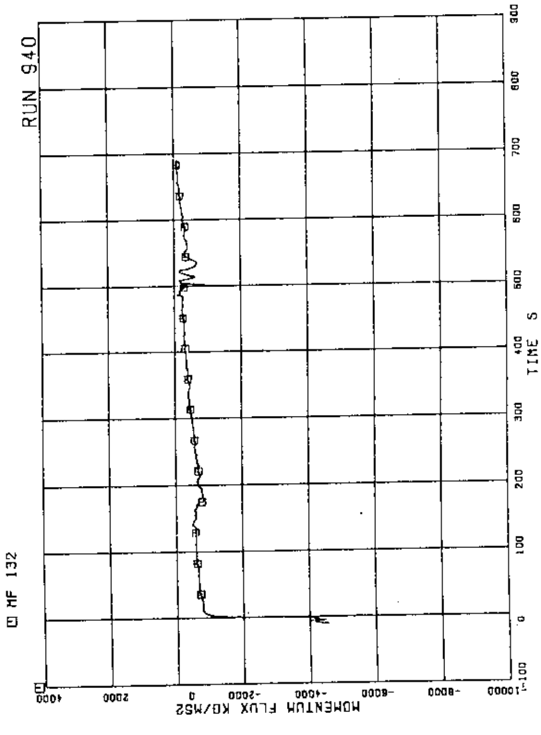

Fig.A.50 Momentum flux at break A spool piece (low range)

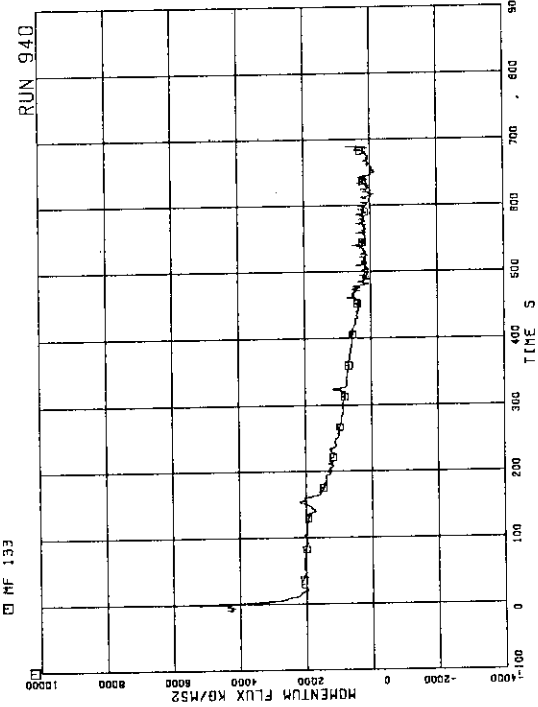

Fig.A.51 Momentum flux at break B spool piece (low range)

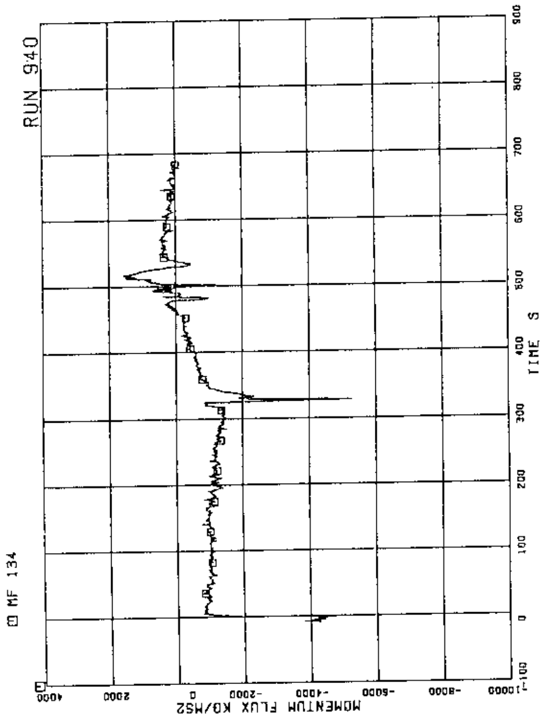

Fig.A.52 Momentum flux at break A spool piece (high range)

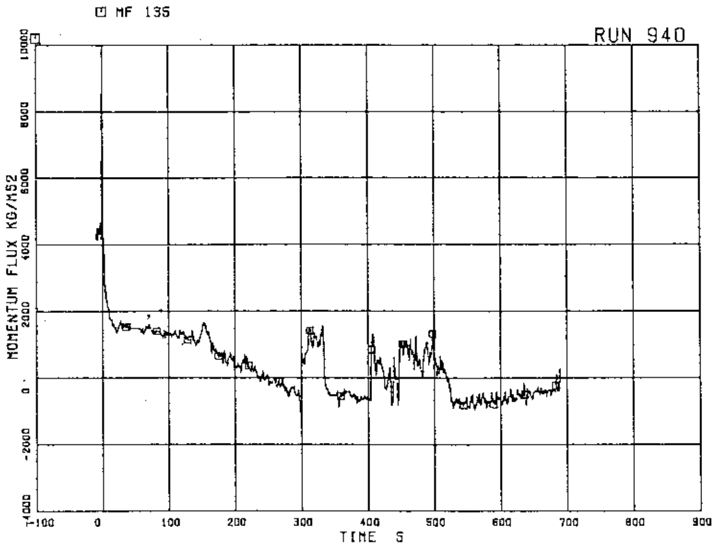

Fig.A.53 Momentum flux at break B spool piece (high range)

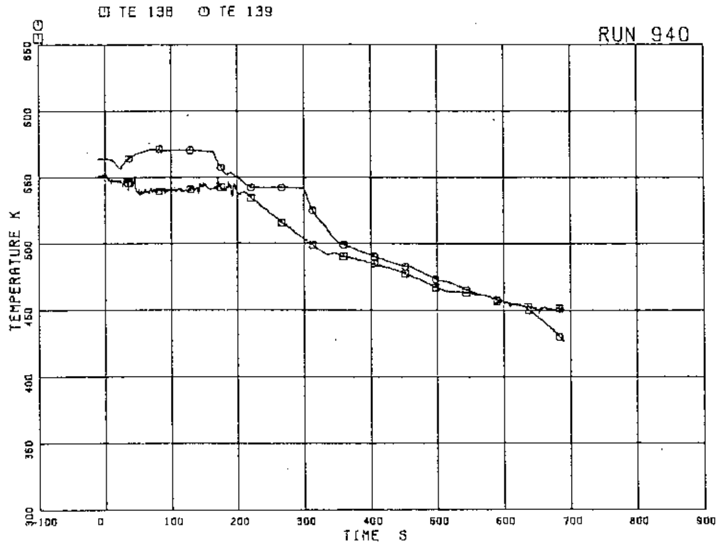

Fig.A.54 Fluid temperatures in lower plenum and upper plenum

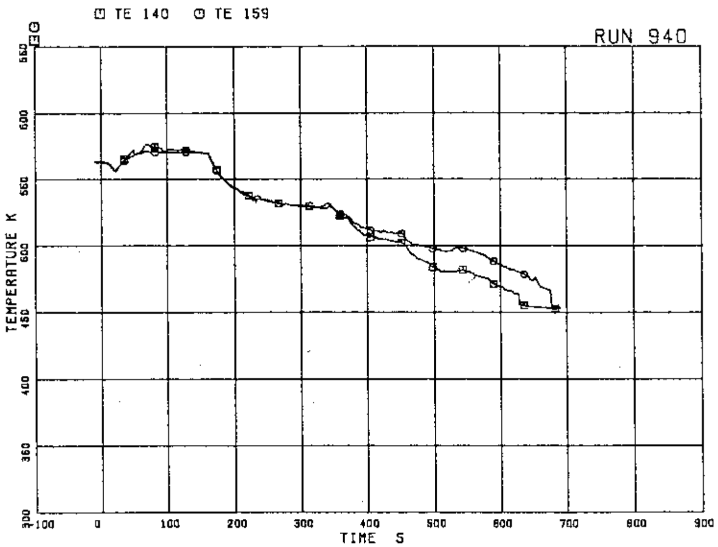

Fig.A.55 Fluid temperatures in steam dome and MSL

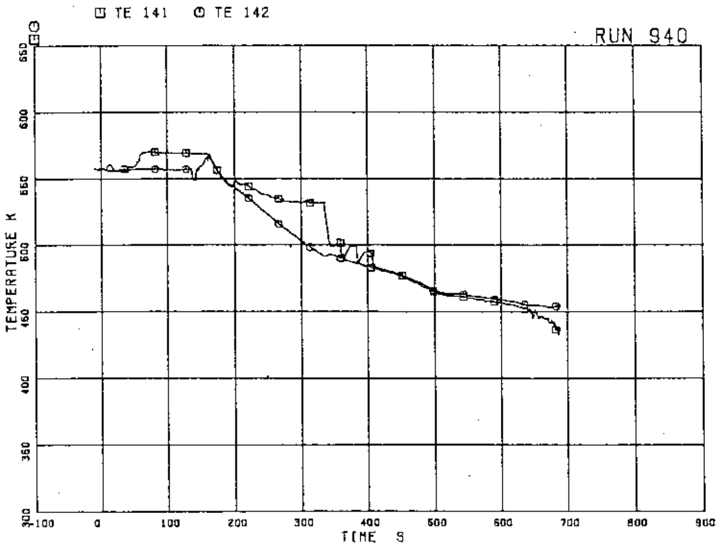

Fig.A.56 Fluid temperatures in downcomer

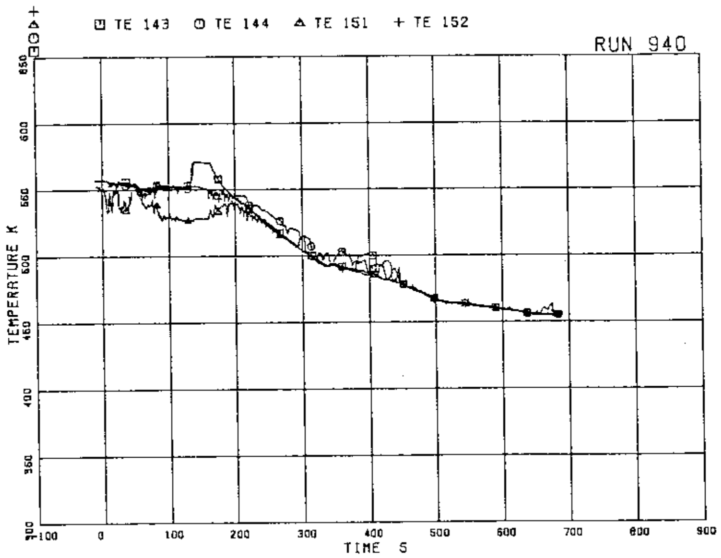

Fig.A.57 Fluid temperatures in intact recirculation loop

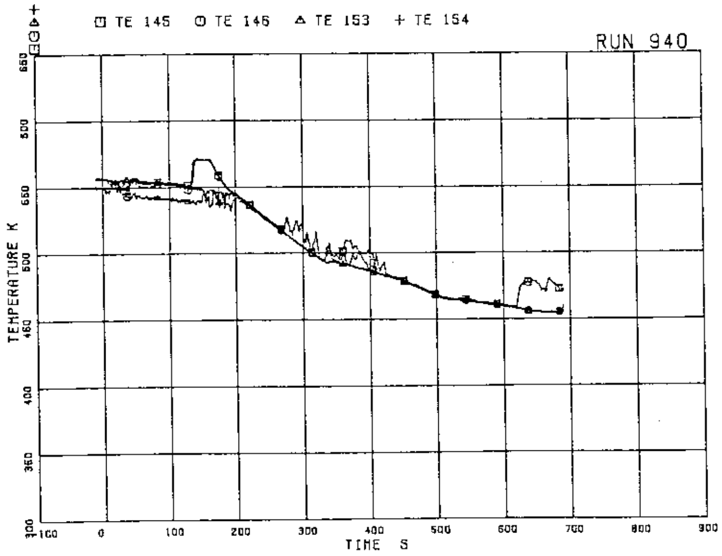

Fig.A.58 Fluid temperatures in broken recirculation loop

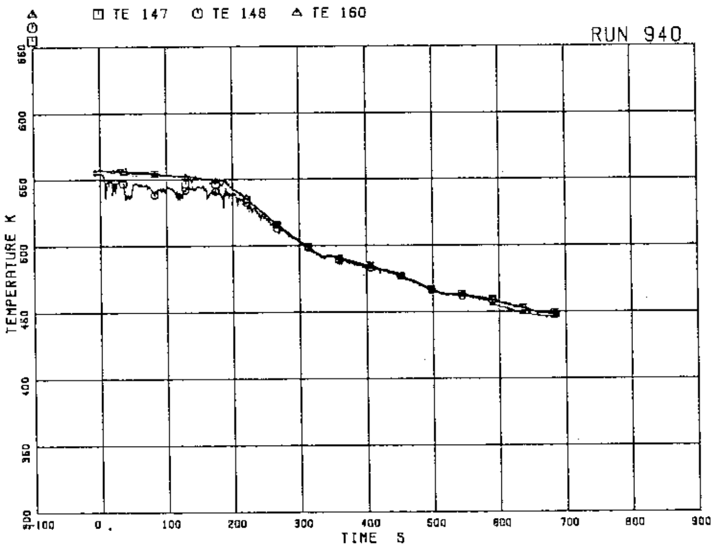

Fig.A.59 Fluid temperatures at JP 1,2 outlet

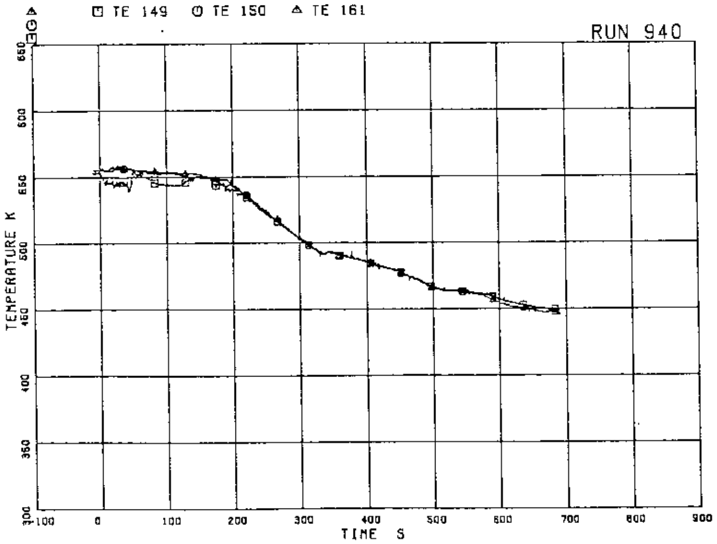

Fig.A.60 Fluid temperatures at JP 3,4 outlet

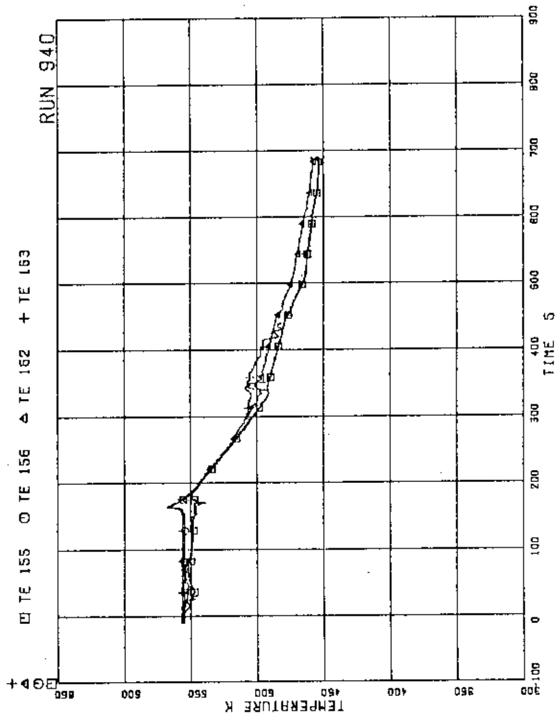

Fig.A.61 Fluid temperatures near breaks A and B

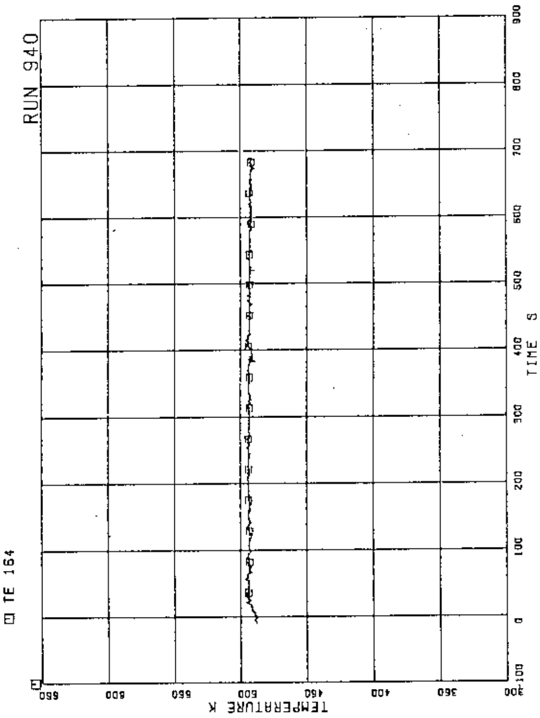

Fig.A.62 Feedwater temperature

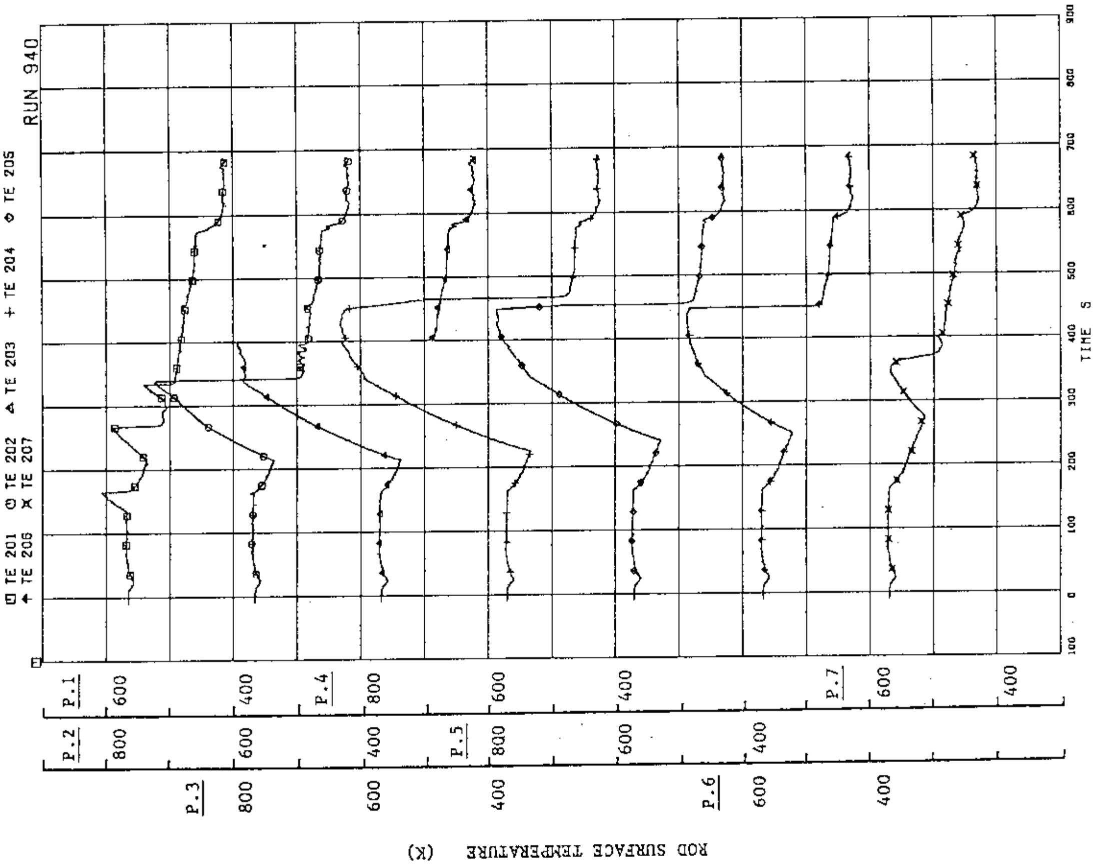

Fig.A.63 Surface temperatures of fuel rod A11

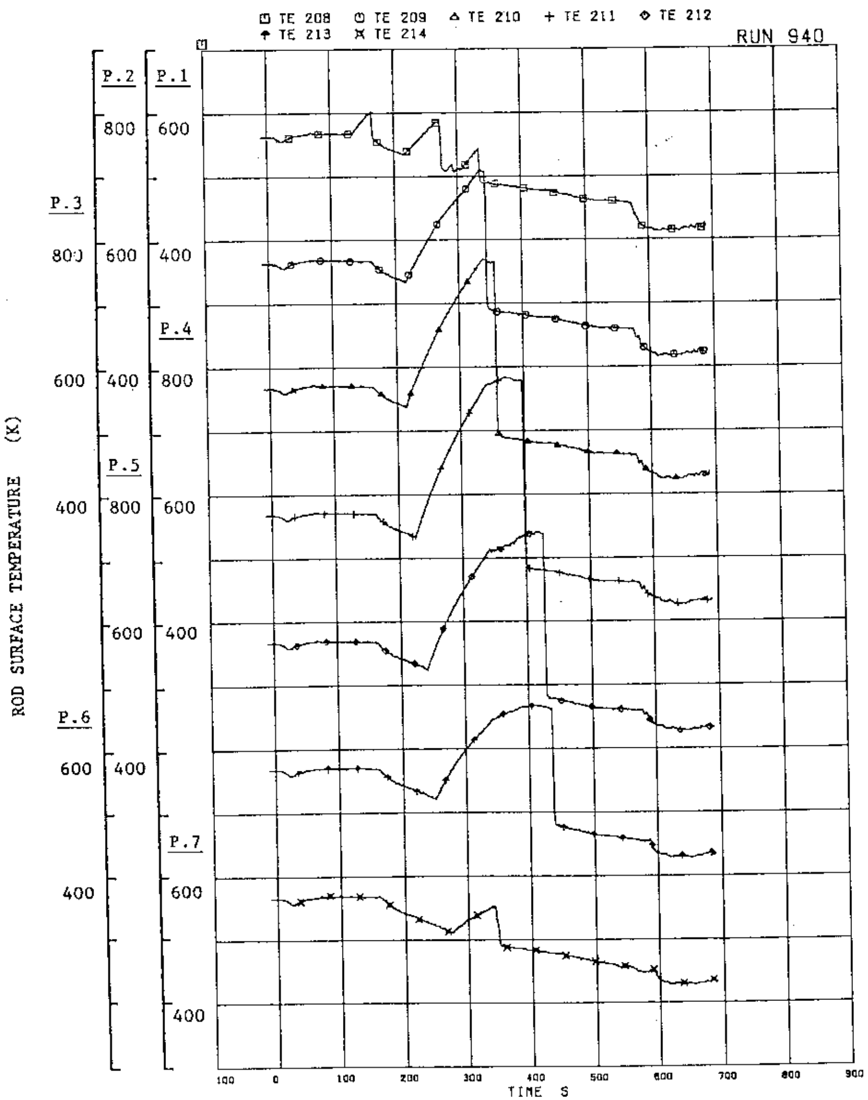

Fig.A.64 Surface temperatures of fuel rod A12

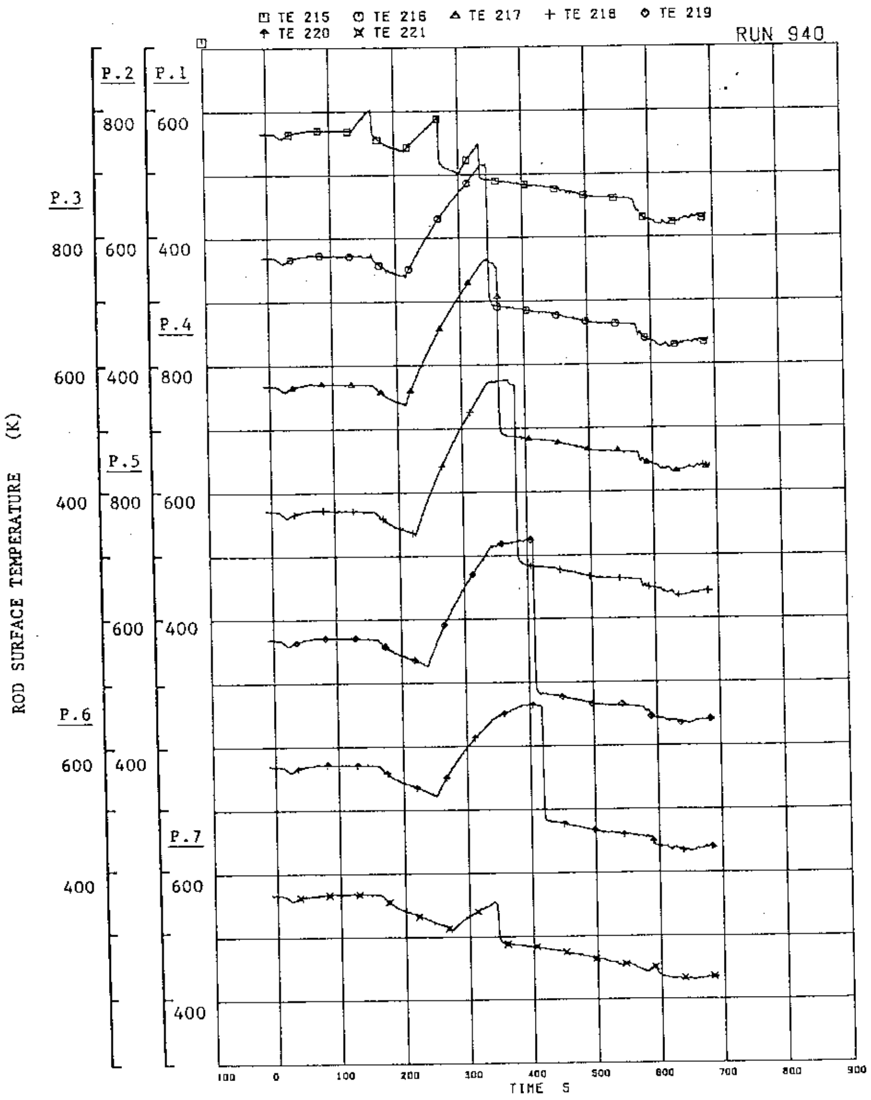

Fig.A.65 Surface temperatures of fuel rod A13

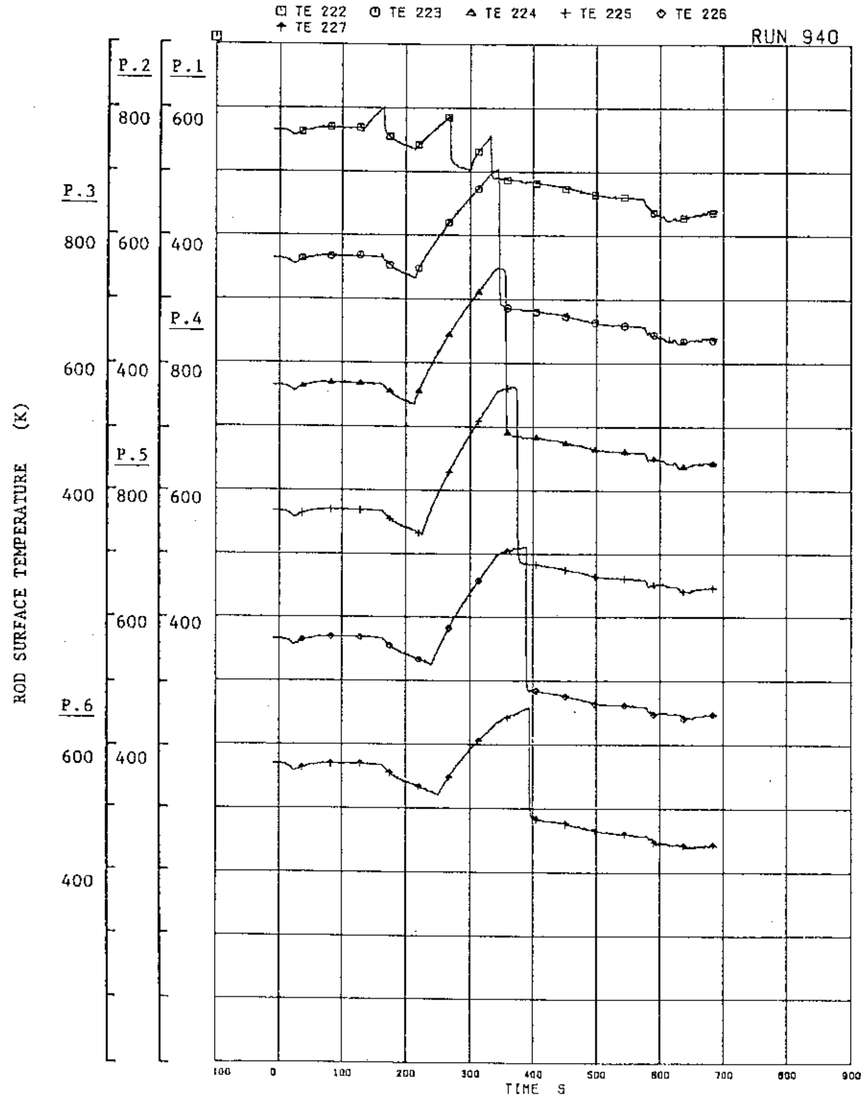

Fig.A.66 Surface temperatures of fuel rod A14

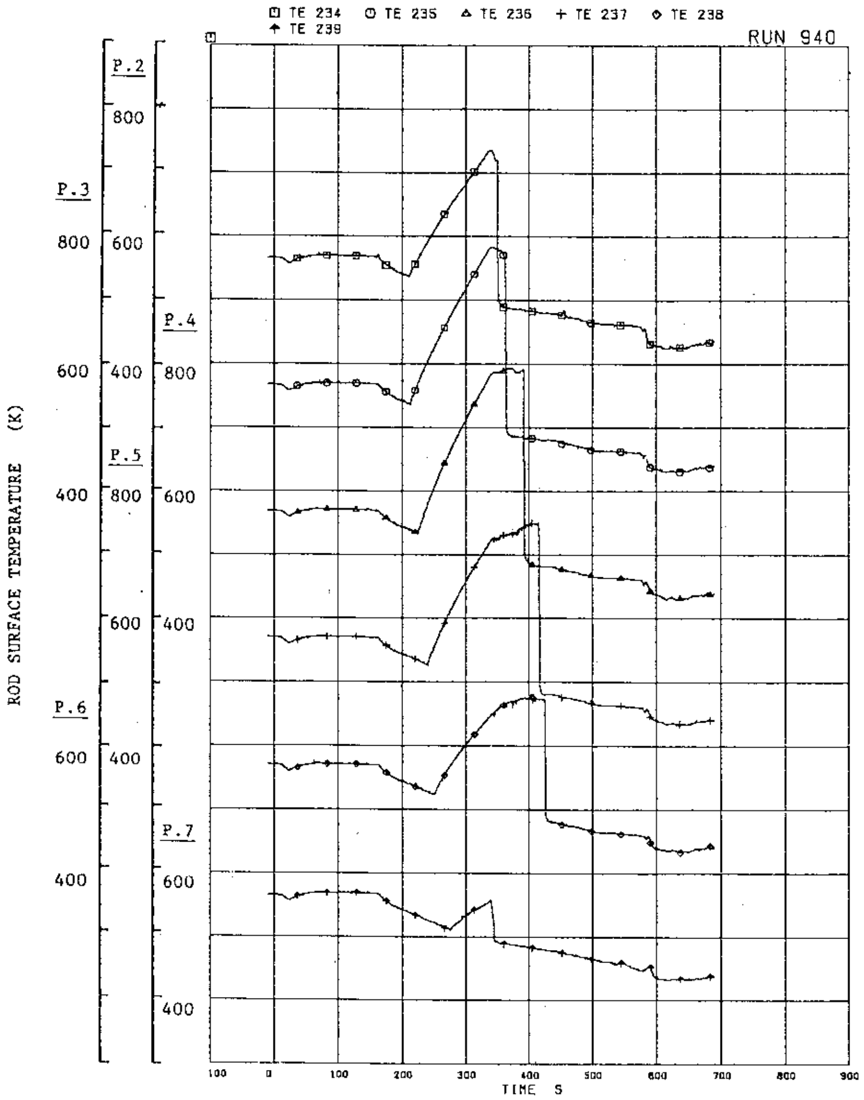

Fig.A.67 Surface temperatures of fuel rod A22

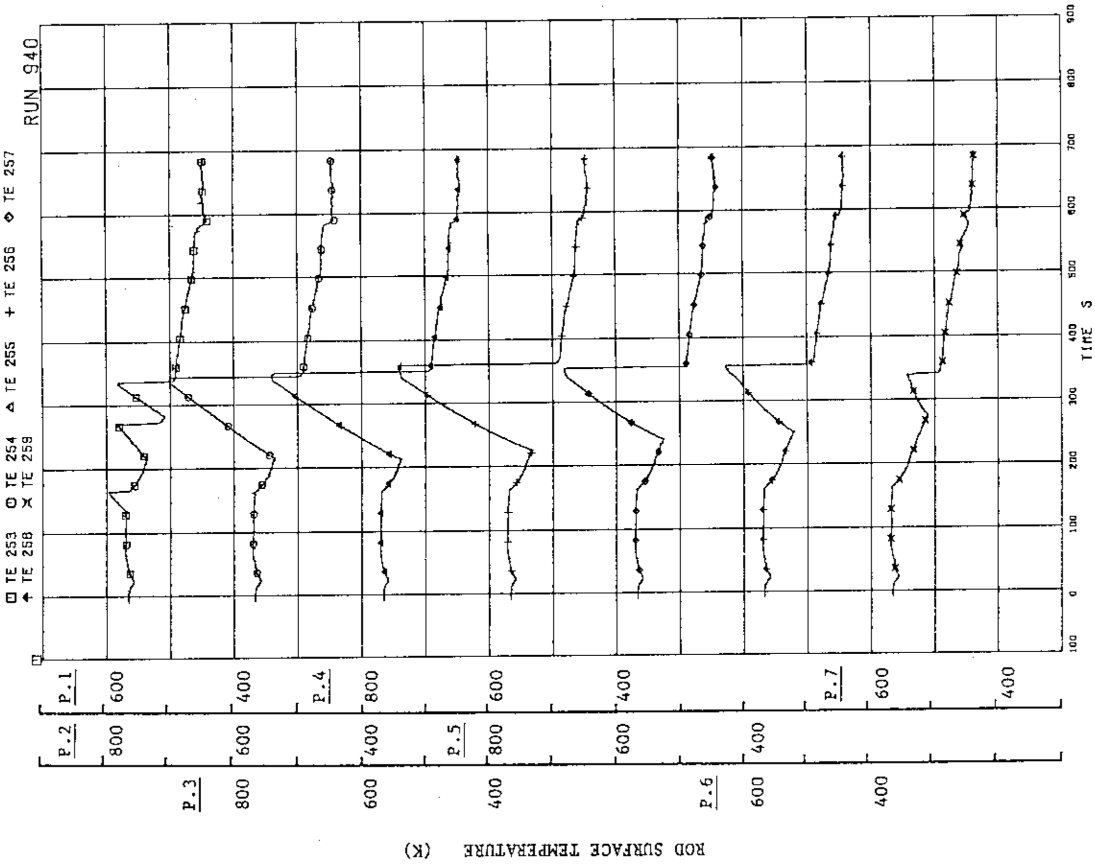

Fig.A.69 Surface temperatures of fuel rod A33

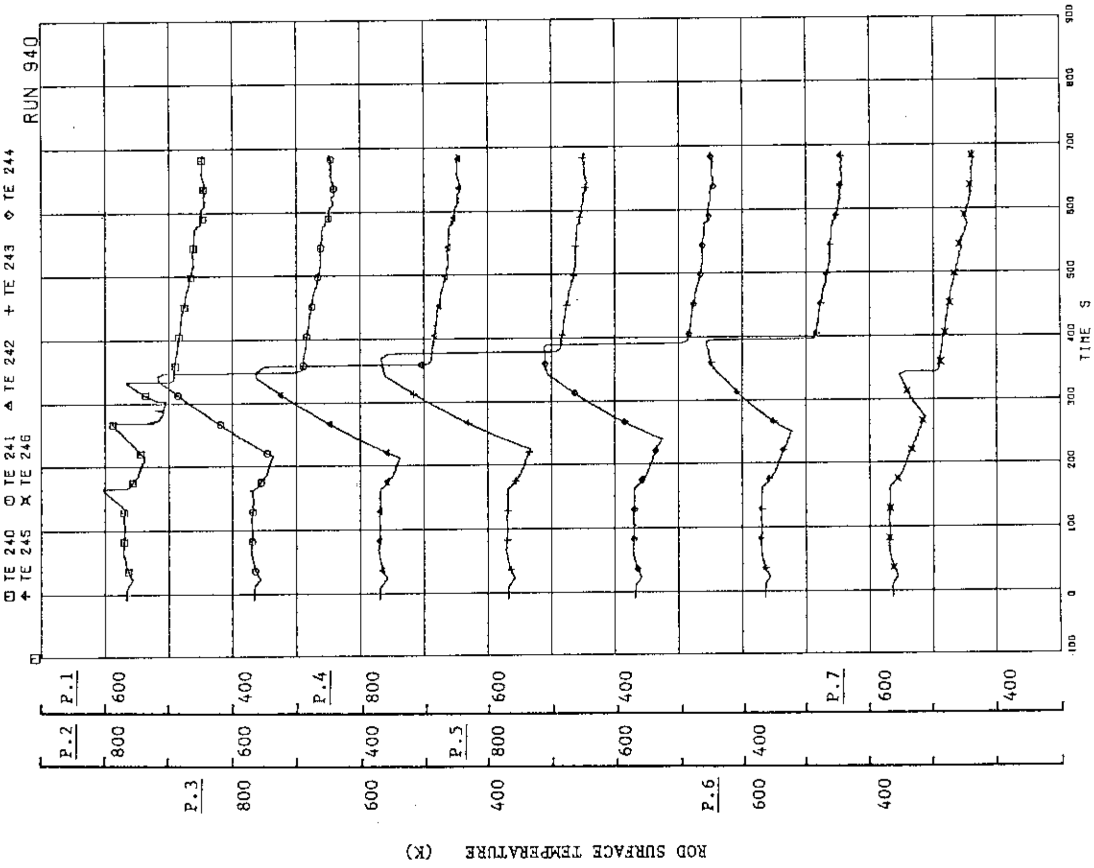

Fig.A.68 Surface temperatures of fuel rod A24

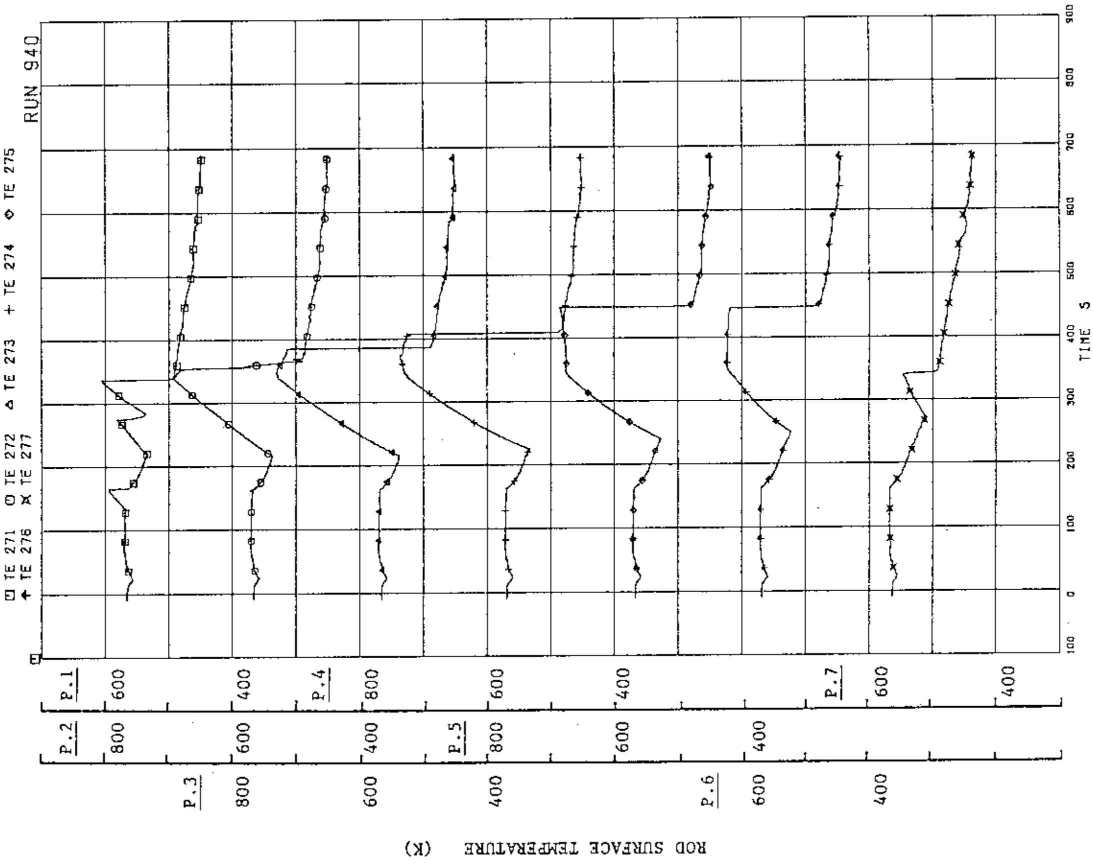

Fig.A.71 Surface temperatures of fuel rod A44

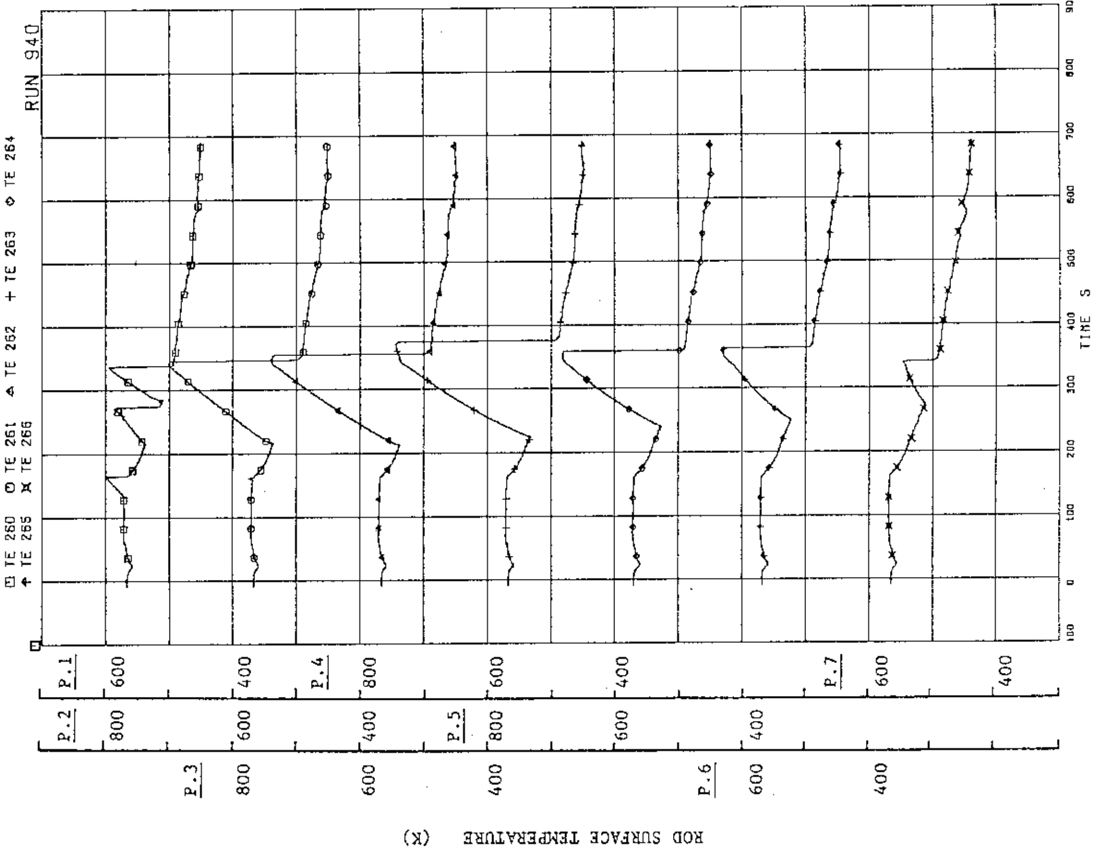

Fig.A.70 Surface temperatures of fuel rod A34

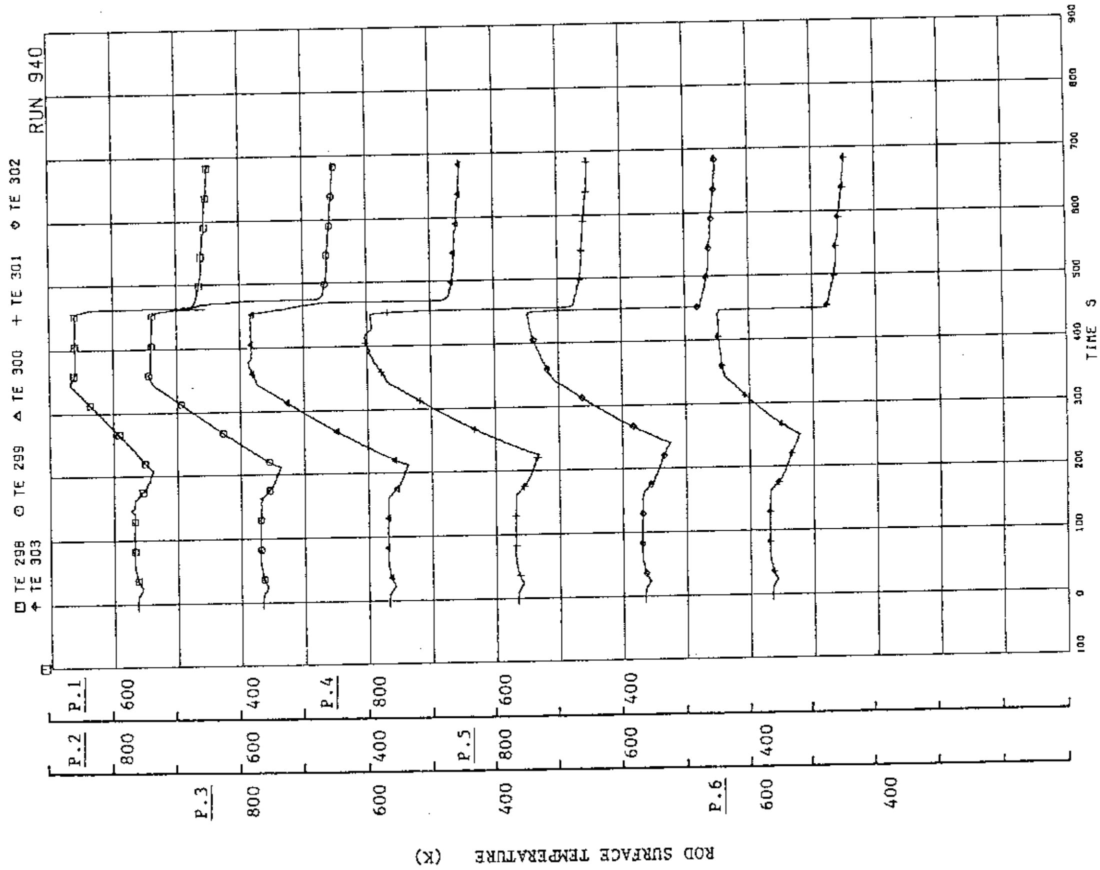

Fig.A.72 Surface temperatures of fuel rod A77

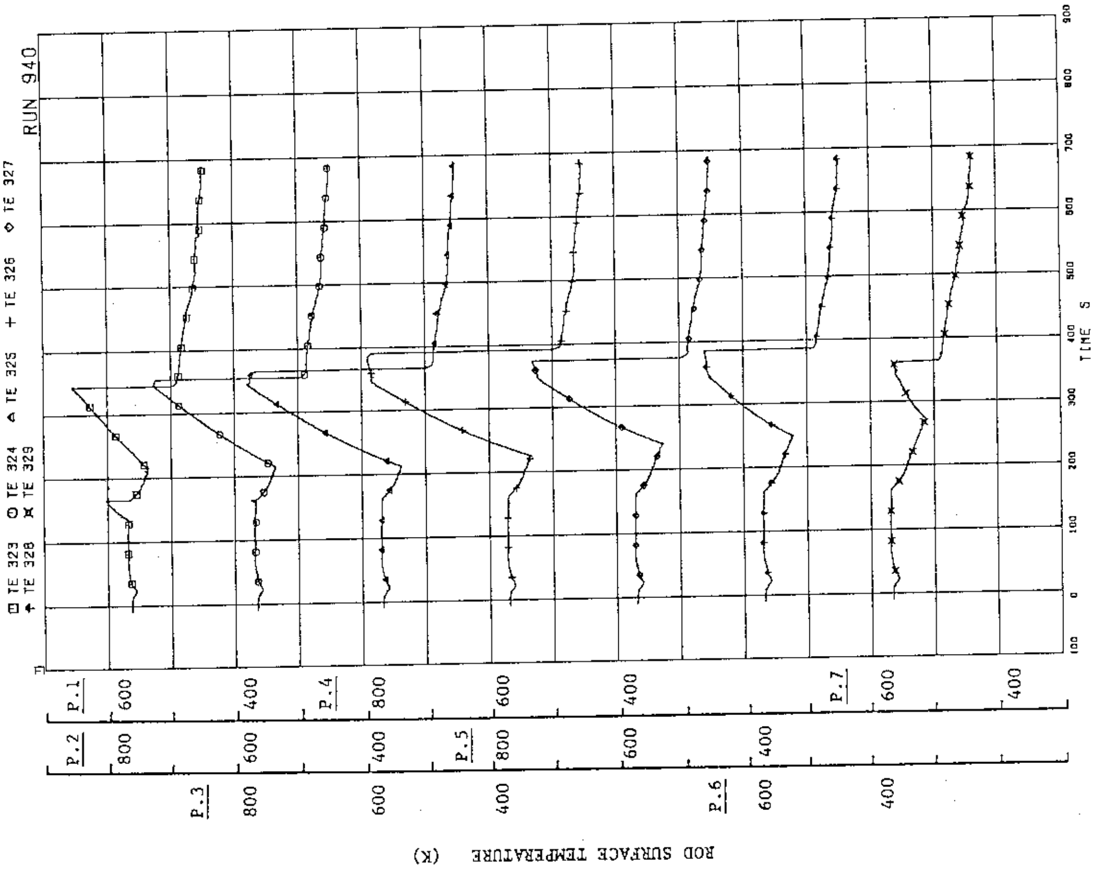

Fig.A.73 Surface temperatures of fuel rod A88

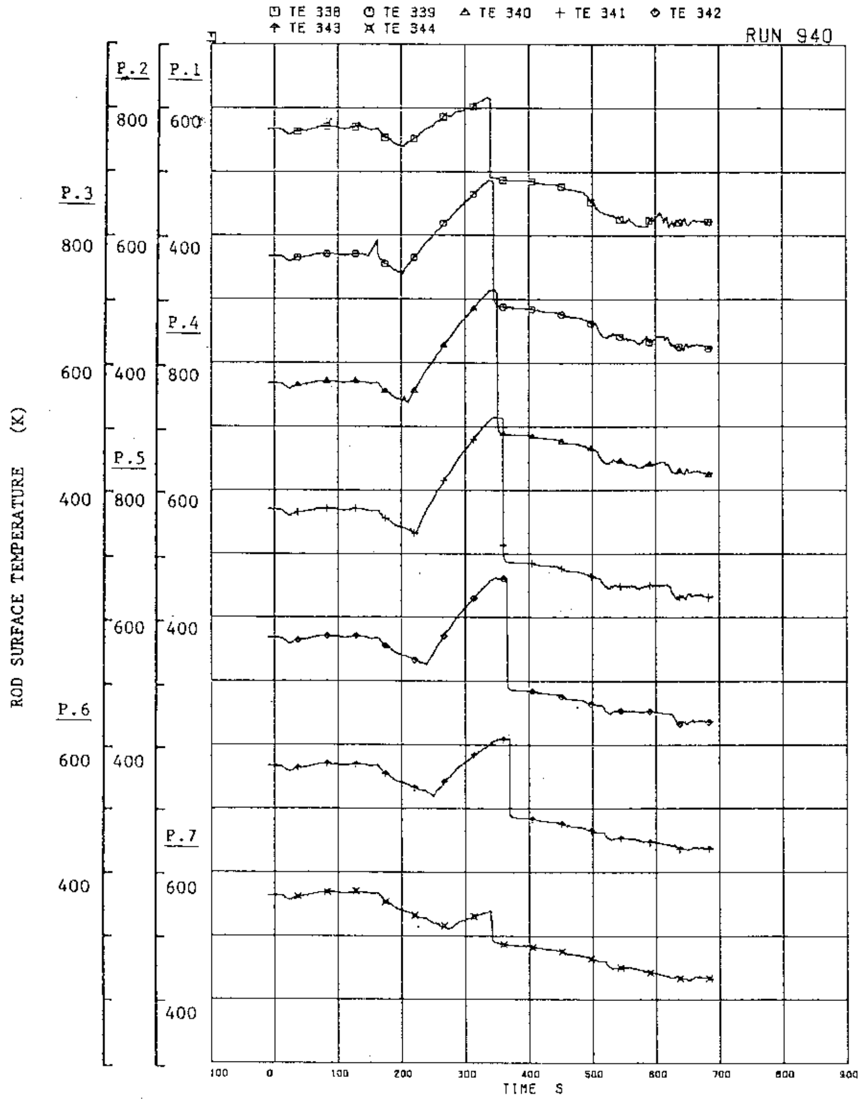

Fig.A.74 Surface temperatures of fuel rod B22

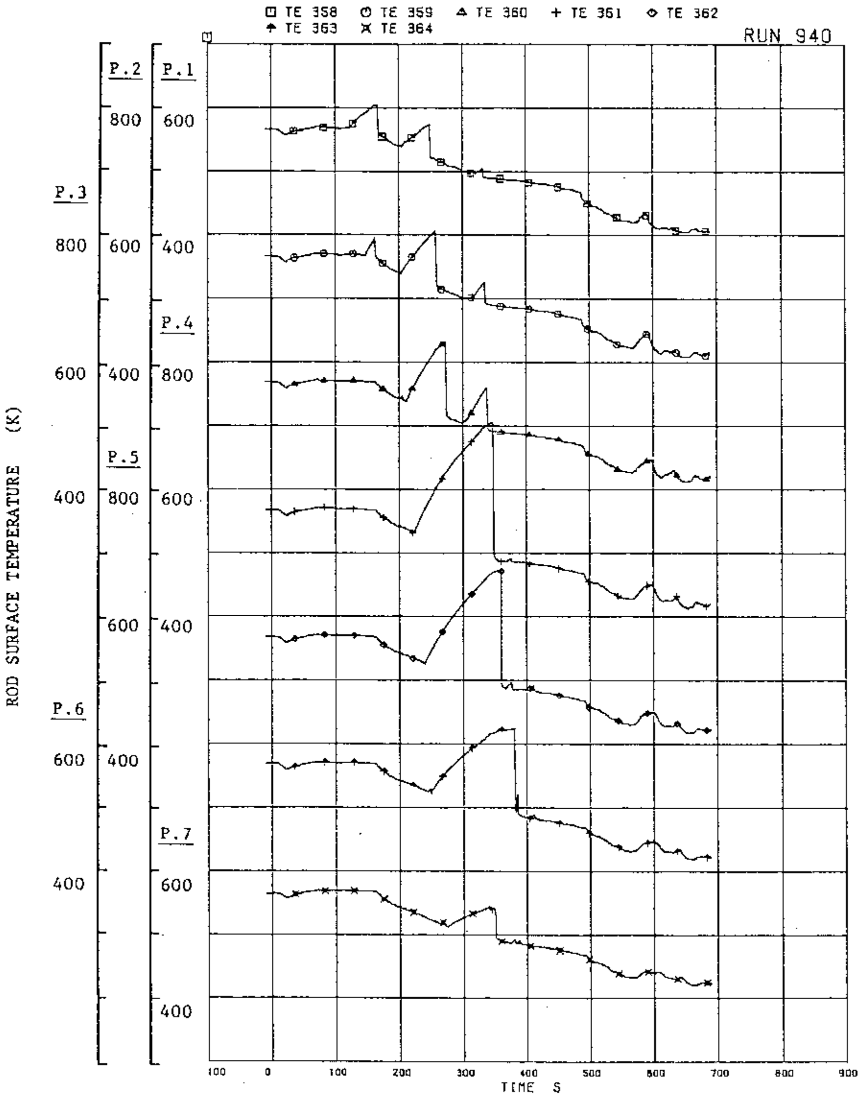

Fig.A.75 Surface temperatures of fuel rod C11

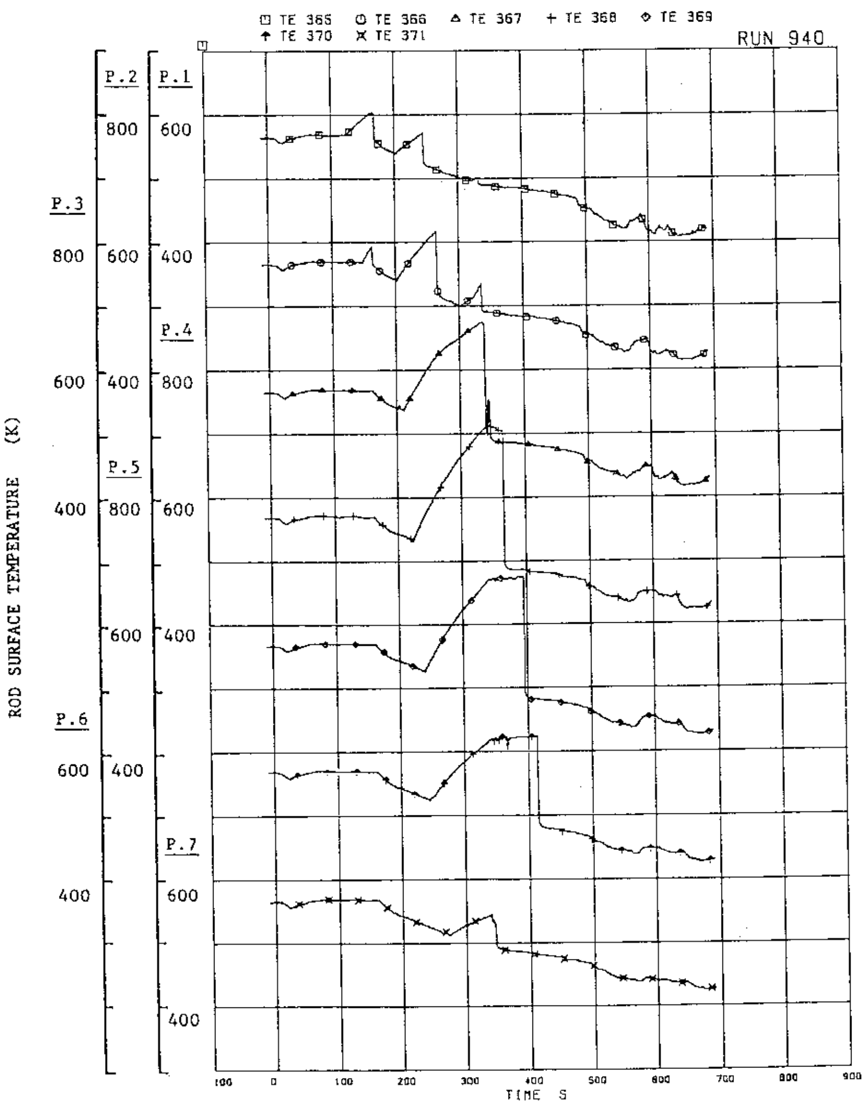

Fig.A.76 Surface temperatures of fuel rod C13

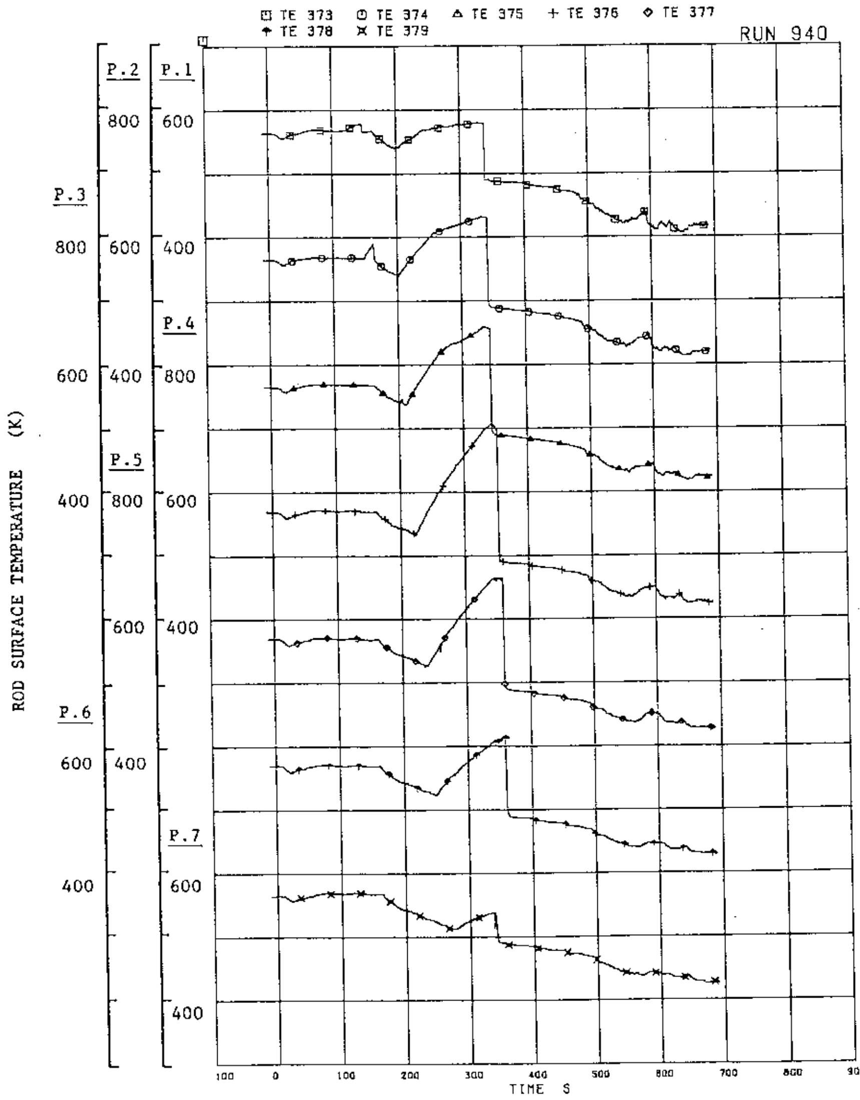

Fig.A.77 Surface temperatures of fuel rod C22

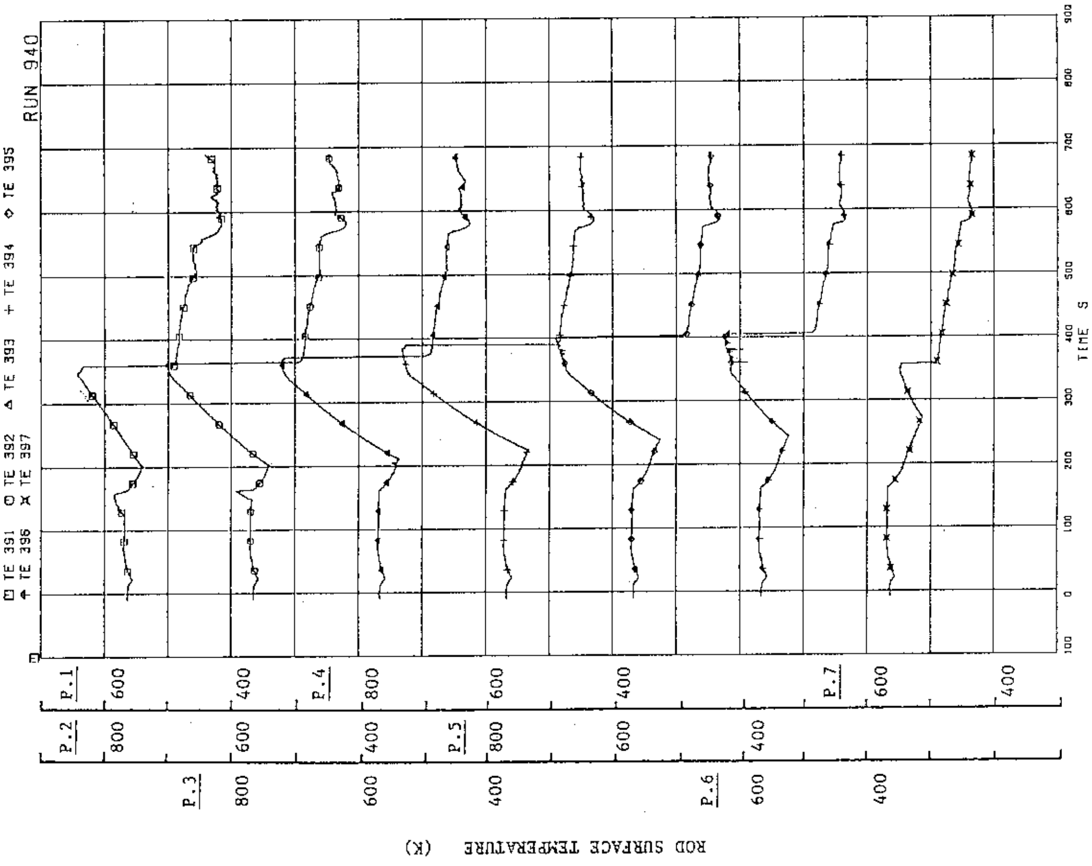

Fig.A.79 Surface temperatures of fuel rod C77

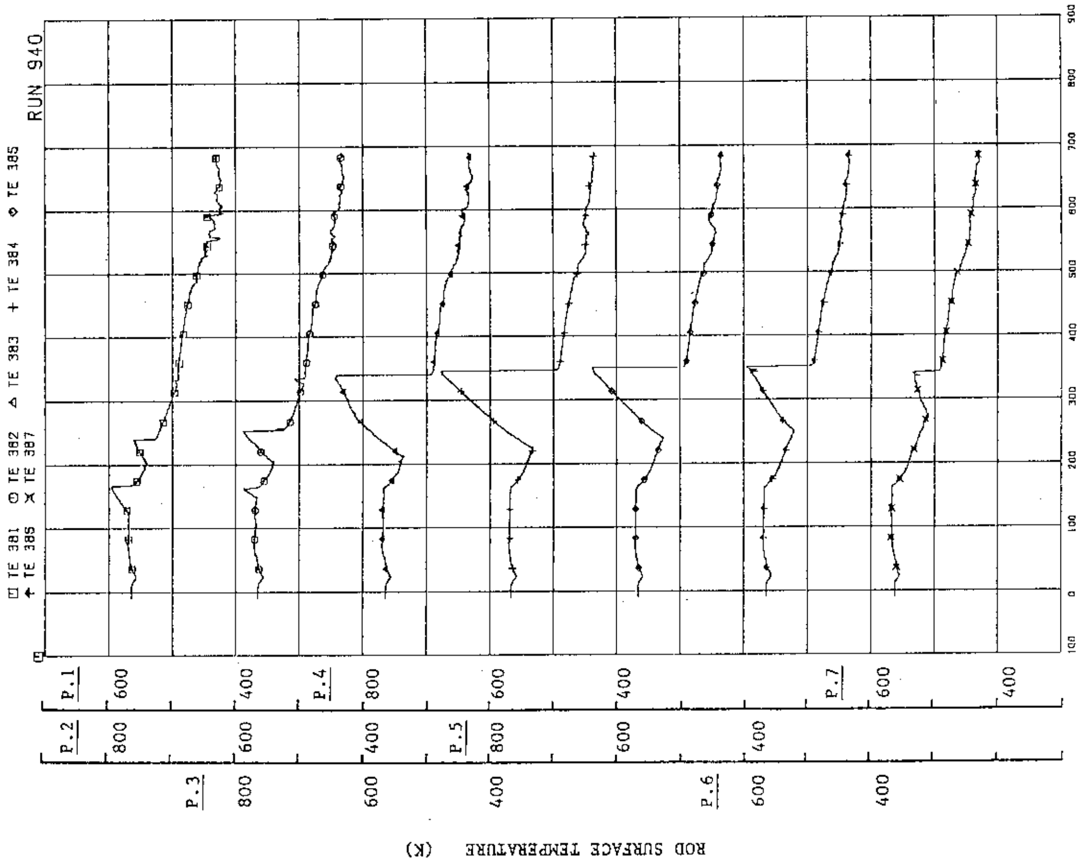

Fig.A.78 Surface temperatures of fuel rod C33

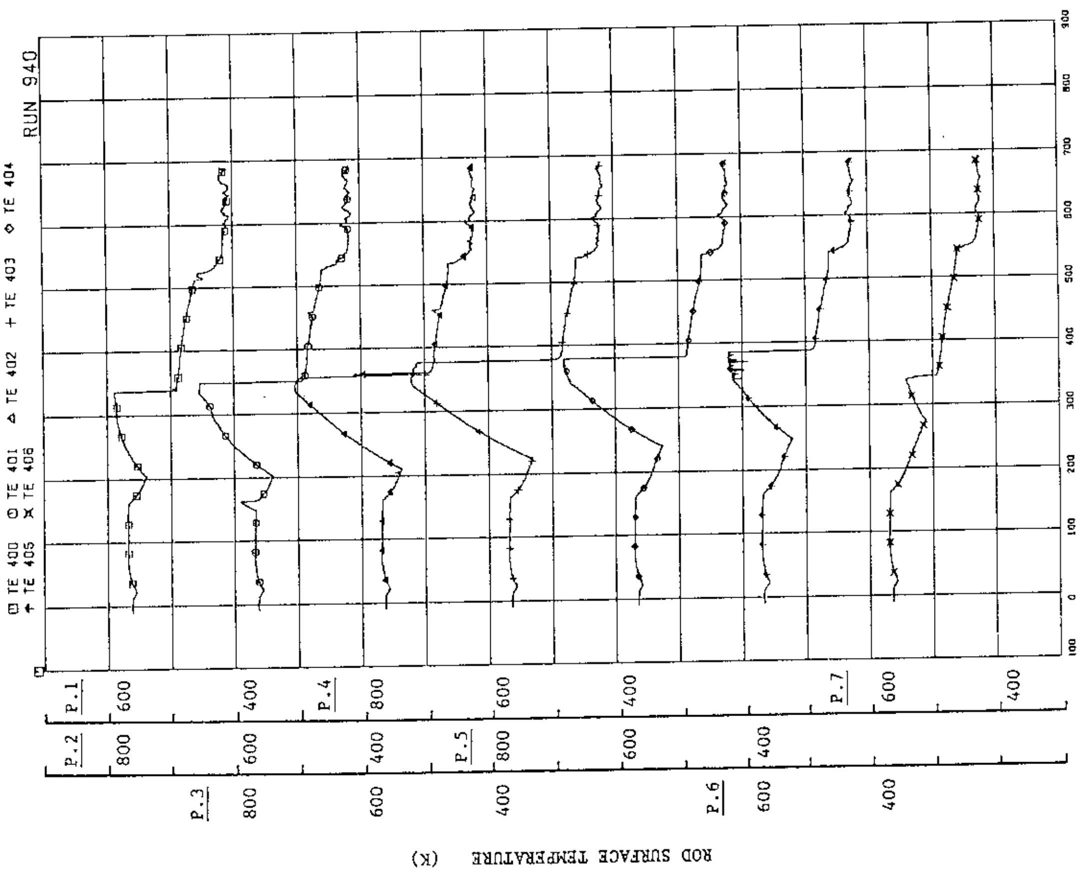

Fig.A.80 Surface temperatures of fuel rod D22

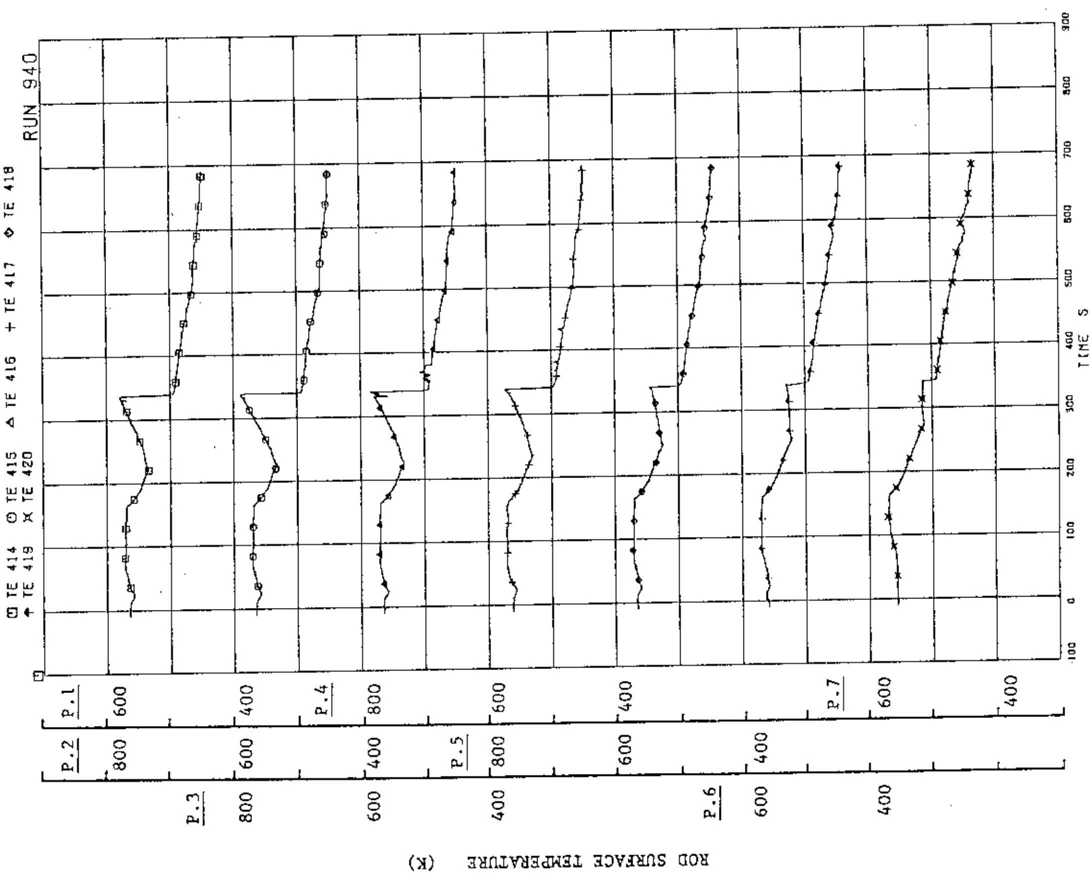

Fig.A.81 Surface temperatures of water rod simulator A45

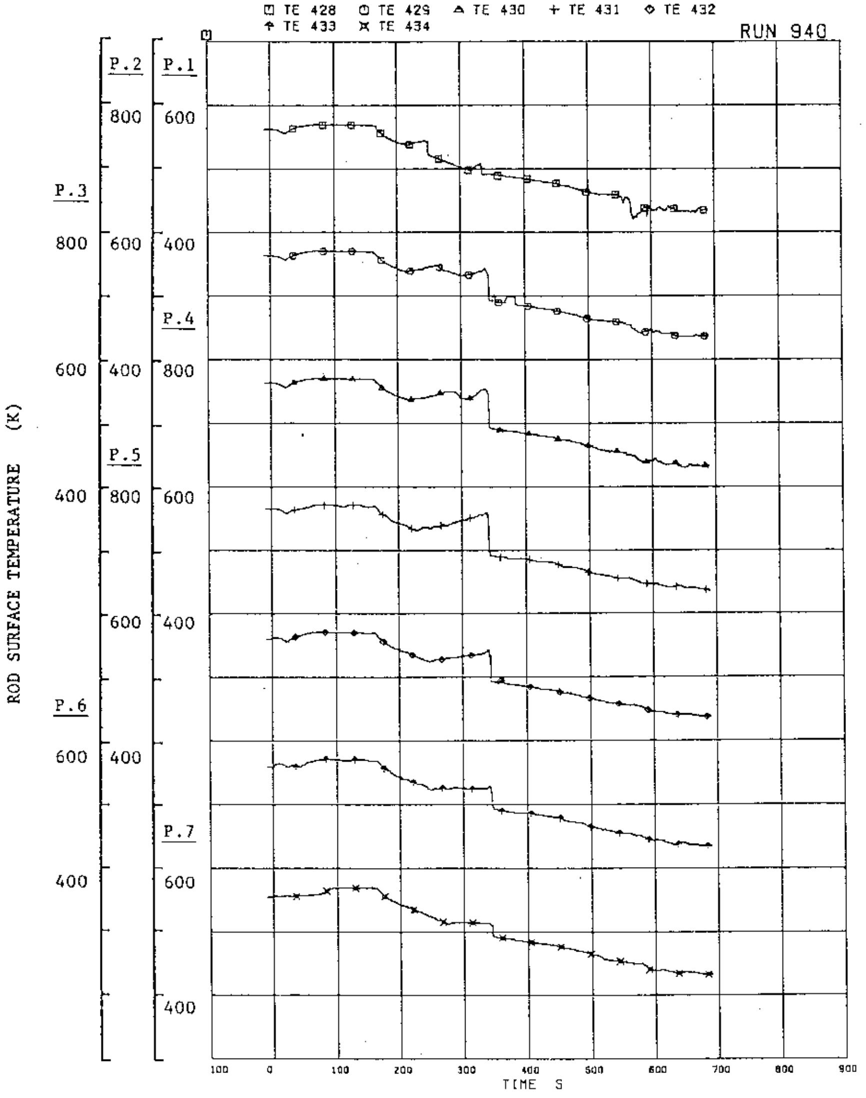

Fig.A.82 Surface temperatures of water rod simulator C45

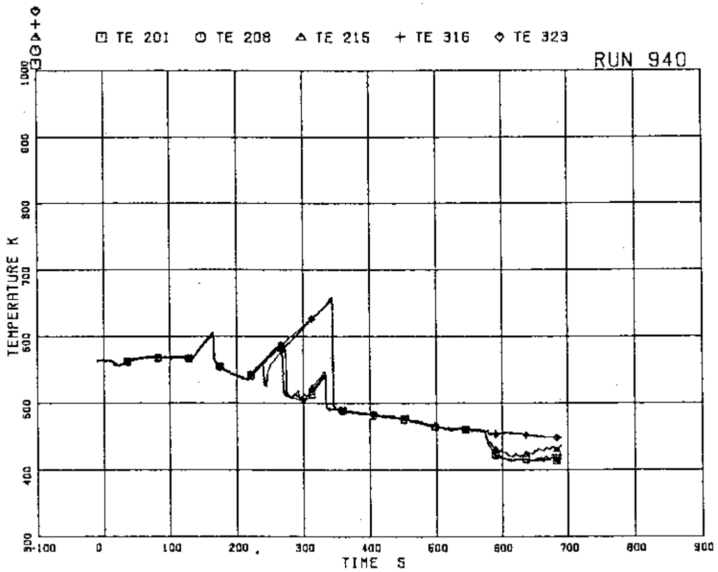

Fig.A.83 Surface temperatures of fuel rods A11, A12, A13, A87 and A88 at position 1

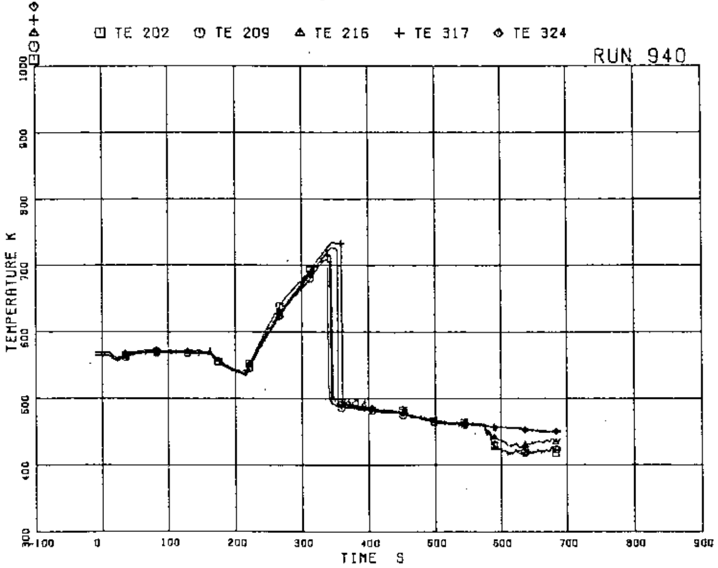

Fig.A.84 Surface temperatures of fuel rods A11, A12, A13, A87 and A88 at position 2

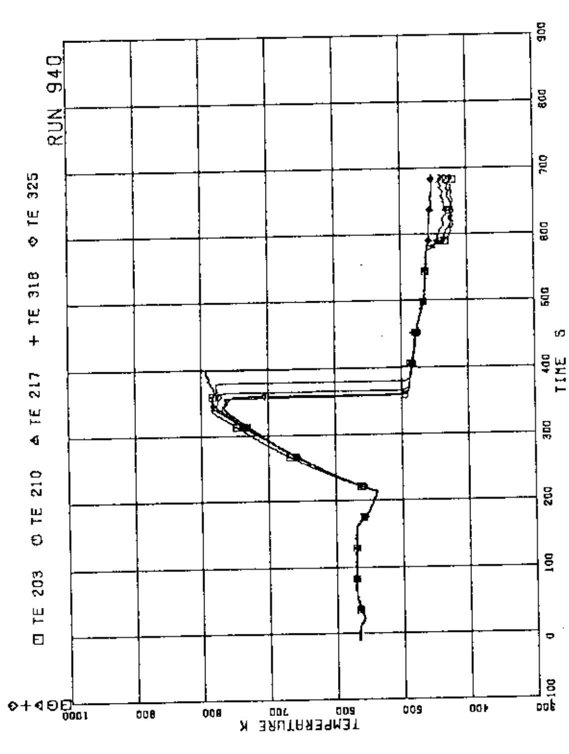

Fig.A.85 Surface temperatures of fuel rods A11, A12, A13, A87 and A88 at position 3

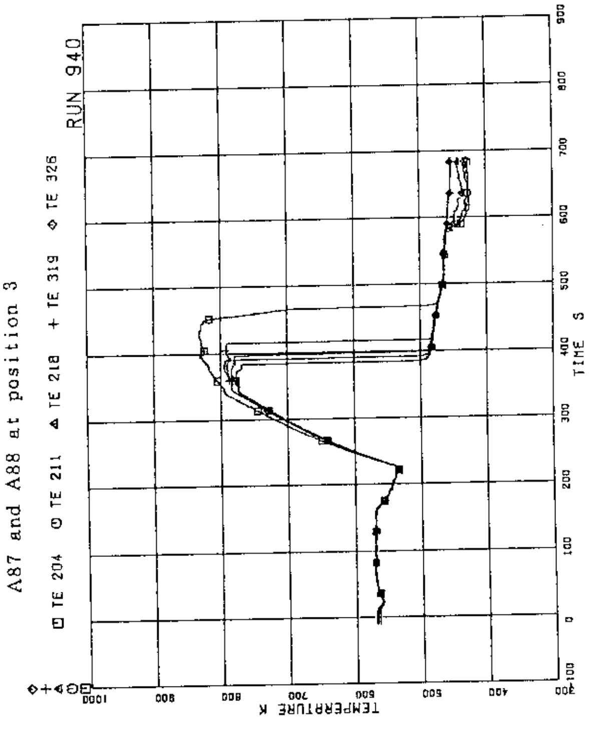

Fig.A.86 Surface temperatures of fuel rods A11, A12, A13, A87 and A88 at position 4

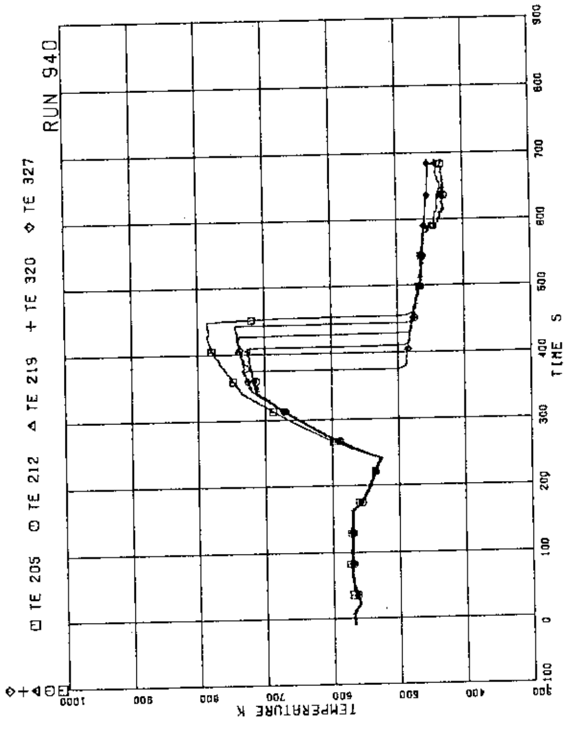

Fig.A.87 Surface temperatures of fuel rods A11, A12, A13, A87 and A88 at position 5

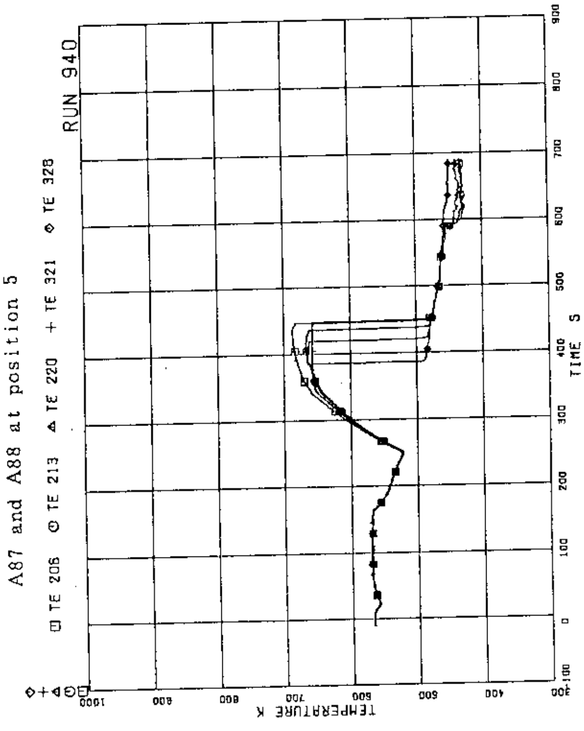

Fig.A.88 Surface temperatures of fuel rods A11, A12, A13, A87 and A88 at position 6

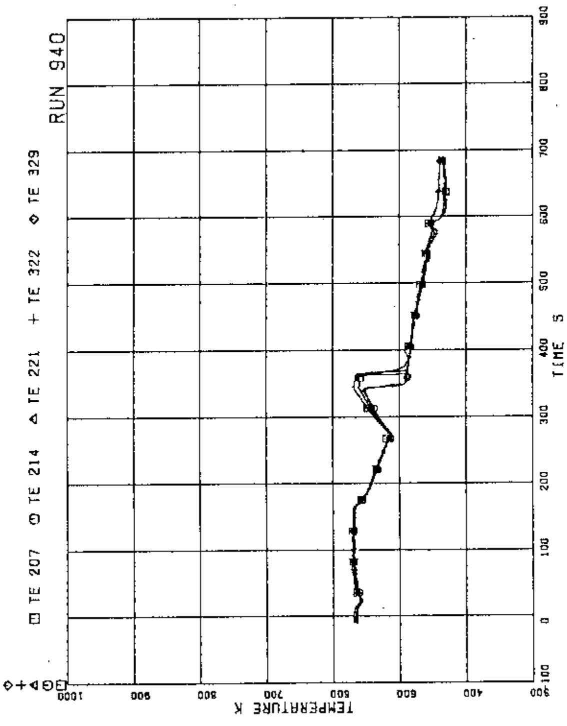

Fig.A.89 Surface temperatures of fuel rods A11, A12, A13, A87 and A88 at position 7

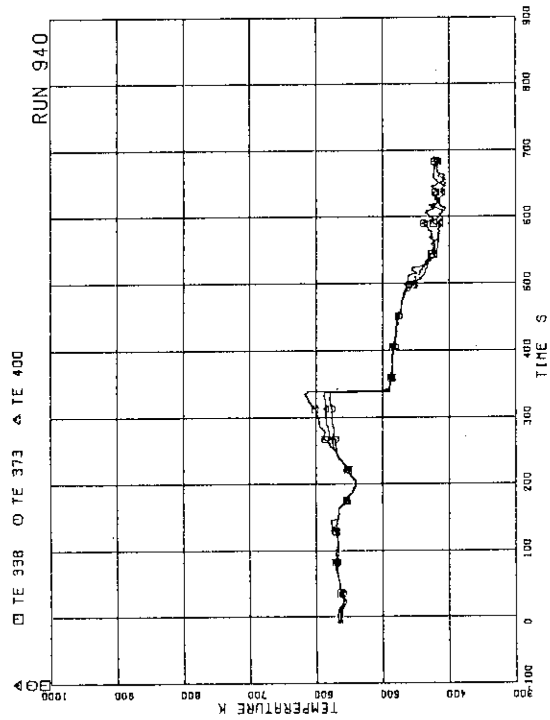

Fig.A.90 Surface temperatures of fuel rods B22, C22 and D22 at position 1

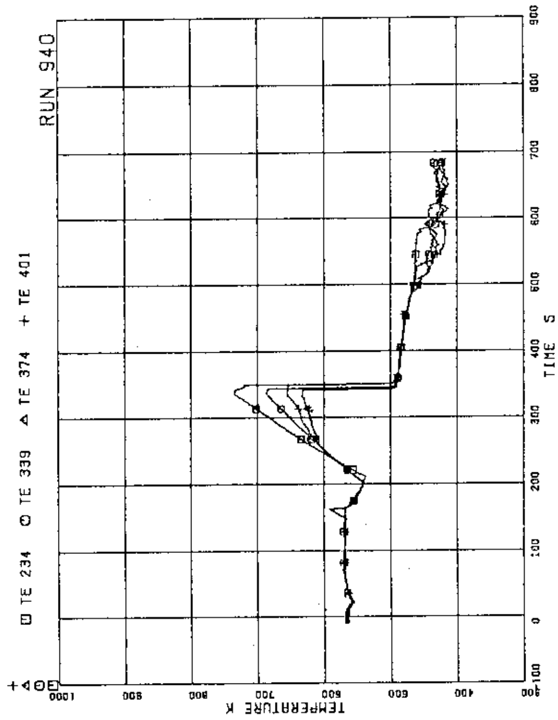

Fig.A.91 Surface temperatures of fuel rods A22, B22, C22 and D22 at position 2

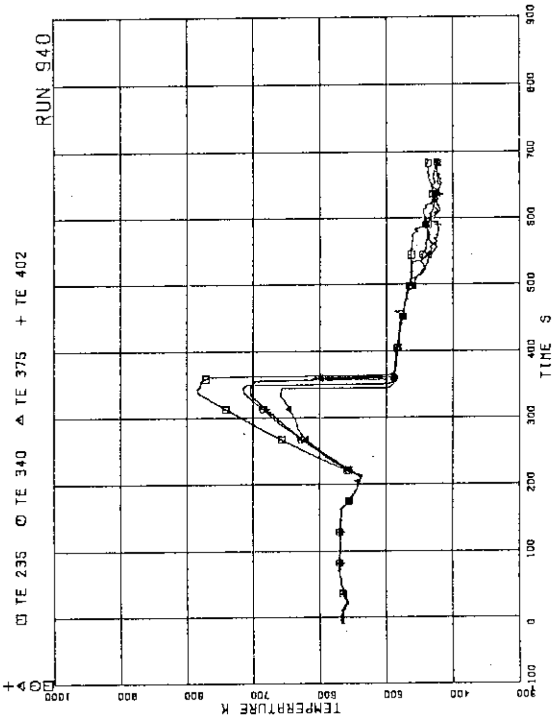

Fig.A.92 Surface temperatures of fuel rods A22, B22, C22 and D22 at position 3

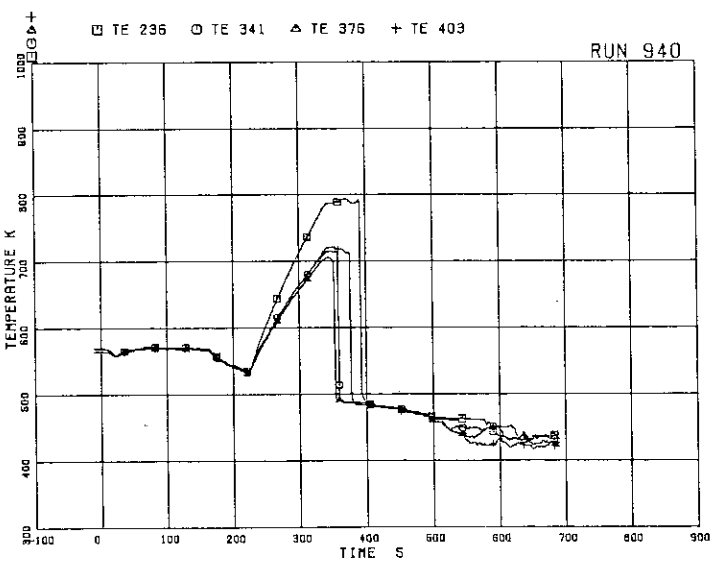

Fig.A.93 Surface temperatures of fuel rods A22, B22, C22 and D22 at position 4

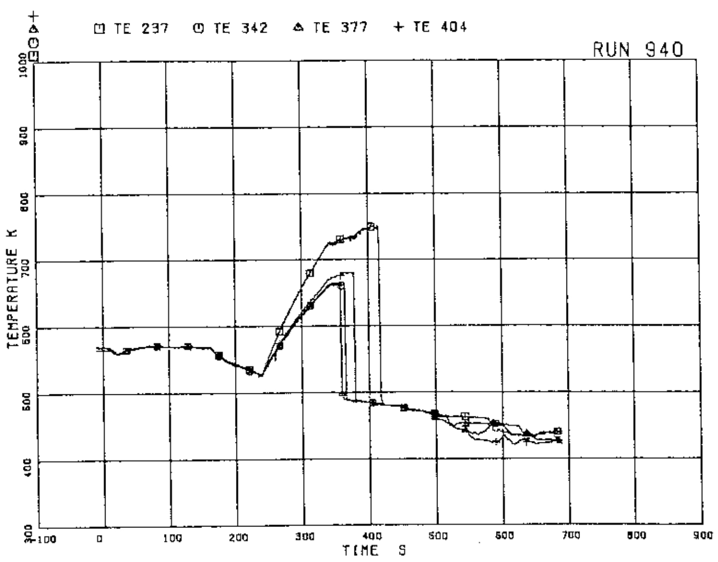

Fig.A.94 Surface temperatures of fuel rods A22, B22, C22 and D22 at position 5

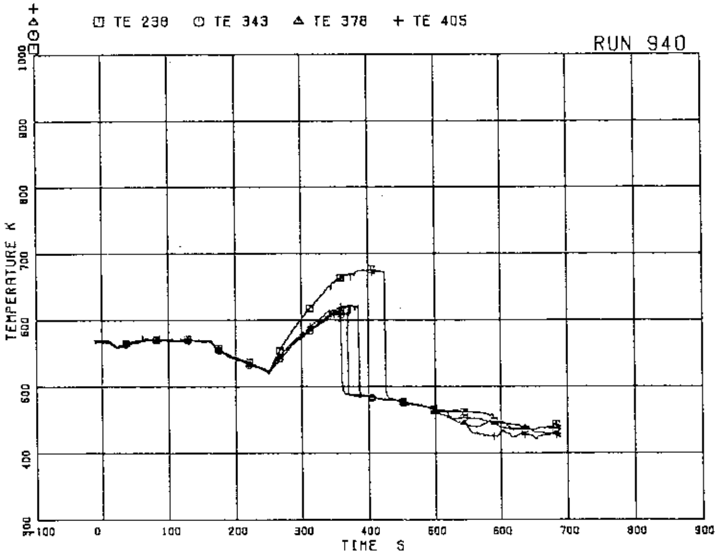

Fig.A.95 Surface temperatures of fuel rods A22, B22, C22 and D22 at position 6

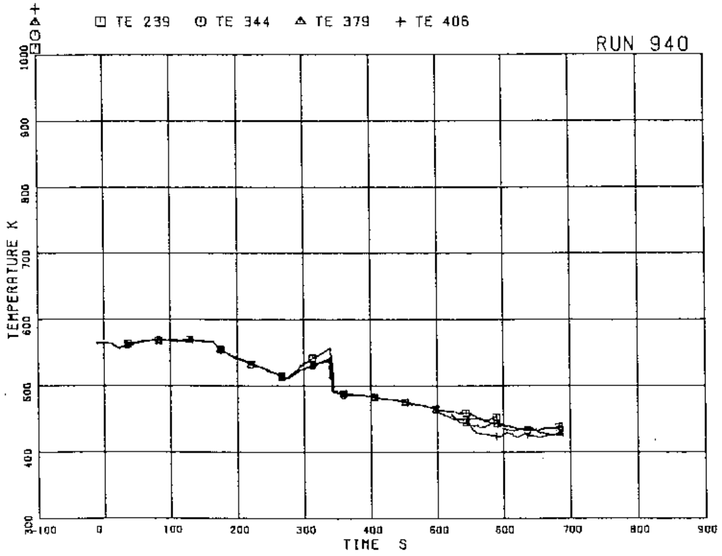

Fig.A.96 Surface temperatures of fuel rods A22, B22, C22 and D22 at position 7

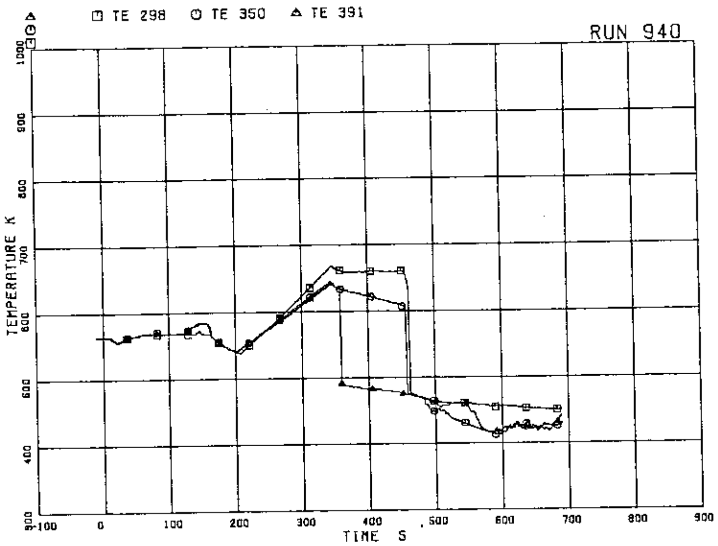

Fig.A.97 Surface temperatures of fuel rods A77, B77 and C77 at position 1

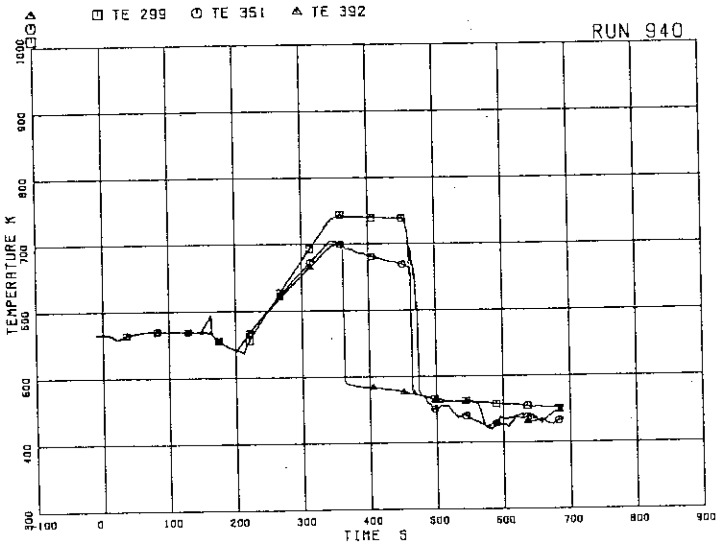

Fig.A.98 Surface temperatures of fuel rods A77, B77 and C77 at position 2

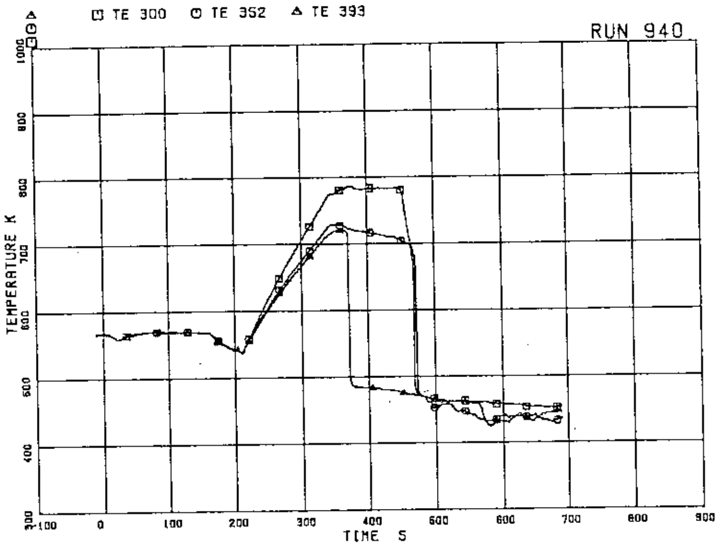

Fig.A.99 Surface temperatures of fuel rods A77, B77 and C77 at position 3

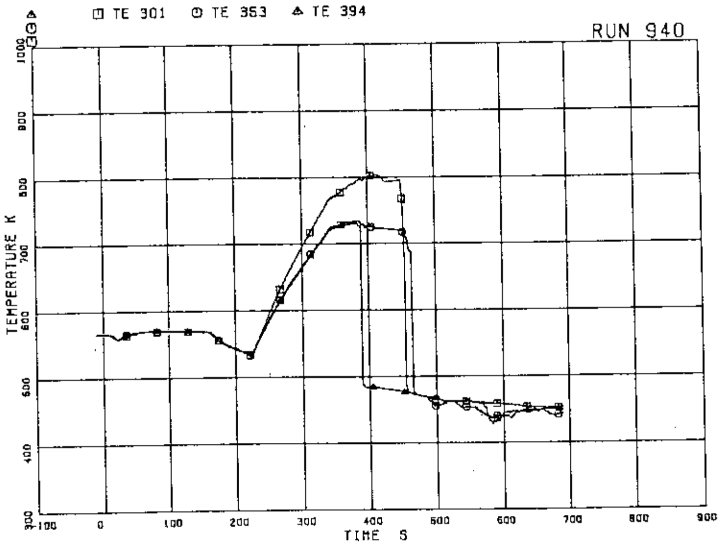

Fig.A.100 Surface temperatures of fuel rods A77, B77 and C77 at position 4

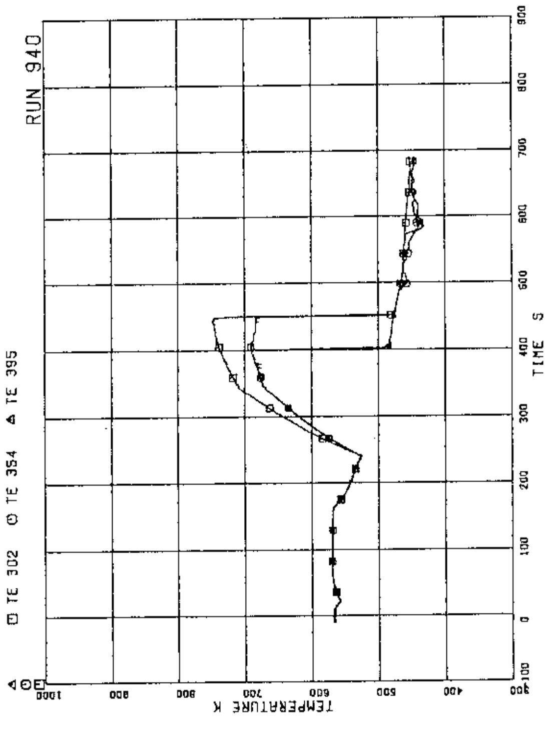

Fig.A.101 Surface temperatures of fuel rods A77, B77 and C77 at position 5

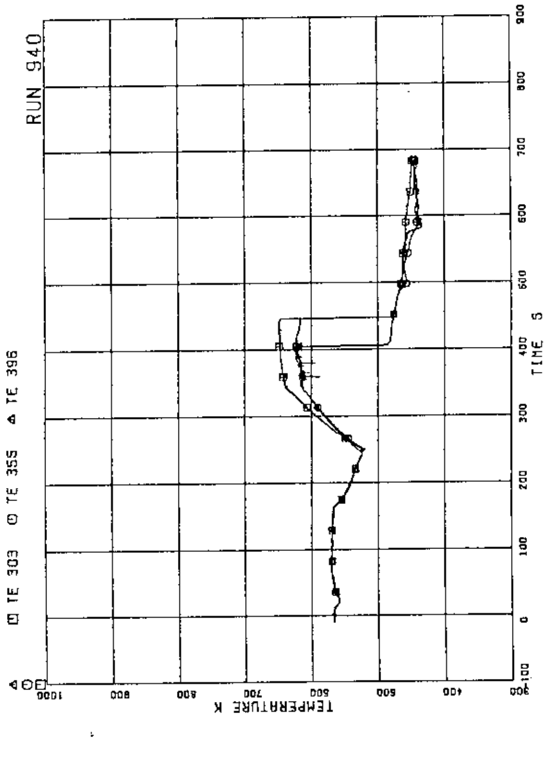

Fig.A.102 Surface temperatures of fuel rods A77, B77 and C77 at position 6

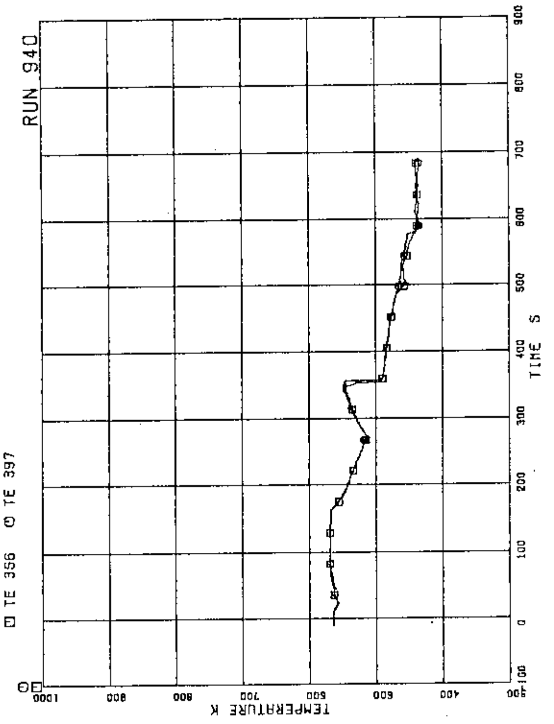

Fig.A.103 Surface temperature of fuel rod A77, B77 and C77 at position 7

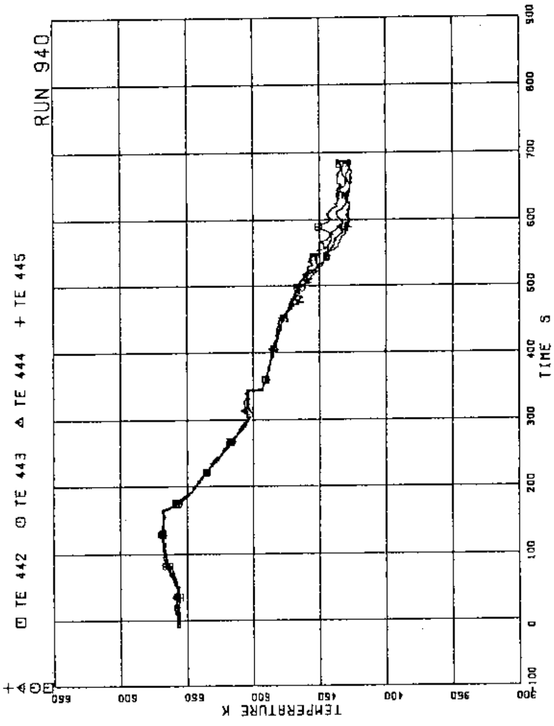

Fig.A.104 Fluid temperatures at channel inlet

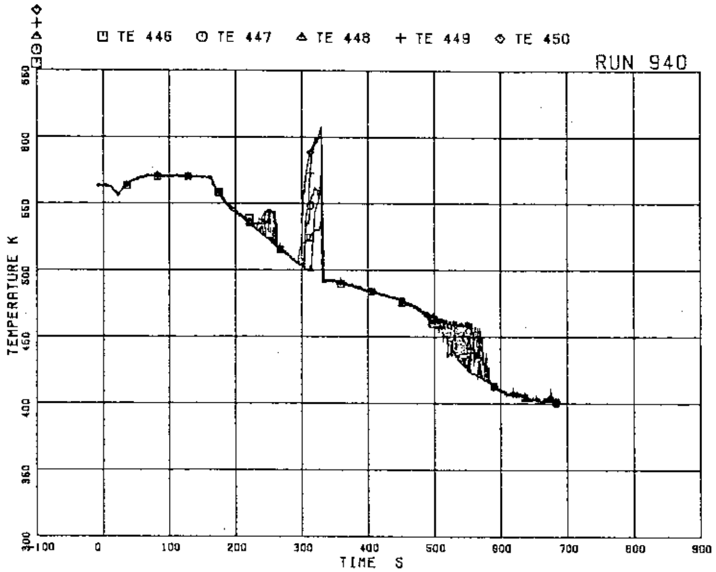

Fig.A.105 Fluid temperatures at channel A outlet

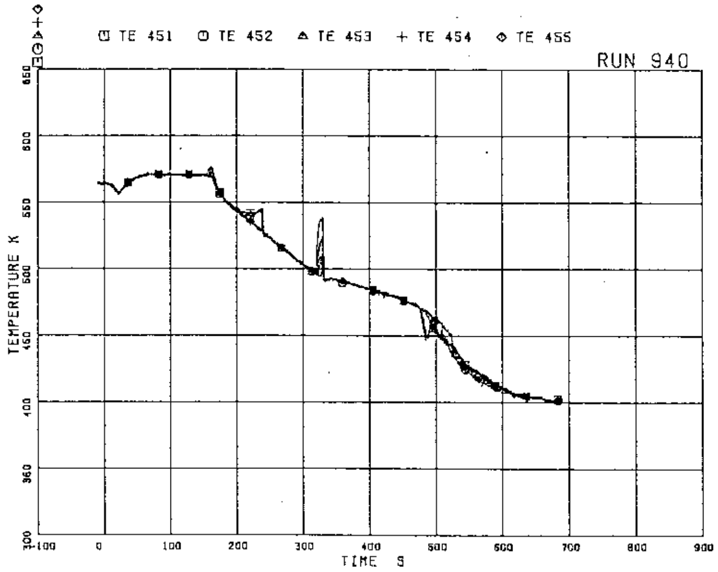

Fig.A.106 Fluid temperatures at channel C outlet

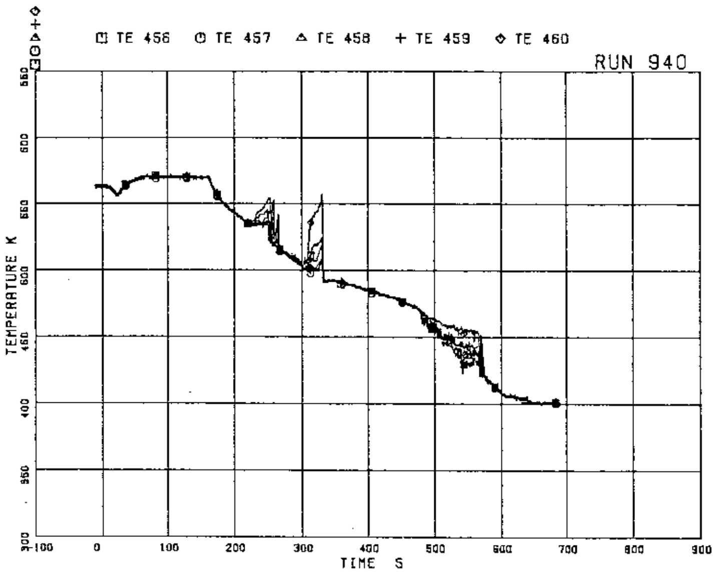

Fig.A.107 Fluid temperatures above UTP of channel A, openings 1 to 5

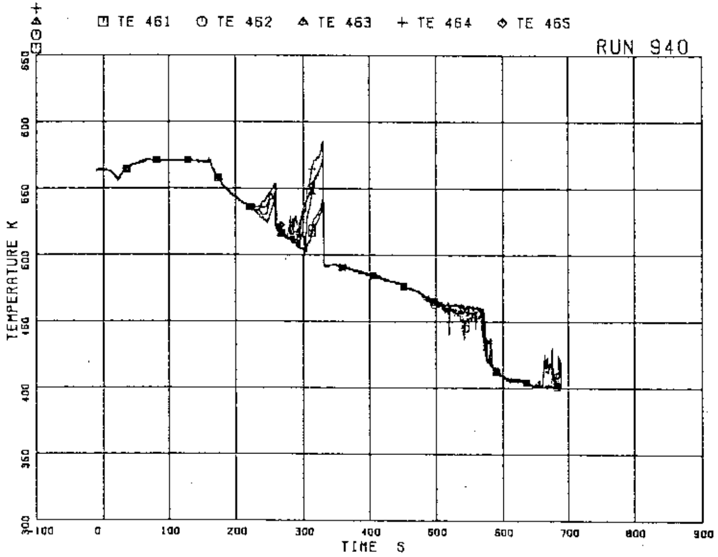

Fig.A.108 Fluid temperatures above UTP of channel A, openings 6 to 10

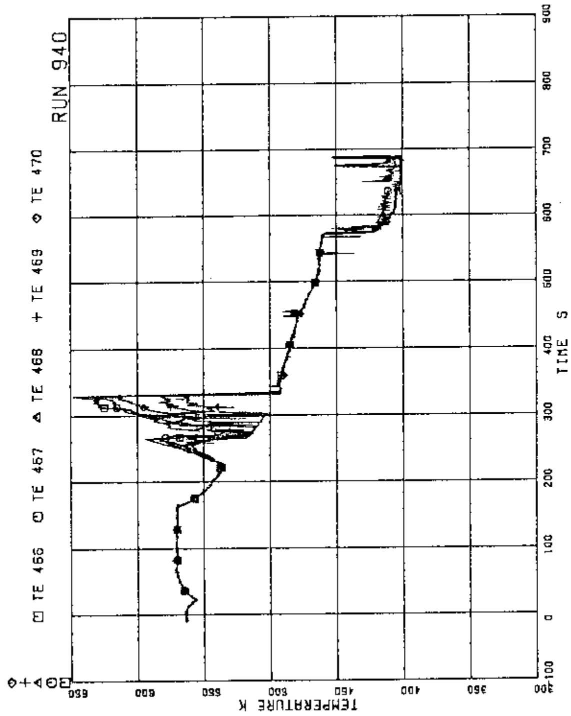

Fig.A.109 Fluid temperatures below UTP of channel A, openings 1 to 5

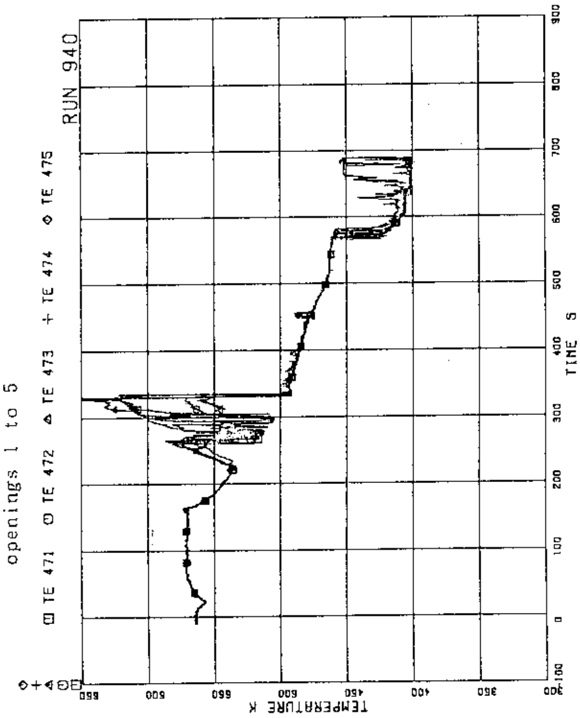

Fig.A.110 Fluid temperatures below UTP of channel A, openings 6 to 10

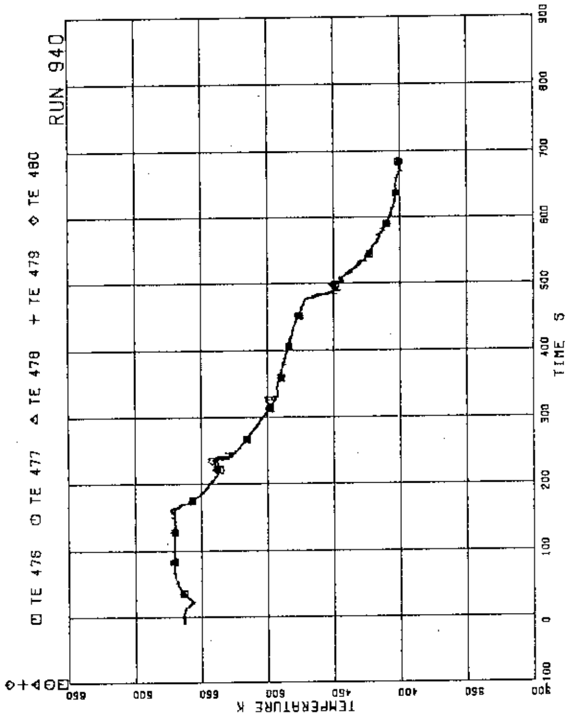

Fig.A.111 Fluid temperatures above UTP of channel C, openings 1 to 5

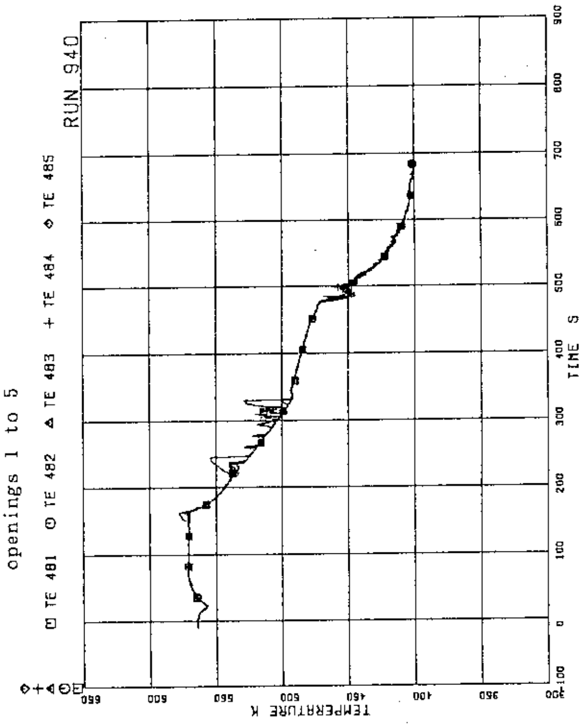

Fig.A.112 Fluid temperatures above UTP of channel C, openings 6 to 10

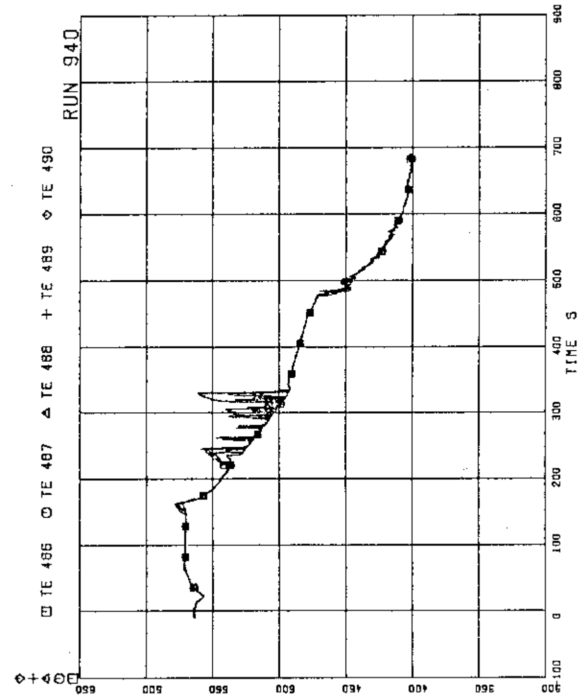

Fig.A.113 Fluid temperatures below UTP of channel C, openings 1 to 5

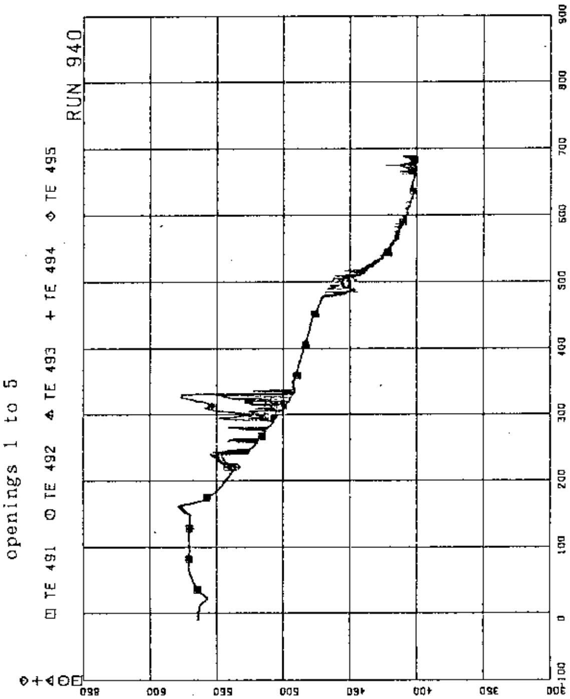

Fig.A.114 Fluid temperatures below UTP of channel C, openings 6 to 10

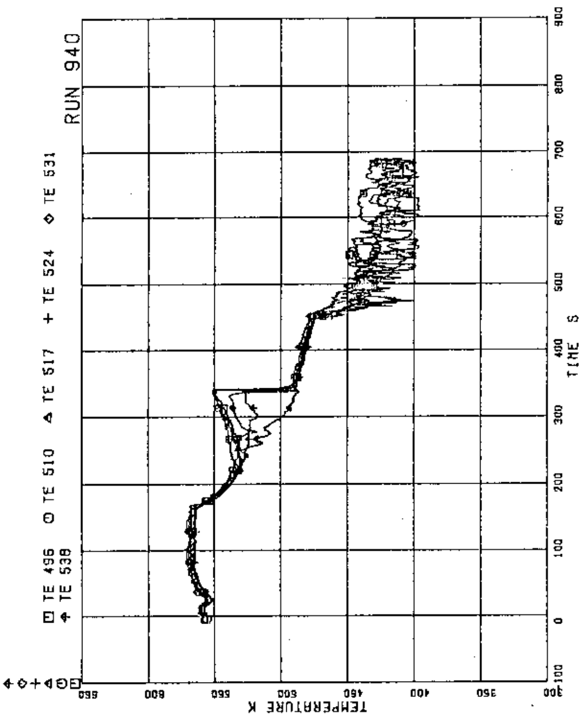

Fig.A.115 Inner and outer surface temperatures of channel box at pos. 1

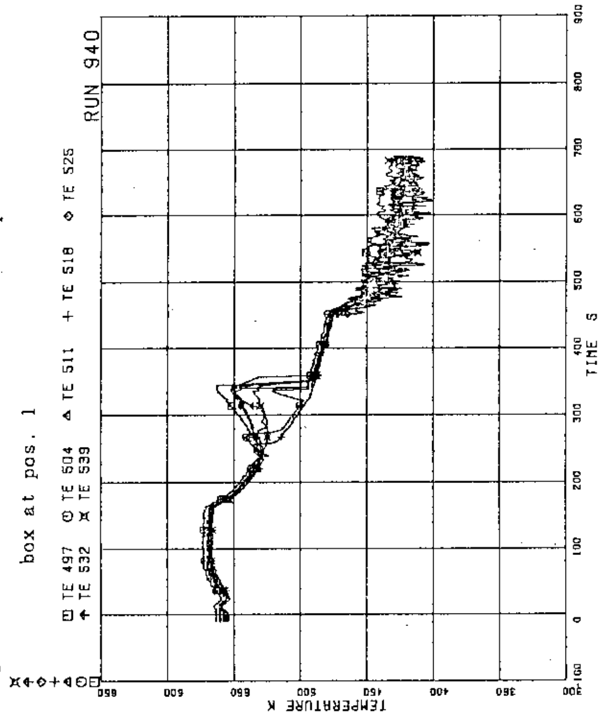

Fig.A.116 Inner and outer surface temperatures of channel box at pos. 2

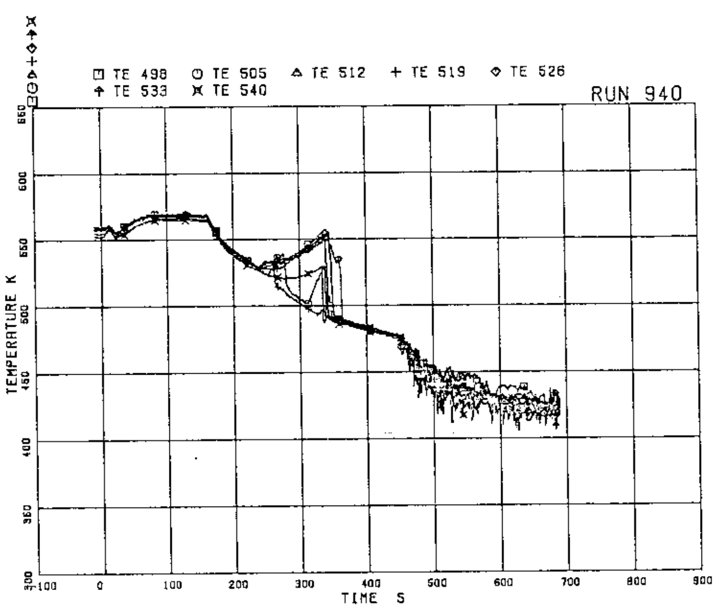

Fig.A.117 Inner and outer surface temperatures of channel box at pos. 3

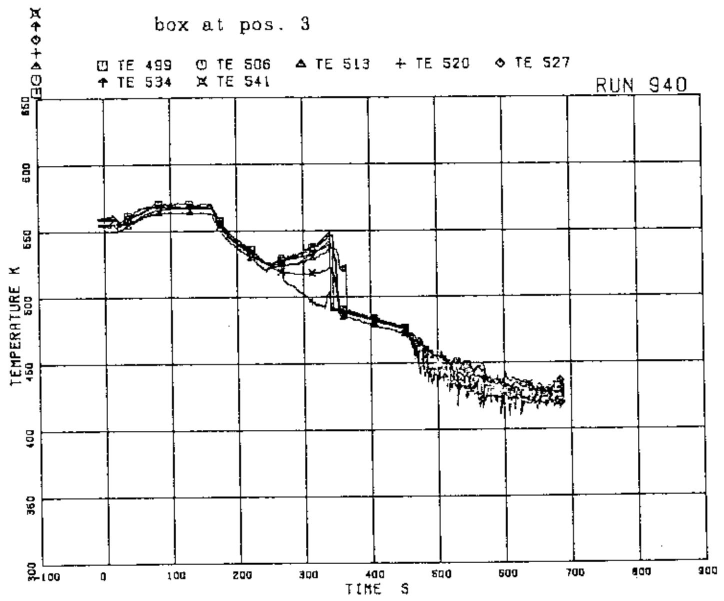

Fig.A.118 Inner and outer surface temperatures of channel box at pos. 4

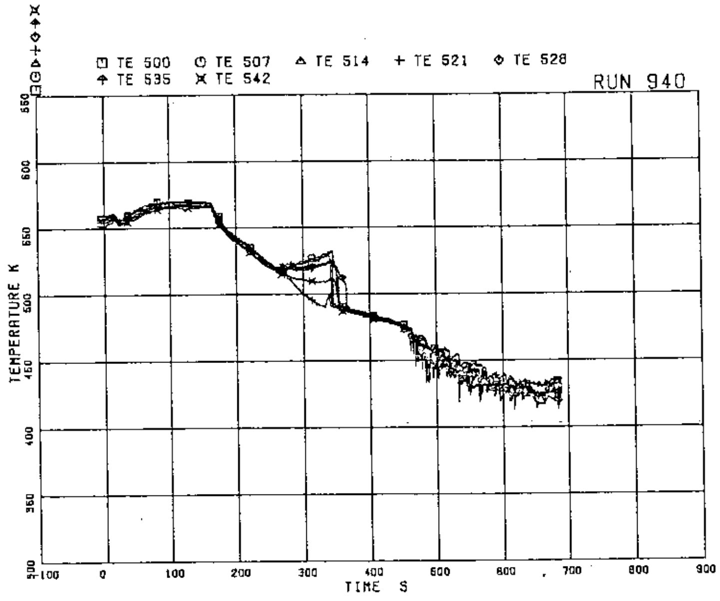

Fig.A.119 Inner and outer surface temperatures of channel box at pos. 5

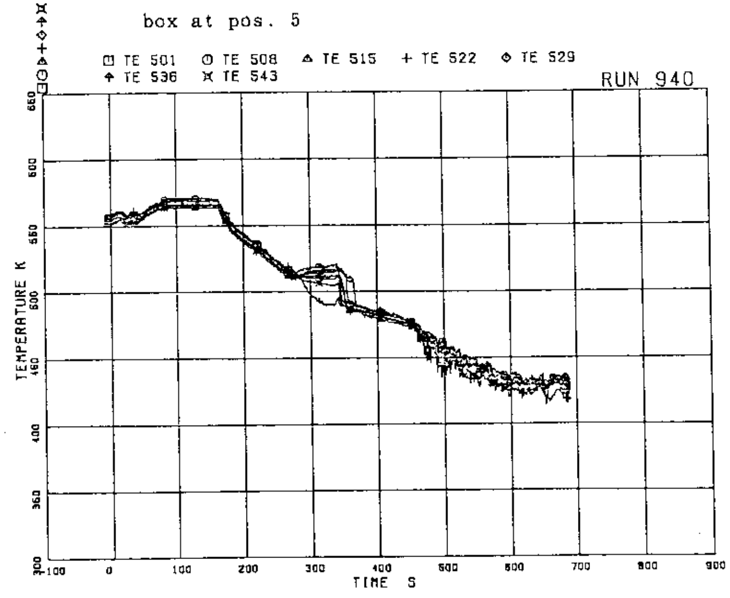

Fig.A.120 Inner and outer surface temperatures of channel box at pos. 6

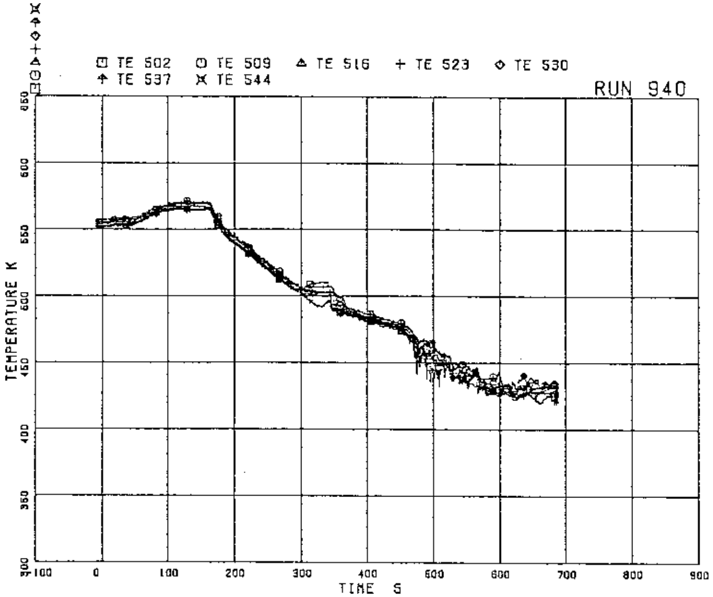

Fig.A.121 Inner and outer surface temperatures of channel box at pos. 7

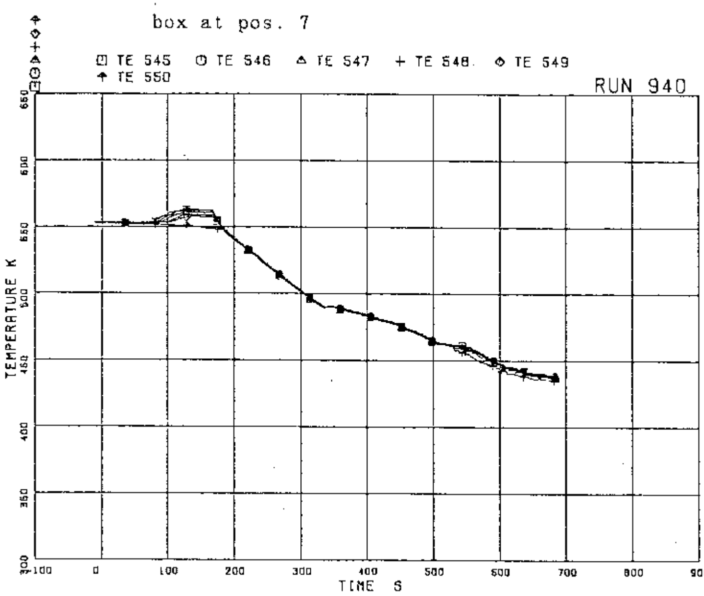

Fig.A.122 Fluid temperatures in lower plnum, center

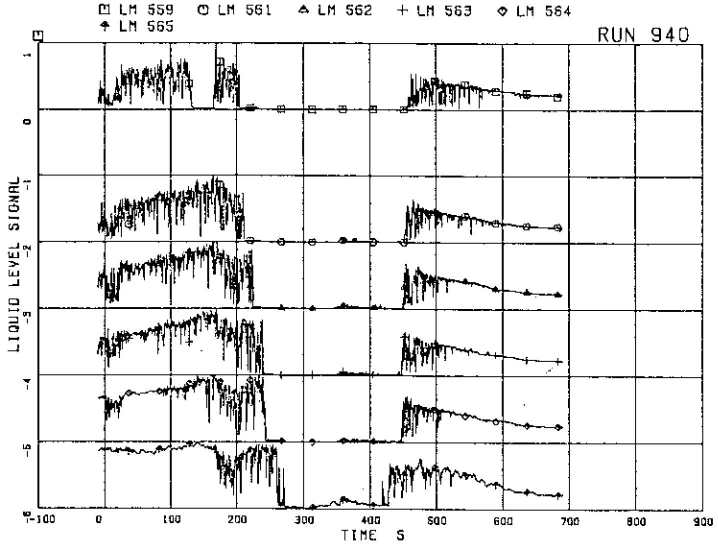

Fig.A.123 Liquid level signals in channel box A, location A1

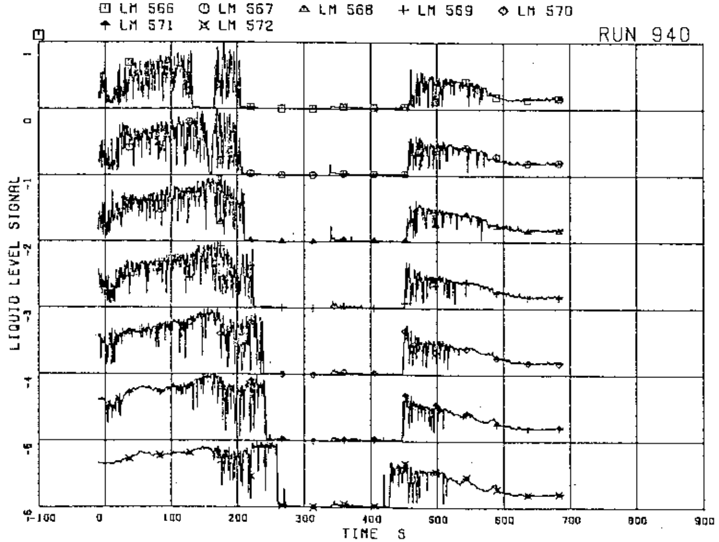

Fig.A.124 Liquid level signals in channel box A, location A2

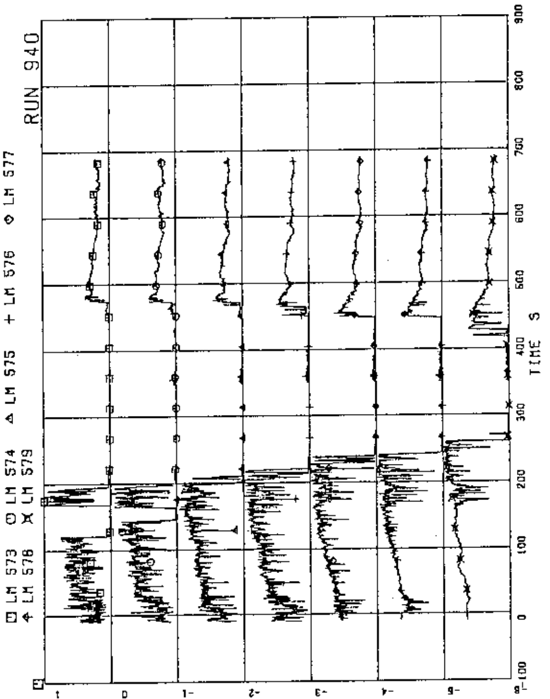

Fig.A.125 Liquid level signals in channel box B

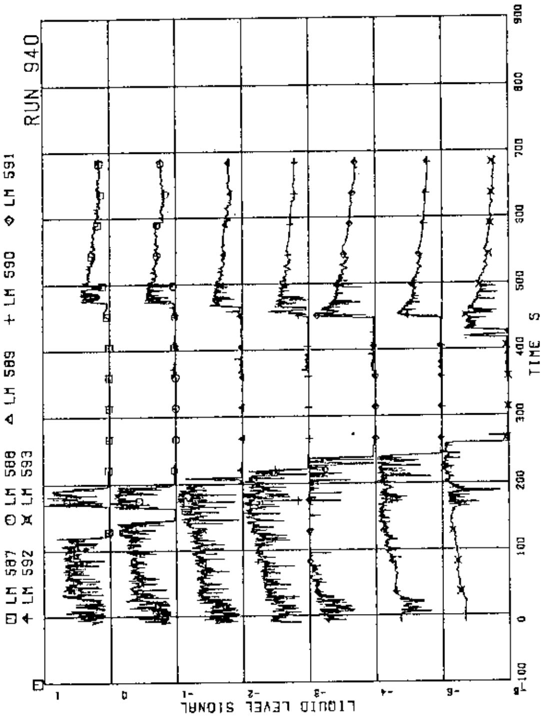

Fig.A.127 Liquid level signals in channel box D

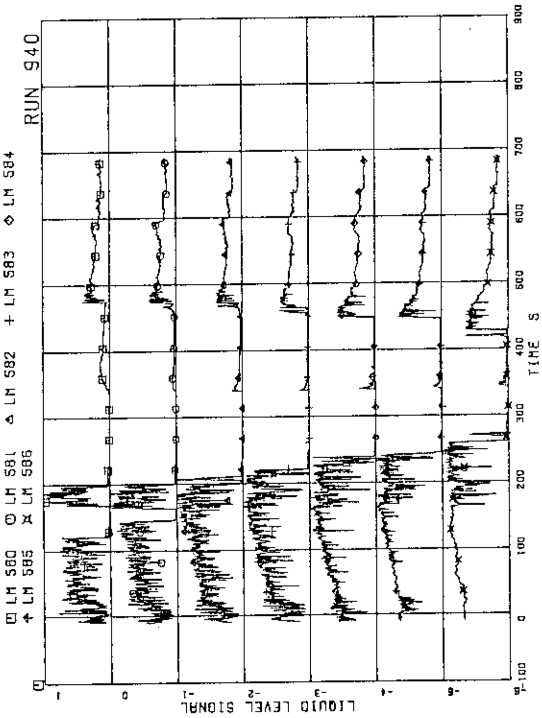

Fig.A.126 Liquid level signals in channel box C

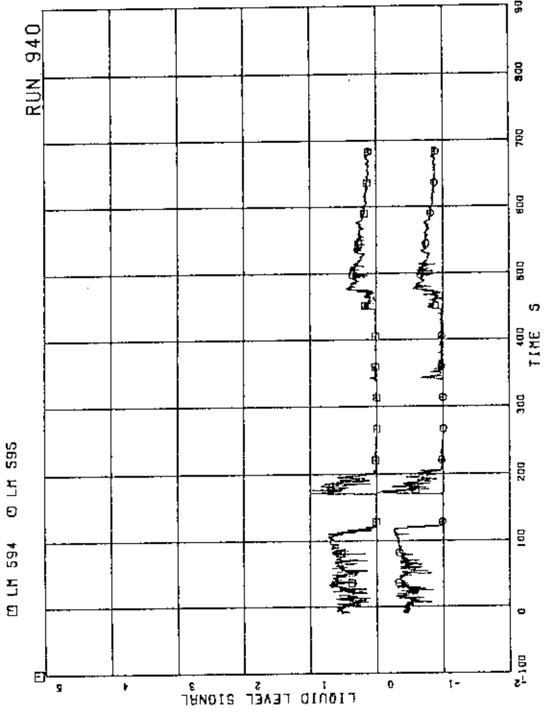

Fig.A.128 Liquid level signals in channel A outlet, location A1

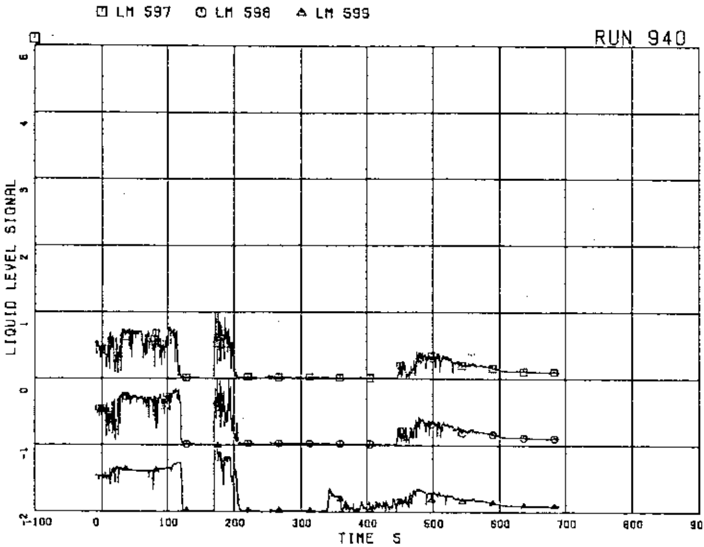

Fig.A.129 Liquid level signals in channel A outlet, location A2

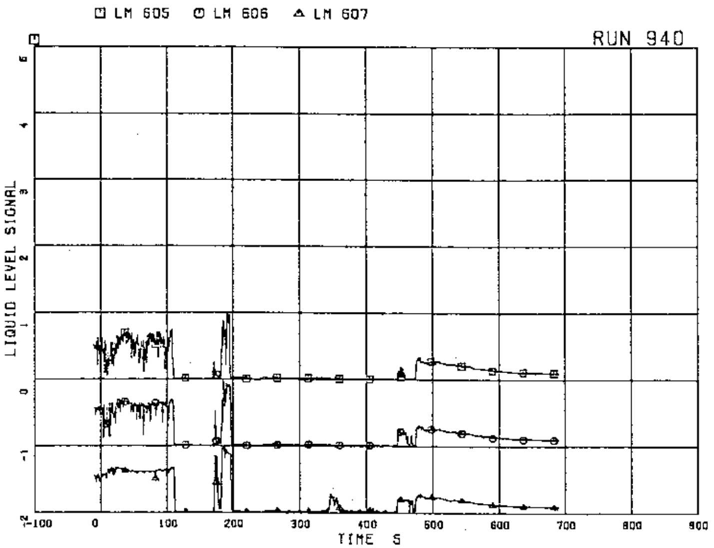

Fig.A.131 Liquid level signals in channel C outlet, location C1

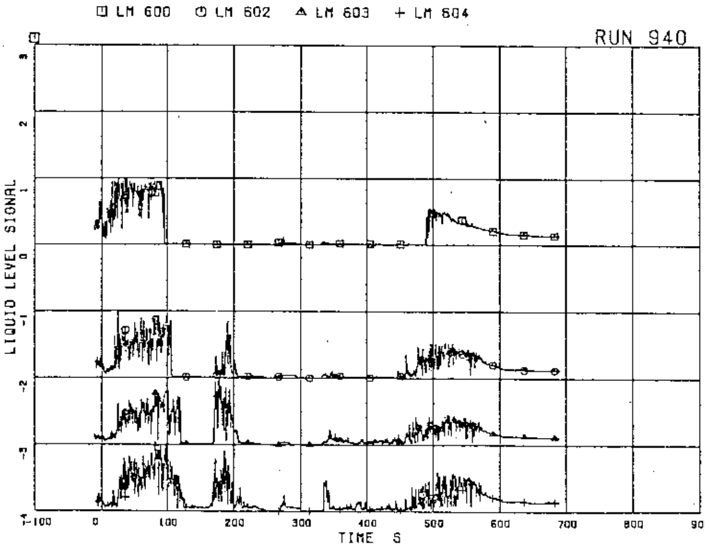

Fig.A.130 Liquid level signals in channel A outlet, center

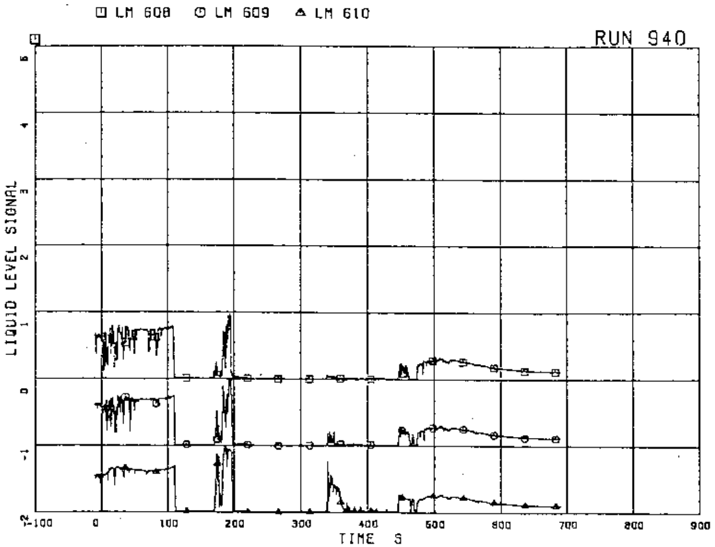

Fig.A.132 Liquid level signals in channel C outlet, location C2

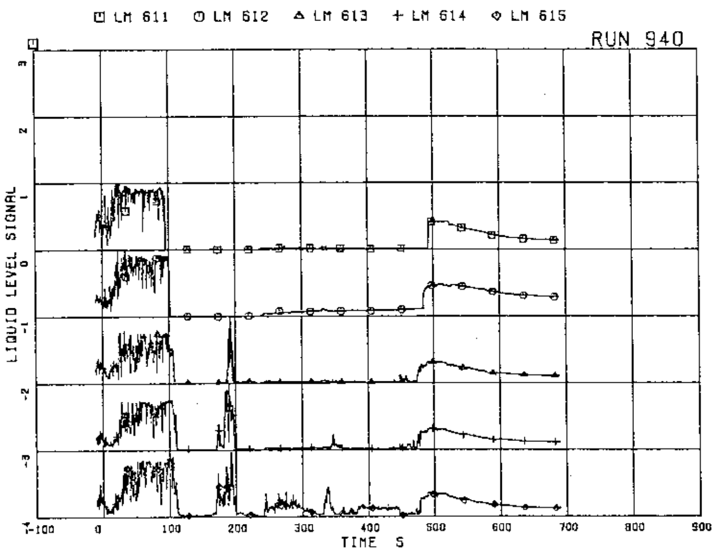

Fig.A.133 Liquid level signals in channel C outlet, center

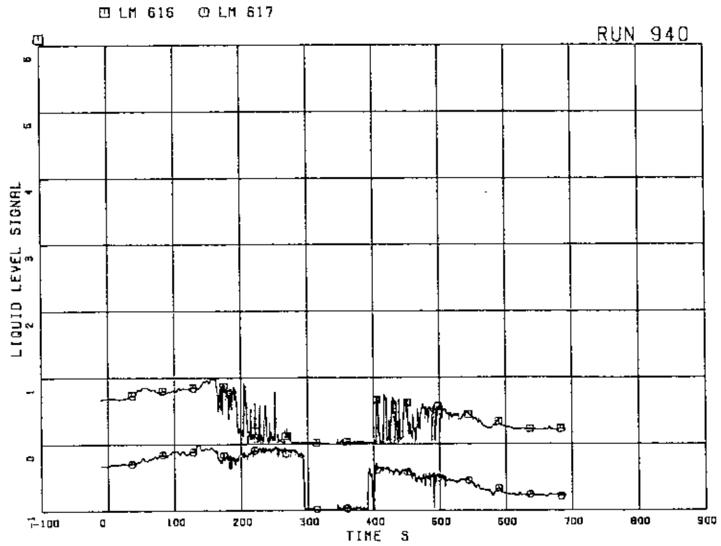

Fig.A.134 Liquid level signals in channel A inlet

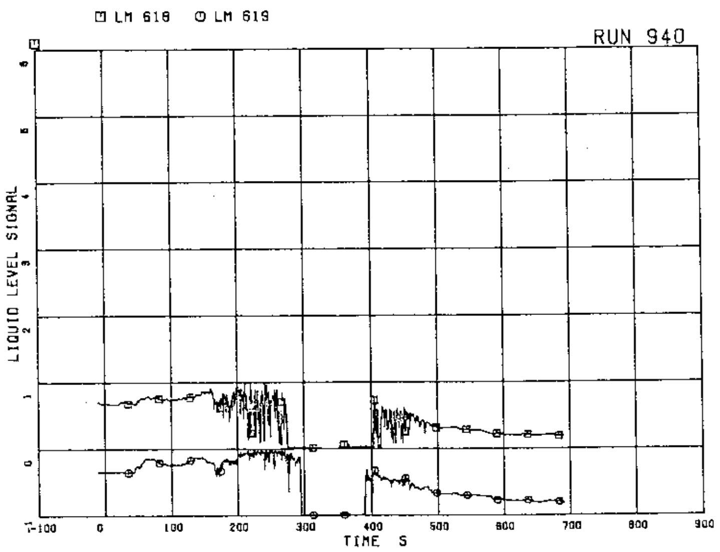

Fig.A.135 Liquid level signals in channel B inlet

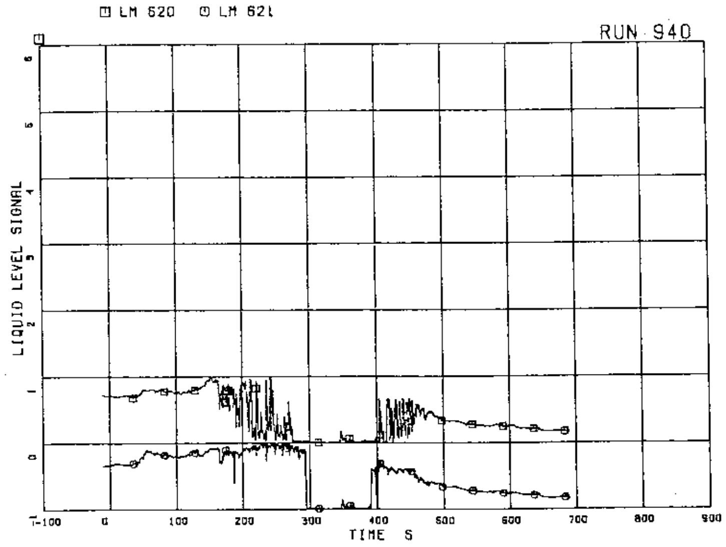

Fig.A.136 Liquid level signals in channel C inlet

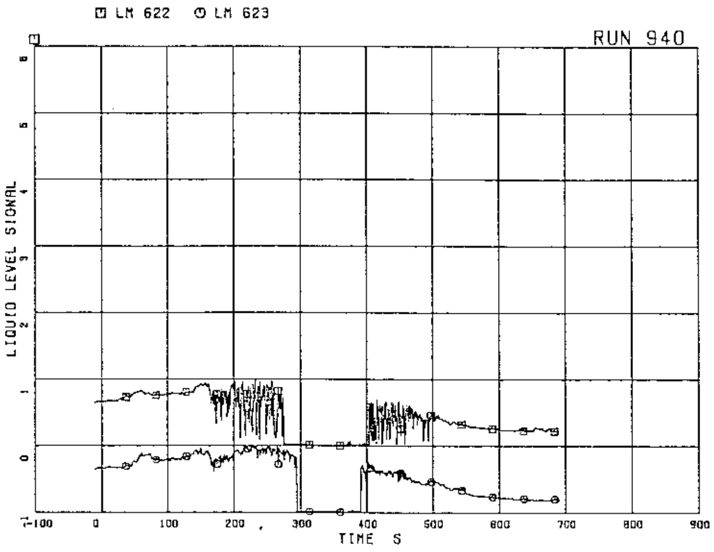

Fig.A.137 Liquid level signals in channel D inlet

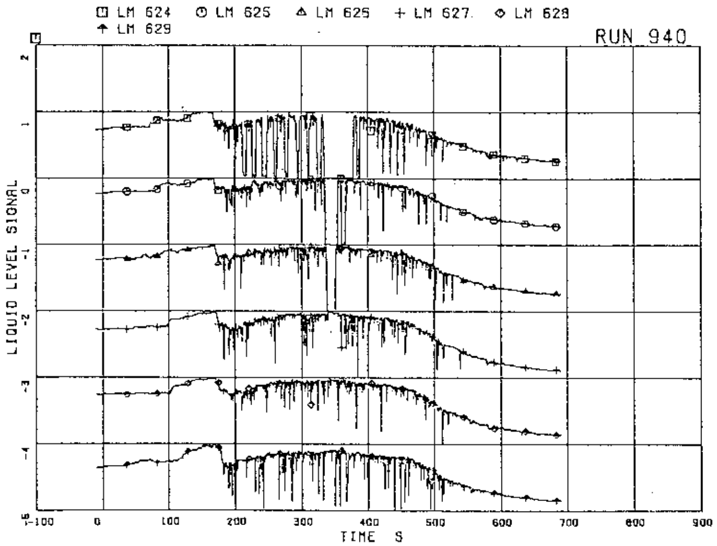

Fig.A.138 Liquid level signals in lower plenum, north

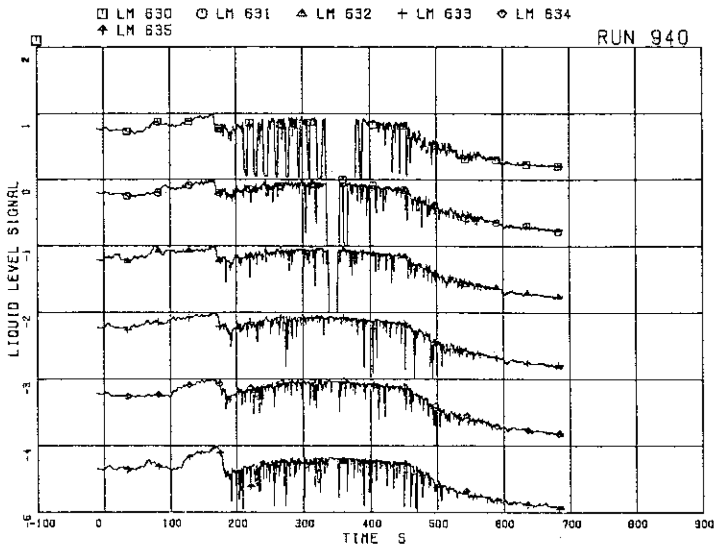

Fig.A.139 Liquid level signals in lower plenum, south

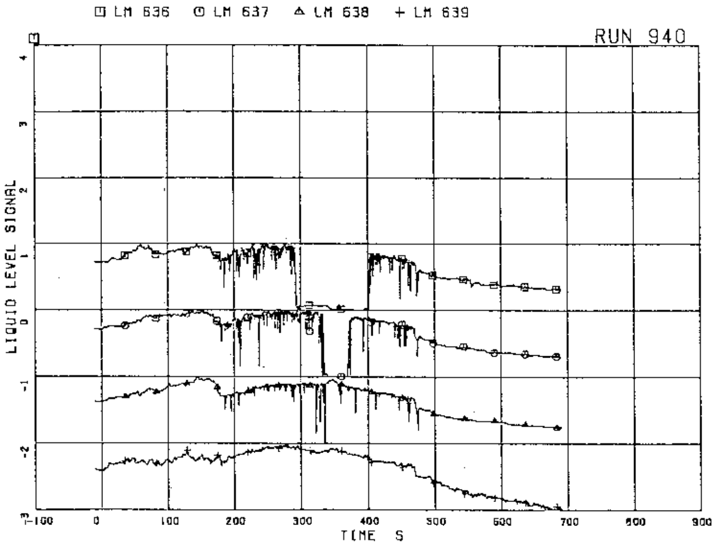

Fig.A.140 Liquid level signals in guide tube, north

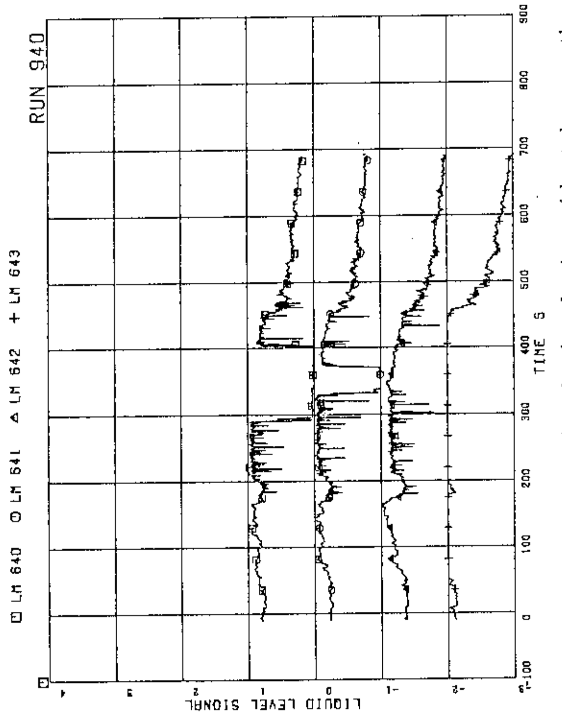

Fig.A.141 Liquid level signals in guide tube, south

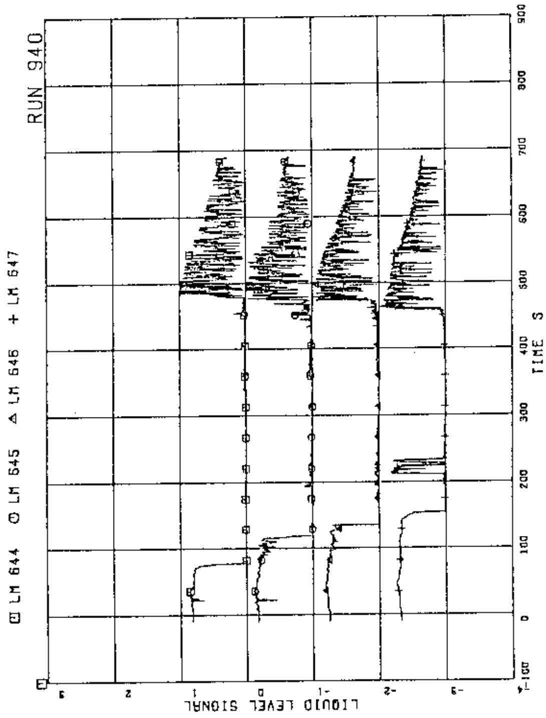

Fig.A.142 Liquid level signals in downcomer, D side

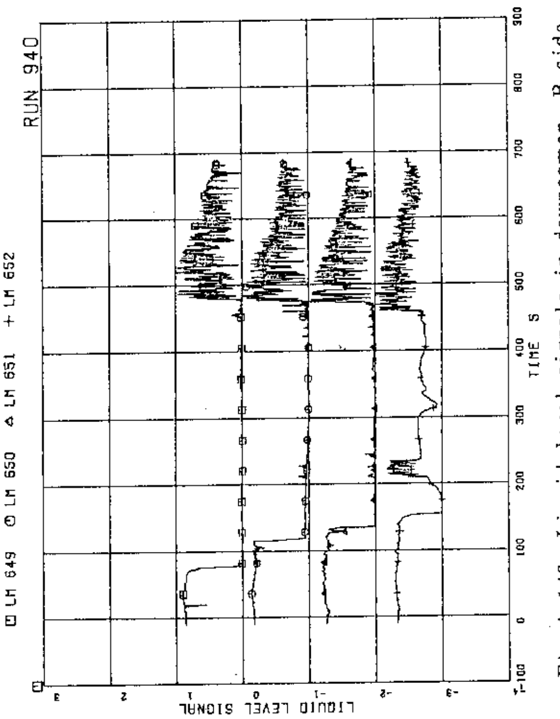

Fig.A.143 Liquid level signals in downcomer, B side

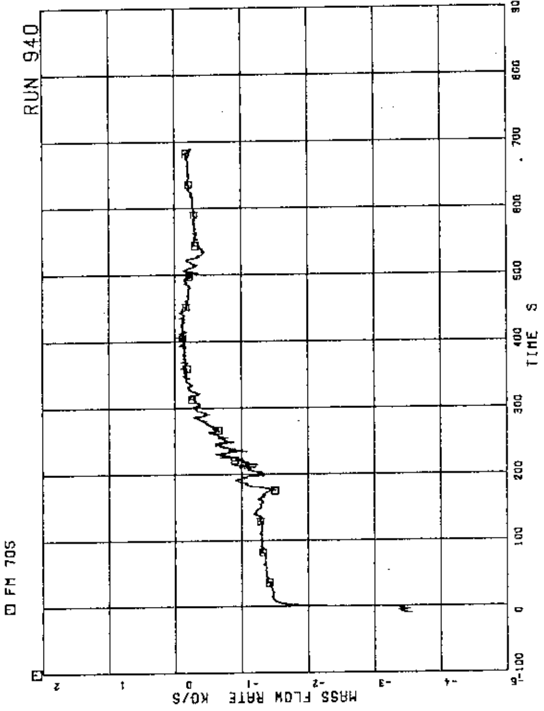

Fig.A.144 Flow rate at MRP side of break (based on low range drag disk data)

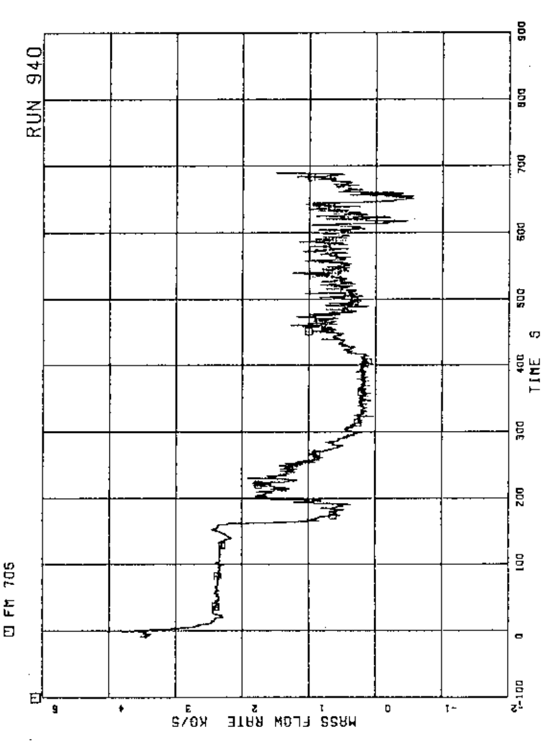

Fig.A.145 Flow rate at PV side of break (based on low range drag disk data)

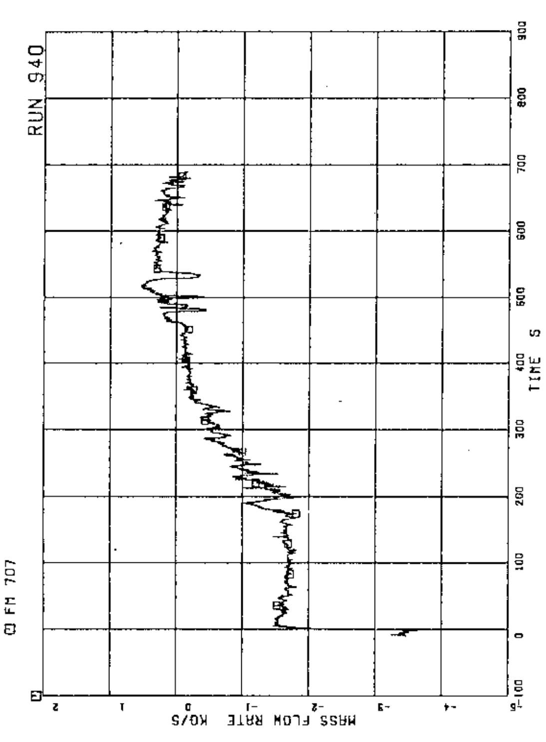

Fig.A.146 Flow rate at MRP side of break (based on high range drag disk data)

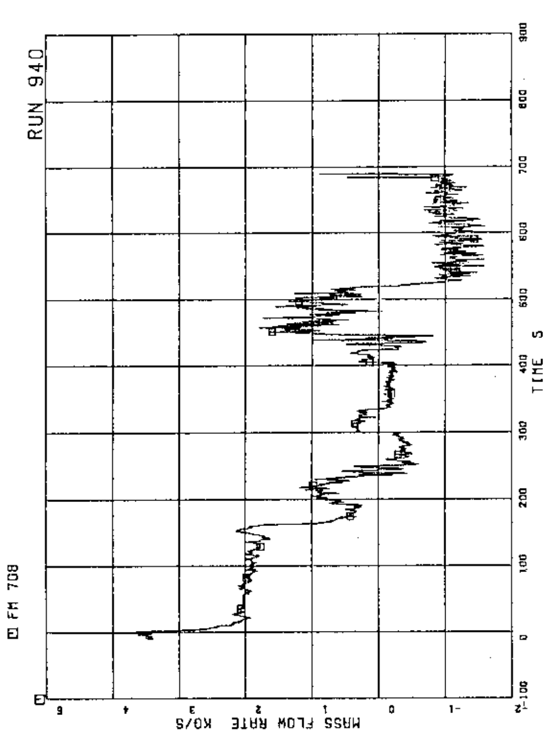

Fig.A.147 Flow rate at PV side of break (based on high range drag disk data)

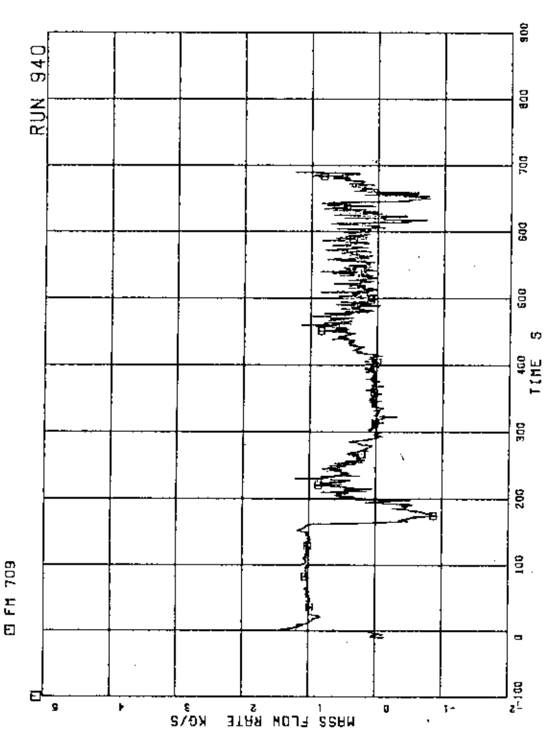

Fig.A.148 Total discharge flow rate from break (based on low range drag disk data)

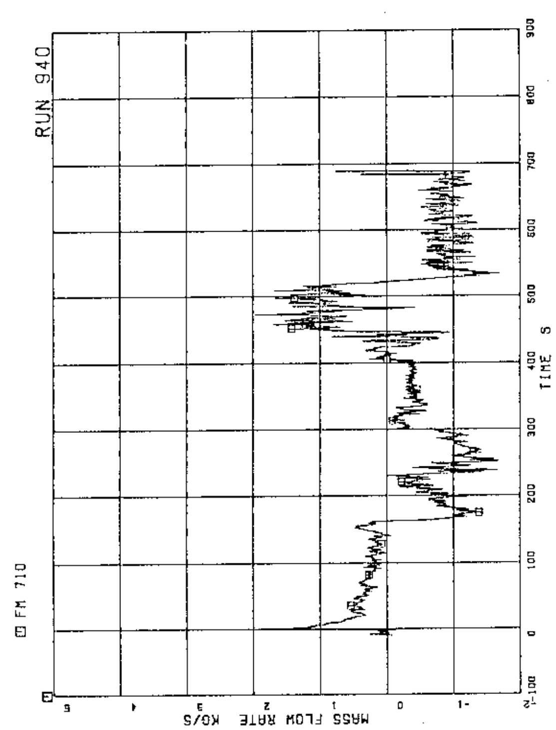

Fig.A.149 Total discharge flow rate from break (based on high range drag disk data)

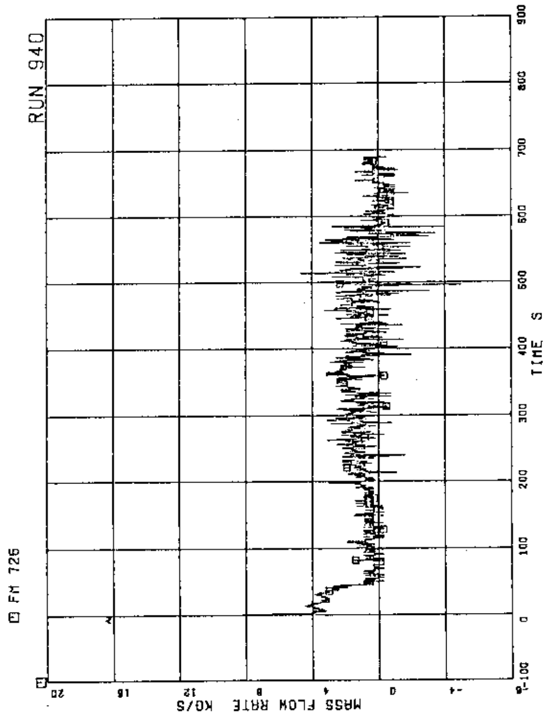

Fig.A.150 Total JP outlet flow rate (pos. flow)

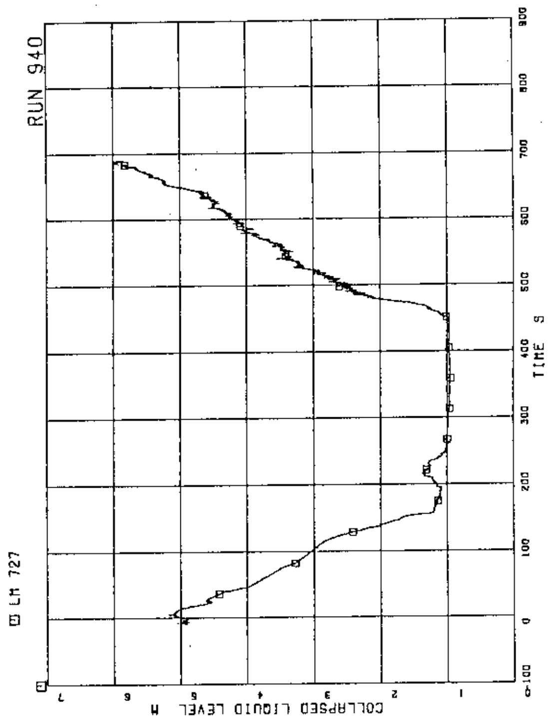

Fig.A.151 Collapsed liquid level in downcomer

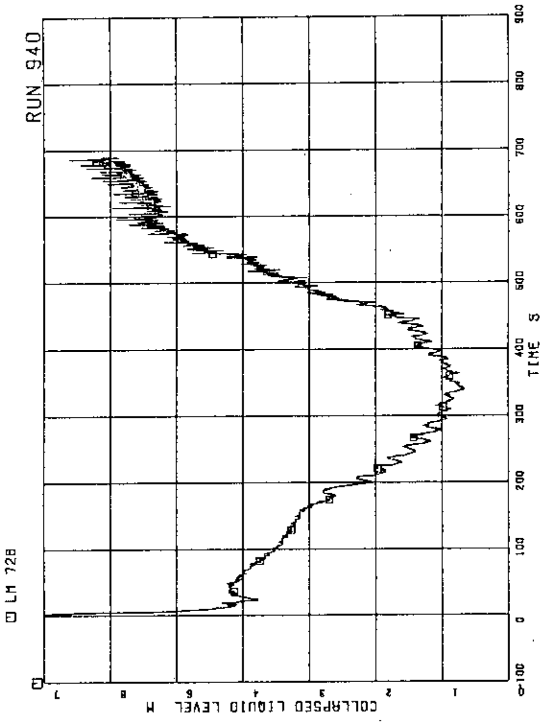

Fig.A.152 Collapsed liquid level inside core-shroud
CORE SHROUD

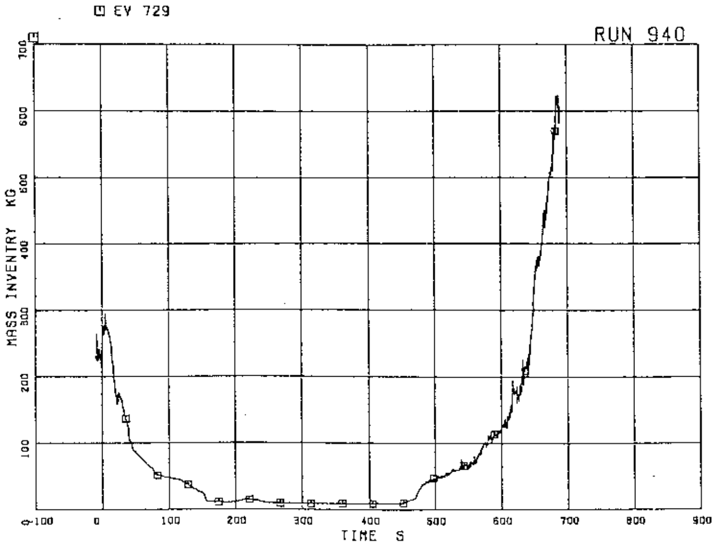

Fig.A.153 Fluid inventory in downcomer

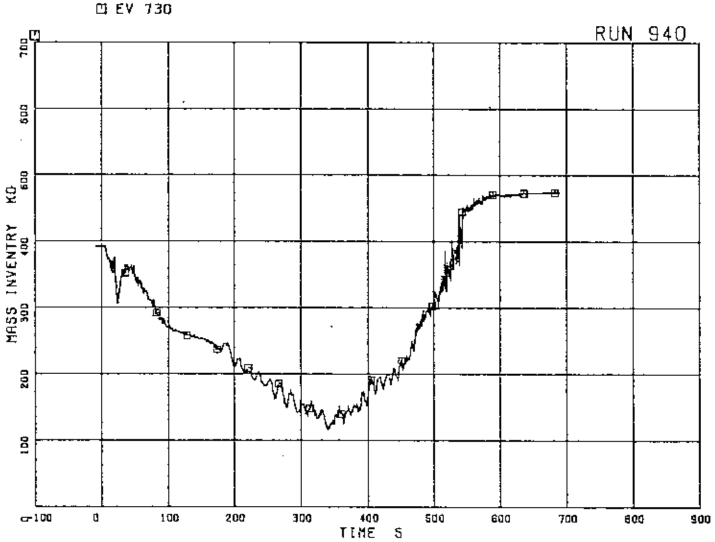

Fig.A.154 Fluid inventory inside core shroud

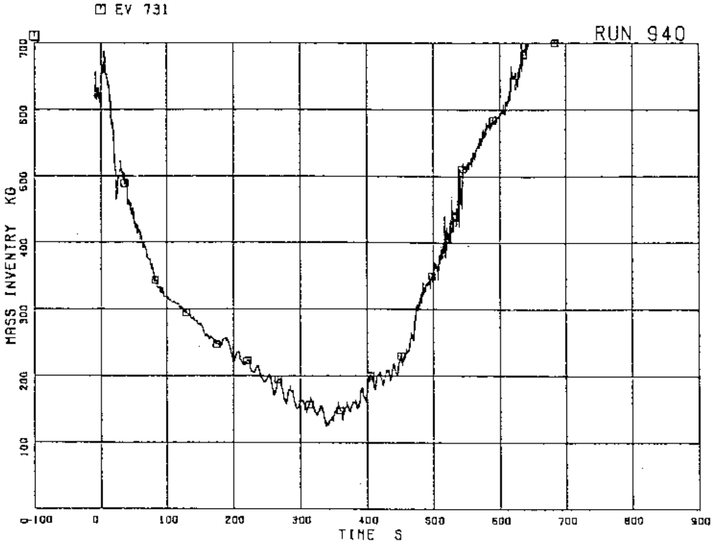

Fig.A.155 Total fluid inventory in pressure vessel

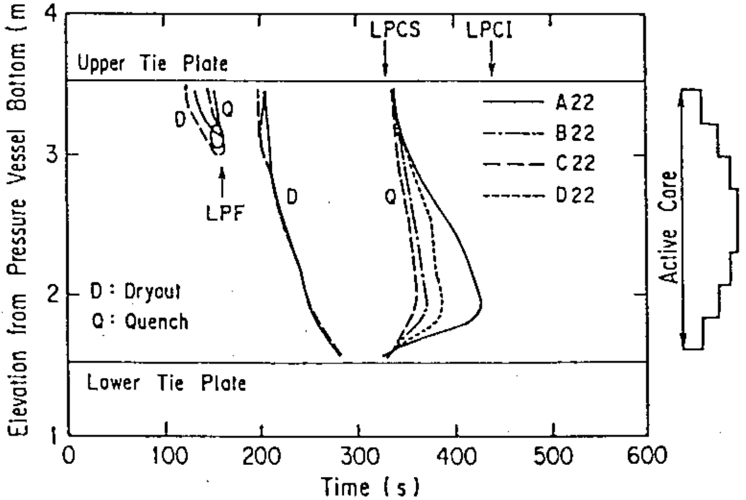

Fig.A.156 Dryout and quench fronts on A22, B22, C22 and D22 rods in RUN 940

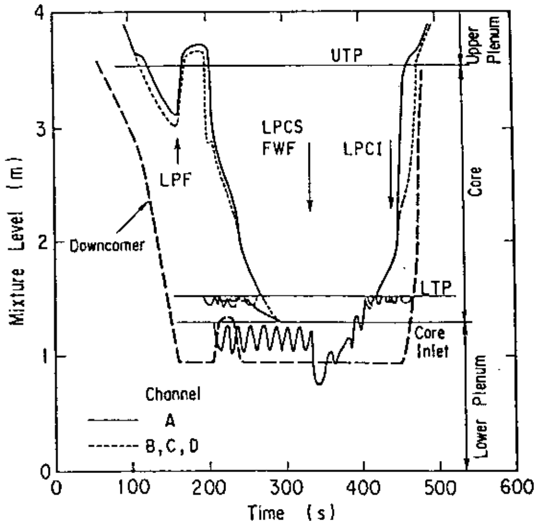

Fig.A.157 Core mixture level transients in RUN 940

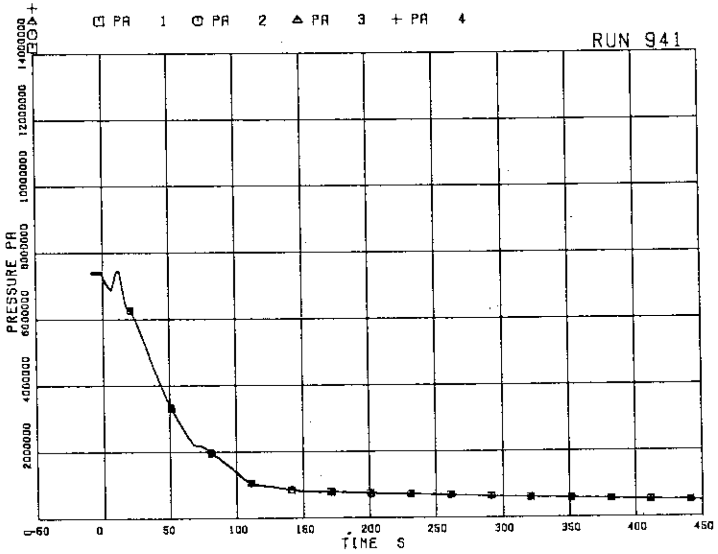

Fig.B.1 Pressure in PV (pressure vessel)

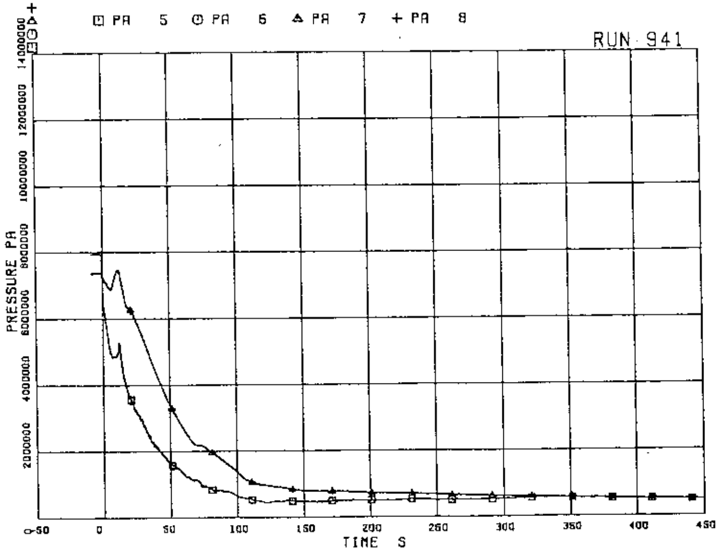

Fig.B.2 Pressure in broken loop JP (Jet Pump)

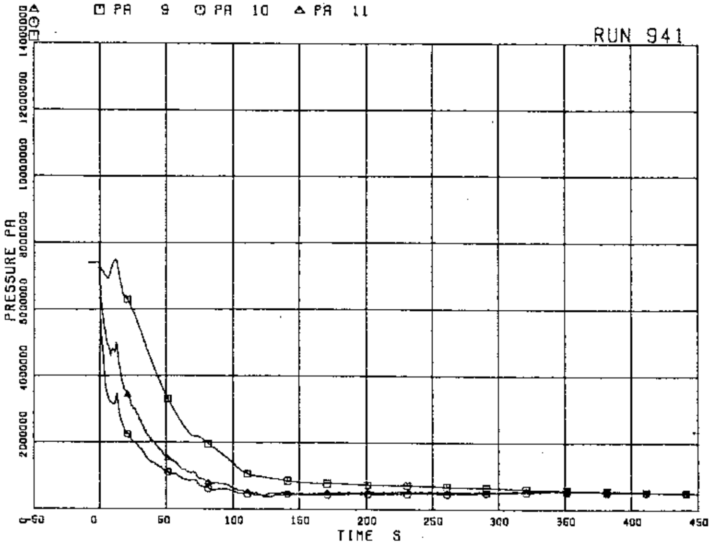

Fig.B.3　Pressure near MRP (Main Recirculation Loop)

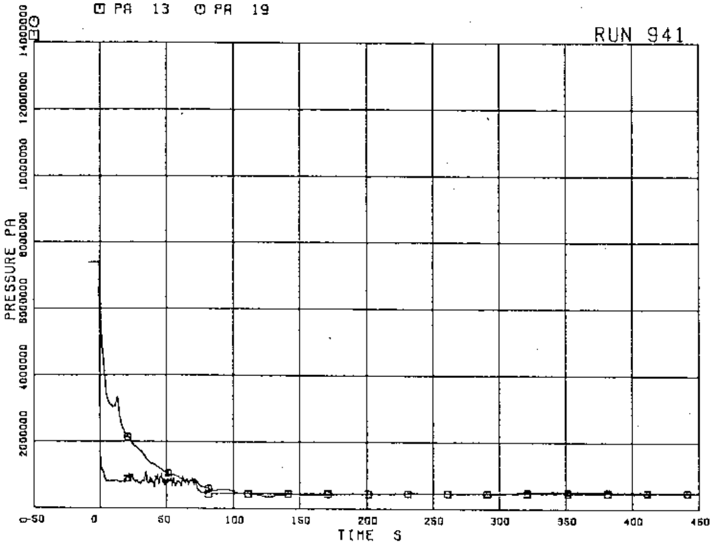

Fig.B.4　Pressure at MRP side of break

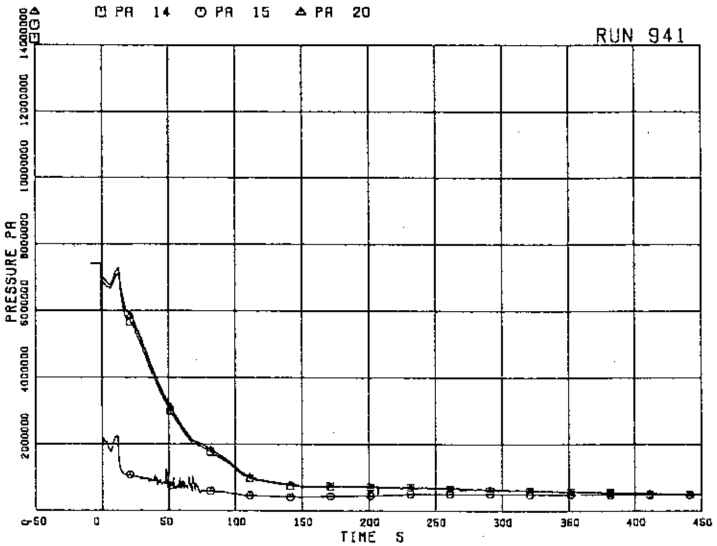

Fig.B.5　Pressure at PV side of break

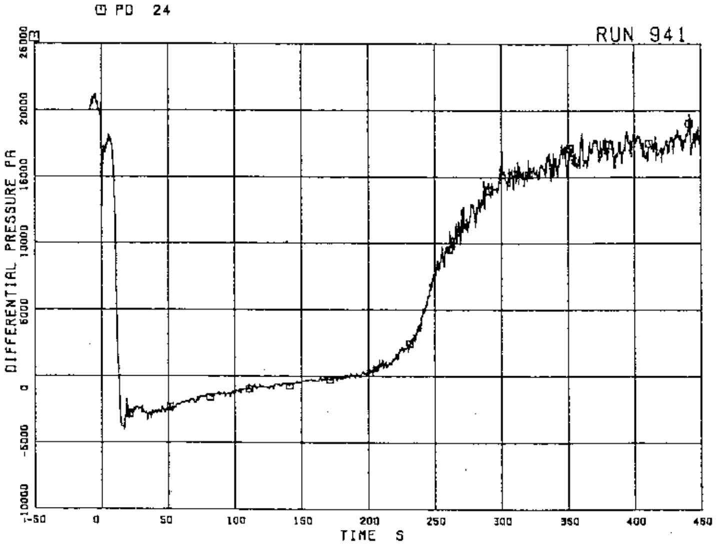

Fig.B.6　(DC) Downcomer Head

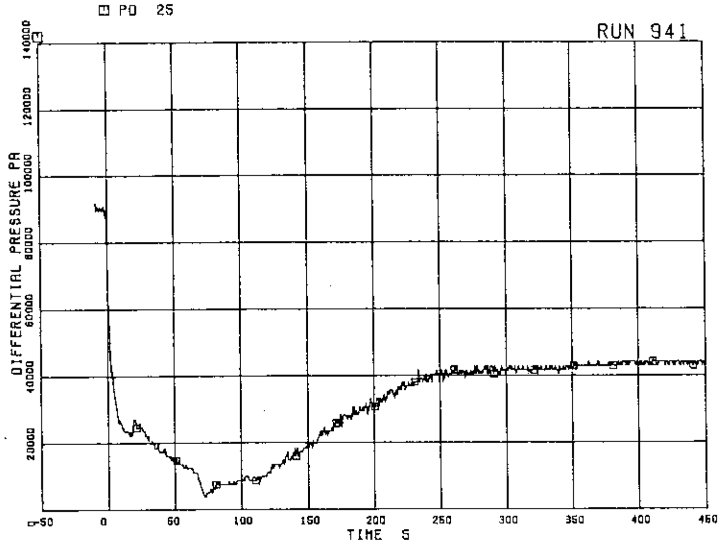

Fig.B.7 Differential pressure between PV bottom and top

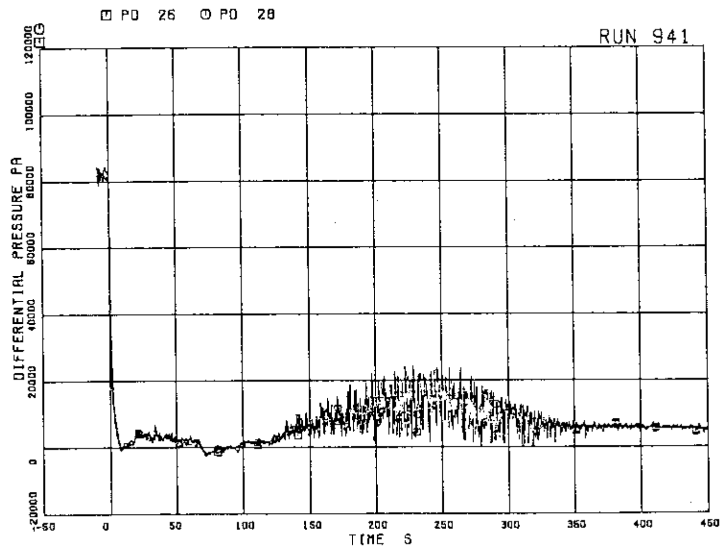

Fig.B.8 Differential pressure between JP-1,2 discharge and suction

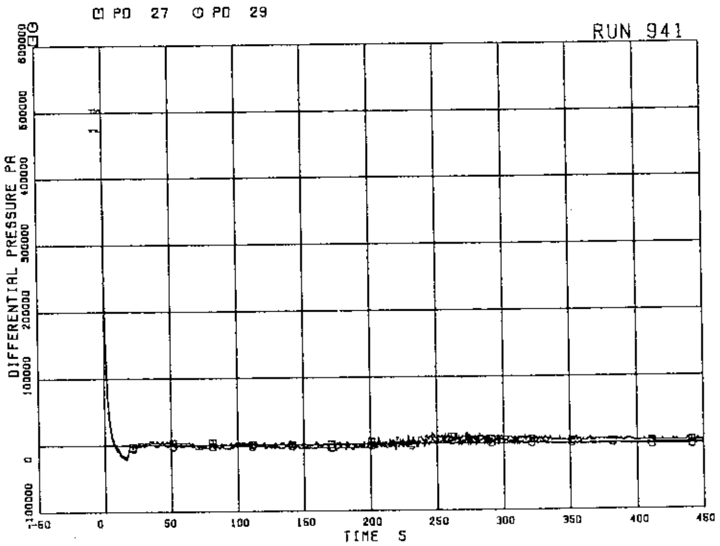

Fig.B.9 Differential pressure between JP-1,2 drive and suction

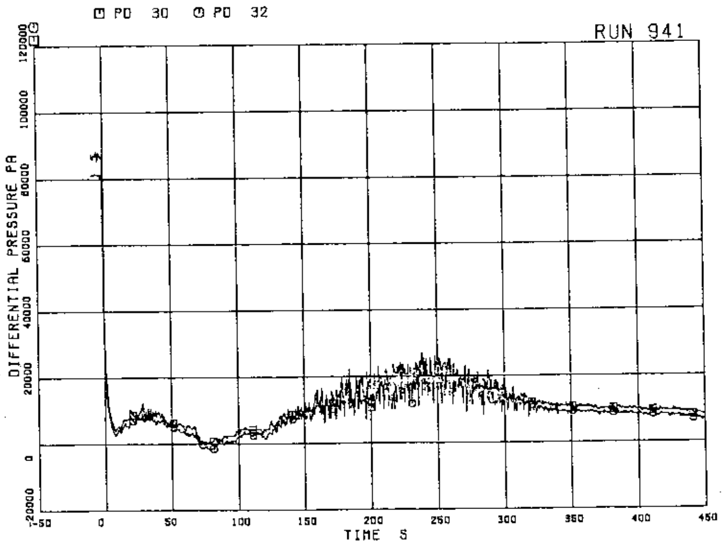

Fig.B.10 Differential pressure between JP-3,4 discharge and suction

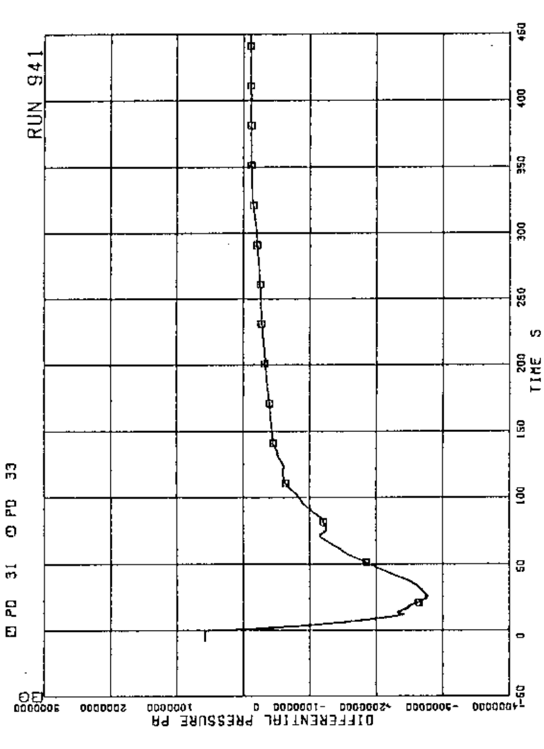

Fig.B.11 Differential pressure between JP-3,4 drive and suction

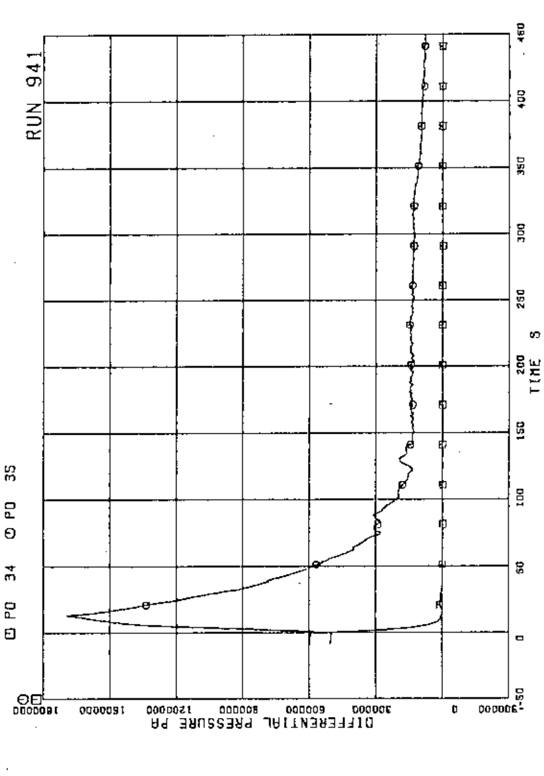

Fig.B.12 Differential pressure beetween MRP delivery and suction

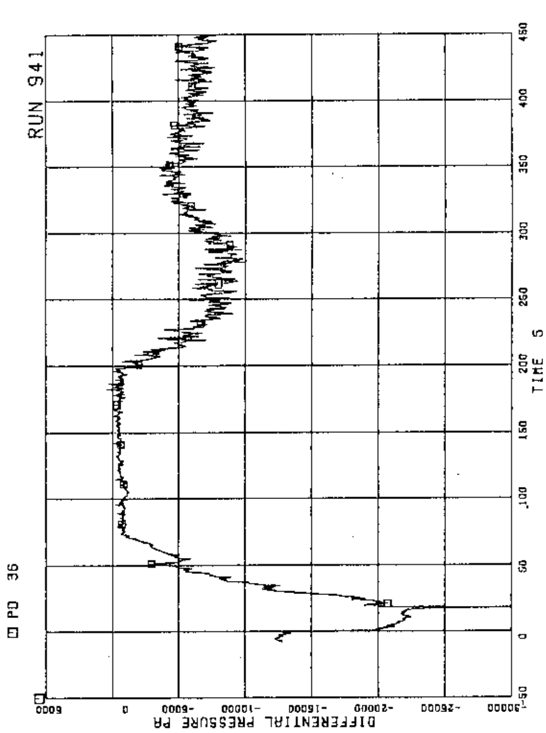

Fig.B.13 Differential pressure between downcomer bottom and MRP1 suction

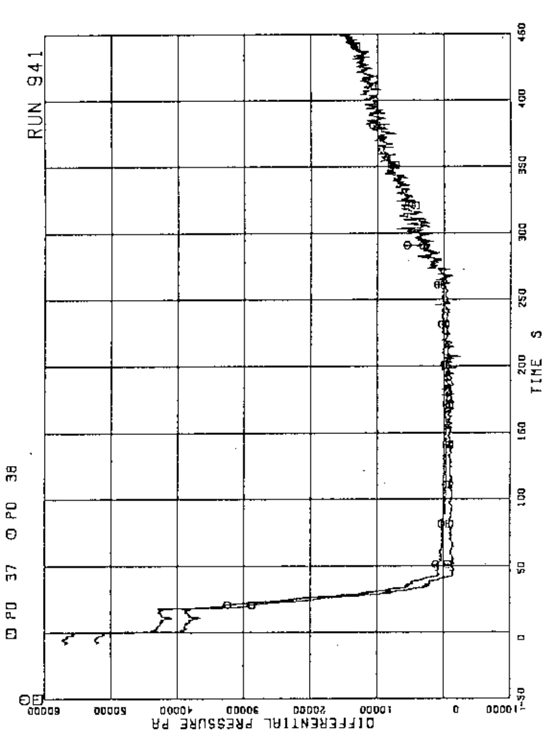

Fig.B.14 Differential pressure between MRP1 delivery and JP-1,2 drive

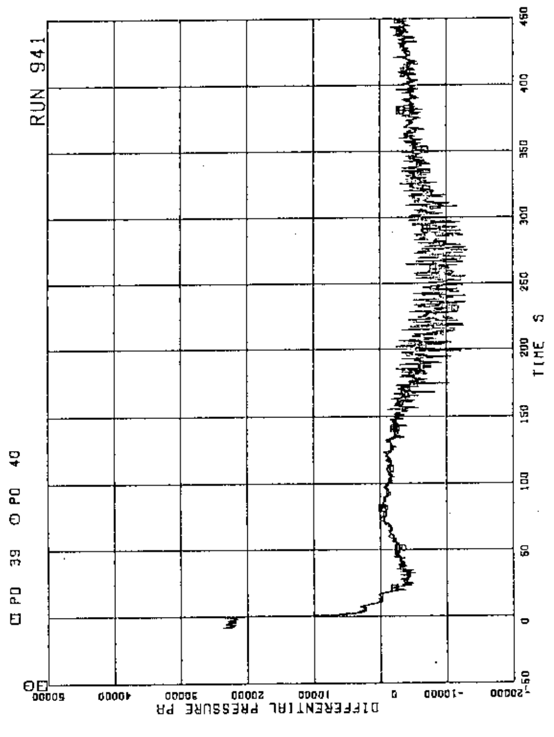

Fig.B.15 Differential pressure between downcomer middle and JP-1,2 suction

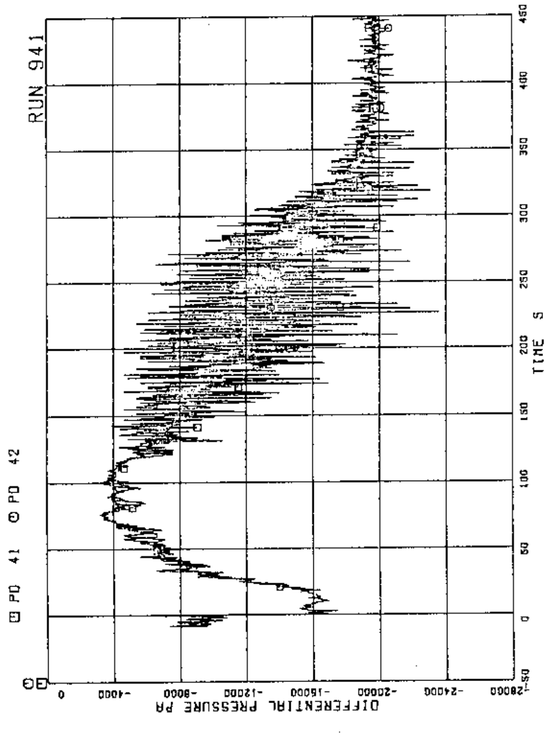

Fig.B.16 Differential pressure between JP-1,2 discharge and LP

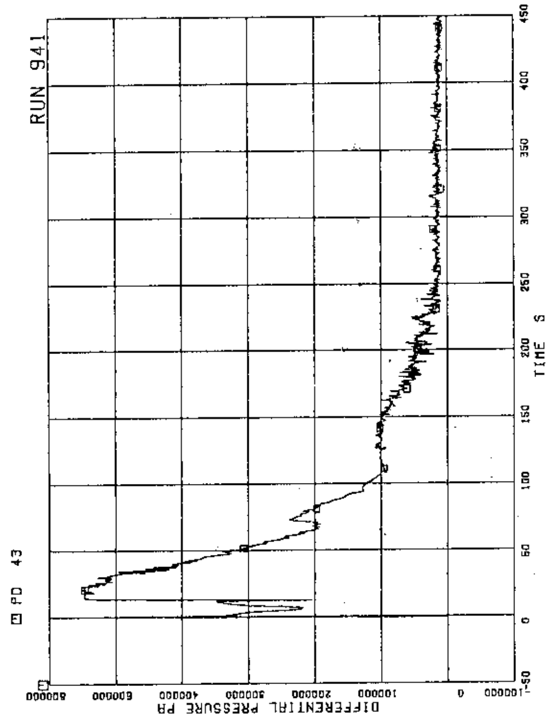

Fig.B.17 Differential pressure between downcomer bottom and break B

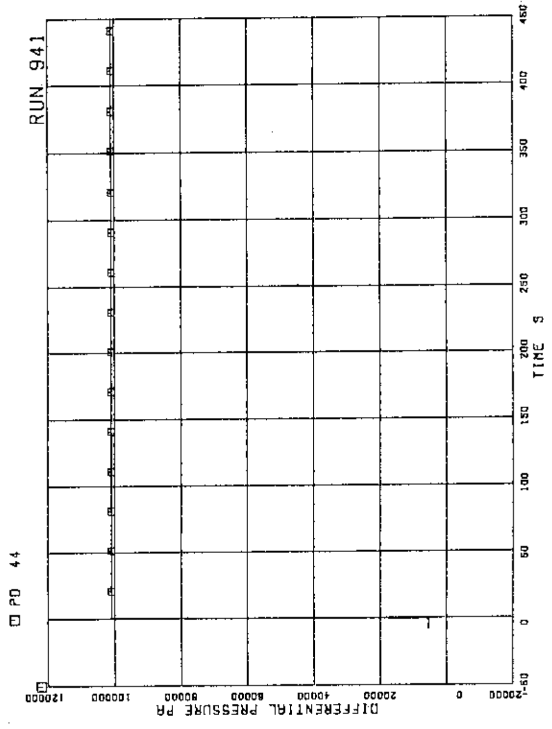

Fig.B.18 Differential pressure between breaks A and B

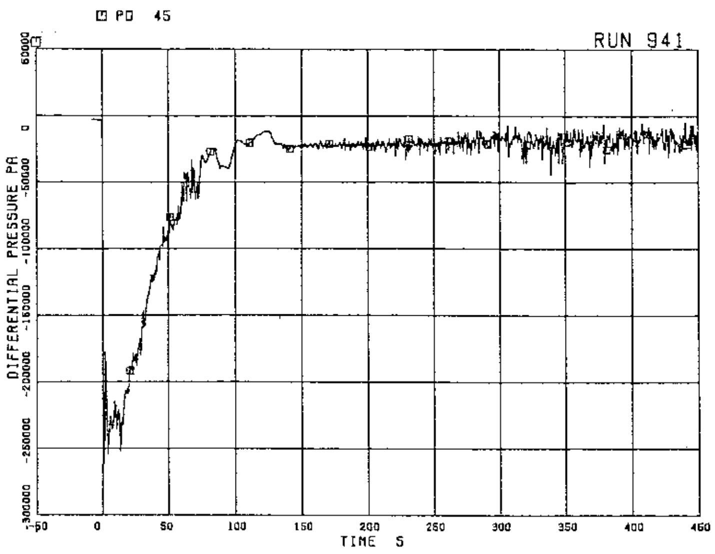

Fig.B.19 Differential pressure between break A and MRP2 suction

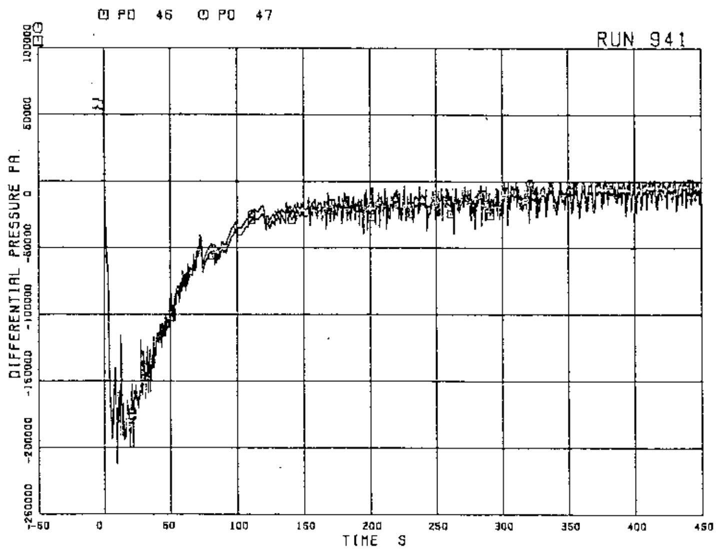

Fig.B.20 Differential pressure between MRP2 dilivery and JP-3,4 drive

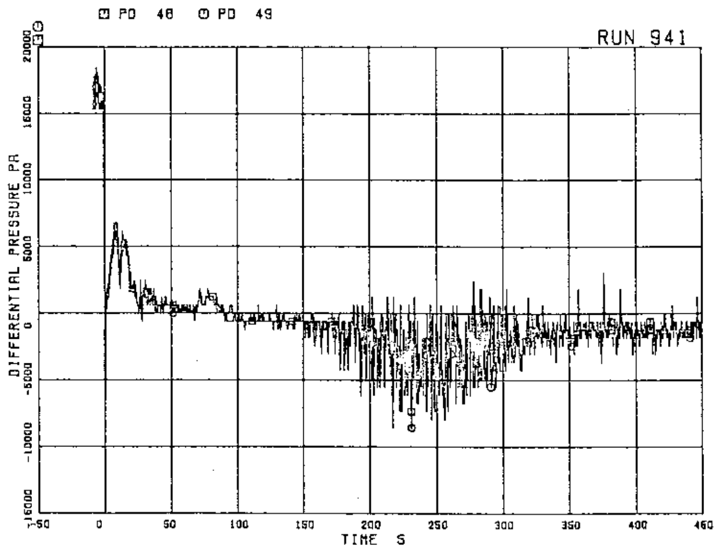

Fig.B.21 Differential pressure between downcomer middle and JP-3,4 suction

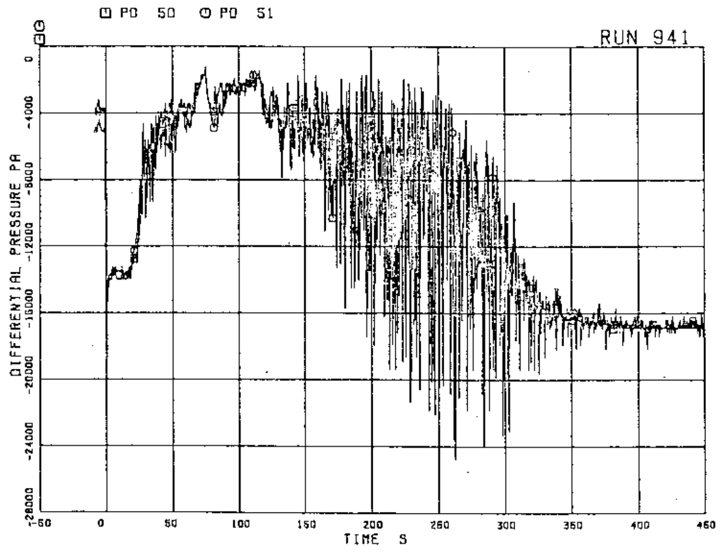

Fig.B.22 Differential pressures between JP-3,4 discharge and confluence

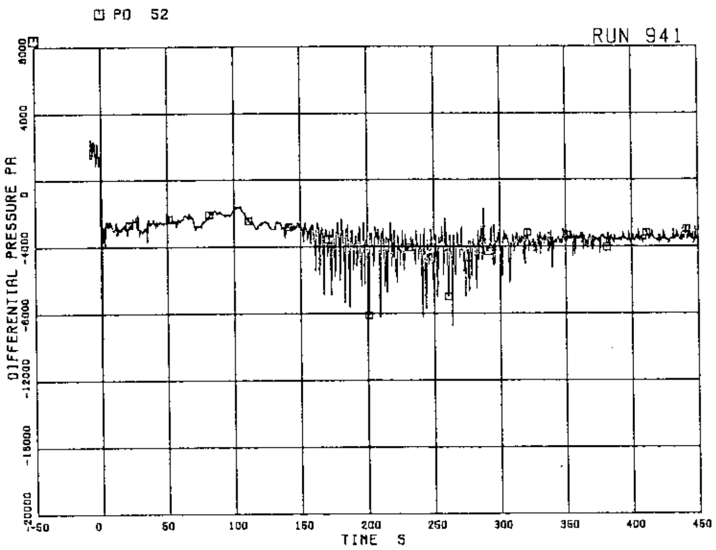

Fig.B.23 Differential pressure between JP-3,4 confluence in broken loop and LP

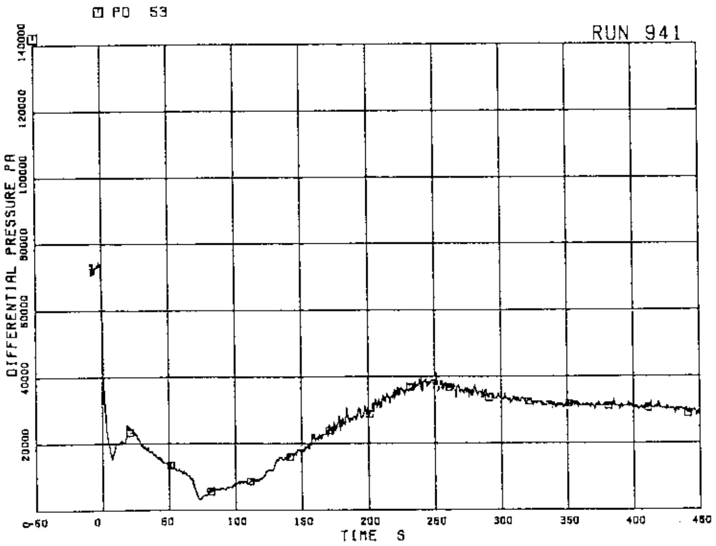

Fig.B.24 Differential pressure between lower plenum and downcomer middle

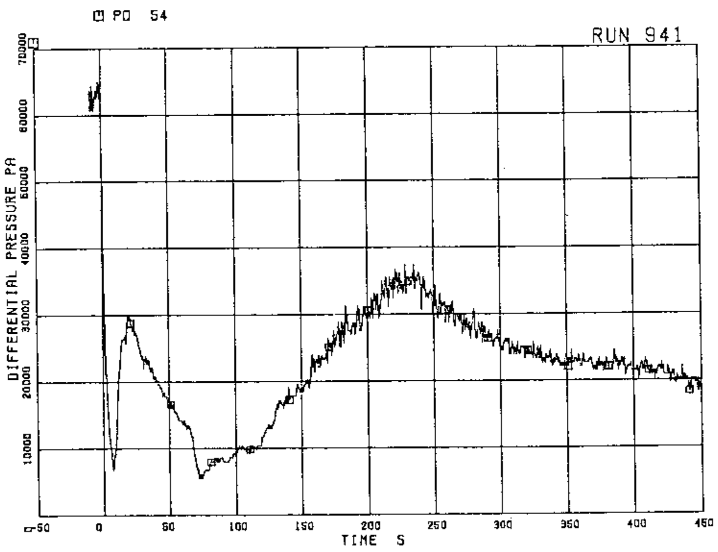

Fig.B.25 Differential pressure between lower plenum and downcomer bottom

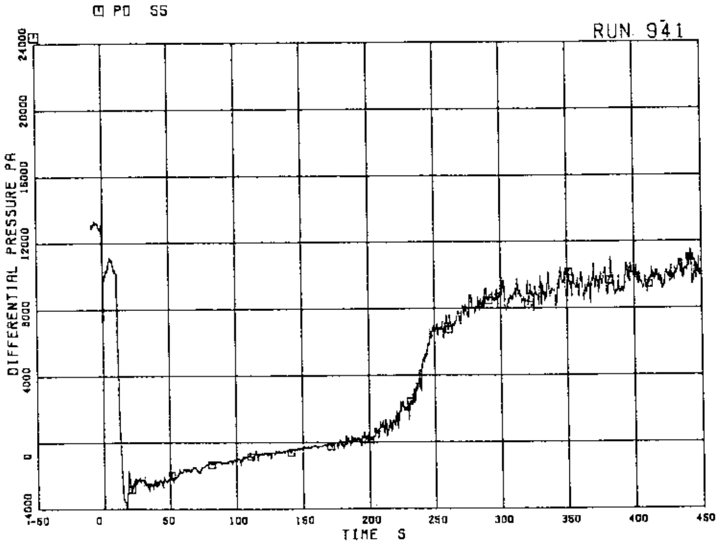

Fig.B.26 Differential pressure between downcomer bottom and downcomer middle

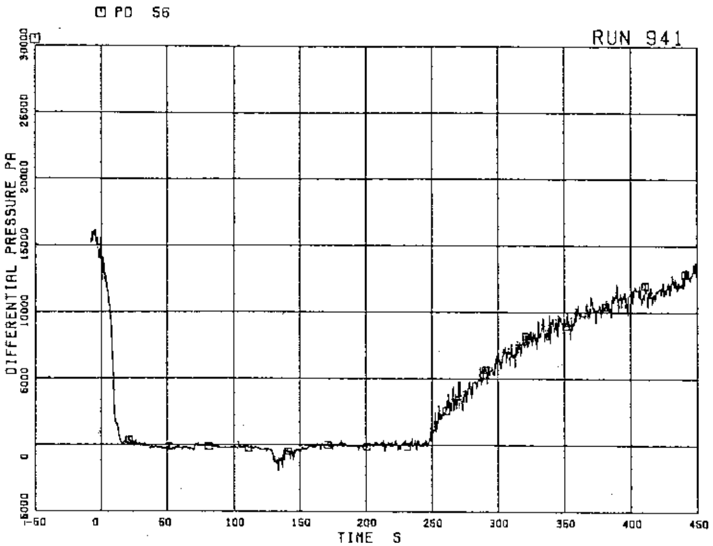

Fig.B.27 Differential pressure between downcomer middle and steam dome

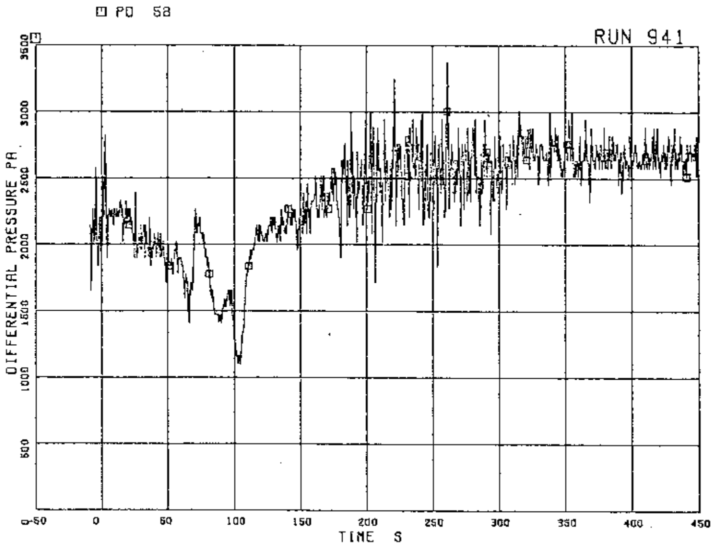

Fig.B.28 Differential pressure between LP bottom and LP middle

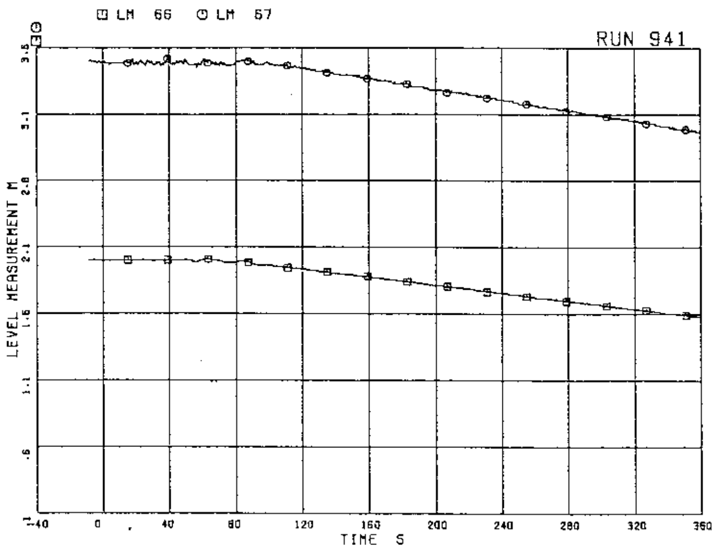

Fig.B.29 Liquid levels in ECCS tanks

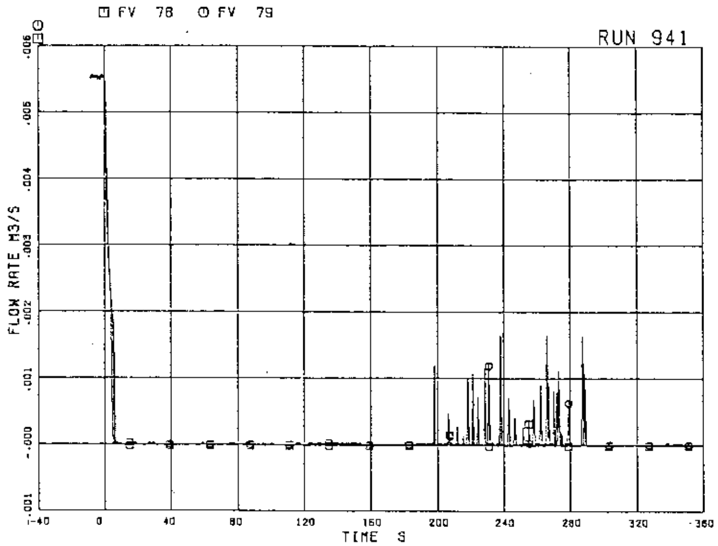

Fig.B.30 JP-1,2 discharge flow rates (pos. flow)

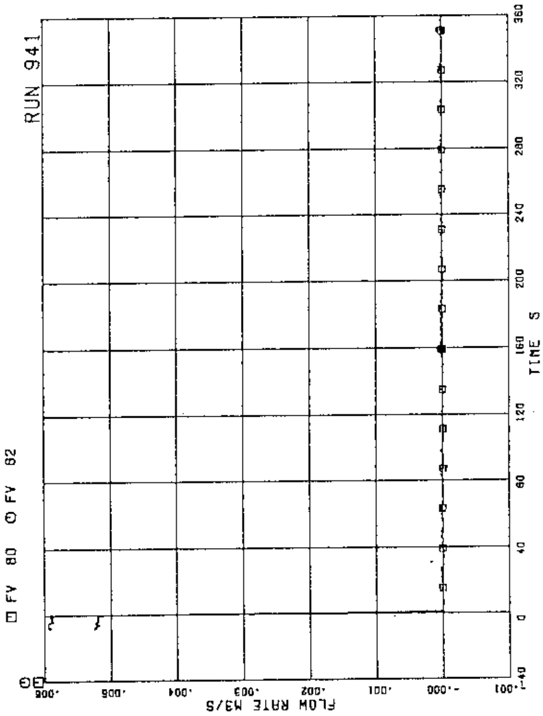

Fig.B.31 JP-3,4 discharge flow rates (pos. flow)

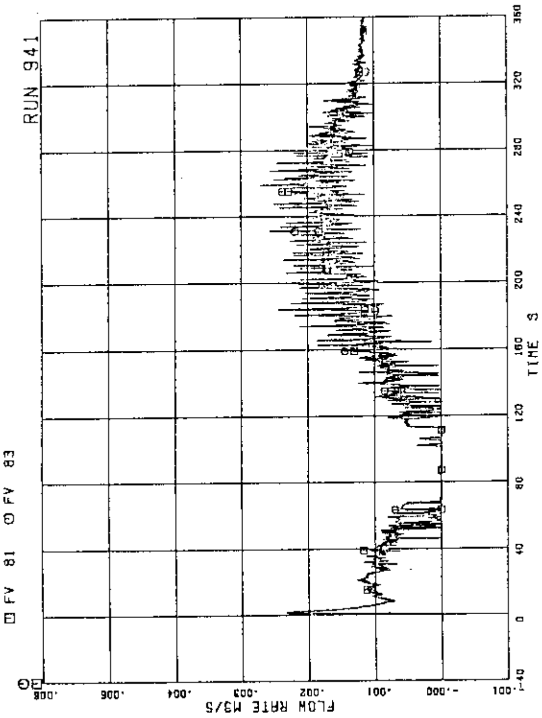

Fig.B.32 JP-3,4 discharge flow rates (neg. flow)

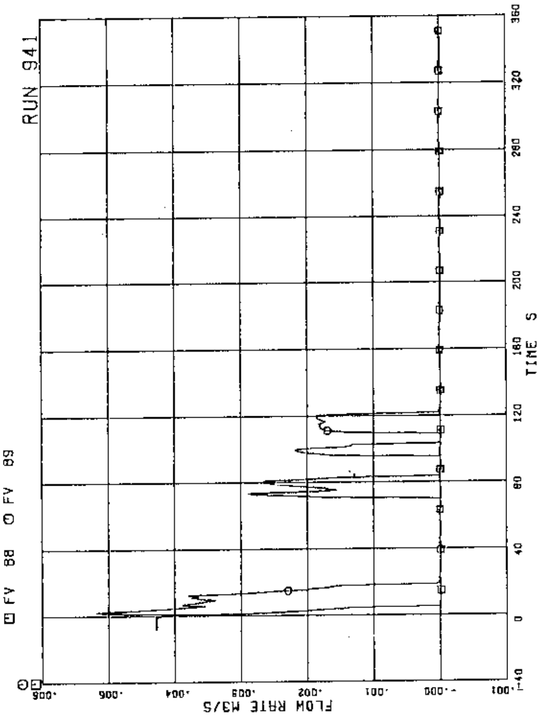

Fig.B.33 MRP discharge flow rate

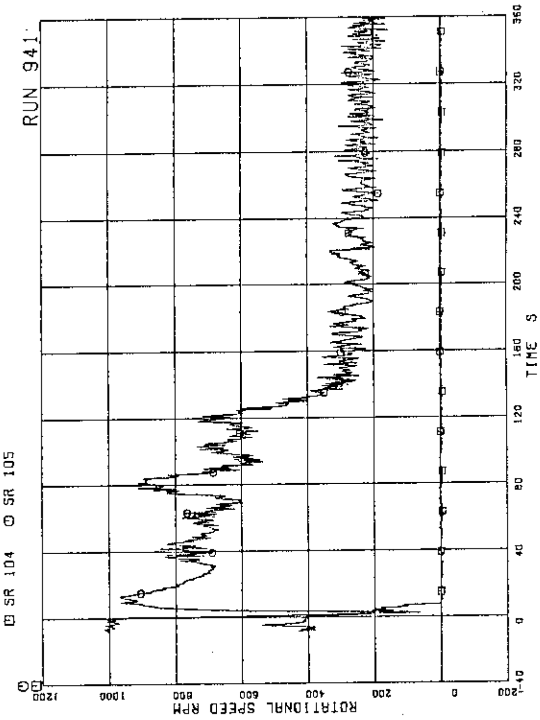

Fig.B.34 MRP pump speeds

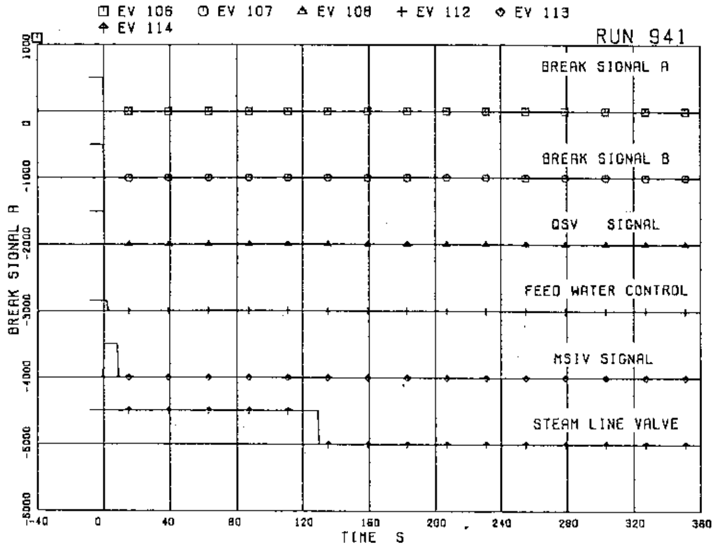

Fig.B.35 Valve operation signals

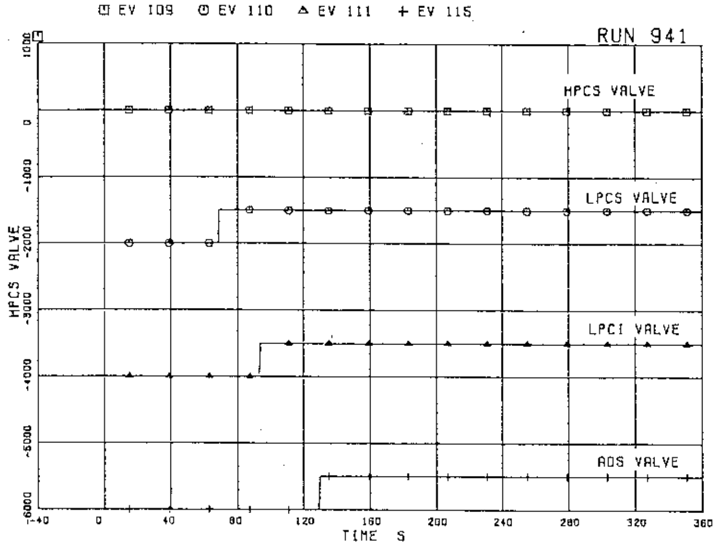

Fig.B.36 ECCS operation signals

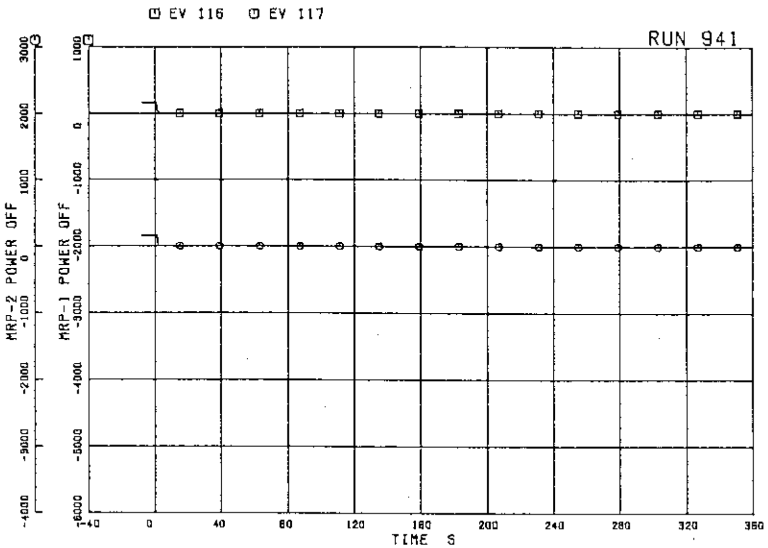

Fig.B.37 MRP operation signals

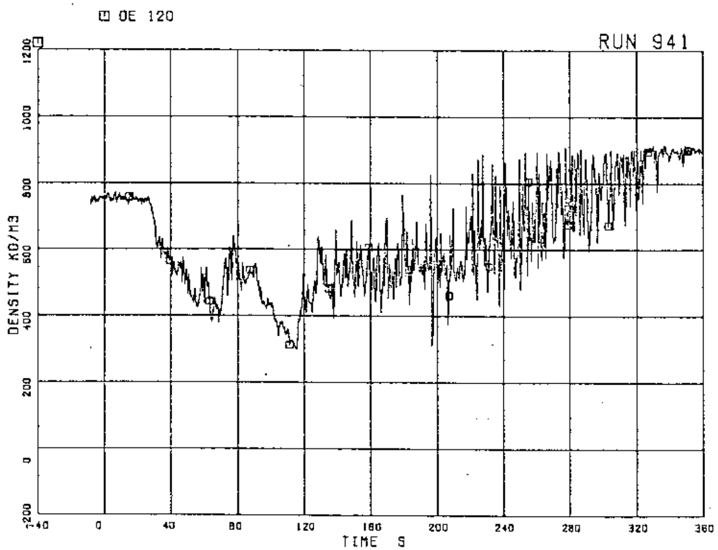

Fig.B.38 Fluid density at JP-1,2 outlet, beam A

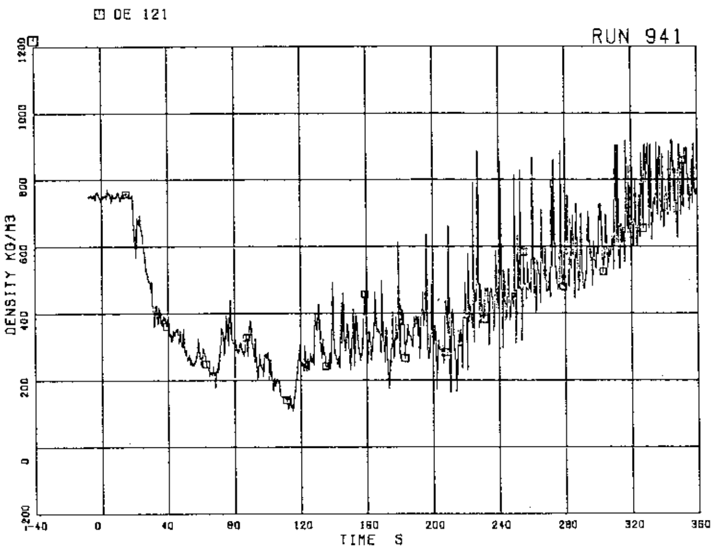

Fig.B.39　Fluid density at JP-1.2 outlet, beam B

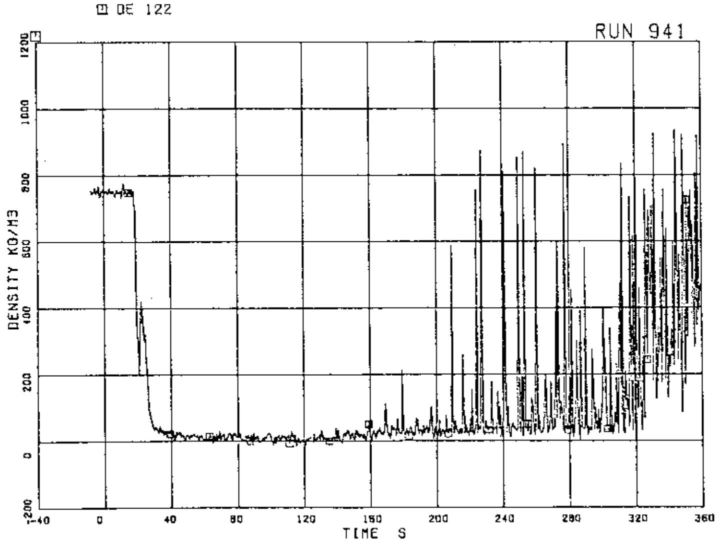

Fig.B.40　Fluid density at JP-1.2 outlet, beam C

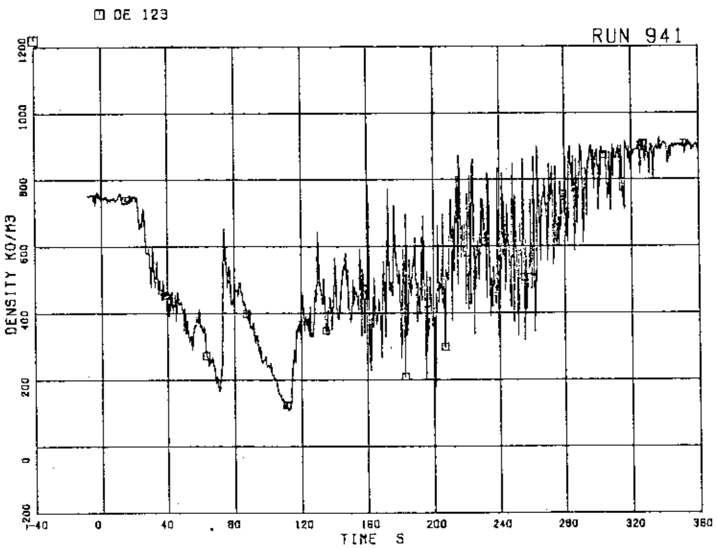

Fig.B.41　Fluid density at JP-3,4 outlet, beam A

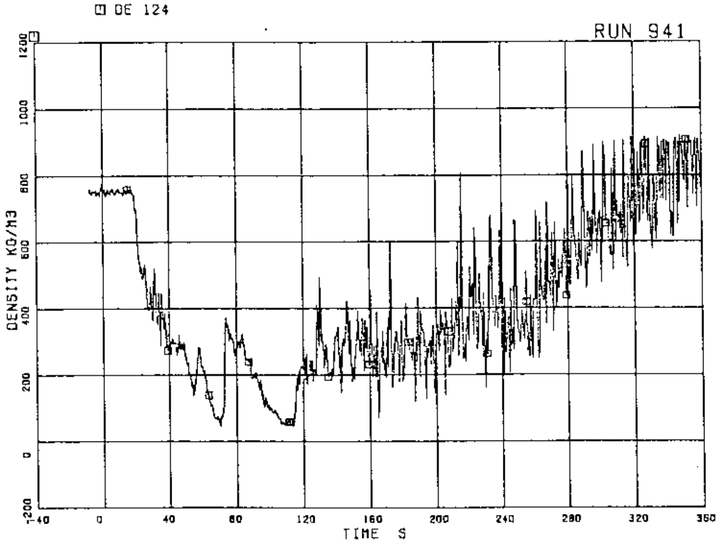

Fig.B.42　Fluid density at JP-3,4 outlet, beam B

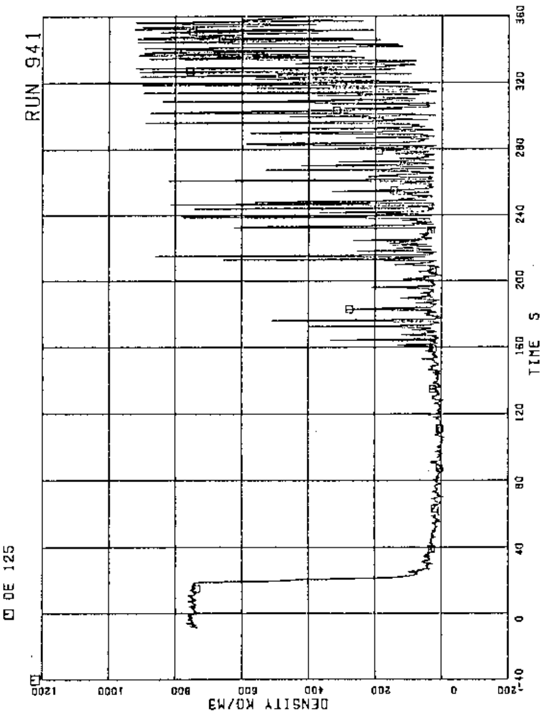

Fig.B.43 Fluid density at JP-3,4 outlet, beam C

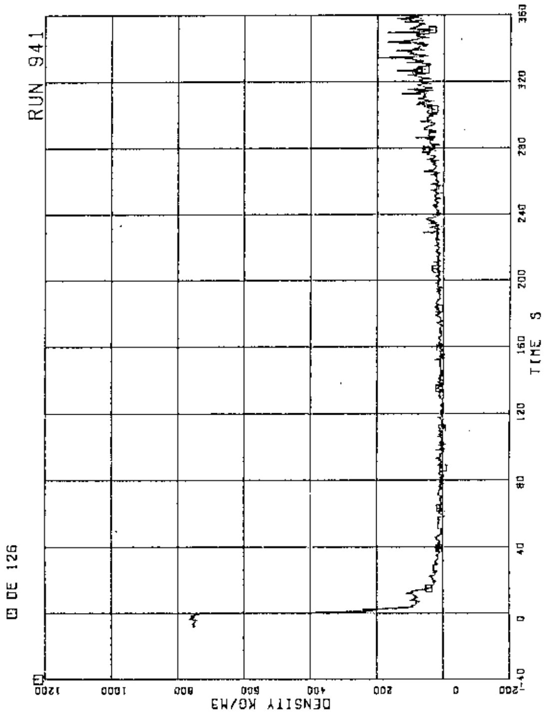

Fig.B.44 Fluid density at MRP-side of break, beam A

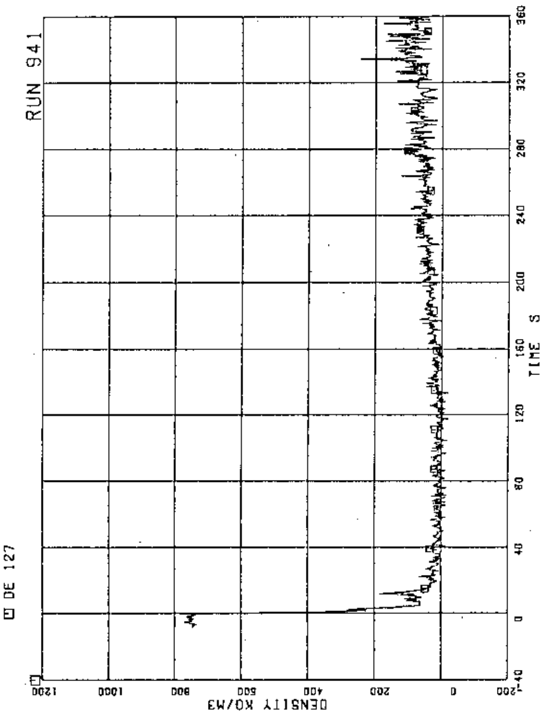

Fig.B.45 Fluid density at MRP-side of break, beam B

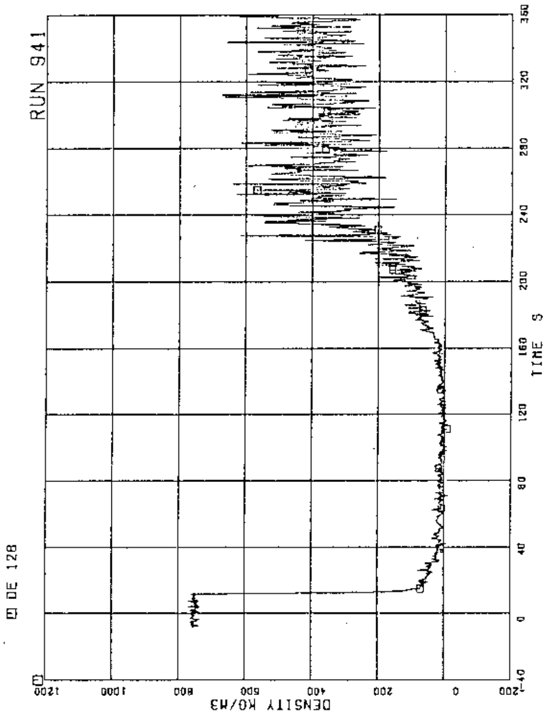

Fig.B.46 Fluid density at PV side of break, beam A

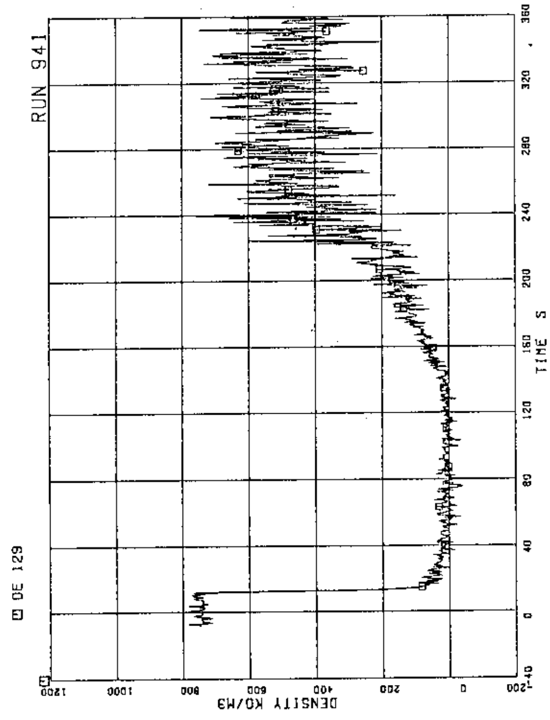

Fig.B.47 Fluid density at PV side of break, beam B

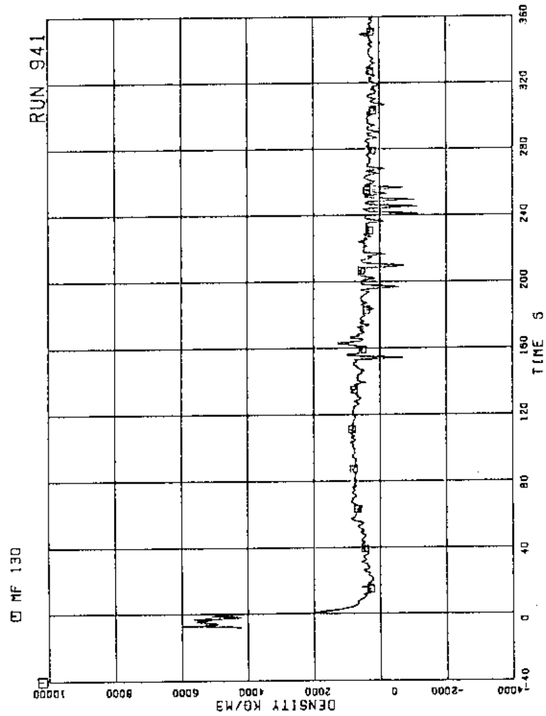

Fig.B.48 Momentum flux at JP 1,2 outlet spool

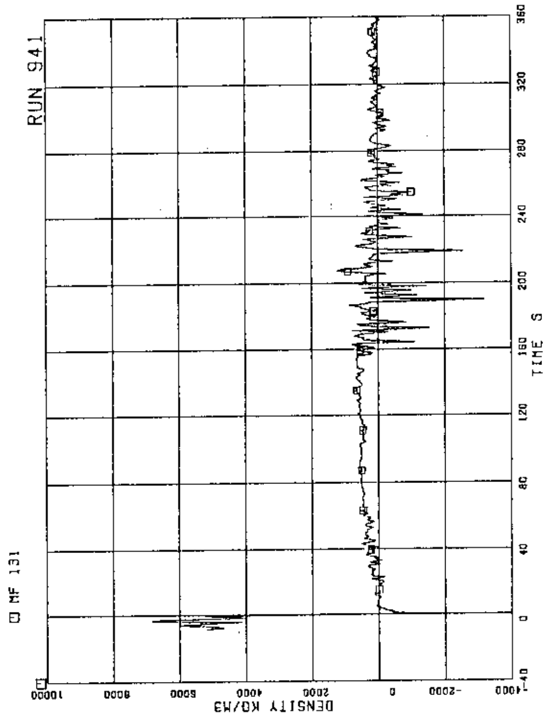

Fig.B.49 Momentum flux at JP 3,4 outlet spool

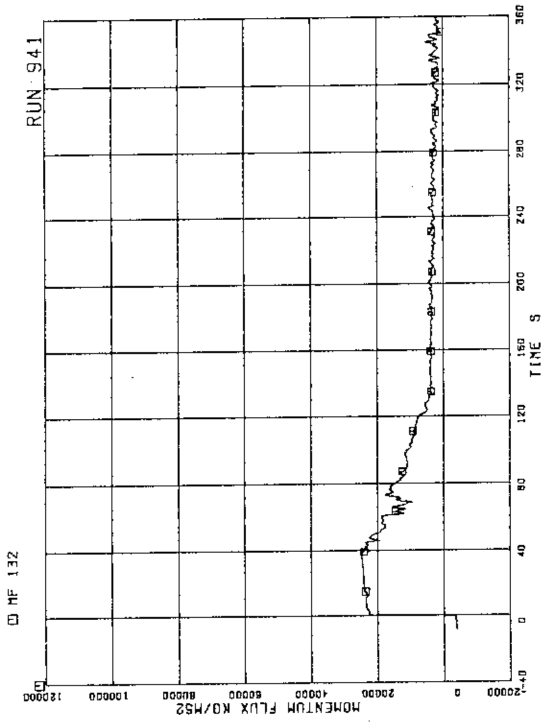

Fig.B.50 Momentum flux at break A spool piece (low range)

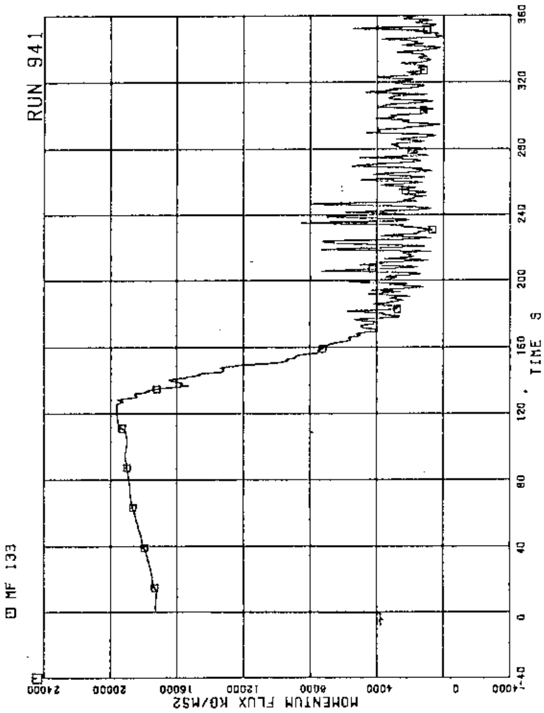

Fig.B.51 Momentum flux at break B spool piece (low range)

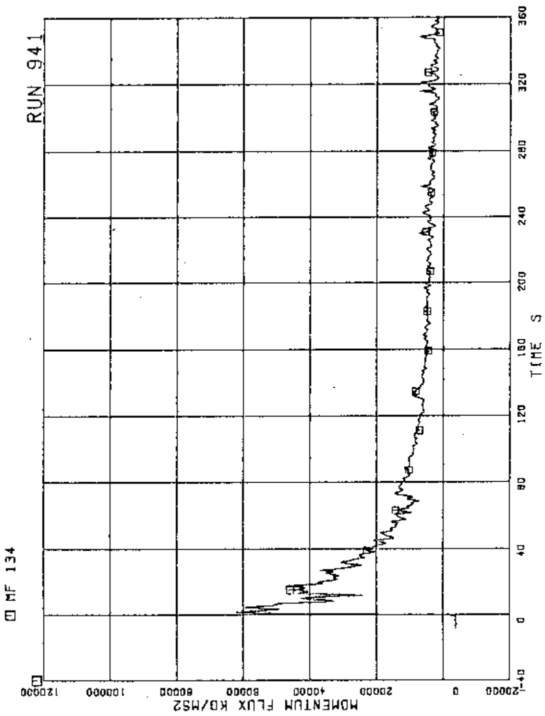

Fig.B.52 Momentum flux at break A spool piece (high range)

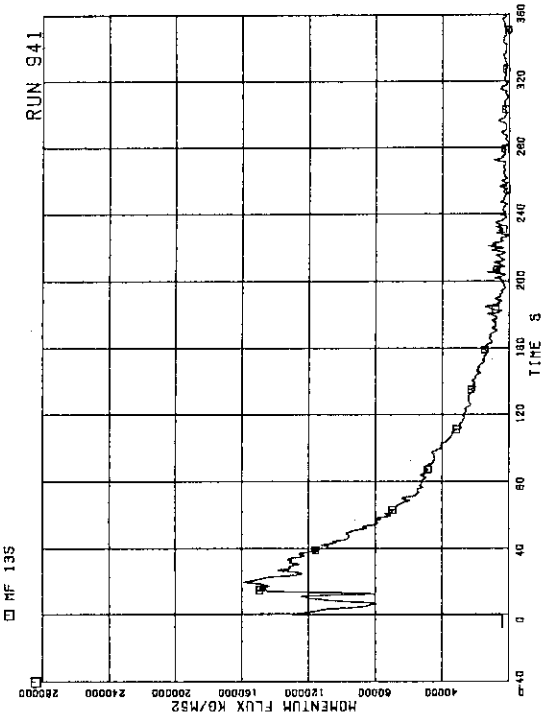

Fig.B.53 Momentum flux at break B spool piece (high range)

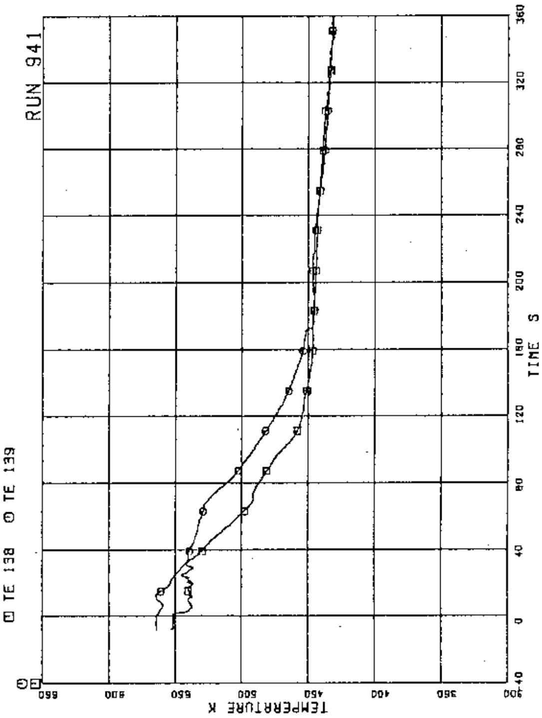

Fig.B.54 Fluid temperatures in lower plenum and upper plenum

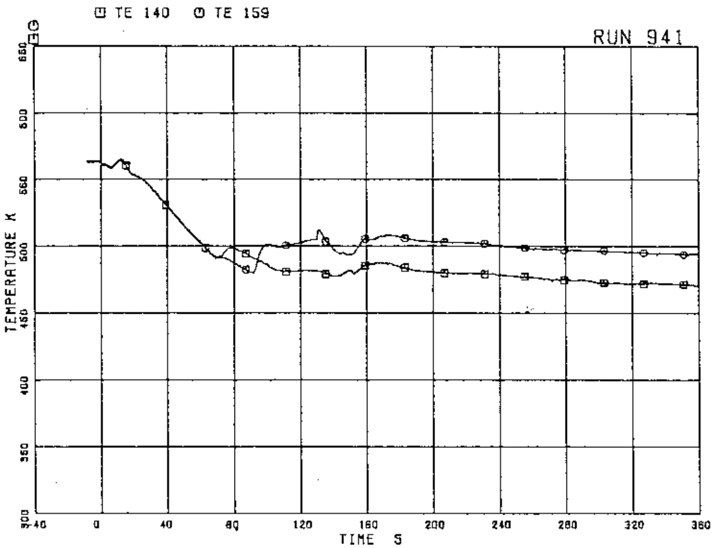

Fig.B.55 Fluid temperatures in steam dome and MSL

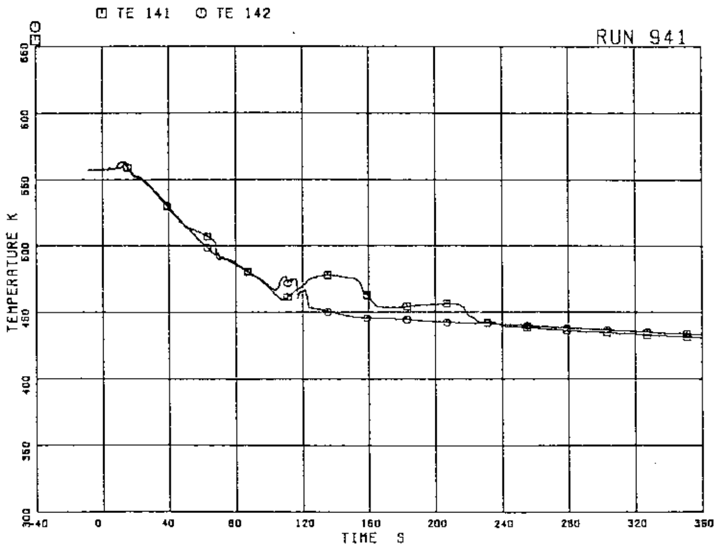

Fig.B.56 Fluid temperatures in downcomer

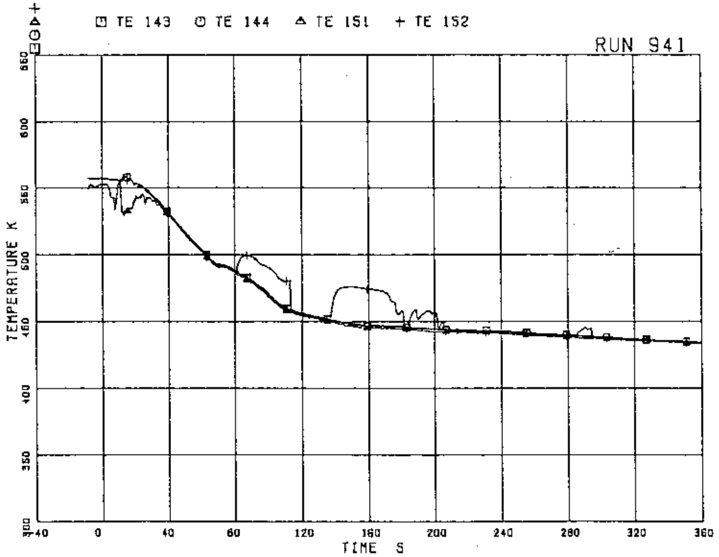

Fig.B.57 Fluid temperatures in intact recirculation loop

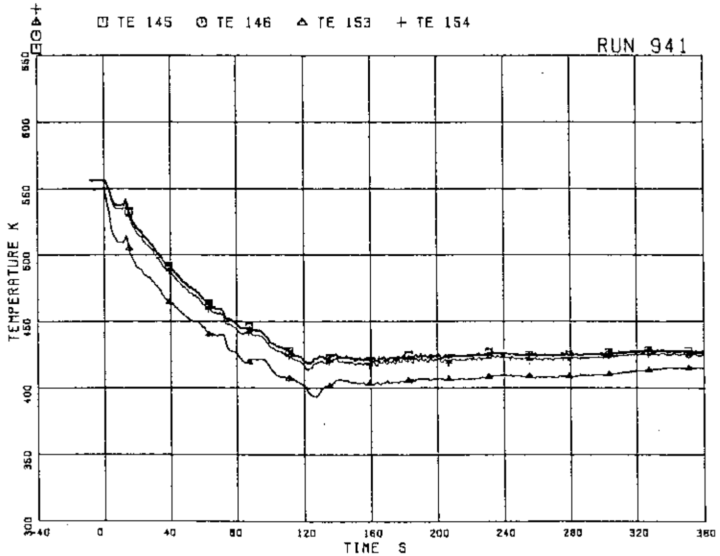

Fig.B.58 Fluid temperatures in broken recirculation loop

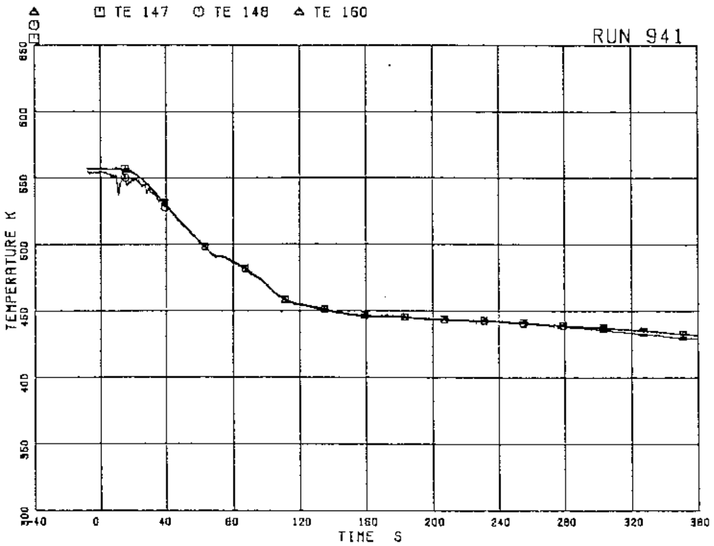

Fig.B.59　Fluid temperatures at JP 1,2 outlet

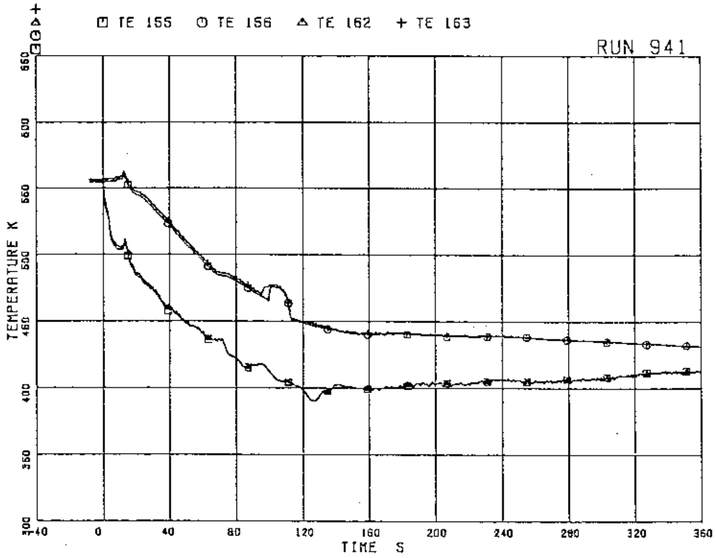

Fig.B.61　Fluid temperatures near breaks A and B

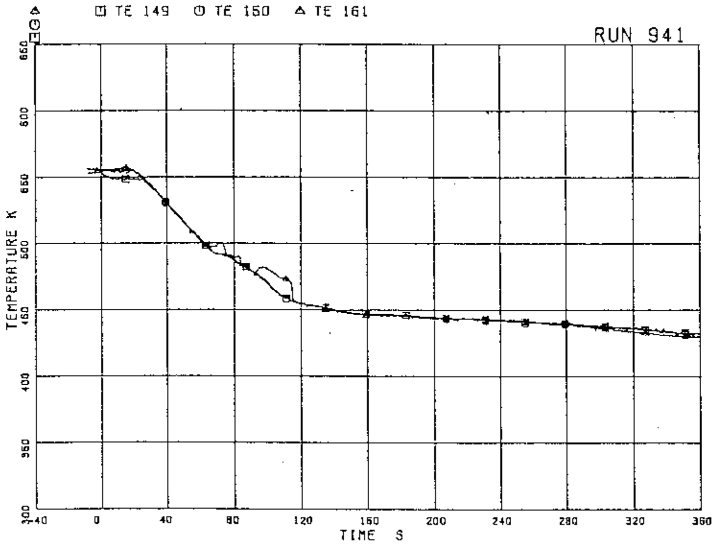

Fig.B.60　Fluid temperatures at JP 3,4 outlet

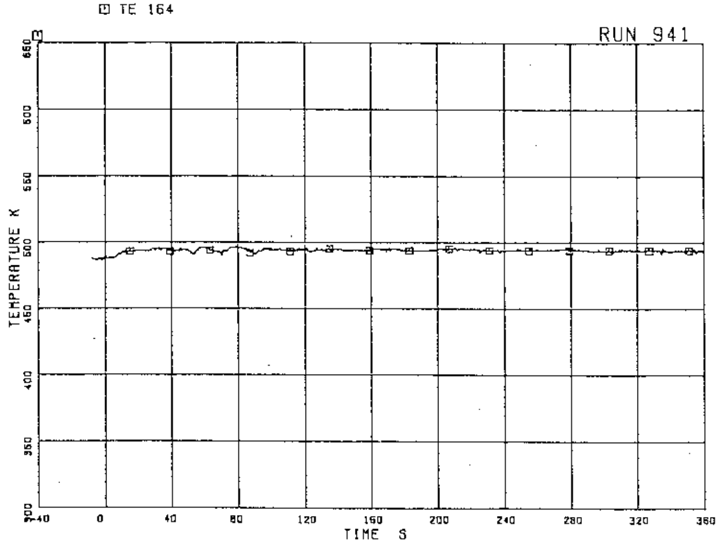

Fig.B.62　Feedwater temperature

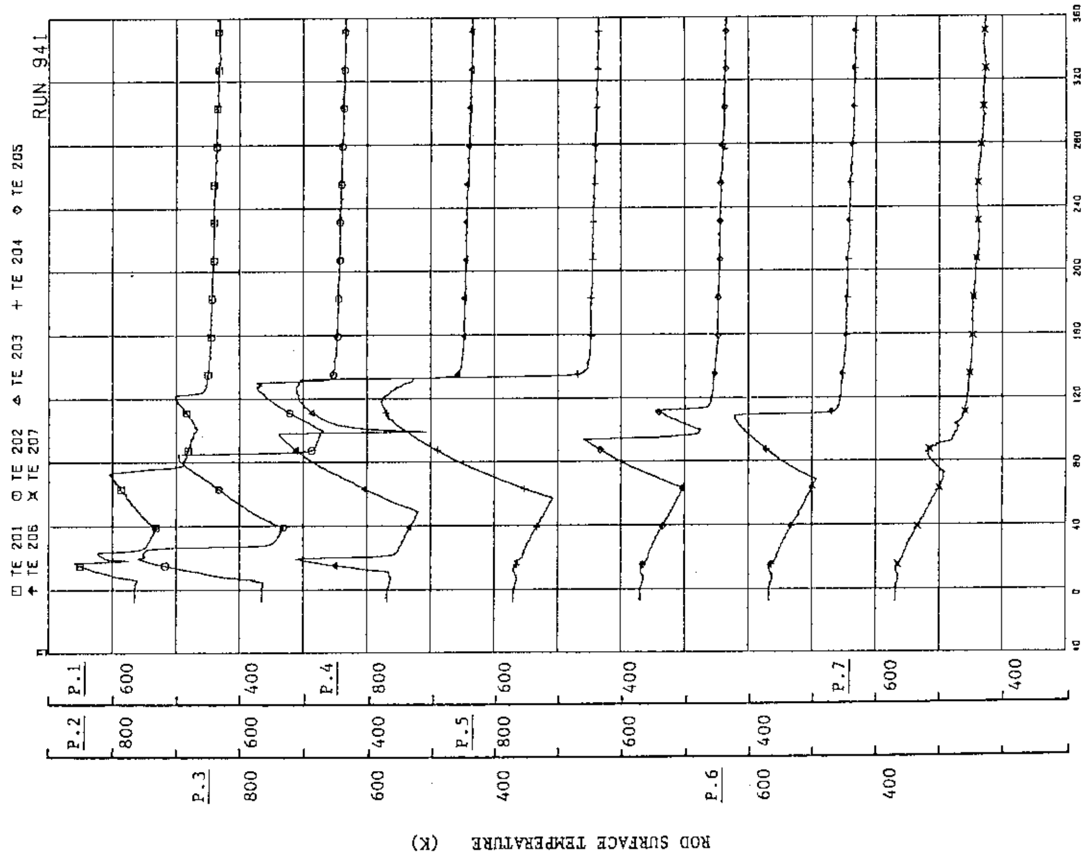

Fig.B.63 Surface temperatures of fuel rod A11

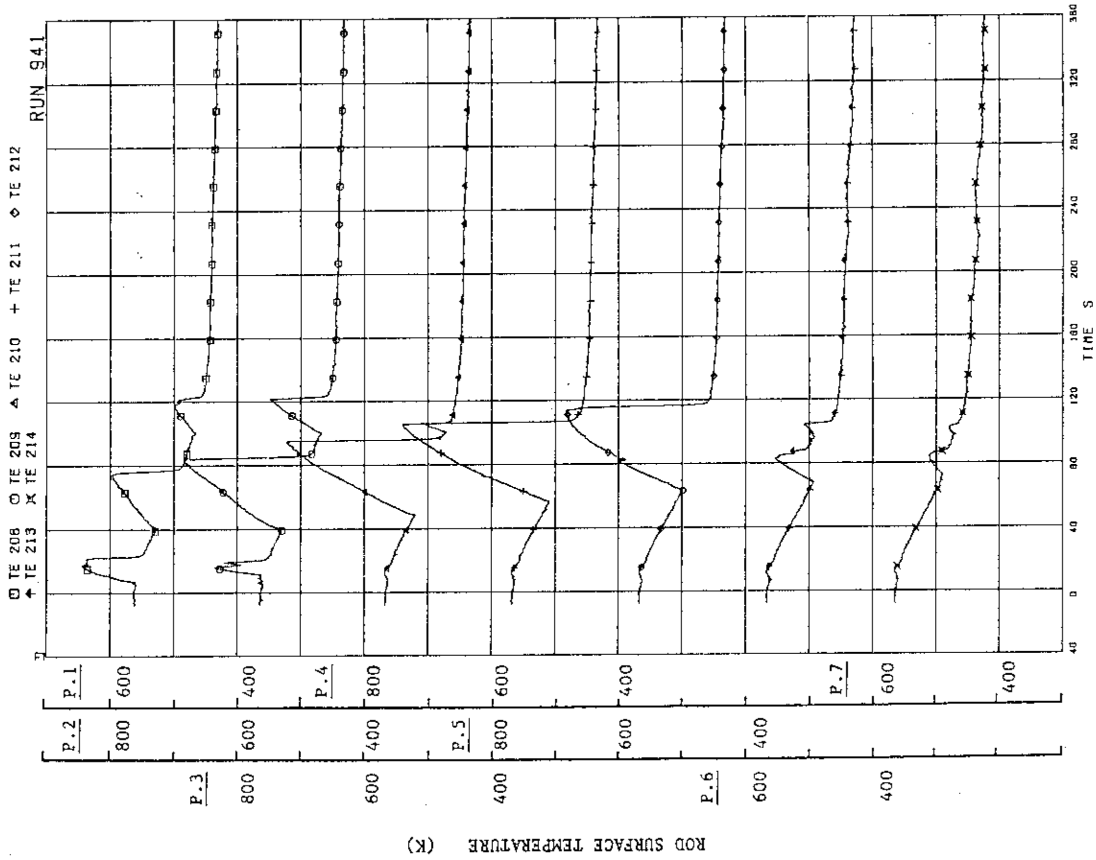

Fig.B.64 Surface temperatures of fuel rod A12

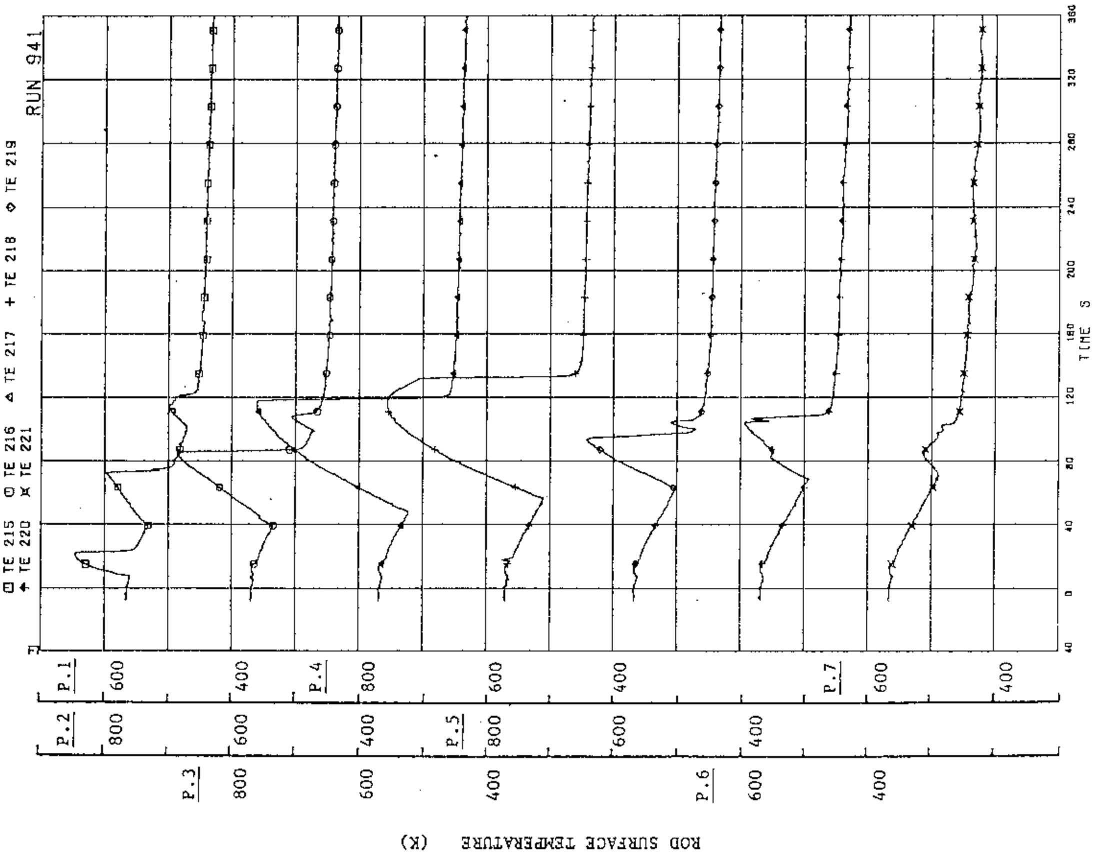

Fig.B.65 Surface temperatures of fuel rod A13

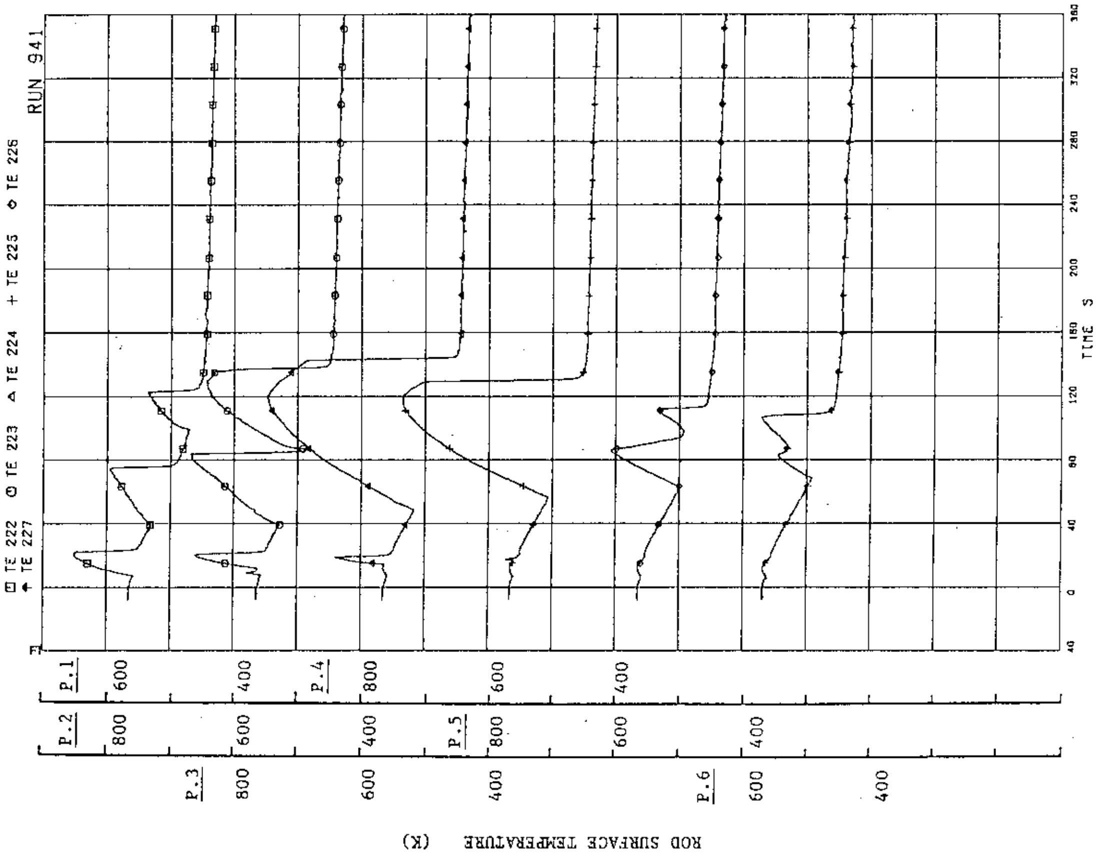

Fig.B.66 Surface temperatures of fuel rod A14

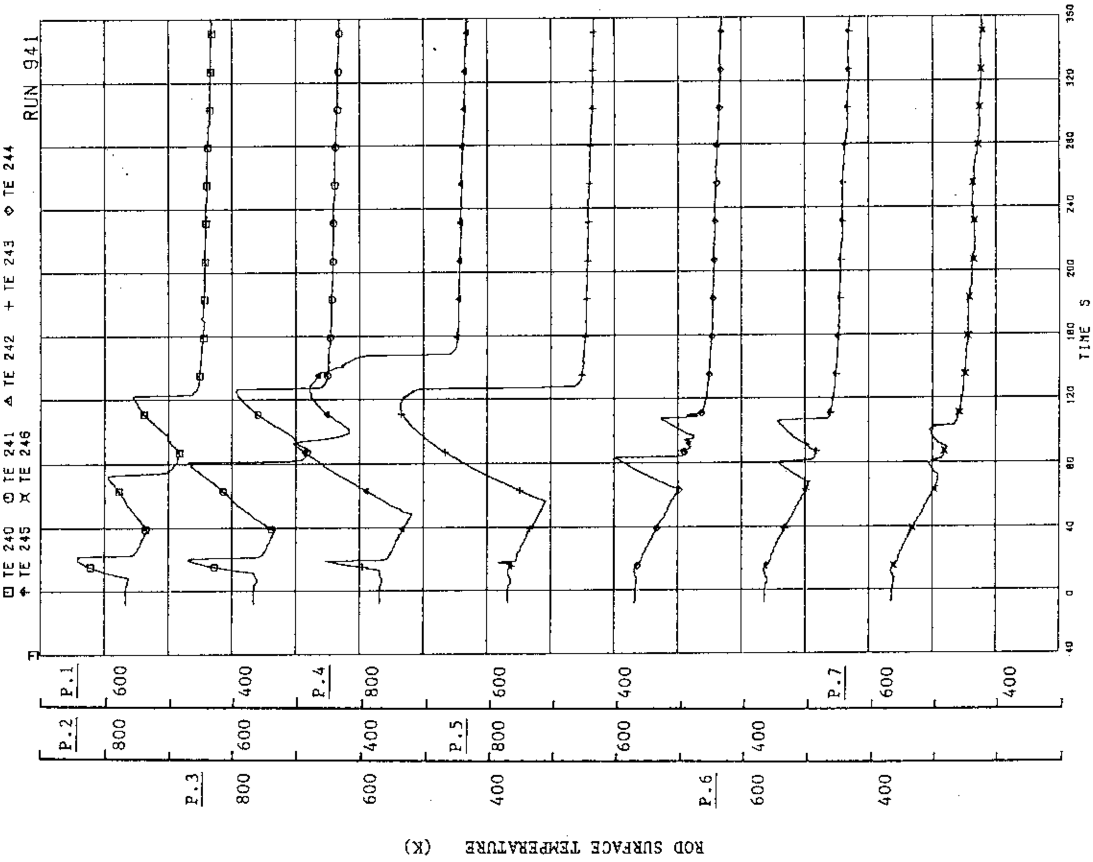

Fig.B.68 Surface temperatures of fuel rod A24

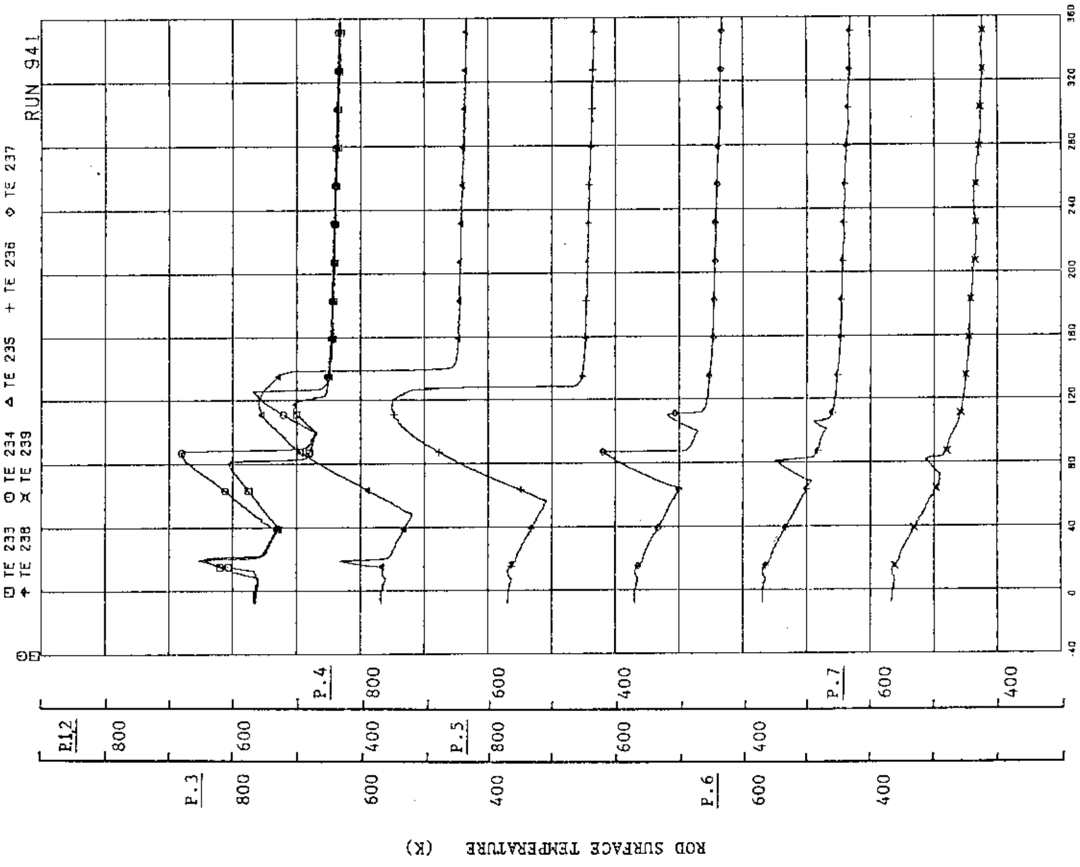

Fig.B.67 Surface temperatures of fuel rod A22

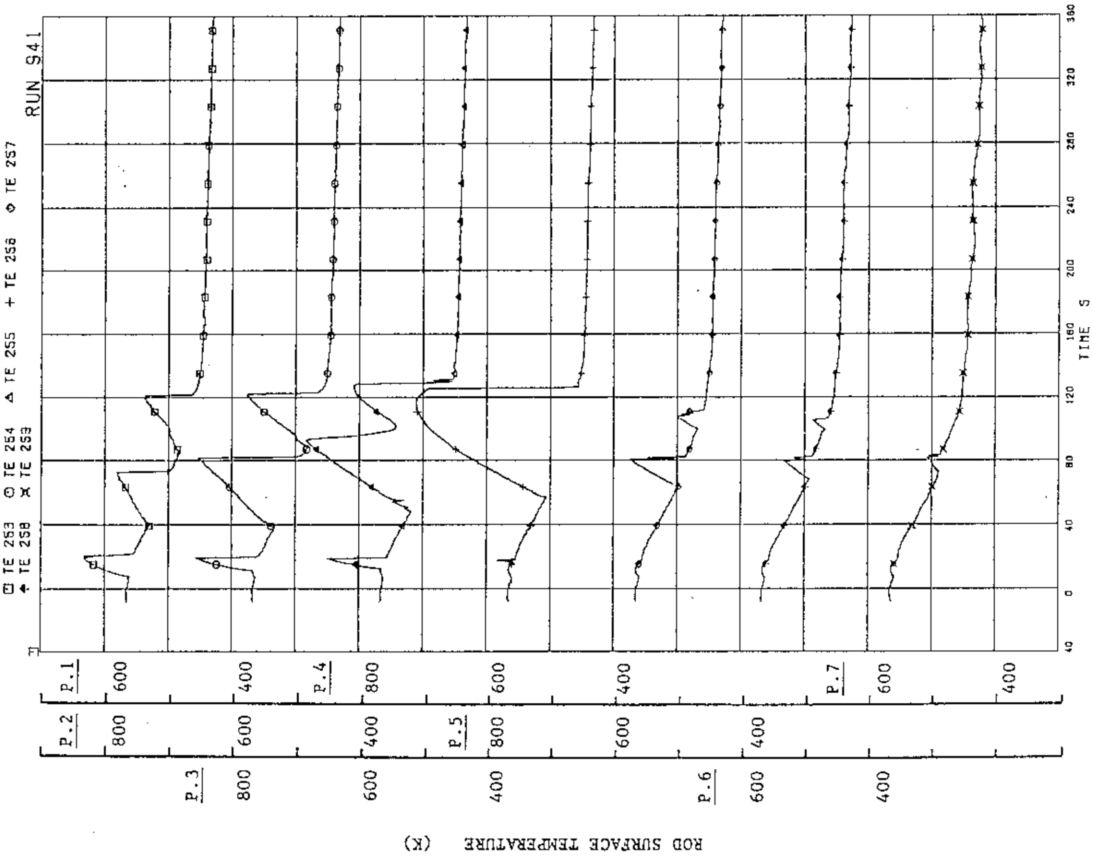

Fig.B.69 Surface temperatures of fuel rod A33

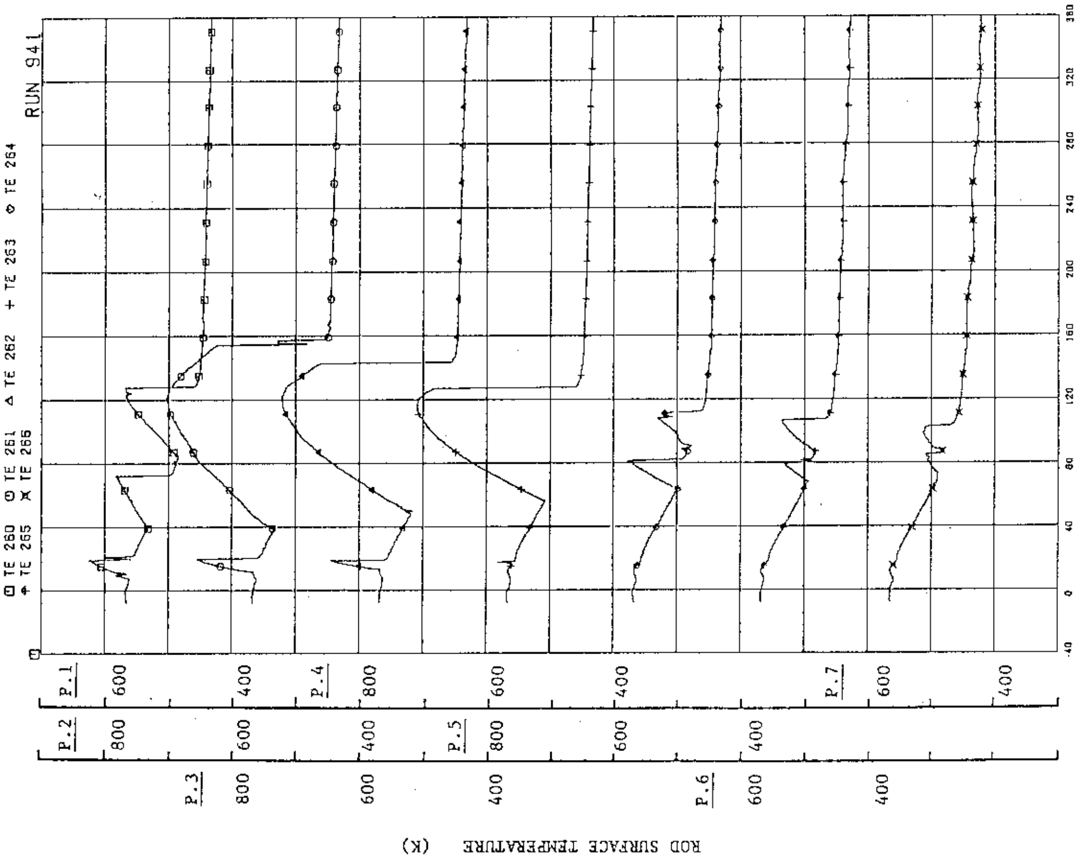

Fig.B.70 Surface temperatures of fuel rod A34

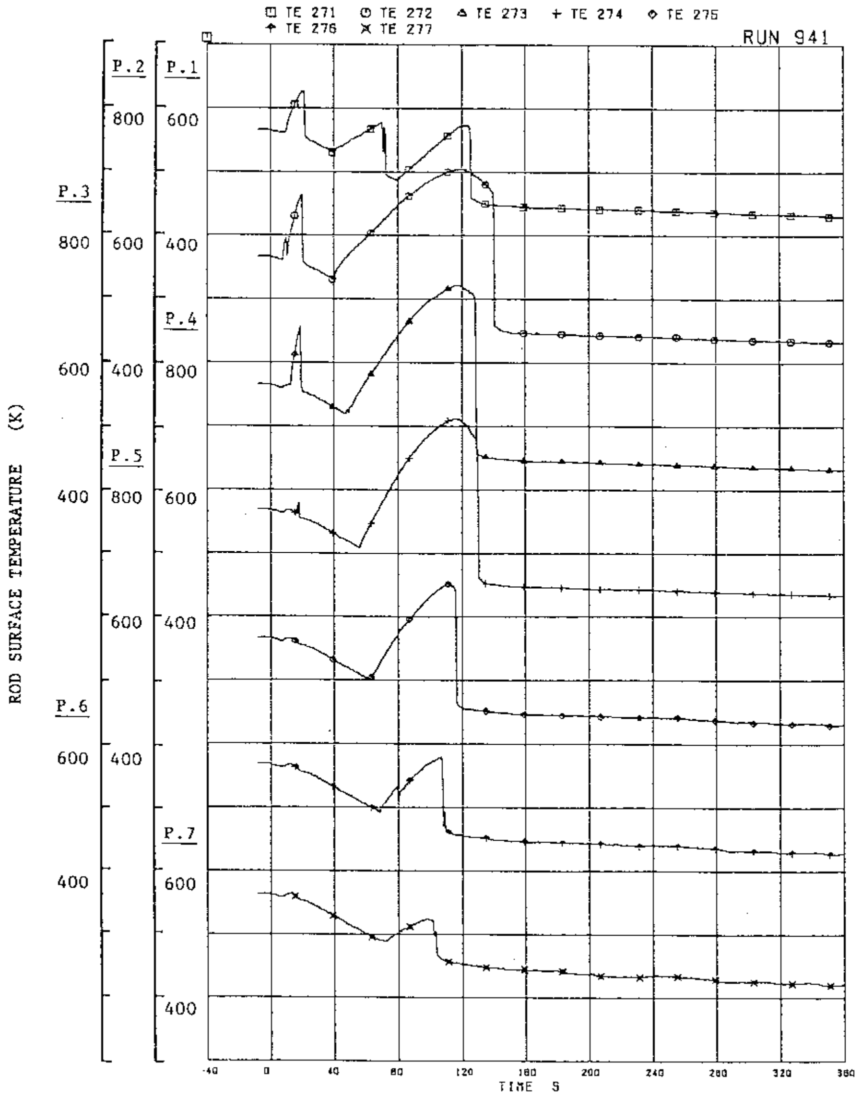

Fig.B.71 Surface temperatures of fuel rod A44

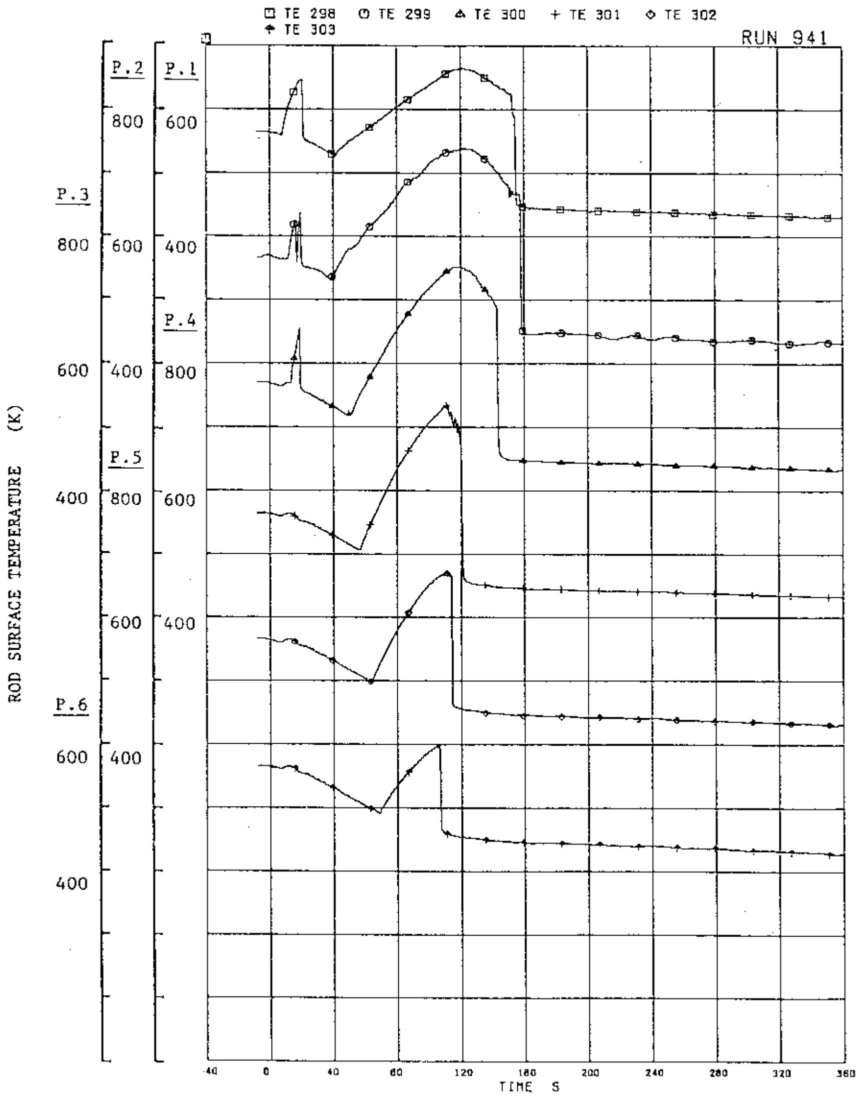

Fig.B.72 Surface temperatures of fuel rod A77

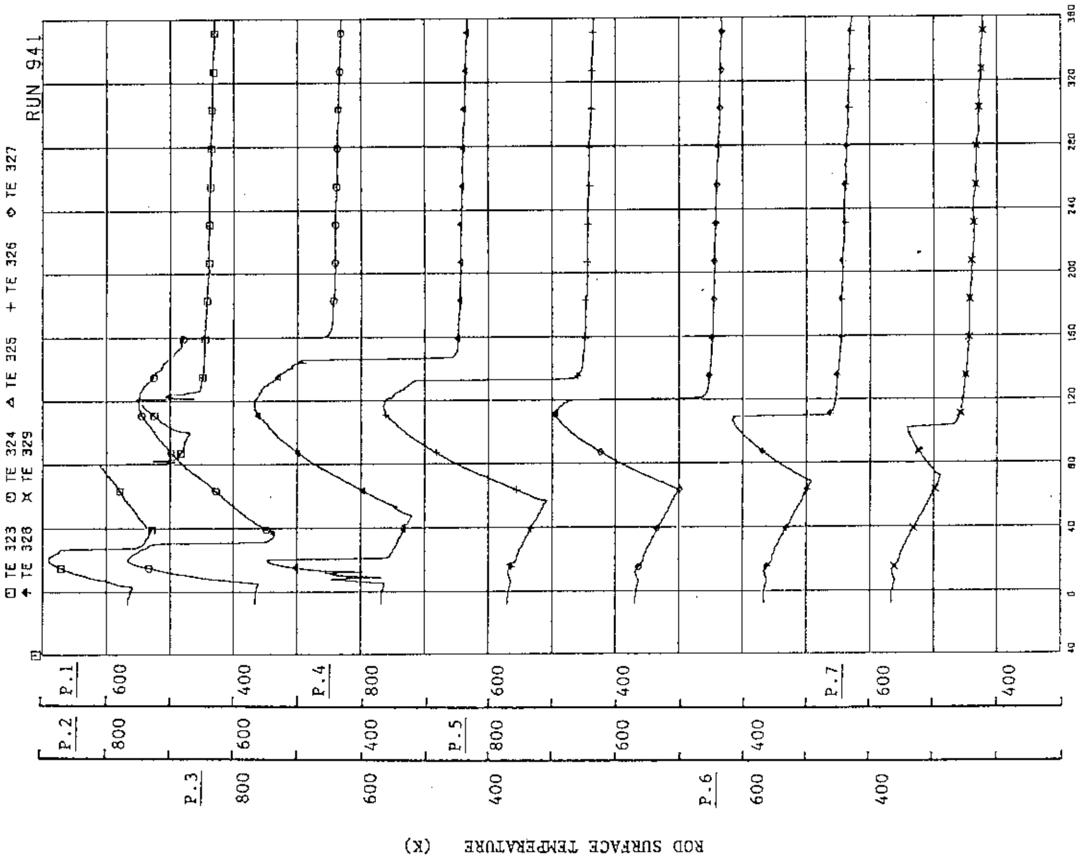

Fig.B.73 Surface temperatures of fuel rod A88

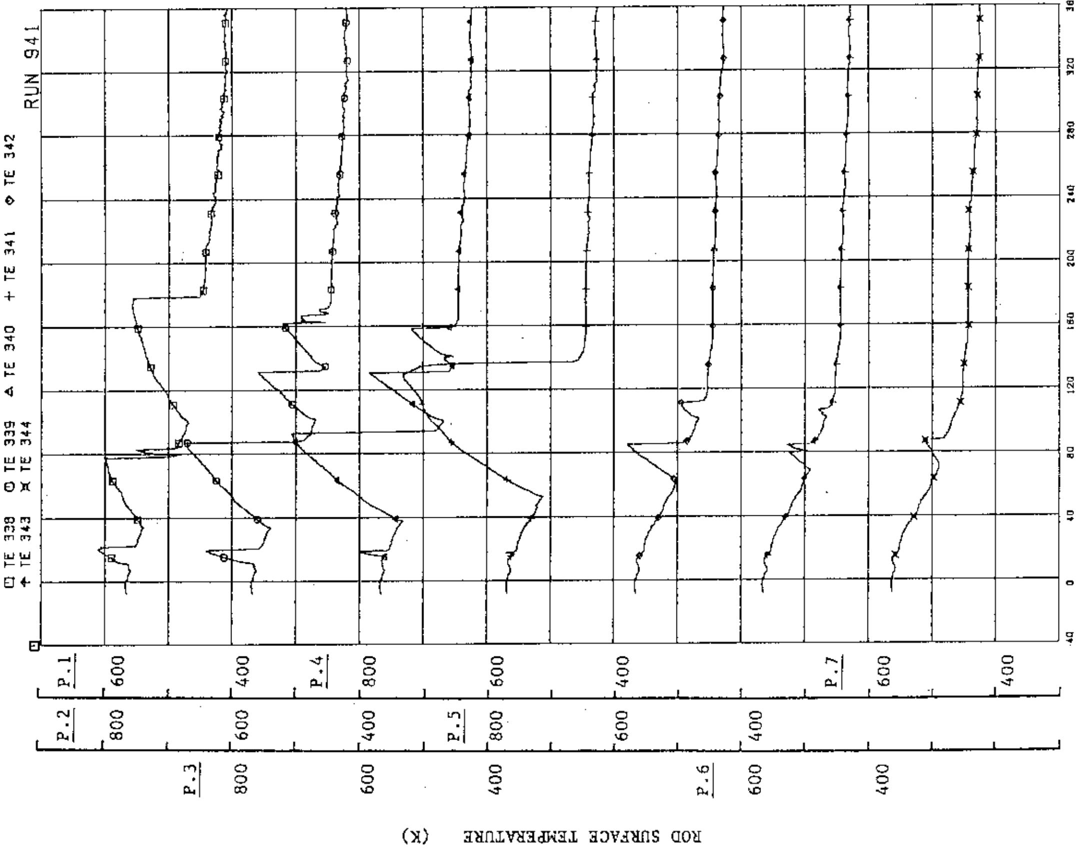

Fig.B.74 Surface temperatures of fuel rod B22

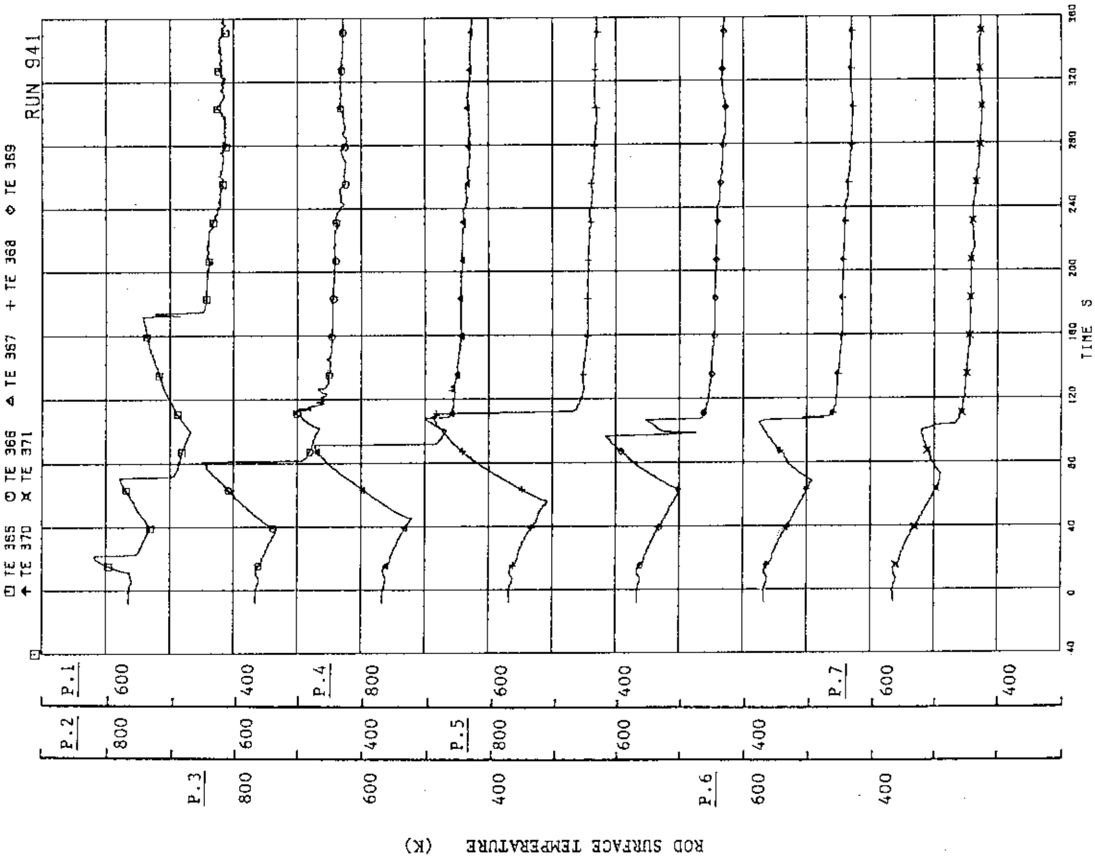

Fig.B.76 Surface temperatures of fuel rod C13

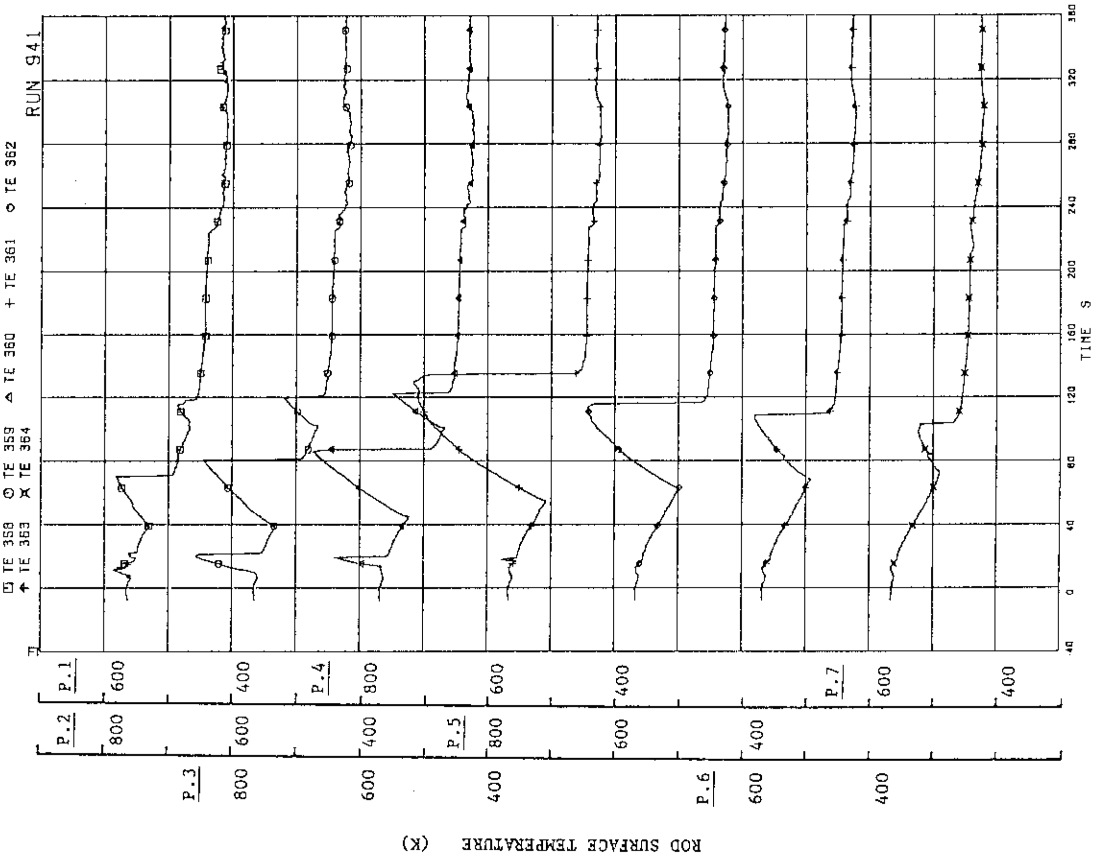

Fig.B.75 Surface temperatures of fuel rod C11

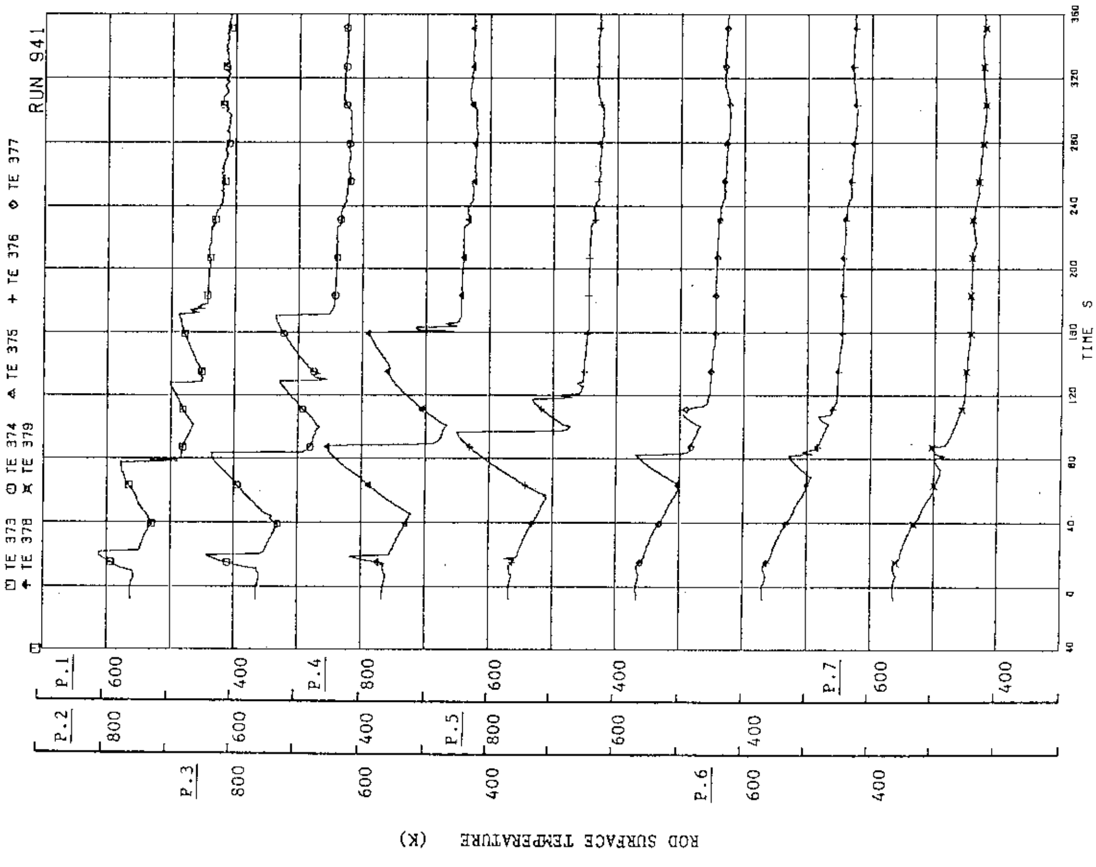

Fig.B.77 Surface temperatures of fuel rod C22

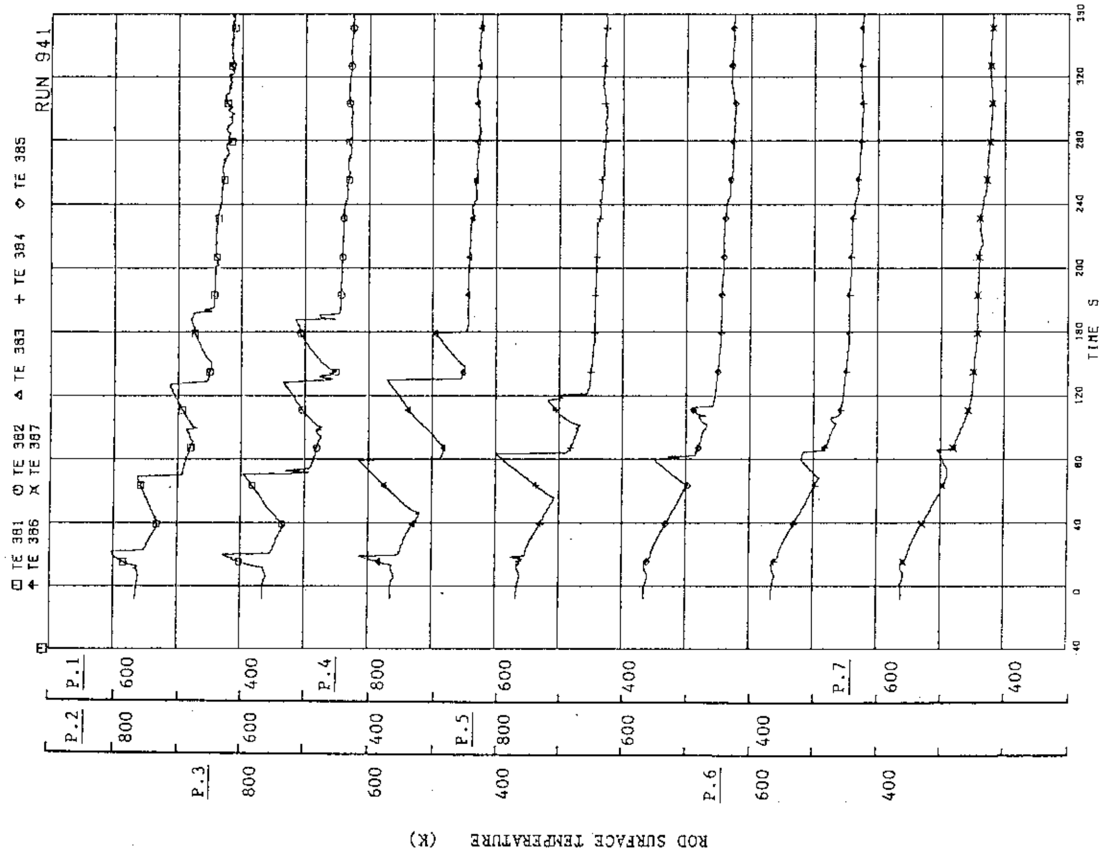

Fig.B.78 Surface temperatures of fuel rod C33

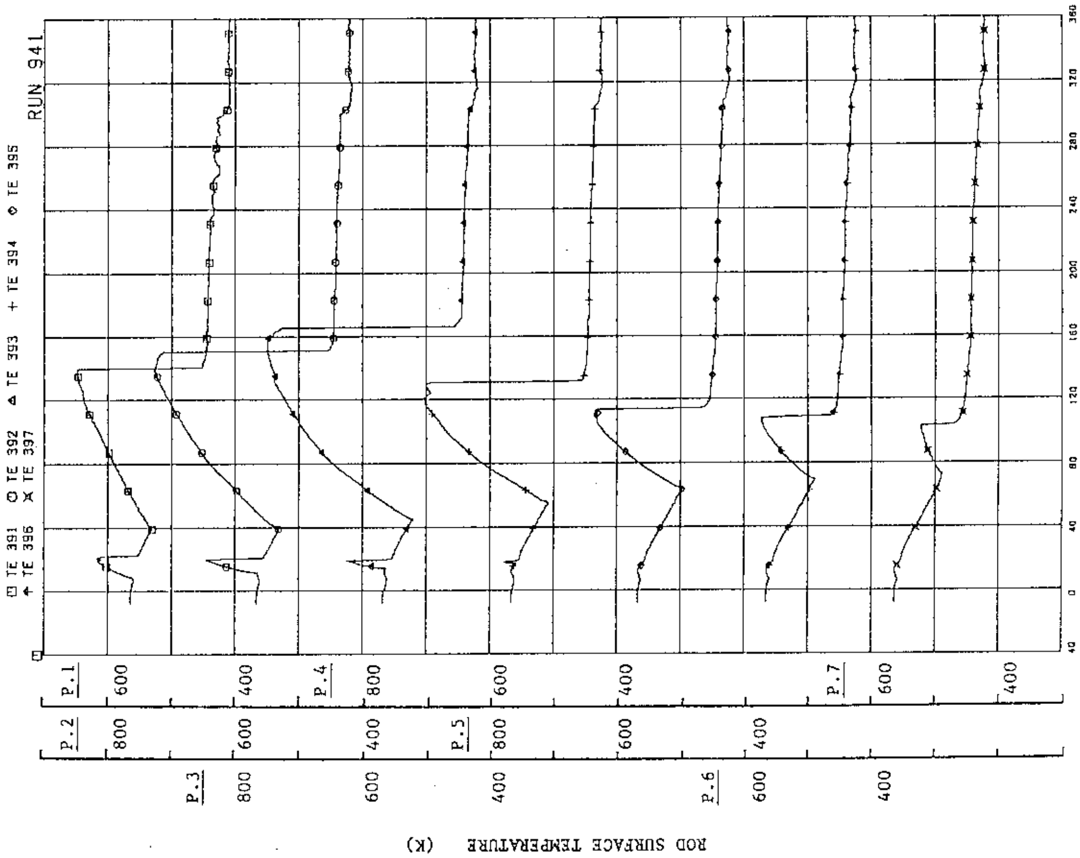

Fig.B.79 Surface temperatures of fuel rod C77

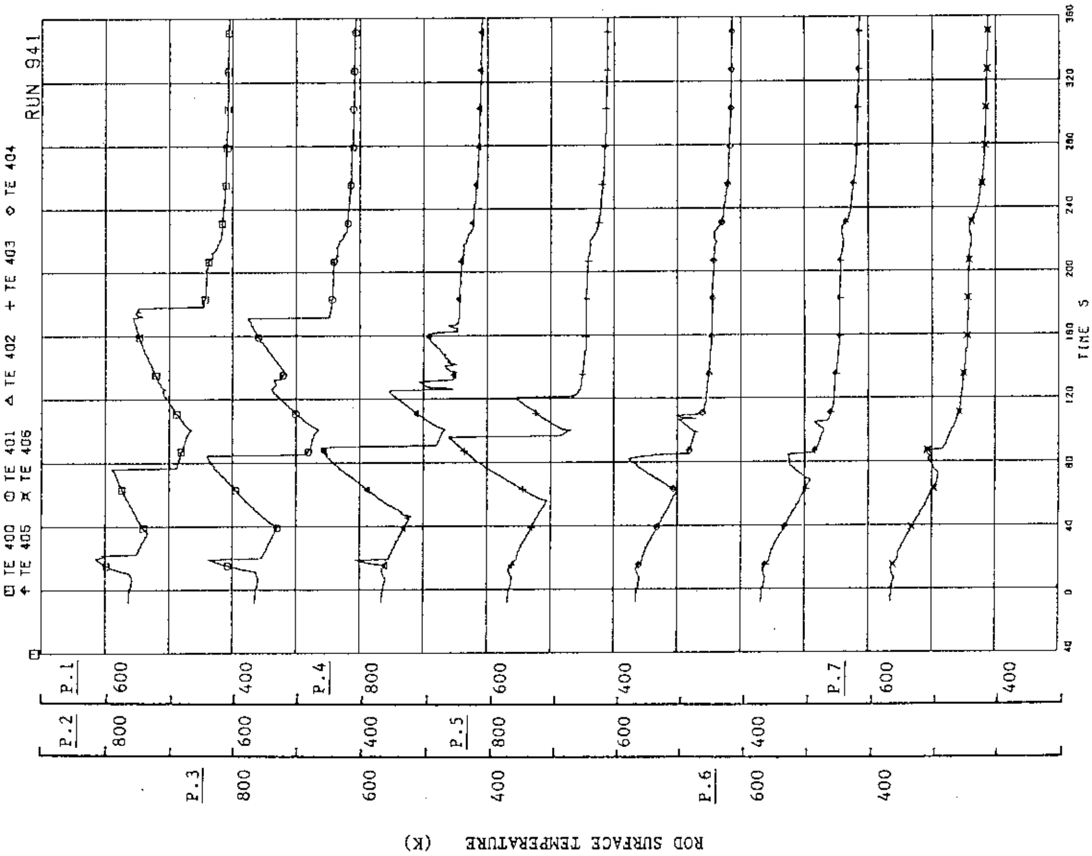

Fig.B.80 Surface temperatures of fuel rod D22

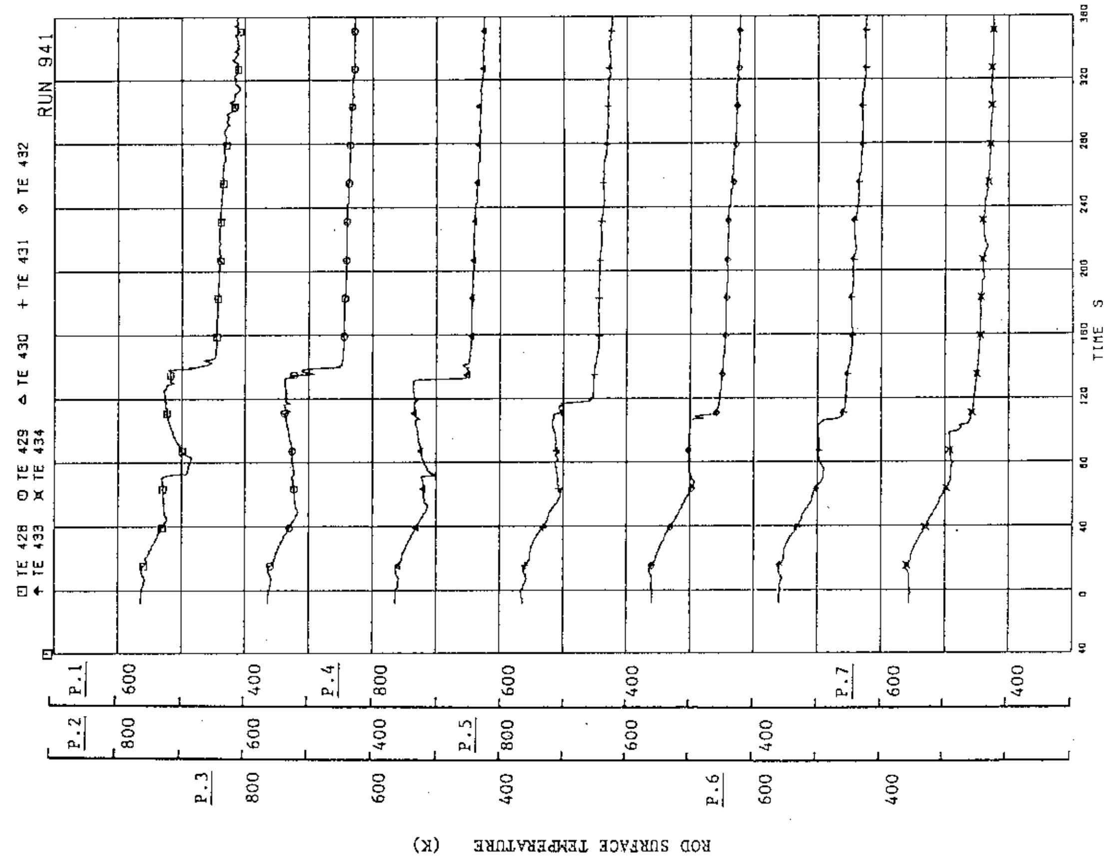

Fig.B.82 Surface temperatures of water rod simulator C45

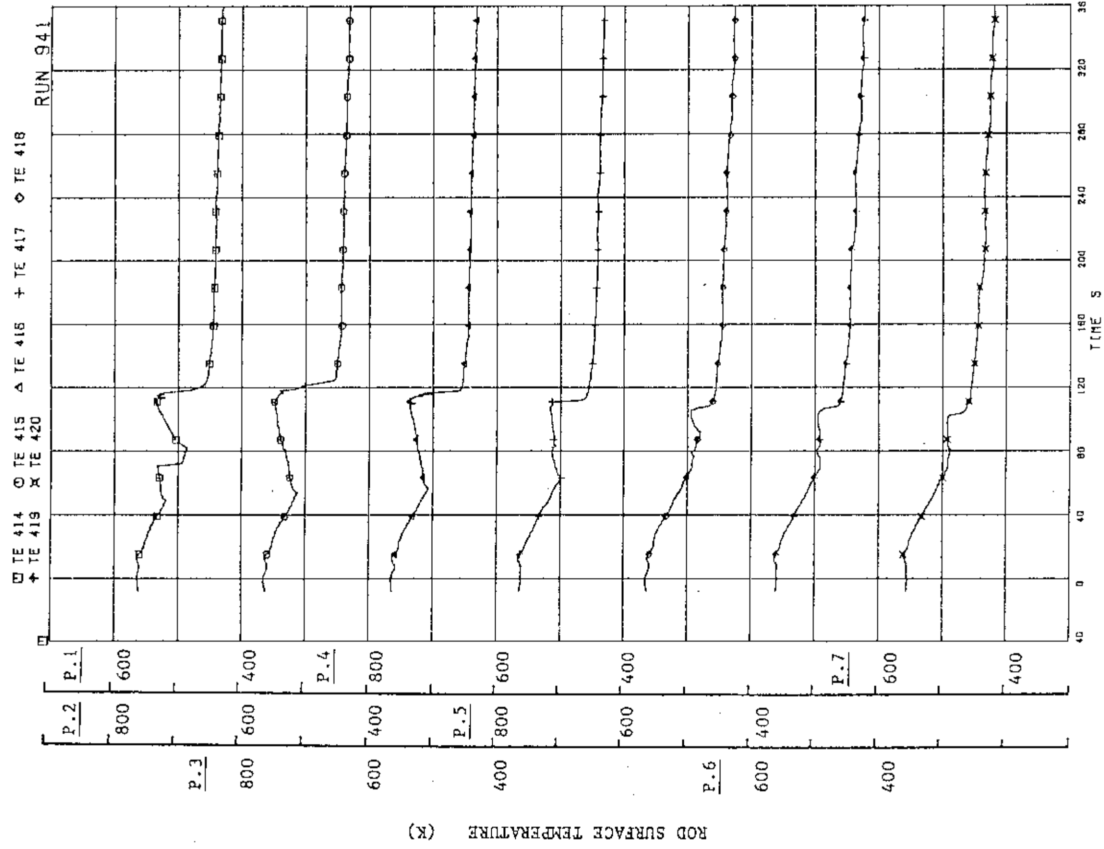

Fig.B.81 Surface temperatures of water rod simulator A45

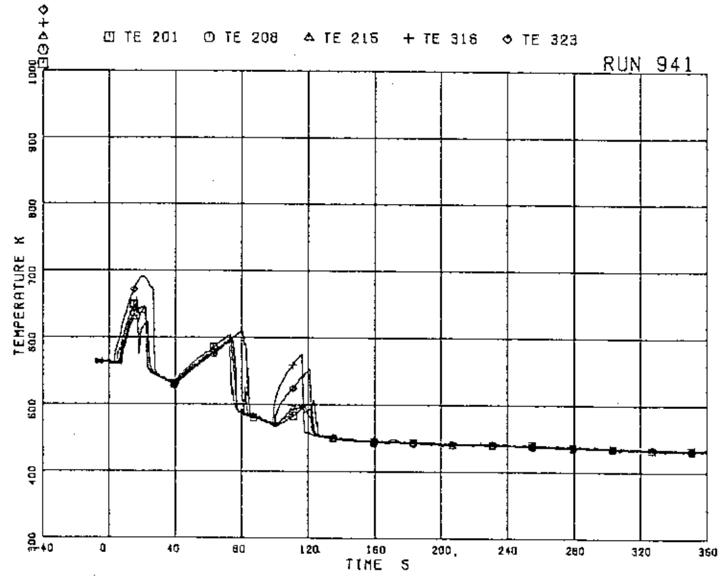

Fig.B.83 Surface temperatures of fuel rods A11, A12, A13, A87 and A88 at position 1

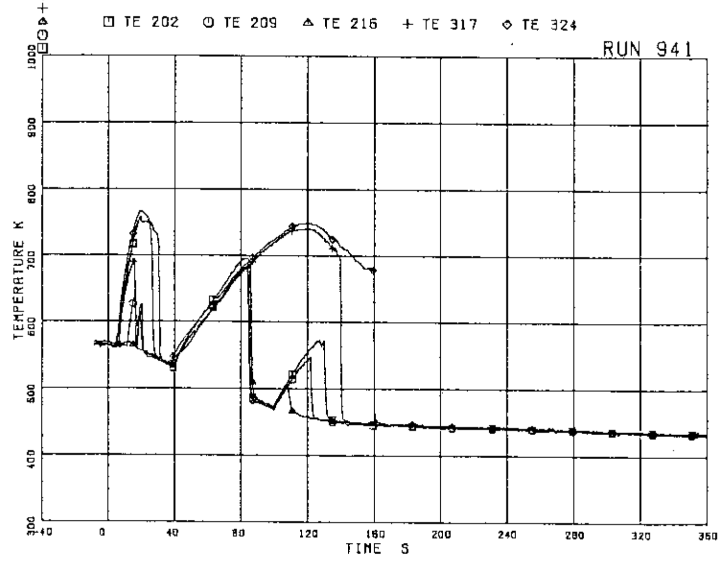

Fig.B.84 Surface temperatures of fuel rods A11, A12, A13, A87 and A88 at position 2

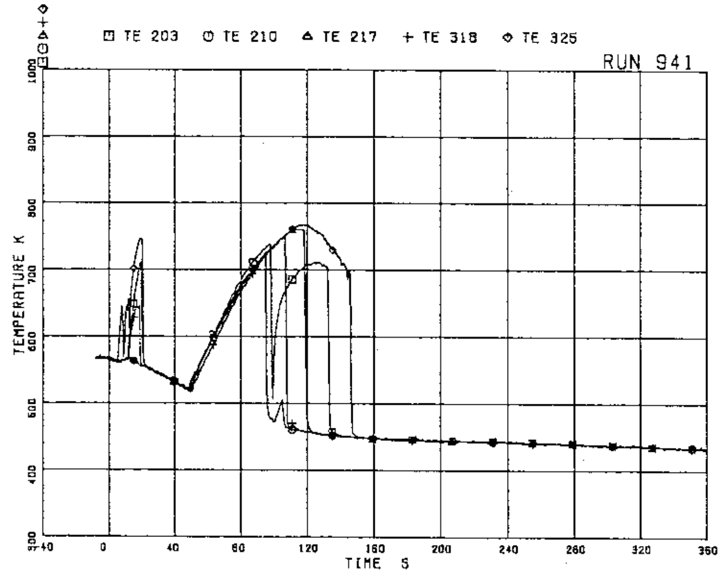

Fig.B.85 Surface temperatures of fuel rods A11, A12, A13, A87 and A88 at position 3

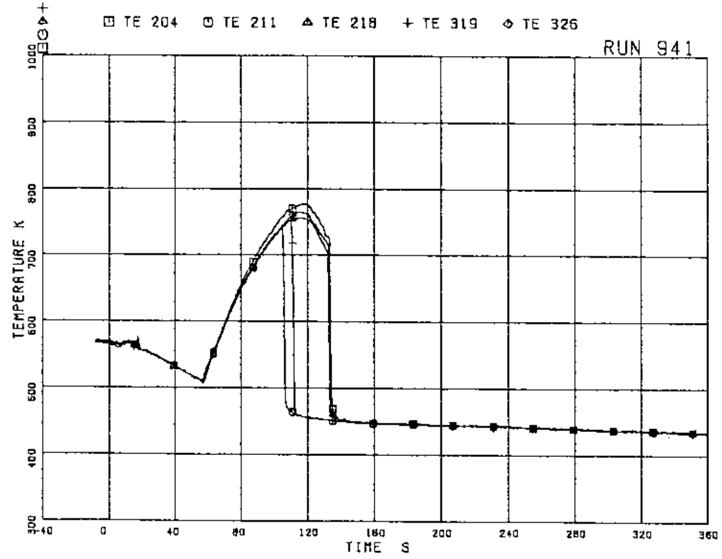

Fig.B.86 Surface temperatures of fuel rods A11, A12, A13, A87 and A88 at position 4

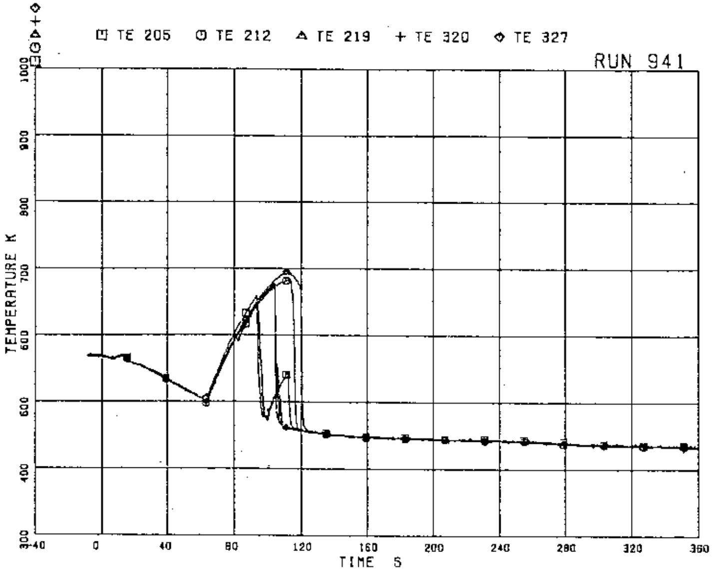

Fig.B.87 Surface temperatures of fuel rods A11, A12, A13, A87 and A88 at position 5

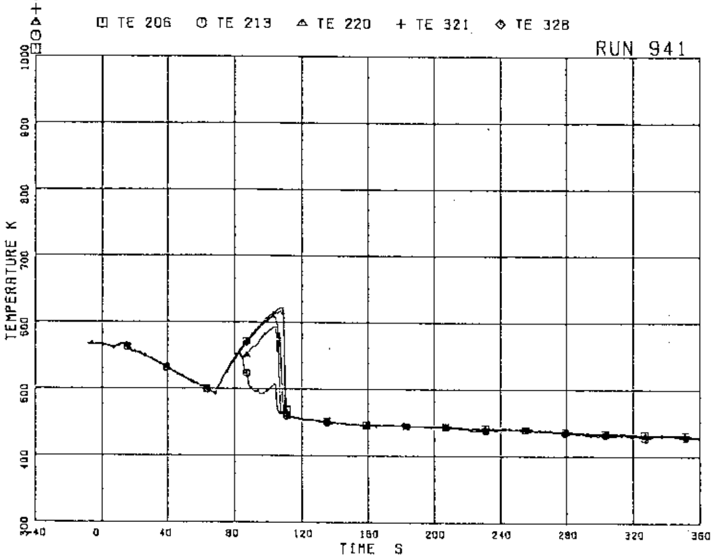

Fig.B.88 Surface temperatures of fuel rods A11, A12, A13, A87 and A88 at position 6

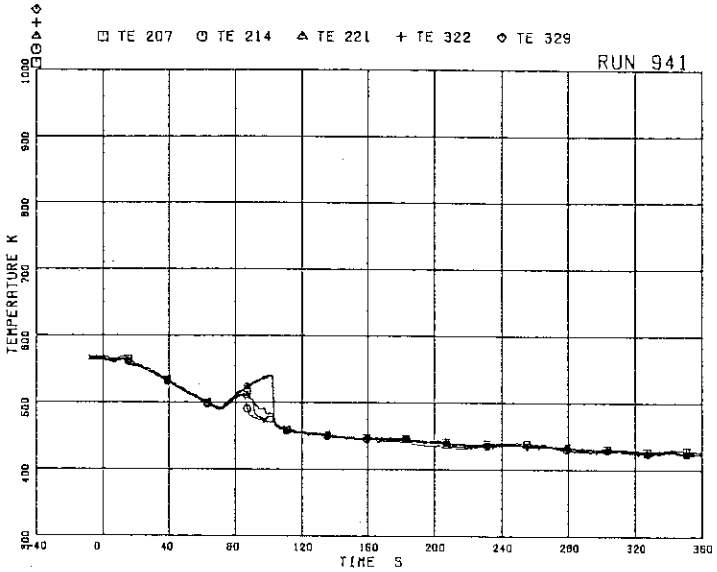

Fig.B.89 Surface temperatures of fuel rods A11, A12, A13, A87 and A88 at position 7

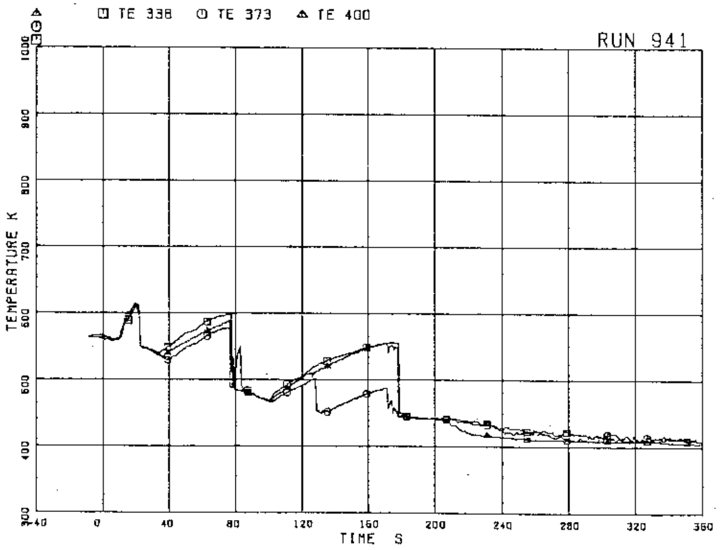

Fig.B.90 Surface temperatures of fuel rods B22, C22 and D22 at position 1

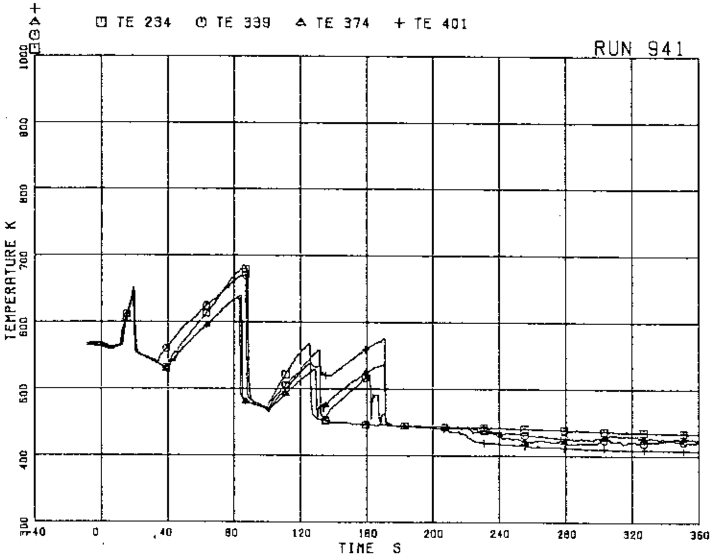

Fig.B.91 Surface temperatures of fuel rods A22, B22, C22 and D22 at position 2

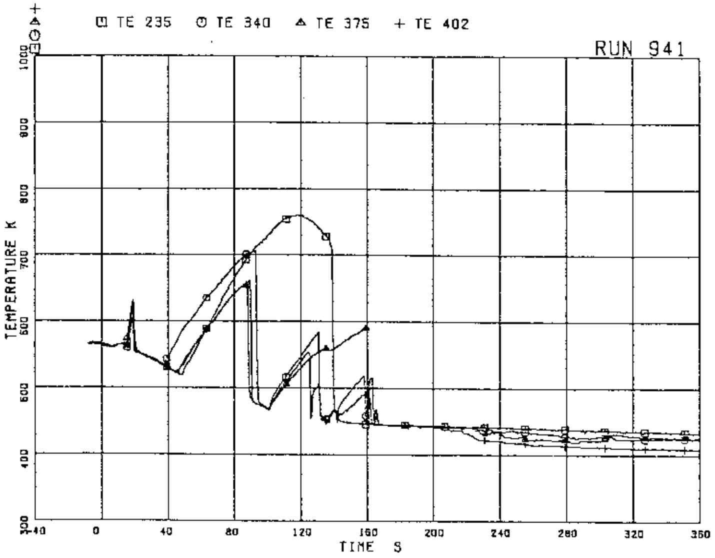

Fig.B.92 Surface temperatures of fuel rods A22, B22, C22 and D22 at position 3

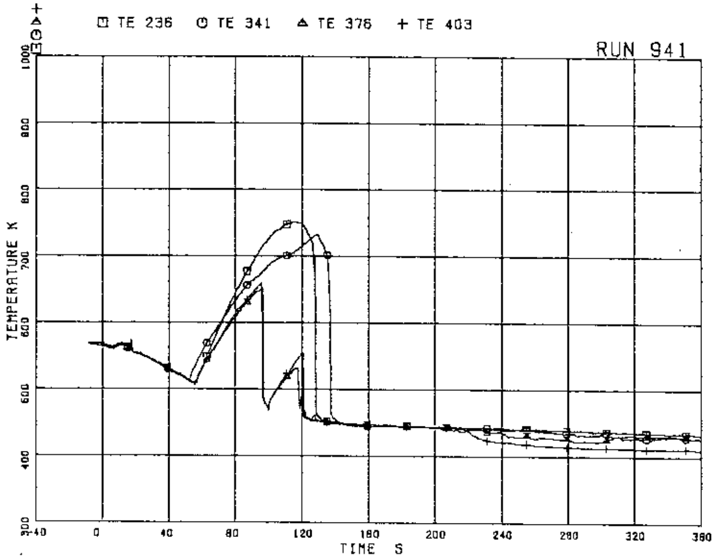

Fig.B.93 Surface temperatures of fuel rods A22, B22, C22 and D22 at position 4

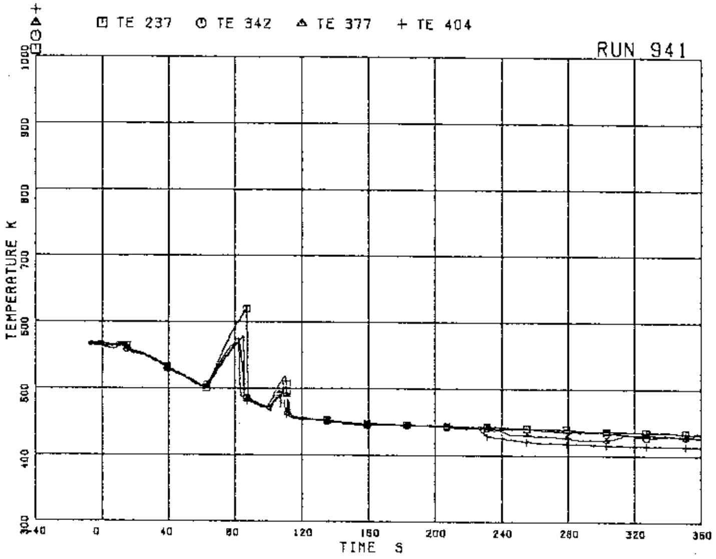

Fig.B.94 Surface temperatures of fuel rods A22, B22, C22 and D22 at position 5

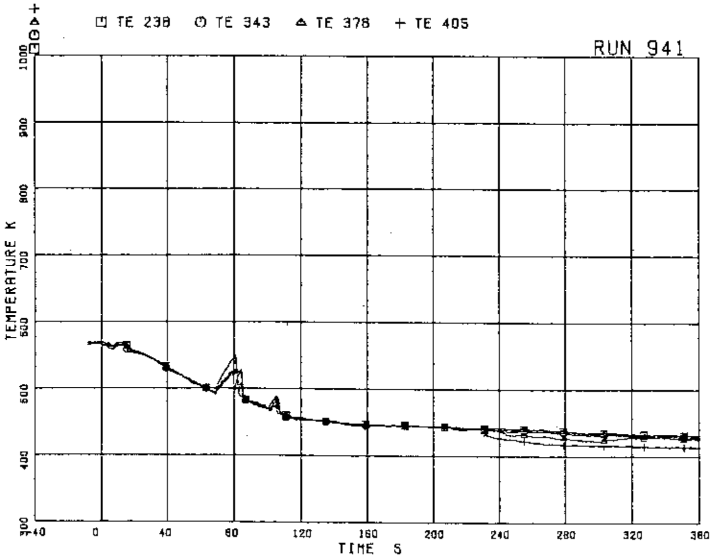

Fig.B.95 Surface temperatures of fuel rods A22, B22, C22 and D22 at position 6

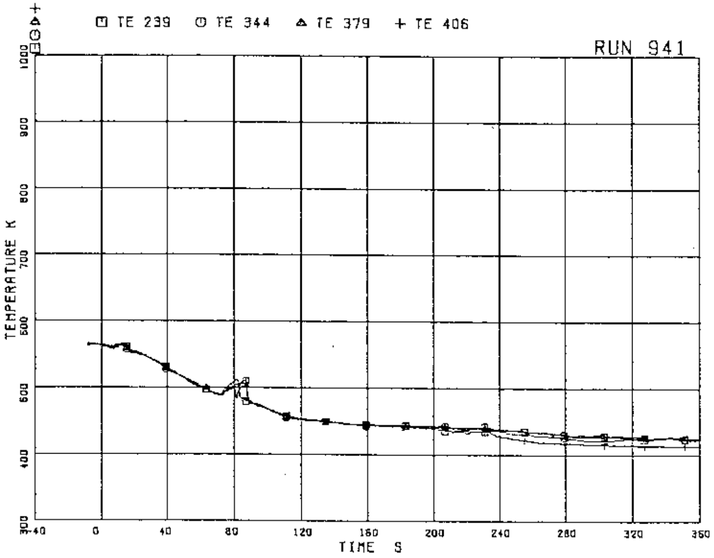

Fig.B.96 Surface temperatures of fuel rods A22, B22, C22 and D22 at position 7

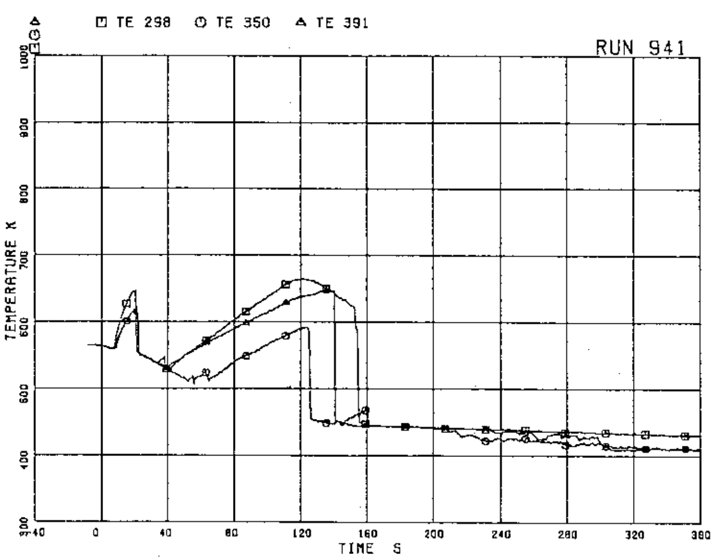

Fig.B.97 Surface temperatures of fuel rods A77, B77 and C77 at position 1

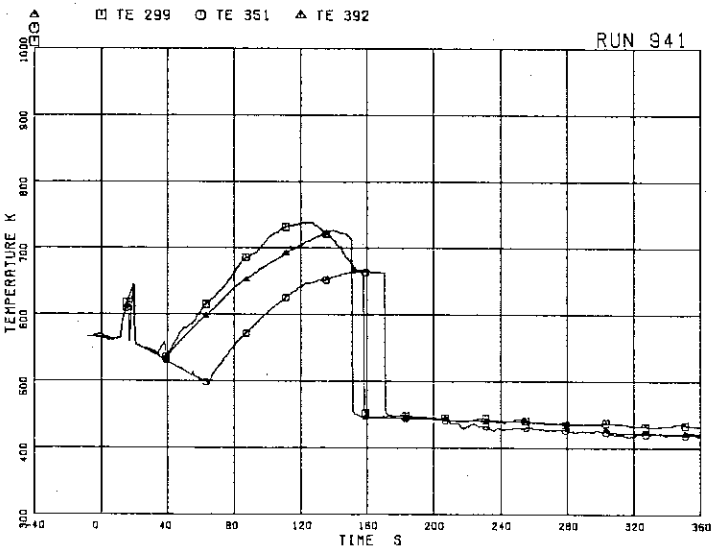

Fig.B.98 Surface temperatures of fuel rods A77, B77 and C77 at position 2

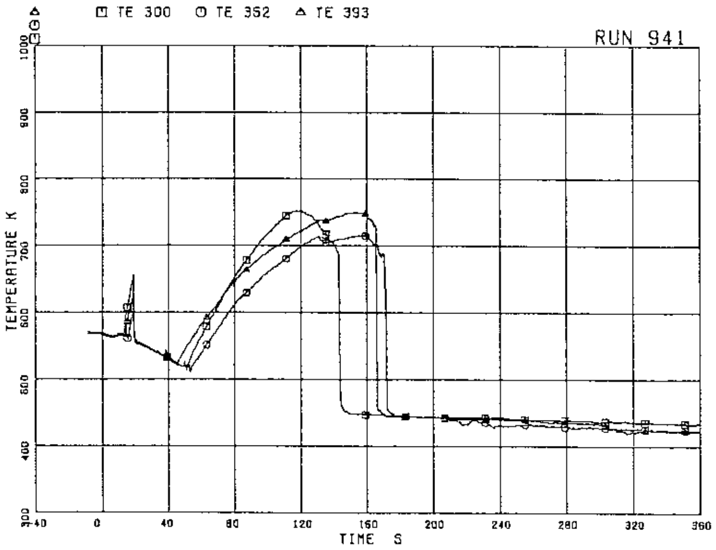

Fig.B.99 Surface temperatures of fuel rods A77, B77 and C77 at position 3

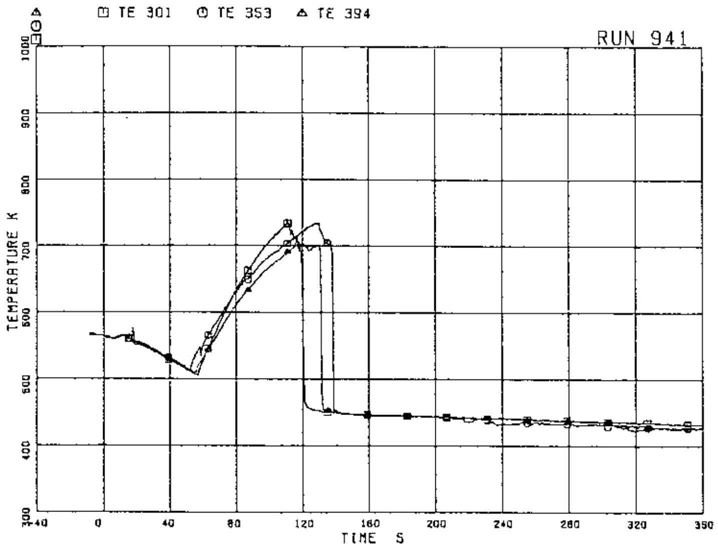

Fig.B.100 Surface temperatures of fuel rods A77, B77 and C77 at position 4

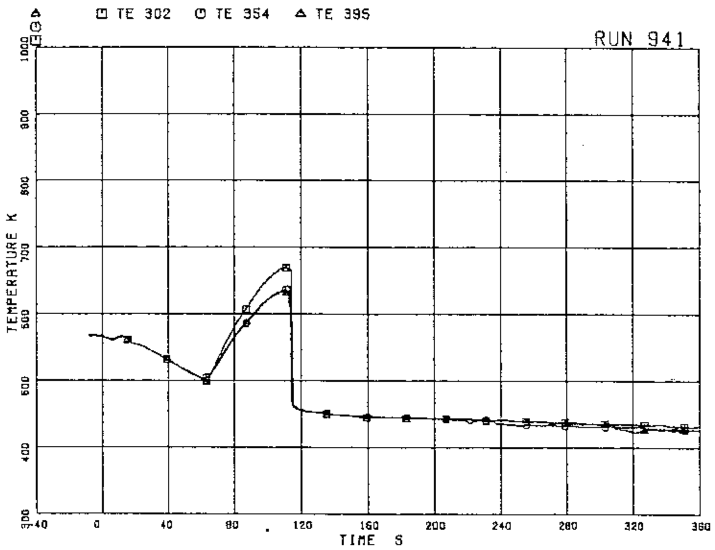

Fig.B.101 Surface temperatures of fuel rods A77, B77 and C77 at position 5

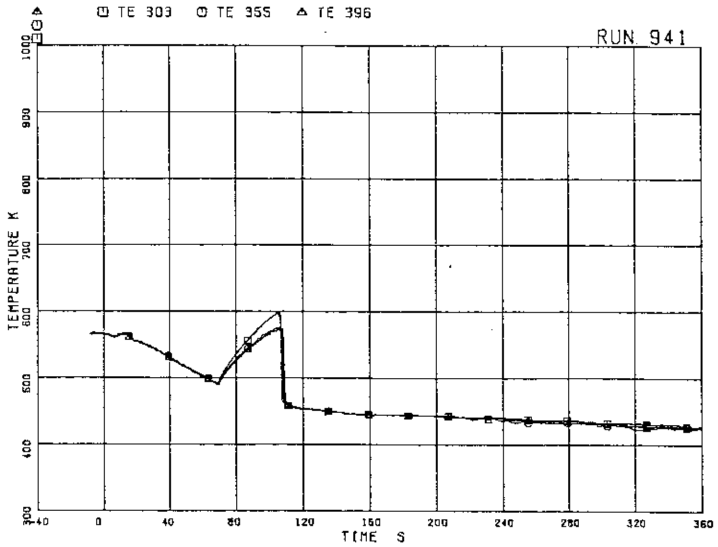

Fig.B.102 Surface temperatures of fuel rods A77, B77 and C77 at position 6

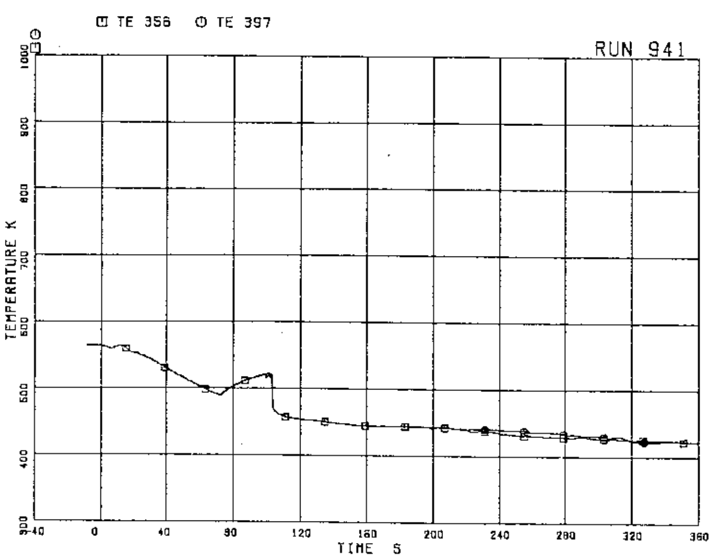

Fig.B.103 Surface temperature of fuel rod A77, B77 and C77 at position 7

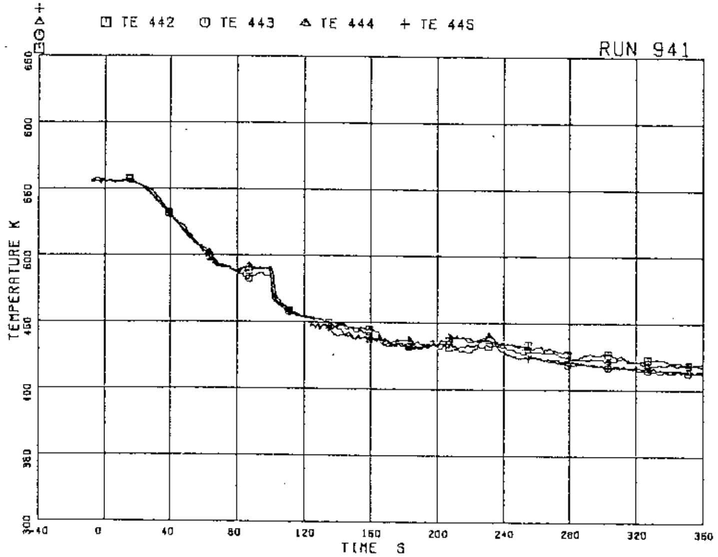

Fig.B.104 Fluid temperatures at channel inlet

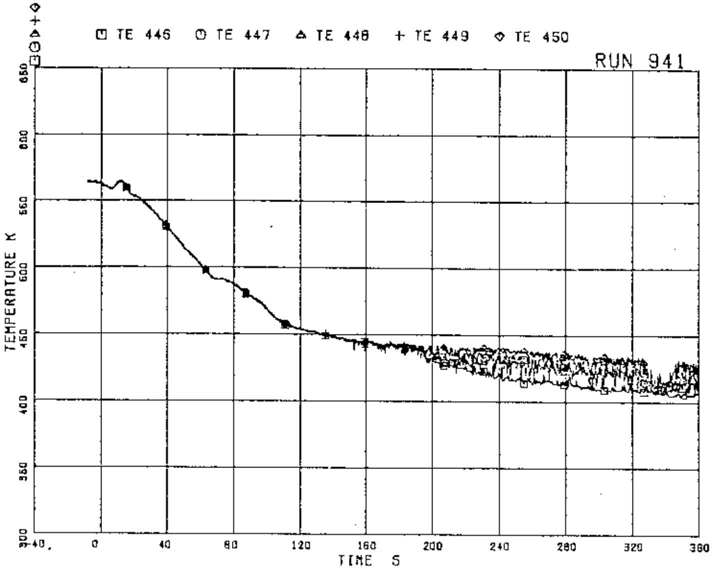

Fig.B.105 Fluid temperatures at channel A outlet

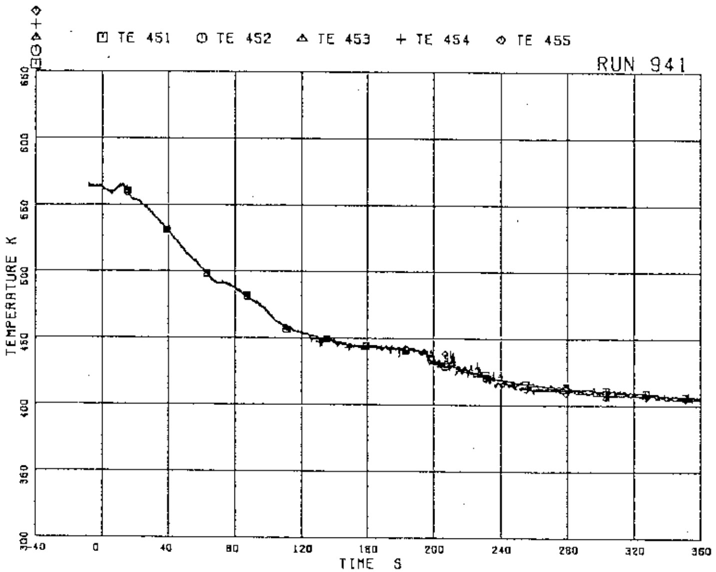

Fig.B.106 Fluid temperatures at channel C outlet

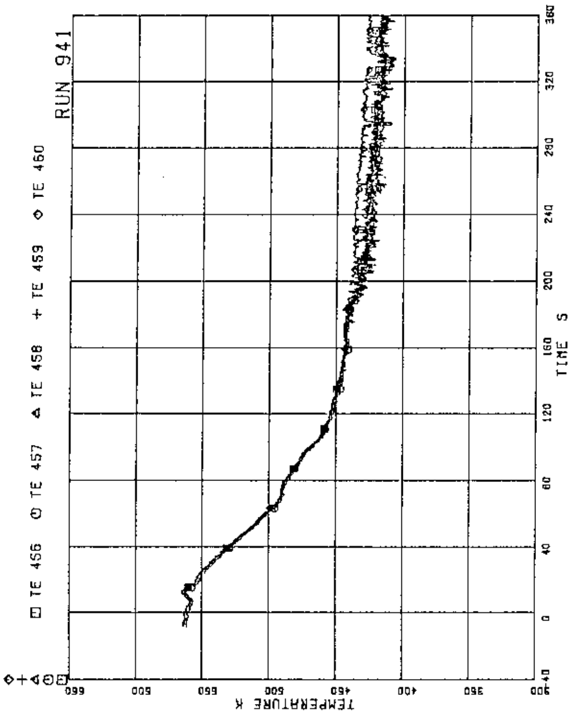

Fig.B.107 Fluid temperatures above UTP of channel A, openings 1 to 5

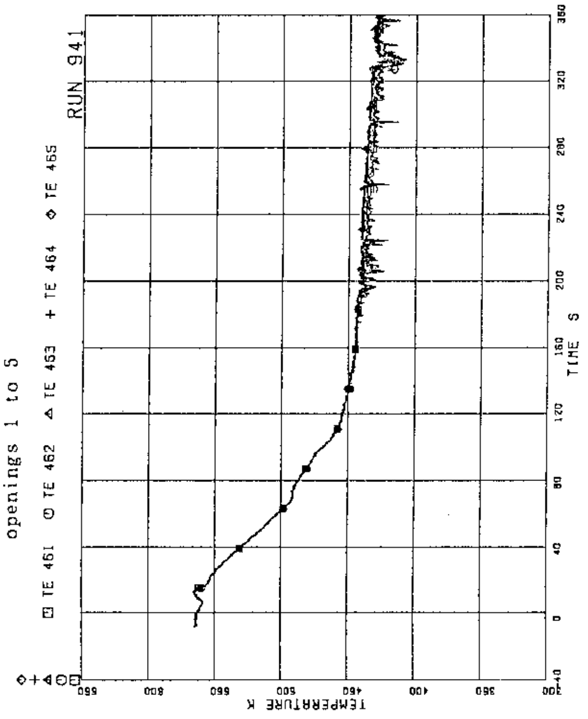

Fig.B.108 Fluid temperatures above UTP of channel A, openings 6 to 10

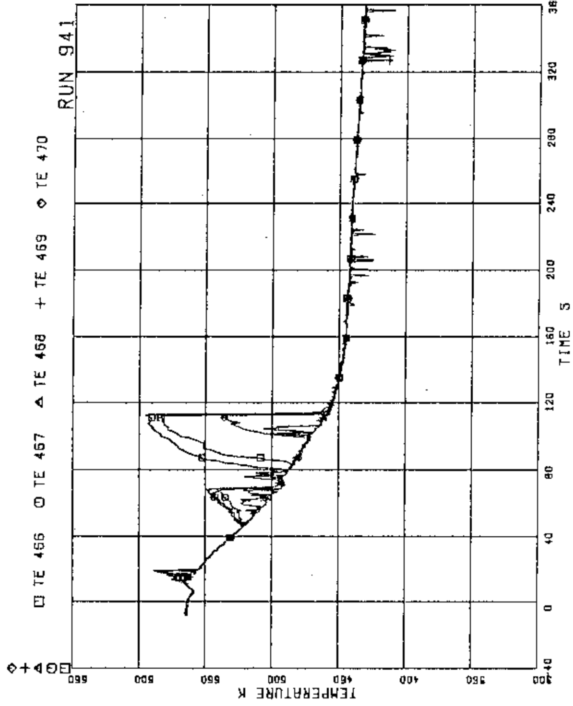

Fig.B.109 Fluid temperatures below UTP of channel A, openings 1 to 5

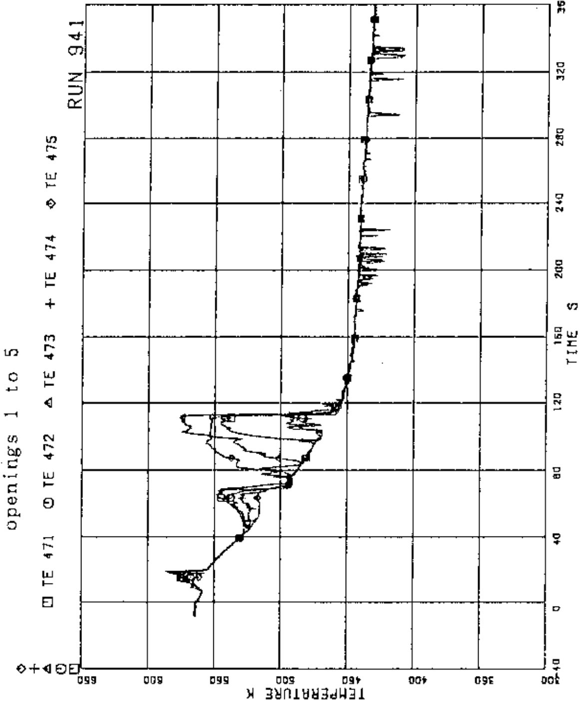

Fig.B.110 Fluid temperatures below UTP of channel A, openings 6 to 10

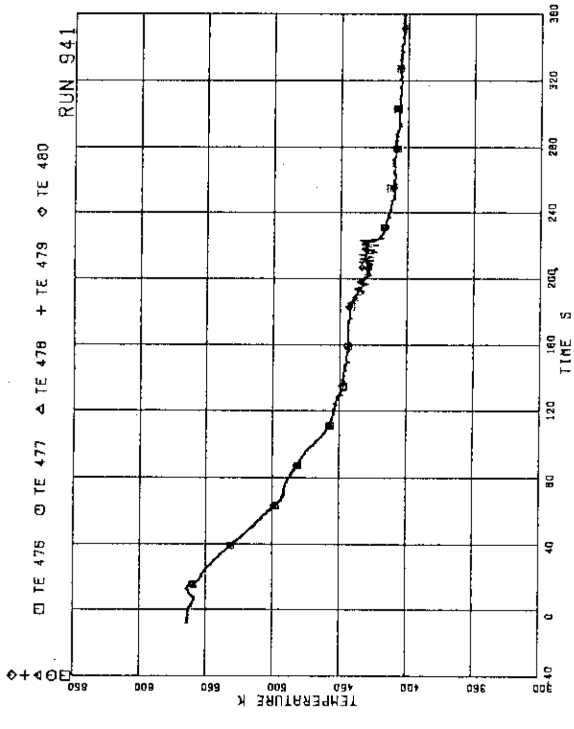

Fig.B.111 Fluid temperatures above UTP of channel C, openings 1 to 5

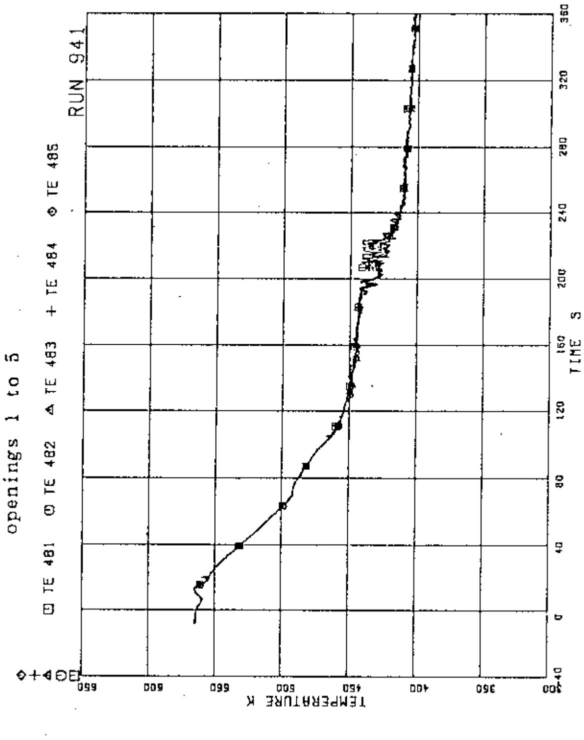

Fig.B.112 Fluid temperatures above UTP of channel C, openings 6 to 10

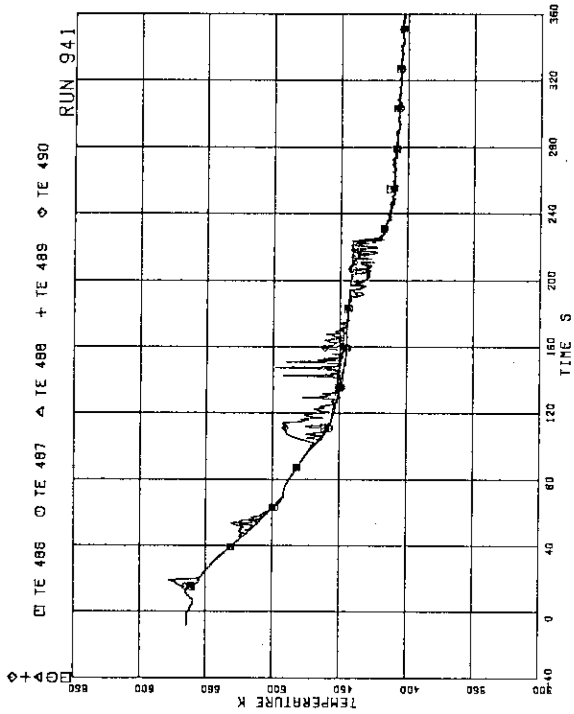

Fig.B.113 Fluid temperatures below UTP of channel C, openings 1 to 5

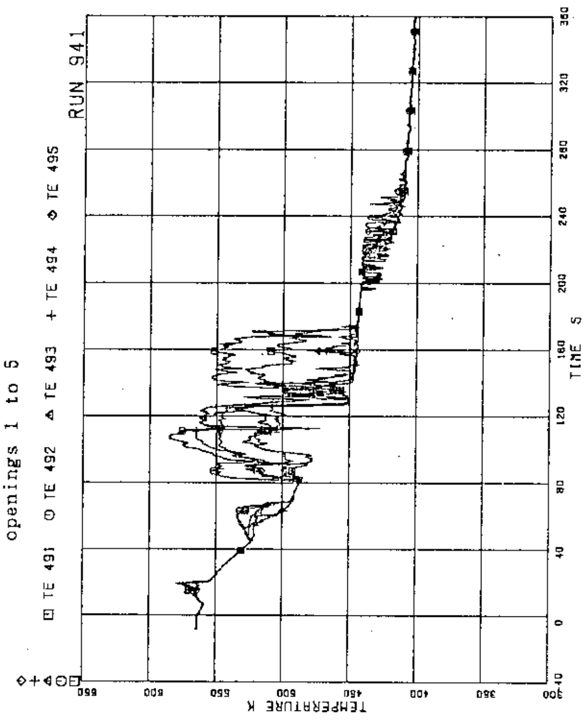

Fig.B.114 Fluid temperatures below UTP of channel C, openings 6 to 10

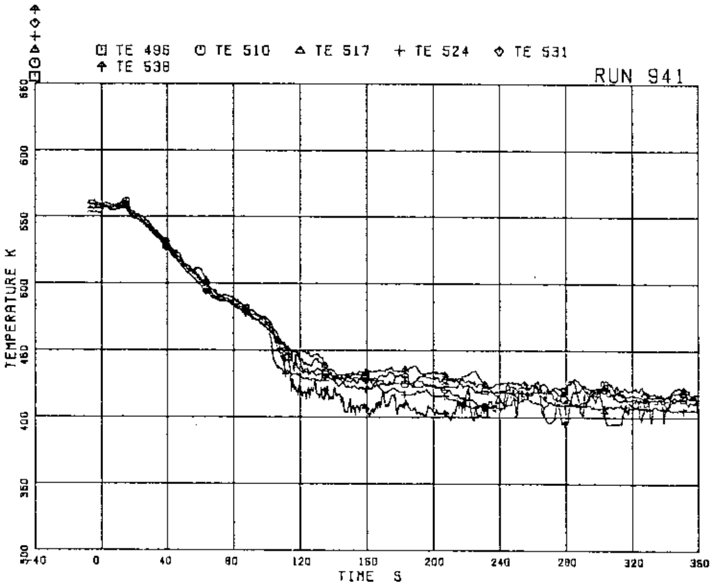

Fig.B.115 Inner and outer surface temperatures of channel box at pos. 1

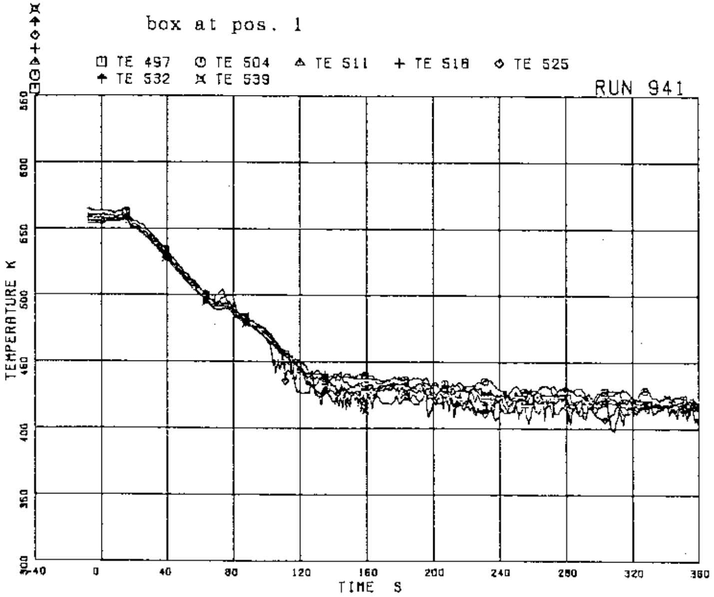

Fig.B.116 Inner and outer surface temperatures of channel box at pos. 2

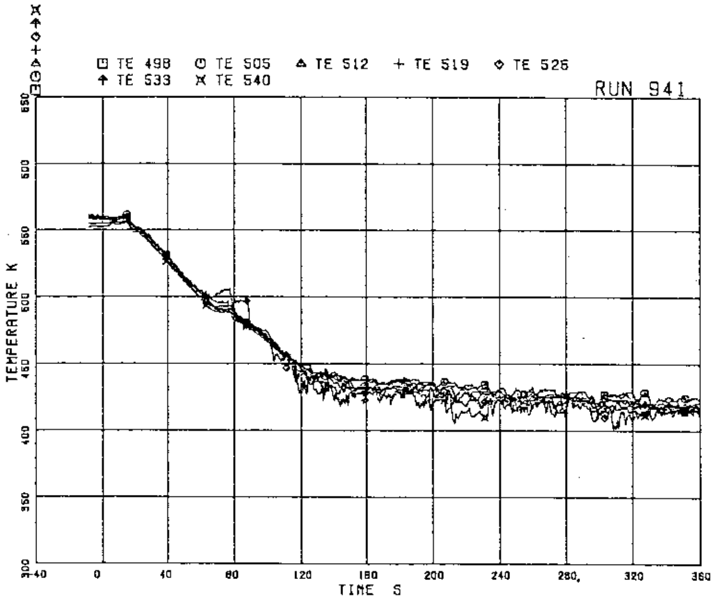

Fig.B.117 Inner and outer surface temperatures of channel box at pos. 3

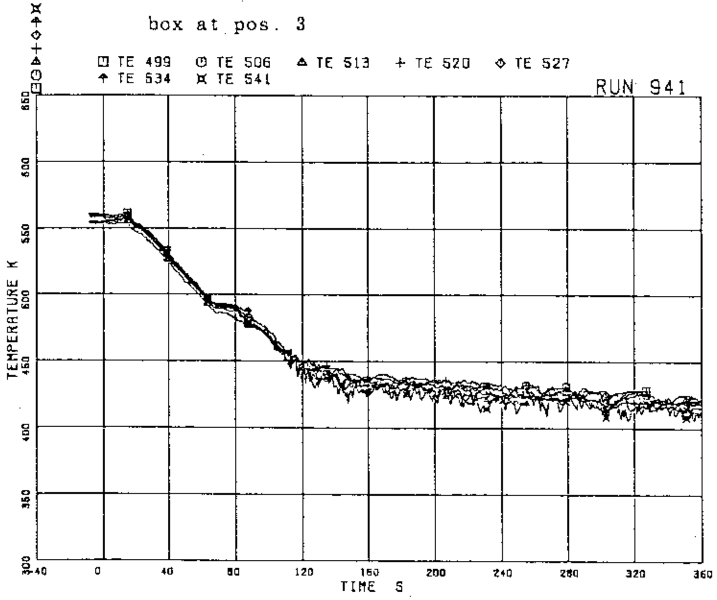

Fig.B.118 Inner and outer surface temperatures of channel box at pos. 4

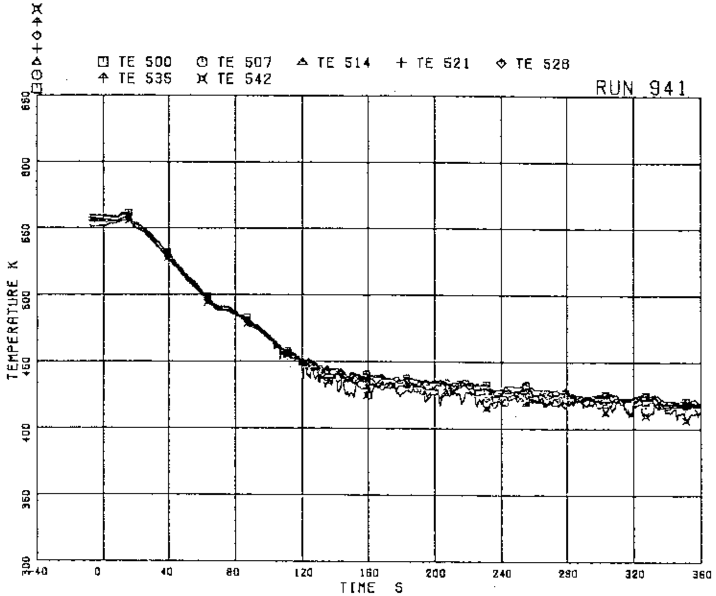

Fig.B.119 Inner and outer surface temperatures of channel box at pos. 5

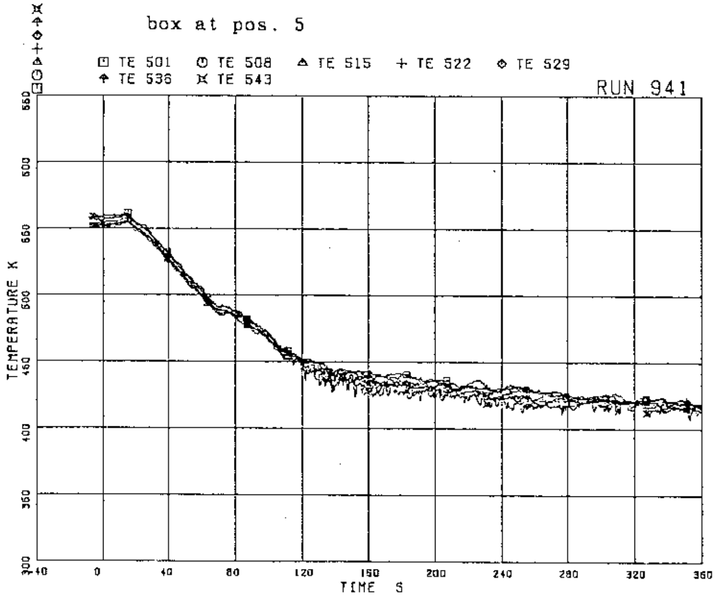

Fig.B.120 Inner and outer surface temperatures of channel box at pos. 6

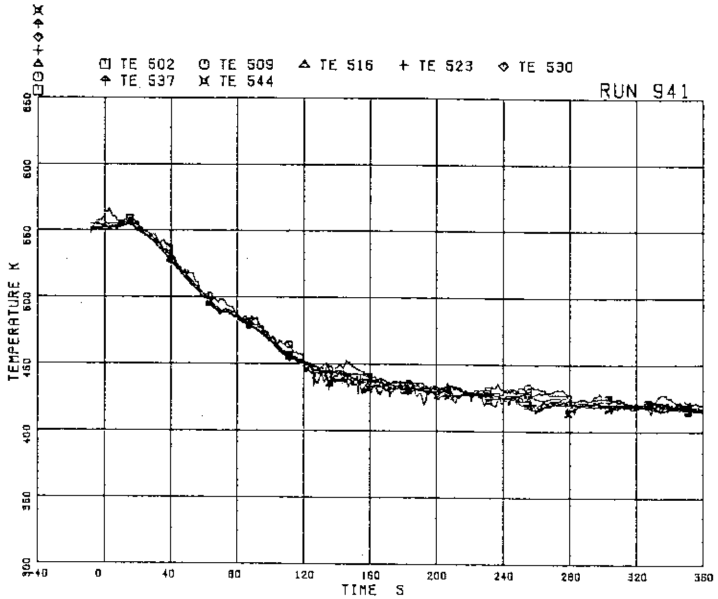

Fig.B.121 Inner and outer surface temperatures of channel box at pos. 7

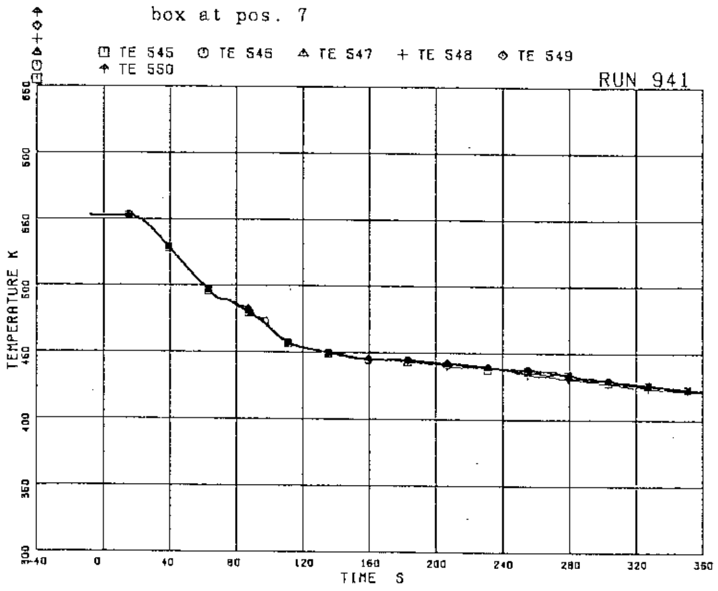

Fig.B.122 Fluid temperatures in lower plnum, center

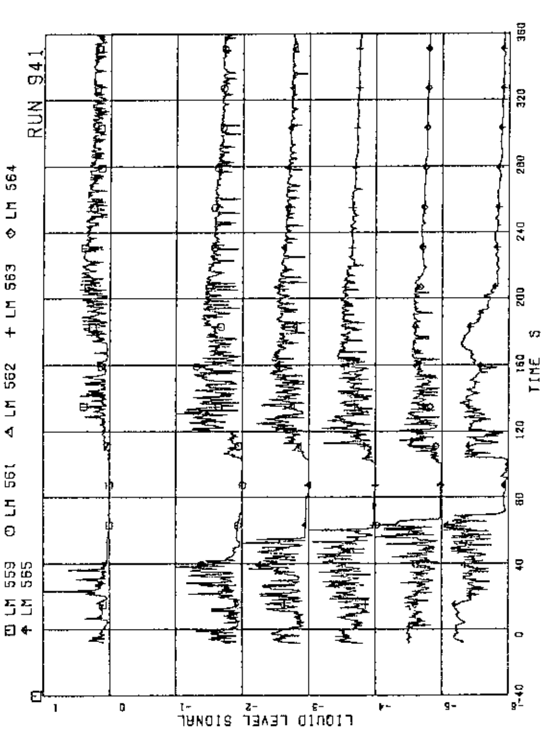

Fig.B.123 Liquid level signals in channel box A, location A1

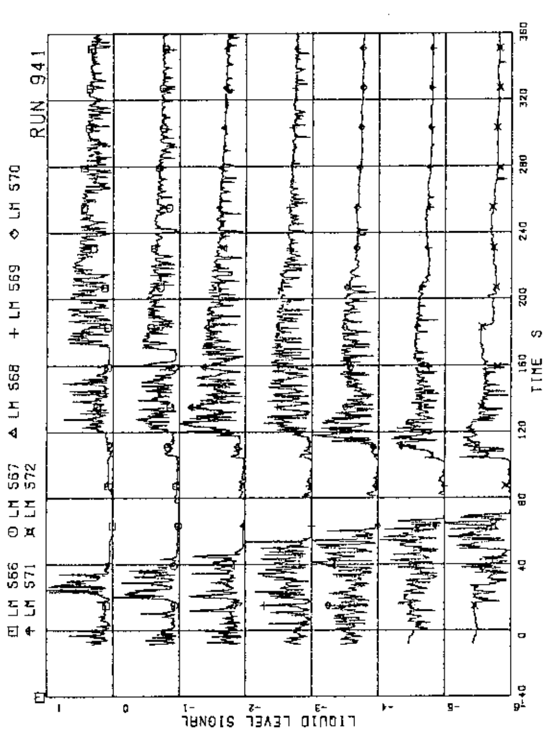

Fig.B.124 Liquid level signals in channel box A, location A2

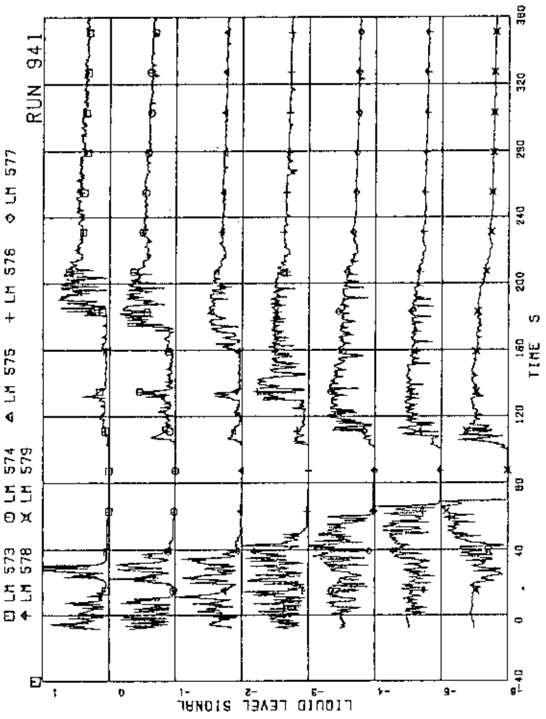

Fig.B.125 Liquid level signals in channel box B

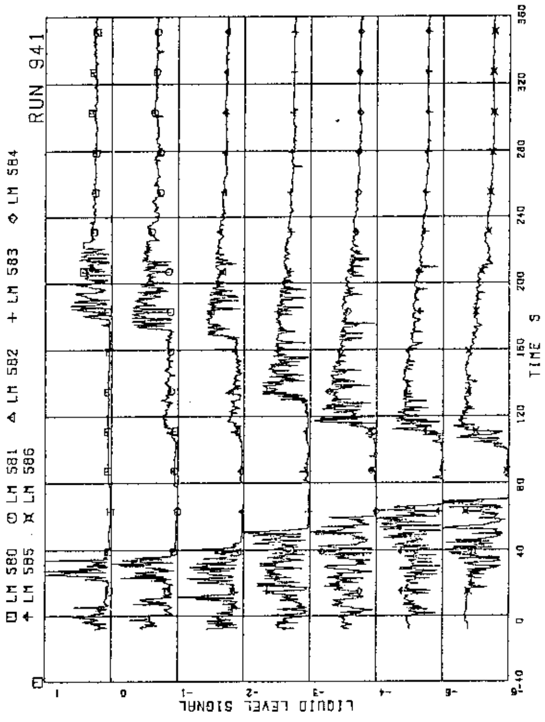

Fig.B.126 Liquid level signals in channel box C

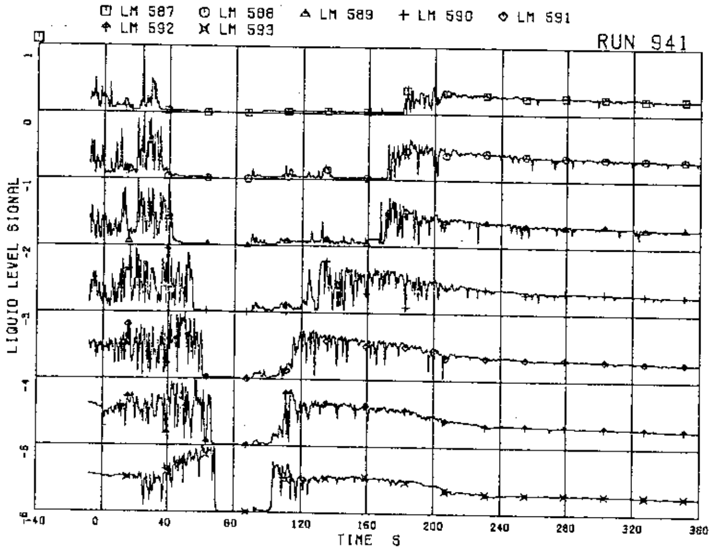

Fig.B.127 Liquid level signals in channel box D

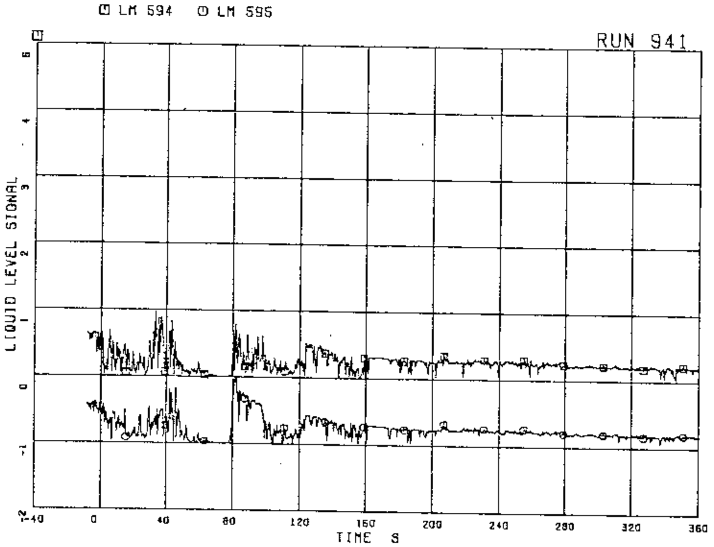

Fig.B.128 Liquid level signals in channel A outlet, location A1

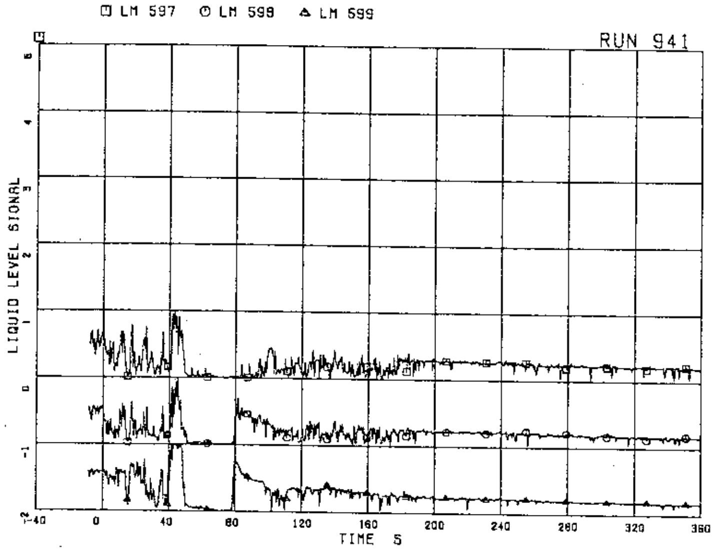

Fig.B.129 Liquid level signals in channel A outlet, location A2

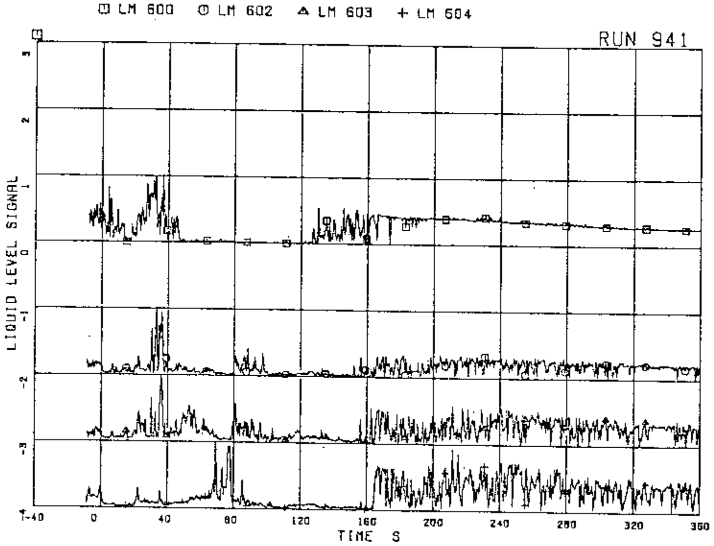

Fig.B.130 Liquid level signals in channel A outlet, center

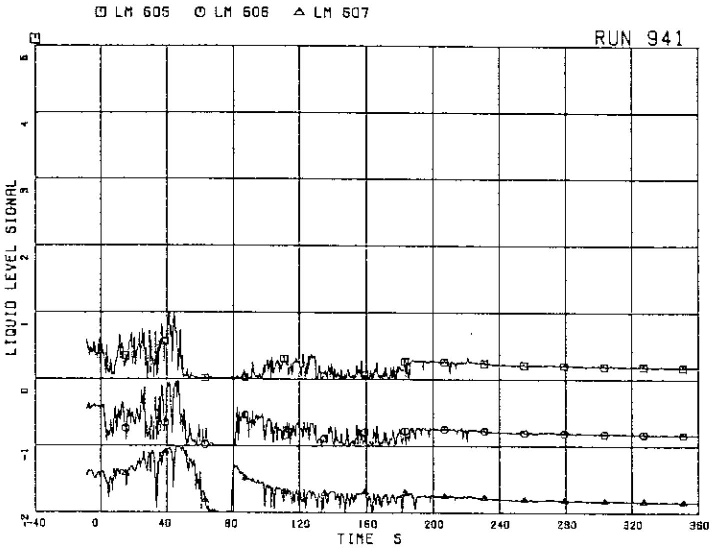

Fig.B.131 Liquid level signals in channel C outlet, location C1

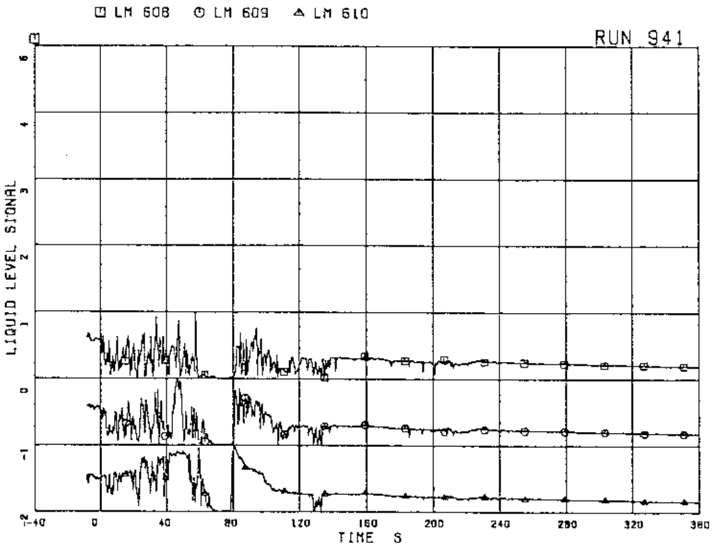

Fig.B.132 Liquid level signals in channel C outlet, location C2

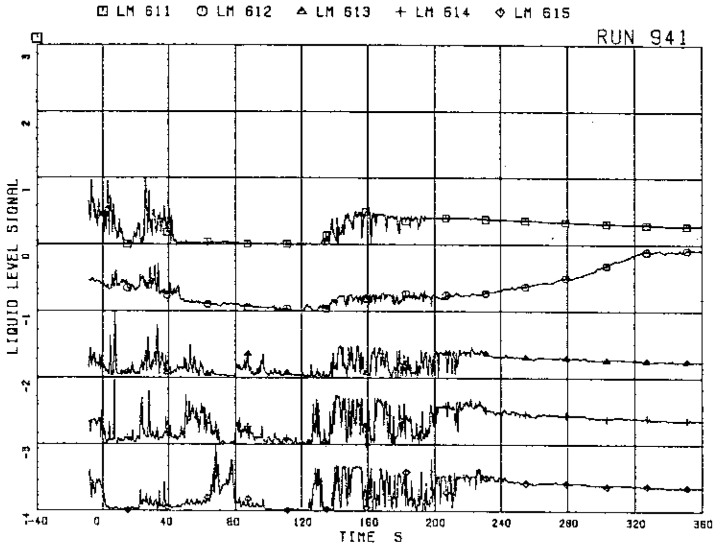

Fig.B.133 Liquid level signals in channel C outlet, center

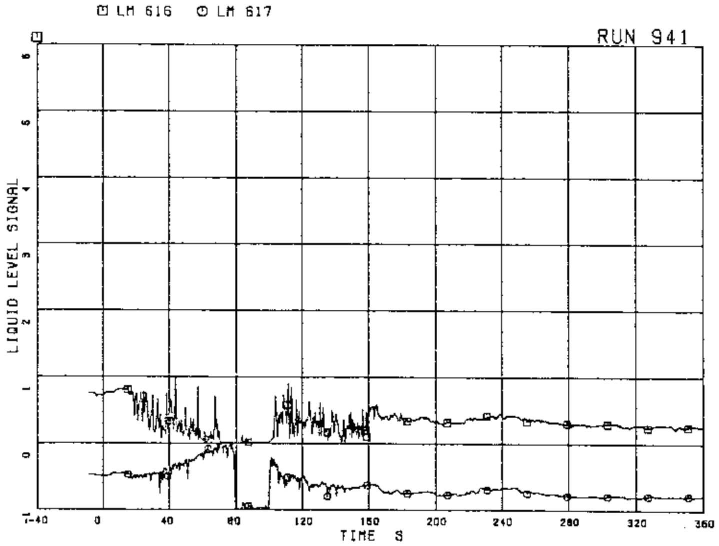

Fig.B.134 Liquid level signals in channel A inlet

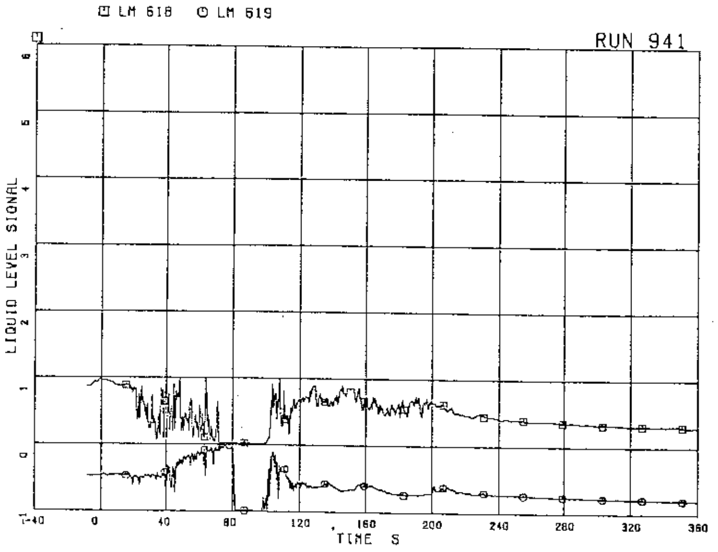

Fig.B.135 Liquid level signals in channel B inlet

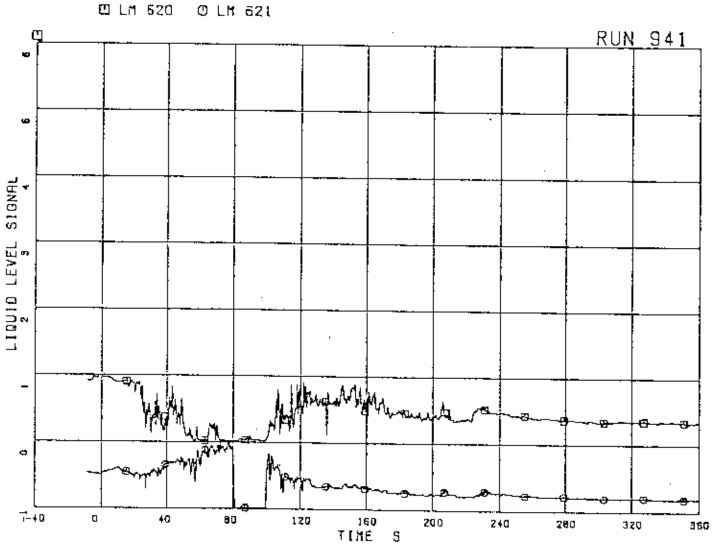

Fig.B.136 Liquid level signals in channel C inlet

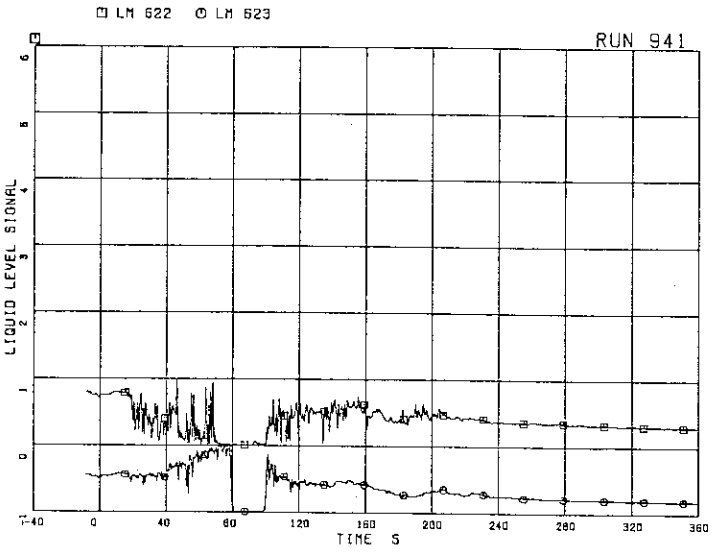

Fig.B.137 Liquid level signals in channel D inlet

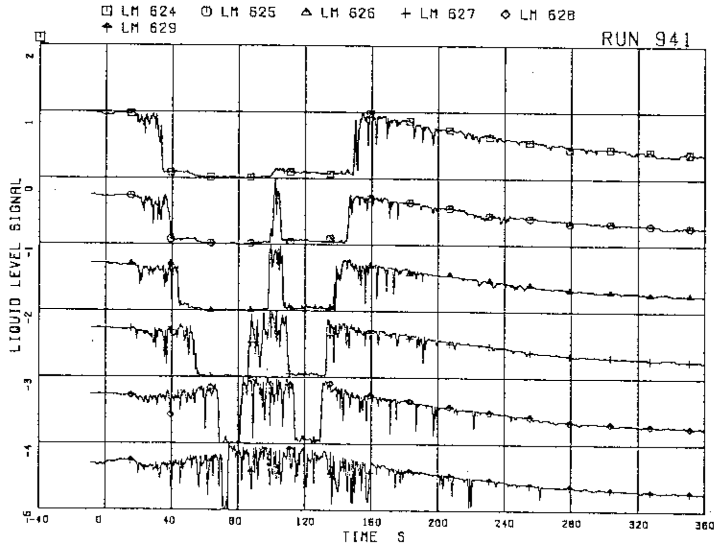

Fig.B.138 Liquid level signals in lower plenum, north

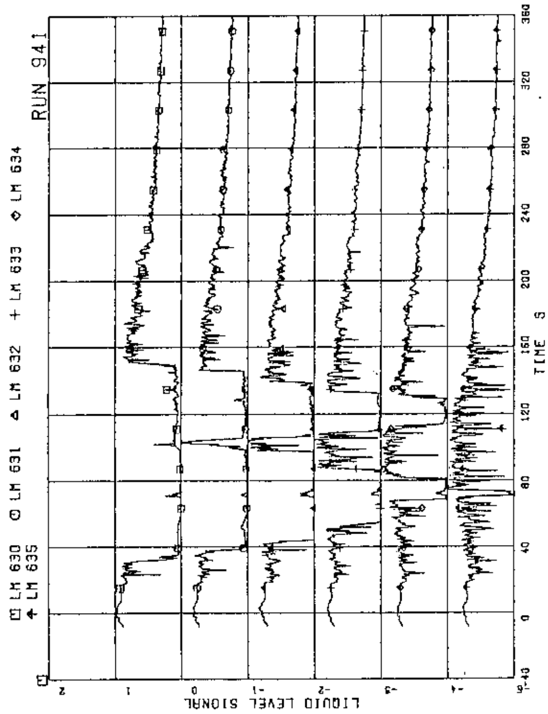

Fig.B.139 Liquid level signals in lower plenum, south

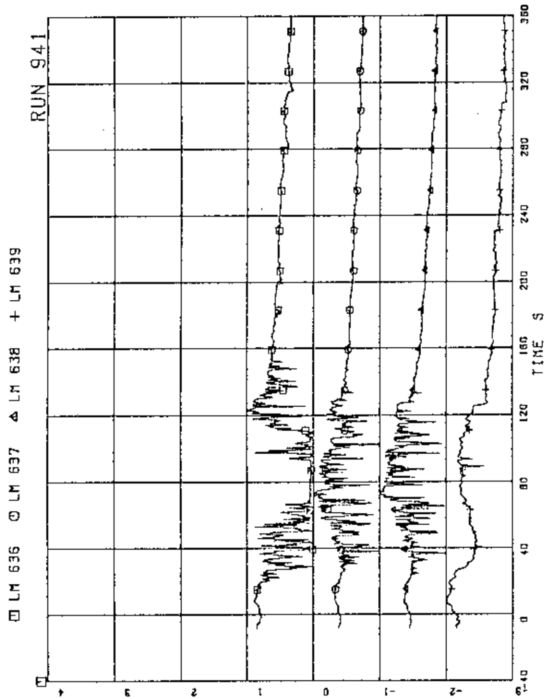

Fig.B.140 Liquid level signals in guide tube, north

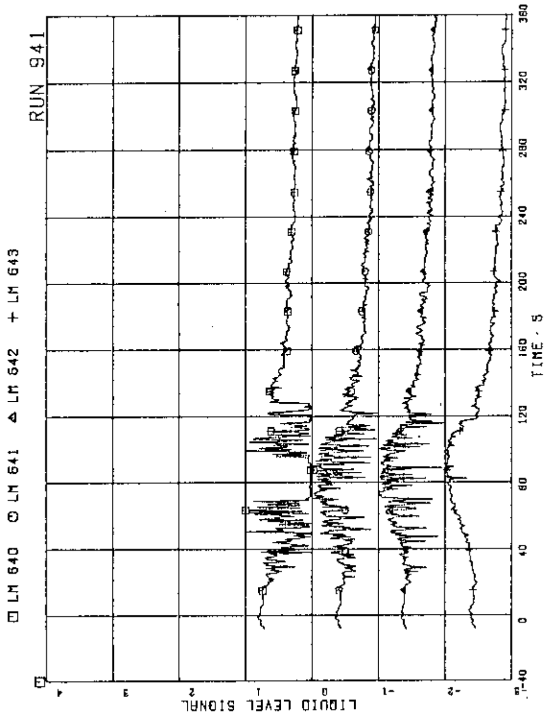

Fig.B.141 Liquid level signals in guide tube, south

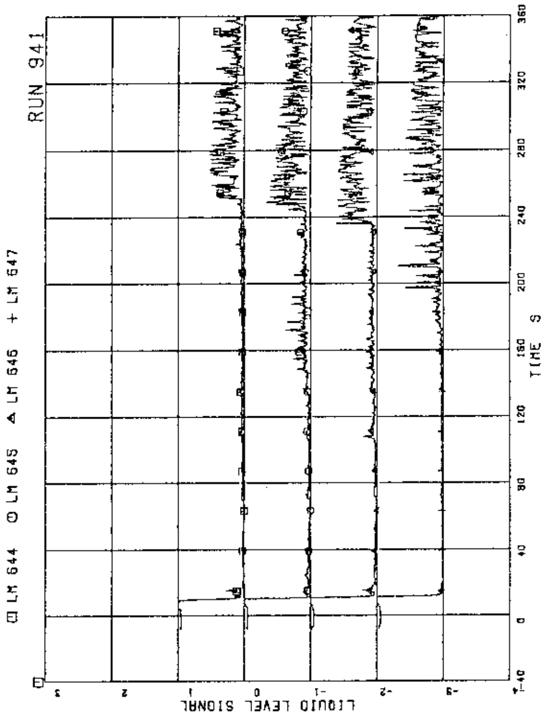

Fig.B.142 Liquid level signals in downcomer, D side

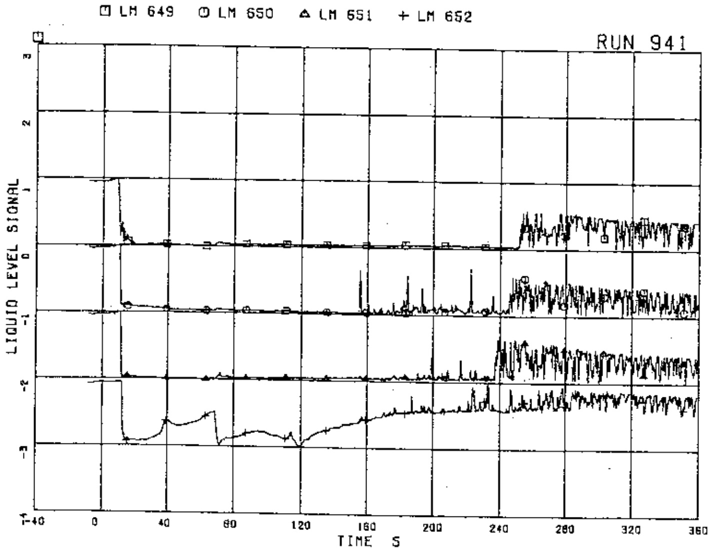

Fig.B.143 Liquid level signals in downcomer, B side
B SIDE

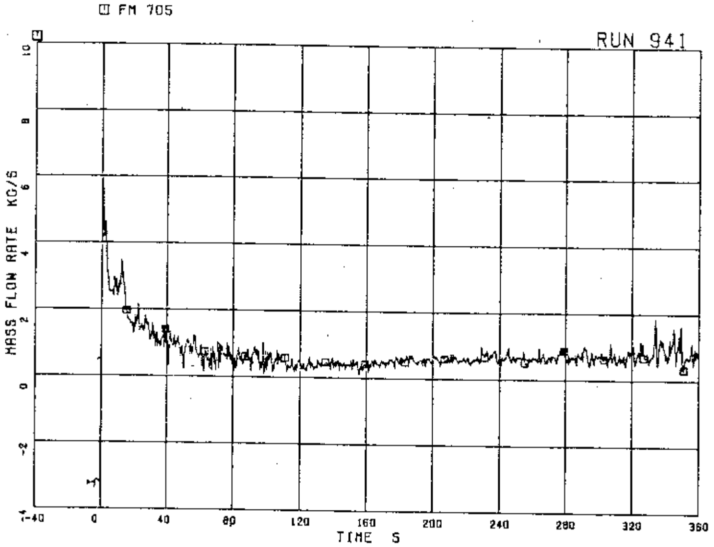

Fig.B.144 Flow rate at MRP side of break (based on low range drag disk data)

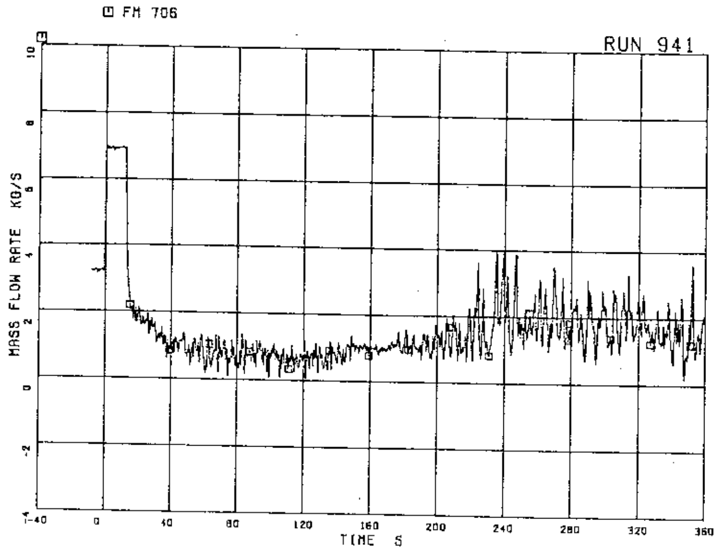

Fig.B.145 Flow rate at PV side of break (based on low range drag disk data)

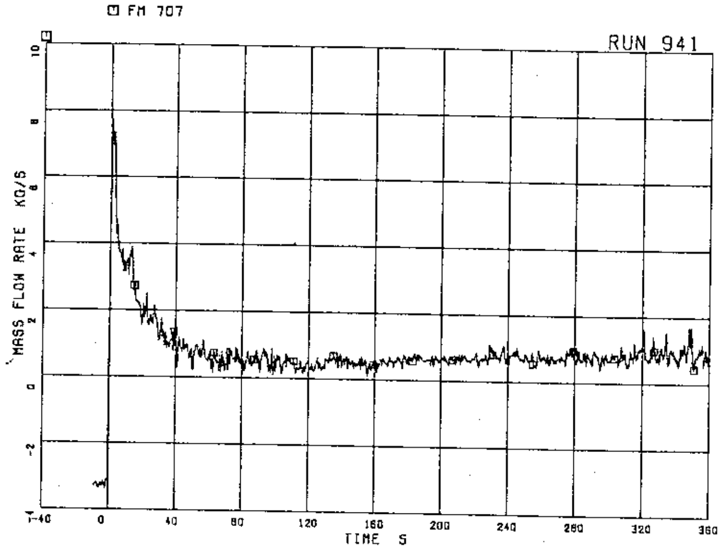

Fig.B.146 Flow rate at MRP side of break (based on high range drag disk data)

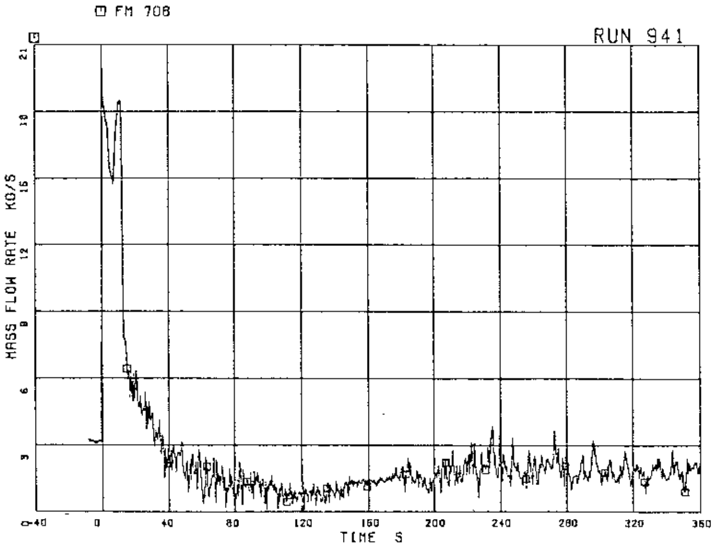

Fig.B.147 Flow rate at PV side of break (based on high range drag disk data)

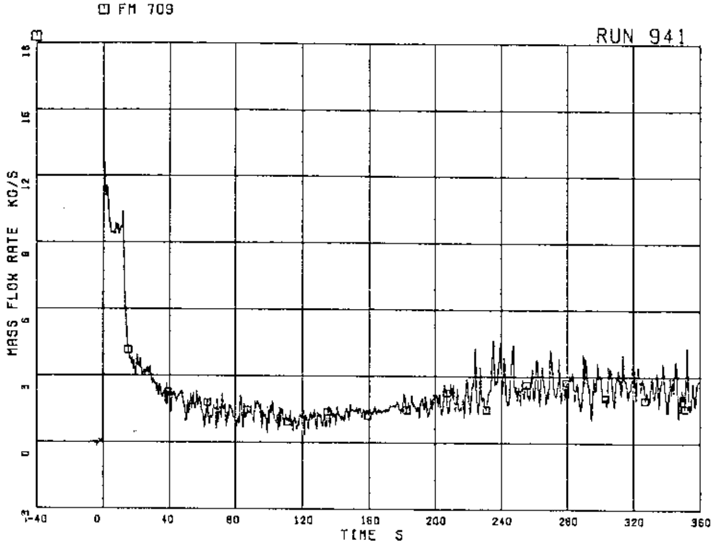

Fig.B.148 Total discharge flow rate from break (based on low range drag disk data)

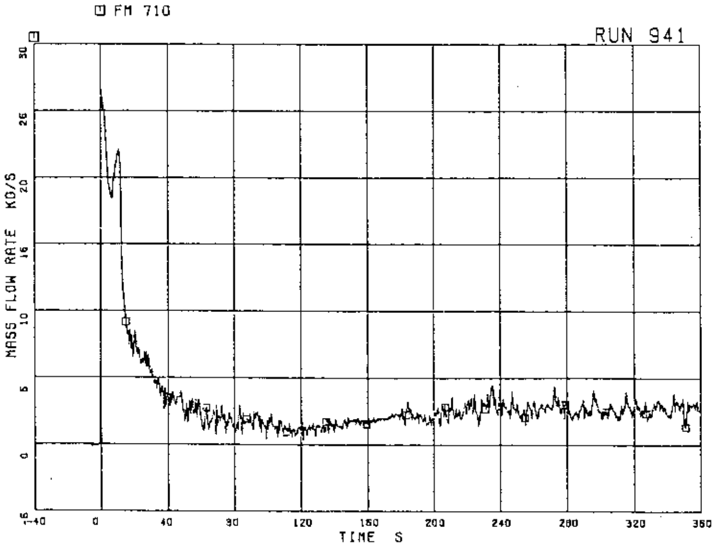

Fig.B.149 Total discharge flow rate from break (based on high range drag disk data)

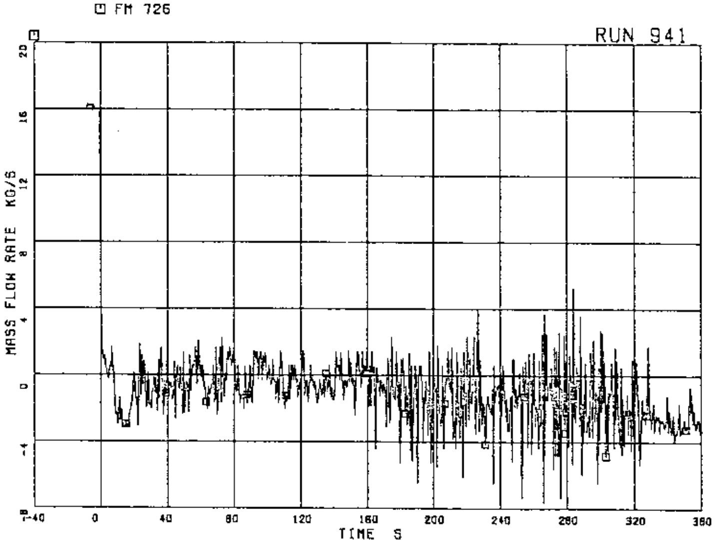

Fig.B.150 Total JP outlet flow rate (pos. flow)

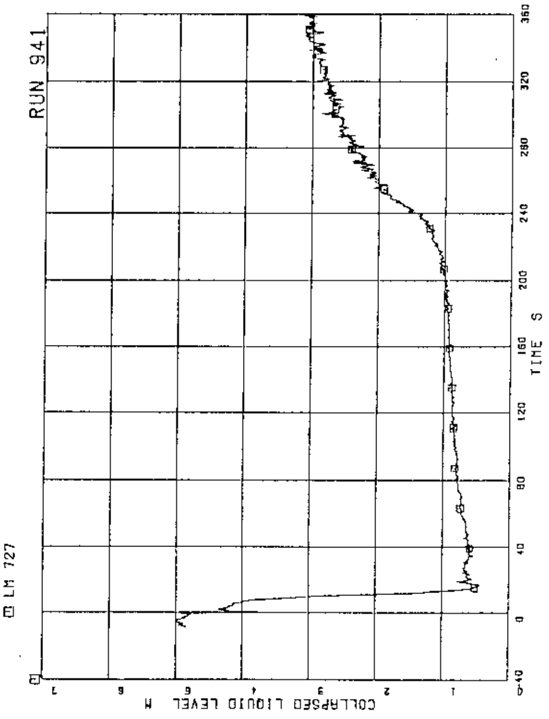

Fig.B.151 Collapsed liquid level in downcomer

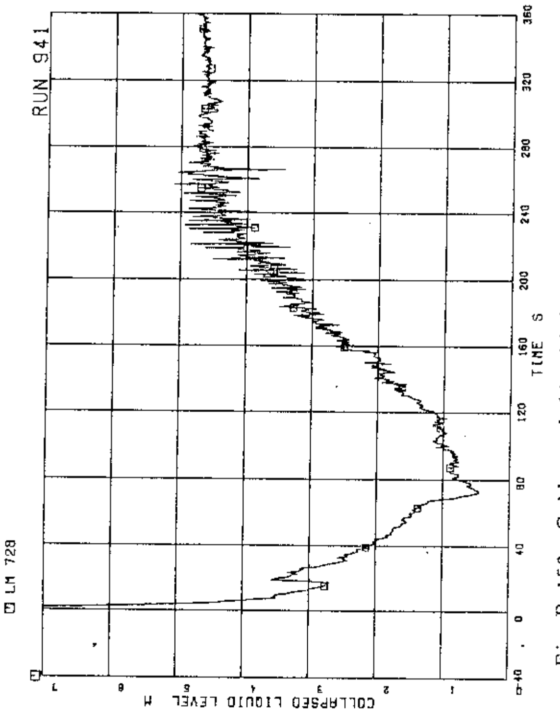

Fig.B.152 Collapsed liquid level inside core-shroud

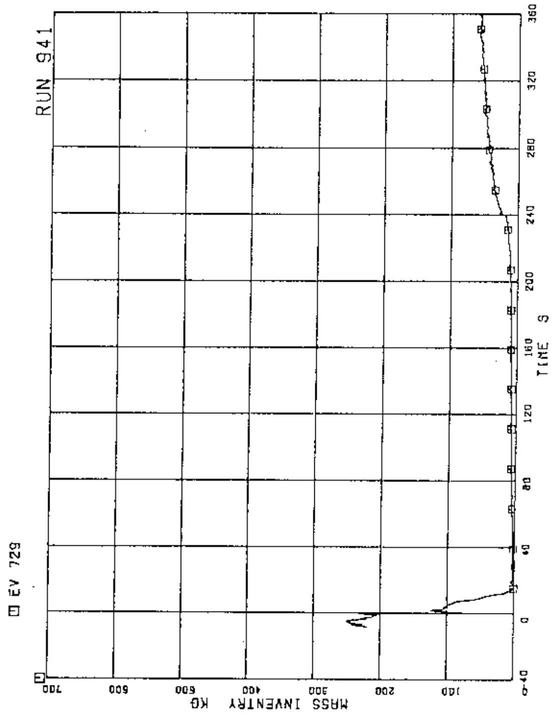

Fig.B.153 Fluid inventory in downcomer

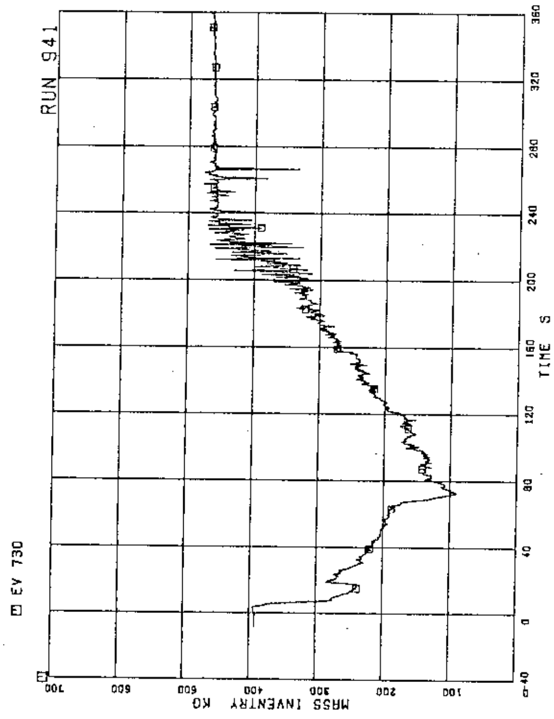

Fig.B.154 Fluid inventory inside core shroud

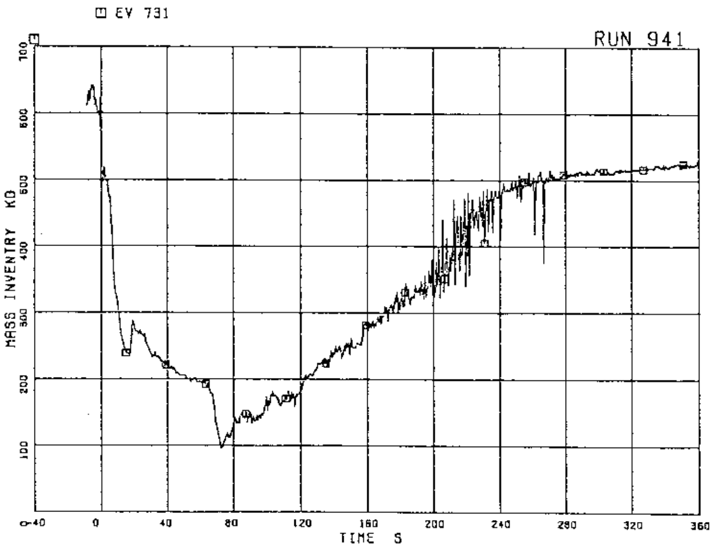

FIG Fig.B.155 Total fluid inventory in pressure vessel

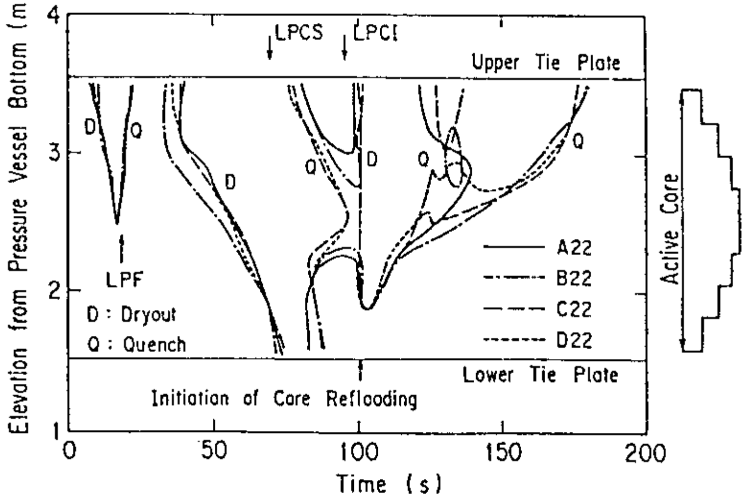

Fig.B.156 Dryout and quench fronts on A22, B22, C22 and D22 rods in RUN 941

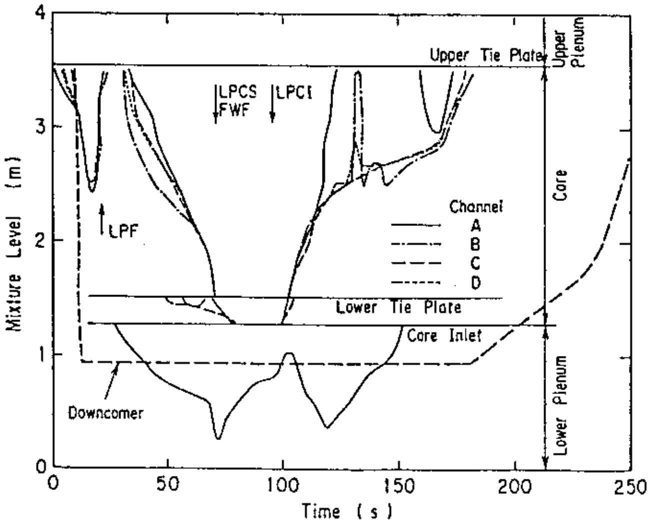

Fig.B.157 Core mixture level transients in RUN 941

Appendix III Maximum Cladding Temperature Distribution of RUNs 940 and 941

Maximum surface temperature at each thermo-couple is searched during a time period after the break and data plotting time, and is recorded with its observation time.

Table A.4 Maximum temperature distribution for RUN 940

	Pos.1	Pos.2	Pos.3	Pos.4	Pos.5	Pos.6	Pos.7
A-11 rod	TE 201	TE 202	TE 203	TE 204	TE 205	TE 206	TE 207
PCT (K)	606.7	723.1	793.9	832.3	786.7	687.1	574.3
Time (s)	165.2	336.0	394.1	425.6	442.4	415.1	70.0
A-12 rod	TE 208	TE 209	TE 210	TE 211	TE 212	TE 213	TE 214
PCT (K)	601.9	708.7	769.9	784.3	741.1	667.9	570.7
Time (s)	165.2	334.6	338.1	370.3	407.4	399.7	98.0
A-13 rod	TE 215	TE 216	TE 217	TE 218	TE 219	TE 220	TE 221
PCT (K)	603.1	715.9	766.3	777.1	726.7	665.5	569.5
Time (s)	164.5	338.1	342.3	369.6	398.3	387.8	120.4
A-14 rod	TE 222	TE 223	TE 224	TE 225	TE 226	TE 227	TE 228
PCT (K)	599.5	703.9	749.5	763.9	711.1	658.3	------
Time (s)	164.5	342.3	343.0	365.4	385.7	393.4	------
A-15 rod	TE 229			TE 230			
PCT (K)	598.3			769.9			
Time (s)	162.4			372.4			
A-17 rod	TE 231			TE 232			
PCT (K)	630.7			832.3			
Time (s)	332.5			445.9			
A-22 rod	TE 233	TE 234	TE 235	TE 236	TE 237	TE 238	TE 239
PCT (K)	629.5	735.1	784.3	794.7	750.6	676.1	570.1
Time (s)	331.8	337.4	338.8	371.0	415.1	393.4	64.4
A-24 rod	TE 240	TE 241	TE 242	TE 243	TE 244	TE 245	TE 246
PCT (K)	601.8	717.7	763.8	767.5	712.0	657.1	571.0
Time (s)	161.7	343.7	343.7	366.1	385.0	387.8	68.6

	Pos.1	Pos.2	Pos.3	Pos.4	Pos.5	Pos.6	Pos.7
A-26 rod	TE 247			TE 248			
PCT (K)	643.8			791.9			
Time (s)	331.8			389.9			
A-28 rod	TE 249			TE 250			
PCT (K)	641.0			810.7			
Time (s)	331.8			401.8			
A-31 rod	TE 251			TE 252			
PCT (K)	630.5			833.2			
Time (s)	335.3			395.5			
A-33 rod	TE 253	TE 254	TE 255	TE 256	TE 257	TE 258	TE 259
PCT (K)	596.1	702.6	741.2	742.1	681.8	627.6	570.1
Time (s)	162.4	338.1	343.7	354.9	348.6	352.8	70.0
A-34 rod	TE 260	TE 261	TE 262	TE 263	TE 264	TE 265	TE 266
PCT (K)	598.0	700.7	740.3	744.0	682.7	630.5	570.1
Time (s)	163.8	339.5	345.8	365.4	353.5	353.5	95.9
A-37 rod	TE 267			TE 268			
PCT (K)	794.7			650.5			
Time (s)	386.4			333.2			
A-42 rod	TE 269			TE 270			
PCT (K)	643.8			802.2			
Time (s)	335.3			385.7			
A-44 rod	TE 271	TE 272	TE 273	TE 274	TE 275	TE 276	TE 277
PCT (K)	605.6	691.2	730.8	736.5	685.6	624.8	569.1
Time (s)	336.7	337.4	346.5	370.3	447.3	360.5	106.4

Table A.4 Maximum temperature distribution for RUN 940 (Cont'd)

	Pos.1	Pos.2	Pos.3	Pos.4	Pos.5	Pos.6	Pos.7
A-48 rod	TE 278			TE 279			
PCT (K)	642.9			789.1			
Time (s)	335.3			436.1			
A-51 rod	TE 280			TE 281			
PCT (K)	651.4			807.9			
Time (s)	335.3			420.7			
A-53 rod	TE 282			TE 283			
PCT (K)	640.0			738.4			
Time (s)	336.7			366.8			
A-57 rod	TE 284			TE 285			
PCT (K)	699.7			836.0			
Time (s)	441.7			444.5			
A-62 rod	TE 286			TE 287			
PCT (K)	667.6			794.7			
Time (s)	336.7			366.8			
A-66 rod	TE 288			TE 289			
PCT (K)	627.6			783.5			
Time (s)	345.1			441.7			
A-68 rod	TE 290			TE 291			
PCT (K)	656.2			817.2			
Time (s)	343.7			443.1			
A-71 rod	TE 292			TE 293			
PCT (K)	662.8			841.6			
Time (s)	336.0			415.1			

	Pos.1	Pos.2	Pos.3	Pos.4	Pos.5	Pos.6	Pos.7
A-73 rod	TE 294			TE 295			
PCT (K)	669.5			799.4			
Time (s)	340.2			380.8			
A-75 rod	TE 296			TE 297			
PCT (K)	657.1			791.0			
Time (s)	343.0			380.8			
A-77 rod	TE 298	TE 299	TE 300	TE 301	TE 302	TE 303	TE 304
PCT (K)	668.5	744.0	787.2	804.1	748.7	649.5	------
Time (s)	347.2	357.7	369.6	410.9	443.8	423.5	------
A-82 rod	TE 305			TE 306			
PCT (K)	675.2			------			
Time (s)	340.9			------			
A-84 rod	TE 307			TE 308			
PCT (K)	666.6			806.9			
Time (s)	341.6			395.5			
A-85 rod	TE 309	TE 310	TE 311	TE 312	TE 313	TE 314	TE 315
PCT (K)	663.8	744.0	793.8	806.9	761.9	677.1	570.1
Time (s)	343.7	354.2	362.6	381.5	447.3	403.2	65.8
A-87 rod	TE 316	TE 317	TE 318	TE 319	TE 320	TE 321	TE 322
PCT (K)	659.0	735.5	785.4	794.7	745.0	659.0	569.1
Time (s)	343.7	347.9	343.7	378.7	438.2	385.0	67.2
A-88 rod	TE 323	TE 324	TE 325	TE 326	TE 327	TE 328	TE 329
PCT (K)	654.3	727.1	779.7	791.0	730.8	660.9	570.1
Time (s)	343.0	345.8	344.4	378.7	368.2	383.6	63.0

Table A.4 Maximum temperature distribution for RUN 940 (Cont'd)

	Pos.1	Pos.2	Pos.3	Pos.4	Pos.5	Pos.6	Pos.7
B-11 rod	TE 330	TE 331	TE 332	TE 333	TE 334	TE 335	TE 336
PCT (K)	603.7	685.6	723.3	722.4	693.1	630.5	------
Time (s)	163.8	342.3	343.0	346.5	440.3	418.6	------
B-13 rod				TE 337			
PCT (K)				723.3			
Time (s)				356.3			
B-22 rod	TE 338	TE 339	TE 340	TE 341	TE 342	TE 343	TE 344
PCT (K)	617.1	687.5	715.8	714.8	662.8	609.5	570.1
Time (s)	333.2	336.7	345.1	342.3	352.1	350.0	84.0
B-31 rod				TE 345			
PCT (K)				713.9			
Time (s)				366.8			
B-33 rod				TE 346			
PCT (K)				681.8			
Time (s)				339.5			
B-51 rod				TE 347			
PCT (K)				700.7			
Time (s)				358.4			
B-53 rod				TE 348			
PCT (K)				676.1			
Time (s)				345.1			
B-66 rod				TE 349			
PCT (K)				704.5			
Time (s)				393.4			

	Pos.1	Pos.2	Pos.3	Pos.4	Pos.5	Pos.6	Pos.7
B-77 rod	TE 350	TE 351	TE 352	TE 353	TE 354	TE 355	TE 356
PCT (K)	645.7	706.4	729.9	735.5	691.2	623.8	570.1
Time (s)	343.7	345.1	345.8	382.2	403.9	403.9	85.4
B-86 rod				TE 357			
PCT (K)				752.5			
Time (s)				445.2			
C-11 rod	TE 358	TE 359	TE 360	TE 361	TE 362	TE 363	TE 364
PCT (K)	605.6	606.6	631.4	705.4	673.3	624.8	570.1
Time (s)	163.8	256.9	270.2	344.4	356.3	378.0	70.7
C-13 rod	TE 365	TE 366	TE 367	TE 368	TE 369	TE 370	TE 371
PCT (K)	603.7	617.1	674.2	713.0	675.2	623.8	570.1
Time (s)	163.1	263.9	332.5	345.8	357.7	406.7	130.9
C-15 rod				TE 372			
PCT (K)				713.9			
Time (s)				355.6			
C-22 rod	TE 373	TE 374	TE 375	TE 376	TE 377	TE 378	TE 379
PCT (K)	579.7	632.4	660.0	706.4	665.7	616.2	571.0
Time (s)	323.4	331.1	332.5	343.7	350.7	358.4	118.3
C-31 rod				TE 380			
PCT (K)				712.0			
Time (s)				344.4			
C-33 rod	TE 381	TE 382	TE 383	TE 384	TE 385	TE 386	TE 387
PCT (K)	596.1	588.4	643.8	677.1	638.1	596.1	568.1
Time (s)	165.2	252.7	333.2	342.3	344.4	349.3	81.9

Table A.4 Maximum temperature distribution for RUN 940 (Cont'd)

	Pos.1	Pos.2	Pos.3	Pos.4	Pos.5	Pos.6	Pos.7
C-35 rod				TE 388			
PCT (K)				696.9			
Time (s)				357.0			
C-66 rod				TE 389			
PCT (K)				696.9			
Time (s)				382.2			
C-68 rod				TE 390			
PCT (K)				745.9			
Time (s)				448.0			
C-77 rod	TE 391	TE 392	TE 393	TE 394	TE 395	TE 396	TE 397
PCT (K)	642.9	699.7	721.4	731.8	690.3	626.7	570.1
Time (s)	347.9	352.1	354.2	380.1	397.6	399.7	79.1
D-11 rod				TE 398			
PCT (K)				729.9			
Time (s)				358.4			
D-13 rod				TE 399			
PCT (K)				729.0			
Time (s)				352.8			
D-22 rod	TE 400	TE 401	TE 402	TE 403	TE 404	TE 405	TE 406
PCT (K)	589.3	655.2	704.5	721.4	681.8	622.9	570.1
Time (s)	332.5	332.5	335.3	345.1	370.3	375.9	75.6
D-31 rod				TE 407			
PCT (K)				729.9			
Time (s)				352.8			

	Pos.1	Pos.2	Pos.3	Pos.4	Pos.5	Pos.6	Pos.7
D-33 rod				TE 408			
PCT (K)				678.0			
Time (s)				347.9			
D-51 rod				TE 409			
PCT (K)				712.0			
Time (s)				357.7			
D-53 rod				TE 410			
PCT (K)				678.9			
Time (s)				378.0			
D-66 rod				TE 411			
PCT (K)				712.4			
Time (s)				427.7			
D-77 rod				TE 412			
PCT (K)				729.1			
Time (s)				396.2			
D-86 rod				TE 413			
PCT (K)				745.0			
Time (s)				445.2			

Table A.5 Maximum temperature distribution for RUN 941

	Pos.1	Pos.2	Pos.3	Pos.4	Pos.5	Pos.6	Pos.7
A-11 rod	TE 201	TE 202	TE 203	TE 204	TE 205	TE 206	TE 207
PCT (K)	659.5	759.1	738.7	778.3	659.5	622.3	568.4
Time (s)	16.8	19.8	97.2	118.2	93.6	108.0	0.0
A-12 rod	TE 208	TE 209	TE 210	TE 211	TE 212	TE 213	TE 214
PCT (K)	643.9	684.7	723.1	739.9	682.3	566.3	564.2
Time (s)	17.4	84.0	94.2	105.0	112.2	0.0	0.0
A-13 rod	TE 215	TE 216	TE 217	TE 218	TE 219	TE 220	TE 221
PCT (K)	646.3	684.7	761.5	755.5	641.5	593.5	566.1
Time (s)	21.0	85.2	115.8	113.4	93.0	103.2	0.0
A-14 rod	TE 222	TE 223	TE 224	TE 225	TE 226	TE 227	TE 228
PCT (K)	651.1	667.9	748.3	735.1	607.9	571.9	------
Time (s)	20.4	82.8	119.4	115.2	85.8	106.8	------
A-15 rod	TE 229			TE 230			
PCT (K)	652.3			738.7			
Time (s)	20.4			115.2			
A-17 rod	TE 231			TE 232			
PCT (K)	661.1			752.0			
Time (s)	19.2			112.2			
A-22 rod	TE 233	TE 234	TE 235	TE 236	TE 237	TE 238	TE 239
PCT (K)	642.7	679.9	760.3	751.5	620.0	569.2	565.4
Time (s)	19.8	84.6	117.6	114.6	87.0	0.0	0.0
A-24 rod	TE 240	TE 241	TE 242	TE 243	TE 244	TE 245	TE 246
PCT (K)	641.9	668.5	703.5	736.5	598.0	566.2	564.0
Time (s)	19.2	19.2	92.4	114.0	83.4	12.0	0.0

	Pos.1	Pos.2	Pos.3	Pos.4	Pos.5	Pos.6	Pos.7
A-26 rod	TE 247			TE 248			
PCT (K)	643.8			743.1			
Time (s)	19.8			114.0			
A-28 rod	TE 249			TE 250			
PCT (K)	678.0			766.6			
Time (s)	18.6			115.2			
A-31 rod	TE 251			TE 252			
PCT (K)	673.3			783.5			
Time (s)	19.2			115.8			
A-33 rod	TE 253	TE 254	TE 255	TE 256	TE 257	TE 258	TE 259
PCT (K)	632.4	656.2	682.7	711.1	573.9	567.0	565.1
Time (s)	18.6	19.2	92.4	115.8	80.4	0.0	0.0
A-34 rod	TE 260	TE 261	TE 262	TE 263	TE 264	TE 265	TE 266
PCT (K)	623.8	702.6	721.4	709.2	576.8	567.6	564.7
Time (s)	19.2	119.4	117.6	112.2	81.0	0.0	0.0
A-37 rod	TE 267			TE 268			
PCT (K)	739.3			643.8			
Time (s)	114.0			19.8			
A-42 rod	TE 269			TE 270			
PCT (K)	643.8			762.8			
Time (s)	19.2			115.8			
A-44 rod	TE 271	TE 272	TE 273	TE 274	TE 275	TE 276	TE 277
PCT (K)	625.7	704.5	721.4	712.0	652.4	579.7	563.4
Time (s)	19.8	117.6	115.8	115.2	111.6	106.8	0.0

Table A.5 Maximum temperature distribution for RUN 941 (Cont'd)

	Pos.1	Pos.2	Pos.3	Pos.4	Pos.5	Pos.6	Pos.7
A-48 rod	TE 278			TE 279			
PCT (K)	652.4			738.4			
Time (s)	19.2			115.2			
A-51 rod	TE 280			TE 281			
PCT (K)	657.1			767.5			
Time (s)	20.4			116.4			
A-53 rod	TE 282			TE 283			
PCT (K)	624.8			712.0			
Time (s)	19.2			115.8			
A-57 rod	TE 284			TE 285			
PCT (K)	656.2			742.1			
Time (s)	118.2			111.6			
A-62 rod	TE 286			TE 287			
PCT (K)	626.7			764.7			
Time (s)	19.2			114.6			
A-66 rod	TE 288			TE 289			
PCT (K)	629.5			711.1			
Time (s)	122.4			116.4			
A-68 rod	TE 290			TE 291			
PCT (K)	667.6			763.8			
Time (s)	19.8			116.4			
A-71 rod	TE 292			TE 293			
PCT (K)	662.8			790.0			
Time (s)	16.8			116.4			

	Pos.1	Pos.2	Pos.3	Pos.4	Pos.5	Pos.6	Pos.7
A-73 rod	TE 294			TE 295			
PCT (K)	624.8			760.9			
Time (s)	19.2			115.2			
A-75 rod	TE 296			TE 297			
PCT (K)	647.6			738.4			
Time (s)	120.6			114.0			
A-77 rod	TE 298	TE 299	TE 300	TE 301	TE 302	TE 303	TE 304
PCT (K)	664.7	738.4	752.5	734.6	669.5	598.0	------
Time (s)	121.2	120.6	117.0	111.6	109.2	105.0	------
A-82 rod	TE 305			TE 306			
PCT (K)	666.6			------			
Time (s)	18.0			------			
A-84 rod	TE 307			TE 308			
PCT (K)	660.0			766.6			
Time (s)	19.2			116.4			
A-85 rod	TE 309	TE 310	TE 311	TE 312	TE 313	TE 314	TE 315
PCT (K)	666.6	751.5	768.5	761.9	687.5	615.2	565.8
Time (s)	19.2	120.0	115.8	116.4	107.4	106.8	0.0
A-87 rod	TE 316	TE 317	TE 318	TE 319	TE 320	TE 321	TE 322
PCT (K)	648.6	740.3	749.7	753.4	677.1	608.5	564.4
Time (s)	16.2	118.8	106.2	109.2	103.8	102.6	0.0
A-88 rod	TE 323	TE 324	TE 325	TE 326	TE 327	TE 328	TE 329
PCT (K)	690.3	766.6	767.5	764.7	696.0	617.1	565.6
Time (s)	19.2	19.2	120.0	114.6	110.4	106.8	0.0

Table A.5 Maximum temperature distribution for RUN 941 (Cont'd)

	Pos.1	Pos.2	Pos.3	Pos.4	Pos.5	Pos.6	Pos.7
B-11 rod	TE 330	TE 331	TE 332	TE 333	TE 334	TE 335	TE 336
PCT (K)	621.9	676.1	776.9	746.8	647.6	576.8	------
Time (s)	19.8	84.0	155.4	128.4	110.4	106.2	------
B-13 rod				TE 337			
PCT (K)				745.9			
Time (s)				128.4			
B-22 rod	TE 338	TE 339	TE 340	TE 341	TE 342	TE 343	TE 344
PCT (K)	609.5	670.4	706.4	731.8	578.8	566.2	563.2
Time (s)	19.8	84.6	92.4	129.0	84.6	0.0	0.0
B-31 rod				TE 345			
PCT (K)				732.7			
Time (s)				128.4			
B-33 rod				TE 346			
PCT (K)				687.5			
Time (s)				129.6			
B-51 rod				TE 347			
PCT (K)				716.7			
Time (s)				129.0			
B-53 rod				TE 348			
PCT (K)				682.7			
Time (s)				129.0			
B-66 rod				TE 349			
PCT (K)				691.2			
Time (s)				129.0			

	Pos.1	Pos.2	Pos.3	Pos.4	Pos.5	Pos.6	Pos.7
B-77 rod	TE 350	TE 351	TE 352	TE 353	TE 354	TE 355	TE 356
PCT (K)	618.1	664.7	714.8	733.7	636.2	576.8	564.7
Time (s)	19.8	150.0	154.2	127.8	110.4	106.2	0.0
B-86 rod				TE 357			
PCT (K)				713.9			
Time (s)				108.0			
C-11 rod	TE 358	TE 359	TE 360	TE 361	TE 362	TE 363	TE 364
PCT (K)	585.5	656.2	673.3	715.8	642.9	580.7	564.8
Time (s)	11.4	19.8	85.8	128.4	110.4	107.4	0.0
C-13 rod	TE 365	TE 366	TE 367	TE 368	TE 369	TE 370	TE 371
PCT (K)	618.1	648.6	673.3	686.5	616.2	574.9	564.3
Time (s)	20.4	80.4	90.6	108.6	96.6	105.0	0.0
C-15 rod				TE 372			
PCT (K)				702.6			
Time (s)				129.6			
C-22 rod	TE 373	TE 374	TE 375	TE 376	TE 377	TE 378	TE 379
PCT (K)	612.3	643.8	655.2	651.4	568.1	569.1	563.9
Time (s)	19.8	19.8	88.2	96.6	0.0	0.0	0.0
C-31 rod				TE 380			
PCT (K)				693.1			
Time (s)				129.6			
C-33 rod	TE 381	TE 382	TE 383	TE 384	TE 385	TE 386	TE 387
PCT (K)	601.8	627.6	615.2	598.9	565.0	564.7	562.3
Time (s)	19.8	19.8	79.2	83.4	0.0	0.0	0.6

Table A.5 Maximum temperature distribution for RUN 941 (Cont'd)

	Pos.1	Pos.2	Pos.3	Pos.4	Pos.5	Pos.6	Pos.7
C-35 rod				TE 388			
PCT (K)				674.2			
Time (s)				129.6			
C-66 rod				TE 389			
PCT (K)				664.7			
Time (s)				120.0			
C-68 rod				TE 390			
PCT (K)				723.3			
Time (s)				129.0			
C-77 rod	TE 391	TE 392	TE 393	TE 394	TE 395	TE 396	TE 397
PCT (K)	647.6	727.1	749.7	702.6	637.1	573.9	563.4
Time (s)	136.2	139.2	152.4	117.0	110.4	106.8	0.0
D-11 rod				TE 398			
PCT (K)				722.4			
Time (s)				120.6			
D-13 rod				TE 399			
PCT (K)				722.4			
Time (s)				121.8			
D-22 rod	TE 400	TE 401	TE 402	TE 403	TE 404	TE 405	TE 406
PCT (K)	615.2	640.0	660.9	660.0	575.9	567.2	563.8
Time (s)	19.8	84.0	88.8	96.0	82.2	0.0	0.0
D-31 rod				TE 407			
PCT (K)				719.5			
Time (s)				120.6			
D-33 rod				TE 408			
PCT (K)				591.3			
Time (s)				81.6			
D-51 rod				TE 409			
PCT (K)				700.7			
Time (s)				120.6			
D-53 rod				TE 410			
PCT (K)				672.3			
Time (s)				120.6			
D-66 rod				TE 411			
PCT (K)				662.0			
Time (s)				120.6			
D-77 rod				TE 412			
PCT (K)				696.7			
Time (s)				120.6			
D-86 rod				TE 413			
PCT (K)				696.9			
Time (s)				110.4			